CCLRC
Rutherford Appleton Laboratory

COUNCIL FOR THE CENTRAL LABORATORY
OF THE RESEARCH COUNCILS

Central Laser Facility

Annual Report 2002/2003

© **Council for the Central Laboratory of the Research Councils 2003**

Enquiries about copyright, reproduction and requests for additional copies of this report should be addressed to:

Council for the Central Laboratory of the Research Councils
Library and Information Services
CCLRC Rutherford Appleton Laboratory
Chilton
Didcot
Oxfordshire
OX11 0QX
Tel: 01235 445384 Fax: 01235 446403
E-mail: library@rl.ac.uk

ISSN 1358-6254

Neither the Council nor the Laboratory accept any responsibility for loss or damage arising from the use of information contained in any of their reports or in any communication about their tests or investigations.

Central Laser Facility

Annual Report 2002/2003

Central Laser Facility
CCLRC Rutherford Appleton Laboratory
Chilton, Didcot
Oxfordshire OX11 0QX
Tel. 44 (0) 1235 445655
Fax. 44 (0) 1235 445888
E-mail. clf@rl.ac.uk
Web site. http://www.clf.rl.ac.uk

RAL Report No. RAL-TR-2003-018

The front cover shows Prof. Mitchell of the University of Rennes, France, studying laser induced dissociation and ionisation of ions using the high power femtosecond Astra laser facility. The work was funded through the EU Access to Research Infrastructures Programme
(Photograph courtesy of RAL Photographic Section).

ISBN 0902376268

Acknowledgements

The production team for this Annual Report was as follows:

Editor	Brian Wyborn
Production	Dave Burgess
Chapter Editors	David Neely, Tony Parker, Colin Danson, Graeme Hirst
Section Editors	Rob Clarke, David Neely, Margaret Notley, Peter Norreys, Andrew Langley, Pavel Matousek, Stan Botchway, Waseem Shaikh, Colin Danson, Mike Towrie, Dave Pepler, Ian Ross
Support	Alison Brown, Chris Reason, RAL BITD.

This report is available on the CLF's Web Site http://www.clf.rl.ac.uk.

The document has been reproduced by the RAL Reprographics Section.

Thanks to all the above for their contribution towards producing this report and of course to all the authors for their submissions.

Contents

High Power Laser Programme - X-ray Laser and Long Pulse Plasma Physics

High Power Laser Programme - Femtosecond Pulse Physics

High Power Laser Programme - Theory and Computation

Lasers for Science Facility Programme

Lasers for Science Facility Programme - Chemistry

Laser Science and Development – Vulcan

Laser Science and Development – Lasers for Science Facility

Laser Science and Development – Instrumentation

Laser Science and Development – Laser Research and Development

Appendices

Operational Statistics

Foreword

M H R Hutchinson

Central Laser Facility, CCLRC Rutherford Appleton Laboratory, Chilton, Didcot, Oxon, OX11 0QX, UK

Email address: *h.hutchinson@rl.ac.uk*

This annual report for the Central Laser Facility (CLF) is an account of the work carried out by its users and staff during the financial year 2002-3.

A highlight of the year has been the completion of the principal elements of the Petawatt upgrade project for Vulcan and the performance of the first experiments at intensities which are the highest produced world-wide. These have included the acceleration of ions and electrons in the laser-produced plasma and electron energies in excess of 500MeV were observed. This is the highest energy observed from any laser-plasma interaction to date. Nuclear reactions can be produced by the high fluxes of protons and γ radiation produced when the laser is focussed to very high intensities and, using the enhanced intensities provided by the Petawatt laser, nuclear transmutation of radioactive material and the production of short-lived isotopes relevant to positron emission tomography were demonstrated. The Astra laser has also been highly productive with successful experiments on a wide range of subjects including multiphoton ionisation, molecular dynamics, X-ray production and the generation of ultra-high magnetic fields.

Within the Lasers for Science Facility, the combination of tunable, ultra-short pulses and the Kerr gating technique enabled a vigorous experimental programme in physics, chemistry and biology to be pursued. The sub-picosecond capabilities of the Ultra-Fast Laboratory has enabled studies of photochemical dynamics of organic and inorganic molecular systems to be studied. The provision of both advanced lasers and the specialist support of CLF staff through the EPSRC–funded Laser Loan Pool has continued to be successful in enabling a wide range of research within UK university laboratories.

The CLF continues to play a critical role, both within the UK and internationally, in the enabling of laser-related research across a broad range of fields. The increased intensity provided by Vulcan has enabled users from the UK and further afield to explore the interaction of light with matter at unprecedented intensities and has placed the CLF at the forefront of laser-plasma research. We look forward with confidence to new research and new opportunities, not only with Vulcan, but across the full range of science carried out within the CLF.

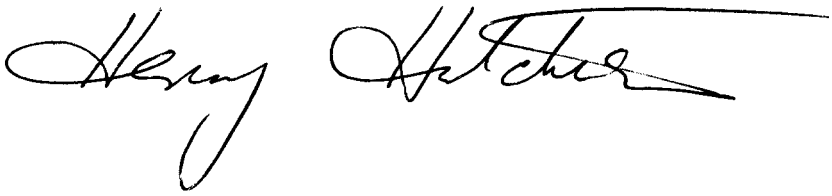

Overview of the Central Laser Facility

B E Wyborn

Central Laser Facility, CCLRC Rutherford Appleton Laboratory, Chilton, Didcot, Oxon, OX11 0QX, UK

Email address: *b.e.wyborn@rl.ac.uk*

Laser Facilities for Users

The Central Laser Facility (CLF) is a world leading centre for research using lasers. Facilities available to users include the Vulcan Nd: glass laser which delivers multi- TW beams to two target areas and a Petawatt beam line to a newly commissioned third target area, the Astra ultra- short pulse interaction facility based on titanium sapphire laser technology, a range of state of the art table top laser systems and specialised diagnostic instruments within the Lasers for Science Facility and the Laser Loan Pool.

Vulcan

Vulcan is a highly versatile large scale Nd: glass laser installation which delivers a maximum of 2.5 kJ of energy in its six 10 cm and two 15 cm beamlines to two target areas, each of which is equipped with frequency conversion optics to enable both 1μm and 0.5 μm operation of all beams. A range of pulse durations are available from 100 ps to 20 ns in various geometries.

A short pulse (700 fs) high irradiance (~10^{20} W cm^{-2}) chirped pulse amplification (CPA) capability is available, with vacuum propagation to target and reflective beam focusing optics. Additional low energy beams, including sub- picosecond CPA probes, are provided for diagnostics with high temporal resolution. The system is fully characterised and equipped with advanced diagnostics.

Vulcan Petawatt Upgrade

The reporting period saw the conclusion to the 3 year development of Vulcan's CPA beamline to the Petawatt level. The project involved the addition of 20 cm disc amplifiers, the construction of a large aperture vacuum beam compressor and a new target chamber within a new target area building.

In order to enable the facility to conduct user experiments an EPSRC grant was awarded to commission the interaction facility and validate the radiation shielding. This was successfully completed in November 2002 followed by the first Petawatt user experiment during December 2002 and January 2003. This was conducted by Dr Karl Krushelnick, Imperial College, London and successfully demonstrated the acceleration of electrons using lasers to energies in excess of 500MeV, the world's highest to date.

Lasers for Science Facility (LSF)

The LSF operates a suite of state of the art table- top laser systems and associated instrumentation giving users access to highly tunable (vuv - ir) and variable pulse width (ns to fs) laser radiation. This includes lasers for ns and ps time- resolved studies and specialises in time-resolved vibrational spectroscopy in the femtosecond and picosecond time domain applications in chemistry, physics, biological and material sciences. The time resolved resonance Raman (TR^3) facility provides unique capabilities to enable highly fluorescent samples to be studied using a 4 ps optical Kerr shutter in combination with a fully tunable kHz femtosecond synchronised pump-probe apparatus based on OPA technology. The same laser source also drives the high brightness PIRATE facility (Picosecond Infrared Absorption and Transient Excitation) giving two independently tunable beams across the mid infra red region of the spectrum for pump / probe experiments. There is also a high average power laser plasma x-ray source and a fast gated (100 ps) confocal microscopy laboratory for fluorescence imaging and optical tweezers for investigating the behaviour of particles in solution (including living cells).

Laser Loan Pool

Commercial laser systems are available from the Laser Loan Pool for periods of up to 6 months at the user's home laboratory. Systems available include nanosecond tunable YAG pumped dye lasers (with frequency up-conversion and down-conversion covering the spectral region from 205 nm to 4500 nm), an excimer laser operating down to 157 nm, a CW frequency doubled argon ion laser and an all solid-state femtosecond Titanium Sapphire laser tunable between 680 nm and 1020 nm. A wide range of ancillary and diagnostic equipment is also available to support user experiments.

Astra

The Astra facility is based on titanium sapphire laser technology which gives users access to high intensity laser pulses at 10 Hz repetition rate.

The facility supplies laser pulses to two target areas simultaneously. Target Area I provides pulses of 50fs duration with an energy of 10 mJ, producing irradiance on target in excess of 10^{16} W cm^{-2}. The Target Area II currently delivers 300 mJ in 50fs with target irradiance at 10^{18} W cm^{-2} regime.

Engineering Services

Mechanical, electrical and computing support is provided for the operation of the laser facilities at the CLF, for the experimental programmes on these facilities and for the CLF's research and development activities. Access to mechanical and electrical CAD tools and workshop facilities enable a rapid response to be provided to users.

Access to Facilities

The mechanism for awarding access to beamtime at all CCLRC facilities will change from April 2003 following the second stage of the Quinquennial Review of the CCLRC. From this date access will be reviewed, awarded and funded by CCLRC. For the latest information please visit the CCLRC Web site at: http://www.cclrc.ac.uk/Activity/FacilityAccess or contact Mrs. Alison Brown (a.j.brown@rl.ac.uk).

During the period covered by this report, beamtime at all CLF facilities was awarded to European researchers and their collaborators through the EU Access to Large Scale Infrastructure programme. The CLF hopes to continue this arrangement in the forthcoming Sixth Framework Programme through a joint application with other European laser facilities. For information on calls for proposals, eligibility criteria, etc. please contact Colin Danson (c.danson@ rl.ac.uk).

Hiring of the facilities and access to CLF expertise is also available on a commercial basis for industrial research and development. Please contact Mrs. Alison Brown for further information (a.j.brown@rl.ac.uk).

CLF Web site

Further information on the CLF, its facilities and the scientific programmes is available on the CLF Web site at http://www.clf.rl.ac.uk.

High Power Laser Programme

1) Short Pulse Plasma Physics

2) X-ray Laser and Long Pulse Plasma Physics

3) Femtosecond Pulse Physics

4) Theory and Computation

Spatially and temporally resolved studies of self-generated Mega-Gauss magnetic fields using the Vulcan laser

A Gopal, M Tatarakis, A E Dangor, M S Wei, F N Beg, K Krushelnick
Plasma physics Group, Imperial College, London, SW7 2AZ, UK

P A Norreys, K L Lancaster, H Habara
Central Laser Facility, CCLRC Rutherford Appleton Laboratory, Chilton, Didcot, Oxon, OX11 0QX, UK

M Zepf

Dept. of Pure and Applied Physics, The Queen's University of Belfast, Belfast, BT7 1NN, UK

Main contact email address: *amrutha.gopal@ic.ac.uk*

Introduction

Magnetic fields of several hundred Mega-Gauss (MG) can be generated as high intensity laser pulses interact with matter[1-4]. Recently, there has been widespread interest in fields of such strength since they may be important for future inertial confinement fusion experiments and as well for the study of some astrophysical phenomena in the laboratory.

Computer simulations have predicted that fields on the order of a GGauss can be produced at laser intensities of 10^{21} W/cm^2. Because of the short timescales over which such fields exist it has been difficult to verify these computational predictions. However, recent experimental investigations have made measurements of these fields[5,6] by studying the polarisation properties of self-generated high order harmonic radiation. Fields of the order of several hundred MGauss were measured using this technique. In this report we report the first quantitative study of the temporal and spatial characteristics of these huge magnetic fields.

During a high power short pulse interaction various phenomena can occur – such as the production of fast electrons, the generation of higher harmonics of the incident laser frequency and the generation of ultra-strong magnetic fields. Different mechanisms that give rise to self-generated magnetic fields are:

a) Non parallel gradients of the plasma temperature and density [1)]
b) Fast electron currents generated inside the target [2)]
c) Spatial and temporal variations of the laser ponderomotive force giving rise to magnetic fields comparable to those of the incident laser[3)]

Previous studies have used external probes such as magnetic tape, frequency doubled probe laser pulses etc. However, these methods are inadequate for measurements in very high density plasma. The first results in this regime were only recently obtained by Tatarakis et al[5,6] using the self-generated harmonics of the incident laser.

By harmonics we mean higher order multiples of the fundamental laser frequency which are generated by the oscillating motion of the critical density surface during the interaction. Previous work on harmonic selection rules[7)] implies that an obliquely incident p-polarised laser pulse generates both p-polarised odd and even harmonics. We have confirmed this result at low intensities where the magnetic field should be very low or negligible. All previous theoretical work suggests that the harmonics are generated at the same time as the magnetic field.

An electromagnetic wave propagating perpendicular to a magnetic field in a plasma experiences birefringence. This is called the Cotton-Mouton effect and occurs as the harmonics propagate through the plasma and results in a change in the polarisation ellipticity of the wave. Consequently, measuring the induced birefringence allows a measurement of the magnetic field present. In order to know the induced ellipticity[8)] it is necessary to measure the Stokes vectors of the polarisation ellipse before and after propagation through the plasma. From this one can estimate the self-generated magnetic field if the propagation length and the angle between the B field and propagation direction are known. In addition to the above method, we have also used the observations of polarisation "cut-offs" to estimate the peak magnetic field present.

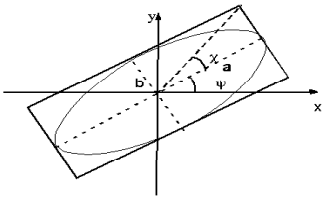

Figure 1. Polarisation ellipse.

Experiment – temporal measurements

In this report we discuss the first measurements of the temporal and spatial behaviour of these huge magnetic fields. A schematic of the experimental set up is shown in Figure 2. In the first section we discuss the temporal measurements using the 3rd harmonic of the fundamental laser frequency. The third harmonic was optimum for these measurements because of the wavelength sensitivity of our detector.

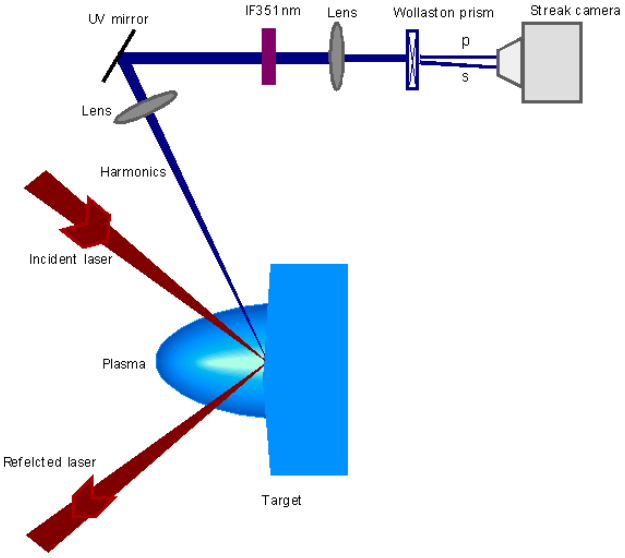

Figure 2. Schematic experimental set up for temporally resolved B field measurement.

The CPA arm of the Vulcan laser was focused to a 10 micron diameter spot using an f/3 off-axis parabolic mirror. The targets used were 5x5mm^2 optically polished glass. For temporally-resolved measurements, longer pulses (~8ps) were used.

Harmonics generated at the critical density surface were collected using f/10 fused silica optics and were directed to the polarimeter setup using UV enhanced aluminium mirrors. At the entrance of the polarimeter narrow band interference filters were inserted to remove other wavelengths. The selected wavelength was directed through a Wollaston prism which splits the beam into s-polarisation and p-polarisation. A 10 cm focal length fused silica lens was used to image the different polarisations onto the entrance slit of the streak camera.

For the calculation of the magnetic field using Stokes vectors, all components of Stokes vector are required. This was not possible in this experimental setup as the slit size of the streak camera was not sufficiently large to accommodate all the beams without overlapping. Consequently, a complete determination of the polarisation properties of the light was not possible. However, the ratio of absolute intensity of the ordinary wave (s-polarisation) to the extra-ordinary wave (p-polarisation) allows a measurement of the initial development of the magnetic field. Shots were taken at different intensities as well as at short pulse duration. However, measurements with short pulses are not precise since the resolution of the streak camera is less than the pulse duration.

Temporally resolved measurements

The results for different laser pulse energies are shown in Figure 3. It is evident that the S/P ratio increases as the intensity increases. Also, it is clear that the s-polarisation peaks when the intensity peaks. At the beginning of the pulse there is no s-polarisation as the magnetic field is low or negligible at low intensities. From the analysis it is likely that the duration of the magnetic field is at least as long as that of the incident laser pulse. At high intensities the s-polarisation signal peaks later than the p-polarisation signal, i.e. the magnetic field peaks after the incident pulse peaks. In the later part of the pulse the ratio changes such that the harmonics are essentially depolarised. This may be because the third harmonic can be generated by other mechanisms which do not produce polarised radiation (i.e., Langmuir wave turbulence and collapse).

Spatially resolved measurements

Simulations done using the OSIRIS 2 1/2D PIC code show that at oblique incidence the ponderomotive force of the laser pushes the plasma to higher density which in turn gives rise to a higher concentration of magnetic field lines. We have set up two simultaneous polarimeters at different angles to study this prediction. The experimental set up is shown in Figure 4.

The experimental setup is similar to that described for the temporal measurement. Harmonics were collected at two different angles – 70 degrees off target normal in both directions. For polarimeter 1, harmonics were collected using f/10 optics and for polarimeter 2 the collection optics were f/6 optics. All of the lenses were made of fused silica. The collected harmonics were directed to the polarimeters outside the target chamber using UV enhanced aluminium mirrors. A typical polarimeter setup is shown in Figure 4.

The mirrors were kept at small angles to ensure that depolarisation effects were minimized. Shots were taken for different laser intensities for 3rd (351nm) and 4th (263nm) harmonics. Calibration shots were taken without polarisers. Shots were also taken for a range of intensities.

The results are shown in Figure 5.

Calculations were performed for different plasma electron densities. Uncertainties in the calculation were due to the calculation of angle between the magnetic field and the harmonic propagation vector.

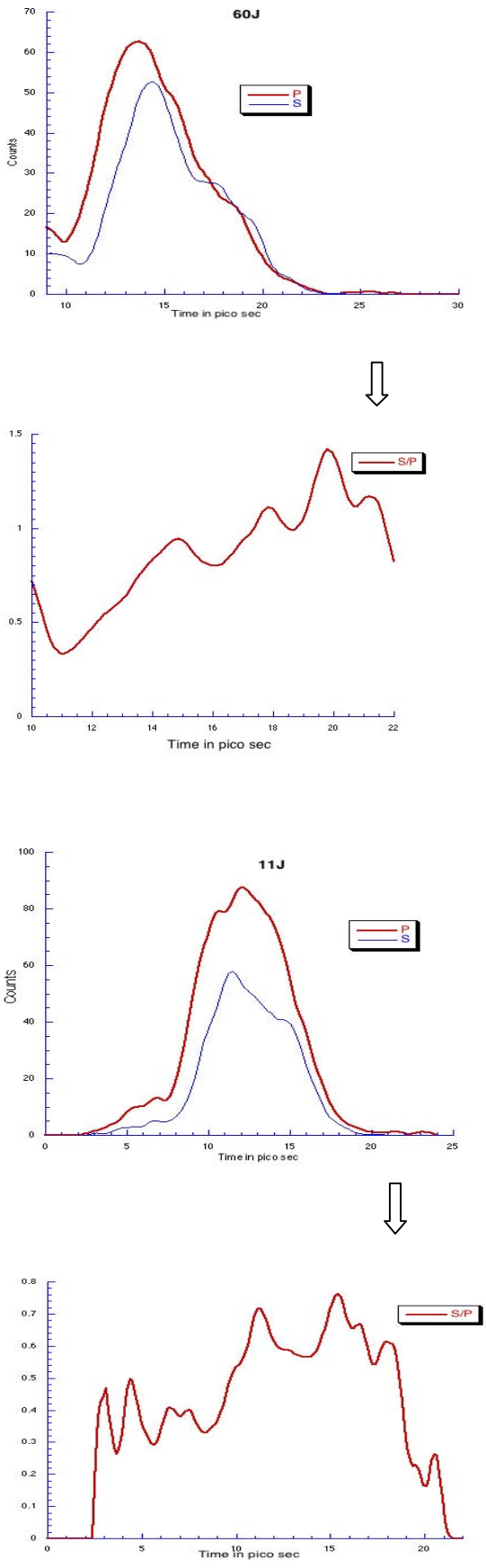

Figure 3. The evolution of s and p harmonics for a high energy shot (60 J) and a low energy shot (11 J) and the ratio of S/P for above shots.

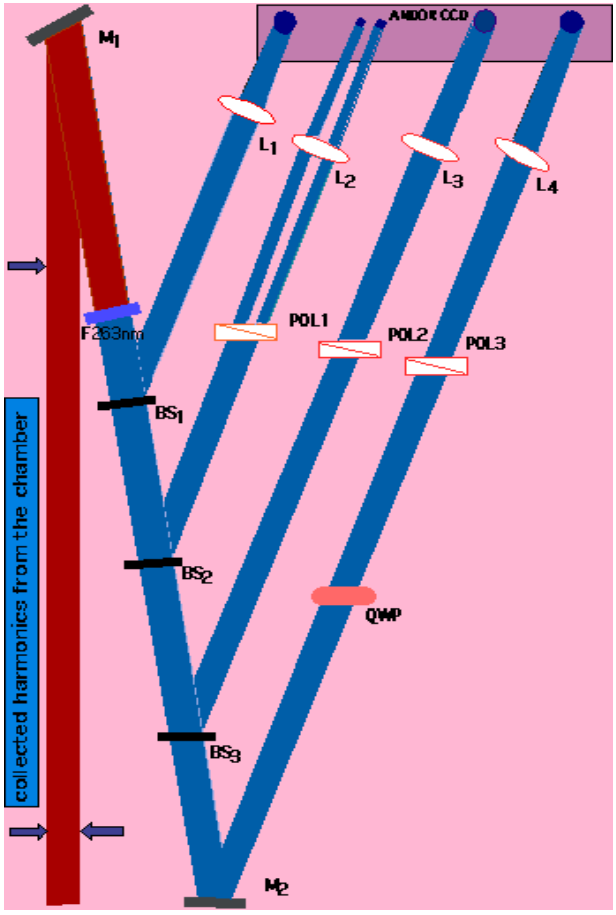

Figure 4. Schematic set up of a polarimeter.

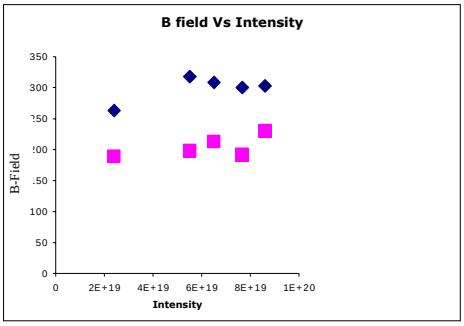

Figure 5. Estimate of magnetic field in direction of laser (blue diamonds) and back away from the laser (pink squares).

Conclusions

In conclusion we have made the first detailed study of the magnetic field using polarimetry of the self-generated harmonics. It was found that the magnetic field duration is at least as long as the incident high intensity laser pulse. Initial measurements of the spatial distribution of the magnetic field suggests that the field is asymmetric as predicted by PIC simulation results.

Such measurements could be improved by the use of externally produced higher order harmonics which could probe through solid-density plasma and allow more precise measurements.

References

1. J. A. Stamper *et al*., Phys. Rev. Lett. 26, 1012 (1971).
2. A. Pukhov and J. Meyer-ter Vehn, Phys. Rev. Lett. 76, 3975 (1996).
3. R.Sudan, Phys. Rev. Lett. 70, 3075 (1993).
4. J. A. Stamper and D. A. Tidman, Phys.Fluids 16, 2004 (1973).
5. M.Tatarakis, I.Watts, F. N. Beg, E. L. Clark, A. E. Dangor, A. Gopal, M. G. Haines, P. A. Norreys, U. Wagner, M. S. Wei, M. Zepf, K. Krushelnick, Nature, 415, 280 (2002).
6. M. Tatarakis, A. Gopal, I. Watts, F. N. Beg, A. E. Dangor, K. Krushelnick, U. Wagner, P. A. Norreys, E. L. Clark, M. Zepf, R. G. Evans, Physics of Plasmas 9, 2244 (2002).
7. R. Lichters, J. Meyer-ter-Vehn, A. Pukhov, Plasma Phys. 3, 3425 (1996).
8. S. E. Segre, Plasma Phys. Controlled Fusion 41, R57 (1999).

Multi-MeV ion production from interactions of high intensity Vulcan Petawatt laser with gas jet targets

M S Wei, S P D Mangles, Z Najmudin, B Walton, A Gopal, M Tatarakis, A E Dangor, K Krushelnick

The Blackett Laboratory, Imperial College, London, SW7 2BZ, UK

E L Clark

Plasma Physics Department, AWE plc, Aldermaston, Reading, RG7 4PR, UK

S Fritzler

Laboratoire d'Optique Apliquée, ENSTA, Ecole Polytechnique, CNRS, 91761 Palaiseau, France

R J Clarke, C Hernandez-Gomez

Central Laser Facility, CCLRC Rutherford Appleton Laboratory, Chilton, Didcot, Oxon, OX11 0QX, UK

Main contact email address: *wei.mingsheng@imperial.ac.uk*

Introduction

Throughout the past decade, the continuing developments in high-intensity, short-pulse laser technology, have stimulated significant interest in electron acceleration from laser-produced plasmas. The interesting physics, which occurs during such interactions is important for applications such as compact particle accelerators[1)] and fast ignition for inertial confinement fusion[2)].

In addition to electron acceleration, energetic ions can also be accelerated quite efficiently through 'Coulomb explosions' which occur during high intensity short pulse laser interaction with underdense plasmas[3,4)]. The ions are accelerated by the strong space-charge force generated by the ponderomotive force of the laser expelling electrons away from the region where the laser is focused in the underdense plasma. Experimentally, Krushelnick et al[3)] have observed helium ions with peak energy 3.6 MeV, deuterons up to 1 MeV and neon ions with energy greater than 6 MeV. In their experiments, a 50 TW laser, having a pulse duration of 0.9 ps was focused to the edge of a supersonic gas jet. The plasma density was up to 5×10^{19} cm^{-3}. From the maximum ion energy measurements, it was inferred that the peak laser intensity in the experiments was a few times higher than the focused intensity in vacuum – primarily due to self-focusing of the high intensity laser by relativistic and charge-displacement processes.

Plasma channel formation as a result of the self-focusing effects has been the subject of intense study as it is crucial for the use of plasma waveguides in laser driven particle accelerators[5)]. The laser power (P_L) required for relativistic self-focusing to dominate diffractive effects is given as $P_L>P_c$, where $P_c\sim17.4(n_c/n_e)$ GW is a critical power; n_e is the plasma electron density and n_c is the density corresponding to the density when the plasma frequency and laser frequency are the same. Studies of the transverse stability of relativistic/charge displacement self-channeling against azimuthal perturbation done by Borisov et al[6)] have predicted that 10^4 times critical power can be easily confined to a single stable channel in an underdense plasma with an appropriate longitudinal gradient of the electron density, e.g. a simple exponential density ramp with plasma scalelength 0.4-0.5 mm. The radius of the laser channel is inversely proportional to the square root of plasma density. Previous studies[4)] using short pulse laser interactions with underdense plasma having P_L more than one order of magnitude larger than P_c have suggested that the maximum ion energy is proportional to the laser energy and pulse duration, but inversely proportional to the fourth power of the laser beam radius. The laser pulse energy losses due to the ion acceleration scale similarly with laser energy and pulse length but inversely proportional to the square of the beam radius. However, the influence of the initial plasma density on relativistic self-focusing and ion acceleration during the interactions in the regime where $P_L>>P_C$ remains unexplored. Here we present the results of experiments where P_L/P_c is up to 2000.

In this report, we present ion measurements from experiments with the Vulcan Petawatt laser, in which a 300 TW laser with a pulse duration 0.6 – 0.8 ps interacts with an underdense gas-jet plasma with varying density (from 4×10^{18} to 1.4×10^{20} cm^{-3}). In this experiment, helium ions with energy up to 13.2(±1) MeV were measured. For the first time we observed that the maximum ion energy has a strong correlation with the plasma density, and increases approximately as the plasma density to the power 0.8, when the pulse duration and the vacuum laser intensity were kept constant. The interactions were also studied by 2-D PIC simulations. The experimental data agrees quantitatively with the simulation results both with regard to the ion energy spectra and the maximum ion energy. The simulations also indicate the contribution of the collisionless shock wave to ion acceleration.

Experimental set-up

Our experiments were performed using the Vulcan Petawatt laser. This laser system can produce laser pulses with an energy up to 312 J and a duration of 0.5-0.7 ps at a wavelength of 1.054 μm. The laser pulse was focused to the edge of a supersonic gas-jet target (2mm nozzle diameter) using an f/3 off axis parabolic mirror. When helium was used as the working gas, the backing pressure in the gas nozzle was varied from 3 bar to 70 bar, which gave plasma densities between $(0.04 - 1.4) \times 10^{20}$ cm^{-3}. The electron density during the interaction was obtained by the sidebands at the laser frequency at multiples of ω_p due to the forward Raman scattering instability. Deuterium gas was also used but at a lower plasma density due to the limitations of the gas jet.

The spectrum of the ions at 100° from the laser propagation direction was measured with a Thomson parabola. Ions with different charge/mass ratio (q/m) can be distinguished since they produce unique parabolic trajectories at the detector plane. Detailed descriptions of the spectrometer can be found in Reference 7. The spectrometer was positioned 80 cm from the interaction region. A 250 μm diameter pinhole was positioned to subtend a solid angle of 7.67×10^{-8} steradian. The detectors used were 1mm thick CR39 nuclear track detectors. After etching the plastic in NaOH solution for 3 hours, the number of the individual pits along the particular parabola was sampled in various energy bins to give the ion spectra.

Experimental results

A typical helium ion spectrum is shown in Figure 1. In this shot, the measured plasma density was 1.4×10^{20} cm^{-3}, the highest density obtained in our experiments. The calculated laser intensity was 2.9×10^{20} Wcm^{-2}. Both He^{2+} and He^{1+} ions have been clearly accelerated to high energy. The maximum energy for He^{2+} is 13.2±1 MeV. It is estimated that the total number of He^{2+} ions with energy greater than 680 keV is 3.8×10^{11}. It should be noted that there is some reduction of the number of fully ionized helium ions having an energy less than

1 MeV. This can be explained by the strong charge-exchange/recombination of ions with the surrounding background neutral gas as they move out of the interaction region. Since the cross-section for charge-exchange ($\sigma \propto 1/\Delta E^3$) is large for the smaller ΔE (kinetic energy difference), slower He^{2+} ions are more likely to lose energy in ionizing the neutral gas. This is proved by the fact that there are still a large number of He^{1+} ions observed with high energies. The He^{2+} ion spectrum also exhibits a 'plateau' profile at the energy range between 6-10 MeV and has a sharp drop to the cut-off point (maximum ion energy recorded on the detector), which have good qualitative agreement with 3-D PIC simulations[8].

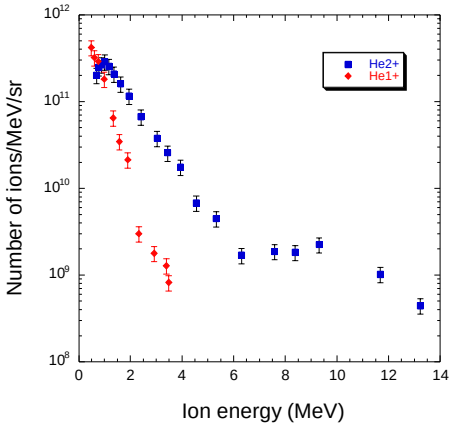

Figure 1. Helium ion spectrum at plasma density 1.4×10^{20} cm^{-3} and laser intensity I ~ 2.9×10^{20} W/cm^2.

Figure 2 shows a typical spectrum with plasma density at 1.7×10^{19} cm^{-3}. The laser intensity (3.7×10^{20} Wcm^{-2}) is slightly higher than that shown in Figure 1. As shown in the spectra, both the number of ions accelerated and the maximum energy of ions obtained were greatly reduced at lower density. The maximum ion energy drops to 2.33 MeV and the total number of He^{2+} ions with energy > 588 KeV is reduced to 7.4×10^{10}. It is found that the ion spectra at low density fit quite well with exponential distribution.

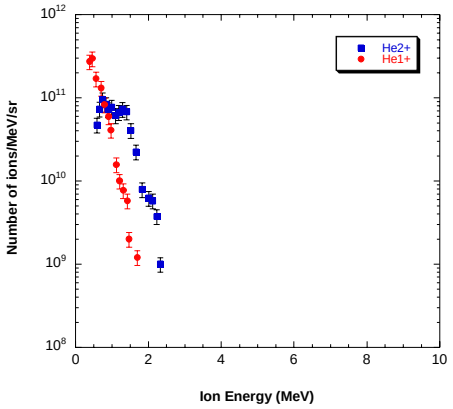

Figure 2. Helium ion spectrum at plasma density 1.7×10^{19} cm^{-3}.

Measurements with deuterium gas also show the same behaviour (see Figure 3). Deuterons with a maximum energy of 1.4 MeV were measured when the plasma density was 1.22×10^{19} cm^{-3}. The spectrum fits well with an exponential profile with an average energy 180±20 keV. When the density is in the range $(4 - 8)\times10^{18}$ cm^{-3}, both the average energy and maximum energy are reduced.

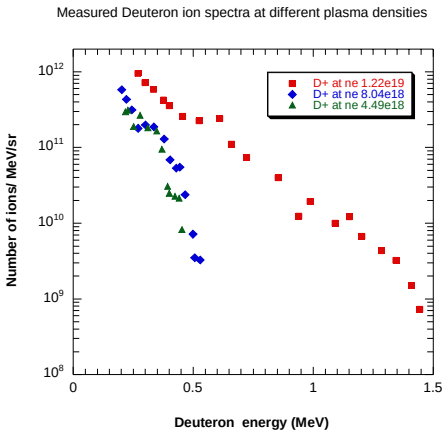

Figure 3. Deuteron spectra at different plasma densities.

A series of shots were taken for a scan in density during the experiments – both with helium and deuterium gas. In Figure 4, we present the maximum ion energy per nucleon plotted against plasma density. The power law fitting ($E_{max} \propto n_e^{0.8}$) shows that the maximum ion energy increases with the plasma density. Indeed no energetic helium ions were measured at a density below 4×10^{18} cm^{-3}.

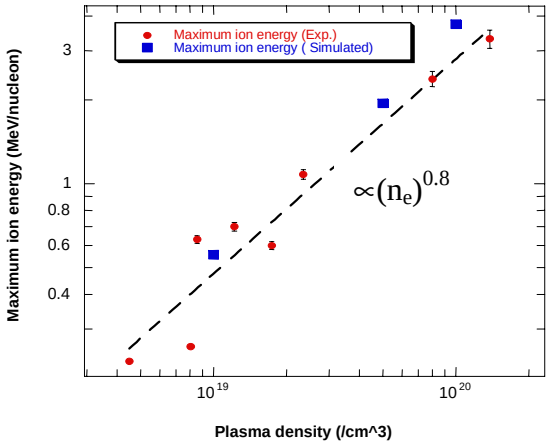

Figure 4. Correlation of the measured maximum ion energy vs. plasma density (red dot). Also shown are the simulation results (blue square). Dashed line is the power law fitting to 0.8.

Preliminary ion angular distribution was measured using several layers of radiochromic film (RCF) strips sitting at radial direction at a distance of 6 cm. Through the use of aluminium filters in front of the RCF, the angular distribution of different energy ranges can be determined from the RCF images. Here we assume RCF signals were dominated by the contribution from the ions, which is roughly correct according to past experience. Measurements with nuclear track detectors will be used to check the results in future experiments. Our measurements showed that ion emissions at low density case were predominantly along 90° with angular spread (FWHM) less than 30° for those ions with energy less than 2 MeV. High energy ions (E > 2 MeV) had even smaller angular spread which was less than 4°. With the increase of the plasma density, the angular spread became much larger. Even the high energy component (E > 3.5 MeV) had an angular spread of about 27° and also those ions were emitted off 90° in the forward direction. Considering our diagnostic viewing angle (100° from the laser axis), the maximum ion energy recorded on our detector may be less than that produced during the interactions.

PIC simulations

To investigate how the plasma density influences the ion acceleration, a series of 2-D PIC simulations using the OSIRIS code[9] were performed at the same laser intensity ($I\sim3\times10^{20}$ Wcm^{-2}, a_0 ~15) but different plasma densities (0.01 n_c , 0.05 n_c and 0.14 n_c) for deuterium plasma. The ratio of laser power over critical power is up to 2000. The plasma density profile has a linear ramp for 0.5 mm, a flat profile for another 0.5 mm and a linear drop to 0 at a distance of 0.5 mm. This density profile in ramping stage is very similar to the real one produced by the gas-jet in the experiment. A linear-polarized laser beam with a duration of 0.65 ps was focused onto the front edge of the gas-jet having a spot size of 10 µm (FWHM) in diameter. 'Moving window' with size 795.8 µm by 99.5 µm in longitudinal and transverse direction, which moves with the laser pulse, was used to study the propagation and interaction of the laser with underdense plasma with the density profile described above.

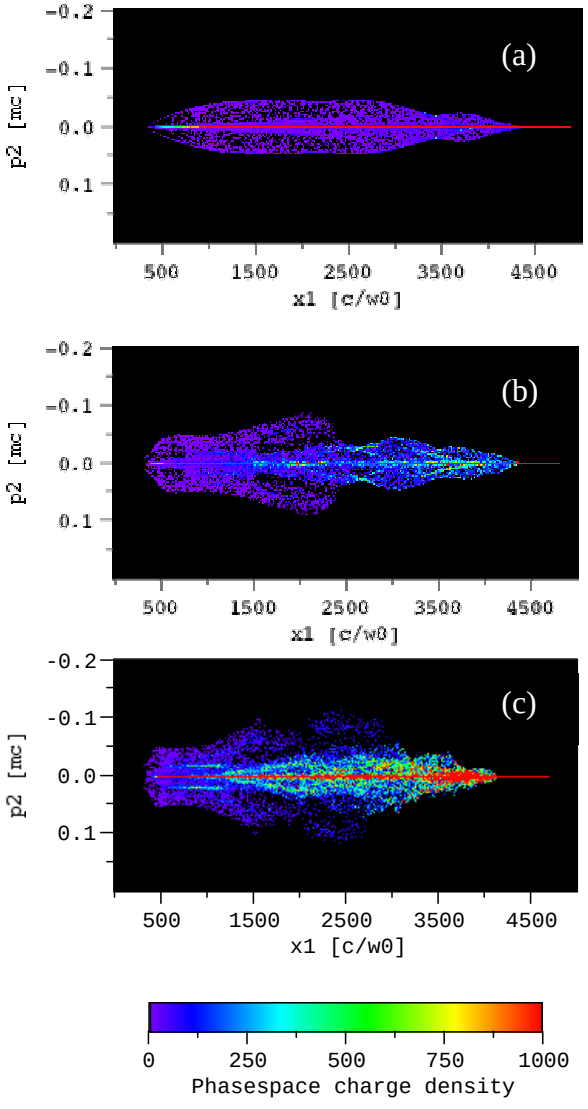

Figure 5. Ion density plot in phase space at same time but different densities (a) 0.01n_c, (b) 0.05 n_c and (c) 0.14n_c.

Figure 5 shows the plots of ion charge density in phase space p2x1 at a time 2.6 ps after the beginning of the simulation for three different density runs. By this time, the laser pulse has propagated in the plasma for about 600 µm. It clearly shows that with the increase of plasma density, ions are accelerated more in the radial direction. It is noted that the ions were accelerated smoothly at lower density. It seems that ions did not see the peak ponderomotive potential in this case. On the other hand, most energetic ions in the high density case are generated from regions of tight focusing after the laser pulse has undergone the relativistic self-focusing and guided in the plasma channel. It is observed that the diameter of the laser beam during the self-focusing at 0.14 n_c was about 4 µm at FWHM and 8 µm at 0.01 n_c. The former is about 1/3 of the vacuum focal spot size. The laser intensity was found to be increased by a factor of 3 with $a_0\sim25$ during the interaction. Most of the energetic ions are located between 270 and 430 µm in longitudinal direction in high plasma density (1.4×10^{20} cm^{-3}) case. Later on strong filamentation instabilities grow and there is no more efficient acceleration of ions.

Simulations with the high plasma density also clearly show that there are two collisionless shocks driven out after the self-focusing in the radial direction. The second shock (also the fast one traveling out at a speed of 0.2c) catches up with the first one (the slower one with speed at 0.1c) and collide with each other. Large populations of ions are accelerated to high energy during this colliding process. Figure 6 presents the time evolution of ion density plots in x2x1 space, which shows this process.

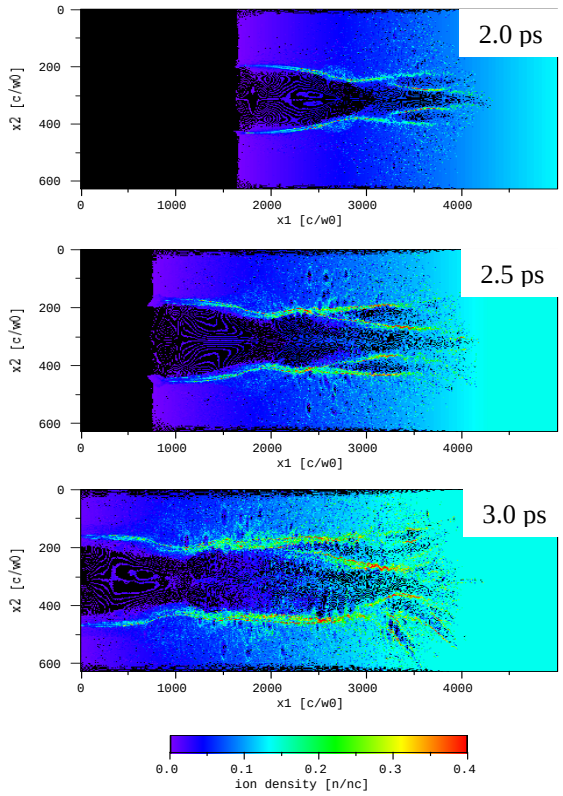

Figure 6. Time evolution of ion density in x2x1 space from simulations at high plasma density($n_e = 1.4\times10^{20}$ cm^{-3}). They clearly show that two shock waves were formed after the self-focusing and then collided and merged together.

Simulated deuteron energy spectra are presented in Figure 7 for different densities at same time during the run (2.8 ps). The spectra do not evolve substantially later on. The increase of ion energy with density is very obvious. The spectra are deduced at 90° with an opening angle of 10°. The maximum ion energy is about 2 times higher than that observed in the experiments. As we discussed earlier, this is probably due to our diagnostic viewing angle. Indeed the maximum ion energy obtained in the simulation at the real experimental observation angle is reduced by a factor of 2 compared with the peak energy at 90°. This agrees well with the observed maximum ion energy. (Note that helium ion energy should be approximately twice the deuteron

energy since Z=2 for He^{2+}). The simulated ion spectrum for the high density case also shows the 'plateau' profile in the high energy component of the ion distribution. The colliding of two shock waves in the simulation may account for this structure.

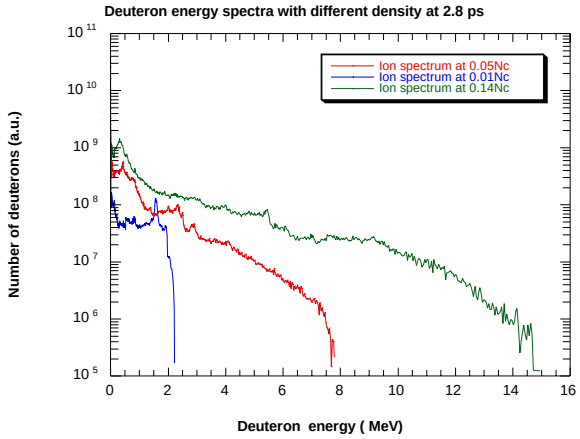

Figure 7. Simulated ion energy spectra for different plasma densities.

Discussions and conclusions

We have experimentally studied ion acceleration due to Coulomb explosion from the interactions of a short laser pulse with an underdense plasma with laser power up to 2000 times critical power for relativistic self-focusing to occur. In this new regime, we find a strong correlation between maximum ion energy against plasma density which is also confirmed by our 2-D PIC simulations. Our study suggests that high plasma density will lead to more efficient ion acceleration. Two possible acceleration processes may contribute to the energetic ion production. One is the enhanced on-axis laser intensity due to laser self-focusing with smaller effective plasma channel radius $R_{sf} \sim n_e^{-1/2}$ at higher density[6], and correspondingly higher ponderomotive potential, during the interactions. Since the maximum ion energy is directly related to the ponderomotive potential of the laser ($U= Zm_ec^2(\gamma-1)$), with the increase of the peak laser intensity, ion energy would also be expected to be higher at higher plasma density. This is precisely what is observed both in experiments and the PIC simulations. On the other hand, simple calculations linking maximum ion energy with enhanced ponderomotive potential due to self-focusing suggest that a second acceleration mechanism may exist at high density. At $0.14n_c$, the degree of self-focusing observed could only accelerate ions to half the maximum energy observed in the simulation. The violent expulsion of ions during the collision of two shock waves suggests that large amounts of ions may obtain high energy from this process. Particle acceleration due to the interaction of shocks is very important in space and astrophysics and as such more experiments need to be performed to investigate this process.

Acknowledgements

The authors acknowledge the assistance of the staff of the Central Laser Facility of the Rutherford Appleton Laboratory in the execution of this work as well as the support of the UK Engineering and Physical Sciences Research Council (EPSRC). We gratefully acknowledge the OSIRIS consortium which consists of UCLA/IST(Portugal)/USC for the use of OSIRIS.

References

1. T. Tajima and J. M. Dawson, Phys. Rev. Letters 43, 267 (1979); P. Sprangle *et al*., Appl. Phys. Letters 53, 2146 (1988); K. Nakajima *et al*., Phys. Rev. Letters 74, 4428 (1995); D. Umstadter *et al*., Science 273, 472 (1996); A. Modena *et al*., Nature 377, 606 (1995); A. Ting *et al*., Physics of Plasmas 4, 1889 (1997); V. Malka *et al*., Science 298, 1596 (2002)
2. M. Tabak *et al*., Physics of Plasmas 1, 1626 (1994)
3. K. Krushelnick, E. L. Clark, Z. Najmudin *et al*, Phys. Rev. Letters 83, 737 (1999)
4. G. S. Sarkisov, V. Yu. Bychenkov, V.N. Novikov *et al*, Phys. Rev. E. 59, 7042 (1999)
5. E. Esarey and P. Sprangle, IEEE Journal of Quantum Electronics 33, 1897 (1997), and references therein; S.-Y. Chen, G. S. Sarkisov, A. Maksimchuk et al., Phys. Rev. Letters 80, 2610 (1998)
6. A. B. Borisov *et al*., Plasma Phys. Control. Fusion 37, 569 (1995); A. B. Borisov *et al*., J. Phys. B 32, 3511 (1999); A. B. Borisov et al., J. Phys. B 34, 2167 (2001)
7. E. L. Clark, Ph.D thesis, University of London (2001)
8. A. Pukhov Rep. Prog. Phys. 66, 47 (2003)
9. R. Hemker, Ph.D Thesis, UCLA, (2000)

Observations of the propagation of high order harmonic radiation through dense plasma

U Wagner, P A Norreys
Central Laser Facility, CCLRC Rutherford Appleton Laboratory, Chilton, Didcot, Oxon, OX11 0QX, UK

A Gopal, M Tatarakis, A E Dangor, M S Wei, F N Beg, K Krushelnick
Plasma physics Group, Imperial College, London, SW7 2AZ, UK

M Zepf
Dept. of Pure and Applied Physics, The Queen's University of Belfast, Belfast, BT7 1NN, UK

Main contact email address: *kmkr@imperial.ac.uk*

Introduction

Recent advances in laser technology have enabled the generation of focused radiation intensities up to ~ 10^{20} Wcm^{-2}. This has led to a number of interesting new observations from the plasmas which can be produced during laser-matter interactions at such extreme intensities. These include the generation of beams of relativistic electrons[1)] , gamma rays[2)] , and energetic protons [3)] as well as the observation of laser induced nuclear reactions [4)]. However, because of the high densities and the small spatial and temporal scales of the plasmas produced in such experiments (< 10 µm, < 1 ps) it remains difficult to diagnose these interactions precisely using conventional techniques.

During such experiments, measurements of the emission of high order harmonics of the fundamental laser frequency can be a powerful diagnostic of the physical processes and plasma conditions in the interaction region [5, 6)]. High order harmonics are useful since they are generated at the same time and from the same location as the high intensity interaction. The generation mechanism for these harmonics is also quite well understood – so it is possible to infer a significant amount of information concerning the interaction merely by measuring the properties of this harmonic radiation.

The production of harmonics up to the 75th order (of 1.053 µm radiation) was previously observed using focused laser intensities up to 10^{19} Wcm^{-2} and was found to have a conversion efficiency of about 10^{-6} in the XUV region [5)]. The harmonics can be understood as being caused by an oscillating current of electrons moved across the vacuum-solid interface by the electric field of the laser pulse or, equivalently, by a simple model based on the phase modulation experienced by the light upon reflection from the oscillating plasma-vacuum boundary [7)]. The efficient generation of these harmonics is also of potential interest as a bright source of XUV radiation.

In this report we show the results from an experiment which has measured the polarisation properties of these high order harmonics after they propagate through high density plasma. We observe the generation of polarised sidebands on the harmonics which are likely due to Thomson scattering of the XUV harmonics in a magnetised high density plasma.

Experimental setup

These experiments were performed using the Vulcan laser system at the Rutherford Appleton Laboratory, which uses the technique of chirped pulse amplification to produce 0.7 - 1.0 ps pulses at 1.053 µm with energies up to 70 J onto target. The rectangular beam, 20 x 11 cm^2, was focused by an off-axis parabolic mirror (f/3). Targets consisted of extremely thin aluminium foil targets (less than 1 µm thick). The energy on target and pulse duration were monitored on a shot-to-shot basis. The intensity on target was up to ~ 9 x 10^{19} Wcm^{-2} and the laser pre-pulse was determined to be about 10^{-6} of the peak intensity using third order auto-correlation techniques[8)]. The sub-critical plasma produced by this prepulse in front of the target was measured by optical probing and found to have a scale-length which was typically less than 10 µm.

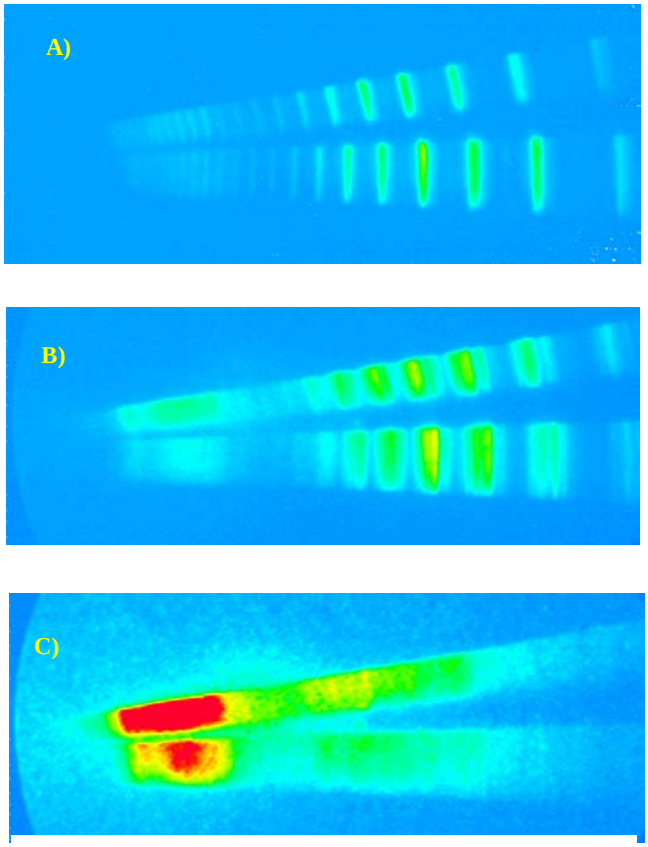

Figure 1. Raw data from experiments 7th (right) to 25th (left) harmonic (s polarisation on top, p polarisation below). A) harmonics from front of target, B) harmonics from rear of target (0.2 µm Al), C) harmonics from rear of target (0.4 µm Al).

In our experiments, a multi-channel XUV-polarimeter was constructed to perform measurements with harmonics of higher order than 5. An XUV-polarimeter is needed as the wavelengths of these harmonics are below 200 nm for Vulcan (which operates at 1053 nm). The VUV-polarisers are a triple-mirror-configuration which are partially polarising due to the Fresnel-reflections on gold-coated mirror surfaces. Two VUV-polarisers were set up orthogonally to measure the p- and the s-components of the harmonics. The polarised beams are then focused onto the slit of an Acton spectrometer, enabling the simultaneous measurement of many harmonic orders. An open microchannel-plate (MCP) coupled to a charge-coupled-device (CCD) by a fiber-optic-bundle was used as the detector.

The XUV polarimeter was positioned at the rear of very thin foils of aluminium (0.2 and 0.4 µm thick) and the harmonic spectrum was measured during interactions at peak laser intensity.

Results

Examples of raw data acquired during the experiment are shown in Figure 1. Lineouts from this data are shown in Figure 2. Figure 1A) shows an example of a spectrum taken from the front of the target while 1B) shows the spectrum of the harmonics after propagation through 0.2 µm Al. Figure 1C) shows the propagation of the harmonics through a thicker plasma (0.4 µm).

The principal observation from this experiment is the significant broadening of the harmonics observed after propagation through the dense plasma. The intensity of the harmonics was also significantly reduced using 0.4 µm (i.e., only the higher frequency part of the spectrum could propagate).

Also, of particular interest is the apparent satellite structure observable on the harmonics in Figure 1B). These satellites are strongly polarised and are likely due to an interaction of the harmonic frequency with strong magnetic fields in the interior of the plasma.

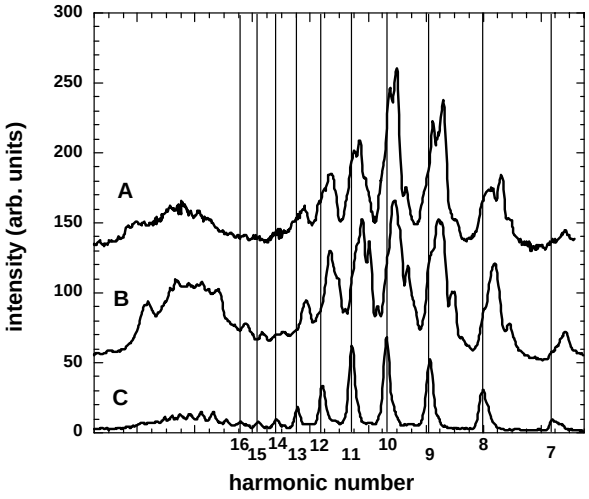

Figure 2. Lineouts from Figure 1. A) polarisation from 1B) (0.2 µm Al)**,** B) s-polarisation from 1B) (0.2 µm Al), C) s-polarisation from 1A).

There have been previous measurements of an electron cyclotron modulation of the Thomson scattered spectrum from early experiments using a theta pinch [9)]. In our experiments, if the observed satellites are caused by Thomson scattering of harmonic radiation with the magnetic field of the plasma, this would suggest that the magnetic field in the overdense region is about 20 MegaGauss in strength. This corresponds to previous theoretical estimates for the internal magnetic field [10)]. Further analysis of these results is ongoing.

References

1. L. Gremillet, *et al.,* Physical Review Letters 83, 5015 (1999); M. I. K. Santala *et al.,* Physical Review Letters 86, 1227 (2001).
2. R. D. Edwards, *et al.*, Applied Physics Letters 80, 2129 (2002); P. A. Norreys, *et al.*, Physics of Plasmas, 6, 2150 (1999); M. H. Key *et al.*, Physics of Plasmas, 5, 1966 (1998).
3. E. L. Clark *et al.,* Physical Review Letters, 84, 670 (2000); R. A. Snavely *et al.*, Physical Review Letters, 85, 2954 (2000); E. L. Clark, *et al.,* Physical Review Letters 85, 1654 (2000); K. Krushelnick, *et al.*, IEEE Transactions in Plasma Science 28, 1184 (2000); A. Maksimchuk *et al., Physical Review Letters*, 84, 4108 (2000).
4. K. W. D. Ledingham *et al.,* Physical Review Letters 84, 899 (2000); M. I. K. Santala, *et al.,* Physical Review Letters 84, 1459 (2000).
5. P. A. Norreys *et al.,* Physical Review Letters 76, 1832 (1996).
6. R. Hassner *et al*., Opt. Lett. 22, 1491 (1997); W. Theobald *et al.,* Physical Review Letters 77, 298 (1996); I. Watts *et al.*, Physical Review Letters 88, 155001 (2002).
7. R. Lichters, J. Meyer-ter-Vehn and A. Pukhov, Phys. Plasmas 3, 3425 (1996); D. von der Linde and K. Rzazewski, Appl. Phys. B - Lasers Opt. 63, 499 (1996).
8. C. N. Danson *et al*., Opt. Comm. 103, 392 (1993).
9. D. E. Evans and P. G. Carolan Phys. Rev. Lett. 25, 1605 (1970).
10. J. R. Davies *et al.* Phys. Rev. E 59, 6032 (1999).

High intensity laser driven z-pinches

F N Beg, E L Clark*, M S Wei, A E Dangor, R G Evans*, A Gopal, M Tatarakis, K Krushelnick
The Blackett Laboratory, Imperial College, London, SW7 2BZ, UK

P A Norreys, M Tolley, K L Lancaster
Central Laser Facility, CCLRC Rutherford Appleton Laboratory, Chilton, Didcot, Oxon, OX11 0QX, UK

M Zepf
Department of Physics, The Queens University, Belfast, BT7 1NN, UK

P McKenna, K W D Ledingham*, T McCanny
Department of Physics, University of Strathclyde, Glasgow, G4 0NG, UK

* *also at AWE plc, Aldermaston, Reading RG7 4PR, UK*

Main contact email address: *f.beg@ic.ac.uk*

Introduction

Since the technique of chirped pulse amplification (CPA)[1)] was first introduced for use in high power laser systems, peak laser intensities have increased dramatically. It is now possible to perform laser-plasma interaction experiments at intensities approaching 10^{21} Wcm^{-2} – a regime in which the physics is qualitatively different from that at lower intensities.

One of the important characteristics of such interactions is the generation of energetic beams of electrons[2)], protons[3)] and gamma rays[4)], which result from the very efficient conversion of laser energy into hot electrons. Because the electrons in the electric field of the laser have relativistic quiver motions, the temperature of the hot electron distribution produced at such extreme intensities becomes very high. A large number of hot electrons having an average energy of the order of 1 MeV can be generated as intensities exceed 10^{19} Wcm^{-2} and the formation of beams therefore leads to the production of significant return currents in the plasma.

There are, in general, two types of return currents produced in such experiments. One occurs as the beam of hot electrons penetrates into the plasma. This beam requires a large neutralising return current of cold plasma electrons moving in the opposite direction in order for the hot beam to propagate (i.e., for beams with currents greater than the Alfvén limit). These currents can cause ohmic heating in regions of the plasma interior which are relatively close to the interaction region. In the experiments described here in which thin wire targets are used (wire thickness ~ laser spot size) this will not be an important source of return current since hot electrons will be much more likely to move around the wire rather than penetrate into the interior.

The other related source of return current is due to the population of very energetic electrons which "escape" the plasma and which create a large electrostatic potential on the target due to charge separation between these electrons and the heavier ions. If the return current can respond quickly to this charge imbalance, more hot electrons can be emitted from the plasma. In general, the numbers of electrons, which can escape in this way are much less than those in the neutralized electron beam which penetrates the plasma during interactions with solid "slab" targets. The peak voltage which can be produced is approximately the ponderomotive potential of the focused laser pulse since this corresponds to the electrostatic potential in the plasma due to the charge separation which can be maintained by the light pressure. When these fast electrons escape the target and establish this potential, a number of phenomena can be observed because of the generation of return currents in response to the resulting large scale electric fields.

There have been several previous experiments using nanosecond duration CO_2 laser pulses (λ = 10.6 μm), which have studied the effect of return currents generated in this way. Benjamin et al.[5)] reported the heating of thin fibres due to the production of return currents. The estimated target voltage was 190 kV. In another experiment, Hauer and Mason [6)] used laser-produced return currents (~ 0.8 MA) to implode a thin cylindrical liner, which was observed to collapse with a velocity of 5-7 x 10^4 ms^{-1}.

In this report, we present the first observations of the effects of such return currents on the physics of the plasma produced during much higher intensity laser plasma interactions (up to 5 x 10^{19} W/cm^2) and, crucially, much shorter pulse duration (typically 1 ps). We provide conclusive evidence that the return currents and target charging in these experiments are especially important since these greatly influence the propagation and energy deposition of the generated electron beams. We show that the fast rising currents associated with PW laser interactions may be sufficient to make detailed studies of radiative collapse in ps Z-pinch configuration, which is presently not possible using pulsed power generators with current risetimes of hundreds of nanoseconds.

Experimental Arrangement

Experiments were carried out using the CPA beam of the Vulcan Nd:glass laser system at Rutherford Appleton Laboratory. The laser wavelength was 1.054 μm, the pulse length was 0.9 – 1.3 psec and the energy incident on target was between 60 and 80 J. The laser was focused onto the target using an off-axis parabolic mirror with a focal length of 60 cm. The peak intensity was up to 5 x 10^{19} Wcm^{-2}. Several wire configurations were used as targets. The targets used were one, two or three parallel wires assembled on the top face of a 3 mm diameter grounded brass stalk. A 50 μm planar aluminum target was also used in conjunction with wires on some shots instead of the wire targets. Here, the p-polarized laser beam was incident at an angle of 45^0 onto such foil targets. The wires were typically hard tempered 20 μm diameter copper which had lengths of 3 or 5 mm. Gold and glass wires were also used. In the case of two or three wire target assemblies, the secondary wires were placed out of the line of the laser propagation direction to avoid any heating due to transmitted or scattered energy from the interaction of the laser beam with the target wire.

The targets were probed perpendicularly to the interaction laser beam using shadowgraphy with a picosecond duration, frequency doubled (527 nm) probe beam. The timing of the probe beam could be varied to study the expansion of the wires. A four frame camera based on gated image intensifiers coupled to CCD detectors was used to obtain images of the target and secondary wires. The framing time was 1 nsec. The timing of the frames was adjusted to obtain images at the time of interaction and at 1 nsec intervals subsequent to the interaction. Notch filters were used to reduce the intensity of self-emission (ω and 2ω) on the detector. A time integrated x-ray pinhole

camera was also used to measure the x-ray emission region with high spatial resolution.

Results

Shots with single wire targets (20 µm thick copper) showed intense optical emission (see Figure 1). This emission was observed to be a maximum near the laser spot but, in addition, it could also be observed along the wire for distances of several hundred microns. Such emission was most intense along the wire in the direction connected to ground and there was little or no emission towards the free end of the wire at a distance more than a few tens of microns from the interaction region. The wire was also observed to expand with a velocity of 5×10^4 m/sec – reaching a diameter of 120 µm in 1.25 nsec (i.e., an average expansion velocity of 3×10^4 m/sec). This optical emission and expansion of the heated wire is due to ohmic heating by the return current generated by fast electrons, which leave the target. In this case, electrons from ground will move to compensate for the charge imbalance generated during the interaction. For ps laser pulse, the rate of rise of the return current is limited by the wire inductance L (here about 150 ps at 100 eV).

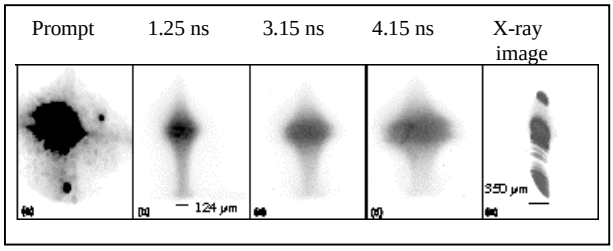

Figure 1. a) A sequence of optical frames showing emission and expansion of the wire target, b) time integrated x-ray image showing m=0 perturbations (hv > 400 eV). Optical and x-ray images have different magnifications.

Our interpretation is that the optical emission is due to return current heating of the wire material since it was observed at large distances from the laser spot and emission was principally from region connected to ground. The expansion velocity of the wire during these experiments is similar to that routinely observed in single wire z-pinch discharge experiments which use a current in the range 100 kA – 1 MA. As in z-pinch experiments, an m=0 MHD instability was observed in wire targets as shown in Figure 1(e). The observed instability has an average wavelength of 110 µm (the largest and shortest wavelengths were 270 and 40 µm respectively). The theoretical wavelength for this instability can be calculated using the model used in Reference 7 and is given by (in microns),

$$\lambda = \frac{2\pi}{k} = 2.41 \times 10^{10} \frac{T_e^2 A^{1/2}}{n_o Z y} ,$$

where $T_e = 10^6$ *K (100 eV)*, $n_0 = 10^{26}$ m^{-3}, $A = 29$ and $Z = 10$ and y is taken to be 1 for the fastest growing mode. This gives a wavelength of 100 µm, which is in rough agreement with the experimental results.

In single wire z-pinch discharges the wavelength of the observed instability increases as the current rises. At very early times in the discharge, the instability has a wavelength of about 100 µm, which increases to 1 mm at later stages of the current pulse. Hence, the presence of short wavelength instabilities in these laser driven z-pinch experiments is likely due to the relatively low temperature of the plasma, which carries the return current (< 100 eV).

For very short current pulses MHD instabilities will not have sufficient time to grow as the current rise is shorter than a typical MHD time. Here, an MHD instability growth time is of the order of 0.1 – 1 nsec (i.e., the Alfvén wave transit time across the pinch). In our experiments the curved emission regions visible in the x-ray image are probably caused by the motion of the plasma after the current has ended and after such instabilities have stopped growing.

Experiments were performed with secondary grounded wires adjacent to the wire targets. Optical images clearly show well localized second harmonic emission from the secondary wire. In Figure 2, a secondary wire was placed 300 µm from the main wire target and a band pass interference filter is used to measure only emission at the second harmonic frequency of the laser. The first optical frame is synchronous with the laser pulse. Intense second harmonic emission can be seen both at the laser spot position and from the secondary wire. The second wire expands to a diameter of 50 µm and the emission from the secondary plasma lasts much longer than that from the target wire. The total emission from the target wire in this case is much less and is of shorter duration than that from target wires when there are no secondary wires in the vicinity of the interaction. This is likely due to intense field emission from the second wire – which subsequently provides most of the return current for the hot electrons, which escape during the interaction. Structured x-ray emission patterns due to MHD m=0 instabilities could also be observed on both wires in time integrated x-ray pinhole images of the interaction. In comparison, when two secondary wires were used, second harmonic emission and plasma formation due to the generation of return current was only observed on one of the secondary wires – the one which was closest to the interaction wire.

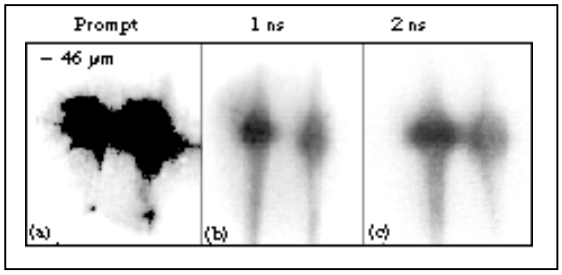

Figure 2. Optical frames showing emission from two wire targets. The laser is incident on the wire from right. The secondary target shows more emission and expansion.

Intense second harmonic emission from the secondary target was also observed in shadowgraphic channels (Figure 3). The secondary target was positioned out of the laser propagation direction at a distance of about 300 µm. A narrow interference filter with a bandwidth of 10 nm peaking at the second harmonic was used. The observed emission is due to the optical transition radiation caused by fast electrons accelerated by the electric field established between the main and secondary targets. Emission takes place when electrons pass from one medium to another and emission from the second wire demonstrates efficient energy coupling.

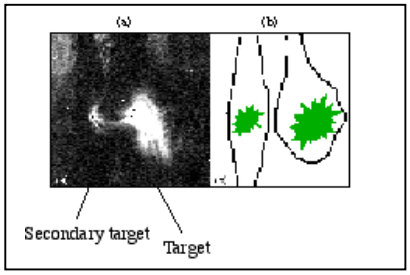

Figure 3. A shadowgram showing well localized second harmonic radiation from a secondary target. The secondary target was at about 300 µm distance from the main target. The schematic of the target arrangement is shown in (b).

In order to rule out other mechanisms, which can heat these wires and produce the optical emission, the laser was focused

on a 50 µm thick aluminum foil target and a wire was placed about 400 microns behind the foil. In this case, m=0 perturbations could also be observed on the secondary target. Figure 4 shows an image of optical emission recorded on the rear surface of the target. Intense optical emission from the rear surface of the target is clearly visible which is likely due to coherent optical transition radiation from the energetic electron beam leaving the target. This emission is also observable in wavelength ranges other than the second harmonics of the laser frequency. This is due to spread in the electron beam energy. Optical emission is also clearly observed from the secondary wire. The structure seen on this wire is similar to that observed in the time integrated x-ray pinhole images when the laser was incident on a single wire.

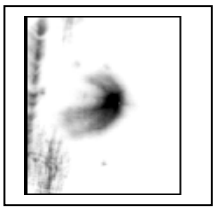

Figure 4. An optical frame showing second harmonic emission from the rear surface of the foil target. The m=0 sausage type instability is observed on a secondary wire target.

The hot electron current can be estimated using a simple energy balance equation[6], $fIA=(J_H/e)kT_H$, where f is the fraction of the absorbed energy into hot electrons, I is the intensity of the laser in W/cm^2, A is the area of the laser spot. This suggests that the hot electron current is approximately 3 MegaAmperes, using an intensity of 5 x 10^{19} W/cm^2, a spot size ~ 10 µm, 10% laser energy in hot electrons with an electron temperature of 1.25 MeV. This consequently would correspond to the magnitude of the return current in the wire near the interaction region. The target potential can also be estimated by assuming a Boltzmann distribution of energies for the hot electrons and the use of Gauss' law. This suggests that the potential is given by $\phi = \frac{Ne}{4\pi\varepsilon_o r}\exp\left(\frac{-(k_B T_{hot} - e\phi)}{k_B T_{hot}}\right)$

where N is the total number of electrons which escape the plasma and T_{hot} is the ponderomotive potential of the focused laser pulse. A target potential of up to 10 MV can be generated for interactions at 10^{21} W/cm^2 and can extend for several centimetres around the target.

In order to get a better understanding of the physical processes in these multi-component plane foil and secondary wire targets we have performed 2-1/2D collisionless PIC simulations using the OSIRIS code [8]. In the simulations, a laser wave at an intensity of 10^{20} W/cm^2 in a focal spot of 5µm diameter is incident in the positive x1 direction on a flat target of about 4µm thickness with a square 'wire' placed 4µm behind the foil. The electron density in the foil and the wire is 20 times the critical density. The dimensions of the target and separation between the secondary wire and the target are much smaller than used in the experiments and are limited by the computational cost. In the simulations the electrons in the foil and in the wire are treated as distinct species and may be plotted separately. Figure 5 shows some of the simulation results. In Figure 5a we plot the longitudinal phase space (p1 vs x1) of the 'foil' electrons at 120 fsec. The electrons in the foil target behave as normal and are strongly bunched at a frequency of 2ω corresponding to the **vxB** force of the laser. Most of the 'foil' electrons are reflected at a Debye sheath on the rear of the foil but some escape the foil leaving a large positive charge on the foil. Figure 5b shows the p1-x1 phase space of the 'wire' electrons at 180 fsec. The electrons from the wire are accelerated towards the foil and reach energies of more than 4 MeV (γ = 8). The white lines drawn in Fig 5b emphasise the bunching of the electrons leaving the wire and showing a similar periodicity to the laser accelerated electrons. This should give rise to the emission of second harmonic (green) light from the un-irradiated wire due to optical transition radiation. Indeed this is in excellent agreement with the experimental observations where well-localized second harmonic emission is observed from the secondary wire.

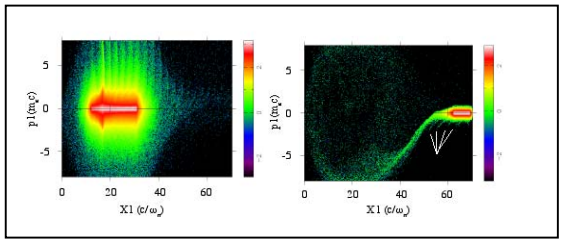

Figure 5. The longitudinal phase space of electrons from a foil target at 120 fs (left) and secondary wire target at 180 fs (right) using 2-1/2 D PIC simulations with OSIRIS code.

In conclusion, we have shown the first results of Ohmic heating of thin wire targets due to the return current in short pulse laser-solid interactions (i.e., laser-driven z-pinches). This current is produced by the escape of fast electrons from the target. We have also shown intense well localized optical emission from the secondary targets due to propagation of fast electrons.

In addition, we have observed growth of short wavelength modes of the m=0 "sausage" instability which is indicative of relatively slower growth due to shorter current pulses. This result may have important implications for future z-pinch experiments. Z-pinches were previously considered a good candidate for thermonuclear fusion experiments – since it was theoretically possible to radiatively "collapse" deuterium/tritium plasmas to high density. However, such experiments using pulsed power drivers showed that the pinch becomes unstable early in the discharge if the current is slowly rising (hundreds of nanoseconds). Short wavelength MHD instabilities grow and eventually destroy the pinch without the occurrence of uniform collapse. However for a laser-driven z-pinch using a laser intensity approaching 10^{21} W/cm^2, it may be possible to increase dramatically the energy and number of fast electrons that escape the target. As a result, return currents produced by escaping fast electrons can exceed multi-MegaAmpere levels and may have a current rise time, which is significantly less than the growth time for unstable MHD modes. Hence, such fast rising currents may be sufficient to make detailed studies of radiative collapse, which is presently not possible using pulsed power generators with current risetimes of hundreds of nanoseconds.

References

1. D. Strickland and G. Mourou, Opt. Comm. 56, 219 (1985).
2. M. Tatarakis *et al.*, Phys. Rev. Lett. 81, 999 (1998); M. Borghesi *et al.*, Phys. Rev. Lett. 83, 4309 (1999); L. Gremillet *et al.*, Phys. Rev. Lett. 83, 5015 (1999).
3. A. P. Fews *et al*, Phys. Rev. Lett. 73, 1801 (1994); E. L. Clark *et al.*, Phys. Rev. Lett. 84, 670 (2000); R. Snavely *et al.*, Phys. Rev. Lett. 85, 2945 (2000); M. I. K. Santala *et al.*, Appl. Phys. Lett. 78, 19 (2001); A. Maksimchuk *et al.*, Phys. Rev. Lett. 84, 4108 (2000); M. Zepf *et al.*, Phys. Rev. Lett. 90, 064801 (2003).
4. F. N. Beg *et al.*, Phys. of Plasmas 4, 447 (1997); R. D. Edwards *et al.*, Appl. Phys. Lett. 80, 2129 (2002).
5. R. F. Benjamin *et al.*, Phys. Rev. Lett. 42, 890 (1979).
6. A. Hauer and R. J. Mason, Phys. Rev. Lett. 6, 459 (1983).
7. M. G. Haines, Phys. Rev. Lett. 47, 917 (1981).
8. R. Hemker, Ph.D. Thesis, UCLA, 2000.

Relativistic electron acceleration with the Vulcan Petawatt laser

S P D Mangles, B Walton, M S Wei, A Gopal, Z Najmudin, A E Dangor, K Krushelnick

Blackett Laboratory, Imperial College, London, SW7 2BZ, UK

S Fritzler

Laboratoire d'Optique Appliquée, École Nationale Supérieure des Techniques Avancées, École Polytecnique, CNRS, UMR 7639, 91761 Palaiseau, France

D Neely, R J Clarke, C Hernandez-Gomez

Central Laser Facility, CCLRC Rutherford Appleton Laboratory, Chilton, Didcot, Oxon, OX11 0QX, UK

Main contact email address: *stuart.mangles@imperial.ac.uk*

Introduction

Laser-plasma acceleration is capable of producing extremely high accelerating electric field gradients that can generate high-energy electrons in very short distances. Experiments carried out with the 'Salle Jaune' laser at LOA[1)] have produced electrons up to 200 MeV in an acceleration length of less than 2 mm. Previous experiments with Vulcan prior to the upgrade have produced electrons up to 120 MeV [2)]. The acceleration mechanism for most previous experiments has been the production of relativistic plasma waves, which can trap and accelerate electrons, although there is some evidence that acceleration by the laser field itself can play a role[3)] through the interaction of the $\boldsymbol{v} \times \boldsymbol{B}$ force of the laser and the density channel caused by the laser beam's ponderomotive force.

Plasma acceleration offers the potential of significantly smaller acceleration facilities, which together with the rapid development of laser technology could allow university laboratory sized accelerators for use in a wide range of experiments. Of particular interest is the generation of short pulse, short wavelength light sources. This can be done by a number of methods: through coherent Thomson scattering from the accelerated electron bunch when a second TW laser is focused onto the bunch[4)]; by stopping the electrons in an appropriate target to produce a short burst of γ rays through bremsstrahlung radiation[5)] or by passing the electron bunch through a wiggler magnetic field to make a table-top free electron laser.

The Vulcan Petawatt upgrade allows experiments to be performed at higher intensities than has been previously available. The intensity, I, of a laser system is often described by the normalised vector potential of the laser field, $a_0 = eA/mc^2 \propto \sqrt{(I\lambda^2)}$ (A is the vector potential of the laser field, m is the electron mass and c is the speed of light). a_0 is also the normalised transverse momentum of the electron motion in the laser field. As a_0 approaches 1 the electron motion becomes relativistic. Previous experiments have been performed with a_0 between 1 and 5. The Vulcan Petawatt Upgrade allows us to access regimes where $a_0 >> 1$ (in the experiment reported here $a_0 \approx 15$).

Experiment

This report details the experimental measurement of energetic electrons produced by focusing the Vulcan Petawatt upgrade onto the edge of a supersonic gas jet. During this experiment Vulcan consistently produced 650 fs FWHM duration pulses delivering ~ 160 J on target. These pulses were focused with an f/3 off axis parabolic mirror to produce a focal spot with an intensity FWHM of ~ 10 µm, thus generating intensities greater than 3×10^{20} Wcm^{-2}.

The experimental set up is shown in Figure 1. The gas jet used has a 2mm diameter supersonic nozzle[6)] and could produce plasma electron densities between 5×10^{18} and 2×10^{20} cm^{-3}. The density was controlled by varying the backing pressure behind the valve of the gas jet. The density was measured using forward Raman scattering data. The gas used was Helium, which at the intensities produced will be fully ionized by the laser early in the interaction.

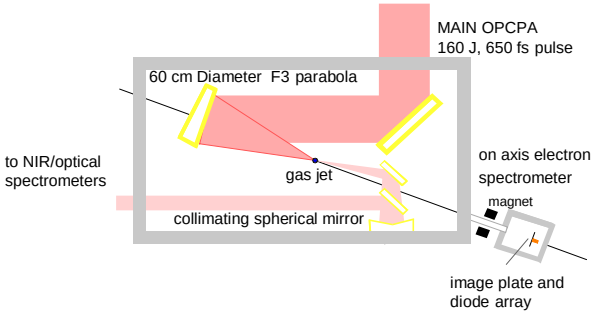

Figure 1. Experimental set-up.

The electrons accelerated along the axis of laser propagation were measured using a magnetic spectrometer. The electrons exited the highly shielded main vacuum chamber through a small (25 mm) diameter tube to a secondary vacuum vessel. This reduced the level of background signal from low energy x-rays and electrons. The entrance to the spectrometer is a 5 mm diameter hole that serves to collimate the electron beam to ensure sufficient energy resolution. The specially designed vacuum chamber allows the electron beam to pass between the pole pieces of an electromagnet that deflects the electrons off-axis. The magnetic field produced by the electromagnet is controlled by varying the current in the magnet coils. Magnetic fields can be produced up to ~ 0.8 T. The magnetic field region between the pole pieces has previously been mapped using a Hall probe and is very uniform, with small fringe fields at the edge of the pole pieces. The correspondence between electron energy and deflection from the axis is found using a charged particle tracking code that takes the fringe fields into account.

The electrons are detected by an image plate, a re-usable film sensitive to ionizing radiation. Two sections of image plate are used, one to measure the electron signal, deflected below the laser axis, and another to measure the background signal above the axis. Since the background is due to x-rays from the interaction itself or from bremsstrahlung radiation emitted by the electrons as they pass through material before the detector plane it is assumed that the background is symmetrical above and below the axis.

Image plates use a process called photo-stimulated luminescence (PSL). Europium atoms in the active layer of the plate are excited into a metastable state when they absorb energy from ionizing radiation incident on the plate. This leaves behind a latent image. To read the data the image plate is scanned with a helium-neon laser. This further excites the europium ions, which then relax by emission of a blue photon. A photo-multiplier then measures these photons and the intensity of PSL is recorded. The scanning and reading is performed with a commercially available scanner. The plates are read twenty minutes after the shot was fired because the scan takes approximately two minutes and the decay of the metastable state is such that twenty minutes after exposure there

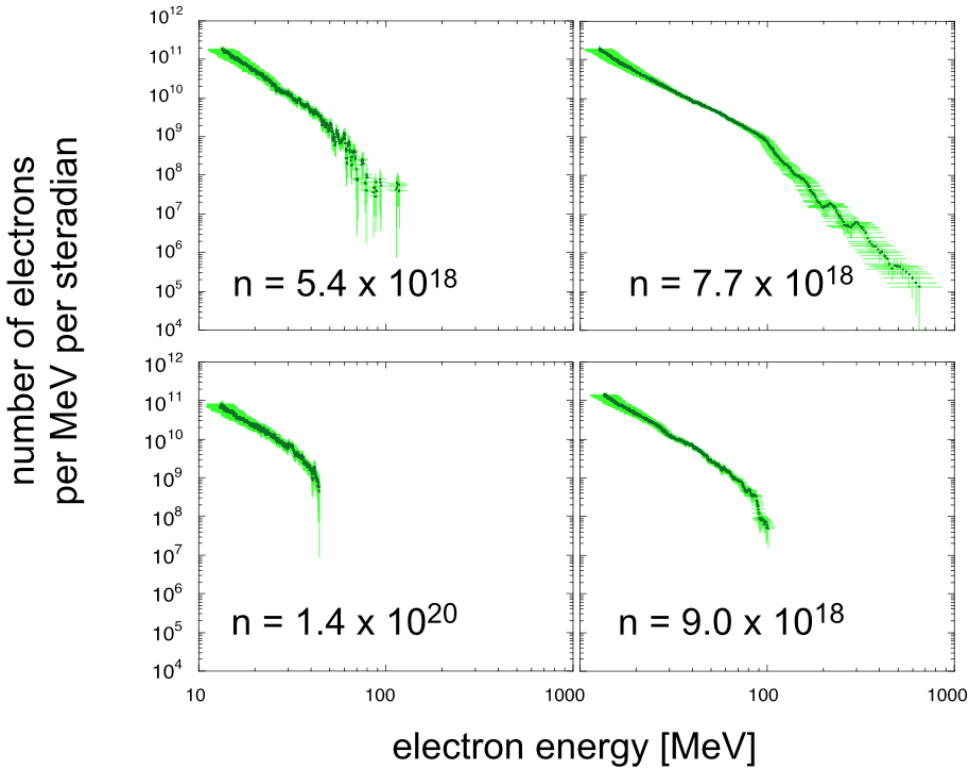

Figure 2. Measured electron spectra at various electron densities.

is no appreciable difference in the signal level between the beginning and end of the scan.

The relationship between PSL intensity and energy deposited in the plate is close to linear. This has been confirmed by x-ray studies[7] and the direct relationship between the number of electrons and signal was calculated by placing a diode array directly behind the image plates. The diodes used have a known response to the number of electrons within a particular energy range incident on them. By calculating the energy lost by the electrons as they travel through the plate before reaching the diodes it is possible to cross-calibrate the diode and image plate signals.

The image plate data exhibits a much larger dynamic range than the diodes and the image nature of the data allows much better noise discrimination. The resolution of the image plates, although not as high as x-ray film is much higher than the diode array. The combination of the resolution and size of the image plates (each is 250 mm long) allows a reasonably broad energy range (for example 10 – 700 MeV) to be measured on this spectrometer in a single shot.

The laser-plasma interaction was also diagnosed by measuring the transmitted spectrum of the laser. A portion of the transmitted beam was collimated and transported out of the vacuum chamber to a pair of near-infrared spectrometers; CCD cameras recorded the spectra on each shot at two different spectral dispersions. This allowed the simultaneous observation of Raman satellites and broadening of the main pulse at high resolution.

Results

Figure 2 shows a number of electron energy spectra obtained from shots with helium gas. These shots have been selected to show the trend observed as the density of the gas jet was varied. Electrons were accelerated to relativistic energies at all densities. The spectra can be characterised by a 'dual power law', where the number of electrons N with energy between E and $E + dE$ is given by $N(E)dE \propto E^{a(E)}$, where $a(E) \sim -5$ over the approximate energy range $10 < E < 100$ MeV and $a(E) \sim -2$ for $E > 100$ MeV. The change in the power law exponent with energy may well indicate that the highest energy electrons are accelerated by a different mechanism than the lower energy electrons. The spectra show all points where (signal/noise) > 1. Figure 3 shows explicitly how the acceleration varies with density. Three measures of the acceleration are shown, the energy at which the spectrum drops below the signal/noise threshold, the low-energy power law exponent and the high-energy power law exponent. All three clearly show a resonance near $n_e = (0.7 \pm 0.1) \times 10^{19}$ cm^{-3}.

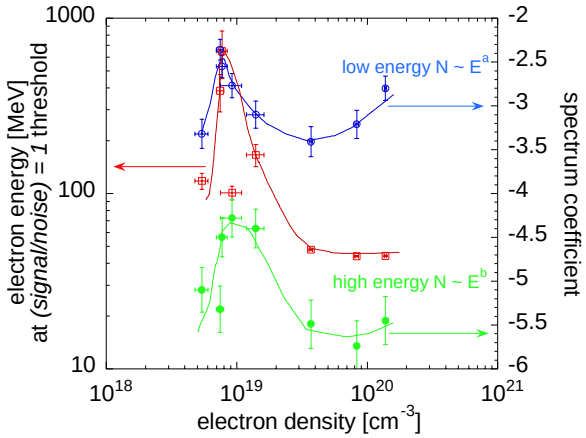

Figure 3. Variation of electron spectrum with density, showing electron energy at (signal/noise) = 1 and power law exponents for low and high energy components.

Figure 4 shows the relationship between the amount of forward Raman scattering (FRS) observed and the electron density. It is clear that the electron acceleration and FRS are uncorrelated. This is in marked contrast to previous experiments[5], and indicates that the acceleration mechanism is not self-modulated laser wakefield acceleration (SM-LWFA) as in previous lower intensity experiments on Vulcan[2,7].

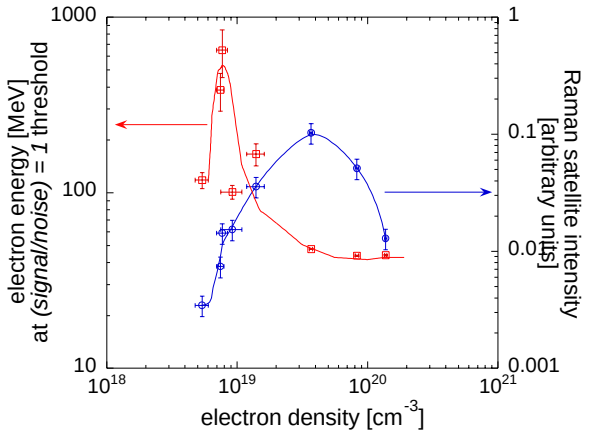

Figure 4. Comparison of density dependence of electron acceleration and Raman satellite intensity.

Other studies of electron acceleration with various lasers have shown different density dependences. A study with a 35 fs, 0.6 J laser pulse[6] showed no such resonance effect with the maximum electron energy broadly matching theoretical predictions for classical laser wakefield acceleration. An experiment with the Astra laser with 70 fs, 0.25 J pulses[9] does show an optimum density for acceleration near 9×10^{19} cm^{-3}. An experiment by Gahn et al.[10] with 200 fs, 0.25 J pulses showed an enhanced acceleration at 2×10^{20} cm^{-3}. In the Gahn study there is strong evidence that the electron acceleration is strongly correlated with channel formation and 3D PIC simulations by Puhkov[3] indicate that direct laser acceleration (DLA) is the dominant mechanism. Simulations of the results of Malka et al show that with the very short pulse used in those experiments the mechanism is predominantly wakefield acceleration.

Simulations

A limited number of 2D-3V PIC code simulations with OSIRIS[11] have been performed on the 24-node BEOWULF cluster available at Imperial College and appear to show that DLA is the dominant acceleration mechanism in the results reported here.

Simulations have been performed at various densities simulating realistic laser pulses incident on a fully ionized plasma with a linear density ramp from vacuum up to bulk plasma density over a distance of ~ 600µm. (This is consistent with the type of nozzle used in these experiments[5]). Each simulation has completed at least 2.5 ps of the experiment. This is not the entire experiment but computational time constraints limit the length that can be simulated. Future work will include the ejection of the electrons from the back of the gas jet.

The PIC code simulations show three apparent acceleration mechanisms. First, electrons are accelerated to ~10 MeV within the front half of the laser pulse. This is due to the ponderomotive force of the laser field. These accelerated electrons are bunched at twice the laser frequency, associated with the $\boldsymbol{v} \times \boldsymbol{B}$ force of the oscillating transverse fields. The acceleration is only in the front half of the pulse because this is where the ponderomotive force associated with the envelope (the intensity gradient) is pushing the electrons forward. Also the position of the peak electron energy during this phase corresponds to the maximum in the intensity gradient. The second acceleration mechanism occurs when the front of the laser pulse self-modulates, forming a plasma wave near the front of the pulse. This plasma wave traps and further accelerates a population of electrons. The electrons are trapped in bunches separated by the local plasma wavelength. Within these bunches the electrons remain bunched at twice the laser frequency indicating that the plasma wave traps electrons that are already accelerated by the ponderomotive force.

In the simulation at $n_e = 10^{19}$ cm^{-3} these are the only two acceleration mechanisms observed but at higher densities a third process occurs a few 100 fs after self-modulation starts. At this time a large number of electrons are accelerated behind the wakefield region but still within the laser pulse to very large energies (up to 800 MeV). The major difference between the low density and high density case is that at $n_e = 10^{19}$ cm^{-3} the magnetic field generated by the current of electrons accelerated by the ponderomotive and wakefield mechanisms is an order of magnitude lower than the higher density cases. This seems to follow the pattern of direct laser acceleration described by Puhkov et al.

As the density is increased above $n_e = 10^{20}$ cm^{-3} the propagation of the laser beam becomes unstable, with filamentation and hosing type instabilities being observed after ~2 ps. Plots of the normalised laser intensity after 2.5 ps for simulations at $n_e = 1.0 \times 10^{19}$ and 1.4×10^{20} cm^{-3} are shown in Figure 5. These instabilities appear to be closely related to self-focusing of the laser pulse.

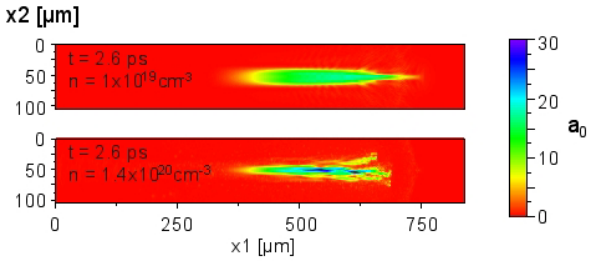

Figure 5. Simulated laser intensity after 2.6ps (780 µm) propagation. The high density case shows manifestation of filamentation and hosing instabilities.

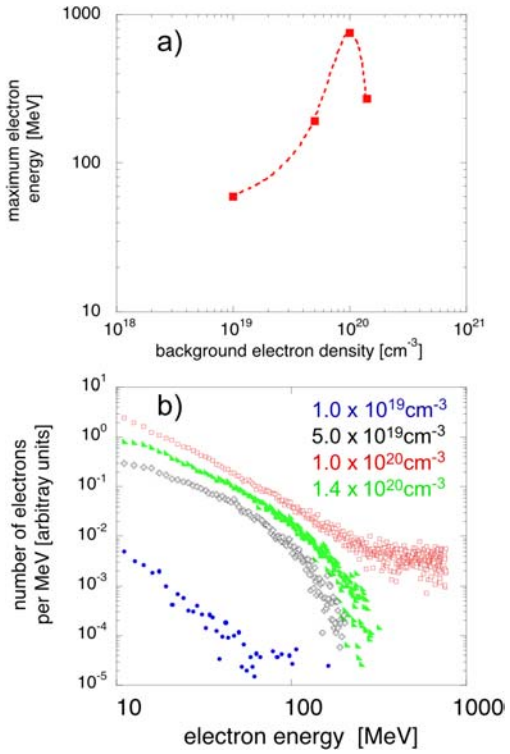

Figure 6. a) electron acceleration density dependence observed in PIC simulations and b) electron energy spectra from the same simulations.

Figure 6a shows the electron energy spectra produced by the PIC code at 2.5 ps. These spectra mimic the experimental electron spectrometer by only including electrons within a cone

angle of ~ 2×10^{-3} radians, matched to the acceptance cone of the real spectrometer. It should be noted however that these spectra are the instantaneous energy spectra taken while the electrons are still within the plasma. The ejection of the electrons from the back of the plasma may play an important role in determining the final energy spectrum since space charge effects as the electron bunch leaves will affect lower energy electrons differently from higher energy electrons.

Figure 6b shows the relationship between maximum electron energy and density from the simulations. This is very similar in shape to the experimental data, except that the peak occurs at $n_e = 10^{20}$ cm^{-3} in the simulations compared with $n_e = 10^{19}$ cm^{-3} in the experiment. The difference in density may be attributed to the close to ideal laser parameters used in the simulation; the laser pulse is a diffraction limited Gaussian spot of 7 µm diameter, corresponding to an f/2.7 focusing optic compared with the f/3.1 optic used during the experiment. Since channel formation and filamentation instabilities are closely related to the initial laser power and intensity it is reasonable to think that they may have a strong effect on the acceleration resonance.

Instabilities in the propagation of the laser pulse could affect the electron acceleration in two ways. Filamentation could break up the accelerating structures (effectively destroying the density channel necessary for DLA) and hosing could deflect the highest energy electrons away from the axis. In the simulations reported here the highest energy electrons do follow the hosing laser beam, although if this deflection were the only cause in the experimentally observed resonance we would expect the degree of acceleration observed above the resonant density to be more random. This is not the case - all shots above the resonant density produced similar spectra. The observed resonance is therefore most likely due to a combination of the two instabilities "switching off" the most efficient acceleration mechanism. Future experiments could use whole beam measurements of the energy spectrum using photo-nuclear techniques[2)] to determine whether the maximum energy is off-axis at high density and transverse optical probing techniques could be used to try to observe the hosing and filamentation instabilities seen in the simulations.

In summary the first 'user experiment' on the Vulcan Petawatt Upgrade has successfully accelerated electrons well beyond 200 MeV. This is the highest energy observed from any laser-plasma interaction to date. It appears that the increase in intensity has moved Vulcan from operating in the SM-LWFA regime to one where a DLA type mechanism is dominant.

Acknowledgements

We gratefully acknowledge the OSIRIS consortium which consists of UCLA/IST(Portugal)/USC for the use of OSIRIS. We would also like to thank the staff of the Central Laser Facility at RAL for help in the successful delivery of the first user experiment on the Vulcan Petawatt upgrade.

References

1. V. Malka *et al*, Science, 298, 1596 (2002)
2. M.I.K. Santala *et al*, Phys. Rev. Lett., 86, 1227 (2001)
3. C. Gahn *et al*, Phys. Rev. Lett., 83, 4772, (1999)
4. R.D. Edwards *et al*, App. Phys. Lett., 80, 2129 (2002)
5. V. Malka *et al*, Rev. Sci. Inst. 71, 2329 (2000)
6. R.D. Edwards, AWE Plc., private communication
7. A. Modena *et al*, Nature (London) 377, 606, (1995)
8. V. Malka *et al*, Phys. Plasmas, 8, 2605, (2001)
9. S.P.D. Mangles, this report, 71, (2003)
10. C. Gahn *et al*, Phys. Plasmas, 9, 987, (2002)
11. R. Hemker, Ph.D Thesis, UCLA, (2000)

Proton emission from wire targets

F N Beg, E L Clark*, M S Wei, A E Dangor, R G Evans*, A Gopal, M Tatarakis, K Krushelnick
The Blackett Laboratory, Imperial College, London, SW7 2BZ, UK

P A Norreys, M Tolley, K L Lancaster, R J Clarke
Central Laser Facility, CCLRC Rutherford Appleton Laboratory, Chilton, Didcot, Oxon, OX11 0QX, UK

M Zepf
Department of Physics, The Queens University, Belfast, BT7 1NN, UK

P McKenna, K W D Ledingham*, T McCanny
Department of Physics, University of Strathclyde, Glasgow, G4 0NG, UK

* *also at AWE plc, Aldermaston, Reading, RG7 4PR, UK*

Main contact email address: *f.beg@ic.ac.uk*

Introduction

Recently, there has been considerable progress in the study of the electron and proton beams[1,2] generated in high intensity short pulse laser solid interactions. The interest in charged particle beams is primarily due to a number of applications such as in table-top accelerators, production of radioisotopes, and in fast ignition for inertial confinement fusion. Most of the applications require highly collimated beams with little divergence and energy spread. It has been proposed[3] that the targets of various materials and configurations can shape the proton angular emission.

In previous experiments[4,5] at $5x10^{19}$ Wcm^{-2} incident on plane targets, we have observed proton emission from thin foil targets of several materials. When diagnosed with a stack of radiochromic film and CR39 detectors behind the target, the protons from the front appear as highly divergent rings from low to high energy. The protons from the back appear as only a low energy, low divergent disc. Maximum proton energies above 40 MeV have been observed. With wedge targets[6], the proton beam was observed to emanate from each of the two rear surfaces clearly indicating that the target geometry is of significant importance.

In this report we present observations of proton emission from wire targets. We show that proton emission depends on location where the wire is irradiated with the laser - either on the tip of the wire or elsewhere along the wire. We also show that the presence of additional wire or foil nearby the target wire affects the spatial structure of the proton emission.

Experimental Setup

Experiments were carried out with the CPA beam of the Vulcan Nd:glass laser system at Rutherford Appleton Laboratory. The laser wavelength was 1.054 µm, the pulse length was 0.9 – 1.3 psec and the energy on target was between 60 and 80 J. The laser was focused with an off-axis parabolic mirror with a focal length of 60 cm to give a focal spot size of 10 µm. The maximum intensity was 5×10^{19} Wcm^{-2}. The diameter of the wire target was 20 µm so that there was no leakage of the laser beam around the wire. The length of the wires was either 3 or 5 mm, usually of copper but glass and gold wires were also used in some shots. The wire axis was perpendicular to the p-polarized laser. In some shots one or two additional wires were placed close by the target wire. These additional wires were positioned so as to avoid any direct illumination from the laser. A schematic of the experimental set up is shown in Figure 1.

A probe beam (527 nm, 1 ps) at 45° to the main interaction beam and perpendicular to the wire axis was used for shadowgraphy. The timing of the probe beam was varied with respect to the main laser beam.

Angular and energy distribution of proton emission were measured using stacks consisting of alternate layers of radiochromic film (RCF) and CR39 plastic nuclear track detectors. The stack was covered in 12 µm aluminium foil to absorb low energy charged particles and plasma radiation. The stopping power of protons in radiochromic film and CR39 is well known – so at a particular layer in the stack the energy of protons producing the signal can be easily determined[4]. The CR39/RCF detector stack was placed behind the target at 45° to the main beam. A stack was also placed in the blow-off direction for some shots. A time integrated x-ray pinhole camera was also used to determine the size of x-ray emitting region with 12 µm resolution.

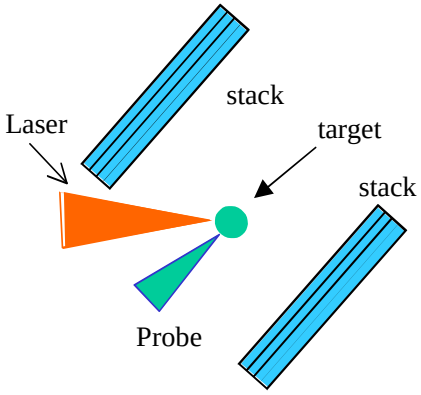

Figure 1. A schematic of the experimental setup.

Results

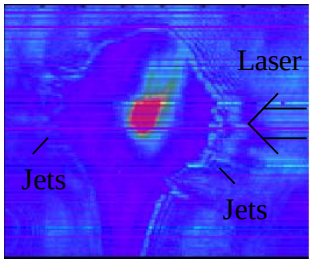

Figure 2. Shadowgram showing expansion of the plasma near the tip of the wire. The jet like structure on the front and rear is evident.

Figure 2 shows a shadowgram at 300 ps after the main laser beam. An interference filter at 2ω was used. The laser was focused at 50 µm below the tip of the wire (9 µm glass). The shadowgram shows expansion of the plasma at the tip of the wire and jet like structures perpendicular to wire axis at the front and rear of the interaction region. Intense second harmonic emission can also be seen.

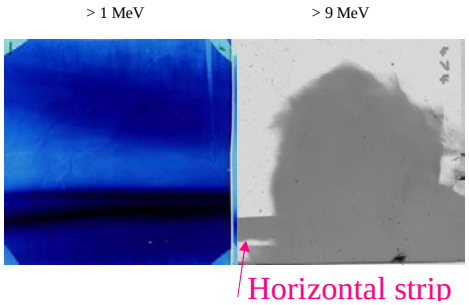

Figure 3. Scanned images of both RCF and CR39 show strip structure. The blob structure is evident only on the CR39 detector.

In Figure 3 the scanned images of radiochromic film (RCF) and CR39 at different depths in the stack are shown. On the first layer of RCF, which is sensitive to proton energy > 1 MeV, three structures are seen - a diffuse stripe above two well-defined intense horizontal stripes 4 millimetres apart. The stripes are uniform along the whole width of the RCF. On the second layer of RCF sensitive to protons > 3 MeV, only the double stripes are present indicating that the diffuse stripe is due to low energy protons. The CR39 layers deep inside the stack, which are sensitive to protons, show that the stripes are due to protons. We infer the maximum proton energy of 9 MeV and angular width of 3.6^0. A blob is also recorded on both CR39 layers. The size of the blob decreases with increasing energy and a cone angle of 22^0 at 9 MeV energy is measured. It is interesting to note that the blob is emitted at 45^0 to the laser beam propagation direction. This may be due to the directionality of the electron beam from the target accelerating protons.

In some shots the focal spot on the wire was moved 2 mm from the tip. The diffuse stripe and blob are not seen. Thus they must be due to the laser being focused near the top. When the stack of RCF/CR39 was moved to the blow-off direction, a horizontal stripe with the same vertical half angle as in the forward direction is observed. This may be due to the stripe being symmetric all the way around the wire, but this has to be checked.

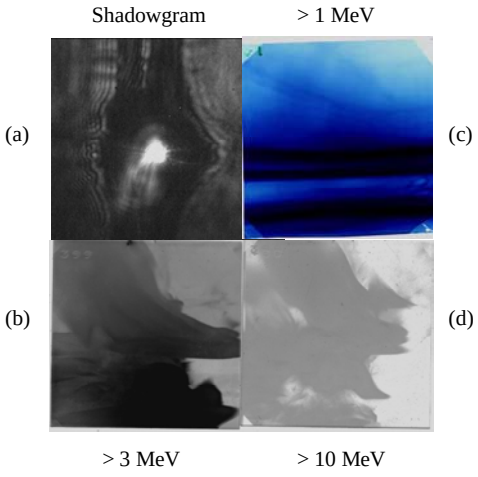

Figure 4. (a) A shadowgram shows a second harmonic emission from the target wire and additional wire. (c)Two sets of stripes can be seen on RCF due to protons (> 1 MeV) and (b) a complex proton structure on CR39 detector with proton energy between 3-9.5 MeV. Stripes are of low energy and are not seen in (d).

Observations were also made with an additional wire close to the target wire. Again a stack of RCF and CR39 was used as shown in Figure 1. Both wires were of equal length and 250 µm apart. The laser was focused halfway down the wire. The shadowgram (see Figure 4) shows intense second harmonic emission from both the target wire and additional wire. The second harmonic emission may be due to coherent optical transition radiation (OTR) produced by the bunches of the relativistic electrons generated at 2ω which is the frequency expected for **JxB** force of the laser. When these relativistic electrons pass through from one medium to another, they emit radiation called optical transition radiation (both coherent and incoherent).

The RCF/CR39 stack shows that there are two sources of protons – two sets of stripes are evident in both RCF and CR39. From the CR39 scans, we can infer that the stripes are due to protons. Both sets of stripes have a half angle of $4\text{-}5^0$. On the CR39 detecting protons above 10 MeV (Figure 4), a complex structure is observed. The two sets of stripes may be due to emission from the wire target and the additional wire. If this is true, we can infer an angle of $16^o \pm 8^o$ between these wires, which is likely to be the case. The proton emission observed implies that there are hot electrons generated at both wires. This is consistent with the shadowgram, which shows coherent OTR emission from both wires and also there is a radial expansion of the wires, which is due to return current heating[7].

Finally, shots were taken with the configuration shown in Figure 5a where a 50 µm aluminium foil is inserted between the two wires. The laser is focused on one wire. The foil plane is tilted with the direction of observation so that only the back surface is in the field of view. The shadowgram in Figure 5b shows intense second harmonic emission from the target wire and from the rear surface of the foil. This is clear evidence that relativistic electrons are accelerated from the target foil. This is consistent with proton emission observed on the stack of RCF/CR39. On the first layer of RCF a disk with a half angle of 16^0 is observed. This disk is also seen on the CR39 layer (> 3 MeV). The absence of the stripe could be due to absorption of protons produced at the target wire by the foil.

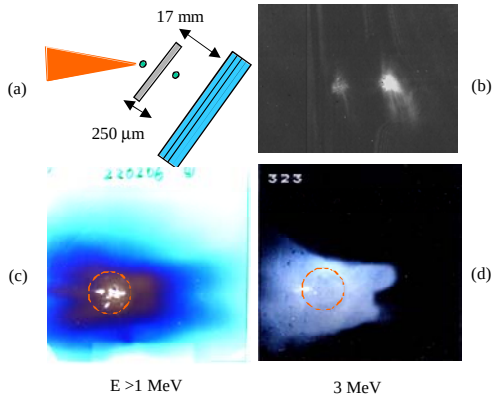

Figure 5. a) Schematic of the target setup. In b) shadowgram shows the second harmonic emission from the rear of the foil. The disk structure due to proton emission is evident in c) on RCF and d) on CR39 detectors. The encircled regions in (c) and (d) show disk structure.

Conclusions

To conclude, we have shown that the protons are generated symmetrically around a wire when a high intensity laser is focused on the wire and if the focal spot is close to the tip of the wire, proton structure modifies. The second harmonic emission is produced due to coherent OTR by bunches of electrons accelerated by the **JxB** force of the laser. Furthermore, coherent OTR and protons are also generated at an additional wire or foil.

Acknowledgements

The authors would like to acknowledge assistance of the staff of the Central Laser Facility of the Rutherford Appleton Laboratory. We also thank the UK Engineering and Physical Sciences Research Council (EPSRC) for the financial support.

References

1. M. Tatarakis *et al*., Phys. Rev. Lett. 81, 999 (1998); M. Borghesi *et al*., Phys. Rev. Lett. 83, 4309 (1999); L. Gremillet *et al*., Phys. Rev. Lett. 83, 5015 (1999).
2. A. P. Fews *et al*, Phys. Rev. Lett. 73, 1801 (1994); E. L.Clark *et al*., Phys. Rev. Lett. 84, 670 (2000); R. Snavely *et al*., Phys. Rev. Lett. 85, 2945 (2000); M. I. K. Santala *et al*., Appl. Phys. Lett. 78, 19 (2001); A. Maksimchuk *et al*., Phys. Rev. Lett. 84, 4108 (2000);
3. A. Pukhov, Rep. Prog. Phys. 66, 47 (2003).
4. E. L. Clark *et al*., Phys. Rev. Lett., 84, 670 (2000); E. L. Clark *et al*., Phys. Rev. Lett. 85, 1654 (2000)
5. M. Zepf *et al*., Phys. Rev. Lett. 90, 064801 (2003).
6. E. L. Clark *et al*., to be published.
7. F. N. Beg *et al*., this report, 14, (2003)

Heavy ion-induced reactions in ultrahigh-intensity laser interactions with heated solid targets

P McKenna, K W D Ledingham*, J Yang, S Shimizu, T McCanny, L Robson

Department of Physics, University of Strathclyde, Glasgow, G4 0NG, UK
**also at AWE plc, Aldermaston, Reading, RG7 4PR, UK*

R P Singhal, I Spencer

Department of Physics and Astronomy, University of Glasgow, Glasgow, G12 8QQ, UK

R J Clarke, P A Norreys, K L Lancaster, S Karsch

Central Laser Facility, CCLRC Rutherford Appleton Laboratory, Chilton, Didcot, Oxon, OX11 0QX, UK

M S Wei, K Krushelnick, P Nilson, S P D Mangles, F N Beg

Blackett Laboratory, Imperial College, Prince Consort Road, London, SW7 2BZ, UK

E L Clark

AWE plc, Aldermaston, Reading, RG7 4PR, UK

J Galy, J Magill

European Commission, Joint Research Centre, Institute for Transuranium Elements, Postfach 2340, 76125 Karlsruhe, Germany

K Spohr, R Chapman

Department of Electronic Engineering and Physics, University of Paisley, PA1 2BE, UK

Main contact email address: *p.mckenna@phys.strath.ac.uk*

Introduction

There is widespread interest in the use of high-intensity (>10^{19} Wcm^{-2}) laser-produced plasmas as sources of energetic ions. Beams of protons with energies up to 58 MeV[1)] and heavier ions with about 5 MeV per nucleon[2,3)] have been demonstrated experimentally. The many exciting applications for these potentially compact sources of energetic ions include isotope production for nuclear medicine[4)] and injectors for future large-scale ion accelerators[2)].

Due to their higher charge-to-mass ratio, protons, which result from water and hydrocarbon contamination layers on the surfaces of solid targets, are more efficiently accelerated than any other ion species and effectively screen the acceleration potential, reducing the efficiency of heavy ion acceleration. It has been demonstrated recently using Thomson parabola ion spectrometers that heating the solid target reduces the contamination layers, and hence the proton flux, increasing the numbers of heavier ions accelerated[3,5)]. The present work further diagnoses the effect of target heating on ion acceleration through measurements of nuclear activation reactions.

Experimental

This work was carried out during separate experiments using the 100 TW and petawatt arms of the Vulcan laser. In the first experiment pulses with energy up to 100 J at a wavelength of 1.053 μm and temporal duration of ~1 ps were focused to a maximum intensity of 5 x 10^{19} Wcm^{-2}, using an f/3 off-axis parabolic mirror. The *p*-polarised laser beam was incident onto 100 μm thick, 5 x 5 mm Al targets at an angle of 45° to the target normal, within a vacuum chamber maintained at 10^{-5} mbar. The Al target foil was radiatively heated to a constant temperature for approximately 20 minutes before laser irradiation. Secondary activation ^{48}Ti samples were positioned at the front of the target (the 'blow-off' direction).

In the second experiment pulses with energy up to 300 J and duration 0.7 ps were focused to a maximum intensity of 6 x 10^{20} Wcm^{-2} onto 100 μm thick Fe foils. The foils were resistively heated to temperatures in excess of 800°C and secondary catcher ^{12}C samples were positioned in the blow-off direction as shown in Figure 1.

In both experiments the secondary catcher samples were analysed after each laser shot using two well-shielded Germanium detectors (25% and 35% efficient). The samples were analysed for sufficiently long counting times to identify the nuclides produced based on their emitted gamma ray energies and their half-lives.

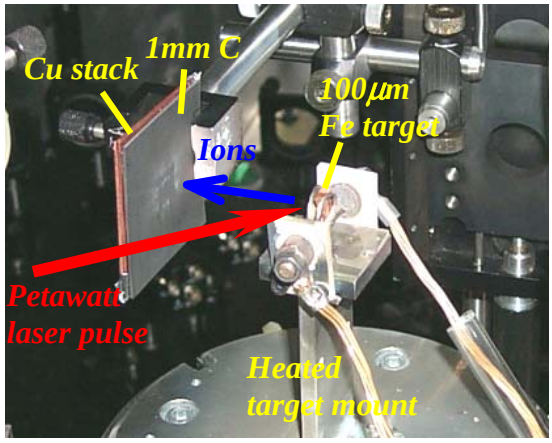

Figure 1. Typical set-up for the heavy ion reaction experiment. The laser is focused onto the primary foil target, which can be either resistively or radiatively heated. Ions accelerated from the resulting plasma induce nuclear reactions in activation samples centred on the target normal axis.

Results

Figure 2 (a) and (c) shows parts of the measured gamma-ray spectrum observed from a ^{48}Ti catcher sample after irradiation of an unheated Al target foil with 73 J of laser energy. Characteristic gamma-ray lines of ^{48}V, ^{47}V and ^{44}Sc are observed, and result from the proton induced reactions (p,n), (p,2n) and (p,α+n) respectively. Using the peaked cross-sections for these reactions it has been determined that ~10^{10} protons with energies in the range 10 to 30 MeV are required to produce the activities observed. Only proton-induced nuclear reactions were observed from the unheated Al target.

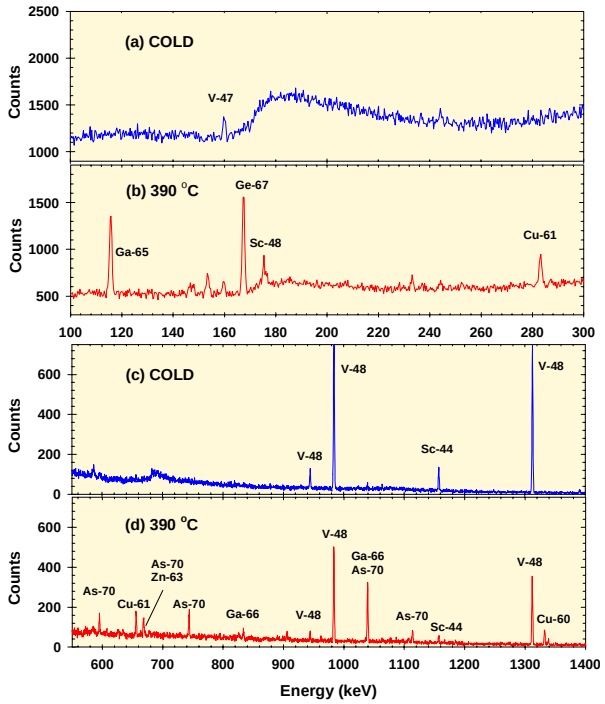

Figure 2. Gamma-ray spectra observed in a Ti sample after irradiation with ions from a primary Al target which was (a) and (c) cold and (b) and (d) heated to 390 °C.

The gamma-ray spectrum obtained from a ^{48}Ti activation sample with an ^{27}Al foil target heated to 390°C is shown in Figure 2(b) and (d). Signature peaks of ^{48}V, and ^{44}Sc are detected with much reduced intensity. The proton flux required to induce the observed activity is reduced by a factor of between three and five with the hot target.

Importantly, a range of additional nuclei are observed with the heated target, namely ^{70}As, ^{69}As, ^{67}Ge, ^{66}Ga, ^{65}Ga, ^{63}Zn, ^{61}Cu and ^{60}Cu. Compound nuclear formation followed by particle evaporation ('fusion-evaporation') is primarily responsible for the production of the observed nuclei. Fast ^{27}Al and ^{16}O ions interact with stationary ^{48}Ti atoms in the secondary catcher material to induce compound nucleus formation. The excited compound nuclei decay by evaporating protons, neutrons and alpha particles leaving residual nuclei, which emit characteristic gamma radiation. The possible reaction channels are identified in Table 1 and the cross-sections for these reactions, as determined using the Monte-Carlo code PACE-2 [6] (projection angular-momentum coupled evaporation), are shown in Figure 3.

Nuclides	Half-life	No. of Nuclei	Reactions
Cold			
^{48}V	15.9 d	5.5 x 10^{6}	^{48}Ti(p,n)^{48}V
^{47}V	32.6 m	6.0 x 10^{5}	^{48}Ti(p,2n)^{47}V
^{44}Sc	3.9 h	8.9 x 10^{3}	^{48}Ti(p,α+n)^{44}Sc
Hot			
^{48}V	15.9 d	1.8 x 10^{6}	^{48}Ti(p,n)^{48}V
^{44}Sc	3.9 h	2.0 x 10^{3}	^{48}Ti(p,α+n)^{44}Sc
^{70}As	52.6 m	7.6 x 10^{3}	^{27}Al+^{48}Ti→^{70}As+1α+1n
^{69}As	15.2 m	1.0 x 10^{4}	^{27}Al+^{48}Ti→^{69}As+1α+2n
^{67}Ge	18.7 m	4.7 x 10^{3}	^{27}Al+^{48}Ti→^{67}Ge+1α+3n+1p
^{66}Ga	9.5 h	8.2 x 10^{4}	^{27}Al+^{48}Ti→^{66}Ga+2α+1n
^{65}Ga	15.2 m	8.6 x 10^{3}	^{27}Al+^{48}Ti→^{65}Ga+2α+2n
^{63}Zn	38.1 m	1.0 x 10^{5}	^{16}O+^{48}Ti→^{63}Zn+1n
			^{27}Al+^{48}Ti→^{63}Zn+2α+3n+1p
^{61}Cu	3.4 h	5.5 x 10^{4}	^{16}O +^{48}Ti→^{61}Cu+2n+1p
			^{27}Al+^{48}Ti→^{61}Cu+3α+2n
^{60}Cu	24.4 m	3.6 x 10^{3}	^{16}O +^{48}Ti→^{60}Cu+3n+1p
			^{27}Al+^{48}Ti→^{60}Cu+3α+3n

Table 1. Residual nuclei observed in the titanium activation target. The numbers of each nuclei produced are per laser shot and have been corrected for detection efficiency and gamma emission probability per disintegration. Proton induced and energetically favourable heavy-ion fusion-evaporation reaction channels are identified.

^{61}Cu, ^{60}Cu and ^{63}Zn could be produced via ^{27}Al+^{48}Ti or ^{16}O+^{48}Ti evaporation reactions, but the relatively high cross-sections at low energies for the latter would suggest this to be the likely channel for the production of ^{61}Cu and ^{60}Cu (Table 1). The acceleration of O ions from an Al target foil has been observed in a previous experiment and is attributed to the presence of H_2O and oxide layers on the target surface[7]. The cross-sections for ^{27}Al+^{48}Ti reactions have more than one peak, suggesting more than one evaporation channel leading to the same residual nuclide. The lowest energy channels are peaked at energies between 80 and 120 MeV for the production of ^{70}As, ^{69}As, ^{67}Ge, ^{66}Ga and ^{65}Ga. The relatively high energies required to observe even the lowest energy reaction channels may explain why these nuclei are not observed with the cold target. Target heating increases the mean Al ion energy, populating these reaction channels with greater efficiency.

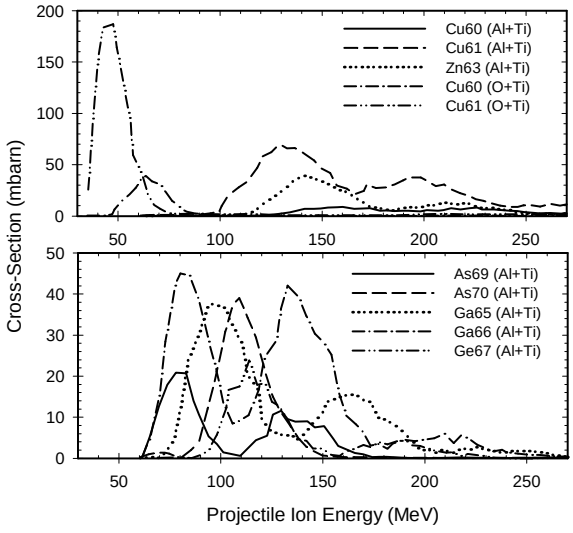

Figure 3. Cross-sections for evaporation from ^{27}Al+^{48}Ti and ^{16}O+^{48}Ti compound nuclei, calculated using the PACE-2 code.

In the second experiment a primary target, ^{56}Fe, with a mass much greater than the contaminants was chosen to remove any ambiguity in identifying the heavy-ion-induced reaction channels. The unheated ^{56}Fe foil target was initially irradiated with a 90 J laser pulse (in Target Area West) and characteristic peaks of ^{67}Ge, ^{66}Ge, ^{66}Ga, ^{65}Ga, ^{63}Zn, ^{62}Zn, ^{61}Cu and ^{60}Cu, were observed in the C secondary material. Later a similar experiment was carried out in the Petawatt Target Area with a 250 J pulse focused onto the unheated Fe target foil. A similar range of isotopes were detected with similar activity, Figure 4(a). However with the Fe target heated to 860°C and with a laser pulse energy of 270 J a significant increase in the activity of these isotopes was observed, as manifested in the increased peak heights of Figure 4(b). The fusion-evaporation reactions leading to the production of these residual isotopes are identified in Table 2 and their cross-sections, as calculated using the PACE2 code are illustrated in Figure 5.

Fortunately the cross-sections for the observed reactions are peaked in different regions of the projectile ion energy spectrum. This has enabled the Fe ion energy distributions to be calculated, by convoluting the cross-sections and stopping powers, over a range of energies extending beyond 400 MeV. The result of these calculations is shown in Figure 6. The effect

of heating the target is to increase the Fe ion flux by about an order of magnitude.

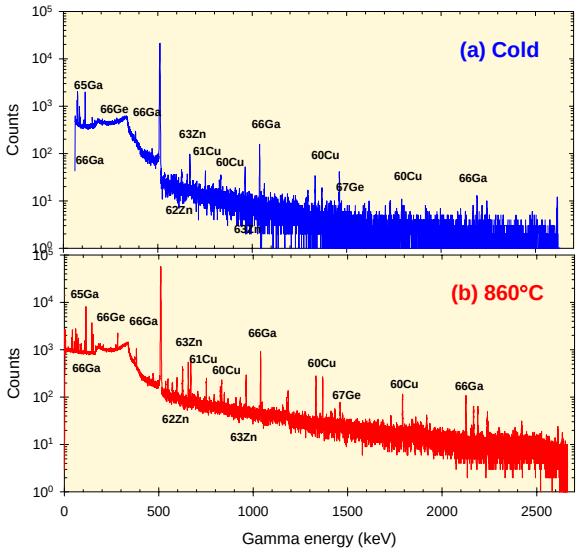

Figure 4. Gamma-ray spectra observed in a C activation sample after irradiation with ions from a primary Fe target foil which was (a) unheated and (b) heated to 860 °C.

^{56}Fe + ^{12}C Reactions	Half-life	Number of nuclei, *N*	
		Unheated	**860°C**
^{67}Ge +1n	18.7 m	1.6 x 10^3	4.3 x 10^4
^{66}Ge +2n	2.3 h	3.3 x 10^3	4.3 x 10^5
^{66}Ga +1n+1p	9.5 h	2.5 x 10^4	3.5 x 10^6
^{65}Ga 2n+1p	15.2 m	8.4 x 10^3	1.7 x 10^6
^{63}Zn +1α+1n	38.9 m	9.5 x 10^3	1.9 x 10^6
^{62}Zn +α+2n	9.3 h		
^{61}Cu +1α+2n+1p	3.4 h	6.3 x 10^3	1.7 x 10^6
^{60}Cu +1α+3n+1p	24.4 m	8.3 x 10^2	2.7 x 10^5

Table 2. List of fusion-evaporation reactions observed in the C activation target. The numbers of each nuclei produced are per laser shot and have been corrected for detection efficiency and gamma emission probability per disintegration.

By mounting Cu activation samples behind the C catcher sample, as shown in Figure 1, it was possible to measure proton induced reactions for the same heated and unheated target shots. The activity of ^{63}Zn produced from (p,n) reactions on ^{63}Cu was decreased by more than two orders of magnitude for the heated target shot.

Conclusions

In conclusion, ion-induced reactions have been used to diagnose ion acceleration in high-intensity laser-plasma interaction experiments with heated and unheated targets. Analysis of the reaction products indicates that sufficient heating of a target foil removes contamination layers and reduces the proton flux by orders of magnitude, resulting in a more efficient acceleration of heavier ions.

The use of target heating to selectively open reaction channels in the study of heavy-ion-induced reactions has been demonstrated. This work also has implications for the use of laser-plasma based ion accelerators as potential injectors for future heavy ion accelerators.

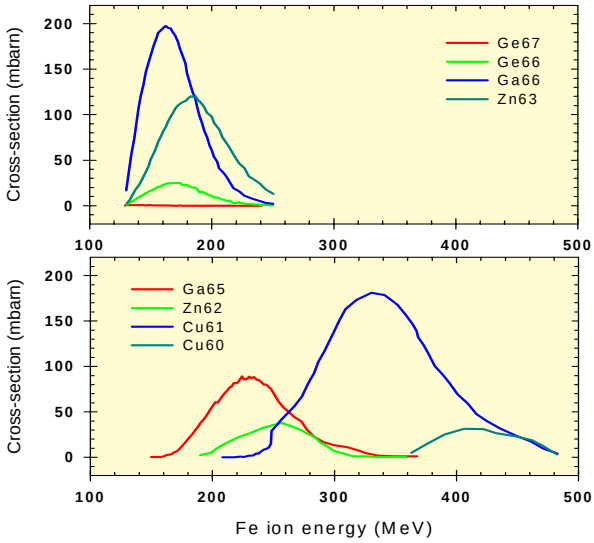

Figure 5. Cross-sections for evaporation from ^{56}Fe+^{12}C compound nuclei, calculated using the PACE-2 code.

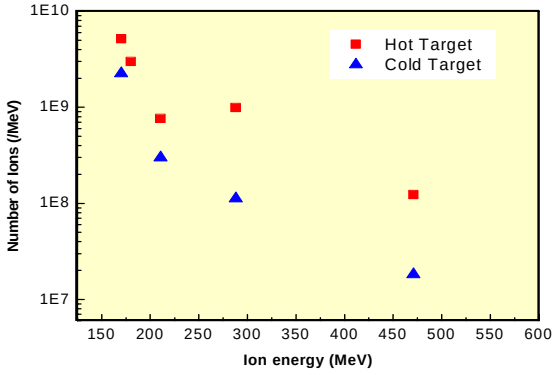

Figure 6. Fe ion energy spectra deduced from measurements of fusion-evaporation reactions. The flux of ions is increased by target heating.

Acknowledgements

We would like to acknowledge the expertise of the Vulcan operations team. PMcK is supported by a Royal Society of Edinburgh/SEELLD research fellowship. SS acknowledges support from the Japanese Society for the Promotion of Science. This work is funded by the EPSRC(UK).

References

1. J. T. Mendonça, J. R. Davies, and M. Eloy, Meas. Sci. Tech. 12, 1801 (2001).
2. K. Krushelnick *et al.* IEEE Transactions on Plasma Science 7, 2055 (2000).
3. M. Hegelich *et al.* Phys. Rev. Lett. 89, 085002 (2002).
4. K. W. D. Ledingham, P. McKenna, and R. P. Singhal Science 300, 1107 (2003).
5. M. Zepf *et al.* Phys. Rev. Lett. 90, 064801-1 (2003).
6. A. Gavron Phys. Rev. C 21, 230 (1980).
7. P. McKenna *et al.* Phys. Rev. Lett., In press (2003).

Fusion-evaporation and direct-interaction nuclear reactions using Vulcan

P McKenna, K W D Ledingham*, T McCanny

Department of Physics, University of Strathclyde, Glasgow, G4 0NG, UK
** also at AWE plc, Aldermaston, Reading, RG7 4PR, UK*

R P Singhal, I Spencer

Department of Physics and Astronomy, University of Glasgow, Glasgow, G12 8QQ, UK

M I K Santala, F N Beg, K Krushelnick, M Tatarakis, M S Wei

Blackett Laboratory, Imperial College, Prince Consort Road, London, SW7 2BZ, UK

E L Clark

AWE plc, Aldermaston, Reading, RG7 4PR, UK

R J Clarke, K L Lancaster, P A Norreys

Central Laser Facility, CCLRC Rutherford Appleton Laboratory, Chilton, Didcot, Oxon, OX11 0QX, UK

K Spohr, R Chapman

Department of Electronic Engineering and Physics, University of Paisley, PA1 2BE, UK

M Zepf

School of Mathematic and Physics, Queens University Belfast, Belfast, BT7 1NN, UK

Main contact email address: *p.mckenna@phys.strath.ac.uk*

Introduction

High intensity, $>10^{19}$ W/cm^2, laser-produced plasmas have been shown to potentially be efficient sources of energetic ions[1,2]. During laser irradiation of a target foil proton fluxes (~10^{12}) are accelerated to energies up to tens of MeV and heavier ions to energies ~5 MeV/nucleon[3,4]. Hydrocarbon and H_2O contamination layers on the target surfaces provide a source of hydrogen, carbon and oxygen ions, which are also accelerated by the quasi-static space charge fields induced.

Important physics in the laser-plasma based acceleration of electron and proton beams has been investigated by systematic measurements of (γ,n) and (p,n) nuclear reactions[5-8]. Measurements of heavy ion emission however have been limited to Thomson parabola ion spectrometers, which generally sample small solid angles (~10^{-5} sr)[3,9] and therefore are not able to measure the integrated ion flux, given that the ion expansion can be influenced by self-generated electric and magnetic fields[9,10].

In this report it is demonstrated that energetic 'heavy' ions, accelerated in laser-ablated plasmas can induce nuclear reactions. Interactions of these fast ions with stationary atoms in adjacent activation samples create compound nuclei that de-excite through the evaporation of protons, neutrons and alphas. High-resolution γ-ray spectra measured from nuclei in activated materials are used to make quantitative measurements of ion emission. This novel source of heavy ions with a broad energy distribution is potentially important in the study of astrophysical nuclear reactions. High intensity lasers are able to provide a quasi-thermal distribution of charged particles at typical astrophysical temperatures, which potentially could be used to determine reaction rates for investigating stellar evolution[11].

Experiment

The experiment was carried out using the 100 TW beam of the Vulcan Nd:Glass laser. The wavelength was ~1 μm and pulse length was ~1 ps. The p-polarised beam was focused using a parabolic mirror onto 100 μm thick aluminum targets at an angle of 45^o and to a peak intensity ~5 x 10^{19} W/cm^2. The target vacuum chamber was maintained at <10^{-4} mbar. Activation targets were exposed to the ions accelerated from the front surface of the primary target foil. A well-shielded Germanium detector (with a relative efficiency of 25%) was used to measure the characteristic gammas emitted by the isotopes produced. Nuclides were identified by the gamma energies and half-lives.

Results

In the first part of the experiment a 1 mm thick ^{27}Al activation sample was positioned along target normal direction, subtending a solid angle of ~4 sr. After 75 J laser pulse irradiation of the primary aluminum foil target, characteristic peaks of ^{34m}Cl, ^{38}K, ^{24}Na, ^{28}Al, ^{29}Al, ^{27}Mg, ^{49}Cr, ^{43}Sc, ^{44}Sc and ^{44m}Sc were measured in the aluminum activation sample, as illustrated in Figure 1. The numbers of each nucleus determined after correction for detection efficiency and the gamma emission probability per disintegration are listed in Table 1. Possible reaction channels are also listed.

Fusion-evaporation reactions are primarily responsible for the production of the observed nuclei. The Monte-Carlo code PACE-2 [12] was used to determine cross-sections for the possible evaporation reactions. PACE-2 calculates the total fusion cross-section for a projectile and target and computes the

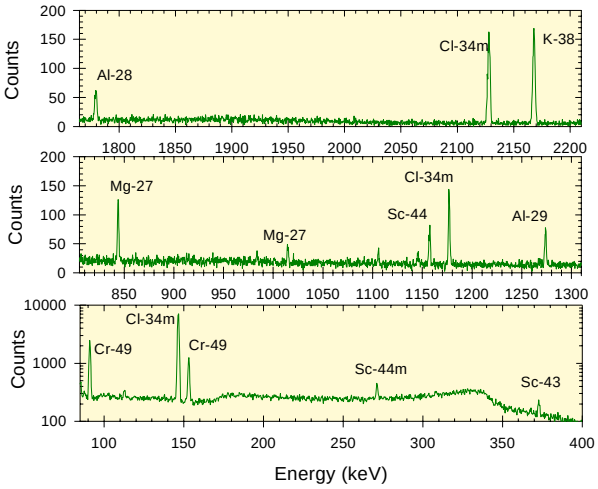

Figure 1. Gamma-ray spectrum in an aluminum activation sample after irradiation with ions from an aluminum target foil. ^{34m}Cl, ^{38}K, ^{28}Al, ^{29}Al, ^{24}Na, ^{27}Mg, ^{49}Cr, ^{43}Sc, ^{44}Sc and ^{44m}Sc peaks are observed.

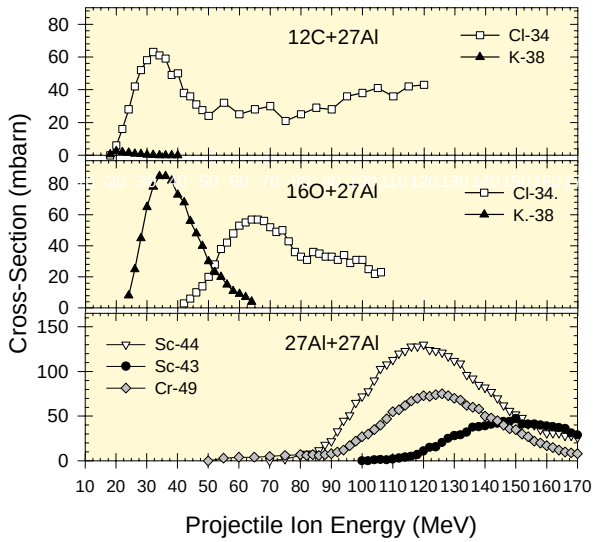

Figure 2. Cross-sections for the production of ^{34}Cl, ^{38}K, ^{49}Cr, ^{43}Sc and ^{44}Sc calculated using the PACE-2 evaporation code for [^{12}C+^{27}Al], [^{16}O+^{27}Al] and [^{27}Al+^{27}Al] compound nucleus formation.

yields for fission exit channels. The cross-sections, shown in Figure 2, are peaked for the most probable evaporation channel, with the high energy tail exhibiting different modes of decay resulting in the same nuclide. The estimated accuracy of the PACE-2 calculations is between 10 and 20%. An experimental cross-section[13] for the isomer ^{34m}Cl was used. The calculated cross-sections and threshold energies were used to identify the reactions.

The PACE-2 calculations indicate large cross-sections for production of ^{49}Cr, ^{43}Sc and ^{44}Sc by evaporation processes from the ^{27}Al+^{27}Al compound nucleus system (Table 1). However, ^{34m}Cl, ^{38}K, ^{24}Na, ^{28}Al, ^{29}Al and ^{27}Mg are unlikely to result from ^{27}Al+^{27}Al compound reactions. The acceleration of contaminant carbon and oxygen ions to produce ^{12}C+^{27}Al and ^{16}O+^{27}Al reactions must be considered as alternative pathways. The cross-sections suggest that ^{34m}Cl and ^{38}K are formed via evaporation of alpha particles and neutrons from the ^{12}C+^{27}Al and ^{16}O+^{27}Al compound nucleus systems, but that ^{24}Na, ^{28}Al, ^{29}Al and ^{27}Mg are unlikely to result from fusion-evaporation reactions. These could result from direct interaction processes.

A second experiment was carried out to highlight possible contributions arising from the acceleration of parasitic ions. A 1 mm thick ^{12}C sample was used as the activation target and a primary ^{27}Al target foil was irradiated with a 68 J laser pulse. Characteristic gammas of ^{34m}Cl, ^{38}K, ^{24}Na, ^{28}Al, ^{29}Al and ^{27}Mg are again observed, Figure 3, and the numbers of each nucleus are listed in Table 1.

The numbers of ^{34m}Cl, ^{24}Na and ^{29}Al nuclei produced in both experiments agree to within ±25%, indicating that they originate via collisions between carbon and aluminium ions. Larger yields of ^{28}Al and ^{27}Mg observed with the aluminum activation target can result from ^{27}Al(n,γ)^{28}Al and ^{27}Al(n,p)^{27}Mg reaction channels, not available with a carbon activation target. A factor ~15 difference in ^{38}K is clearly observed when comparing the ^{34m}Cl and ^{38}K peaks at 2127 and 2167 keV respectively in Figures 1 and 3. ^{38}K could be produced from all three compound nucleus systems (Table 1), although PACE-2 calculations rule out the ^{27}Al+^{27}Al process and indicate a relatively large cross-section of the order of 85 mb at about 35 MeV for ^{16}O+^{27}Al (Figure 2).

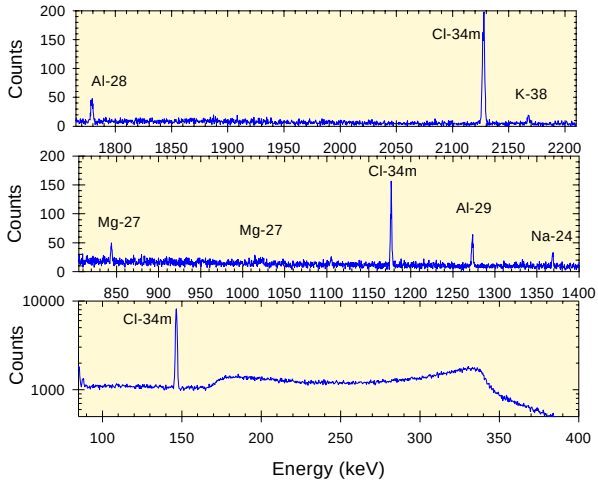

Figure 3. Gamma-ray spectrum in a carbon activation sample after irradiation with ions from an aluminum target foil. ^{34m}Cl, ^{38}K, ^{28}Al, ^{29}Al, ^{24}Na and ^{27}Mg peaks are observed.

The identified fusion-evaporation reactions can be used to quantify ion acceleration. Effectively the calculation involves a convolution of the cross-section and stopping power as the ions propagate into the activation target. About 4 x 10^9 Al ions with energies of 50 MeV and 33 MeV respectively are required to produce the observed quantities of ^{34m}Cl and ^{38}K in the carbon activation target, as shown in Figure 4. An order of magnitude less Al ions of higher energy, ~120 MeV, are needed for the production of the ^{49}Cr and ^{44}Sc nuclei in the aluminum activation target. As already discussed, the factor ~15 increase in the production of ^{38}K in the aluminum target is likely due to the ^{16}O+^{27}Al fusion-evaporation process. For the *additional* ^{38}K nuclei to be produced via this reaction requires ~10^9 ^{16}O ions. This increase in activity cannot be due to the reverse collision system, i.e. ^{27}Al+^{16}O, as the oxygen contamination layer on the secondary target is insufficiently thick to account for the observed activity. The ^{27}Al(n,p)^{27}Mg cross-section, which has a peak of about 105 mb at 10 MeV, would require

Observed nuclei	Half-life	Number of nuclei, *N*		**^{27}Al + ^{27}Al** Reactions	E_{Thres} MeV	**^{12}C + ^{27}Al** Reactions	E_{Thres} MeV	**^{16}O + ^{27}Al** Reactions	E_{Thres} MeV
		^{27}Al sample	**^{12}C sample**						
^{34m}Cl	32.1 mins	2.8 x 10^4	3.0 x 10^4	…		^{34m}Cl +1α+1n	4.8	^{34m}Cl +2α+1n	16.7
^{38}K	7.61 mins	1.7 x 10^4	1.1 x 10^3	^{38}K +3α+3n+1p	87.9	^{38}K +1n	---	^{38}K +1α+1n	5.7
^{28}Al	2.24 mins	6.4 x 10^4	4.6 x 10^4	…		^{28}Al +2α+2p+1n	39.9	^{28}Al +3α+2p+1n	55.7
^{29}Al	6.56 mins	4.5 x 10^3	3.7 x 10^3	…		^{29}Al +2α+2p	26.7	^{29}Al +3α+2p	40.8
^{24}Na	14.98 hrs	1.2 x 10^4	9.2 x 10^3	…		^{24}Na +3α+2p+1n	56.2	^{24}Na +4α+2p+1n	73.0
^{27}Mg	9.46 mins	4.7 x 10^3	1.4 x 10^3	…		^{27}Mg +2α+3p+1n	54.0	^{27}Mg +3α+3p+1n	71.0
^{49}Cr	41.9 mins	7.7 x 10^3		^{49}Cr +1α+1n	---	…		…	
^{43}Sc	3.89 hrs	1.4 x 10^4		^{43}Sc +2α+1p+2n	52.5	…		^{43}Sc	---
^{44}Sc	3.93 hrs	6.8 x 10^3		^{44}Sc +2α+1p+1n	30.0	…		…	
^{44m}Sc	2.44 days	7.3 x 10^4		^{44m}Sc +2α+1p+1n					

Table 1. The number of each nucleus induced per laser shot in the ^{27}Al and ^{12}C secondary samples. The most energetically favoured modes of decay of the compound nucleus systems ^{27}Al+^{27}Al, ^{12}C+^{27}Al and ^{16}O+^{27}Al are considered as candidates for the production of these nuclei. The threshold energy, E_{Thres}, for each reaction is listed.

10^6 neutrons /sr (assuming an isotropic distribution) to account for the *additional* ^{27}Mg observed.

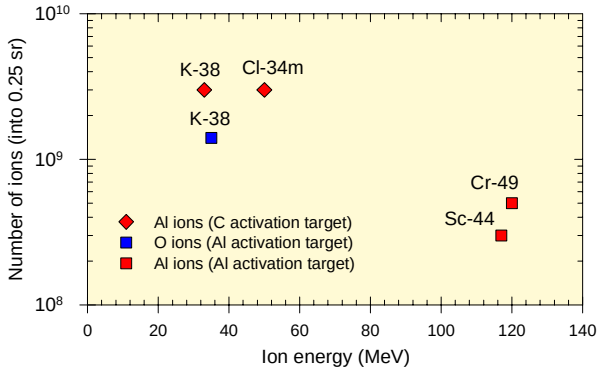

Figure 4. Numbers of ^{27}Al (red) and ^{16}O (blue) ions, with energy above the reaction threshold energy, required to induce the measured activities of the nuclides indicated. Diamond and square symbols correspond to carbon and aluminum activation samples respectively.

Conclusion

In conclusion, through the acceleration of ions in laser-produced plasmas, fusion-evaporation reactions have been induced in secondary targets and successfully used to diagnose heavy-ion acceleration. An indication of the numbers of ions involved in reactions with cross-sections peaked in different regions of the ion energy spectrum is obtained. The technique benefits from the very large dynamic range and insensitivity to electrical noise generated by the laser-plasma interaction. It may also be possible to obtain angularly resolved measurements of energetic heavy ions by using multiple activation foils.

This initial study of heavy-ion induced reactions has shown that the range of reactions induced can be changed by the presence of surface contaminants, highlighting the need for experimentation under controlled conditions, as in traditional nuclear physics. As the peak intensity of laser systems continues to increase in the future such experiments may also prove to be an efficient method to produce unusual nuclear isotopes.

Acknowledgements.

We acknowledge the assistance of the Vulcan operations team. PMcK is supported by a Royal Society of Edinburgh/SEELLD research fellowship.

References

1. E. L. Clark *et al.* Phys. Rev. Lett. 84, 670 (2000).
2. R. A. Snavely *et al.* Phys. Rev. Lett. 85, 2945 (2000).
3. M. Hegelich *et al.* Phys. Rev. Lett. 89, 085002 (2002).
4. K. Krushelnick *et al.* IEEE Transactions on Plasma Science 28, 1184 (2000).
5. I. Spencer *et al.* Nuclear Instruments and Methods in Physics Research B 183, 449 (2001).
6. K. W. D. Ledingham *et al.* Phys. Rev. Lett. 84, 899 (2000).
7. T. E. Cowan *et al.* Phys. Rev. Lett. 84, 903 (2000).
8. M. I. K. Santala *et al.* Phys. Rev. Lett. 86, 1227 (2001).
9. E. L. Clark *et al.* Phys. Rev. Lett. 85, 1654 (2000).
10. M. Tatarakis *et al.* Phys. Rev. Lett. 81, 999 (1998).
11. P. Mohr *et al.* Phys. Lett. B 488, 127 (2000).
12. A. Gavron Phys. Rev. C 21 , 230 (1980).
13. I.-M. Ladenbauer-Bellis, I. L. Preiss, and C. E. Anderson, Phys. Rev. 125, 606 (1962).

Isotope production for positron emission tomography using Vulcan Petawatt

K W D Ledingham*, P McKenna, T McCanny, S Shimizu, J Yang, L Robson

Department of Physics, University of Strathclyde, Glasgow, G4 0NG, UK
**also at AWE plc, Aldermaston, Reading, RG7 4PR, UK*

R P Singhal

Department of Physics and Astronomy, University of Glasgow, Glasgow, G12 8QQ, UK

M J Zweit, J Gillies

Paterson Institute for Cancer Research, Christie Hospital, Manchester, M20 4BX, UK

R J Clarke, P A Norreys

Central Laser Facility, CCLRC Rutherford Appleton Laboratory, Chilton, Didcot, Oxon, OX11 0QX, UK

M S Wei, S P D Mangles, P Nilson, K Krushelnick

Blackett Laboratory, Imperial College, Prince Consort Road, London, SW7 2BZ, UK

M Zepf

Department of Pure and Applied Physics, The Queen's University, Belfast, B17 1NN, UK

Main contact email address: *k.ledingham@phys.strath.ac.uk*

Introduction

The history of positron emission tomography (PET)[1] is linked with many technological advances in nuclear physics, accelerator and detector technology since the beginnings of modern PET in 1973. PET is a powerful medical diagnostic technique requiring the production of short lived positron emitting isotopes, principally ^{11}C, ^{13}N, ^{15}O and ^{18}F, by proton activation of separated isotopes using cyclotrons or Van de Graaff accelerators. Furthermore the technique requires the isotopes to be administered to the patient in suitable pharmaceutical form. Presently favoured is ^{18}F-tagged de-oxyglucose (FDG). Unfortunately this powerful technique, which is used to image blood flow and diagnose cancer tumors, has been greatly limited to just a few sites in the UK due to the cost, size and shielding requirements of the conventional accelerators.

Recently it has been shown that when an intense laser beam interacts with solid targets[2-6], MeV protons are generated capable of producing PET isotopes. In this article we demonstrate intense PET sources of ^{11}C and ^{18}F using the intense petawatt laser beam at Vulcan and also for the first time laser production of FDG. The potential for cheap, easy to shield, table-top laser technology for this purpose is highlighted.

Experimental

The new petawatt arm of the Vulcan Nd:Glass laser at the Rutherford Appleton Laboratory was used in this experimental study. The 60 cm beam was focused to a 5.5 μm diameter spot using a 1.8 m focal length off-axis parabolic mirror, in a vacuum chamber evacuated to ~10^{-4} mbar. The average pulse duration was 750 fs and the energy on target was between 220 and 300 J. The peak intensity was of the order of 6 x 10^{20} Wcm^{-2}. Aluminium, gold and mylar foil targets of various thicknesses were mounted on multiple target wheel assembly as shown in Figure 1, and irradiated by the p-polarised laser beam at an angle of 45^{o}. The protons emanated from contamination layers of water and hydrocarbons on the target surfaces.

To measure the proton energy spectra copper stacks (5cm x 5cm) were positioned along target normal direction and exposed to the protons accelerated from both the front and back surfaces of the target foil, as shown in Figure 1. The activity in the foils from ^{63}Cu(p,n)^{63}Zn with a half-life of 38 minutes[4] was measured in a 3"x3" NaI coincidence system and convoluted with the reaction cross-section and proton stopping powers to produce the energy distributions shown in Figure 2. The spectra are quasi-exponential with the higher energy protons measured behind the target. The number of protons generated per laser shot was typically about 10^{12}.

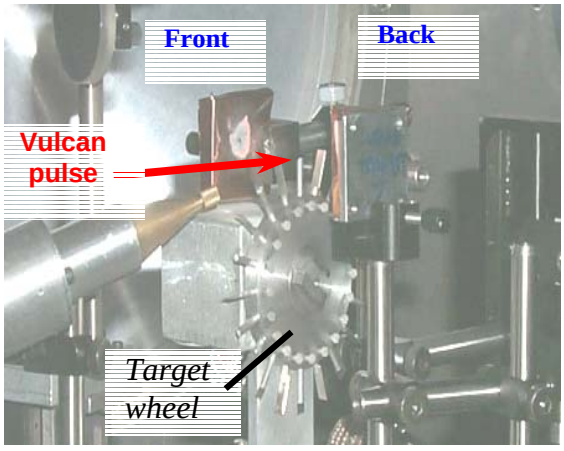

Figure 1. Experiment arrangement. The laser pulse was focused at an angle of 45° onto solid targets mounted on a target wheel. Proton activation of Cu stacks positioned both in the plasma blow-off direction (FRONT) and behind the target (BACK) was used to diagnose proton energy spectra. The Cu stacks were replaced by ^{11}B samples for ^{11}C production.

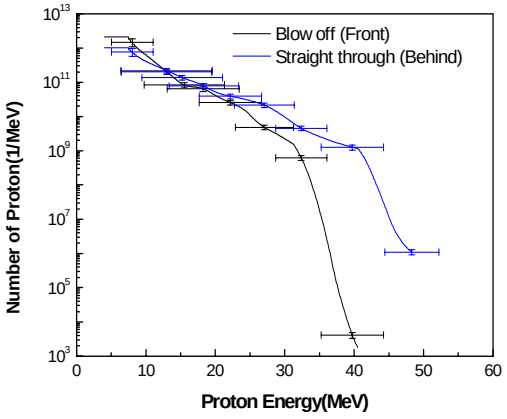

Figure 2. Typical proton spectra in front of and behind the target. The highest energy protons are directed behind the target while the greatest C^{11} activity is generated in front of the target.

The copper stacks were subsequently replaced by boron activation samples (5cm diameter x 3mm thick) and after each laser shot these samples were removed from the vacuum chamber and the ^{11}C activity produced by the (p,n) reaction on ^{11}B was measured in the NaI coincidence system. Figure 3 shows a typical half-life measurement that was initiated one and a half hours after the laser shot because of the radiation hazard due to the high activities induced. The counting rate was converted to initial activity in Bq using a calibrated ^{22}Na source. The activity generated in the secondary targets in front and behind the primary target was thus measured in absolute units.

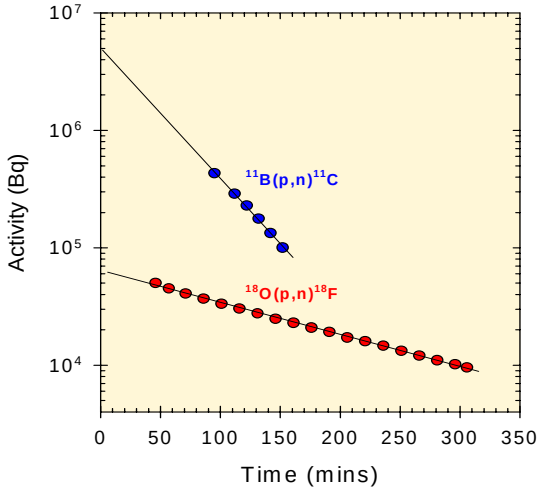

Figure 3. The measured half-lives of ^{11}C and ^{18}F.

Figure 4 shows the ratio of the measured ^{11}C activity behind the target to that in front of the target, as a function of target thickness and material. For thin target foils <5 μm the measured activity is approximately equal front and back (independent of material) and the total activity measured for a 300 J pulse on target ($6x10^{20}$ Wcm^{-2}) is about 10^7 Bq. In front of the target the activity for similar laser energies is independent of both the target thickness and material, whereas the ^{11}C activity measured on the sample behind the target decreased with increasing thickness.

^{18}F is the PET isotope favoured by clinicians because of its longer half-life (110 minutes). Furthermore these isotopes must be administered to the patient in suitable pharmaceutical form with the presently favoured form being ^{18}F-tagged de-oxyglucose (FDG). It was thus necessary to determine how much ^{18}F could be produced per laser shot. The isotope is generated from a (p,n) reaction on the separated isotope ^{18}O. $CaC^{18}O_3$ and enriched water ($H_2{}^{18}O$) samples of high purity were used in the present work. At the highest laser pulse energies 10^5Bq of ^{18}F were produced per laser shot (Figure 3). On one high intensity shot ^{11}B and $H_2{}^{18}O$ samples were placed in front and behind the Al target foil respectively and the ratio of the induced $^{11}C/^{18}F$ activities was measured to be about 30. This was expected due to the quantities of sample involved and the difference in cross-section for these reactions.

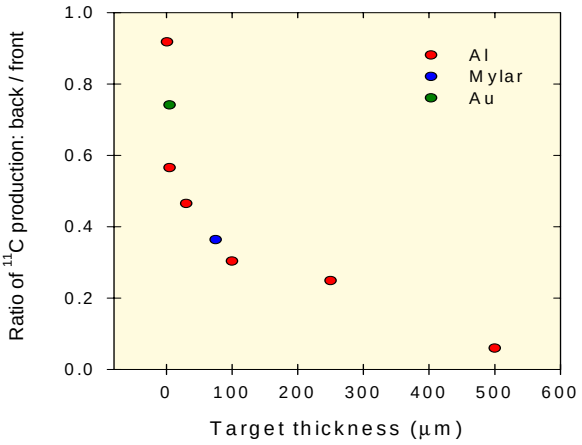

Figure 4. Back/Front ratio of ^{11}C from (p,n) reactions on ^{11}B as a function of target thickness.

Conclusions

We have now demonstrated that considerable quantities of the PET isotopes ^{11}C and ^{18}F can be generated by laser-produced protons from Vulcan. These high energy measurements, together with previous results at lower pulse energies are important in the determination of optimum laser pulse parameters for the design of a future laser system dedicated to isotope production. This work is the first demonstration of laser-driven ^{18}F production and synthesis of [^{18}F]FDG (fluorodeoxyglucose), the work horse tracer for clinical PET.

References

1. R.Nutt, Molecular Imaging and Biology, 4, 11-26, 2002.
2. E.L. Clark *et al* Phys Rev Lett, 84, 670-673, 2000
3. M.I.K.Santala *et al* Appl.Phys.Lett, 78, 19-21, 2001.
4. I.Spencer *et al* NIM B 183, 449-458, 2001

Laser-driven photo-transmutation of long-lived nuclear waste: Application to Iodine-129

K W D Ledingham*, P McKenna, J Yang, T McCanny, S Shimizu, L Robson

Department of Physics, University of Strathclyde, Glasgow G4 0NG, UK
**Also at AWE plc, Aldermaston, Reading, RG7 4PR, UK*

J Magill, J Galy, R Schenkel, J Rebizant

European Commission, Joint Research Centre, Institute for Transuranium Elements, Postfach 2340, 76125 Karlsruhe, Germany

R J Clarke, P A Norreys

Central Laser Facility, CCLRC Rutherford Appleton Laboratory, Chilton, Didcot, Oxon OX11 0QX, UK

R P Singhal

Department of Physics and Astronomy, University of Glasgow, Glasgow G12 8QQ, UK

M S Wei, S P D Mangles, P Nilson, K Krushelnick

Blackett Laboratory, Imperial College, Prince Consort Road, London SW7 2BZ, UK

Main contact email address: *k.ledingham@phys.strath.ac.uk*

Introduction

One of the major problems of the nuclear power industry today is in the management and disposal of high-level radioactive waste. Vitrified high-level waste can be stored for about 50 years before ultimate geological disposal. However, in many countries around the world much research effort is being expended in the possibility of partitioning and transmuting radioactive waste [1)], which can reduce its toxicity by a factor of 100. Recently a number of roadmaps for nuclear waste transmutation have been produced [2)]. Although the most frequently discussed methods involve transmutation by bombardment with neutrons from a reactor, or more recently from a particle accelerator [3)], there have been other suggested approaches to this problem, for example laser-driven high-brightness gamma generation for photo-transmutation [4)]. In a recent UK report on the transmutation of nuclear waste (http://www.ph.surrey.ac.uk/npg/transmutation) the importance of launching new ideas in radioactive waste management was emphasized and it is in this context that the present work introduces a novel method of inducing photo-transmutation reactions using bremsstrahlung produced in a target irradiated by an ultrahigh intensity laser.

Compact multi-terawatt and petawatt pulsed high-intensity laser systems have now been developed in a number of laboratories worldwide. Techniques such as chirped pulse amplification[5)] have facilitated laser pulses of the order of femtoseconds or picoseconds to be temporally stretched by 3 to 4 orders of magnitude for non-destructive amplification in a chain of optical amplifiers. Laser pulses are re-compressed to deliver about 10^3 - 10^5 PWcm^{-2} intensity on target. At these intensities the electron quiver energy in the laser field is fully relativistic and leads to the generation of high brightness beams of energetic gamma rays, protons, neutrons and heavy ions[6-10)].

In this article we report on the use of the Vulcan Petawatt laser to drive the photo-transmutation of long-lived ^{129}I with a half-life of 15.7 million years to ^{128}I with a half-life of 25 min. A laser-generated gamma ray is absorbed into the ^{129}I nucleus, which releases a neutron to undergo transmutation to ^{128}I. This giant dipole resonance (γ,n) reaction is observed in ^{129}I and ^{127}I and the absolute activities of the reaction products ^{128}I and ^{126}I are used for the first time to determine an integrated cross-section for ^{129}I(γ,n)^{128}I, from the known ^{127}I(γ,n)^{126}I cross section.

Experiment

The experiment was performed on the petawatt arm of the Vulcan Nd:glass laser housed at the Rutherford Appleton Laboratory, UK. A 360 J laser pulse, of wavelength λ~1 μm and duration 0.7 ps, was focused using a 1.8 m focal length off-axis parabolic mirror to a spot size of 5.5 μm diameter, to achieve an intensity I of the order of 5 x 10^{20} Wcm^{-2}. The target was a solid piece of gold with dimensions 5 x 5 x 4 mm. Irradiation of the target with intense laser light ponderomotively drives electrons into the target with relativistic energies. The electron energy distribution has been previously shown to be Boltzmann-like[11)] and for the p-polarised, 45° laser irradiation arrangement used in this study, kT (the product of the Boltzmann constant and the electron temperature) is of the order of $0.511(\sqrt{[1+I\lambda^2/6.85\text{x}10^{17}]}-1)$ MeV, where the irradiance $I\lambda^2$ is measured in Wcm^{-2}μm^2 [12)]. The laser irradiance for this experiment was ~5 x 10^{20} Wcm^{-2}μm^2 which would produce a hot electron population with an expected kT of ~6.4 MeV. These hot electrons are stopped in the high-Z gold target, generating bremsstrahlung gamma radiation with a broad energy distribution and similar kT.

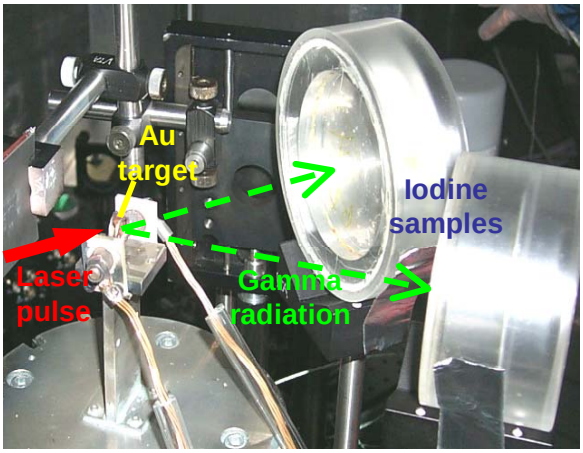

Figure 1. Photograph of the experimental arrangement. The high intensity laser pulse enters from the left of the picture and is focused onto a 4 mm thick Au target. Relativistic electrons from the resulting hot plasma are converted to high-energy bremsstrahlung in the target. Iodine samples encased in Al and Plexiglas are located along the laser and target normal axes. The gamma radiation from the target induces transmutation of the iodine samples through (γ,n) reactions.

In previous experiments the gamma radiation has been shown to be strongly angular dependent on the direction of beam propagation influenced by laser induced preplasma conditions[13)]. In the present experiment two iodine samples were positioned along the laser and target normal directions behind the gold target as shown in Figure 1. The samples were

prepared from waste solution from a fuel processing facility. Iodine was present in the raw waste solution at 1.3 gl^{-1} with isotopic composition 30% ^{127}I, 70% ^{129}I plus short lived ^{131,133}I. A 90% efficient extraction procedure produced iodide as PbI_2 compound with density 3.24 g/cm^3. This powder was then compacted in a 55 mm diameter Al can, which was further encapsulated in a vacuum-tight Plexiglas container. The samples contained 46.2 g and 43.3 g of iodine with isotopic composition 85% ^{129}I and 15% ^{127}I.

After single-shot laser irradiation of the target the characteristic gamma radiation from photo-induced reaction products in the gold target and the iodine samples were measured using two well-shielded intrinsic germanium detectors. The detection efficiency (35%) was calibrated using known sources of ^{152}Eu, ^{57}Co, ^{22}Na, ^{137}Cs and ^{60}Co to facilitate absolute numbers of laser induced reactions to be determined.

Results

Figure 2 shows part of the measured gamma-ray spectrum from the laser-irradiated gold target. The peaks at 332.9 keV and 355.6 keV originate from the decaying isotope ^{196}Au and the peak at 328.4 keV from ^{194}Au, produced by ^{197}Au(γ,n)^{196}Au and ^{197}(γ,3n)^{194}Au reactions. $(6.7\pm0.6)\times10^8$ and $(2.5\pm0.4)\times10^6$ isotopes of ^{196}Au and ^{194}Au were generated respectively. Since the cross-sections for the (γ,n) and (γ,3n) reactions on gold are well known and are peaked at different gamma energies, the bremsstrahlung spectrum can be deduced, using a technique described in detail elsewhere[14]. Assuming a Boltzmann-like energy distribution the k*T* was determined to be (5.5±0.7) MeV. This is in good agreement with the calculated value of 6.4 MeV for a laser irradiance of ~5 x 10^{20} $Wcm^{-2}\mu m^2$.

The iodine samples were analysed using the germanium detectors before and after laser irradiation of the gold target. The background spectrum of Figure 3 was measured for 3 hours and the principal lines observed resulting from the decay include ^{125}Sb. The background activity from the samples was of the order of 2.4×10^8 Bq. A 1mm thick Pb filter was inserted between the iodine samples and the detector in order to reduce the detector dead-time due to the high activity of the β emission from the ^{129}I decay and the X-ray radiation at 29.8 keV, 29.4 keV and 33.6 keV and gamma radiation at 39.6 keV. Calculations have shown that the intensity of a line at 450 keV, which is the region of interest for the experiment, is attenuated about 15% by the addition of this filter.

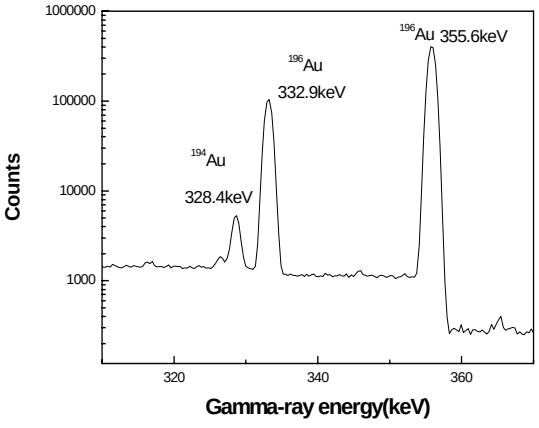

Figure 2. Gamma emission spectrum from the activated gold target after laser irradiation. (γ,n) and (γ,3n) reactions on Au are observed.

Twenty minutes after laser irradiation the iodine samples were returned to the germanium detectors. Figure 3 shows clear peaks at 443.3 keV and 527.1 keV, characteristic of the decay of ^{128}I. Interestingly, both samples had similar peak strengths indicating a wide angular distribution of gamma radiation from the gold target. The decay of ^{128}I was determined by measuring the integrated area of the peaks over successive time intervals, Figure 4. The half-lives of the 442.9 keV and 526.6 keV peaks were (25.8±1.0) minutes and (24.5±1.5) minutes respectively, which agree well with the literature value of 25.0 minutes. In addition, the ratio of the area of the 442.9 keV and 526.6 keV peaks averaged over all of the measured spectra is 10.9, in good agreement with the literature value of 10.4. An additional peak at 949.6 keV was weakly observed and is also attributed to the decay of ^{128}I. From the data we have deduced the total activity of ^{128}I produced at the time of the laser shot to be 1323 Bq. This number was determined after correction for the decay branching ratios, attenuation in the 1 mm thick Pb filter (between the sample and the detector) and self-absorption in the Pb-matrix sample. This corresponds to the production of about 2.9×10^6 isotopes of ^{128}I for the 360 J laser shot.

The iodine samples contained 15% of the isotope ^{127}I. Observed weak peaks at 388.6 keV and 666.3 keV in the measured gamma emission spectra are attributed to the decay of ^{126}I, produced by (γ,n) reactions on ^{127}I. A similar analysis performed on those peaks illustrates the production of 1.7×10^6 ^{126}I isotopes.

Comparison of the numbers of the ^{129}I(γ,n)^{128}I and ^{127}(γ,n)^{126}I reactions induced in the same iodine sample facilitates a ratio of the integrated cross-sections for these reactions to be determined. For a given gamma flux Φ, the number of nuclides N_{128} of ^{128}I and N_{126} of ^{126}I produced are given by: $N_{128}=\sigma_{129}\Phi N_{129}$ and $N_{126}=\sigma_{127}\Phi N_{127}$, where N_{127} (=3.5×10^{22}) and N_{129} (=1.8×10^{23}) are the initial number of atoms of ^{127}I and ^{129}I respectively in the sample and σ_{129} and σ_{127} are the cross-sections for the ^{129}I(γ,n)^{128}I and ^{127}I(γ,n)^{126}I reactions respectively. Assuming the Q-value and width of the cross-sections are similar, the ratio of the integrated cross-sections can be written as:-

$$\frac{\sigma_{\mathrm{int}}^{^{129}I}}{\sigma_{\mathrm{int}}^{^{127}I}} = \frac{N_{128}}{N_{126}} \cdot \frac{N_{127}}{N_{129}}$$

The integrated cross-section for ^{127}I(γ,n)^{126}I is known, 309 mbarns[15], and the value for the ^{129}I(γ,n)^{128}I reaction was determined using 4 measured spectra to be 97±40 mbarns. This is in good agreement with the theoretical cross-section given in the literature as 110 mbarns[15]. Because the present technique involves a simple ratio of measured peak areas of two isotopes of the same element (irradiated under the same conditions), it is

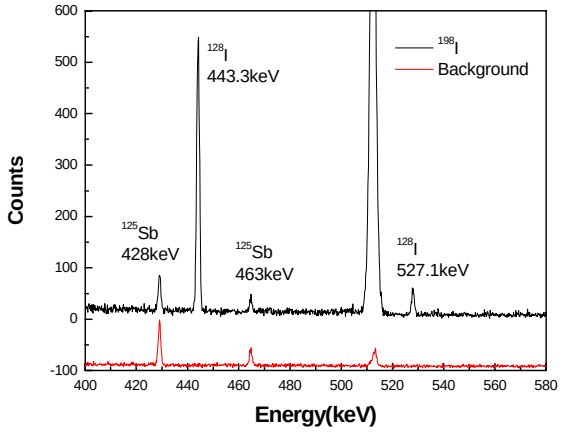

Figure 3. Gamma emission spectra from one of the iodine samples measured before (background) and after laser irradiation of the gold target. Characteristic emission lines of ^{128}I at 442.9 keV and 526.6 keV are clearly observed.

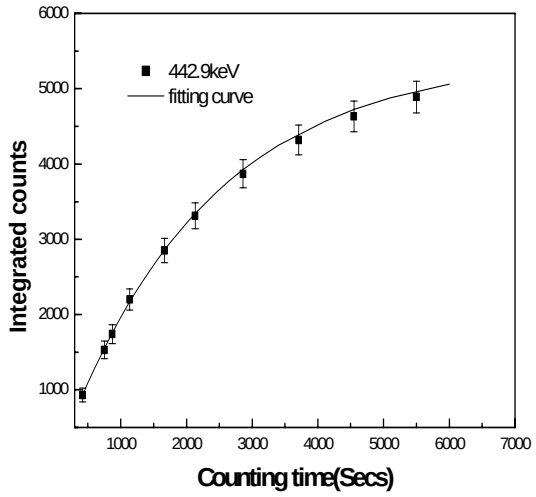

Figure 4. Integrated area of the 442.9 keV emission peak from the decay of ^{128}I measured as a function of time. The measured half-life of (25.8±1.0) minutes agrees well with the literature value of 25 minutes for the half-life of ^{128}I.

superior to methods employing a convolution of the gamma energy spectrum with an assumed cross-section shape. The main uncertainty in the determined integral cross-section resides in the measured gamma-peak areas.

Conclusion

We have demonstrated laser-driven (γ,n) transmutation of an important long lived fission product, ^{129}I, found extensively in radioactive waste, to ^{128}I which decays quickly with a half-life of just 25 minutes. In addition, by comparing the activities of ^{128}I and ^{126}I, and using the known ^{127}I(γ,n)^{126}I cross-section we have determined the unknown integrated cross-section for the ^{129}I(γ,n)^{128}I reaction. We have shown that a single 360 J laser pulse focused to ~5x10^{20} Wcm^{-2} can generate about 2.9x 10^{6} nuclei of ^{128}I. A similar experiment carried out recently on the short-pulsed tabletop laser at the University of Jena [16] at a similar laser intensity, but with pulse energies of about a joule, generated 1.5 nuclei of ^{128}I per laser shot.

A new generation of compact, high-intensity tabletop lasers is currently being designed in a number of laboratories, incorporating novel technology such as optical parametric chirped pulse amplification [17,18]. Several of these laser systems will be geared towards applications such as medical isotope production and transmutation studies of long-lived isotopes. This paper has introduced laser-driven photo-transmutation as a feasible method for experimental research into transmutation reactions, with potential applications to medicine and nuclear waste management.

Acknowledgements

We acknowledge the expertise of the Vulcan laser and target support teams. PMcK is supported by a Royal Society of Edinburgh/SEELLD research fellowship. JY acknowledges support from the China Scholarship Council and SS acknowledges support from the Japan Society for the Promotion of Science. This work is funded by the EPSRC(UK).

References

1. J. Magill *et al*., Nuclear Energy 42 at press (2003)
2. See for example: C. Rubbia (Chairman) A European Roadmap for Developing Accelerator Driven Systems (ADS) for Nuclear Waste Incineration, ENEA Report (ISBN 88-8286-008-6) (2001)
3. C. D. Bowman Annual Rev. Nuc. Part. Sci. 48, 505 (1998)
4. Li D, *et al*., J. Nuc. Sci. Tech. 39, 1247 (2002)
5. D. Strickland and G. Mourou Opt. Comm. 56, 219 (1985).
6. K. W. D. Ledingham *et al*. Science 300, 1107 (2003).
7. E. L. Clark *et al*. Phys. Rev. Lett. 84, 670 (2000).
8. M. I. K. Santala *et al*. App. Phys. Lett. 78, 19 (2001).
9. I. Spencer *et al*. Nuc. Inst. Meth. Phys. Res. B 183, 449 (2001).
10. P. McKenna *et al* Phys. Rev. Lett. In press (2003).
11. G. Malka and J. L. Miquel Phy. Rev. Lett. 77, 75 (1996).
12. S. C. Wilks *et al*. Phys. Rev. Lett. 69, 1383 (1992).
13. M. I. K. Santala *et al*. Phys. Rev. Lett. 84, 1459 (2000).
14. I. Spencer *et al*. Rev. Sci. Inst. 73, 3801 (2002).
15. Handbook on photonuclear data for applications - Cross-sections and Spectra IAEA-TECDOC-1178 (2000).
16. J. Magill *et al*. Applied Physics B: Lasers and Optics at press.
17. I. N. Ross *et al*. Laser and Particle Beams 17, 331 (1999).
18. A. Dubietis *et al*. Opt. Comm. 88, 437 (1992).

Advanced fast ignition studies on the Vulcan laser – cone/shell implosions

P A Norreys, K L Lancaster*, C D Murphy*, H Habara, S Karsch, R J Clarke, J LCollier, R Heathcote, C Hernandez-Gomez, S J Hawkes, D Neely, M H R Hutchinson*

Central Laser Facility, CCLRC Rutherford Appleton Laboratory, Chilton, Didcot, Oxon, OX11 0QX, UK
**also at Blackett Laboratory, Imperial College, Prince Consort Road, London, SW7 2BZ, UK*

R G Evans

Blackett Laboratory, Imperial College, Prince Consort Road, London, SW7 2BZ, UK

M Zepf

Department of Pure and Applied Physics, Queens University of Belfast, Belfast, BT7 1NN, UK

J A King, R R Freeman

Department of Applied Science, University of California, Davis, 1 shields Ave, Davis, CA 95616-8254, USA

S Hatchett, M H Key

Lawrence Livermore National Laboratory, Livermore, CA 94550, USA

R Stephens

General Atomics, P.O. Box 85608, San Diego, CA 92186-5608, USA

C Stoeckl

Laboratory of Laser Energetics, University of Rochester, 250 E. River Road, Rochester, NY 14623-1299, USA

K A Tanaka, T Norimatsu, Y Toyama, R Kodama

Institute of Laser Engineering, Osaka University, Suita, 565-0841, Osaka, Japan

Main contact email address: *p.norreys@rl.ac.uk*

Introduction

One of the most attractive fast-track paths to fusion energy is now being explored in laser fusion research - the advanced fast ignition concept[1]. The first demonstrations of this new concept have been reported at the Rutherford Appleton Laboratory[2] and at Osaka University[3]. A 100TW short-duration laser pulse was coupled to a novel target geometry that allowed simultaneous compression and significant heating. The results indicated a highly efficient coupling of the short pulse laser energy to the heating of the compressed plasma.

The next step was to conduct experiments at a laser power equivalent to a full-scale ignition system, albeit at 1/20 of that required for ignition. The first equivalent power experiments using a Peta-Watt class laser system as the heating source were reported last year in the journal *Nature* as a rapid communication, in light of their timeliness and importance[4]. A three orders of magnitude enhancement of fusion products was demonstrated, confirming that the high heating efficiency is maintained as the short-pulse laser energy is substantially increased. Measurements using perfectly synchronised lasers for the fast heating and compression indicate that it may be possible to use longer pulses (>10ps) to achieve ignition.

Work at RAL this year has concentrated on an important objective related to these new observations, namely confirmation of the results at an independent laboratory using similar laser conditions.

Experimental configuration

To minimise changes between the experiments at RAL and ILE, hollow deuterated plastic shells with similar diameter and thickness were used. The target area and chamber were configured so that the 100 TW beam was coupled to the nanosecond drive beams in 6-beam cubic symmetry, illustrated in Figures 1 & 2. The main difference between the two experiments was the frequency of the main drive beams ($2\omega_0$ for ILE, ω_0 for this experiment) to maintain the incident energy on target.

Pulses from the SAM oscillator were stretched to 300 ps and amplified in 2 preamplifiers. They were then split into two halves. One half was amplified unchanged in the outer arm of the rod chain to generate the 80J / 0.8ps-1.1ps beam to target. The second half went through a second, specially designed stretcher to increase the pulse duration to 900ps[5]. This pulse was then amplified in a third preamplifier before being introduced into the inner arm of the Vulcan rod chain to generate the main-6 drive beams. Each of the six 10.8cm beams delivered 150J to target using f2.5 lenses. The 100 TW

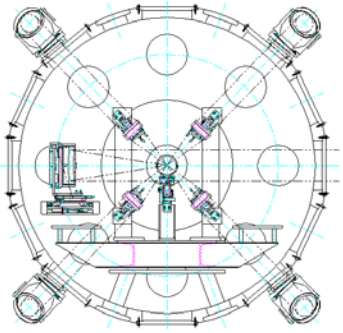

Figure 1. East-west view of the target chamber showing four of the main drive beams focused by f2.5 lenses and the 100 TW beam focused by an off-axis parabolic mirror.

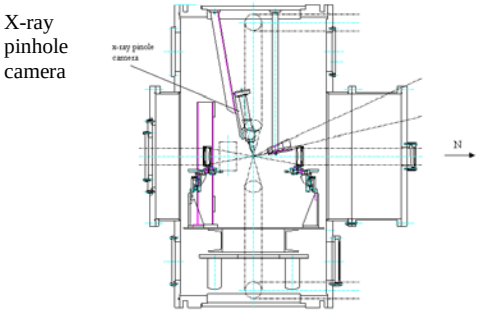

Figure 2. North-south view showing two opposing drive beams on the horizontal plane with the X-ray pinhole camera .

beam was introduced in the horizontal plane at 15 degrees from the east-west axis (the drive beams were at 45 degrees to the horizontal, as illustrated in Figure 1). Figure 2 shows the north-south view of the chamber where the beams were introduced on the horizontal axis.

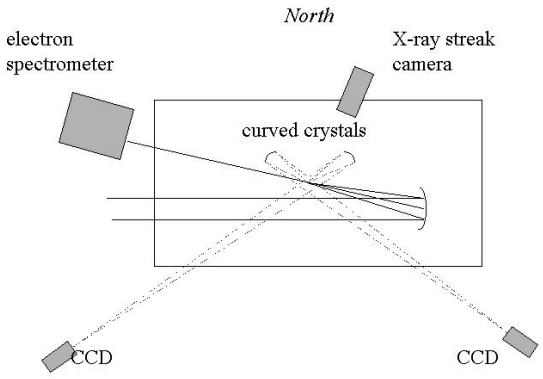

Figure 3. Arrangement of plasma diagnostics in the horizontal plane.

Phase zone plates producing 500μm focal spots were used in initial implosions. It was found that the energy coupling efficiency to the implosion was poor due to the tangential focus generated by the phase plates. In the results reported below, the beams were overlapped onto the sphere without phase plates using the f2.5 aspheric lenses.

The plasma diagnostics are illustrated in Figure 3 and included the LANSA and current mode time-of-flight neutron detectors set up outside the chamber that are described in detail elsewhere in this annual report[6,7].

The X-ray pinhole camera was filtered by 25μm-thick Be, so that it was sensitive to photons above 1keV. The detector was Kodak DEF X-ray film. The camera had a magnification of ×10. The pinhole size was 10μm and was set in 7μm thick Pt substrate.

A Kentech X-ray streak camera was coupled to 10μm slit that was placed 15cm from the target at a magnification of ×5 to provide a one dimensional streaked image of the implosion.

An electron spectrometer was employed directly along the 100 TW laser axis from the off-axis parabolic mirror on the horizontal plane to detect the electron spectra generated by the CPA pulse. The spectrometer, illustrated in Figure 4, consisted of a pair of 1.0T permanent magnets with dimensions 15cm×3cm separated by 3cm. These produce a magnetic field in the gap of 0.14T. The magnetic field deflected electrons onto a Fujifilm BAS-SR 2025 image plate (diameter 20cm×25cm) located on the top of the magnet structure in Figure 4. The image plates work by photo-stimulated luminescence, i.e. ionizing particles induce electrons in the substrate to occupy meta-stable levels that are de-excited by longer wavelength laser radiation used in the reader. The information was digitally recorded using a FUJIFILM BAS-1800II[8] reader after 80 minutes. The spectrometer was located 1m from the target and was capable of detecting electrons in the energy range 0.1 – 80 MeV.

Two spherically curved crystals were used for X-ray imaging. The first was used for backlighting in the initial phase of the experiment and the second was used for direct K_α imaging of Cu impurity (hν=8.05keV) doped into the shell during the heating phase.

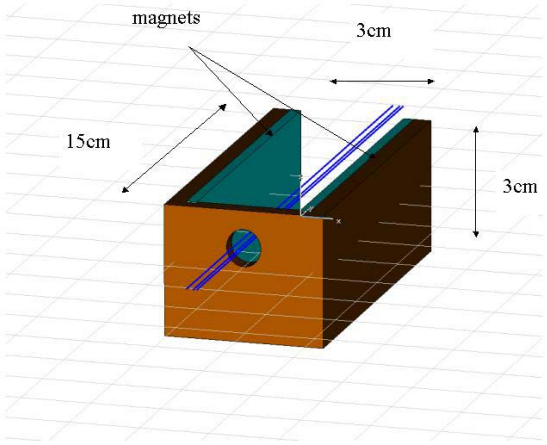

Figure 4. Illustration of the interior of the electron spectrometer. The entrance hole is 1cm diameter. The centre of the hole is located 1cm below the top of the magnets. The image plate was located 15mm from the top of this structure.

Ti K_α radiation (hν=4.51 keV) was used for the X-ray radiographic studies. The areal density was obtained by measurement of the attenuation of the monochromatic X-rays through the compressed matter. Snapshots were made at different times on consecutive shots to determine the peak stagnation time of the implosion. In this case, the 100 TW beam was defocused by several millimeters to produce a 1mm×0.5mm focal spot on a 25μm thick Ti foil giving an intensity on target of 1.6×10^{16} Wcm^{-2}. The K_α radiation generated was imaged using a spherically curved crystal onto to a Princeton Instruments 16-bit X-ray CCD camera.

Implosion dynamics.

A 1% fraction of Cu was doped into the deuterated polystyrene shells. The shells had a diameter of 486μm and a wall thickness of 6 μm. Identical shells were mounted on Au cones as illustrated in Figure 5 and were manufactured at the General Atomics Corp. The inner edge of the cone had an opening half angle of 13°. The outer edge had a half angle of 22°. A collar on the Au material located the shell in position such that the cone tip was 40μm from the stagnation point.

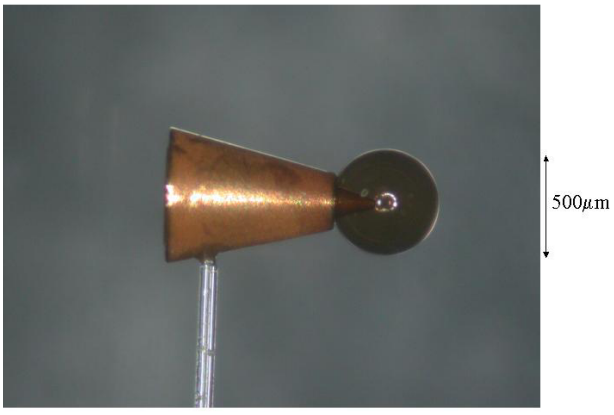

Figure 5. Photograph of the cone shell assembly.

To determine stagnation time, identical diameter and thickness spherical shells were irradiated with the 1 kJ, nanosecond drive laser pulse. Figure 6 shows a radiograph of such a spherical shell taken 1ns after the peak of the pulse. It can be seen that the shell has not moved significantly – which indicates that stagnation occurs well after the drive laser has finished and the shell is coasting to peak compression. Significant

decompression of the shell occurs in the coasting phase after the drive pulse is finished.

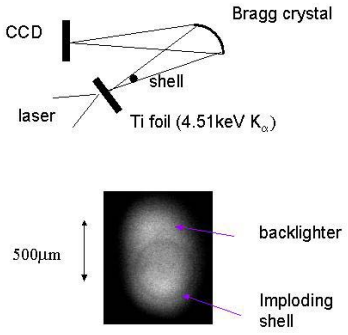

Figure 6. Imploding shell taken 1ns after peak of drive pulse.

Figure 7 shows radiographs of the implosion taken after different times. Stagnation occurs at 3.1 ns after the peak of the drive pulse. The compressed core diameter is 100μm FWHM. Comparison of the measured X-ray absorption with opacities calculated using the LASNEX 1D hydrocode indicate that peak compressed densities of 4gcm^{-3} were achieved.

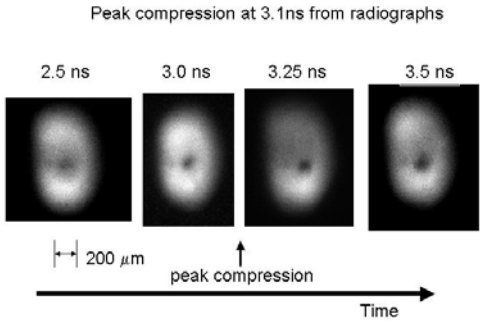

Figure 7. Snapshots of implosions taken at different times.

The next step was to radiograph a cone-shell implosion at peak compression. This is shown in Figure 8. The cone shell was rotated so that the implosion symmetry was as close as possible to that used for the next heating phase. For illustration, a cone-shell target was rotated to provide the same view angle as the radiograph set-up. Both the outer collar and the surface of the Au guide cone located inside the shell are clearly distinguishable in the radiograph. The image demonstrates that the 100-μm diameter compressed plasma is formed close to the tip of the cone, corresponding to a peak areal density of 40 mgcm^{-2}.

Comparisons of the compressed density that can be achieved in hydrodynamic simulations with and without radiation transport included indicates that this process plays a central role in limiting the compressed density. The 1D Lagrangian hydrodynamic code MEDUSA (that does not include radiation transport) predicts, for example, compressed densities of 350gcm^{-3} and ~10μm core diameter, even when the absorbed energy is adjusted to match to the measured stagnation time. Similar results were obtained from 1D LASNEX code without radiation transport, but when this was included, the predicted density was significantly reduced - to 9gcm^{-3} with 80μm core diameter. The measured and calculated densities are therefore in reasonable agreement when radiation transport is taken into account.

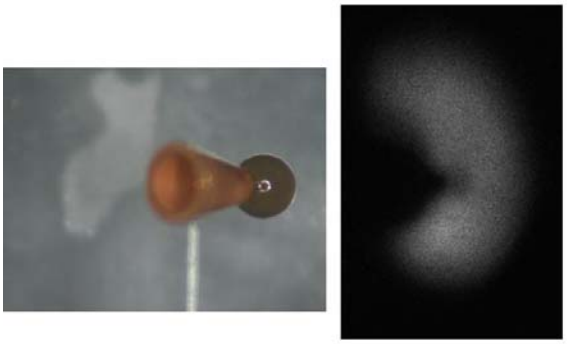

Figure 8. Radiograph of a cone-shell implosion taken 3.1ns after the peak of the drive pulse (right) showing the compressed plasma formed close to the tip of the cone. The image on the left illustrates the angle of view.

Radiative transport allows x-rays from the laser deposition region to penetrate and preheat the dense shell, making the shell much less compressible at stagnation. Whether or not radiative pre-heat is included in the simulations, the shell at stagnation is well off the degenerate adiabat, but the entropy differences are large between the two cases. With radiation transport included, the entropy of highest density at peak ρR is ~3.6e8 joules/gm/keV. Without the transport included, the entropy is ~2.0e8 joules/gm/keV. The pressure for a given density is a factor of about 6.3 higher with radiation (or, put the other way, without radiation the density is a factor of 3.1 greater for a given pressure). Moreover the capsule without radiation reaches a much higher stagnation pressure, because what is being held constant is the amount of work the imploding shell's kinetic energy can do: so a relatively high P at a given V means the kinetic energy of the shell with radiation is all used up before V changes much.

Figure 9 shows two X-ray images of the implosion with and without the cone insert. There is no X-ray emission from the core visible. This indicates that the residual thermal energy is low (~50 eV) at stagnation. These results confirm that there was little chance of diagnosing the implosion by neutron spectroscopy – as the temperature (even with increase due to the short pulse heating) is too low for any significant number of thermonuclear reactions to occur.

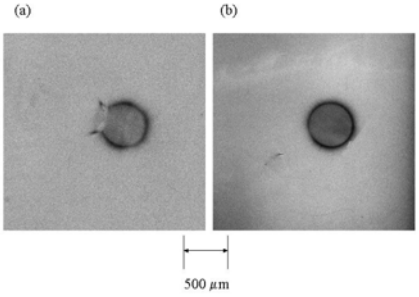

Figure 9. X-ray pinhole images of (a) cone/shell implosion (b) shell implosion. No core is present, even when the 100TW beam was focused into the cone to heat the plasma at stagnation.

Heating with 10 ps pulses

The measurements above confirm that the compressed density is 4gcm^{-3} and the areal density is 40mgcm^{-2}. These conditions are somewhat lower than those obtained earlier at Osaka

University. There the compressed density was 50-70gcm^{-3} and the areal density was 200mgcm^{-2}. The latter conditions more closely match the range of MeV electrons generated by the 100TW heating beam.

In an attempt to match the range of fast electrons to realized compressed density in the experiment, the pulse duration of the short pulse beam was increased to 10ps, providing an intensity on target of 2.5×10^{18} Wcm^{-2}. Figure 10 shows two electron spectra under these conditions. The first is when the now 10TW beam was focused onto a single Cu foil at this maximum intensity. The second was for a hollow Au cone without an implosion. It can be seen that the number of electrons differs by no more than a factor of 3 in the range 1 – 10 MeV.

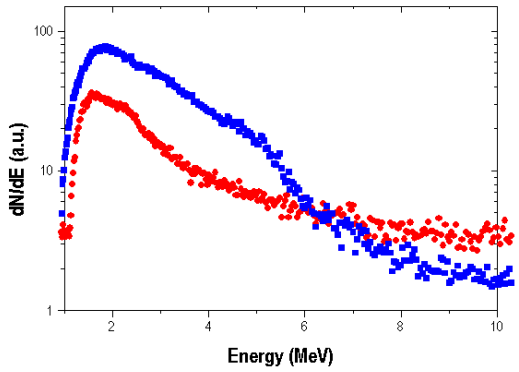

Figure 10. Comparison of electron spectra obtained with a 25µm thick Cu foil (blue) and a free standing cone target (red) .

There was no electron signal in the spectrometer when the 10ps duration heating beam was introduced into a cone shell implosion. There was also no noticeable increase X-ray emission observed in the X-ray pinhole images. This indicates that substantial hydrodynamic motion must occur under these conditions. The much longer rising edge of the 10ps heating pulse allows the material at the end to break through and start to fill the cone with plasma. The critical density surface is pushed much further back into the cone – resulting in a much lower focused intensity (due to the Rayleigh range of the focusing optic) than that at tight focus. It can be concluded from these measurements that the rising edge of a cone-shell implosion must be carefully controlled to generate a steep rising edge.

Heating with 1 ps pulses

Figure 11 shows two electron spectra taken when the pulse duration was minimized. The first is when the 100 TW beam was focused onto a single Cu foil at maximum intensity. The electron distribution for the foil case is well described by a simple exp(-*E*/*kT*) Maxwellian distribution with *kT=4MeV*. This is in reasonable agreement with a ponderomotive potential for an intensity on target of 1×10^{20} Wcm^{-2}, suggesting there may be some self-focusing due to hole-boring occurring during the interaction. The second spectrum in Figure 11 (red) was obtained during a cone/shell implosion at stagnation with a 1ps duration heating pulse. It is clearly seen, however, that electrons below 7 MeV are severely attenuated. The number of electrons at 2.5MeV is reduced by a factor of 8, taking into account the factor of 3 difference between foil and stand-alone cone that is seen again in the electron distribution above 7MeV.

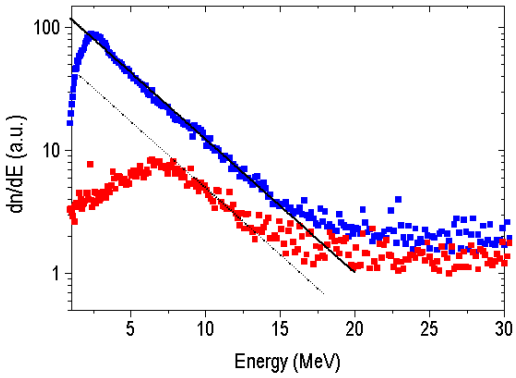

Figure 11. Comparison of electron spectra obtained with a 25µm thick Cu foil (blue) and a cone/shell implosion at stagnation with the 100 TW beam (red). The high energy components of both spectra are well described by exp(-E/kT) distributions with kT = 4 MeV (solid lines).

One possibility is that the fast electrons undergo small angle scattering in the compressed plasma, thus increasing the cone angle of the escaping electrons. Since the electron spectrometer subtends only a small solid angle, this effect would reduce the numbers of MeV electrons being detected. Suppose that the fast electrons are emitted in a ~20° cone angle before they traversed the compressed plasma. This would correspond to a solid angle of ~π/4 sr. The reduction in electron numbers can only be accounted for provided that 50% of the 2.5MeV electrons were scattered isotropically into 4π sr – which appears unlikely.

Discussion

To look at this question of the transport of MeV electrons in further detail, two dimensional computer simulations using the LSP code were undertaken, Figure 12. The LSP simulations were performed with an injected electron beam into the CD plasma whose density was varied between 1gcm^{-3} – 2gcm^{-3} – 4gcm^{-3}. The mesh resolution is 400 × 600 cells with 0.25micron size. The target is 150µm x 100µm. The code treated the background electrons as a fluid, whereas the injected electrons were treated as particles. The fluid background had a perfect gas equation of state and Spitzer transport coefficients. The code assumed a parallel electron beam temperature of kT = 2.5MeV and a transverse temperature of kT = 300keV.

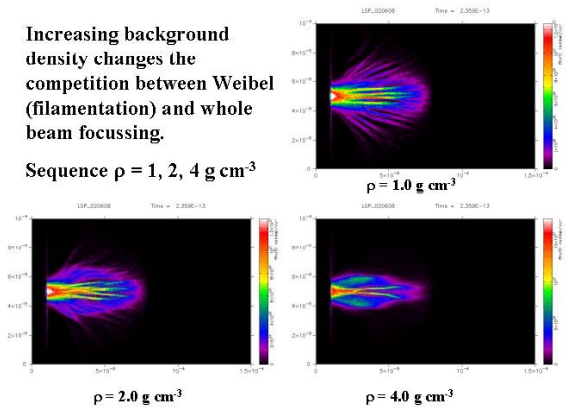

Figure 12. LSP simulations of electron beam density taken at 235fs into the pulse for three different densities. More collimated flow is indicated for the 4gcm^{-3} plasma.

The results of the simulations indicate that a higher background density promotes the collimation of the injected electron beam, due to the competition between Weibel and whole beam self-focusing. However, it also reduces the peak background temperature reached for these higher densities. This is due to the fact that collisional heating is proportional to density, the resistive heating is independent of density and the heat capacity proportional to density. These simulations indicate that it may be difficult to resistively heat high density plasmas for fast ignition.

This brings us back to the question of the missing electrons in Figure 11. If the electron beam is more collimated inside the over-dense region, then the electron spectrometer might be expected to register more electrons escaping the target, not fewer. Of course, it is conceivable that electrons that escape the target could miss the entrance to the electron spectrometer if the target is misaligned in some manner, but great care was taken to ensure that the cone/shell implosions were aligned correctly.

Another possibility is that anomalous resistivity is playing an important role in these interactions. The LSP simulations assume Spitzer resistivity for the background electrons. This is calculated assuming that the small angle scattering events are single electron-electron collisions that are summed over the Maxwellian distribution. When the magnetic field is large enough, for example in the presence of fine-scale filamentary structures generated by the magnetic Weibel or tearing mode instabilities, the Lamor radius of the colder electrons in the return current can be smaller than the Debye length. In this situation, multiple scattering events can occur with the same electron or ion. This quickly leads to the onset of turbulence and results in a substantial increase in the plasma resistivity. Sentoku et al., for example, has recently calculated that there is as much as 10^3 increase in resistivity compared with classical Spitzer values for PW laser-plasma interactions[9]. Anomalous resistivity may also account for the ballooning effect (where the X-ray spot size was always much larger than the focal spot dimensions).

Summary

Cone shell implosions have been performed on the Vulcan laser using the full 1-kJ output of the system. X-ray radiographic studies have indicated that compressed densities of 4gcm^{-3} and areal densities of 40mgcm^{-2} were achieved. X-radiation preheat, combined with lower ablation pressures, indicate that 1053nm drive is unlikely to be useful in full-scale ignition designs, due to the limited compressed densities that can be achieved.

Heating with 10ps pulses confirms that careful control of the rising edge of the compressed pulse is necessary to avoid hydrodynamic motion and plasma filling the cone. Nearly an order of magnitude reduction in the number of 2.5 MeV electrons escaping the target to the electron spectrometer was observed when 1ps pulses were used. Computer simulations show that the higher density of the compressed plasma promotes more collimated flows, but at the cost of reduced background heating. They also suggest that it is difficult to resistively heat higher density (200 gcm^{-3}) plasmas for fast ignition, when classical resistivity is used. Our results indicate, however, that anomalous resistivity may be playing an important role. Of course, this effect requires further detailed investigation.

Acknowledgements

The authors gratefully acknowledge the assistance of all the staff at the Central Laser Facility. This work was supported by the United Kingdom Engineering and Physical Sciences Research Council grant number GR/R16778. American and Japanese colleagues acknowledge support from the US National Science Foundation and the Japan Society for the Promotion of Science respectively.

References

1. M.Tabak *et al.* Physics of Plasmas 1, 1626 (1994); S.Hatchett and M.Tabak (private communication 2000).
2. P.A.Norreys *et al.* Physics of Plasmas 7, 3721 (2000)
3. R.Kodama, *et al.*, Nature 412, 798 (2001)
4. R.Kodama *et al.* Nature 418 922 (2002)
5. S.Hawkes *et al.* CLF Annual Report 2002/03 (this report), 183.
6. H.Habara *et al.* CLF Annual Report 2002/03 (this report), 185.
7. H.Habara *et al.* CLF Annual Report 2002/03 (this report), 43, and 45.
8. see Website http://home.fujifilm.com/products/science/bas1800_2/index.html
9. Y.Sentoku *et al.* Phys. Rev. Lett. 90, 155001 (2003).
10. R.Stephens *et al.* Phys Rev E (submitted 2003)

Picosecond radiography of a laser driven implosion

A J Mackinnon, P K Patel, S Hatchett, J Koch, T H Phillips, R Town, M H Key
Lawrence Livermore National Laboratory, Livermore, CA 94551, USA

L Romagnani, M Borghesi,
Dept of Physics, Queens University, Belfast, UK

J A King, R Snavely, R R Freeman,
Dept. of Applied Science, University of California, Davis, CA 94551, USA

R J Clarke, H Habara, R Heathcote, K L Lancaster, P A Norreys,
Central Laser Facility, CCLRC Rutherford Appleton Laboratory, Chilton, Didcot, Oxon, OX11 0QX, UK

R Stephens, T C Cowan
General Atomics, San Diego, USA

Main contact email address: *mackinnon2@llnl.gov*

Proton radiography of laser produced plasmas

Proton radiography using laser generated ion beams is a rapidly advancing area of research[1]. The proton probe beams used in these experiments are produced when femtosecond or picosecond laser pulses are focused, with irradiance in the range $I\lambda^2$ of $3x10^{18}$ to $5x10^{20}$ Wcm^{-2} onto thin foil targets. Up to 10^{11} -10^{13} protons, with energies up to 20-50 MeV in a quasi-exponential spectrum of mean energy 3-7 MeV, have been observed along the target rear surface normal, within a half angle of about 5-25 degrees[2]. Models predict that the protons are accelerated in a timescale of the order of a few times the laser pulse length[3], while penumbral edge measurements have shown that the proton source size is very small (~1-10μm) and the beam has a very low emittance (~$1x10^{-3}$ mm-rad).

Proton beams with multi-MeV proton energy, low emittance and short pulse length are particularly suitable for radiographic applications of dense plasmas and solid materials. For example 50-100MeV protons produced by a PW laser would be sufficiently energetic to probe cold, compressed NIF (National Ignition Facility) cores, while the lower energy protons could be used to diagnose electric and magnetic fields inside hohlraums. Multiple scattering strongly influences the imaging properties of these proton beams and in some cases limits the achievable resolution. Modelling of the effect of multiple scattering on proton radiography is currently being undertaken using Monte-Carlo proton transport codes. The first proton probing experiments of electromagnetic field structures in low-density laser-produced plasmas have been carried out at the Rutherford Appleton Laboratory[1]. However the utility of proton radiography in dense laser-compressed materials typical of those that exist in laser driven implosion has yet to be studied in detail. An experiment to investigate proton probing of a laser driven implosion was carried out on the 100TW Vulcan laser system to investigate the suitability of proton radiography to diagnose overdense plasmas.

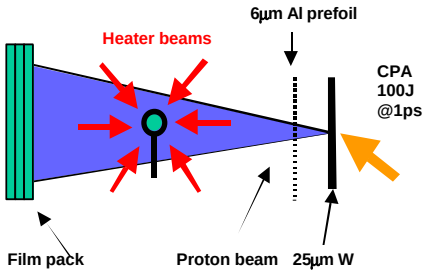

Figure 1. Geometry for proton radiography of the 6 beam implosion.

As shown in Figure 1, six beams of Vulcan (each 1μm wavelength, 1ns duration) were focused onto a microballoon at an irradiance of $1x10^{13}$ Wcm^{-2} and without phase plates. The individual beam energy was in the range of 100-150J giving a maximum energy on target of 900J. The targets were plastic microballoons (CD_2), 500μm in diameter and with two different wall thickness: 3μm and 7μm. The heater beams were arranged such that they illuminated the target tangentially from six orthogonal directions, giving the best symmetry for the implosion.

The implosion was diagnosed by two types of picosecond backlighters, namely laser produced protons in the MeV range or x-rays from Titanium K_α at 4.5KeV. These diagnostics were obtained by focusing a 50-100J CPA laser pulse, duration 1ps onto a solid foil at high laser irradiance (~$5x10^{17}$ Wcm^{-2} for K_α and $5x10^{19}Wcm^{-2}$ for proton radiography). The synchronization of the 1ns heater beams to the picosecond backlighter beam was measured to within 100ps using an optical streak camera. For the protons the source was used as a point projection imager of the target. The protons were obtained from a 25μm Tungsten foil and the proton beam produced an exponential spectrum of mean temperature 3MeV and a high-energy cut-off around 15-20MeV. The detector consisted of a multilayer pack containing spatially resolving dosimetry film (RCF) and particle track detectors (CR-39). This arrangement gave a diagnostic in which each layer was filtered by the preceding layer, giving a series of images on each shot each with a slightly different energy, ranging from 3 to 15MeV. For the K_α measurement a spherical quartz mirror was used to image the microballoon onto an x-ray sensitive CCD camera at a wavelength of 4.5KeV [4] with 5μm spatial resolution. For the K_α measurement the backlighter consisted of a Titanium foil and the spherical crystal imaged the implosion along the same axis as that used by the proton radiography.

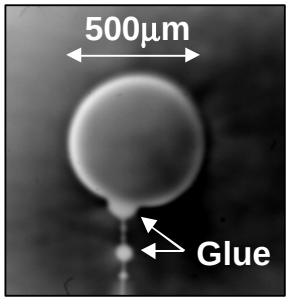

Figure 2. Proton radiograph, in 7MeV protons, of a 500μm diameter microballoon with a 7μm wall thickness.

Experimentally it was found that few or no protons were produced on shots when the back surface of the proton target

was exposed to the coronal plasma surrounding the imploding balloon.

To overcome this a 6µm aluminum foil was used to shield the proton foil from the hot coronal plasma produced during the implosion. This observation is consistent with the formation of a preformed plasma on the rear of the proton target before the arrival of the CPA laser pulse. Such a plasma at the rear surface of the target can reduce the accelerating electric field and disrupts the proton acceleration mechanism[5]. The aluminum pre-foil protected the back surface of the proton backlighter foil from scattered or specularly reflected light from the heater beams and low energy x-rays or fast ions from the implosion plasma and thus prevented the formation of a pre-plasma which would degrade the proton beam.

A proton radiograph in 7 MeV protons, of a cold (undriven) microballoon is shown in Figure 2. The balloon has good contrast and the shell is well resolved as shown in Figure 3. Analysis of the sharpness of the edges of the balloon gives resolution of ~7-10µm for this proton energy (the main limitation on the resolution in this experiment is actually due to the proton pre-foil rather than the intrinsic emittance of the proton source).

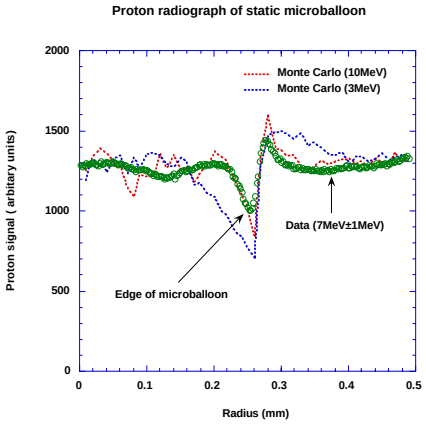

Figure 3. Radial line-out taken through center of proton radiograph. Radial line-outs from Monte-Carlo simulations of proton transport through a 500µm diameter, 7µm wall microballoon at 3 and 10MeV are also shown.

As shown in Figure 3 the balloon impresses a 30% modulation onto the proton beam with a characteristic shape where the proton signal first reduces below the background then overshoots just outside the shell. This behavior is consistent with multiple small angle scattering of the protons as they go through the microballoon wall[6]. Figure 3 also shows the output of proton Monte-Carlo simulations of a point source propagating through the microballoon using 3 and 10MeV protons. It can be seen that these simulations agree well with the data, reproducing the shape of the edge of the balloon and confirming that multiple scattering is responsible for modulating the proton beam and forming the image of the balloon.

The evolution of the capsule density profile during the implosion was studied by varying the delay between the backlighter and the implosion beams.

Figure 4 shows a proton image of a capsule where the drive was very asymmetrical due to significant timing difference between some of the drive beams. In this case the laser beams on the left hand side of the image arrived between 1 and 2ns before the laser beams on the right-hand-side. This led to the significant distortions with the shell travelling much further inwards on the left compared to the right of Figure 4. With more symmetrical drive conditions the capsule remains roughly spherical as the implosion proceeds. Figure 5 shows a proton radiograph taken of an imploding balloon taken 2ns after the start peak of the heater beams where the beams are more precisely synchronized. It can be seen that the implosion has retained roughly spherical symmetry with the overall diameter of the shell reducing to 300µm and with capsule walls that are still largely intact.

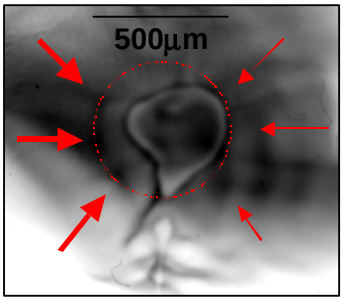

Figure 4. Proton radiograph of an imploding microballoon (7µm wall) with asymmetric drive due to mistimed heater beams (the beams shown on the left of the figure).

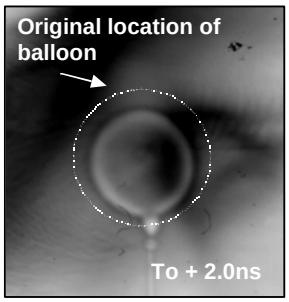

Figure 5. Proton radiograph (7MeV protons) taken 2ns after the peak of the heater beams (7µm wall).

Even though free from the gross asymmetries observed in the implosion of Figure 4, it is clear from this radiograph that the implosion still suffers from significant asymmetric drive conditions, the upper part of the shell having travelled almost twice the distance of the lower part of the shell. The implosion was overdriven from the upper laser beams in this part of the experiment. The remaining asymmetry observed in Figure 5 is also clearly evident as the implosion proceeded towards stagnation, as shown in the radiograph at T_o + 3ns in Figure 6. At this time the shell has assembled to a core with a full width half maximum (FWHM) of 80-90µm. (It should be noted that this capsule has a 3µm wall and so has imploded faster than the 7µm shell). The core has formed in the lower third of the original shell, consistent with more drive from the upper beams, and is not spherical. The elliptical core has a minimum diameter (fwhm) of 73µm and a maximum diameter of 85µm. Proton radiography clearly resolves this asymmetry and allows the density profile to be inferred. In order to obtain an estimate of the density profile in the core Monte-Carlo simulations of a Gaussian shaped density featured were carried out. (Simulations of a more realistic density profile generated from detailed hydrocode simulations are underway to further investigate relationship between the radiograph and the density profile).

Figure 7 shows a line-out across the minor diameter of the core feature, together with the output from a Monte-Carlo simulation taken with 15MeV proton. The simulations were scaled to directly compare with the data but this was done without changing the modulation level of the simulation. The peak density of the core and the fwhm of the function were treated as variable parameters until the best match with the data was obtained. A profile with a peak density of 3g/cc and

fwhm diameter of 80μm for the Gaussian function gave good agreement with the data, as shown in Figure 7.

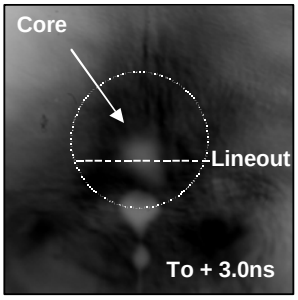

Figure 6. Proton radiograph of compressed core of a shell with a 3μm wall thickness.

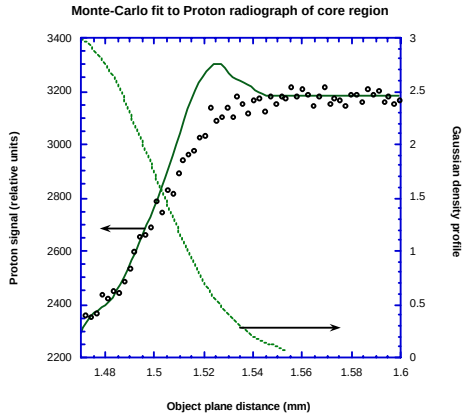

Figure 7. Line-out through density profile shown in Figure 6, together with Monte Carlo simulations of a Gaussian core profile with peak density 3g/cc and a diameter (fwhm) of 80μm.

Although this analysis is in the preliminary stages it can be seen that there is good agreement between these simple simulations and the data. Further work is underway to improve the realism of the simulations by including factors such as the filter and film response and finite emittance of the proton source.

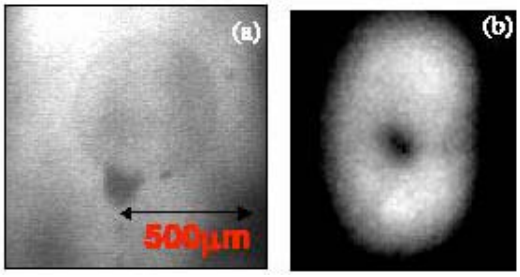

Figure 8. (a) K_α image of static, undriven microballoon. (b) Image of compressed core at T_o+3ns. The core feature is the ellipsoidal region of low transmission close to the centre of the image and tilted by 50 degrees to the horizontal axis of the figure and with a fwhm diameter of 96μm.

Independent confirmation of the proton radiography method was obtained with K_α radiography at 4.5 keV. Figure 8(a) shows an x-ray radiograph of a cold (undriven) microballoon taken with the spherical imaging crystal. Although the resolution of this method is high (around 5μm), it is clear from a direct comparison between Figure 8(a) and Figure 2 that the contrast for the static micro-balloon image with the 4.5keV photons is very much less than that observed with the 7 MeV protons. One reason for this is that the contrast in the x-ray backlighter images was optimized for the higher density conditions expected when the shell is compressed. These data show the utility of proton radiography compared to x-ray radiography for diagnosing early time distortions in the implosion process with high resolution and very good image contrast. A K_α x-ray image of imploded, high density compressed core is shown in Figure 8(b). This image was taken at T_o + 3ns, under similar laser conditions to that of the proton radiographs shown in Figure 5. This K_α image shows an ellipsoidal core, with an identical orientation to the core image obtained with the proton radiographs. A horizontal line-out through Figure 8(b) is shown in Figure 9. The diameter of the core feature in the horizontal direction was measured to be 96μm, in reasonable agreement with the proton radiography measurement of 80-90μm obtained from Figures 6 and 7.

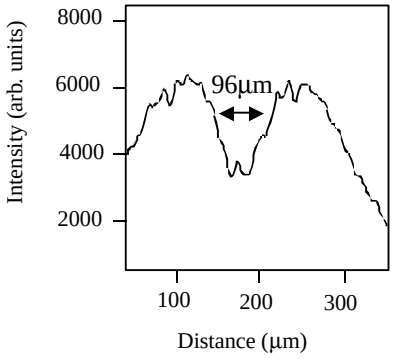

Figure 9. Line-out through K_α radiograph of core feature shown in Figure 8(b).

Conclusions

Proton and K_α radiography of a laser driven implosion with picosecond resolution have been demonstrated for the first time. Proton radiography exhibits high temporal, spatial resolution throughout all stages of the implosion. The K_α technique also gives good resolution but only gives high contrast images when the density is high. Preliminary analysis of the density profiles measured by proton radiography of cold shells and imploded cores shows good agreement with simple Monte-Carlo models. This work has shown that proton radiography is a promising candidate for looking at density perturbations throughout a laser driven implosion. More experimental and theoretical work is underway to fully investigate the utility of this very promising technique for radiography of highly overdense shocked material in ICF relevant plasmas.

Acknowledgments

This work was performed under the auspices of the U.S. Department of Energy by the Lawrence Livermore National Laboratory under contract No. W-7405-ENF-48 and EPSRC grants. AJM acknowledges partial support from an IRCEP advanced fellowship from Queens University, Belfast.

References

1. M. Borghesi, *et al.*, Plasma.Phys.Cont. Fus. 43, A267-A276 (2001); M. Borghesi, *et al.*, Physics of Plasmas, 9, 2214 (2002).
2. E.L.Clark *et al.*, Phys. Rev. Lett 84, 670 (2000), A.Maksimchuk *et al.*, Phys. Rev. Lett. 84, 4108 (2000). R.Snavely, *et al.*, Phys. Rev. Lett. 85, 2945 (2000).
3. Y. Sentoku, Phys.Plasmas. 5, 2009 (2003).
4. J. Koch *et al.*, Rev Sci Inst. 74, 2130 (2003).
5. A.J.Mackinnon *et al.*, 86 1769 Phys. Rev. Lett. (2001).
6. L. Romagnani *et al.*, CLF Annual Report 01/02, 26 (2002)

Ion acceleration measurements via neutron spectroscopy using the Vulcan 100TW facility

H Habara, K L Lancaster*, S Karsch, C D Murphy*, R J Clarke, J L Collier, S J Hawkes, R Heathcote, C Hernandez-Gomez, M H R Hutchinson*, D Neely, P A Norreys

Central Laser Facility, CCLRC Rutherford Appleton Laboratory, Chilton, Didcot, Oxon, OX11 0QX, UK.

** also at Blackett Laboratory, Imperial College, Prince Consort Road, London, SW7 2BZ, UK*

K A Tanaka, T Norimatsu, Y Toyama, R Kodama

Institute of Laser Engineering, Osaka University, Suita, 565-0841, Osaka, Japan

R G Evans

The Blackett Laboratory, Imperial College, Prince Consort Road, London, SW7 2BZ, UK

R R Freeman, J A King

Department of Applied Science, University of California, Davis, 1 shields Ave, Davis, CA 95616-8254, USA.

M H Key

Lawrence Livermore National Laboratory, Livermore, CA 94550, USA

C Stoeckl

Laboratory of Laser Energetics, University of Rochester, 250 E. River Road, Rochester, NY 14623-1299, USA

R Stephens

General Atomics, P.O. Box 85608, San Diego, CA 92186-5608, USA

M Zepf

Department of Pure and Applied Physics, Queens University of Belfast, Belfast, BT7 1NN, UK

Main contact email address : *H. Habara@rl.ac.uk*

Introduction

Ion acceleration processes in high-power laser-plasma interactions are an extremely important area of research in the fast ignitor (FI) scheme[1)] as a source of additional heating. These energetic particle sources are also expected to have many research applications e.g. in nuclear physics[2)] astrophysics[3)] and in biological and medical applications.

In recent studies, energetic ions with energies of over 1 MeV have been reported in intense laser-plasma interactions[4-6)]. The ion acceleration at the surface of the solid target has been shown to be affected by the plasma density scale-length as well as the precise electron acceleration processes[7)]. For example, when the contrast ratio of pedestal to main pulse is 10^{-4}:1, the ion acceleration is due to charge separation[8)], whereas for lower contrast ratios of 10^{-3}:1, hole-boring predominates[9)]. It is therefore very important to investigate the dependence on the scale-length of the preformed plasma, particularly for shorter scale-lengths where the higher acceleration gradients can be expected.

Given this, we have studied the ion acceleration at the solid surface with a short scale-length plasma. The ion acceleration inside the target was investigated by neutron spectroscopy generated from nuclear fusion reactions of accelerated ions (via the beam fusion process). Neutron measurements can be used to derive the accelerated ion momentum distribution inside the over-dense plasma, avoiding the influence of strong electric and magnetic fields around the target[10)]. In this paper, the momentum distribution of accelerated ions is presented by unfolding the neutron spectra by numerical analysis using a 3-dimensional Monte-Carlo fitting procedure.

Experiment

The experiments were performed at Rutherford Appleton Laboratory using the Vulcan laser facility[11)]. This laser system produces pulses up to 80J at a wavelength 1.05μm with pulse duration of 0.9-1.2ps. The beam irradiated plane deuterated plastic target at normal incidence and was focused using an f/4 off axis parabolic mirror. The far field pattern indicated 30% laser energy concentrated within 10μm diameter, therefore the peak laser intensity is 2.5×10^{19}W/cm^2. The contrast ratio between pedestal and main is 10^{-7}:1.

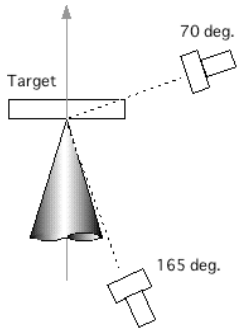

Figure 1. Experimental setup.

The neutron energy spectra were detected by a plastic scintillator combined with photomultiplier-tube through the time-of-flight (TOF) method. Figure 1 shows the experimental setup. Two detectors were set at 71° and 165° from the target normal at 2.3m and 1.9m distance from the target. Each detector has 10cm lead blocks in front of it (to reduce the gamma noise which causes the detector to saturate) as well as 5cm blocks at the side of the detector. The energy resolution of the detector was about 200keV and the valid detectable range was under 15MeV. The detection efficiency and the response function are well calibrated from the thermal neutron signal generated from implosion experiment using a deuterium-filled glass micro balloon.

The momentum distribution of the accelerated ions was evaluated by 3-dimensional Monte-Carlo calculations[12)] to fit the calculation to the experimental spectra. The calculations were performed with a number of distinct momentum distributions, e.g. Maxwellian, monoenergetic, isotropic, anisotropic, and so on.

Figure 2 shows the obtained neutron spectra at (a) 71° and (b) 165° from the target normal. The neutron yield per steradian

in the forward and backward direction was $2.81\times10^{6}\times(1.0\pm2.0)$ and $2.65\times10^{6}\times(1.0\pm2.5)$, similar to yields observed previously on Vulcan[13]. On the other hand, the calculated neutron count at the same direction per steradian per ion are each 3.97×10^{-8} and 3.04×10^{-8}. Consequently, the total ion energy was about 1.2 (1.0±2.5) J, corresponding to between 1%-5% of the laser energy contained within the focal spot. The spectrum taken from the detector at the front of the target indicates a Doppler shift of the peak to the lower energy, suggesting the ions are accelerated into the target. On the other hand, the neutron spectrum obtained from detectors at the side of the target showed the peak that was split at 2.1 and 2.8 MeV. The split suggests the ion acceleration is predominantly in the radial direction rather than the transverse direction.

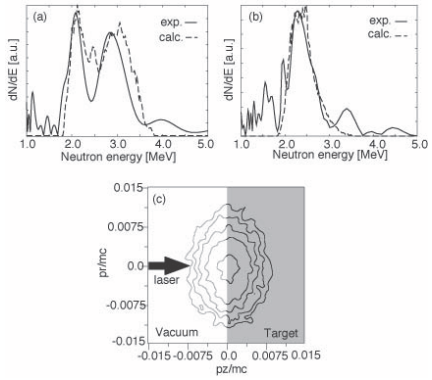

Figure 2. Neutron spectra detected at (a) side and (b) front of the target. (c) Ion momentum distribution from Monte-Carlo fitting.

Detailed analyses were carried out using a Monte-Carlo fitting procedure to the experimental spectra. The dashed lines in Figure 2 (a) and (b) show the well fitted spectra assuming the anisotropic ion momentum distribution as shown by the contour plot in Figure 2 (c). The gray and clear zone indicate the target and vacuum region, respectively. The contour lines in the figure are plotted by every $10^{0.4}$ of relative ion number. The distribution has a Maxwellian energy distribution with temperatures of 40keV for transverse direction and 80keV for radial direction.

Discussion

The results show the inhibition of ion acceleration to the normal direction and radial expansion. This indicates that under these conditions, the ions are not accelerated by the static field induced by the charge separation, but in a manner that is similar with the result from the "hole-boring model" for longer scale-length interactions. However, the contrast ratio of our laser system is order of 10^{-7}, therefore a steep electron density gradient can be expected. The electron density gradients are calculated by a 2-dimensional magnetic hydro-code, POLLUX[12], assuming that the pedestal has a Gaussian shape with 300ps duration from the temporal window of the optical switch in the laser system. Figure 3 shows the density gradient at 150ps from the beginning of the pedestal, just when the main pulse arrives on the target. In the result, the scale length of the gradient is about 3µm. However, the plasma has a long corona tail with a density of $10^{20}/cm^3$ over almost 10µm, which is equivalent with the result from shadowgraphic images[14].

The main pulse irradiated in the plasma can make a hole in the corona and then create a “bow-like” shock wave as described in PIC calculation done by Wilks[15] or Sentoku[9].

The ion energy can be also understood by shock acceleration. Figure 4 shows the energy distribution of ions accelerated to forward (blow-off), side, and backward (into the bulk) directions calculated by the POLLUX code. In this calculation, the main pulse with a 1ps duration, 10µm spot size and intensity of 2.5×10^{19} W/cm^2 interacting with the existing plasma as shown in Figure 3.

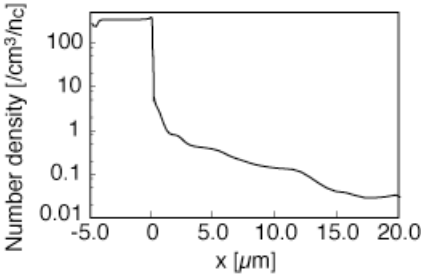

Figure 3. Plasma electron density profile created by laser pedestal.

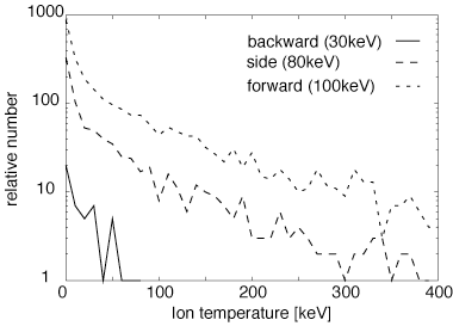

Figure 4. Ion distribution accelerated into the target (backward), to the side, and in the blow off (forward) directions.

Here, the ion temperature directed into the target (backward) and side is 30 and 80keV, respectively, agreeing well with the experimental results. The region where the ions are accelerated reaches Mach numbers from 1.0 to 1.6, which satisfies the shock acceleration condition.

Summary

We have measured the momentum distribution of accelerated ions by ultra-intense laser light. The distribution shows that the ions are accelerated to the side rather than in the transverse direction. This result indicates the ion acceleration is by the shock wave formed on the hole-boring surface in the long-coronal plasma.

Acknowledgement

The authors gratefully acknowledge the help and support of the engineering, laser operations, target preparation and the staff at the Central Laser Facility in the execution of this work.

References

1. M. Tabak, *et al*. Phys. Plasmas 1 1626 (1994).
2. K. W. D. Ledingham *et al*. Phys. Rev. Lett. 84 899 (2000).
3. D. R. Farley *et al*. Phys. Rev. Lett. 83 1982 (1999).
4. A. P. Fews, *et al*. Phys. Rev. Lett. 73 1801 (1994).
5. K. Krushelnick *et al*. Phys. Plasmas 7 2055 (2000)
6. T. Ditmire, *et al*. Nature 398 489 (1999).
7. M. I. K. Santala *et al*. Phys. Rev. Lett. 84 1459 (2000).
8. A. Maksimchuk, *et al*. Phys. Rev. Lett. 84 4108 (2000).
9. N. Izumi *et al*. Phys. Rev. E 65 36413 (2002).
10. C. N. Danson, *et al*. Opt. Commun. 103 392 (1993).
11. H. Habara *et al*. Phys. Plasmas to be published.
12. G. J. Pert J. Comput. Physics 43 111 (1981).
13. P.A.Norreys *et al*. Plasma Phys. & Controlled Fusion 40, 175-182 (1998).
14. P. A. Norreys *et al*. Phys. Plasmas 6 2150 (1999).
15. S. C. Wilks *et al*. Phys. Rev. Lett. 69 1383 (1992)

Characterisation of ^{7}Li(p,n)^{7}Be neutron yields from laser produced ion beams

K L Lancaster*, S Karsch, H Habara, C D Murphy*, R J Clarke, J LCollier, R Heathcote, S J Hawkes, C Hernandez-Gomez, M H R Hutchinson, D Neely, P A Norreys

Central Laser Facility, CCLRC Rutherford Appleton Laboratory, Chilton, Didcot, Oxon, OX 11 0QX, UK
** also at the Blackett Laboratory, Imperial college, London, SW7 2BZ, UK*

M S Wei, F N Beg, E L Clark, K Krushelnick

The Blackett Laboratory ,Imperial college, London, SW7 2BZ, UK

R R Freeman, J A King

Department of Applied science, University of California, Davis, 1 shields Ave, Davis, California, USA

M H Key

Lawrence Livermore National Laboratory, Livermore, CA, USA

K A Tanaka, T Norimatsu, Y Toyama, R Kodama

Institute of Laser engineering, Osaka University, Japan

K W D Ledingham, P McKenna

Department of Physics, University of Strathclyde, Glasgow, G4 0NG, UK

R Stephens

General Atomics, San Diego, CA, USA

C Stoeckl

University of Rochester, USA

M Zepf

Department of Pure and Applied Physics, Queens university, Belfast, UK

Main contact email address: *K.L.Lancaster@rl.ac.uk*

Introduction

There has been considerable research into energetic proton and ion beams produced in short pulse, high intensity, laser-plasma interactions[1-9]. The protons appear to be accelerated from two regions of the target. At the front of the target, ion acceleration can occur by a number of mechanisms: electrostatic sheath expansion into the vacuum, a Coulomb explosion of a channel formed in the pre-formed plasma generated by the pedestal of the laser pulse, hole-boring induced by charge separation, and by electrostatic shocks. At the rear surface of the target, an electrostatic sheath, generated by fast electrons that reach there but cannot escape the target due to space charge build up, also accelerates ions.

These laser produced proton beams can be used to induce reactions in secondary cold targets to produce a bright source of neutrons. Neutrons from laser-plasma interactions could be developed as a source for fast neutron radiography[10]. Neutrons provide a good method of differentiating between high and low Z materials due to the fact that they are attenuated by atomic nuclei. Low Z ions scatter neutrons more easily than high Z ions. X-rays, by contrast, are attenuated by electrons and are less able to distinguish between nuclei with different atomic mass. Both thermal and fast neutrons can be used for imaging purposes, but fast neutrons are ideal for imaging the interior of dense objects that would attenuate thermal neutrons.

There are several methods of fast neutron radiography. The first one relies on time-of-flight gamma-ray emission from nuclei excited by the neutron beam along with neutron transmission measurement to gain a spatially resolved picture of elemental composition with position[11]. This method has been proposed for the detection of hidden drugs and buried layers of different elemental composition. Secondly it is possible to employ neutron resonance radiography[12] to determine elemental composition. By varying the energy of the neutron beam, resonances in the cross section of neutrons incident on particular nuclei can be utilized. Neutron scattering is maximised at these resonances and leads to a reduction in neutron transmission. By spatially resolving the neutron flux an image of the element's line density can be obtained. Even the non-resonant scattering depends on material density fluctuations and can be used in a similar way to obtain an image[13].

We present here the first study of (p,n) reactions induced in secondary LiF targets from laser-produced proton beams that reveals both high neutron fluxes - up to 3×10^{8} sr^{-1} - and an anisotropy in the angular distribution of neutrons. Similar measurements were made by Disdier et al[14] using the D(d,n)^{3}He reaction. The Vulcan laser facility provided a 1ps, 1.053 μm pulse with a rectangular near-field beam profile (200mm×110mm). The full aperture beam was focused on target using f/4.5 and f/3.5 off axis parabolas at both normal and 135º incidence to the target normal respectively. In these experiments, the laser was focused to a 10μm focal spot. The energy contained within that spot was ~30% of the total incident energy (up to 80 J), giving focused intensities up to 2.5×10^{19} Wcm^{-2}.

Experimental layout

Thin foil targets of Mylar (50μm) and copper (25μm) were used to produce proton beams with equivalence to References 1-7. A secondary LiF catcher target (3.4 mm thick) was used to generate neutrons via the ^{7}Li(p,n)^{7}Be reaction. The primary and secondary targets were separated by a distance of 0.5cm.

Several methods of neutron detection were employed to obtain a picture of the angular distribution of the neutrons. Current mode time-of-flight (TOF) detectors consisting of plastic scintillators, which detect neutrons via elastic scattering off protons in the scintillator, coupled to photomultiplier tubes were used to diagnose the energy of the neutrons. Time of flight signals were recorded on an oscilloscope.

Plastic nuclear track detectors (CR-39), shielded with 2mm of lead front and back, were also used to measure neutron yield via damage caused by 'knock-on' protons. After exposure, the detectors are etched in concentrated sodium hydroxide solution at 80°C for 3 hours. Knock-on protons propagate in the track detector and damage the polymer bonds via ionization. After

etching the damage tracks are revealed as pits in the surface of the detector. Typical proton tracks have a diameter ~10μm. By counting the total number of pits and correcting for the solid angle and sensitivity, it is possible to infer a neutron yield. The sensitivity of knock-on protons in CR-39 detectors to neutrons with energies of 2.5 MeV is 1.0×10^{-4} [15]. As our peak neutron energies are near this value it is reasonable to assume this sensitivity.

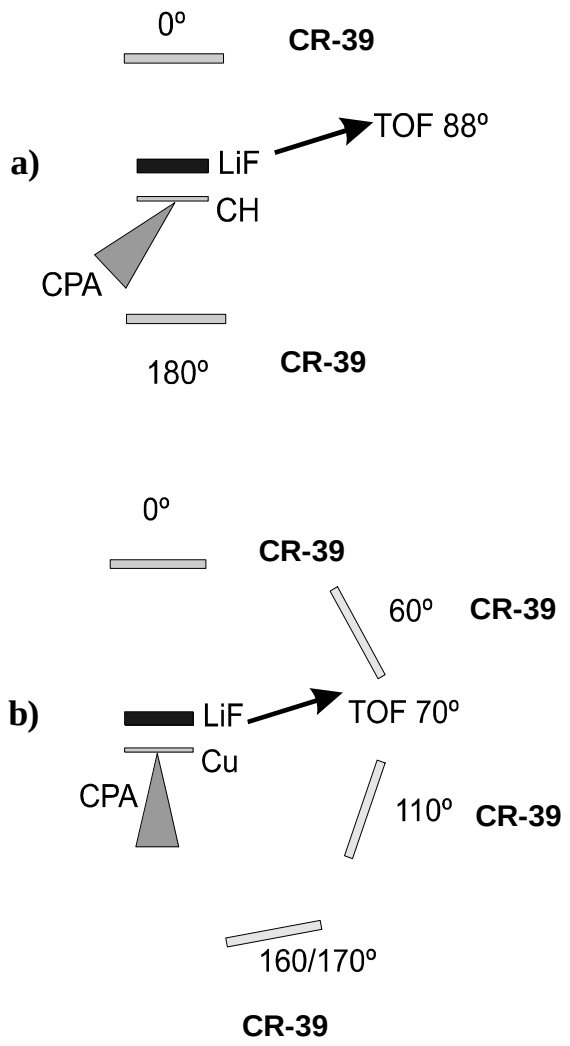

Figure 1. a) Experimental set-up with CH primary target, b) experimental set-up with Cu primary target.

In this report, all angles are defined with respect to the target normal from the rear surface as depicted in Figure 1. In the first neutron production experiment, Mylar primary and LiF secondary targets were used. An f/3.5 off axis parabola focused a 1ps, 1.053 μm pulse onto target at 135º. CR-39 was placed in at 0º and at 180º to obtain the yield in these directions. A time of flight detector was placed 2.32m away at an angle of 88º. In the second experiment, copper primary and LiF secondary targets were used. An f/4.5 off axis parabola focused a 1ps, 1.053 μm pulse at normal incidence to the target. CR-39 was placed close to the target (7-10cm) at 0º, 60º, 110º, and 160º to obtain the angular distribution of neutrons. The current mode TOF detector was placed 2.25 m away at an angle of 70º.

Results and discussion

Figure 2(a) shows a typical time of flight measurement obtained using the Copper primary targets. The neutron energy peaks at ~2.1 MeV. Figure 2(b) shows a typical time of flight spectrum with CH primary targets. The neutron energy peaks at ~1.8 MeV.

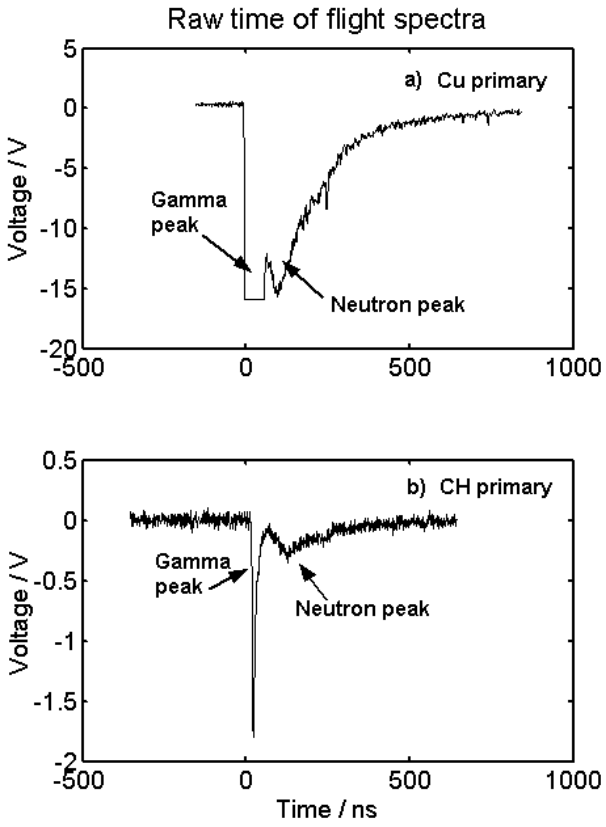

Figure 2. Two raw neutron time of flight spectra, a) Neutron spectrum produced from using a Cu primary target and b) Neutron spectrum produced from using a CH primary target.

The black squares in Figure 3 represent measurements of the angular distribution of neutrons at various angles for an energy on target of 69 J and an intensity of 2×10^{19} Wcm^{-2}. The target consisted of 50μm-thick Mylar plastic. The peak yield was found to be up to 2×10^{8} sr^{-1} at 0º and 3×10^{8} sr^{-1} at 180º. The red and blue squares in Figure 3 represent measurements of the angular distribution of neutrons using the Cu primary targets. The peak yield was up to 1.5×10^{8} sr^{-1} at 0º and 2×10^{8} sr^{-1} at 180º.

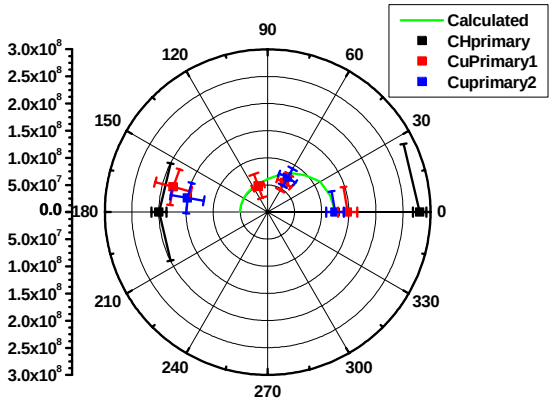

Figure 3. Measured and simulated neutron angular distribution. Solid line represents the simulated distribution, black squares represent the CH measurements, blue and red squares represent the Cu Measurements.

From the IAEA Drosg-2000 code the cross-section for the $^{7}Li(p,n)$ reaction shows that the neutron yield at 0º should be a factor of three greater than at 180º. The solid line in Figure 3 represents this distribution and was generated by the Monte-

Carlo code by S. Karsch[16] using the Drosg cross sections. The yields on this line are arbitrary but it shows the relative distribution at each angle. The measured and simulated distributions match well in the forward hemisphere but there is a discrepancy of 180º. Other reactions must be contributing to the final yield here. Firstly there are several Li(p,n) reactions that can occur within the target. The ^{7}Li(p,n$_0$)^{7}Be reaction has a threshold at 1.881MeV. At 2.372 MeV the first excited state reaction, ^{7}Li(p,n$_1$)^{7}Be*, will occur. At 3.697 MeV the three-body breakup reaction, ^{7}Li(p,n ^{3}He)^{4}He, will occur[17].The higher order Li reactions are insignificant here as the cross section is small. At worst the measured difference between 0º and 180º in this paper is 1×10^{8} sr^{-1} so other reactions must be considered.

The CR-39 was shielded with lead and so the ^{208}Pb(p,n) ^{208}Bi reaction may be significant for the 180° blow-off direction where energetic protons were incident directly onto the Pb material. In the other directions, this reaction is not considered important – in the forward direction, the protons are stopped in the LiF target, and at oblique angles the detectors are well outside the measured cone angle of the proton beams. The cross-section for this reaction is ~5 barn at 25 MeV. The yield of protons produced at 180º can be greater than that at 0º and will be at a minimum at 90º. At 0º all protons should be stopped in the LiF tablet and so the Li(p,n) neutrons will make up a significant part of the yield here. However at 180º there may be a significant contribution from the ^{208}Pb(p,n) ^{208}Bi reaction. To obtain a more qualitative estimate of the significance of the ^{208}Pb(p,n)^{208}Bi reaction a Monte-Carlo code was used to provide an estimate of the yield of neutrons produced by this reaction.

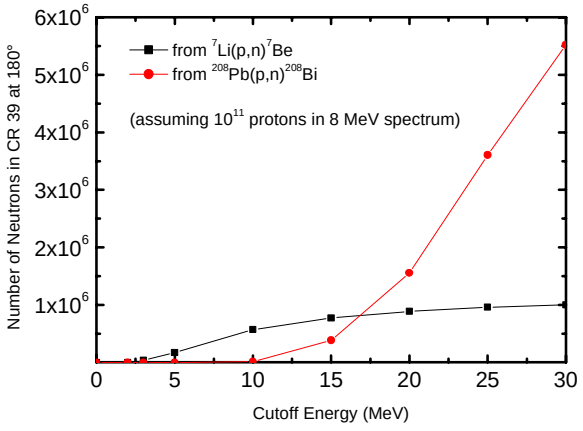

Figure 4. Monte-carlo generated neutron numbers with incident proton cutoff energy for ^{208}Pb(p,n) ^{208}Bi (red) and ^{7}Li(p,n)^{7}Be (black).

The fast rise in the ^{208}Pb(p,n)^{208}Bi cross section with energy (Figure 4) above 10 MeV causes a strong dependence of the neutron yield from this reaction on the hot part of the proton spectrum. To model this we assumed protons in an exponential spectrum of temperature 8 MeV and a 40º divergence hitting either the LiF tablet or the lead shielding of the detector at 180º. We varied the cut-off of the proton spectrum from 5 to 30 MeV and plotted the neutrons entering the detector at 180º from both reactions. Because of the geometry of the experiment nearly half of the neutrons generated in the lead enter the CR-39 and they constitute a significant amount of the total measured neutrons for cut-off energies greater than 15 MeV. Although the proton spectrum in the blow-off direction was not measured in this experiment it was determined in a previous experiment to extend between 15 and 25 MeV. This makes the assumption of the lead causing the high yield at 180º very likely. Note that all the other positions of CR-39 are either obstructed by the LiF tablet or are outside the blow-off direction so that the lead reaction is strongly suppressed here.

Error analysis

To assist in the error analysis, a test slide of CR-39 was etched alongside the exposed slides to obtain a measurement of background levels. This slide was analysed in exactly the same way as the exposed slides and a background count was obtained.

The spread on the number of positive counts on each slide,$\sqrt{n}$, was summed in quadrature with the background error to obtain a value for the absolute error of each measurement. The error bars on the polar plot in Figure 3 represent these errors. The error on the angle measurement arises from the fact that the detector has a finite size and so will cover a small range of angles.

Discussion

To be useful a yield of ~$10^{11\text{-}13}$ sr^{-1} is needed and so a total yield of $10^{12\text{-}14}$ neutrons must be available. To produce this yield of neutrons the laser must deliver more energy. From simple scaling of current experiments it is possible to infer the laser energy needed to produce such yields. The neutron yield, $Y_n \propto \sigma E \eta$ where σ is the cross section, E is the laser energy on target and η is the conversion efficiency of laser energy to protons. The conversion efficiency of laser energy to protons has been seen to increase with increasing laser energy. Measurements on the Vulcan system show a conversion efficiency of between 0.1 and 5% [18]. At energies > 400J it has been shown that the conversion efficiency increases to 12%[19]. However, with higher energy lasers the protons will be more energetic and the average proton energy will increase. The giant resonance in the cross section of the ^{7}Li(p,n)^{7}Be reaction spans an incident proton energy range of 3-7MeV up to a value of 320mb and so for higher energies a different reaction should be utilised. It is preferable to utilize an element that has a peak in the (p,n) cross section for higher energy protons such as ^{56}Fe(p,n)^{56}Co. This reaction has a cross section of ~1 barn for 25 MeV incident proton energy. The proton range will increase with proton energy so the thickness of the target should be increased.

From this relation a laser of ~4KJ, such as the OMEGA EP laser under construction at LLE, should produce a neutron yield in this range provided the range and cross section are matched accordingly. It may also be possible to exploit such neutron production techniques on high-rep rate, tabletop lasers[10] to produce a compact source of neutrons for these purposes.

By using laser produced ion beams to produce neutrons it may be possible to couple such neutron sources to dense, high energy density plasmas generated by much longer pulses in Z-pinches and other pulsed power devices.

To exploit neutron radiography in the current scheme it is planned to conduct experiments in which laser produced neutrons pass through a test object and are attenuated according to the materials present. A neutron imaging plate or a standard image plate such as BAS-TR coupled with a polyethylene converter can be used to detect the neutrons[20]. It may also be possible to activate a sample with the neutrons and then place this on to a standard image plate to obtain an image.

Conclusions

We have presented neutron yields from ^{7}Li(p,n) reactions using laser-generated proton beams from Cu and CH primary foils incident on a LiF secondary target. The CH foil produced neutron yields of up to 3×10^{8} neutrons / steradian for p-polarized irradiation and the Cu foils produced neutron yields of up to 2×10^{8} neutrons / steradian for normal incidence irradiation. The yields for all foil types were slightly higher at

180º compared to 0º. This may be attributed to the $^{208}Pb(p,n)^{208}Bi$ reaction in the lead shielding on the CR-39. This reaction should not be significant at 0º as all the protons should be stopped in the LiF tablet. Between 0º and 60/110º the distribution agrees well with the calculated distribution and it is therefore probable that the yields here are due to reactions in the LiF tablet.

Acknowledgements

The authors gratefully acknowledge the support of all of the staff of the Central Laser Facility without whose assistance this work would not have been possible. The work was supported by the United Kingdom's Engineering and Physical Sciences Research Council. American and Japanese colleagues acknowledge support from the US National Science Foundation and the Japan Society for the Promotion of Science respectively.

References

1. E.L. Clark *et al*., Phys. Rev. Lett. 84, 670 (2000)
2. R.A.Snavely *et al*., Phys. Rev. Lett. 85, 2945 (2000)
3. M. Zepf *et al*., Phys. Rev. Lett. 90, 064801 (2003)
4. K. Krushelnick *et al*., Phys. Plasmas 7, 2055 (2000)
5. A. Mackinnon *et al*., Phys. Rev. Lett. 86, 1769 (2001)
6. M. Roth *et al*., Phys. Rev. Spec. Top. 5, 061301 (2002)
7. A. Maksimchuck *et al*., Phys. Rev. Lett. 84, 4108 (2000)
8. M. Hegelich *et al*., Phys. Rev. Lett. 89, 085002 (2002)
9. K.W.D Ledingham *et al*., Science 300 ,1107 (2003)
10. L.J.Perkins *et al*., Nuclear Fusion 40 ,1 (2000)
11. R. Loveman *et al*., Nucl. Instrum. Meth. B 99, 765 (1995)
12. G. Chen *et al*., IEEE T. Nucl. Sci. 49, 1919 (2002)
13. J.S. Brzosko *et al*., Nucl. Instrum. Meth. B 72, 119 (1992)
14. L. Disdier *et al*., Phys. Rev. Lett. 82, 1454 (1999)
15. J.A.Frenje *et al*., Rev. Sci. Instrum. 73, 2597 (2002)
16. S. Karsch *et al*., Phys. Rev. Lett. 91, 015001 (2003)
17. M. Drosg., Nucl. Sci. Eng. 106, 279 (1990)
18. M. Zepf *et al*., Phys. Plasmas 8, 2323 (2001)
19. RA Snavely *et al*., Phys. Rev. Lett. 85 ,2945 (2000)
20. M. Matsubayashi *et al*., Nucl. Instrum Meth A 463, 324 (2001)

Time resolved emission for a Ne-like nickel X-ray laser

Y Abou-Ali, G J Tallents, M Edwards, R E King, G J Pert

Department of Physics, University of York, Heslington, York, YO10 5DD,UK

A Demir

Department of Physics, University of Kocaeli, Kocaeli, 41000, Turkey

Main contact email address: *yaa100@york.ac.uk*

Introduction

The measurement of the pulse duration of X-ray laser output is important for potential applications and to help understand gain and propagation conditions. In this article, we simulate using the EHYBRID[1)] code the temporal variation of X-ray lasing at 23.1 nm for Ne-like nickel and compare this with experimental measurements.

The duration of gain of an X-ray laser is typically 2 – 10 times longer than the output pulse duration[2)]. A direct measure of gain duration from the emission of resonance lines is not possible as resonance line emission from the upper laser level of Ne-like and Ni-like ions is forbidden. In this article, we show using a simulation code that an estimate of the spatially-averaged duration of X-ray laser gain can be obtained by temporally resolving the spectrally integrated continuum and resonance line emission arising from states near in energy to the upper laser level.

Experiment

In a recent experiment[3)], X-ray lasing was produced in Ne-like nickel at 23.1 nm ($3s^2 2p^5 3p\ ^1S_0 \rightarrow 3s^2 2p^5 3s\ ^1P_1$) by irradiating solid nickel slabs with two beams of wavelength 1.06 μm from the Vulcan glass laser. A pre-plasma was formed with a background pulse of duration 280 ps and peak irradiance 2×10^{13} Wcm^{-2} in a line focus of length 16 mm and width 100 μm. The main pulse irradiance had a duration of 1.2 ps and peak irradiance 7×10^{15} Wcm^{-2} in a line focus of length 12 mm and width 100 μm. The main pulse was incident at a travelling wave speed of light c along the target length. The X-ray laser output was recorded using a flat field grating spectrometer with a 1200 lines/mm aperiodic ruled grating and an Axis Photonique streak camera[4)] positioned at the spectrometer detection plane. The grating was positioned horizontally, so that the variation of the X-ray laser beam intensity with horizontal angle from the vertical target surface could be observed at the spectrometer detection plane. The spectrometer was initially operated with a CCD detection system to check the position of the X-ray laser beam. The streak camera was subsequently positioned with a vertical entrance aperture at the position of peak X-ray laser output recorded by the CCD camera. The peak-to-peak delay between the background and main pulse was varied to optimise the X-ray laser output using the flat field spectrometer with CCD detection. For results reported in this article, we used a delay between pulses of 300 ps.

Another simple streaked slit diagnostic[5)] was developed to record resonance line emission from states near in energy to the upper lasing levels. A Kentech streak camera with a thin gold photocathode (0.3 μm deposited on 1 μm aluminium) viewed the plasma transversely from the front side at an angle of 82.5° to the focal line. The estimated temporal resolution of ≈ 6 ps with this streak camera is dominated by the 500 μm wide entrance slit. A space resolving slit of width 270 μm positioned normal to the timing slit gave spatial resolution ≈ 0.7 mm along the line focus length. A filter of 2.4 μm thick aluminium was employed so that emission in the 0.6-1.8 nm wavelength range was recorded with the diagnostic.

Results

We have used EHYBRID[1)], RAYTRACE[6)] and our spectral emission post-processor[7)] code to evaluate the X-ray lasing duration and resonance line output of nickel for comparison with the experimental results. The hydrodynamic with atomic physics code EHYBRID simulates laser interaction with a solid target as used to create X-ray laser media. EHYBRID approximates the lateral plasma expansion from a slab target by assuming a self-similar density profile in the direction perpendicular to the line focus and the incident laser beam. In the direction towards the laser, the code solves the fluid equation of continuity and the Navier-Stokes equation to calculate the density profile. Energy transport in the direction parallel to the laser is reduced from the free streaming limit by a flux limiter of 0.1. The code evaluates inverse bremsstrahlung absorption, with resonance and other critical density absorption taken into account by dumping 30% of the input laser energy at the critical density. The code does not explicitly model other laser absorption mechanisms such as quarter critical processes. Following King et al[8)], we only input to the code 1/3 of the experimental laser energy so as to allow for un-modelled laser interaction processes such as laser scatter.

The temporal variation of the Ne-like nickel output at 23.1 nm as recorded with the streaked spectrometer using an image intensifier is shown in Figure 1. We believe that the streak camera may have been operated just into saturation (with a slight excess of photo-electrons), which degraded the temporal resolution. It is likely that the observed double humped temporal profile for Ne-like nickel output at 23.1 nm is due to saturation. Superimposed on Figure 1 is a simulated temporal variation of the Ne-like nickel X-ray laser output at 23.1 nm using RAYTRACE post-processing of the space-time output from the EHYBRID code. The simulated duration of X-ray lasing (≈12 ps) agrees with the measured laser duration.

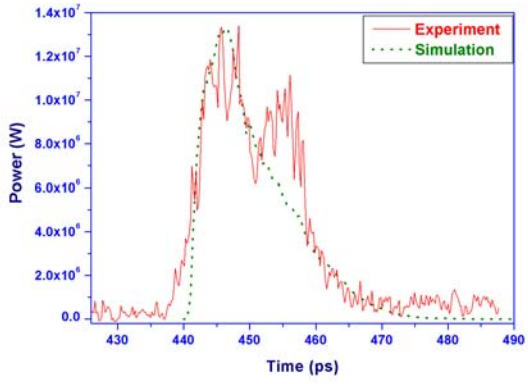

Figure 1. The simulated temporal variation of the Ne-like nickel X-ray laser output at 23.1 nm after ray tracing superimposed on the experimental temporal variation of the Ne-like nickel output recorded using a flat field spectrometer and a fast streak camera.

To simulate the resonance line emission of nickel, the original EHYBRID code was modified to calculate the spontaneous transition rates A_{ij} from the absorption oscillator strengths used in the evaluation of the ionisation balance. 112 Ne-like $1s^22s^22p^6$-$1s^22p^5nl$ (n=3-5, l=s,p,d) and 642 F-like $1s^22s^22p^5$-$1s^22p^4nl$ (n=3-5, l=s,p,d) resonance line intensities have been calculated for the simulation of the spectral emission from the nickel plasma. Resonance lines are often optically thick as they have strong oscillator strengths. Opacity is modelled through an approximate escape factor based on the Holstein function for Doppler broadened lines[9]. Line intensities are evaluated in a post-processor to EHYBRID using the simulated N_i population densities and T escape factor.

In addition to spectral line intensities, the emission due to free-free Bremsstrahlung and free-bound continuum emission is evaluated from EHYBRID deduced plasma parameters in our post-processor. The scattering of a free electron by a heavy charge centre gives rise to Bremsstrahlung radiation. The capture of free-electrons into a bound state of an ion, with the accompanying emission of radiation of energy $h\nu$ produces a continuous spectrum of radiation for $h\nu>\chi_n$ (where χ_n is the ionisation energy from level n of the ion). Free-bound emission arising from recombination of free electrons with O-like, F-like, Ne-like, Na-like, Mg and Al-like ions has been considered.

Spectrally integrated time-resolved experimental and theoretical transverse emission in the 0.6-1.8 nm spectral region emitted from a nickel plasma and recorded by a streaked slit diagnostic is shown in Figure 2. As the streaked slit camera was not absolutely calibrated for intensity, the amplitude of the experimental measurement has been adjusted to fit the simulated emitted power for Figure 2. The emission recorded by the streaked slit diagnostic comprises mainly continuum emission in the 0.6 to 1.8 nm spectral range and resonance lines of Ne-like nickel (resonance emission in the range 0.95 to 1.45 nm from states with electron configurations ($2s^22p^53s$, $2s^22p^53d$, and $2s^22p^63p$) plus F-like lines. The upper limit of recorded continuum emission is determined by the 3.4 μm thickness Al filter and the lower limit by the fall-off in continuum emission at shorter wavelengths. Our simulations show that the free-bound and free-free continuum emission dominate line emission for the spectrally integrated slit camera. The simulated percentage from the different emission processes after spectral and time integration for the experimental filtering used in the streaked slit diagnostic has components of 67% from free-bound continuum, 23% from free-free continuum, 6% from F-like lines and 4% from Ne-like lines. The simulated duration of temporal output of continuum and resonance lines (≈35 ps) for Ni is in agreement with measurements made using the streak camera.

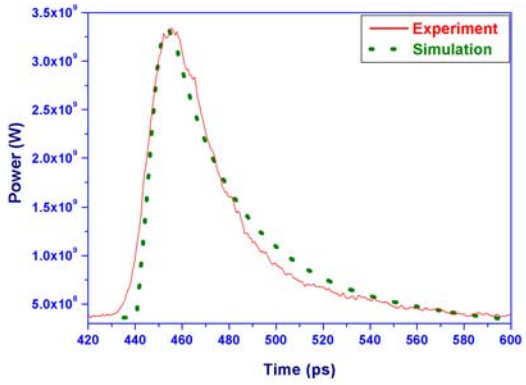

Figure 2. Spectrally integrated time-resolved experimental and simulated transverse emission in the 0.6-1.8 nm spectral region emitted from a nickel plasma and recorded by a streaked slit diagnostic.

Simulation studies show that under the above experimental conditions, the temporal duration of the spectral peak of the gain coefficient for Ne-like lasing at 23.1 nm is 29 ps. This is shorter than the simulated and experimental temporal duration of the spatially integrated continuum and resonance line emission by 24% (see Figure 2). However, lower gain spatial positions at longer distances from the target surface show significantly longer gain coefficient durations (Figure 3). The laser output is determined by a weighted average over all spatial positions depending on the ray paths for the X-ray laser beam.

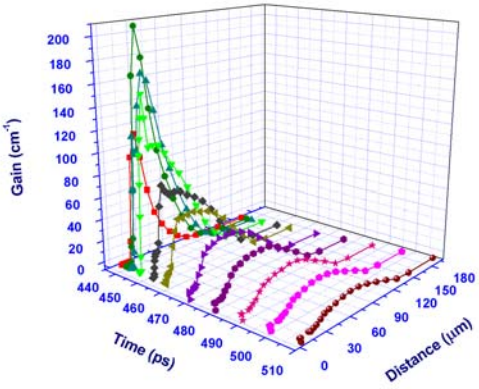

Figure 3. Simulated gain coefficient in the Ne-like Ni X-ray laser at 23.1 nm as a function of time and distance from the target. The gain duration increases and the value of peak gain decreases with distance from the peak gain cell (away from the target surface). The main pumping laser pulse of 1.2 ps duration peaks at time 440 ps.

Conclusion

X-ray laser output at 23.1 nm and the intensity of resonance lines and continuum emission between 0.6-1.8 nm emitted from a nickel plasma has been simulated using the EHYBRID fluid and atomic physics code. A post processor code coupled to the EHYBRID code has been developed to model the transverse emission of resonance lines and continuum emission in the keV spectral region and X-ray laser output has been simulated using a RAYTRACE post-processor to the EHYBRID code. The simulated duration of X-ray lasing (≈12 ps) agrees with the measured laser duration and the temporal output of continuum and resonance lines has been found to be in agreement with measurements made using a streak camera. We have shown that an estimate of the spatially-averaged duration of the X-ray laser gain can be obtained from spectrally integrated continuum and resonance line emission from states near in energy to the upper lasing level as obtained with a simple streaked slit diagnostic.

References

1. G J Pert., J. Fluid Mech. 131 401, (1983)
2. F Strati and G J Tallents., Phys. Rev. A. 64 013807, (2001)
3. Y Abou-Ali *et al*., Optics Commun. 215 397, (2003)
4. Axis-Photonique Inc., Varennes, Canada.
5. Y Abou-Ali *et al*., AIP Conference Proceedings. 641 3-8, (2002)
6. J A Plowes *et al*., Opt. Commun, 116 260, (1995)
7. Y Abou-Ali *et al*., J. Phys. B, to be published
8. R E King *et al*., Phys. Rev. A. 64 053810, (2001)
9. T Holstein., Phys. Rev.72 1212, (1947)

Experiment on collisionless interaction between counter-streaming plasmas in a magnetic field

C Courtois, R A D Grundy, A D Ash, D M Chambers, N C Woolsey

Department of Physics, University of York, Heslington, York, YO10 5DD, UK

R O Dendy, P Helander, K G McClements

UKAEA, Culham Science Centre, Abingdon, OX14 3DB, UK

B Lings, K Rosolankova

Department of Physics, University of Oxford, Park Road, Oxford, OX4 1PP, UK

Main contact email address: *ncw2@york.ac.uk*

Introduction

The possibility of simulating astrophysical phenomena[1] in laser plasma experiments is interesting from a basic plasma physics point of view because of the production of well-defined plasmas, the control of input conditions, and the ability to repeat and make detailed measurements. These studies are usually based on scaling laws[2], where dimensionless parameters are matched between the experiment and the astrophysical object of interest. An interesting example is the development of collisionless shocks observed in supernova remnants (SNR), which occur when the ejected stellar matter interacts at high speed, initially with the circumstellar medium and later the interstellar medium (ISM). These magnetized shocks are also believed to be at the origin of cosmic rays with energies up to 10^{15} eV and through these cosmic rays contribute to heating of the ISM[3]. The energy dissipation in these shocks, and the acceleration mechanisms are not governed by ordinary Coulomb collision, but involve wave-particle processes.

In a previous experiment[4], we outlined experimental techniques for the possible laboratory simulation of collisionless shock relevant to a young SNR, approximately 100 years after the supernova explosion. This experiment combined the supersonic expansion of a laser-exploded plasma with a strong magnetic field. It was proposed that a collisionless shock might form as two such exploding plasmas interact in a counter-streaming geometry. The plasmas were produced by intense laser irradiation of thin plastic foils such that the velocity of expansion ensured the particle mean free paths exceed the size of the experiment. A strong magnetic field was applied to the experiment to ensure the ion gyro-radius remains smaller than the experiment size, and induce a so-called collisionless *effective* collisionality. In this case an effective collisionality can be assumed *if* the plasma is magnetized and whilst the ions are sufficiently cold. If magnetized, a collisionless interaction will occur and heat the plasma resulting in an increase in the ion gyro-radius.

In forming an experimental simulation it is necessary to define a similarity that allows scaling across many orders of magnitude. Here the similarity relevant to the magnetic field is the plasma β. In a SNR the plasma β, the ratio of the plasma kinetic pressure to the magnetic-field pressure, is large (>> 1) so that the magnetic field does not dominate the plasma dynamics. However, a previous experiment showed that a scaled magnetic field did affect the dynamics of two counter-streaming plasmas through the observation of a steepened electron density gradient. This observation requires further investigation and is the subject of this article. (All the expressions in this article are in cgs units).

Experiment

The experiment was carried out using the Vulcan facility at the Rutherford Appleton Laboratory. Two face parallel, 0.1 μm thick C_8H_8 foils are mounted across a 1.2 mm hole on either 50 μm thick copper or 250 μm thick mylar washers separated by 1 mm. Mylar washers were used for some of the shots without magnetic field and for all the shots with magnetic field to prevent possible field disturbance due to induced eddy currents. These foils are irradiated simultaneously with one to two intense laser beams per foil at peak intensity of 0.6 to 1.2 × 10^{14} W/cm^2, in 80 ps pulse duration and 1.053 μm wavelength. Plasmas are created, accelerated and collide by irradiating the non-opposing surfaces of the two foils as shown in Figure 1. Phase zone plates are used to spatially smooth laser focal spot profiles and increase the diameter to 1 mm. This is twice the expansion distance to the collision point and allows the plasma expansion to be approximated as planar and 1-dimensional. The foils are placed at the centre of a pulsed electromagnet producing a homogeneous and longitudinal 7.5T, 1 ms duration, magnetic field. This field is sufficient to ensure the plasma β >> 1, and should not affect the expansion of an exploding plasma. Laser access through the electromagnet to the target is restricted to one laser beam per foil. The pressure in the experimental chamber was maintained around 10^{-4} mbar. The plasma expansion is studied with a CPA (25 ps pulse duration), frequency doubled, spatially smoothed collinear laser probe beam which passes between the foils, perpendicularly to the foil surfaces and to the (1-dimensional) plasma flow. This probe can be delayed relative to the main laser beams forming the plasmas. The polarization of the probe beam is fixed at 45° relative to the foil surfaces using a high extinction ratio (10^4-10^5) Glan Taylor prism polarizer placed before the experimental chamber. The probed plasma is imaged by an f6 achromat lens and analyzed using an interferometer based on a Wollaston prism. The maximum electron density probed with this optical system is around 5 × 10^{19} cm^{-3} along a 1 mm chord through the plasma. In addition, ion time of flight is measured with a series of Faraday cups placed around the target. This allows an estimate of an ion temperature assuming a Maxwell Boltzmann distribution for the ion population.

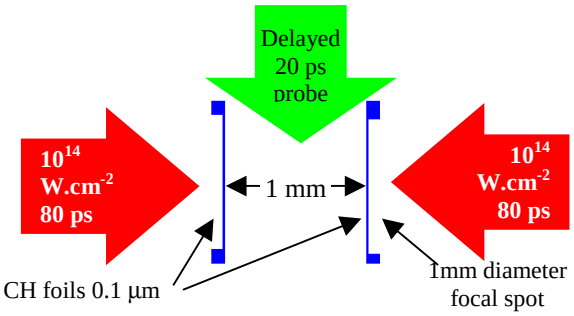

Figure 1. This shows the opposing foil geometry and probe alignment. The probe is delayed relative to the peak of the drive lasers by 250 to 750 ps. The magnetic field orientation is down the page, perpendicular to the plasma flow.

Experimental results

Data is recorded as 25 ps duration snapshots between 250 ps and 1 ns following the laser driven explosion of the foil targets. The role of the magnetic field on single foil plasmas is

described in Section A and two foil plasmas in a counter-streaming geometry in Section B.

A. Plasma expansion from one exploding foil

Interferometric data recorded with probe delays between 250 ps and 750 ps *without* a magnetic field show the electron density, n_e, of the expanding plasma is low, around $n_e = 10^{18}$ cm^{-3} and that the expansion speed of the plasma leading edge, is $V_{exp} = 1.5 \times 10^8$ cm/s with two incident laser beams (i.e.~80 J on target) and $V_{exp} = 1.1 \times 10^8$ cm/s with one beam (i.e.~40 J). The production of fast expanding plasmas with low density and low atomic number (hence the use of plastic) is important for achieving a collision free interaction in a counter-streaming experiment.

Reproduced in Figure 2 are interferometric results from a magnetic field free, 2(a), and a 7.5 T (7.5 x 10^4 Gauss) magnetic field present, 2(b). These foils were exploded with one laser beam containing 42 J and 39 J respectively and images recorded at a relatively long delay of 750 ps. The extracted central horizontal electron densities, assuming a uniform and 0.1 cm thick plasma, are compared in Figure 2(c). Field free data is shown as squares and 7.5 T data as triangles.

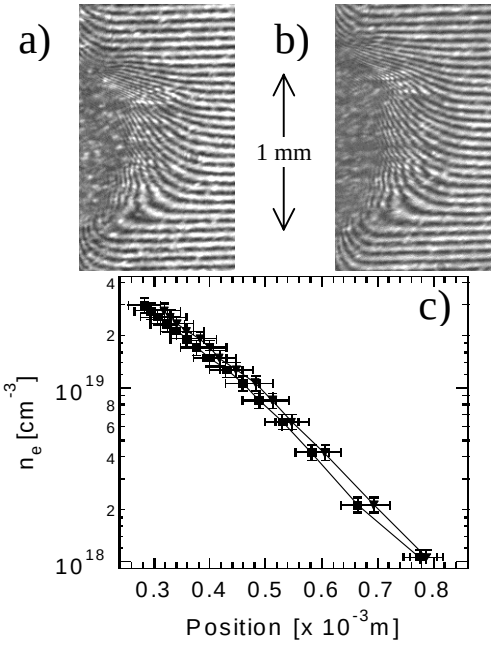

Figure 2. Interferograms of one exploding foil (a) at 750 ps delay without magnetic field and 42 J energy and (b) with 7.5 T magnetic field and 39 J energy. Graph (c) shows the horizontal profiles of n_e at the centre of the foil respectively without, square points, and with, triangle points, a B field.

B. Counter-streaming plasma interaction

Interferograms indicating the density profiles of two exploding foils at 500 ps probe delay are shown in Figure 3. The result for a field free experiment is shown in Figure 3(a) and 41 J on the left foil and 44 J on the right foil, and the experiment with 7.5 T magnetic field and 41 J on the left foil and 50 J on the right foil shown in Figure 3(b). Laser beams come from the left and right sides of each interferogram. The extracted central horizontal electron densities are compared in Figure 3(c) again assuming a uniform and 0.1 cm thick plasma. Magnetic field free data is shown as squares and 7.5 T data as triangles. The position zero corresponds to the experimentally determined minimum of interference fringe shift in the region between the two foils.

Discussion

The extracted densities without a magnetic field, Figure 3(a), show an approximately parabolic shape with a minimum of density in the region where counter-streaming plasmas interact,

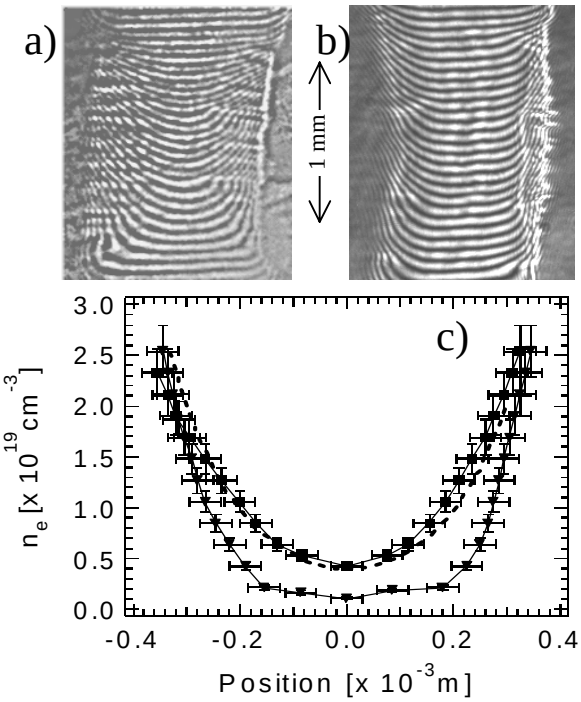

Figure 3. Interferograms of two exploding foils at 500 ps delay without (a) (41 J and left foil, 44 J on right foil) and with 7.5 T magnetic field (b) (41 J on left foil, 50 J on right foil). (c) Horizontal profiles of the n_e at the centre of the foil respectively without (square) and with (triangle) B field. The dashed line is discussed in the text.

as expected if a collision free interaction is anticipated. This measurement is compared to an artificial curve (dotted line) where results from one exploding foil have been added to simulate a collision-free interaction between two opposing exploding foils placed at –0.5 and 0.5 cm respectively. The shape and magnitude of the n_e are similar to the experimental result particularly in the collision area. The conclusion that plasma interpenetration has occurred, and that plasma expansion has not slowed is supported by Faraday cup results that indicated the ion temperature is approximately 100 eV, with a small fraction of ions (<10%) heated to above 1 keV. There is no evidence of a density increase or a retarded expansion in the interferometry.

These results should be compared with the n_e extracted from Figure 3(b) and shown as triangles in Figure 3(c). Here the shape is significantly altered, with density profiles from the exploding foils steepened and separated by an extended region where the n_e is relatively flat. This flat region is around 350 μm wide with low n_e. It appears the plasmas are slowed and less developed in the presence of the magnetic field.

The central region of 7.5 T data in Figure 3(b) is enlarged in Figure 4(a) and the extracted n_e shown in Figure 4(b). These figures show additional structure, a bright feature on the interferogram, with a width around 150 μm, and a small increase in n_e either side of the density minimum, in the flat region identified earlier respectively. These density features are related in some way to the magnetic field. Unfortunately, the electromagnet excluded the use of the Faraday cups.

Experimental data indicate that the n_e evolution of laser driven exploding single foil is similar, and independent of whether a magnetic field up to 7.5 T is present or not, and for at least 750 ps into the expansion. This is expected as the experimental parameters were chosen to ensure that the plasma $\beta >> 1$, that is the plasma pressure exceeds the magnetic field pressure. When a 7.5 T magnetic field is applied on the system, we are not able to measure an effect on the expansion of one exploding foil for distances of propagation comparable to the foils separation.

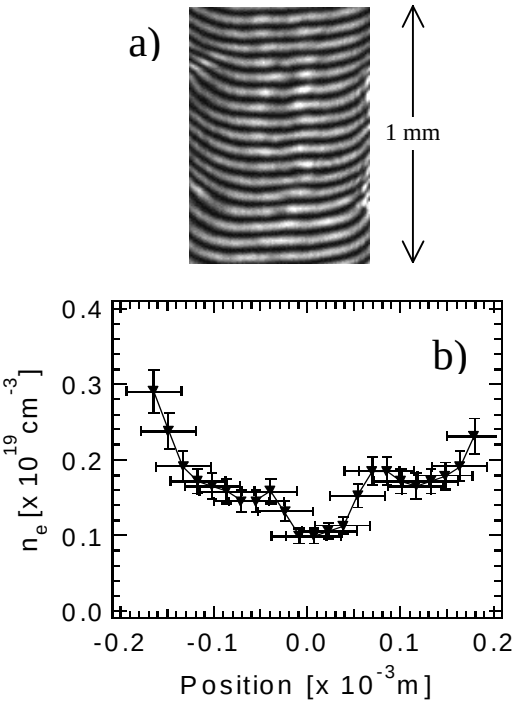

Figure 4. In (a) is an enlargement of the centre of the Figure 3(b), showing the interaction area and in (b) the extracted n_e.

Calculations support this observation. However as the plasma expands beyond 1 mm, the magnetic pressure is expected to become comparable to the thermal pressure and the magnetic field will affect the plasma expansion. This illustrates that the expansion of the plasma, during the timescales and with the sensitivity required by the experiment, is *not* affected by this magnetic field.

High expansion velocities, low plasma densities, and low atomic number are all required to ensure that the interaction between two counter-streaming exploding plasmas is collision free, at least during the stages of the interaction of interest here (i.e. between 250 ps to 750 ps). Assuming the plastic foils are fully ionized, using extracted electron densities, and flow velocities the ion-ion mean free path, the most relevant parameter, exceeds the size of the system[6]. Data shown in Figure 3 clearly indicate that an interpenetration of the two plasma streams occurs, and that collisions are not important at the time of measurement. This is reinforced by comparison with the artificial result constructed from the addition of single foil data. Furthermore, for our experimental conditions, collisionless coupling between the counter-streaming plasmas due to an electrostatic instability[7] is not expected to occur.

This result should be compared to the observation in the presence of a 7.5 T magnetic field. The density profile is notably altered, with steepened density profiles separated by an extended, uniform, low-density region in the interaction area. Furthermore, small yet significant increases in density are observed in this low-density region. Again, as a result of the high kinetic energy it is difficult to explain these features in terms of a magnetic field retarding the plasma flow, or in terms of field compression between the leading edges of the two plasmas. An alternative explanation is that the magnetic field indirectly affects the interaction of the plasmas, for example through a collisionless coupling. This suggestion will require further study. Coupling mechanisms are not well understood, yet it is unlikely to be due to ion-ion two-stream instability[8] as $V_a < V_{exp}$ in our experiment. Momentum is mainly carried by ions, thus the most significant collisionless coupling mechanism must involve the counter-streaming ions.

We have stated that a collisionless coupling requires a magnetic field in the plasma. However, magnetic field penetration into the plasma is an area of uncertainty. It is believed to occur when the skin current drift velocity, induced by an external magnetic field, exceeds the local sound speed. Ion-acoustic turbulence results, and an anomalous resistivity is induced as electrons scatter on this instability. The result is an enhanced magnetic field penetration[9]. In this case the limiting skin current can be written $j < \alpha n_e e C_s$, and is proportional to the sound speed, with the parameter α of order unity and smaller than $(m_i/Zm_e)^{1/2}$. Field penetration occurs to the skin depth $\delta_e = c/\omega_{pe}$, A lower value for the magnetic field to drive this instability is given by $(B^2/8\pi)/(n_e m_e V T_e{}^2) > Zm_e/2m_i$, where ω_{pe} is the plasma frequency. In this experiment, as the plasma pressure is larger than magnetic field pressure, this inequality is satisfied. For conditions relevant here, the magnetic field penetration length can be written $Bc/(4\pi n_e e \alpha C_s)$ resulting in a penetration of ~100 μm.

Conclusion

In this experiment, we have investigated the laser-driven explosion of one thin plastic foil and two thin plastic foils in an opposing geometry. These experiments were repeated with and without a magnetic field. It is clear that the magnetic field is not sufficiently strong to affect the expansion dynamics of a single foil, yet as two similar counter-streaming plasmas interact with a magnetic field transverse to the plasma flow the density is affected. Three features are noted. First, the density profiles are steepened, second an extended low-density region is observed, and third density increases are observed either side of the collision point. Experimental results indicate that the interaction between the two plasmas is collision-free, and that the magnetic field strength is insufficient to retard the plasma flow. We have suggested that ion acoustic turbulence occurs resulting in an anomalous resistivity, and estimated magnetic field penetration to 100 μm. If this occurs, this would result in a collisionless coupling as the leading edges of the plasmas start to interpenetrate.

Acknowledgments

We express our thanks to Dr. Karl Krushelnick and Imperial College for the loan of the electromagnet, and to the Central Laser Facility staff for their advice and help.

References

1. B. A. Remington, *et al*, Phys. Plasma 7, 1641, (2000).
2. D. D. Ryutov, *et al*, Phys. Plasma 8, 1804, (2001).
3. R. Enomoto, *et al*, Nature 416, 823 (2002).
4. N. C. Woolsey, *et al*, Phys. Plasma 8, 2439, (2001).
5. R. Z. Sagdeev, *et al*, Scientific American, April (1991).
6. N. C. Chenias-Popovics, *et al*, Phys. Plasma 4, 190, (1997).
7. T. E. Stringer, *et al*, J. Nucl. Energy, 6, 267, (1964).
8. K. Papadopoulos, *et al*, Physics of Fluids, 14, 849, (1971).
9. J. Aparicio, *et al*, Phys. Plasma 5, 3180, (1998).

Measurement of multiple plane diffraction from shock compressed crystals

J Hawreliak, K Rosolankova, B Lings, F Kerr, J S Wark

Department of Physics, Clarendon Laboratory, University of Oxford, Oxford, OX1 3PU, UK

D Kalantar

Lawrence Livermore National Laboratory, Livermore, California, 94550, USA

D M Chambers, A D Ash, N C Woolsey

Department of Physics, University of York, Heslington, York, YO10 5DD, UK

Main contact email address: *j.hawreliak@physics.ox.ac.uk*

Introduction

Materials shock-compressed at pressures exceeding the Hugoniot elastic limit deform plastically. Plastic deformation is thought to be due to the generation and movement of dislocation in the crystal which permanently and irreversibly change the crystal structure. It is this change and effect of the dislocations we aim to study using in-situ x-ray diffraction [1)].

The Vulcan laser at the Rutherford Appleton Laboratory is one of the few facilities where it is possible to study the lattice structure of a shock loaded crystal using *in situ* diffraction. A high-intensity laser is required to generate the large shock pressures required to induce plasticity, and another synchronous beam is required to generate the x-ray source for diffraction. On a large scale, multi-beam facility like Vulcan it is possible to shock the crystal and use in-situ diffraction to diagnose the response of the crystal.

This report will describe an experiment conducted on the Vulcan laser system to study shock loaded materials with in-situ diffraction. The primary diagnostic is the large angle film detector[2)] which records the time integrated diffraction signal from multiple lattice planes. The information from multiple planes simultaneously is required to diagnose the state of the material being compressed.

Experiment

To study the structure of a solid requires some knowledge of the relative location of the atoms in the material. X-ray Bragg diffraction is an excellent method to study crystal structure. A constructive interference peak in the x-ray scattering signal appears at the Bragg condition:

$$n\lambda = 2d \cdot \sin(\theta) \quad (1)$$

where the incident and diffracted angle, θ, is the same and is determined with respect to the lattice plane with lattice spacing, d, and x-ray wavelength λ (Figure 1).

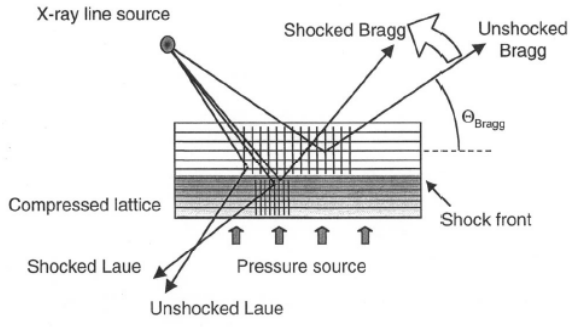

Figure 1. A schematic diagram showing the set-up of in-situ diffraction.

The compression of the lattice will cause a change in the lattice spacing, d, which will be observed as a change in the angle at which the Bragg condition is satisfied. With the large angle film detector a small source placed close to the crystal surface allows many planes to be recorded simultaneously.

The target consists of two separate pieces (Figure 2); a backlighter mount and a crystal mount. The two components have independent x,y,z motion to allow flexibility in the alignment on a shot to shot basis. The crystal mount is designed so that the entire crystal is shocked and the diffraction will occur over a 1.2 x 1.6mm region in the centre of the 3x3 mm crystal. The beveled edges of the crystal mount minimize the shadow of the mount on the film. The backlighter is a half pin 400μm in radius with a 45° half cone machined out of the tip. The backlighter foil is placed on the flat side covering the cone shaped hole and a gold foil is placed on the curved side to block the film from direct exposure from the x-ray source. The size of the x-ray backlighter source is determined by the focal spot size of the laser beams, which is ~100μm in diameter. The x-ray wavelength is determined by the K-shell (He-like) x-rays from the backlighter foil. The location of the backlighter is generally set such that the x-ray source is 400μm above the surface of the crystal and 1mm from the exposed region of the crystal.

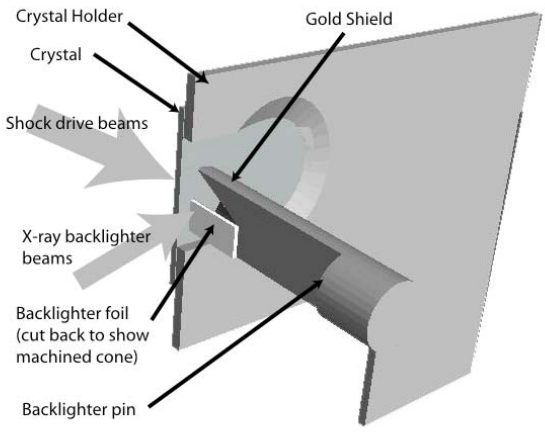

Figure 2. Schematic diagram of the target set-up.

The large angle film pack is designed to collect x-ray diffraction from multiple lattice planes. Standard detectors would be placed in a location covering only a small angular range covering diffraction from one set of planes. The wide angle film pack covers π steradians of solid angle from the crystal. The film pack consists of three individual film holders: one rectangular section (142 x 71mm) and two triangle pieces (one side length 142mm long and a peak 71mm high bisecting the length). Each film holder has a 0.75mm thick beryllium light shield which is covered with 20μm of mylar and 6μm of aluminized mylar to protect from stray laser light and target debris, where the Al-mylar is replaced every shot. The film packs contain DEF film and thin metal foils appropriate for filtering the x-ray backlighter. When aligned, the large angle film detector will cover 90° in one direction from parallel to the crystal surface to the normal and 180° in the orthogonal direction. The film pack is situated so the crystal target is

located 51mm along the normal from the centre of the rectangular film pack.

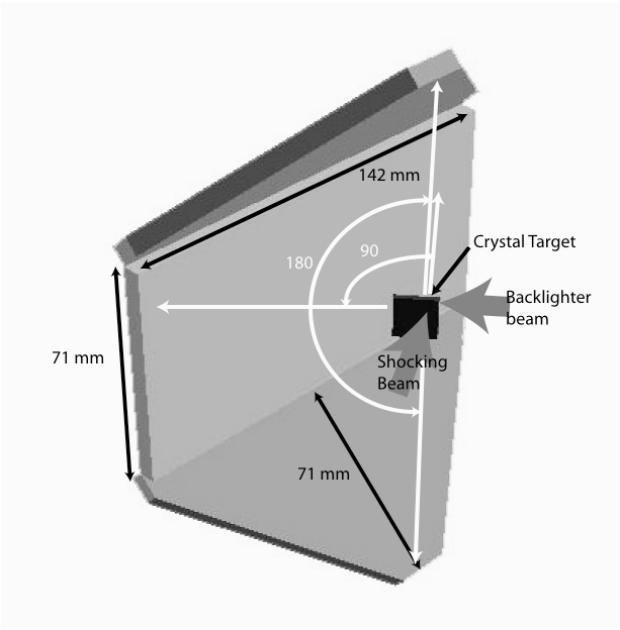

Figure 3. The geometry of the large angle film pack. The black numbers give the dimensions of the film pack and the white numbers show the angular coverage of the film pack.

Analysis of Wide Angle Film Pack

Figure 4 is an example of diffraction of an Fe backlighter from a Si crystal recorded on the large angle film pack. The different lines on the film are associated with diffraction from different lattice planes. As described in Equation (1), diffraction only occurs when the Bragg condition is met. In the experimental geometry the physical size of the crystal/backlighter targets are much smaller than the dimensions of the film pack which allows the diffraction signal on the film to be described as conic sections corresponding to different lattice planes. The cone that describes the diffraction from each lattice plane has the apex at the location of the crystal, the cone angle determined by Equation (1) by the spacing of the lattice plane and the wavelength of the x-ray backlighter and the axis of the cone is parallel to the h,k,l vector normal to its corresponding plane, Figure 5.

The analysis of the data requires a method of characterizing the orientation of the crystal before it is compressed. The combination of a finite shock speed, finite x-ray burst and finite probe depth allow unshocked and shocked information about the crystal to be recorded on the film on a single shot. The x-ray source duration was set to 1 ns by the length of the laser pulse. The timing of the x-ray pulse and the shock driving pulse was set such that an unshocked signal would be recorded at the start of the x-ray pulse and the shock wave would move into the diffraction volume while the x-ray source was still on. This characterizes the crystal and highlights the effects of the shock on the crystal. By fitting the uncompressed diffraction lines it is possible to characterize the orientation of the crystal and calibrate the film. In Figure 4, the sharp unshocked diffraction lines can be seen as well as the shock-compressed lines showing a change in the crystal lattice spacing. The compression of the different lattice planes will be used to determine the response of the crystal as a whole.

Discussion

The experiment was successful in showing the advantage of using the large angle film pack to study the diffraction from shock compressed crystals. Having diffraction information from different lattice planes will allow an interpretation of how the crystal structure changes plastically when a material is shock compressed. At the moment the data is being analyzed to determine the changes in the different lattice plane spacing. These results will be compared with molecular dynamic simulations that model the motion of individual atoms in a material under compression.

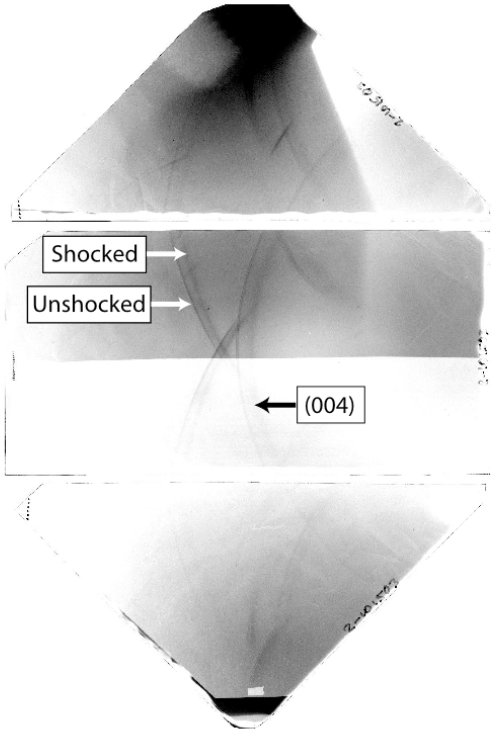

Figure 4. Experimental image of an Fe backlighter diffracting from a shocked Si crystal. The change in intensity through the rectangular section of the large angle film pack is due to multiple filtering.

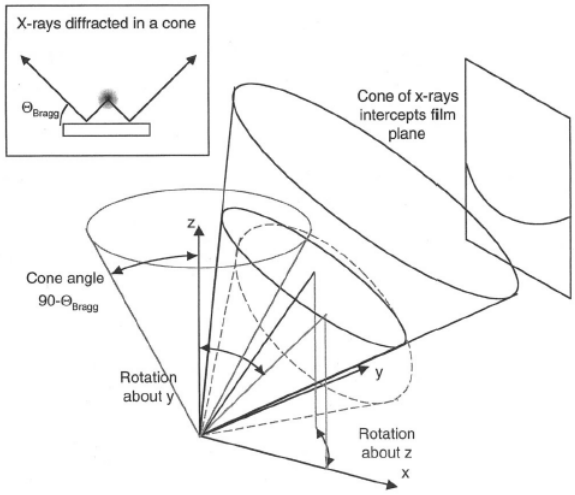

Figure 5. Geometry of the diffraction associated with different lines on the film.

References

1. A Loveridge-Smith, A Allen, J Belak, T Boehly, A Hauer, B Holian, D Kalantar, G Kyrala, R W Lee, P Lomdahl, M Meyers, D Paisley, S Pollaine, B Remington, D C Swift, S Weber, and J S Wark PRL 86, 2349(2001)

2. D H Kalantar, E Bringa, M Caturla, J Colvin, K T Lorenz, M Kurmar, J Stolken, A M Allen, K Rosolankova, J S Wark, M A Meyers, M Schneider and T R Boehly Rev. Sci. Instr. 74, 1929 (2003)

Studies of soft x-ray driven tamped ablative systems

J Pasley, P Nilson, M G Haines

Plasma Physics Group, Blackett Laboratory, Imperial College London, South Kensington, London, SW7 2BZ, UK

M M Notley, M Tolley, D Neely

Central Laser Facility, CCLRC Rutherford Appleton Laboratory, Chilton, Didcot, Oxon, OX11 0QX, UK

W Nazarov

Chemistry Department, University of Dundee, Dundee, DD1 4HN, UK

Main contact email address: *j.pasley@imperial.ac.uk*

Introduction

In discussion of Indirect Drive Inertial Confinement Fusion reference is often made to the 'rocket-like' acceleration of the fuel capsule. However, radiation implosion (RI) can potentially take on a number of different guises. Not all of these variants rely upon rocket-like behavior:-

- Rocket-like RI: implosion driven primarily by subsonic (/transonic) ablation of the low-Z capsule surface.
- Gun-like RI: implosion driven primarily by a material (/radiation) pressure reservoir that surrounds a high-Z coated fuel capsule.

In the latter system, the high-Z pusher will certainly ablate and give rise to some rocket-like acceleration- but the ablation wave in the pusher will stall after a few nanoseconds (ns). The high opacity of the exhaust makes this inevitable. After this has happened, the capsule is dependent upon the surrounding (low-Z / photon) fluid crushing it into the required conditions.

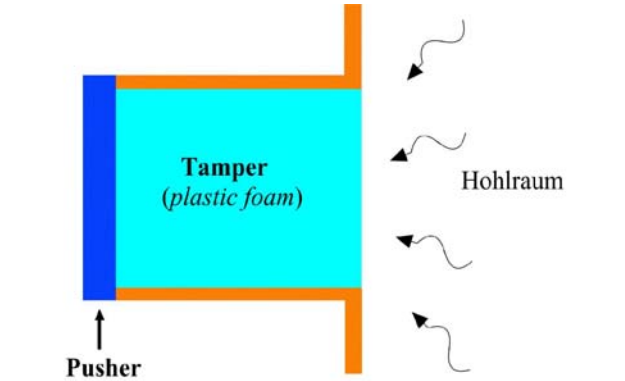

Figure 1. Generic tamped ablative target as used in the experiment.

With the available driver energies, it is difficult to mock-up material pressure driven gun-like RI in the laboratory, even in 1-D. This is principally down to the fact that any candidate pressure reservoir needs to be either completely confined or else very thick. If it is not confined then the material also needs to be heated rapidly enough that rarefaction waves propagating in from the driver facing surface(s) do not have time to reach the pusher during the time period of interest. Since the reservoir material must also be dense enough to exert a useful pressure once heated, this places considerable demands upon the driver.

With the energies available on Vulcan, the closest possible approach to material pressure driven acceleration is what we refer to as 'tamped ablation'. This system mimics the early time dynamics of the material pressure driven system in a non-convergent geometry. However, the energies available necessitate that the tamper material is of very low density and of limited thickness- so restricting the magnitude and duration of the material pressure drive. The targets we employed took the general form illustrated in Figure 1.

In order to ensure rapid heating of the plastic tamper material the x-ray drive temperature must be quite high (in excess of 100eV). Where energy is limited, this implies a relatively short rise time for the x-ray drive. Using the Vulcan laser the drive must peak no later than ~ 2ns if the hohlraum is to reach the required temperatures. This means that even if a particularly high-Z pusher is chosen, the rocket-like acceleration mechanism will still be available for most of the time period of interest. So the acceleration mechanism is neither profoundly 'gun-like' nor clearly 'rocket-like', but is somewhere in between the two [1].

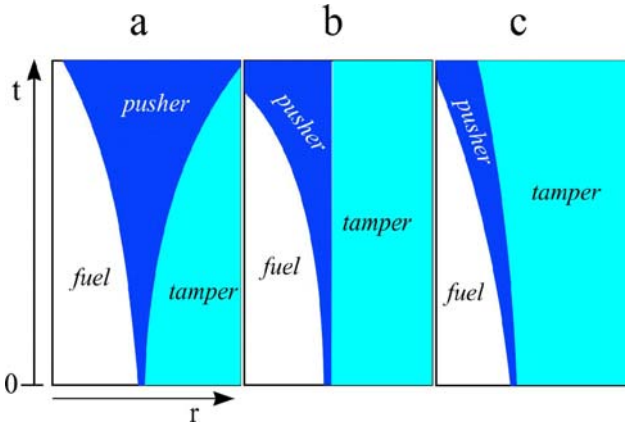

Figure 2. a) under-tamped, b) critically tamped, c) over-tamped.

The tamper material will have a relatively low opacity to the hotter components of the soft x-ray drive when cold, and will be nearly transparent to the drive once heated. Consequently the driver-facing surface of the pusher will experience radiant heating throughout the time period of interest. Considering the motion of the heated pusher material, we can suggest that initially it is sure to expand out into the, as yet, relatively cold tamper [2]. This is due to the fact that the mean free path (m.f.p) of the hot photons that have reached the pusher will be orders of magnitude less in the pusher than in the tamper- so the energy density in the surface of the pusher will far exceed that in the neighbouring tamper material. As time progresses the tamper will be heated to an increasing depth by the propagation of a heat wave driven primarily by the softer components of the drive. Once this heat wave approaches the boundary of the pusher material, three possible scenarios arise. These are illustrated in Figure 2. The ablated pusher material will either be snow-ploughed back into the dense pusher, remain quasi-static, or else continue to expand into the tamper. We designate these three possibilities 'over-tamped', 'critically-tamped' and 'under-tamped' respectively.

There are also three possible mechanisms for heating in the tamper[3]: subsonic ionisation, where a shock leads the heating wave; transonic ionisation, where the heat-wave is closely tied to the shock (separation < 1 radiation m.f.p.) and finally

supersonic ionisation, where the heat wave propagates sufficiently rapidly that the material does not have time to form a shock. In this latter case, whilst no shock wave will form, the material will still be accelerated somewhat by the passage of the heat front, although this acceleration becomes negligible in the highly supersonic regime. In the other two cases, the ionization wave is followed immediately by a rarefaction (assuming the tamper is not itself restricted from moving.) Subsonic and supersonic ionisation fronts are stable, assuming that the heated tamper material is relatively transparent to the drive (i.e. low-Z). Transonic fronts tend to collapse into the stable subsonic configuration if the drive temperature is held constant. The above three types of ionisation wave are illustrated in Figure 3.

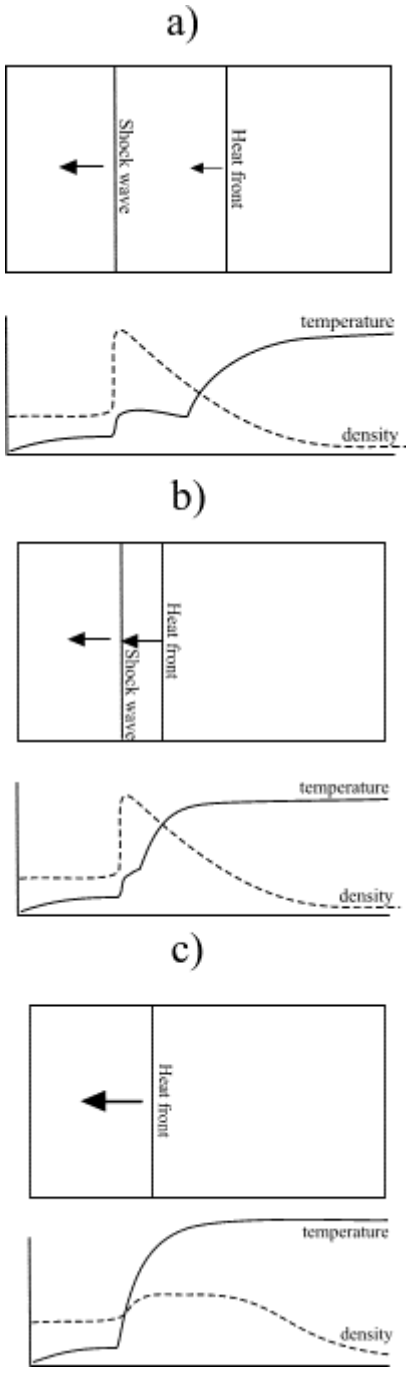

Figure 3. Three classes of ionisation wave: a) subsonic, b) transonic, c) supersonic.

Each of the three types of ionisation wave has a different pressure vs. radiation temperature scaling associated with it [4]. In the subsonic regime, pressure scales[5] approximately with $T^{3.5}$. Around the transonic point the scaling becomes more complicated- the pressure reaches a peak at the transonic point, then falls off. This drop in pressure is due to the disappearance of the shock wave upon entering the supersonic regime. Once the propagation becomes significantly supersonic, the scaling becomes approximately linear with temperature ($\cong nkT$ where n is the number density of particles (ions + electrons) and k is the Boltzmann constant). If the temperature becomes extremely high, then the radiation pressure will dominate, and the scaling will adopt a T^4 like dependency. This trend is illustrated for 200 mg/cc CH plastic in Figure 4 (analytical calculation.)

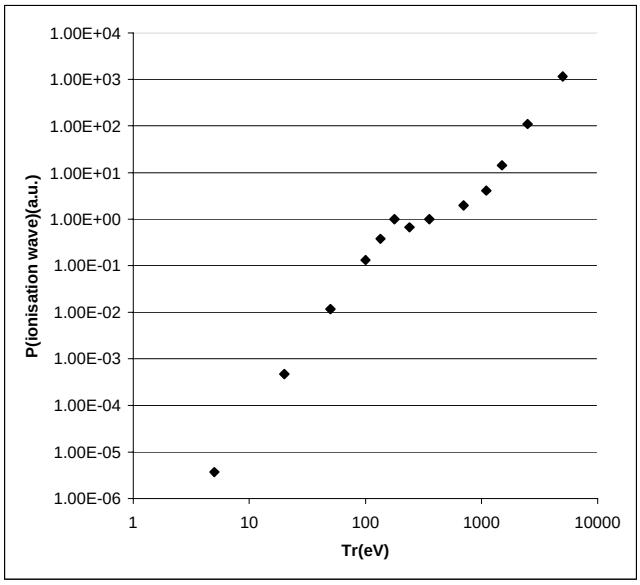

Figure 4. Pressure associated with an ionisation wave in 200 mg/cc CH plastic. Up to around 180 eV the scaling goes as $T^{3.5}$ peaking at the transonic point, rising linearly with T through the supersonic (material pressure dominated) regime, and then adopting a T^4 dependence at temperatures somewhat above 1 keV, where radiation pressure comes into dominance. This is an analytical calculation, but gives a fair idea of the scaling. The pressure is normalised to that at the transonic point.

In addition to the material pressure associated with the heated tamper material that surrounds the pusher, there is also the ram-pressure that is associated with arrival of the ionisation wave at the driver-facing surface of the pusher. Ram pressure is the pressure due to the momentum coupling between the ionisation wave accelerated tamper material and the pusher[6]. In the subsonic case, this amounts to simple shock acceleration as the shock lead ionisation wave reaches the pusher. In the supersonic case, the rarefaction can lag significantly behind the heat front, so a weaker yet more prolonged impetus is conveyed.

In high-Z materials, such as may be found in the pusher, the ionisation wave propagation is almost inevitably subsonic and diffusive, except in the very earliest stages of penetration. This diffusive behavior results in the ablation pressure having a strongly negative time dependence, and greatly increases the time such materials take to burn-through relative to their low-Z counterparts. This makes high-Z materials relatively ineffectual for rocket-like ICF, but highly suited to material pressure driven systems, where they are merely required to protect the fuel from radiative pre-heating. In our experiment we employed both chlorinated plastic and gold-coated chlorinated plastic pushers. However the rise time of the radiation pulse was sufficiently

short that these materials were still able to make fair use of the drive.

Going back to rocket-like ICF for a moment, it is worth noting that subsonic ionisation is equivalent to the usual ablation mechanism that is seen in rocket-like indirect drive ICF targets. It is also permissible to stand on the edge of transonic behaviour in such systems (the final 'shock' in the NIF baseline target is actually a transonic ionisation wave[7].) However the use of supersonic ionisation demands the use of a tamper-pusher system in order to avoid fuel preheat[4].

Experimental arrangement

The experiment was conducted in Vulcan Target Area East in Feb-Mar 2003. All beams were frequency doubled. The main-6 cluster configuration (6 beam cone with a half angle of 13°), along with B7 propagating along the axis of the cluster, were used to heat the hohlraum. The eighth beam was incident upon a gold backlighter disk.

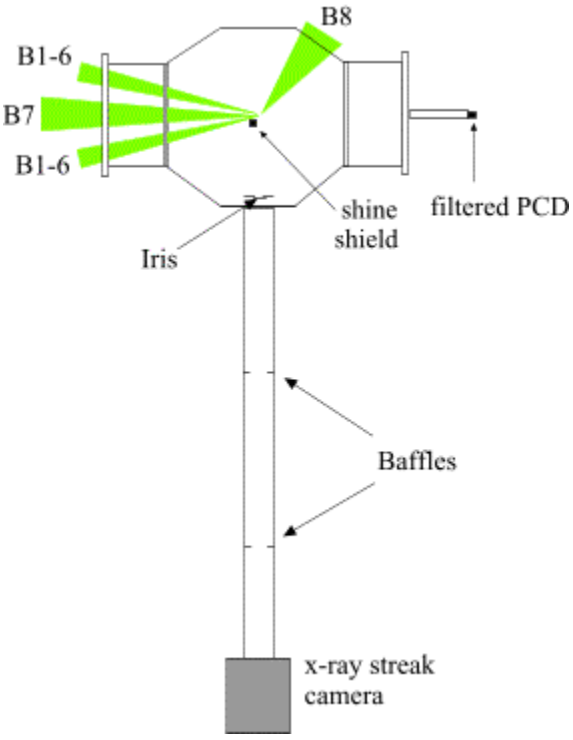

Figure 5. The experimental arrangement.

The major diagnostic was high magnification X-UV imaging[8] of the rear (non-driver facing) surface of the pusher. This system employed a spherical multi-layer mirror, operating at 50 angstroms, imaging to a high magnification (2x) x-ray streak camera. The target chamber arrangement is illustrated in Figure 5. The imaging tube was of sufficient length that an overall magnification of ~140 was obtained. The iris and baffle assemblies served to minimise the level of scattered light entering the diagnostic. The shine shield prevented x-rays propagating directly to the streak camera from either the target or the backlighter.

Figure 6 illustrates the arrangement at target chamber centre. The purpose of the mask is to preserve the surface of the X-UV mirror. The mirror is rotated behind the mask between shots, and a new area of the surface is employed (/destroyed!) in each shot.

The driver for the hohlraum consisted of the main-6 operating at maximum energy in a 2 ns square pulse, and B7 operating at maximum energy over 4 ns. This gave a maximum energy into the hohlraum of ~1 kJ in green. A cross section through the hohlraum is shown in Figure 7. The hohlraum has a two-chamber design, the object of which is to maximise the achievable radiation temperature. The main 6 are incident in a ring on the annular gold wall surrounding the target package.

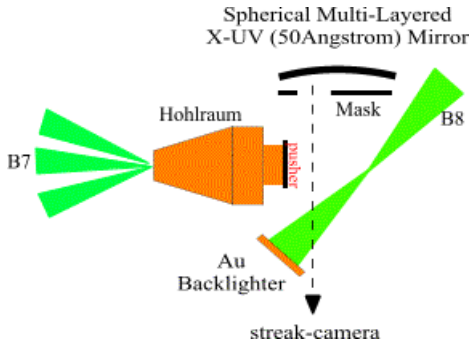

Figure 6. The arrangement at target chamber centre.

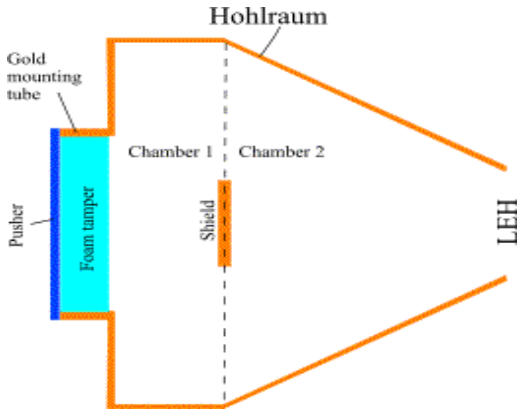

Figure 7. Cross section through the hohlraum. LEH designates the Laser Entrance Hole.

Beam 7 is incident upon the thick gold shield that 'divides' the hohlraum into two distinct chambers. This arrangement reduces the radiation losses from chamber 1, where the target package is mounted, by placing a heated buffer (chamber 2) between it and the LEH. The hohlraum is 1.33 mm in length, and 1 mm in diameter. The target package incorporates either a 150 or 200μm deep 500μm diameter $C_{15}H_{20}O_6$ foam tamper (mounted in a gold cylinder of equal length) in intimate contact with a 30μm thick C_8H_7Cl pusher, which in some cases was coated with 0.01μm of gold on the driver-facing surface. For each ablator/ foam length combination a pusher-only shot was taken, to determine the dynamics in absence of any tamping. The hohlraum temperature evolution was monitored on shots in which neither foam nor foil were present- giving the CH/Aluminum filtered PCD array[9] a clear view into the hohlraum through the hole in which the target package would ordinarily be mounted. The temporal evolution of hohlraum temperature is shown in Figure 8.

The 4ns pulse length of beam 7 resulted in our achieving a remarkably flat-topped temperature profile, the peak temperature being approximately 132 eV (+/- 5 eV).

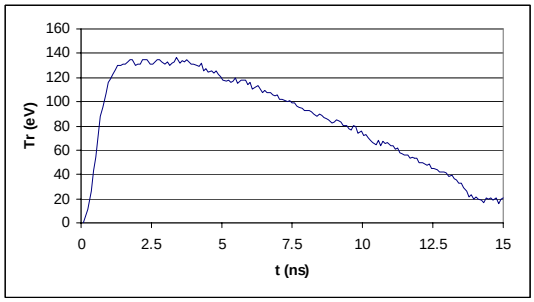

Figure 8. Hohlraum temperature evolution.

Results and analysis

A sample of typical data from the imaging system is shown in Figure 9.

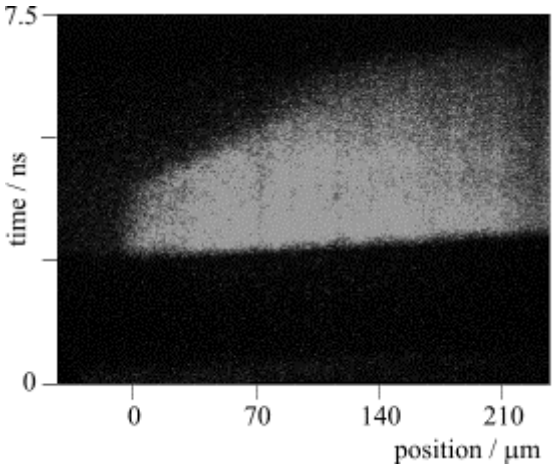

Figure 9. Streak data for the 200µm length 70 mg/cc foam tamped pusher (no gold flash).

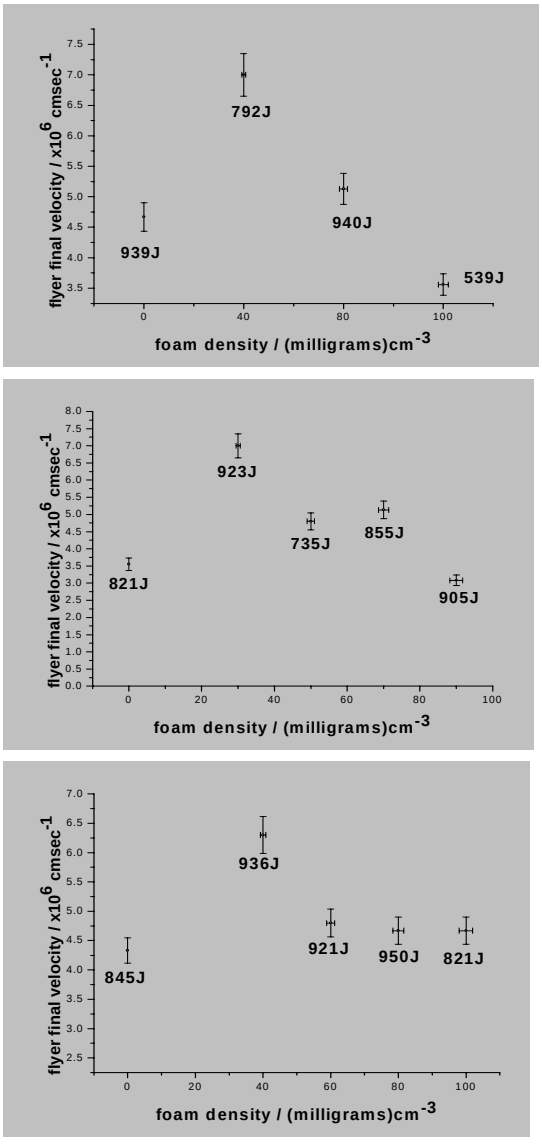

Figure 10. Final velocity of pusher rear surface. Top: 150µm length, no gold flash. Middle: 200 µm length, no gold flash. Bottom: 150 µm length, gold-flashed pusher.

As can be seen from Figure 9, after the first couple of nanoseconds of flight, the pusher's rear surface ceases accelerating and proceeds at a relatively constant velocity. Since the pushers were all initially of the same mass, this final velocity serves as an order of merit, by which the efficiency of the acceleration process may be measured. Figure 10 illustrates the final velocities achieved in all of the shots for which streaked trajectory data was produced.

In every case, the results show that the final velocity peaks in the targets in which the pushers were tamped with material in which ionisation wave propagation would be expected to be either transonic, or slightly supersonic. The combination of material pressure, ram pressure and subsonic ablation of the pusher has combined to deliver a significantly greater impulse to the pusher than subsonic ablation alone. As expected, the effects of the tamping are most dramatic in the targets where the tamper was thick or the pusher was coated with gold.

Conclusions

The above analysis is only preliminary. However, it does appear that combining a rocket-like and a gun-like acceleration mechanism can, in some cases, result in considerably greater impulse being delivered to the payload than with the rocket-like mechanism alone. This confirms previous results taken by Willi et al on the Phébus laser system in 1999[10].

Acknowledgements

This work was funded 50% by the EPSRC and 50% by the MoD. We would also like to acknowledge the support of AWE Aldermaston staff.

References

1. 'Radiation and Material-Pressure Hydrodynamics', 1998 ICF Annual Report, Lawrence Livermore National Laboratory, UCRL-LR-105820-98
2. J. Edwards, S.G. Glendinning, L. J. Suter, B. A. Remington, O. Landen, R. E. Turner, T. J. Shepard, B. Lasinski, K. Budil, H. Robey, J. Kane, H. Louis, R. Wallace, P. Graham, M. Dunne, B.R. Thomas, 'Turbulent hydrodynamics experiments using a new plasma piston', Phys. Plasmas 7, 5, 2099-2106, (2000).
3. S.P. Hatchett, 'Ablation Gas Dynamics of Low-Z Materials Illuminated by Soft X-Rays', Lawrence Livermore National Laboratory, UCRL-JC--108348
4. Steve Haan, Lectures to the 1st High Energy Density Physics Summer School, Santa Cruz, 2002, Lawrence Livermore National Laboratory, UCRL-MI-150131
5. John Lindl, 'Inertial Confinement Fusion- The Quest for Ignition and Energy Gain Using Indirect Drive', Phys. Plasma 2 ,11, 3933-4024, (1995).
6. Communication with Mike Dunne (AWE Aldermaston)
7. Communication with Steve Haan (Lawrence Livermore National Laboratory)
8. J. Edwards, M. Dunne, R. Taylor, O. Willi, C. A. Back, S. J. Rose, 'Experimental Measurement of the Dynamics of Foil Targets under the Impact of Intense Pulses of Soft X Radiation', PRL 71, 21, 3477-3480, (1993).
9. G. C. Idzorek, R. J. Bartlett, 'Silicon photodiode characterization from 1 eV to 10 keV', Proc. SPIE 3114, 349-356, (1997).
10. O. Willi, J. Pasley, A. Iwase, W. Nazarov, S. J. Rose 'Increase in the drive pressure in soft x-ray irradiated foam foil packages', proc. Inertial Fusion Sciences and Applications 1999.

Mapping of self-generated magnetic fields using harmonic polarimetry

A Gopal, M Tatarakis, A E Dangor, K Krushelnick

Blackett Laboratory, Imperial College, London, SW7 2AZ, UK

K Cassou

Universite Paris-Sud (XI), Orsay, France

Main contact email address: *amrutha.gopal@imperial.ac.uk*

Introduction

The study of self-generated magnetic fields in laser-produced plasmas has been an active area of research over the past several years. It is well known that when a high power, short duration laser pulse interacts with plasma very large magnetic fields can be produced. Such fields can be many MegaGauss in strength. Even though there are numerous mechanisms which can give rise to these magnetic fields – three are of particular importance.

These are: i) as plasma is ablated during the interaction, non-parallel gradients of plasma temperature and density can give rise to growing magnetic fields[1)] ii) the current of fast electrons generated during the interaction can generate magnetic fields via the Weibel instability[2)] iii) the radiation pressure associated with the incident laser pulse can generate a current of electrons within the skin depth of the plasma near the critical density surface which is an additional source of azimuthal magnetic field[3)]. Detailed theoretical and computational studies have shown that these fields are azimuthal (around the laser interaction region) and the strength of such fields can exceed that of the laser pulse itself [5,6)].

There have been previous experimental studies of these phenomena using external probes such as magnetic tapes, induction coils and frequency doubled probe laser beams. However, such probes are unable to make measurements in the highest density regions of the plasma where the largest magnetic fields are predicted to exist. Hence, measurements of the properties of self-generated harmonics (which are generated simultaneously from the interaction region) can be of great importance in experiments.

Previously, we have studied self-generated magnetic fields in laser-produced plasmas using such methods. In this report, we present the results of initial measurements which demonstrate the use of a new technique to measure the complete magnetic field profile in a single shot. This technique also allows the measurement of scattered radiation from the interaction over a wide range of angles which is useful for studying laser scattering phenomena. In our previous studies we have made measurements of harmonics scattered into a small solid angle in order to calculate the magnetic field through which the harmonic radiation passes. This consequently gives only a measurement of the fields existing within a small region of the plasma.

In order to map the entire profile of these magnetic fields we have used an ellipsoidal collection optic which can refocus harmonics emitted in all directions from the interaction onto a detector. The image on the detector can subsequently be used to produce a 2 dimensional map of the field which surrounds the interaction region in a single shot.

An ellipsoidal collector has two conjugate foci. Light collected from one focal point passes through the second focus after reflection. In our experiment we then re-collimate the light and direct it onto the detector (see Figure 1). Note that in our experiments the image on the detector was always in the near field and consequently simple geometrical optics allowed us to determine the angle at which the light was emitted.

In these experiments, the Astra laser system was used. This laser operated at a wavelength of 800 nm and produced pulses which were 70 fsec in duration and had typical energies of 200 mJ. The beam was focused using an f/3 off axis parabolic mirror onto a target which consisted of a short rod of aluminium. The estimated laser intensity was 5 x 10^{18} W/cm^2. The target rod had one end which was polished and this end was placed at the first focal point of an aluminised ellipsoidal collector. Harmonics generated from the interaction region will be reflected and refocused to the second focal point. The beam emerging from the second focal point was then collimated using a lens, directed out of the vacuum chamber and sent through a polarimeter before reaching the detector (a 16 bit CCD camera). Unlike in previous studies, in this polarimeter set-up only one channel was used. Shots were taken individually to calculate the Stokes vector of the light so that the magnetic field which induced the ellipticity in the harmonics could be estimated.

Shots were also taken at different intensities for different harmonics. Figure 2 shows an example of a set of raw data of the 4th harmonic emission from the experiment.

Using this data the angular dependence of the ellipticity could be determined (i.e. the Stokes vectors could be calculated). Subsequently the angular variation of the magnetic field surrounding the interaction region could be determined and compared to theoretical modelling. Further analysis of these results is ongoing.

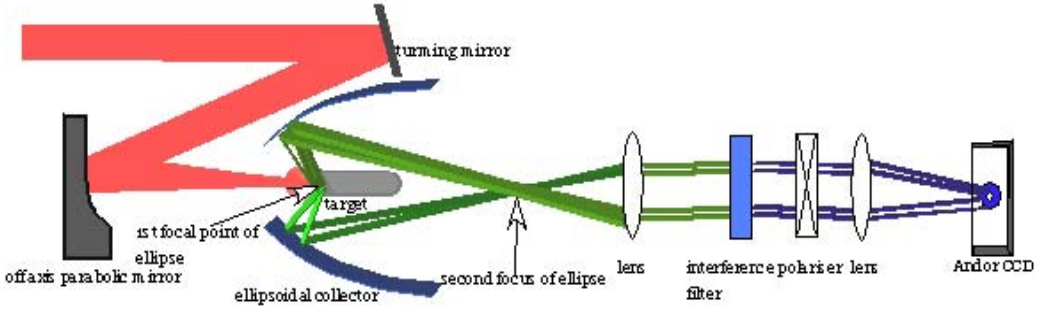

Figure 1. Schematic experimental set up.

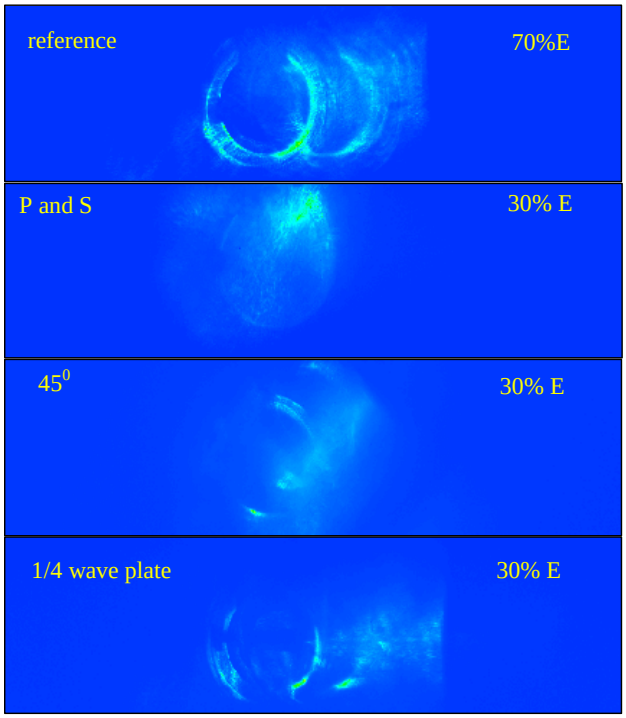

Figure 2. Raw data taken with different polariser settings (200nm).

References

1. J. A. Stamper *et al*. Phys. Rev. Lett., 26,1012 (1971).
2. Pukhov and J. Meyer-ter Vehn, Phys.Rev.Lett, 76, 3975 (1996).
3. R. Sudan, Phys. Rev. Lett. 70, 3075 (1993).
4. J. A. Stamper and D. A. Tidman, Phys. Fluids 16, 2004 (1973).
5. M. Tatarakis, I. Watts, F. N. Beg, E. L. Clark, A. E. Dangor, A. Gopal, M. G. Haines, P. A. Norreys, U. Wagner, M. S. Wei, M. Zepf, K. Krushelnick, Nature 415, 280, (2002).
6. M. Tatarakis, A. Gopal, I. Watts, F. N. Beg, A. E. Dangor, K. Krushelnick, U. Wagner,P. A. Norreys, E. L. Clark, M. Zepf, R. G. Evans, Physics of Plasmas 9, 2244 (2002).

Self generated magnetic field measurements from laser produced high density plasmas using the Astra laser system

A Gopal, M Tatarakis, A E Dangor, K Krushelnick

Plasma physics Group, Imperial College, London, SW7 2BZ, UK

K Cassou

Universite Paris-Sud(XI), Orsay,Paris, France

Main contact email address: *amrutha.gopal@ic.ac.uk*

Introduction

Present state-of-the-art short pulse laser systems are capable of producing pulses of less than a picosecond in duration and which can have powers greater than a Petawatt. If such pulses are focused, the intensity produced is sufficient to strip electrons from atoms instantaneously and create plasma. Electron motion in these laser fields becomes relativistic at intensities higher than 10^{18} Wcm^{-2} and laser-plasma interactions in this regime can give rise to a wide range of new phenomena such as the generation of energetic electrons, ions, and x-rays, the production of high order harmonics of the incident laser frequency and the creation of very strong magnetic fields. These phenomena have been predicted by both theoretical and computational studies and are presently the subject of experimental investigation using high intensity laser systems in laboratories around the world.

When a high power, ultra short laser pulse interacts with matter, a current of fast electrons can be produced which propagates in the laser direction and which creates a return current in the adjacent cold plasma. This results in the production of a strong azimuthal magnetic field[1]. Non-parallel gradients of plasma temperature and density in the ablated plasma can also give rise to MegaGauss magnetic fields[2]. In addition, the radiation pressure associated with the laser pulse creates huge toroidal magnetic fields[3]. At higher intensities (~10^{21}W/cm^2) these self-generated fields can become comparable to the laser B-field.

In previous studies, using external probing techniques, fields of the order of tens of MegaGauss have been measured – which is significantly less that the peak magnetic fields predicted by theory[3]. These very high magnetic fields are predicted to be localised near the critical density surface – hence probing with frequency doubled laser pulses is very difficult in these high density regions. Consequently, in this report we describe the use of the technique of polarimetry using the self-generated harmonics of the incident laser which has recently been developed as a method for measuring magnetic fields[4,5] in high density plasmas.

Since laser harmonics are generated at the same time as the magnetic fields in the critical density region and have the same polarisation as the original beam, the depolarisation effect of the magnetic field on the harmonics can act as method to estimate the magnitude of the magnetic fields. In the presence of a magnetic field, plasma acts as a birefringent medium – hence, the polarisation of the harmonics propagating out of the magnetised plasma becomes elliptical. This is called the Cotton-Mouton effect. Measuring the ellipticity of the harmonics enables a direct measurement of the magnetic fields through which the harmonics propagated.

The polarisation properties of electromagnetic waves can be represented using Stokes vectors. Therefore, measuring the Stokes vectors of the harmonics before and after propagating through the plasma enables the calculation of the transition matrix and consequently the determination of the magnetic field.

Let, S_{in} and S_{out} be the initial and final Stokes vectors respectively. They are related by:

$$S_{out} = M \bullet S_{in}$$

where M is the resultant transition matrix such that,

$$M = M_P \cdot M_n \cdot M_{n-1} \cdots M_1$$

where M_P is Muller matrix of the plasma and $M_n \cdot M_{n-1} \cdots M$ are the Muller matrices of optical components present before the detector.

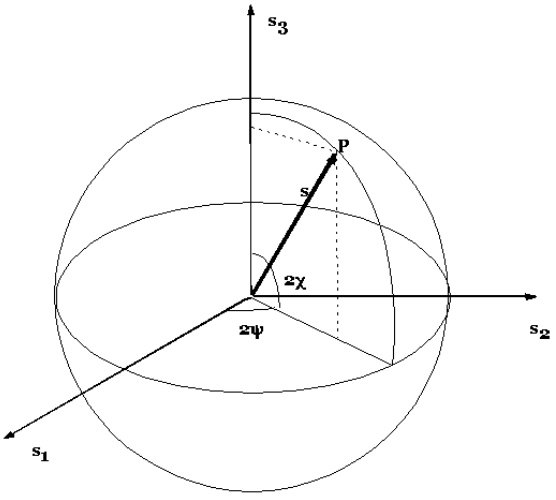

Figure 1. Poincare sphere. Schematic representation of Stokes vectors.

The evolution of the polarisation vector for an ordinary and extraordinary wave with refractive indices μ_1 and μ_2 is given by the equation,

$$\frac{ds(z)}{dz} = \Omega \times s(z),$$

where, $\Omega = -\frac{\omega}{c}(\mu_1 - \mu_2)s_{c2}$ and s_{c2} is the polarisation vector such that;

$$\mu_1^2 = 1 - \frac{\omega_p^2}{\omega^2} \text{ and } \mu_2^2 = 1 - \frac{\omega_p^2}{\omega^2}\left(\frac{\omega^2 - \omega_p^2}{\omega^2 - \omega_p^2 - \omega_c^2}\right)$$

Experiment

The experimental setup is shown in Figure 2. The Astra laser system was used and the 70 fsec, 250 mJ beam was focused to a spot of 10 microns diameter using an off-axis parabolic mirror. The targets used were 5 mm diameter aluminium rods polished at 45^0 on one end. A retro-reflection technique was used to align the targets. The maximum energy available per pulse was 250 mJ and shots with varying energy were taken by reducing the energies to 1% of maximum using a rotatable half-wave plate and a polariser. The harmonics generated were collected using fused silica lenses and the collimated beam of harmonics was directed to the polarimeter which was set up outside the vacuum chamber. At the entrance of the polarimeter a narrow band interference filter was placed to select the correct harmonic wavelength. The beam was then split into four channels using beam splitters. The first channel was the reference channel – without polarisers. The second channel consists of a Rochon polariser set at an angle of 0^0. Since the separation angle of the polariser was small we were able to image both s and p polarizations using the same lens. The third channel consisted of a second Rochon polariser positioned at an angle of 45^0. The fourth arm included a quarter wave plate followed by a polariser at 45^0. Consequently, by using data from all channels complete knowledge concerning the Stokes vectors of the harmonic could be obtained.

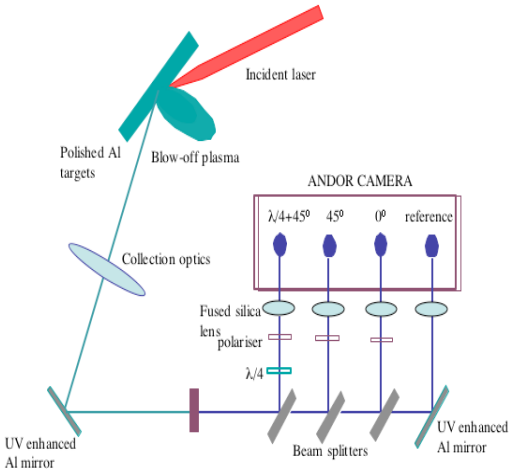

Figure 2. Schematic of experimental setup.

Beams from each channel were focused using a 20 cm fused silica lens. A 16 bit UV Andor CCD camera was used as the detector. We selected the second, 5/2 and third harmonics of the incident laser. Measurements using the 4^{th} harmonic were difficult due to the low harmonic intensity. Shots taken without polarisers and the quarter wave plate give the relative intensity of the light passing through each channel. Thus, we can calculate the reduced Stokes parameters and thereby infer the magnetic field. The angle between magnetic field lines and harmonics are taken as 15^0. The path length and density scalelength were estimated using 2D PIC simulations.

An example of the typical raw data is shown in Figure 3.

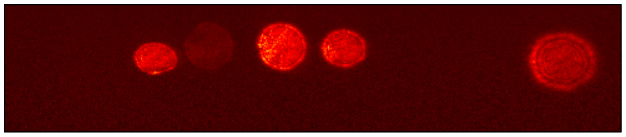

Figure 3. Raw data.

Results

The magnetic field was calculated for different wavelength harmonics at various intensities. Figure 4 shows the results for the third harmonic.

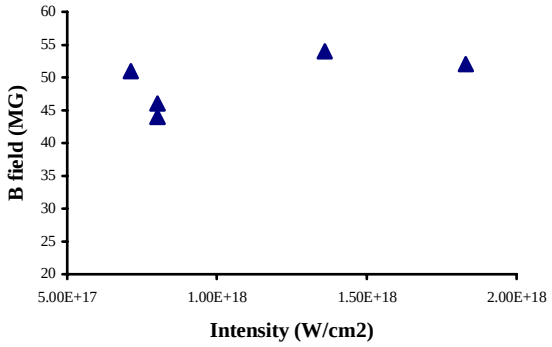

Figure 4. Measured magnetic fields.

These preliminary results using the third harmonic suggest a magnetic field which increases with intensity. However, an $I^{1/2}$ dependence is not observable. The measured magnetic fields are in reasonable agreement with previous low intensity Vulcan results.

References

1. A. Pukhov and J. Meyer-ter Vehn, Phys. Rev. Lett, 76, 3975 (1996).
2. J. A. Stamper, K. Papadopoulos, R. N. Sudan, Phys. Rev. Lett., 26, 1012 (1971).
3. R. Sudan, Phys. Rev. Lett, 70, 3075 (1993).
4. M. Tatarakis, I. Watts, F. N. Beg, E. L. Clark, A. E. Dangor, A. Gopal, M. G. Haines, P. A. Norreys, U. Wagner, M. S. Wei, M. Zepf, K. Krushelnick, Nature, 415, 280 (2002).
5. M. Tatarakis, A. Gopal, I. Watts, F. N. Beg, A. E. Dangor, K. Krushelnick, U. Wagner, P. A. Norreys, E. L. Clark, M. Zepf, R. G. Evans, Physics of Plasmas 9, 2244 (2002).

Multiple ionisation of a C^+ target by ultrafast high intensity laser pulses

S L Stebbings, T R J Goodworth, W A Bryan, W R Newell

Department of Physics and Astronomy, University College London, Gower Street, London, WC1E 6BT, UK

I M G Johnston, I D Williams

Department of Physics, Queen's University Belfast, Belfast, BT7 1NN, UK

J B A Mitchell, S Carles, J L Le Garrec, S D Le Picard

Universite de Rennes1, Campus de Beaulieu, 35042 Rennes Cedex, France

A J Langley, E J Divall, C J Hooker

Central Laser Facility, CCLRC Rutherford Appleton Laboratory, Chilton, Didcot, Oxon, OX11 0QX, UK

Main contact email address: *s.stebbings@ucl.ac.uk*

Introduction

Theoretical and experimental studies have concentrated on the ionisation dynamics of neutral atomic targets, in particular the rare gases, within intense laser fields. However, to fully test current theory, it is necessary to investigate a wide range of targets. In addition to studying neutral targets, we have originally used ion beams as the initial targets. With this in mind, we report on the multiple ionisation of C^+ within an intense laser field of intensity > 10^{16} Wcm^{-2}.

Two independent intensity-scanning techniques, the z-scan[1)] and conventional full volume intensity variation, are presented here for C^{2+} and C^{3+} ions. This has enabled the full and unambiguous identification of individual ionisation processes from the precursor C^+ ion.

Experiment

The ion beam apparatus has been used in previous experiments and is described in detail elsewhere[2)]. The C^+ ions were produced from high purity $CO_{(g)}$ in an oscillating-electron type ion source. These ions were then extracted and momentum selected to produce a 1.1kV ion beam of diameter 1.8mm, which intersected the laser beam propagation (z) axis at 90^0 on focus in the interaction region.

Linearly polarized laser pulses, 65fs, 790nm were produced from the Astra Ti:Sapphire laser. These were then focused using an f/15 lens to give a peak intensity of $3x10^{16}$ Wcm^{-2} and a diffraction limited spot size of 8μm.

To scan the focused laser beam through the ion beam, the lens was mounted on a computer controlled translation stage that drives it over a distance of 25mm along the z-axis relative to the optimum focusing position (z scanning). Scanning the laser beam through the ion beam means the target C^+ ions are subject to different intensities.

In addition to these z-scans, ion yields of C^{2+} and C^{3+} were measured as a function of laser intensity using a half waveplate to vary the peak intensity, with the lens at z=0.000mm.

Analysis of the multiply charged ions i.e. C^{2+} and C^{3+} was achieved by spatially separating them from the primary ion beam and their subsequent detection in an off-axis channeltron, to produce time of flight spectra for each charge state. The primary C^+ ion beam was collected in a well-baffled Faraday cup.

Results and Discussion

Figure 1 shows the z-scan of C^{2+}, the signal following a typical Gaussian volume shape, apart from the feature at z=4.500mm (modelled by curve A). This is due to the presence of metastable C^+ within the ion beam.

At z=2.500mm, there is sufficient intensity to cause further ionisation to C^{3+}, depleting the C^{2+} signal producing volume. Therefore the C^{3+} signal producing volume (by curve C) must be subtracted from the total theoretical volume curve fit.

At z<1.00mm, the Gaussian volume does not fit the experimental data. Due to the optics used, there will be diffraction rings present. At z<1.00mm, the intensity within the first couple of rings will be sufficient to cause ionisation, thus increasing the total expected signal.

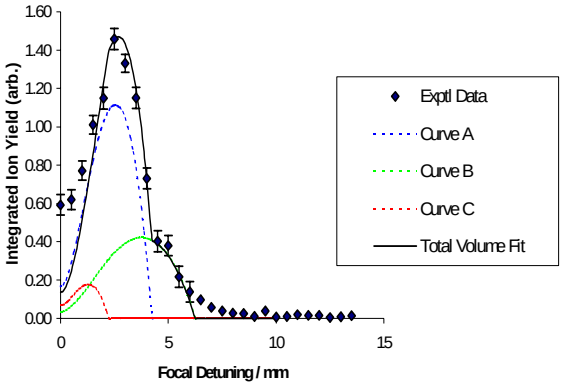

Figure 1. C^{2+} Z-Scan, curve A corresponds to a 24.7 eV ionisation process, B to 20.3 eV and C to 41.7eV.

Conversely, Figure 2 shows the z-scan of C^{3+}, where the volume fit is not as qualitatively good as for C^{2+}. This is due to a decrease in signal by an order of magnitude.

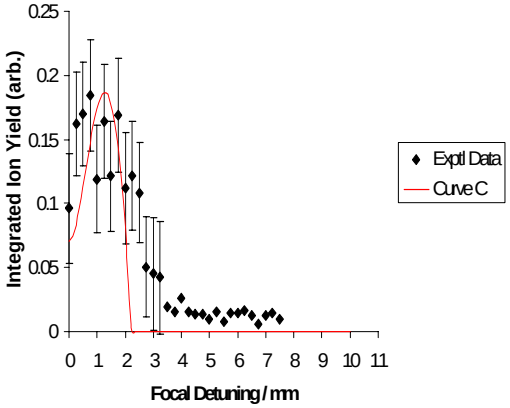

Figure 2. C^{3+} Z-Scan, curve C corresponding to the 41.7 eV process (also shown in Figure 1).

The maximum is also at a lower z-value implying the saturation intensity (corresponding to an ionisation energy of 41.7 eV) for the process lies close to the peak laser intensity.

From the curves A, B and C in Figure 1, the saturation intensities were obtained and used in the classical field ionisation model[3)] to get the corresponding ionisation energies

of 20.3, 24.7 and 41.7eV. These ionisation energies correspond to different processes, which are summarised in Figure 3.

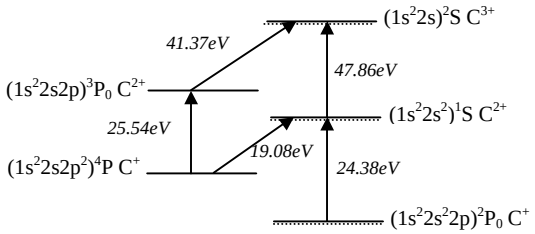

Curve	Ionisation Energy, expt[1]	Ionisation Energy, theory	Initial State	Final State
A	20.3 eV	19.08 eV	$^4P\ C^+$	$^1S\ C^{2+}$
B	24.7 eV	24.38 eV	$^2P_0\ C^+$	$^1S\ C^{2+}$
C	41.7 eV	41.37 eV	$^3P_0\ C^{2+}$	$^2S\ C^{3+}$

Figure 3. Energy level diagram of C^+ and identified ionisation processes.

The z-scan technique has the effect of volume enhancement for low energy processes. The metastable ionisation process (20.3 eV, curve B in Figure 1) has a natural volume enhancement of two relative to curve A. Convolving this with the fitted volume curves in Figure 1, implies the 20.3 eV process is six times weaker than the 24.7 eV process (curve A).

Unlike the other identified ionisation processes, the $^4P\ C^+ \Rightarrow {}^1S\ C^{2+}$ is spin forbidden. Ionisation of the quartet state, would leave the atomic core with both spins aligned, as opposed to the spin up – spin down configuration of $^1S\ C^{2+}$ state. Therefore, for this process to occur, the carbon ion must undergo a spin flip probably caused by magnetic field interaction.

Quasi-classical tunnelling (ADK) theory[4)] has been applied to the intensity scans of C^{2+} and C^{3+} in Figures 4 and 5 respectively.

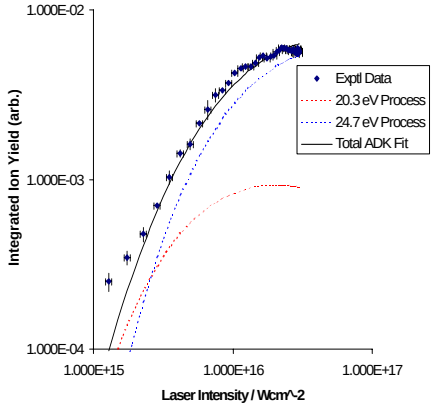

Figure 4. Intensity scan and ADK fit to C^{2+}.

The total ADK fit to C^{2+} is a sum of the 20.3 eV and 24.7 eV processes, in a ratio of approximately 1:6. This ratio is compatible with the findings in the C^{2+} z-scan.

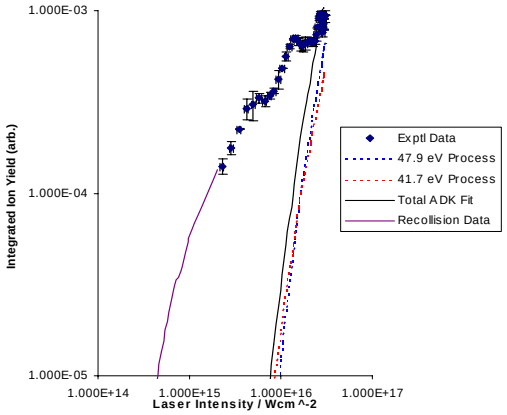

Figure 5. Intensity scan and ADK fit to C^{3+}.

Figure 5 shows the total ADK fit to C^{3+}. Here, the ADK theory fit isn't as good as that for C^{2+}. At intensities < 10^{16} Wcm^{-2}, the signal arises from non sequential ionisation due either to recollisions of the electron with the ground or metastable states. Calculations by H. van der Hart of the recollision process are shown.

References

1. A A A El Zein *et al*, Phys. Scripta, T92 119, (2001)
2. J B Greenwood *et al*, Phys. Rev. Letts., 88 233001, (2002)
3. J H Posthumus *et al*, J. Phys. B, 28 L349, (1995)
4. M V Ammosov *et al*, Zh. Eksp. Teor., Fig 91 2008, (1986)

Ionization pathways in intense field two- and three-body Coulomb explosion of carbonyl sulphide (OCS)

W A Bryan, W R Newell

Department of Physics and Astronomy, University College London, Gower Street, London, WC1E 6BT, UK

J H Sanderson

Department of Physics, University of Waterloo, Waterloo, Ontario, Canada N2L3G1

A J Langley

Central Laser Facility, CCLRC Rutherford Appleton Laboratory, Chilton, Didcot, Oxon, OX11 0QX, UK

Main contact email address: *w.bryan@ucl.ac.uk*

Introduction

The first investigation of the multiple ionization of a molecule by an ultrafast laser pulse was performed by Frasinski et al[1] in 1989, and interest in the field has flourished since. Indeed, contemporary investigation of intense ultrafast interactions with atoms and molecules has flourished into a new field of light-matter physics. Examination of experimental results has brought to the fore the importance of a number of unexpected processes, and a number of theoretical considerations indicate molecular ionization cannot be treated as the action of a single electron. Specifically, *ab initio* calculations of the distortion of carbon dioxide during multiple ionization by a static electric field[2] indicate the presence of charge-exchange pathways leading to experimentally observed geometries[3,4] and ionization proceeding through the most negative atomic site. The successful culmination of theoretical investigations into the applicability of Thomas-Fermi theory to ultrafast ionization in molecules has led to a recent publication concerning the ionization of CO_2 and N_2O[5]. This hydrodynamic treatment of a group of active electrons appears to hold considerable promise, given an impressive agreement between experimental and theoretical results.

When a high power ultrafast laser pulse is focused into a diffuse gas target, the intensity in the confocal volume exposes a triatomic molecule to ~10^{16} Wcm^{-2} at focus, decreasing to ~10^{13} Wcm^{-2} in the low intensity lobes before and after the focus. Depending on the location and orientation of the molecule, the laser pulse can initiate a number of complex processes, including laser-induced reorientation[3], low energy dissociation with the removal of 0, 1 or 2 electrons[6] and two- or three-body Coulomb explosion (2BCE and 3BCE respectively)[7,8] with the removal of at least 3 electrons. The laser pulse has also been observed to modify the geometry of triatomics undergoing 3BCE[3,4,6-8]; these processes are still undergoing investigation.

It is common that two or more high intensity processes overlap, and that the effects of two competing processes manifest in a similar manner. 3BCE is further complicated in many-electron triatomics by the large number of possible ionization channels, labelled according to the convention $OCS^{(m+n+p)+} \rightarrow O^{m+} + C^{n+} + S^{p+}$ being referred to as the (m, n, p) channel. Transitions between these channels will be referred to as "ionization pathways" to follow the discussions of Menon et al, who recently performed a thorough investigation into ionization of nitrogen and iodine[9].

The current work continues our investigation of the behaviour of carbonyl sulphide (OCS) in a femtosecond laser pulse [9]. Previous publications investigated modifications of the ground state geometry of the exploding molecule by the laser field, invoking enhanced ionization to describe the experimentally observed bond lengths and bend angles for five ionization channels. These publications evaluated the prospect of using 50 fs laser pulses for Coulomb Imaging small molecules. The present work complements the earlier publication, discussing the dynamics of the molecule during electron removal. Specifically, dissociation and 2BCE were investigated using two-dimensional covariance mapping (2DCM). Measurements of the kinetic energy of the product ions are reported. The 2DCM technique has been used to investigate 3BCE. However, given that OCS is comprised of three atomic species, and that the charge-to-mass ratio of oxygen and sulphur atoms is degenerate under certain conditions, three-dimensional covariance mapping (3DCM) of Coulomb explosion of OCS has been performed. This allows unambiguous identification of all ionization pathways and the measurement of their relative strengths. The kinetic energy release associated with each of these pathways is also reported.

Experimental

As in previous experimental studies, the RAL (UK) Astra laser facility was the source of the femtosecond laser pulses, as detailed in previous publications[3,7,8]. Ti: Sapphire seed pulses at 790 nm were amplified by CPA[10] to a pulse energy of 10 mJ in 50 fs at a repetition rate of 10 Hz. The laser pulses were focused by an f = 25 cm lens into the source region of a Wiley-McLaren[11] time-of-flight mass spectrometer (TOFMS), where they interact with a gas target at intensity 3×10^{16} Wcm^{-2}. Product ions were extracted from the source region, and detected using a pair of micro-channel plates after 11 cm of field-free drift. Throughout the present work, the laser polarization direction is parallel to the axis of the TOFMS. Unlike previous Ion Momentum Imaging (IMI) experiments[3,7,8], the detector is exposed to the full confocal volume and operated in high efficiency mode. When performing IMI using the same apparatus, an extraction field of 300 Vcm^{-1} is applied, and an aperture placed between the micro-channel plates and the interaction region, whereas CM experiments are performed without an aperture and an extraction field of greater than 600 Vcm^{-1}. The output of the TOFMS is monitored on a Tektronix TDS-744A digital storage oscilloscope (DSO). Time-of-flight spectra are recorded on the DSO, and stored on a laboratory PC.

Data processing

Following data collection, it was necessary to remove an instrumental 'ringing' effect from the raw TOF data. This was performed by passing a three-point median filter over the data, followed by the application of a peak detection routine, which examines the relationship between the amplitude of a peak *i* and subsequent peaks *i + 1, 2, 3*…. If peaks *i + 1, 2, 3*… are damped oscillations of *i* then they are discarded from the spectrum. The two- and three-dimensional covariance coefficients are then calculated according to the following equations. The two-dimensional covariance coefficient $C_2(x,y)$ is defined in Equation 1:

$$C_2(x,y) = < xy > - < x >< y > \qquad (1)$$

where *x* and *y* are *N* single shot time-of-flight spectra, *N* is the number of laser shots and < > is the average overall *N* for all *n* points in the TOF spectrum. In Equation 1, vector multiplication is used. The three-dimensional covariance

coefficient $C_3(x,y,z)$ is defined in Equation 2, where z is a third representation of the single shot TOF data.

$$C_3(x,y,z) = < xyz > - < xy >< z > - < xz >< y > - < yz >< x > + 2 < x >< y >< z > \quad (2)$$

Depending on the process under investigation, either $C_2(x,y)$ (2BCE) or $C_3(x,y,z)$ (3BCE) is evaluated for all n points on the TOF spectrum, resulting in an n^2 matrix in the case of $C_2(x,y)$ and an n^3 matrix in the case of $C_3(x,y,z)$. A full discussion of the application of covariance mapping to triatomic molecules is given in Reference 12. To test the performance of the experimental apparatus with respect to false correlations, a series of two-dimensional maps were recorded with the order of 3000 laser shots as a function of target gas pressure. At a pressure of 3×10^{-9} mbar, the contribution of false correlations to the covariance map became negligible. Of the order of 10^5 individual TOF spectra were recorded directly to hard disk. Shot-to-shot variations in laser pulse energy were allowed while collecting data, as this random fluctuation is vital for the covariance technique[12].

Results – 2BCE of OCS

A contour representation of an OCS 2DCM is presented in Figure 1 over a time-of-flight ranging from C^+ to OCS^+. An electric field of 600 Vcm^{-1} is applied across the extraction region. The covariance islands are identified by average TOF spectra below and to the left of the map. Examining Figure 1, a number of 2BCE channels may be identified: OCS^{2+} to $CO^+ + S^+$ and OCS^{3+} to $CO^+ + S^{2+}$, referred to as (1, 1) and (1, 2) respectively. The kinetic energy release (KER) associated with these channels is presented later in Table 1. Importantly, correlations involving either CS^+ or SO^+ are not observed, indicating a limitation to the possible number of ionization routes. These channels are expected in the 2BCE of OCS, as the OC bond is considerably stronger that the CS bond. Correlations also present on Figure 1 are $S^+ + O^+$ and $S^+ + C^+$ respectively. The forward component of these correlations is falsely correlated with OCS^{2+}, which is unavoidable - the volume of the focus generating OCS^{2+} is large, hence the ion is present in most single-shot TOF spectra. The backward components are clear of any such complication, and arrive at the same TOF, thus allowing the (1,1,1) channel to be identified, as shown in Table 1.

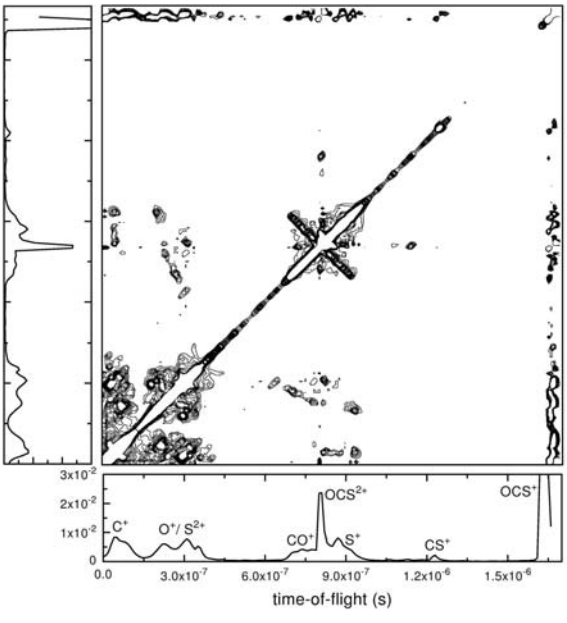

Figure 1. Contour representation of a two-dimensional covariance map (2DCM) of OCS between C^+ and OCS^+.

Figure 2 is a contour representation of the 2DCM of the atomic ions produced by the 3BCE of OCS between t = 0 and t = 600 ns. Starting in the bottom left-hand corner of Figure 2 and moving toward the top right anticlockwise through the body of the map illustrates a variation of ionization product strength with charge state for each species proceeding broadly as (O^{2+}, O^{3+}, O^+), (C^{2+}, C^{3+}, C^+) and (S^{4+}, S^{3+}, S^{2+}, S^{5+}). However, as discussed earlier, in the 2DCM, 3BCE correlations overlap hence these assignments could be the result of a number of 3BCE channels involving identical pairs of ions. This dependence of signal strength with charge state is to be expected, given that the detector is exposed to the full confocal volume. Looking at a number of correlations in Figure 2, a number of observations may be made concerning 3BCE processes. The charge-to-mass degeneracy of oxygen and sulphur is not present in S^{3+}, revealing the relative directions of the ions. The $C^+ + S^{3+}$ (weak), $C^{2+} + S^{3+}$ (strong) and $C^{3+} + S^{3+}$ (medium strong) correlations are all forwards-backwards, common to 2BCE of diatomic molecules. With this in mind and returning to Reference 8 briefly, the sulphur ion is ejected along the polarization direction, while the momentum of the carbon ion is resolved in the opposite direction. To conserve the total momentum of the system, the oxygen ion would be expected to move in the opposite direction to the sulphur ions. The $O^+ + S^{3+}$ (med) and $[O^+ + S^{4+}]$ or $[O^{2+} + S^{2+}]$ (med) correlations in Figure 2 confirm this by also being forward-backward correlations. The combination of these observations identifies the behaviour generating the $[O^+ / S^{2+}] + C^+$ correlation in Figure 2: an overlap of the forward-backward correlation of $C^+ + S^{2+}$ and the forward-forward correlation of $O^+ + C^+$. Thus it appears this group of correlations is due to the (1, 1, 2) channel. Analogous behaviour is seen towards the bottom left hand side of Figure 2. However, it is impossible to separate these higher-order channels because of the temporal overlap ions in time-of-flight region between 0 and 450 ns.

Results – 3BCE of OCS

To resolve the 3BCE channels, we turn to the 3DCM results. Due to the extra dimension introduced into the calculation, the correlation islands on the 2DCM become correlation volumes in the 3DCM. True 3BCE correlations appear as small volumes of positive covariance within the map volume. Identifying the locations of these correlations is complicated by the presence of three auto-correlation (AC) planes, which transverse the map at x = y, x = z and y = z. As in the case of the AC line in a 2DCM,

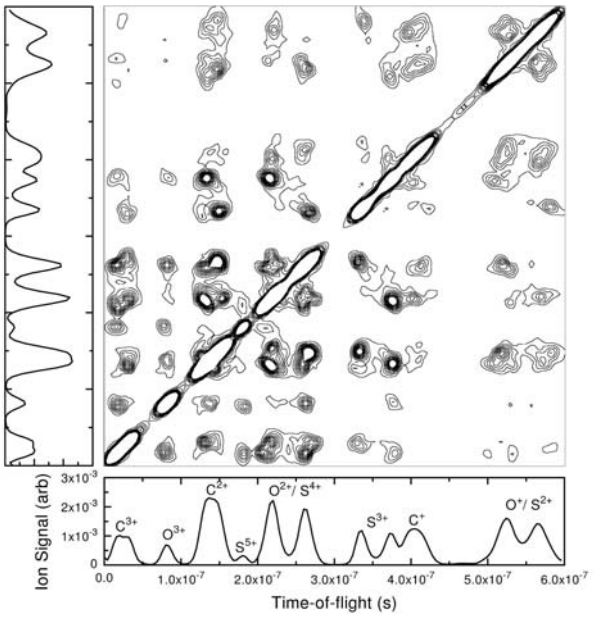

Figure 2. Contour representation of 2DCM of 3BCE fragments produced in the laser-OCS interaction.

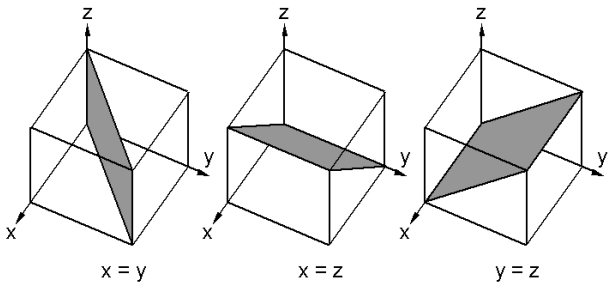

Figure 3. Illustration of the orientation of the three auto-correlation planes passing through the 3DCM.

volumes of the 3DCM in the vicinity of the AC planes have a stronger covariance than the correlations, but are essentially meaningless. The geometry of the AC planes is illustrated in Figure 3, the 3DCM containing the addition of these components.

Research Systems IDL (Interactive Data Language) 5.5 was used to examine the OCS 3DCM, allowing us to present, for the first time, visualisations through the body of the 3DCM. Previous studies present slices through the 3DCM. However by viewing the dataset in three-dimensions, the location of local maxima may be identified easily. A voxel (volume element) projection of the 3DCM between t = 0 and t = 300 ns is presented in Figure 4: this visualisation is generated in two steps. Firstly a transparency threshold T_t is defined, such that if $C_3(x, y, z) < T_t$, the point (x, y, z) is treated as transparent. Secondly, a three-dimensional transform is applied, allowing arbitrary rotation, translation and oblique display of the 3DCM onto an image plane, in this case, defined as the plane of the Figure. Visualising the 3DCM in this manner is similar to taking an x-ray of the dataset, with the covariance coefficient equivalent to density. The position of the AC planes in Figure 4 may be identified through a comparison with Figure 3. The dark

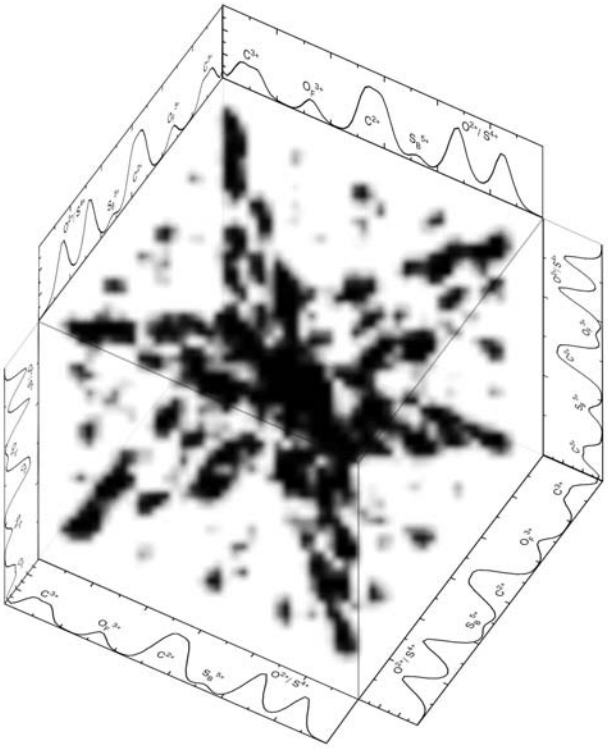

Figure 4. Voxel Projection of 3DCM of the 3BCE of OCS. The autocorrelation planes may be identified by comparison with Figure 3. Dark regions off the autocorrelation planes are true 3-body correlations.

volumes between the AC planes are true correlations, generated only by 3BCE channels, identified in part by average TOF spectra displayed parallel to the x, y, z axes.

Figure 5 is an iso-surface representation of the 3DCM, an iso-surface in 3D being the equivalent of a contour in 2D. The image plane in Figure 5 is defined normal to the line x = y = z, dramatically reducing the impact of the AC planes, as each of the AC planes x = y, x = z and y = z is normal to the image plane. A series of iso-surfaces is used to examine the 3DCM, thus identifying the 3BCE channels. For a particular threshold value, T the transition between $C_3(x,y,z) < T$ and $C_3(x,y,z) > T$ describes the iso-surface. True correlations are then identified in the regions between the AC planes by adjusting the threshold value. The $C_3(x,y,z)$ volume is investigated by varying T and noting local maxima in the regions bounded by the AC planes. The total kinetic energy release (KER) associated with each island is presented in Table 1, along with an estimate of the relative strength of the channel in the range 0 to 5, with 5 strongest. Channel strength is gauged by integrating the correlation volumes. The channels identified in the 2DCM are also included in Table 1.

In the case of a diatomic molecule Coulomb exploding, it is trivial to estimate the bond length at the point of explosion. However, in the case of 3BCE of OCS, which, as illustrated in Table 1, is heavily predisposed to asymmetric Coulomb explosion, such a calculation is not straightforward. To address this, the following technique was applied. The bend-angle distribution for OCS exposed to identical laser conditions[8] is known, and using an element of the Monte-Carlo software developed as part of the IMI technique, the 3BCE of OCS is simulated in momentum space for a range of CO and CS bonds. The bond lengths reported in Table 1 are those in strongest agreement with the 3DCM presented in Figures 4 and 5, and are simulated simultaneously, hence are bound by conservation of momentum.

To investigate transitions between the 16 3BCE channels shown in Table 1, a development of the diatomic 'ionization pathways' system[9] is used, with the addition of an extra dimension to account for the third atom in the system. The 3BCE ionization pathways for OCS are presented in Figure 6, where each intersection on the triangular grid represents a numerically possible channel, each open circle represents an experimentally

Figure 5. Iso-surface representation of the 3DCM of OCS.

Channel	KER (eV)	r_{OC} (Å)	r_{CS} (Å)	Strength
1,1[a)]	4.1	-	2.9	0.5
1,2[a)]	7.6	-	3.2	0.2
1,1,1[b)]	12.3	2.5	3.5	0.7
1,1,1[c)]	14.9	2	3	1
1,1,2	17.9	2.6	3.7	1.5
1,2,2	34	2.3	3.5	2
1,2,3	38.9	2.8	3.9	1
2,2,2	46.3	2.6	3.8	1.5
1,2,4	48.3	2.5	4.1	1
2,2,3	55.8	2.7	4	3
2,3,2	59.7	2.8	4.2	2.5
1,3,4	66	2.6	4.2	1
2,2,4	63	2.9	4.3	4
2,3,3	73	3	4.1	4
2,3,4	81	3.1	4.5	5
3,2,4	78	3.2	4.2	2
3,3,4	96	3.3	4.9	4
3,3,5	105	3.4	5.2	2

Table 1. OCS 2- and 3BCE channels identified from 2DCM and 3DCM, recorded at a peak intensity of 3×10^{16} Wcm^{-2} with a 790 nm 55 fs laser pulse. KER denotes the Kinetic Energy Release of the channel in question, and Strength is estimated between 0 (weakest) to 5 (strongest). Notes: a) OC bond length assumed to be 1.1Å, and CE treated as diatomic. b) Population 1 from (1,1,1) channel. c) Population 2 from (1,1,1) channel.

possible channel, and the solid circles represent observed channels. The distinction between numerically and experimentally possible channels is whether each of the component ions are observed in the TOF spectrum, or whether all three ions are correlated. For example, the (3,1,5) channel is numerically possible as O^{3+}, C^{+} and S^{5+} are all observed individually, but are not correlated. The solid arrows in Figure 6 indicate observed ionization pathways, where transfer between successive layers indicates ionization.

The most striking feature of the OCS-3BCE pathway diagram is the apparent 'cascade' of observed channels developing from the (1,1,1) channel at the apex, forming a network of ionization pathways which may be followed during the laser pulse. In the case of the higher charge states, it is apparent from Figure 6 that a particular channel may be accessed by a variety of routes. The behaviour of the molecule as it progresses through this diagram is currently being investigated, as it appears that it may be possible to isolate charge-exchange processes during ionization.

Returning to Table 1, a general trend between the low total charge 2- and 3BCE and high total charge 3BCE channels is observed: there is an increase in both the OC and CS bonds during ionization. We are investigating this behaviour using a number of theoretical methods, and will publish shortly.

Conclusions

Using two- and three-dimensional covariance mapping, we have recently investigated the order of electron removal during the Coulomb explosion of OCS. A large number of three-body channels have been identified, and fitted into a network of

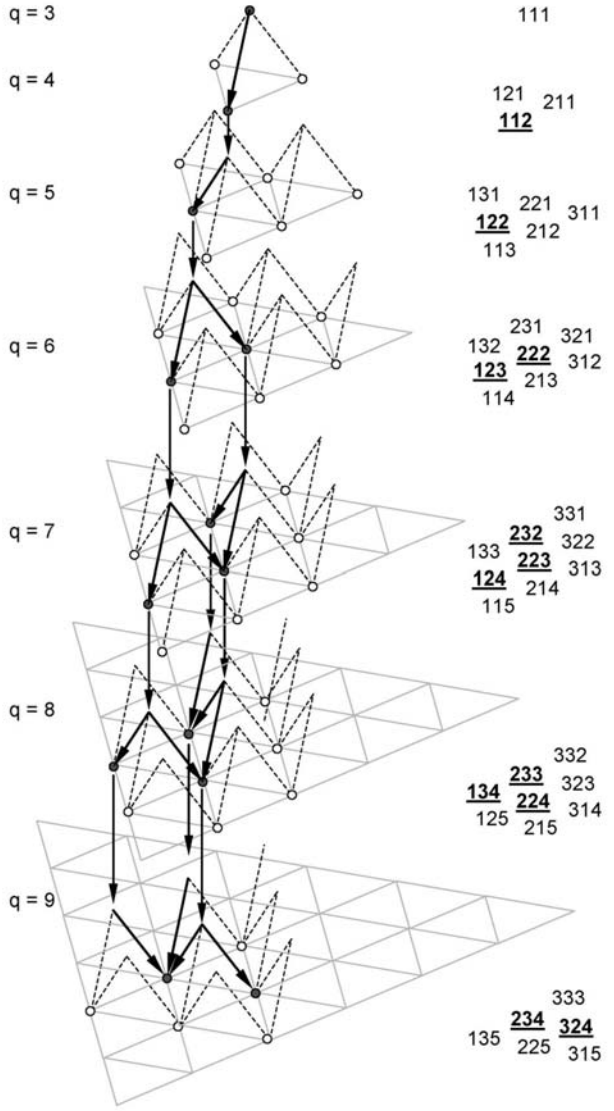

Figure 6. OCS-3BCE Ionization Pathway diagram. Channels of equal total charge (q) are grouped onto levels, identified in the key to the right. Progress down through the diagram illustrates electron removal. The (3,3,4) and (3,3,5) channels are left off.

ionization pathways. The evolution of the molecule while passing through this network is currently being studied.

References

1. L J Frasinski *et al*, Science 246 1029 (1989)
2. H Kono *et al*, J. Phys. Chem. A 105 5627 (2001)
3. W A Bryan *et al*, J. Phys. B: At. Mol. Phys. 33 745 (2000)
4. A Hishkawa *et al*, Phys. Rev. Lett. 83 1127 (1999)
5. Ph Hering *et al*, Phys. Rev. Lett. 85 2288 (2000)
6. A Hishikawa *et al*, Chem. Phys. Lett. 361 245 (2002)
7. J H Sanderson *et al*, Phys. Rev. A 59 R2567 (1999)
8. J H Sanderson *et al*, Phys. Rev. A 65 043403 (2002)
9. S V Menon *et al*, J. Phys. B: At. Mol. Phys. 35 2961 (2002)
10. D Strickland and G Mourou, Opt. Commun. 56 219 (1985)
11. W C Wiley and I H McLaren, Rev. Sci. Instrum. 26 1150 (1955)
12. L J Frasinki *et al*, Phys. Lett. A 156 227 (1991)

Laser-plasma electron acceleration with Astra

S P D Mangles, B Walton, Z Najmudin, K Krushelnick

Blackett Laboratory, Imperial College London, SW7 2BZ, UK

V Malka, M Manclossi

Laboratoire d'Optique Appliquée, École Nationale Supérieure des Techniques Avancées, École Polytecnique, CNRS, UMR 7639, 91761 Palaiseau, France

N Lopes, C Carias, G Mendes

GoLP/Centro de Física de Plasmas, Instituto Superior Técnico, 1049-001 Lisboa, Portugal

F Dorchies

CELIA, Université Bordeaux 1, 33405, Talence, France

Main contact email address: *stuart.mangles@imperial.ac.uk*

Introduction

Successful laser-plasma electron acceleration experiments have been performed on a number of laser systems. The majority of these have been performed on large laser facilities such as Vulcan at the Rutherford Appleton Laboratory[1)] or at LULI at Ecole Polytehcnique[2)]. One of the goals of laser-plasma accelerator development is to produce small size "table-top" accelerators for use in university laboratory size experiments.

Small laser systems have been shown to be able to produce very significant electron acceleration comparable with very large facilities. The 30 fs, 1 J laser system at LOA has produced 200 MeV [3)] electrons compared with the 650 fs, 160 J Vulcan Petawatt upgrade which has produced similar energy electrons (>500 MeV) [4)].

Table top lasers could be used to deliver high repetition rate electron bunches that could be used in a variety of experiments, including the production of bursts of intense short wavelength radiation by a number of mechanisms including stopping the bunch in a converter to produce gamma rays though bremsstrahlung[5)], focusing a second TW laser onto the bunch to produce intense Thomson scattering[6)], or passing the bunch though a periodic magnetic field structure such as a wiggler to produce a free electron laser.

Experiment

This report details the first successful electron acceleration experiment performed on Astra. The experiment consisted of focusing the 250 mJ, 70 fs FWHM pulses with an f/3 off axis parabolic mirror onto the edge of a supersonic gas jet to produce intensities on the order of 2×10^{18} Wcm^{-2}. The plasma wave generated by these pulses can then trap and accelerate electrons from within the plasma. The experimental set up is shown in Figure 1.

The plasma densities used range from 1.5×10^{19} to 1.5×10^{20} cm^{-3} which correspond to the FWHM of the laser pulse, $c\tau$, ranging from 2.5 to 8 plasma wavelengths. This corresponds to a regime where self-modulation can occur and at the higher densities this is expected to be the dominant acceleration mechanism.

The plasma density was controlled by varying the backing pressure of the gas jet valve. The electron density as a function of backing pressure was found by forward Raman scattering (FRS) measurements performed during this experiment and in other longer pulse experiments with the same gas jet nozzle. The plasma density varied linearly with backing pressure.

The electron energy spectrum was measured using an on axis magnetic spectrometer. This consists of an electromagnet that deflects electrons away from the axis. An array of diodes was placed behind the magnet to measure the electron signal (below) and the x-ray background signal (above) the laser axis.

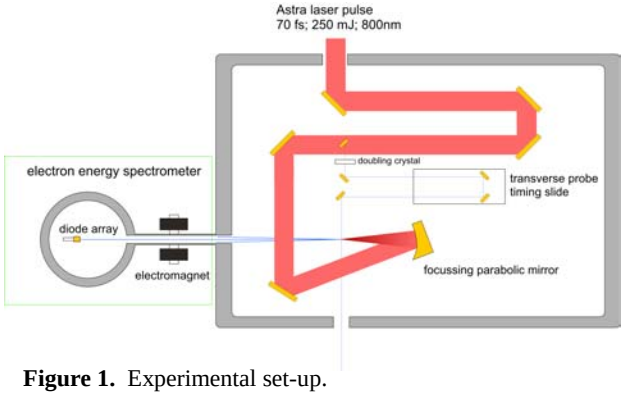

Figure 1. Experimental set-up.

The magnet and diodes were set up to measure a reasonably small range of energies of a few MeV in a single shot. A more complete spectrum was built up by varying the magnetic field while keeping the other experimental parameters the same over a series of shots. A typical spectrum was built up over approximately 15 shots. This also allows a measure of the shot to shot variation in the interaction.

Other diagnostics used in this experiment included a measurement of the transmitted laser spectrum. Transverse probing with frequency doubled light was also performed which was used to produce shadowgraphy of the plasma. This probe was independently timed, and was used to look for pre-pulse effects and plasma channel formation.

Results

Electron acceleration was observed over a range of electron densities. With the density below 7.3×10^{19} cm^{-3} no electrons were observed. This corresponds to $c\tau = 2.5\lambda_p$. It is probable that below this density the growth rate of FRS is not fast enough to produce a high enough amplitude plasma wave that can trap a significant number of electrons. When the pulse length approaches the plasma wavelength standard wakefield production (from the ponderomotive force associated with the front and back of the laser pulse) should dominate over self-modulation, but this is not particularly efficient until the pulse length is shorter than the plasma wavelength.

Figure 2 shows the energy spectra observed at four different densities. Shown on each plot is a power law fit of the form $N(E)dE = aE^b$, where $N(E)dE$ is the number of electrons per steradian with energies between E and $E+dE$ and a and b are the fit parameters. There is a suggestion of departure from this simple distribution at 9×10^{19} cm^{-3} but a higher resolution spectrum would be required to confirm this. The main source of error in the number of observed electrons was found to be shot-to shot variations. Notably this is greatest at higher pressures. At 1.6×10^{20} cm^{-3} the shot-to-shot variation was more than an order of magnitude.

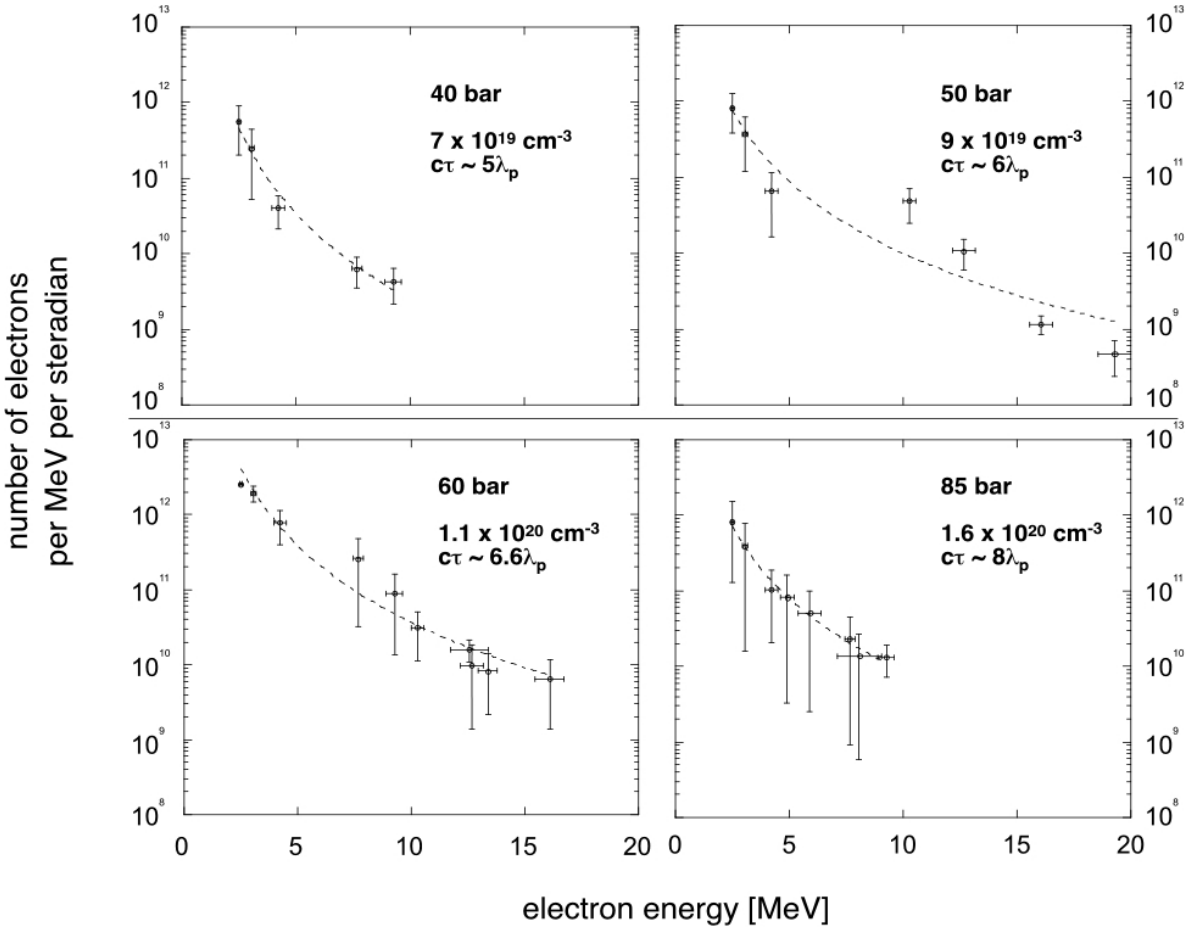

Figure 2. Measured electron energy spectra at various electron densities. Vertical error bars reflect shot-to-shot variation. Dashed lines are power law fits to the data of the form $N(E)dE = aE^b$.

On high density shots Raman satellites were observed. The plasma density that can be inferred from these shots matches the densities produced by the same gas-jet nozzle in another subsequent experiment[4].

Electron acceleration was not observed with electron densities below ~ 7 $\times 10^{19}$ cm^{-3} ($c\tau$ ~ 5 λ_p). The optimum acceleration was observed at a density of ~9 $\times 10^{19}$ cm^{-3} ($c\tau$ ~ 6 λ_p).

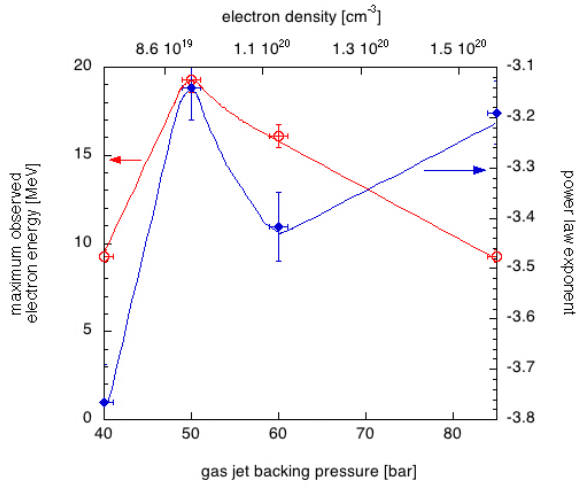

Figure 3. Variation of electron acceleration with gas jet backing pressure (and electron density). Red circles show maximum observed electron energy and blue diamonds show power law exponent for each pressure.

To visualize the density dependence of the electron acceleration two parameters are plotted against valve backing pressure and electron density in Figure 3. The maximum observed electron energy clearly shows an optimum density near 9 $\times 10^{19}$ cm^{-3} (50 bar) and the power law exponent also shows a peak at this density, although this rises again at higher density. The high level of shot to shot variation at high pressures may well indicate that the process is limited by propagation instabilities.

The exact acceleration mechanism needs further study, both experimentally and theoretically, as with the parameters used in the experiment we move from self-modulated wakefield acceleration (at high density) towards classical wakefield acceleration (at low density). The role of the laser field itself in the acceleration should not be discounted.

To summarise we have demonstrated that the Astra laser can be used to produce relativistic bunches of electrons with a broad energy spread up to 20 MeV. This acceleration is not observed below a minimum density and is probably affected by propagation instabilities at high density, resulting in an optimum density near 9 $\times 10^{19}$ cm^{-3}.

References

1. A. Modena *et al*, Nature 377, 606 (1995); M.I.K. Santala *et al*, Phys. Rev. Lett., 86, 1227 (2001)
2. F. Amiranoff *et al*, Phys. Rev. Lett., 81, 995–998 (1998)
3. V. Malka *et al*, Science, 298, 1596 (2002)
4. R.D. Edwards *et al*, App. Phys. Lett., 80, 2129 (2002)
5. W.P. Leemans *et al*, Phys. Rev. Lett., 77, 4182, (1996)
6. S.P.D Mangles *et al*, this report, 17.

Generation and characterization of short pulse Ti Kα radiation

F Y Khattak, A M McEvoy, J Angulo, M Lamb, D Riley

School of Mathematics and Physics, Queen's University of Belfast, University Road, Belfast, BT7 INN, N. Ireland, UK

P S Foster, R J Clarke, M M Notley, D Neely

Central Laser Facility, CCLRC Rutherford Appleton Laboratory, Chilton, Didcot, Oxon, OX11 0QX, UK

Main contact email address: *F. Khattak@qub.ac.uk*

Introduction

The interaction of femtosecond, terawatt laser pulses with solid targets can give rise to the generation of dense plasma emitting short bursts of high fluence K_α line radiation. Conversion efficiency up to ~10^{-4} [1)] and of duration less than twice the pulse length[2)] has already been demonstrated theoretically. Over the past few years, a number of publications[1-8)] have reported on the numerical, theoretical and experimental study of K_α radiation. Such radiation has potential applications in various fields, for example, x-ray lasers[1,9)], medical diagnostics[10)], x-ray diffraction and crystallography[11)]. Much of the earlier reported work has been concentrated on an effort to increase the K_α yield efficiency. To our knowledge, no report has been published on a K_α source with reduced background noise level. We report, here, on experiments generating bright K_α line emission by 67 fs laser beam interaction with both coated and uncoated Ti foil targets enabling us to achieve a relatively clean source. We are able to show an enhancement in the K_α yield for a plastic coated Ti foil when irradiated by a defocused beam.

Experimental Arrangement

The experiment reported here was carried out at the Rutherford Appleton Laboratory, using Astra, the multi-terawatt femtosecond laser facility [12)], delivering up to 300 mJ, infrared (800 nm), p-polarized pulses. The pulse shape is characterized by employing a single-shot third order autocorrelator with a dynamic response of 10^6. The main pulse is superimposed on a residual uncompressed CPA pedestal and ASE. It has a prepulse arriving 13ns ahead of the main pulse. The main pulse has an average full width half maximum (FWHM) of 67 fs with a good degree of reproducibility (±5 fs). The prepulse is ~10^7 times weaker in energy than the main pulse and the contrast of the residual uncompressed pedestal is measured to be 10^{-6} at 10 ps ahead of the main pulse and rises to 10^{-4} at 1.5 ps ahead of the main pulse. The ASE starts 2 ns ahead of the main pulse and rises linearly from a background of 10^{-8} of the main pulse to a level of 10^{-6} in 1 ns and then stays constant until the main pulse arrives.

An f/2.5 off-axis gold-coated parabola was used to focus the beam at an angle of 45º to the target plane. The focal spot intensity distribution for different focal offsets was recorded in the low energy mode of the laser with the help of a retro-system making use of a leakage through one of the turning mirrors inside the interaction chamber. The full width at half maximum (FWHM) of the focal spot at the best focus was measured to be 3 μm x 8 μm. The FWHM contains about 25% of the total energy. The focal spot was varied by moving the parabola off the best focus position along the line-of-focus by a known amount with the help of a micro-controller, towards the target and away from the target (referred to as positive off-set and negative off-set respectively). With the positive off-set a convergent beam interacts with the target while in the case of the negative off-set the focus lies before the target and a divergent beam interacts with the target. As we go off the best focus, the focal spot starts breaking up into numerous hotspots and, therefore, the energy distribution in the focal spot changes. The energy on target was monitored for every shot with a calibrated fast photo-diode and the maximum energy recorded on target was ~230 mJ. The maximum intensity on target exceeds 10^{18} Wcm^{-2} at the best focus.

Ti foils with a thickness of 12.5 μm, both bare and coated with 0.2 μm of CH, were used. After every shot, the target was moved by 2 mm with an external computer controlled micro-drive to get a fresh surface of the target for the laser interaction. In all cases, the beam was tight focused on the foil, using the retro viewing system, before moving the parabola to the desired offset position. By moving a target in and out several times the system was found to be reproducible to better than 20 μm in the position of best focus. Using the average beam waist of 5.5 μm at best focus, Gaussian beam optics predicts an effective Rayleigh range of about 30 μm. A thin glass pellicle, not shown in Figure 1 for clarity, was used in front of the target to protect the parabola from the plasma debris. The time integrated K_α line emission of titanium (4510.84 eV), was recorded with a Von Hamos (VH) spectrometer[13)] filtered with 25 μm beryllium and aluminised-Mylar (1000 Å-7 μm). The spectrometer comprises a cylindrically curved, 25 mm wide and 15 mm arc-length, LiF (200) crystal, (5 cm radius of curvature), on a micro-controlled base stage in a lightproof metal box. The VH spectrometer collects radiation over a large angle and thus provides enhanced detection efficiency. A cooled x-ray CCD system, coupled to the spectrometer in its imaging plane, detects and records the signal. This CCD has a quantum efficiency of approximately 65% for the Ti K_α photons[14)]. The line of sight of the spectrometer (crystal centre and the source position) made an angle of around 48º with the horizontal plane.

The reflectivity of the LiF (200) crystal was calibrated using a 1.85 GBq ^{55}Fe source which emitted Mn K_α photons at 5.9 keV and 6.4 keV. The source was positioned so that the emitted photons were incident onto the crystal at the Bragg angle of 31º. Diffracted photons were detected with a CCD. The quantum efficiency of the CCD was known to be 50% at this photon energy. The diffracted signal could be compared to directly detected photons using the same CCD. A value for the reflectivity of the crystal was calculated to be 0.061 ± 0.003 mrad. The reflectivity of a perfect LiF(200) crystal for a Ti-K_α line is about 10% greater than that for a Mn-K_α line[15)]. Assuming the same proportionate difference in reflectivity for the two lines, we extrapolated the reflectivity of our LiF(200) crystal to be 0.067 ± 0.003 mrad for the Ti-K_α line.

Results

Figure 1(a) shows K_α emission from the front of a 12.5 μm thick bare Ti foil irradiated at an angle of 45º to the normal of the target plane with 67 fs, p-polarized pulses. Shots with the energy-on-target range of 160 mJ ± 20% are included. The radiation collected within the solid angle of the spectrometer are extrapolated to the sphere by assuming uniform emission into 4π solid angle. Only a few error bars (± 20 μm in offset and ± 10% in yield) are shown for clarity of the graph. The errors in yield represent the potential systematic error in energy monitoring and spectrometer efficiency. As we go away from the tight focus, for both positive and negative offsets (decreasing the irradiance on the target), the signal gets weaker and goes below the detection level of the CCD system beyond around 400 μm offset. The yield varies in a roughly symmetric manner around the best focus except for the shots at 125 μm and 175 μm positive offset. The reason for this anomaly is unclear; at the intermediate offset of 150 μm the data is in line

with expectation. In Figure 1(b), the yield from the front of a Ti target coated with 0.2 μm CH is plotted. The data presented is in the laser energy range of 200 mJ ± 20%. The reason for the difference in average laser energy between the data sets is simply due to different levels of optimisation for the laser from one day to the next. This did not affect the relative pre-pulse or ASE levels significantly. Again we show error bars on only few data points for the purpose of clarity. The yield in this case is distinctly different from that of the bare Ti foil, in two ways. Firstly, the yield remains well above the detection level of our CCD system up to an offset exceeding 1000 μm. Secondly, the yield rises as we move closer to the best focus up to about 400 μm offset. Then it reduces to a lower value, almost by a factor of two, and starts rising again as we approach tight focus. The maximum yield at best focus is about the same as that in the case of bare Ti.

Whilst Figures 1(a) and 1(b) show the spread of the individual data points, in Figure 1(c) we compare the results of the yield from bare Ti to that from CH coated Ti foil averaged over a number of shots at each focus (up to 10). The error bars represent ± 20 micron in the offset and the standard error in the mean for the yield. This figure clearly shows the enhancement of yield for CH coated targets at large defocus. In both the cases, the K_α yield decreases sharply as we move away from the best focus up to about 150 μm offset. Moving further away from the best focus, the two sets of data follow different curves. At 400 μm offset, the yield from the coated target is an order of magnitude higher than that from the bare target. At the larger offset positions, as the hard x-ray background is considerably lower than that at the best focus due to reduced irradiance, we are able to generate a relatively clean source of K_α radiation. In Figure 1(d) we have combined the negative and positive offset results (excluding the anomalous points) to show average yield versus the estimated intensity. For offsets greater than the Rayleigh range of the beam we have used geometric optics to calculate the focal spot size and assumed 100% of the incident energy in the focal spot. The yield error bars again represent the standard error in the mean.

Discussion

At the irradiance of ~3×10^{16} Wcm^{-2} (defocusing by about 400 μm), HYADES [16] simulations give the scale-lengths around the critical density zone to be ~0.9 μm and 3.6 μm for the coated and uncoated targets respectively. Using these simulated scale-lengths and a simple approach that assumes resonance absorption occurs according to the Ginzberg model[17], we estimate resonance absorption levels of ~20% for the coated targets and ~0.002% for the uncoated targets. This would explain why we have no significant K_α production for the bare targets beyond about 400 μm offset, despite the irradiance being high enough to generate fast electrons of more than sufficient energy [6].

The optimum scale-length for resonance absorption, at 45° incidence, should be around 0.2 μm. However, the hydrodynamic simulations suggest that this does not occur unless the irradiance is below ~10^{15} Wcm^{-2} at which point the fast electron temperature is too low for significant K-alpha production. In the case of tight focus, (~10^{18} Wcm^{-2}) the HYADES simulations suggest the density scale-length is longer than 20μm in both cases when the main pulse arrives. Clearly the resistance of CH to being broken down has little effect under such high incident irradiances. The question that arises is why is tight focus then the most efficient case? With such a long scale-length one would expect 45° to be well away from the optimum resonance absorption angle. The most likely explanation is that, at tight focus, the focal spot is 3 x 8 μm in size, whilst the pre-formed plasma has a scale-length of order 30-50 μm according to our 1-D model. This means in fact that the expansion at the time of arrival of the main pulse is in reality closer to spherical than planar. Consequently, the incident laser pulse is no longer incident at 45° to the density gradient but at some much smaller and more optimised angle. For a scale-length of 30 microns we would expect the optimised angle to be of order ~7°, which is well within the cone of f/2.5 focusing, which would allow strong resonance absorption even at nominally normal incidence.

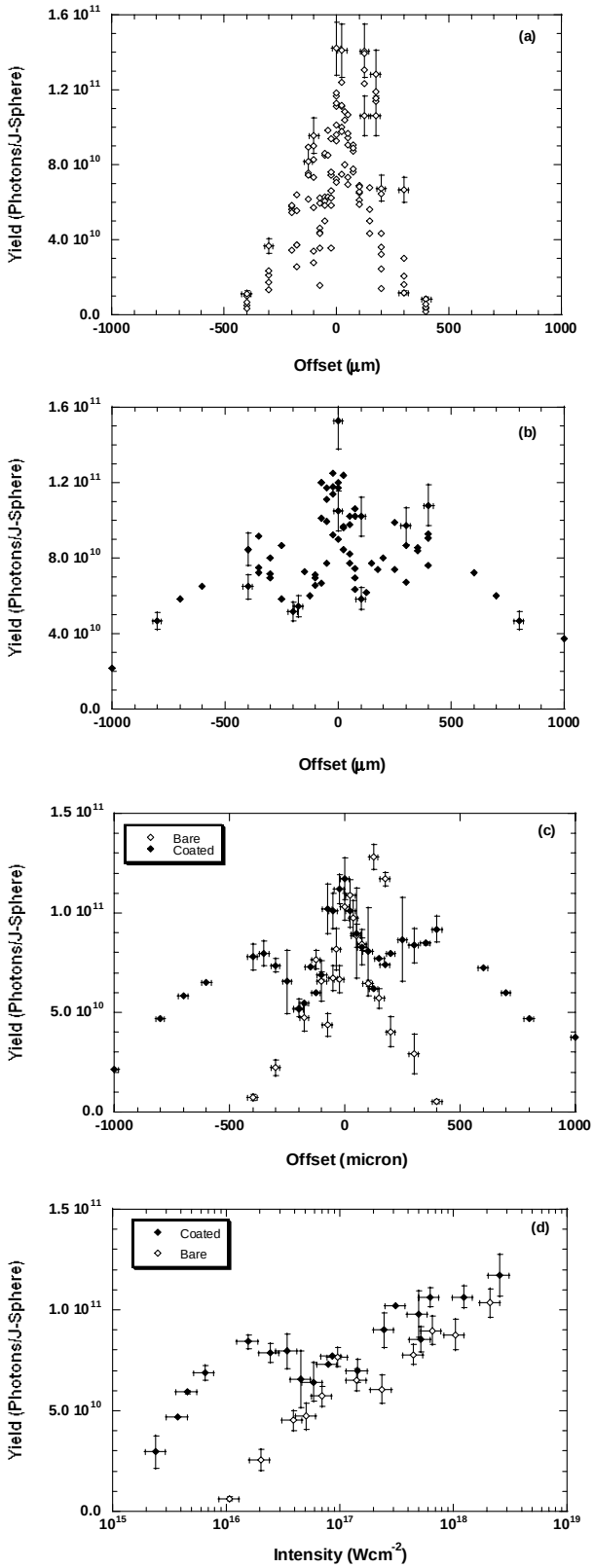

Figure 1. Measured single-shot K_α photons yield as a function of focus offset from Ti foils (a) bare (b) CH coated. (c) Comparison of average K_α yield from bare and CH coated Ti foils, as a function of offset. (d) Shows the combined results.

An important assumption is that there is no time in such a short pulse for profile steepening to occur. To show this we have used a Particle in Cell (PIC) 1-D "boost" code[18,19] which is able to simulate oblique incidence of a P-polarised beam onto a pre-formed plasma. The conditions of the simulation have to be considered. The hydrodynamic simulation suggests that even at tight focus, the pre-formed plasma prior to the main pulse is only ~100 eV, too low for a PIC code simulation at such plasma density. However, a simple simulation suggests that, for a Ti preformed plasma, collisional absorption of ~15% occurs, raising the temperature to ~6 keV at the peak of the pulse. The PIC code does not include collisional absorption so we set the temperature to 6 keV initially.

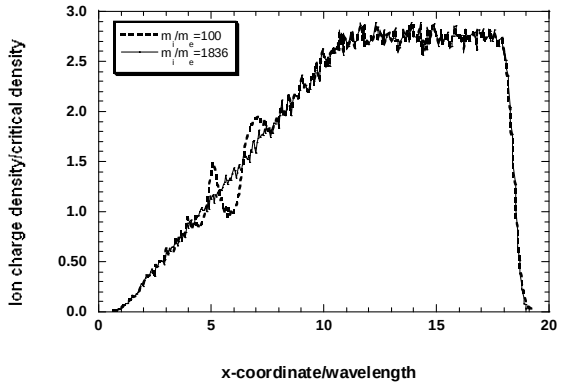

Figure 2. Results of PIC code simulation for two different ion masses ($m_i = 100m_e$, and $m_i = 1836m_e$) showing the ion charge density (in terms of critical density) as a function of position (in terms of wavelength) at the peak of the main pulse (67 fs, 800 nm, $2x10^{18}$ Wcm^{-2}).

Figure 2 shows the results of such a simulation using an incident intensity of ~$2x10^{18}$ Wcm^{-2} corresponding to a light pressure of order 660 Mbar, so we can see that the exact initial temperature of the simulation is not a crucial factor as it corresponds to only ~9 Mbar. We can see that even assuming the minimum ion mass possible (m_i/m_e=1836) there is no profile steepening at the peak of the pulse. For comparison we show a theoretical case where we assume m_i/m_e=100. We can see strong profile steepening occurs easily, illustrating that the code can in fact reproduce this physics but that it requires longer than the pulse duration if anything like a realistic ion mass is assumed. In fact the hydrodynamic simulations suggest that at the highest intensity, the CH is burnt through and the turning point density (~0.5 of critical at 45° incidence) is within the Ti plasma with its even higher ion mass.

Conclusions

In summary, the experimental situation is complex. With oblique incidence and a non-uniform focal spot it is strictly speaking a 3-D problem. However, we have been able to use simplified approaches to illustrate several points. Firstly, at modest irradiances, the parylene coating results in a shorter scale-length. This enhances resonance absorption and thus K-alpha production. Secondly, even at the peak irradiance, where light pressure far exceeds plasma pressure at around critical density, there is no time for profile steepening to occur during the main pulse. The behaviour of the coated targets would seem to proceed along the following lines: as the irradiance increases from 10^{15} Wcm^{-2}, the yield increases due to the fast electron temperature becoming more optimised, despite the scale-length becoming steadily less optimised for 45° incidence. Above about 10^{16} Wcm^{-2} the efficiency drops as the fast electron temperature moves to higher than optimum (c.f. ~6 $x10^{15}$ Wcm^{-2} predicted by Reich *et. al.*[6]). At even higher irradiances, the plasma expansion is moving away from planar to spherical and the effective angle of incidence becomes smaller and more optimised for the longer scale-length and so peak efficiency at tight focus is achieved. For the bare targets, the scale-length is even less optimised at modest irradiance and only at the higher irradiances, where expansion is less planar, is significant yield achieved.

Acknowledgements

We would like to thank the target preparation and the Astra laser staff of the Rutherford Appleton Laboratory. This work was supported by EPSRC grant GR/R09572/01.

References

1. Eder D C, Pretzler G, Fill E, Eidmann K and Saemann A, Appl.Phys. B 70, 211 (2000)
2. Reich Ch, Gibbon P, Uschmann I and Förster E, Phys. Rev. Lett. 84, 4846 (2000)
3. Rousse A, Auderbert P, Geindre J P, Fallies F, Gauthier J C, Mysyrowicz A, Grillon G and Antonetti A, Phys. Rev. E 50, 2200 (1994)
4. Wharton K B, Boley C D, Komashko A M, Rubenchik A M, Zweiback J, Crane J, Hays G, Cowan T E and Ditmire T, Phys. Rev. E 64, 025401 (2001)
5. Feurer T, Morak A, Uschmann I, Ziener Ch, Schwoerer H, Reich Ch, Gibbon P, Förster E, Sauerbrey R, Ortner K and Becker C R, Phys. Rev. E 65, 016412 (2001)
6. Von Der Linde D, Sokolowski-tinten K, Blome Ch, Dietrich C, Zhou P, Tarasevitch A, Cavalleri A, Siders C W, Barty C P J, Aquier J, Wilson K R, Uschmann I and Förster E, Laser and Particle Beams 19, 15 (2001)
7. Ziener Ch, Uschmann I, Stobrawa G, Reich Ch, Gibbon P, Feurer T, Morak A, Düsterer S, Schwoerer H, Förster E and Sauerbrey R, Phys. Rev. E 65, 066411 (2002)
8. Salzmann D, Reich Ch, Uschmann I, Förster E and Gibbon P, Phys. Rev. E 65, 036402 (2002)
9. Moon S J, and Eder D C, Phys. Rev. A 57, 1391 (1998)
10. Svanberg S, Meas. Sci. Technol., 12, 1777 (2001)
11. Rousse A, Rischel C and Gauthier J C, Rev. Mod. Phys. 73, 17 (2001)
12. Langley A J, Divall E J, Hooker C H, Hutchinson M H R, Lecot A J-M P, Marshall D, Payne M E and Taday P F, Central Laser Facility Annual Report, RAL-TR-2000-034, 196, (2000)
13. Notley M, Damerell A, Leach J, Neely D, Tallents G, Lin J, Smith R and Peteche S J, Central Laser Facility Annual Report, RAL-TR-1998-080 , 166
14. http://www.andor-tech.com/specstore/
15. Henke B L, Gullikson E M and J. C. Davis, Atomic Data and Nuclear Data Tables 54, 181 (1993)
16. Larsen J T and Lane S M, J. Quant. Spectorsc. Radiat. Transfer 51, 179 (1994)
17. Ginzburg V, Propagation of Electromagnetic Waves in Plasma, Gordon and Breach Science Publishers, and Kruer W, (1961), The Physics of Laser Plasma Interactions, Addison-Wesley Publishing Company, Inc. California, USA (1988)
18. Lichters R, Pfund R and Meyer-ter-Vehn J, LPIC++ -- A Parallel One-dimensional Relativistic Electromagnetic Particle-In-Cell Code for Simulating Laser-Plasma Interaction, (1999) Report MPQ-125, Max-Planck-Institute for Quantum Optics, Garching (Germany)and http://www.mpq.mpg.de/library/mpq-reports.html# (1999)
19. Lichters R, Meyer-ter-Vehn J and Pukhov A, Phys. Plasmas 3, 3425 (1996)

High contrast for TW-PW lasers – plasma mirrors operated in the near field

B Dromey, S Kar, M Zepf

School of Mathematics and Physics, Queen's University of Belfast, Belfast, BT7 1NN, UK

P S Foster

Central Laser Facility, CCLRC Rutherford Appleton Laboratory, Chilton, Didcot, Oxon, OX11 0QX, UK

Main contact email address: *m.zepf@qub.ac.uk*

Introduction

There has been a dramatic increase in the peak intensity that can be achieved at the focus of a short-pulse laser, with intensities in excess of 10^{21} Wcm^{-2} now a reality[1]. However the improvement in pulse contrast – the ratio between the peak intensity and intensity of any prepulses and amplified spontaneous emission (ASE) – has not kept pace with this development. The key challenge is to achieve contrast ratios large enough to prevent significant plasma formation on solid targets prior to the arrival of the main pulse. While an intensity of ~10^{13} Wcm^{-2} creates a plasma on all known target materials for even the shortest pulses, it has been shown that even a non-ionising intensity of 10^{8} Wcm^{-2} over sufficiently long periods can significantly alter the laser-matter interaction[2].

This implies that a peak intensity to prepulse intensity contrast of >1:10^{-9} is required. In a chirped pulse amplification (CPA) laser system it is very difficult to get a contrast of greater than 1:10^{-7} directly from the laser amplifier itself. The typical sources are prepulses leaked by the Pockels Cell, ASE and spectral bandwidth limitations on the main pulse itself.

One possible method of prepulse suppression is the use of self-induced plasma shuttering[3,4], more commonly referred to as a plasma mirror (PM). For a sufficiently intense laser pulse incident on a dielectric material ionization takes place on the leading edge of the pulse and the peak of the pulse then interacts with a dense plasma. The shuttering effect is achieved by the rapid change in reflectivity as the substrate evolves from a solid (with a reflectivity R~10^{-3}-10^{-2} for an anti-reflection (AR) coated glass slab) into plasma with near unity reflectivity. The laser intensity is chosen so that the intensity of any prepulse energy is below the ionization (i.e., damage) threshold of the glass and experiences the cold reflectivity, while the primary femtosecond pulse easily ionizes the target and reflects off the plasma.

With the advent of lasers capable of 10^{19} – 10^{21} Wcm^{-2} the issue of higher pulse contrast has become a high priority in short pulse laser development[1]. Past studies of PMs have either been limited to studying the reflectivity[3] or have investigated the performance of PMs at a fixed intensity in the laser focus[4]. Positioning a PM in the focus may be appropriate for medium power lasers (P~0.1 TW) where the required intensities can easily be achieved using a lens or mirror of reasonable f-number. But it is inappropriate for lasers with higher powers (TW-PW), where the ideal intensity range can correspond to focal areas of >1cm^2. Placing the plasma mirror in the near field of a laser, however, raises the possibility of severely distorting the phase and amplitude of the pulse due to inhomogeneous plasma expansion and reflectivity. This is in stark contrast to the in-focus case, where the PM acts as the reflective analog of a spatial pinhole filter and spatially inhomogeneous plasma formation thus improves beam quality[4].

Experimental setup

The experiments were performed on Astra. An f/8 off-axis parabola was used to focus the incident pulse onto the surface of an MgF AR coated polished fused silica target at an angle of incidence of ~10°. An identical parabola was used to recollimate the specularly reflected light.

Far field measurements were performed in the focus of an f/64 lens, while the near field was observed by imaging the diffuse reflection off a screen. Incident and specularly reflected energy were measured with a calorimeter. The incident pulse shape from a high contrast diode measurement with 300ps temporal resolution showed an ASE of >1:10^{-8} at 2ns rising to 1:2x10^{-7} at 500ps. Distinct prepulses, with a contrast ratio of 1:2x10^{-6} and 1:10^{-7} were detected preceding the main pulse by approximately 13ns and 16ns respectively. The temporal shape of the laser pulse close to the peak was diagnosed using a scanning third order autocorrelation device (TOAD). The intensity was varied by changing the energy on target or by defocusing the laser. The target was moved after each incident pulse to ensure that a fresh surface was illuminated by the next shot.

Plasma Mirror Characterisation

For a PM to be of any practical use, the reflectivity must be high and the reflected beam quality should ideally show no degradation relative to the incident beam. Consequently the PM must remain flat to a small fraction of the laser wavelength λ. In practice this demands that the plasma does not have adequate time to expand significantly, thus leaving the initial surface shape intact[4]. This puts an upper limit on the maximum pulse duration and, more precisely, on the time Δt that can elapse between the time of plasma formation and the peak of the pulse. The time Δt can be estimated by assuming that the overall surface modulation will only be a small fraction of the total expansion, i.e. we can tolerate a critical surface expansion of only λ or less. Based on these assumptions we can make a rough estimate $\Delta t_{max} \sim \lambda/c_s = 2.5$ps, based on an expansion velocity of $c_s = 3x10^7 cms^{-1}$, λ=0.8μm.

Several ps after plasma formation one would expect significant distortion of the PM and consequently non-specular reflection and an increase in absorption due to the longer scale length[5]. This hypothesis is borne out by the data of Ziener et al.[3] which shows that the transition from high specular reflectivity (~80%) to low specular reflectivity (<10%) occurs at much lower peak intensities for 500fs pulses (~5x$10^{15}$$Wcm^{-2}$) than for 90fs pulses (~5x10^{16} Wcm^{-2}). The sharp drop in specular reflectivity is due to the rapid onset of non-specular reflection, i.e. a distorted PM surface, rather than a sharp decrease in overall reflectivity. In the experiment reported here, the reflectivity of the target was measured for a range of intensities, and excellent agreement was observed with an earlier experiment[3] performed on the same laser.

As with most high power lasers Astra exhibits significant modulation in the laser near field close to the focus. This will result in the plasma formation taking place at different times across the PM and with differing expansion velocities. The intensity variation therefore seeds the non-uniform expansion of the plasma across the PM surface and ultimately leads to significant distortions in the reflected wavefront and the sharp drop in specular reflectivity. However, since the reflectivity scales $R \propto I^{1/2}$, the reflectivity will only vary by a small amount across the PM even for a significant intensity modulation. Consequently, the near field profiles of the collimated beam after the PM display a modulation depth comparable to the original beam.

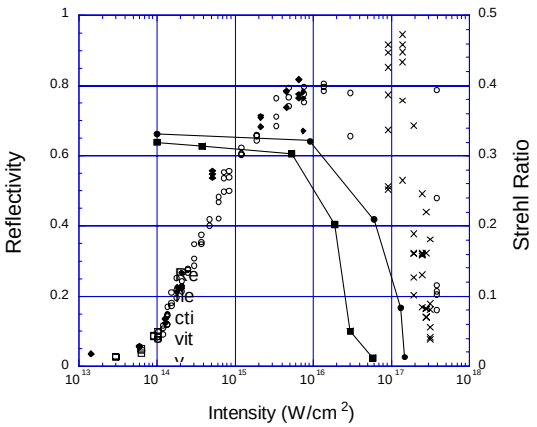

Figure 1. Comparison of the Strehl ratio and the specular reflectivity. Note the rapid drop of the Strehl ratio while the reflectivity remains high.

It is instructive to contrast the reflectivity with the quality of the reflected beam. Figure 1 shows two data sets of the Strehl ratio vs. intensity. In the first data set the Strehl ratio of the reflected beam begins to dip at around 10^{16}Wcm^{-2}. In the second it remains high until $5x10^{16}$ Wcm^{-2}. These two data sets were taken under nominally the same conditions. The difference between the two Strehl ratio measurements is thought to originate from small fluctuations in laser alignment leading to slightly different contrast ratios at a few ps from the peak of the pulse. The pulse contrast at this level is not measured on a shot to shot basis, however repeated measurements do show that the contrast ratio is sensitive to small changes in alignment. TOAD measurements also show significant shot to shot variation in the pulse contrast at 1ps prior to the peak (1:10^{-4} level). These fluctuations lead to a change in the time between the onset of plasma formation and the peak of the pulse Δt, allowing greater plasma expansion and therefore more distortion of the reflected wavefront.

Based purely on the observation of reflectivity and near field beam profile the best intensity range for the plasma mirror would appear to be around 1-$5x10^{16}$ where the reflectivity is reliably >65%. Close inspection of Figure 1 reveals the effect of the varying pulse contrast in the reflectivity measurements as well. The reflectivity can be seen to be highly reproducible up to around 10^{16} Wcm^{-2}. Above this the reflectivity begins to drop on some shots, but can remain high up to 10^{17} Wcm^{-2}. At this intensity point the shot to shot scatter in reflectivity spans 5 - 95%. These results are qualitatively very different from those obtained by previous authors[4], although the pulse contrast conditions and intensities were almost identical. Gold observes an improvement, as opposed to a degradation, in the beam quality due to the spatial filtering effect of the PM. This contrasting behaviour is also evident in the near field of the collimated reflected beam, which shows a slight enhancement of the modulation depth for our case, rather than a smoothing of the profile as reported by Gold. The key difference between the two measurements is the fact that the PM was operated in the near field in this experiment as opposed to the focus in the results reported by Gold.

A comparison of the TOAD measurements with and without the PM places an upper limit on the switch time of the PM of 500fs. This is in good agreement with previous experiments performed on the onset of reflectivity using 70fs pulses by von der Linde et al.[6], which measured a reflectivity rise-time of 200fs. Von der Linde et al. postulate that the rise-time is determined by the timescale required for avalanche ionisation to ionise the PM surface to the critical density. Since the frequency of subsequent collisions of the free electrons with the bound electrons in the target is then determined by the laser frequency, one can reasonably assume that the time required to reach critical density depends only weakly on the laser intensity. Consequently, one would expect to require a higher peak intensity to achieve maximum reflectivity when using pulses with a faster rise-time. That this is indeed the case can be seen in the data in for 90 and 500fs pulses in Reference 3. As in previous experiments, the contrast enhancement is in excellent agreement with the ratio of plasma reflectivity (0.8) to cold substrate reflectivity (1.5%) (~50). Higher contrast enhancement is easily achievable by using a substrate optimised for minimum cold reflectivity. In agreement with previous measurements[4] a substantial blue-shift of the reflected spectrum was observed. This blue-shift is due to Doppler-shifting caused by the motion of the critical surface towards the incoming laser beam. Under our conditions a blue-shift of 1 and 4 nm was observed for $2x10^{16}$Wcm^{-2} and $5x10^{16}$Wcm^{-2} respectively. This corresponds to expansion velocities for the critical surface of $c_s=4x10^7$cms^{-1} and $c_s=1.5x10^8$cms^{-1} respectively. Taking Δt~2ps for our pulseshape and an average velocity of $c_s/2$, this corresponds to a total expansion of 1.6 μm prior to the peak of the pulse or 2λ. This agrees well with our earlier estimate for the onset of non-specular reflectivity.

The results presented here suggest that it should be easily possible to achieve extremely high contrast ratios by cascading several plasma mirrors placed in the near field of a high power laser beam. Since the critical parameter for the onset of degraded focusability is the time from plasma formation to the peak of the pulse Δt, higher peak intensities on subsequent PMs are not expected to have any deleterious effect, despite the higher peak intensity. This can be easily understood by considering that the contrast enhancement due to the first PM will be greater than the increase in peak intensity from one PM to the next. The parameter Δt is therefore effectively fixed by the interaction of the laser with the first PM.

Conclusion

In conclusion, a plasma mirror has been characterised in the near field mode, which is the geometry relevant to improving the pulse contrast of modern TW to PW lasers. A range of operating intensities has been identified that allows high reflectivity to be combined with negligible phase-front distortion of the reflected beam and a contrast enhancement that corresponds to the ratio of PM reflectivity to cold reflectivity. The behaviour of a PM in near field mode differs substantially from the far-field mode investigated in previous publications. A rapid deterioration of the Strehl ratio is observed at high intensities where specular reflectivity is still high. The best Strehl ratio that can be achieved is that of the original beam, in contrast to the enhancement of focusability observed in far-field mode. Cascading of plasma mirrors in the near field with higher intensities should allow extremely high contrast ratios to be achieved with modest loss in total energy. This opens up the path to ultra-high contrast laser pulses with a pulse contrast of 1:10^{-10} at less than 500 fs from the peak of the pulse. Such pulses will give access to a completely new regime of high intensity laser solid interactions.

References

1. M. D. Perry *et al*, Opt. Lett. 24, 160 (1999)
2. K.B. Wharton, *et al*. Phys Rev E, 64 , 025401 (2001)
3. Ch. Ziener *et al*., J. Appl. Phys. 93, 768 (2003)
4. D.M. Gold, Opt. Lett. 19, 2006 (1994).
5. P. Gibbon, A. R. Bell Phys. Rev. Lett., 68, 1535 (1992).
6. D. von der Linde *et al*, J. Opt. Soc. Am. B., 13, 216 (1997)

Electron bunch acceleration - do we need a plasma?

R A Cairns

School of Mathematics and Statistics, University of St Andrews, North Haugh, St Andrews, Fife, KY16 9SS, UK

Main contact email address: *rac@st-andrews.ac.uk*

Introduction

This contribution consists first of a theoretical contribution where I construct a first order envelope equation describing the evolution of an electromagnetic pulse driving a wakefield and show how it gives a completely consistent description of energy transfer from the pulse to the wake. Then I go on to suggest that instead of transferring energy to a wake then from the wake to an electron bunch, it should be possible to transfer energy directly to a suitable electron bunch with greater overall efficiency. Unlike some vacuum acceleration schemes which have been proposed in the past, this does not depend on single electron dynamics in a focus, but depends on the electron bunch being dense enough to behave like a non-neutral plasma and affect the laser pulse propagation. A qualitative consideration of the nature of the interaction in three dimensions suggests that the mechanism could compress as well as accelerate the bunch.

Envelope equation

Various authors have proposed envelope equations to describe the evolution of a pulse as it drives a wakefield [1,2], but include second order derivatives, which rather goes against the spirit of an envelope equation. The problem lies in the use of an eikonal based on the initial wave frequency, while in reality the wave frequency changes because we do not have a stationary plasma in the laboratory frame.

The starting point is the wave equation for the vector potential associated with the laser pulse [1-3]

$$\left(\frac{\partial^2}{\partial t^2} - c^2\nabla^2\right)\mathbf{A} = \omega_p^2\mathbf{A} \qquad (1)$$

with

$$\omega_p^2 = \frac{n_e e^2}{\varepsilon_0 m_e \gamma}. \qquad (2)$$

The relativistic correction to the electron mass, due to both oscillation in the field of the pulse and to fluid motion of the electrons, is conveniently included in the definition of the plasma frequency. If the wave is assumed to be circularly polarised the problem of rapid oscillation of γ producing harmonics is avoided.

To follow the pulse (or different parts of it if we want to see how its shape evolves) we use the standard ray tracing equations [4] :-

$$\begin{aligned}\frac{d\mathbf{r}}{dt} &= -\frac{\partial D/\partial\mathbf{k}}{\partial D/\partial\omega}\\ \frac{d\mathbf{k}}{dt} &= \frac{\partial D/\partial\mathbf{r}}{\partial D/\partial\omega}\\ \frac{d\omega}{dt} &= -\frac{\partial D/\partial t}{\partial D/\partial\omega}\end{aligned} \qquad (3)$$

with

$$D = \omega^2 - \omega_p^2 - k^2c^2. \qquad (4)$$

Since a circularly polarised wave behaves just like a linear wave with a modified electron mass, we use the usual expression for wave energy density [5] which yields :-

$$\frac{1}{2}\frac{\partial}{\partial\omega}\left[\omega\left(1-\frac{\omega_p^2}{\omega^2}\right)\right]E^2 + \frac{1}{2\mu_0}B^2 \qquad (5)$$

or, in terms of the vector potential :-

$$\frac{m\varepsilon_0}{e^2}\omega^2A^2 \qquad (6)$$

where use has been made of the dispersion relation D=0 and the vector potential is in units of mc/e.

Making an eikonal approximation with :-

$$\mathbf{A} = \mathbf{a}(\mathbf{r},t)\exp(i\Psi(\mathbf{r},t)) \qquad (7)$$

and

$$\mathbf{k} = \nabla\Psi \qquad \omega = -\frac{\partial\Psi}{\partial t} \qquad (8)$$

gives, from Equation (1) :-

$$2c^2(\mathbf{k}.\nabla)\mathbf{a} + c^2(\mathbf{a}.\nabla)\mathbf{k} + 2\omega\frac{\partial\mathbf{a}}{\partial t} + \frac{\partial\omega}{\partial t}\mathbf{a} = 0 \qquad (9)$$

where second derivatives have been neglected in the usual way. A more physically transparent version can be obtained by multiplying by the complex conjugate of **a** and adding the result to its complex conjugate, giving :-

$$\frac{\partial}{\partial t}(\omega a^2) + \nabla.(\mathbf{v}_g\omega a^2) = 0 \qquad (10)$$

which, comparing with Equation (6) for the energy density, can be seen to have the simple interpretation that wave quanta are conserved as we follow the ray path (ie we move with the group velocity). The need to take account of the changing frequency is clear, since otherwise we just get the amplitude constant along the ray path. This is why an eikonal approximation based on the initial frequency needs higher order derivatives, which just bring in the frequency change in a less obvious way.

Now we can use Equation (10) to consider energy conservation. by writing it in the equivalent form :-

$$\frac{\partial}{\partial t}(\omega^2a^2) + \nabla.(\mathbf{v}_g\omega^2a^2) = \omega a^2\frac{d\omega}{dt}. \qquad (11)$$

The derivative on the right hand side here is the total derivative following the ray path, so it equals :-

$$\frac{1}{2}a^2\frac{\partial\omega_p^2}{\partial t}. \qquad (12)$$

From the form of Equation (11), it is clear that the expression (12), multiplied by $m\varepsilon_0/e^2$ represents the rate of energy transfer from the plasma to the wave.

We now turn to the electron dynamics and introduce a fluid momentum ***p*** which varies on a much longer time scale than the oscillation period of the electromagnetic pulse. On this slow time scale the fast oscillations can be averaged to produce a ponderomotive force, as in standard derivations of the beat wave equations. It is convenient to take ***p*** to be normalised to m_ec, in which case :-

$$\gamma^2 = 1 + a^2 + p^2. \qquad (13)$$

From Equation (13), together with the cold fluid equations for the electrons, it can be shown after some algebra which there is not space to give here, that the rate of transfer of energy (in units of $m_e c^2$) to the wave, as given by Equation (12) is equal to

$$-\frac{\partial}{\partial t}\left(n\gamma-\frac{1}{2}a^2\frac{n}{\gamma}\right)-\nabla.(n\gamma\mathbf{v})-mc^2\mathbf{E}_0.\mathbf{J} \qquad (14)$$

The various terms in Equation (14) can be interpreted as follows. In the first, $n\gamma$ is the total particle energy density. However, as can be seen from Equation (13) this includes the energy of the fast oscillation. This is subtracted off, which is consistent with its inclusion in the wave energy as given by Equation (5). The second term is just the divergence of the energy flux which, in a cold plasma, contains no contribution from the fast oscillation. In the final term $\mathbf{E}_0$ is the slowly varying component of the electric field, coming from the electron charge density rather than the electromagnetic wave. This term represents the transfer of energy to the slowly varying part of the electromagnetic field.

Electron bunch acceleration

We have now obtained a very general expression for the transfer of energy from an electromagnetic pulse to electrons. With the usual quasistatic approximation for wakefield generation, the electron density profile is assumed to be a function of *z-Vt*, where *V* is the pulse group velocity (usually well approximated by *c*). The rate at which energy is transferred to the wake thus depends on the electron density gradient (or, more exactly, the gradient of n/γ) and the general expression given by Equation (12) can be shown to be consistent with the usual wakefield equations [1-3]. In order to accelerate an electron bunch using a wakefield, the bunch must be of a length shorter than the wakefield wavelength, so that all of it is in an accelerating field [6]. Also, if a reasonable fraction of the wake energy is to be transferred to the electrons, the density of the bunch must be of the same order as the background plasma density. Less dense bunches can, of course, be accelerated but only at the expense of low energy efficiency.

If a suitable bunch can be produced, then it will have density gradients comparable to those in the wakefield and if the electromagnetic pulse is slowed down by it enough to remain on its trailing edge, then energy will be transferred to the bunch at a rate comparable to its transfer to a wakefield. This energy will go directly to the electron bunch whereas transfer of energy from a wakefield to a bunch is only efficient if a very carefully tailored bunch is placed in exactly the right place relative to the driving pulse, a non-trivial technical problem.

The efficiency with which energy could, in principle, be transferred to an electron bunch can be calculated by going to the rest frame of the bunch. As argued above, we want the electron density to be high enough for the group velocity of the electromagnetic wave to be slowed down to the speed of the pulse in the laboratory frame. In the rest frame this translates into the condition that the bunch density is above critical, so in this frame the wave is reflected and its frequency is unchanged. In the laboratory frame the wave overtakes the bunch, moves up the density gradient and is slowed down until it is moving with the speed of the bunch then moves back down the density gradient and is eventually reflected. Transforming between the rest frame and laboratory frame, we get the ratio of initial to final frequency in the latter to be:-

$$\frac{1-V/c}{1+V/c} \qquad (15)$$

which is a small number for a relativistic bunch. From the conservation law, Equation (10), this is also the ratio of initial to final energy in the wave. This indicates that direct energy transfer in a one dimensional system could be almost 100% efficient, but there is, of course, the question of what might happen in a real, three dimensional system. Qualitatively we can see that rays will be refracted as in Figure 1, so there will be an inward focusing force on the electrons.

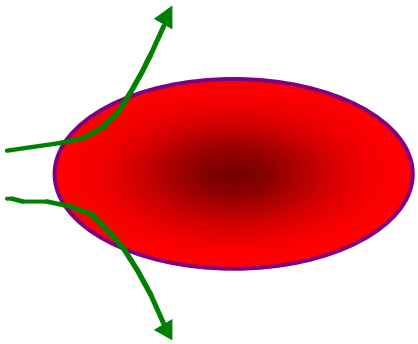

Figure 1. Ray paths in an electron bunch.

Intuitively it seems possible that a suitable electromagnetic pulse could produce a smooth compression in both parallel and perpendicular directions and overall acceleration of the bunch, the problem resembling the old one of producing smooth compression of a shell.

Conclusions

It has been shown that, in order to follow evolution of a pulse generating a wakefield, envelope equations with second order terms can be replaced by the standard ray tracing equations, supplemented by a condition equivalent to conservation of quanta which says that ωa^2 is constant along the ray path. This formulation has been shown to be consistent with a detailed consideration of the energy balance.

Turning to the question of electron acceleration, the suggestion is made that direct acceleration of an electron bunch might be much better than using a wakefield. If suitable bunches can be produced then the rate of energy transfer may be comparable to that from a pulse to a wake, and the problem of efficient transfer from the wake to an electron bunch is avoided. While more detailed work is needed, it seems possible that both acceleration and focusing of a real bunch in three dimensions might be possible. This idea differs from other schemes of vacuum acceleration which rely on electron dynamics in a beam focus. Here the bunch must be dense enough to behave like a non-neutral plasma and affect the wave propagation.

Acknowledgements

This work was carried out as part of the X-Alpha project, supported by EPSRC grant GR/R88090/01. I am grateful to Albert Reitsma, Bob Bingham and Dino Jaroszynsky for valuable comments.

References

1. U de Angelis Physica Scripta T 30, 210, (1990)
2. S V Bulanov *et al*
   Phys. Fluids B 4, 1935, (1992)
3. P Sprangle, E Esarey and A Ting
   Phys. Rev. A 41, 4463, (1990)
4. S Weinberg
   Phys. Rev. 126, 1899, (1962).
5. T H Stix
   Waves in Plasmas, AIP, New York (1992)
6. A Reitsma
   PhD Thesis, University of Eindhoven, (2002)
   (http://alexandria.tue.nl/extra2/200212656.pdf)

Combining B-spline basis techniques with R-matrix Floquet theory

H W van der Hart, C McKenna, L Feng

Department of Applied Mathematics and Theoretical Physics, Queen's University of Belfast, Belfast, BT7 1NN, UK

Main contact email address: *h.vdhart@qub.ac.uk*

Introduction

Over the last two decades laser technology has developed rapidly, enabling experimentalists to study the behaviour of atoms and molecules subjected to ultra-short ultra-intense laser light. These intensities are sufficiently high for the normal atomic dynamics to be severely distorted. This distortion has been observed to result in a large number of non-perturbative features, such as high-harmonic generation, plateau features in above-threshold ionization, and the larger-than-expected production of doubly ionized systems.

Theoretical support has proven to be invaluable in elucidating the physics of the detailed atomic response to an intense laser field. Many theoretical approaches have been developed to describe this response. The first type of approach is to solve the Schrödinger equation directly. While this is quite feasible for one-electron systems, for 3D two-electron systems a substantial amount of computational resources are required[1]. The second type of approach is an S-matrix approach[2]. In this approach, one approximates the full interaction by including only the most important types of interactions. A third type of approach is the R-matrix Floquet approach[3], in which the time-dependent Schrödinger equation is transformed into a time-independent one. This time-independent equation is then solved using well-established R-matrix techniques.

The advantage of the R-matrix Floquet approach is that it is, in principle, capable of investigating any atomic system. The only requirement is that one has a good description of the atom under investigation, as well as the system left after ionization. When the atoms become more complex, this becomes difficult to achieve using *ab-initio* wave functions, as huge expansions are required to describe subtle effects such as (dielectronic) core polarization. It is thus advantageous to combine the R-matrix Floquet approach with model potentials, which have proven to be very accurate for atoms such as Ca[4]. The first part of this report is to show that by combining model potential approaches with R-matrix Floquet theory, it is possible to get excellent results for photoionization of Ca.

In order to get high-quality results for Ca, we have used B-spline basis sets. B-splines have rapidly obtained widespread use in atomic physics[5], because they can be adapted readily to the problem under investigation. This means that a B-spline based code, which is optimized to the study of bound states, can in principle be adapted to continuum-state problems with minimal effort. Only the knot set, the small set of parameters defining the basis set, needs to be changed.

This flexibility of B-spline basis sets is demonstrated in the second part by reporting on two-photon double ionization of He. When the frequency is chosen carefully, two-photon double ionization requires energy transfer from one electron to a second one. By studying double ionization, we therefore gain insight into the influence of electron-electron repulsion on the atomic dynamics. Technology does not yet allow for these processes to be studied experimentally, but it is expected that the development of fourth-generation light sources (4GLS) will enable the investigation of these processes. The theoretical description of double ionization processes is non-trivial, since analytic solutions do not exist for the wave function of two continuum electrons. B-spline basis sets have proven to be highly suited for describing the double continuum[6]. The combination of these basis sets with R-matrix Floquet theory is thus essential for obtaining accurate cross sections.

Multiphoton ionization of Ca

Single- and two-photon ionization calculations of Ca using a combination of B-spline basis sets, model potential techniques and R-matrix Floquet theory, have recently been published[7]. One difficulty in applying R-matrix Floquet theory to Ca is the need to describe both its atomic and ionic states accurately simultaneously. Core polarization is important, and by our use of B-spline basis sets within the R-matrix Floquet method, we allow its inclusion by adopting a model potential approach. This involves representing only the two valence electrons of Ca explicitly and using model potentials to replace all electron-core interactions. Six states of Ca^+ are retained as target states. Figure 1 shows a schematic energy level diagram of Ca, in which we compare the energy levels we obtain for Ca^+ and Ca with known experimental values[8]. The agreement between theory and experiment for the binding energy of Ca is highly satisfactory and excellent agreement is also achieved for the five excited state energies.

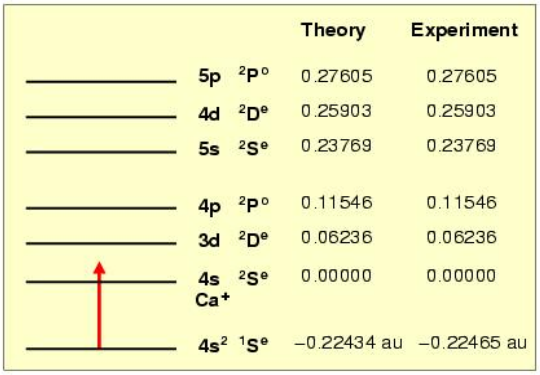

Figure 1. Schematic energy level diagram of Ca. Energy levels of Ca^+ and Ca are in atomic units (au), relative to the 4s $^2S^e$ ground state of Ca^+. The experimental values have been averaged over the different *J*-levels.

We use our approach to calculate the single-photon ionization cross-section above the first ionization threshold of Ca. This investigation is motivated by the fact that this energy region has been used quite extensively to test atomic theory, by examining the agreement with experiment for resonances converging onto the 3d $^2D^e$ threshold. Two dominant resonance features lie within this region: 3d5p $^1P^o$ and 3d6p $^1P^o$. The main challenge is to obtain an accurate description of the very narrow 3d6p resonance. No quantitative agreement has yet been achieved between theory and experiment as to the absolute magnitude of this resonance. We examine our approach to address this problem.

Figure 2 shows our results for the single-photon ionization cross-section for the energy region between 0.238 and 0.266 au, and a comparison with the best known theoretical[9] and experimental[10] results. Good agreement exists between all three results for the 3d5p resonance. With regard to the magnitude of the narrow 3d6p resonance, we achieve a distinct improvement between theory and experiment over earlier work. A difference of about only 6% remains between our present theoretical result and experiment.

The present results demonstrate that the combination of B-spline basis techniques with R-matrix Floquet theory

provides the most accurate theoretical results available to date. We can therefore extend these calculations to higher intensities where the laser field will distort the atomic dynamics in a non-perturbative manner. As a first example on this path, we have investigated the shape of the 3d6p resonance as a function of intensity, and we found[7] an example of laser induced degenerate states[11] at an intensity just below 5×10^{10} W/cm^2.

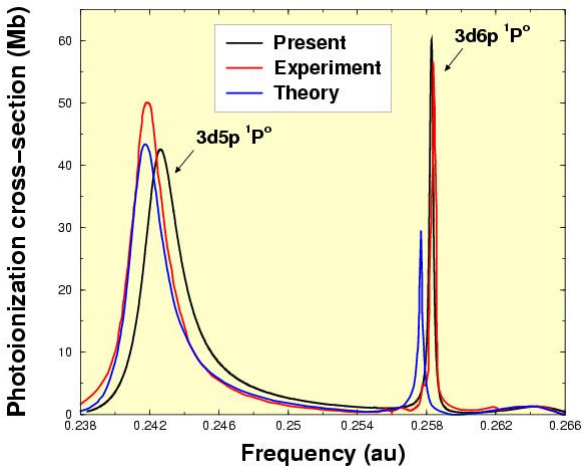

Figure 2. The calculated photoionization cross-section of Ca above the first ionization threshold is compared with the best known theoretical[8] and experimental[9] results.

Two-photon double ionization of He

Double photoionization of He is a process of fundamental importance to atomic physics, since it is a direct demonstration of the influence of electron-electron repulsion. In the absence of dielectronic interactions, no energy can be shared between the two electrons. Since photoabsorption is a single-electron process, in the absence of these interactions no double ionization can take place. Hence double ionization presents a signature of dielectronic interactions, and over the last decade great strides have been made in understanding double photoionization.

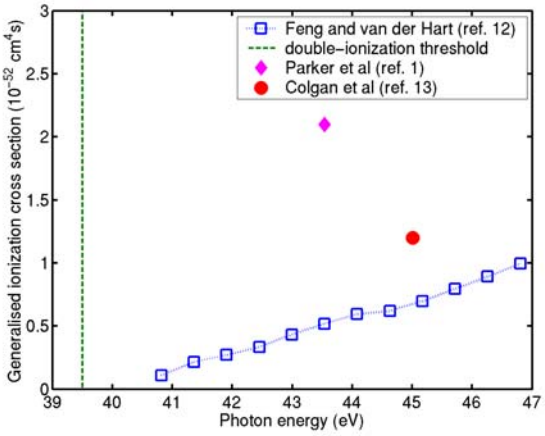

Figure 3. Two-photon double ionization cross sections as a function of photon energy. Results obtained using the B-spline based R-matrix Floquet approach[12] are compared to results from time-dependent calculations performed by Parker et al[1] and by Colgan et al[13].

At first glance, two-photon double ionization appears to be of less significance. Since both electrons can absorb a photon, double escape can take place without requiring any dielectronic interactions. For well-chosen photon energies, this is actually incorrect. At a photon energy of 45 eV, two photons suffice to eject both electrons from He, as the threshold energy is 39.5 eV. On the other hand, the sequential pathway He → He$^+$ → He^{2+} requires three photons, since He$^+$ ionization requires a photon energy of at least 54.4 eV. Two-photon double ionization thus requires that the electrons interact.

Figure 3 shows cross sections for two-photon double ionization obtained by our B-spline based R-matrix Floquet approach[12]. The cross sections are compared to the theoretical results obtained by Parker et al[1] and by Colgan and Pindzola[13]. Although the difference with the latter results is of the order of 70%, this is good agreement bearing in mind that results obtained by perturbative theory[13] differ from ours by a factor of 10. The present results differ by a factor of 4 from the results by Parker et al[1]. This difference is not serious, as we expect these calculations by Parker et al[1] to overestimate the cross sections. Their calculations were performed at an intensity of 5×10^{15} W/cm^2. Multiphoton transitions involving more than 2 photons may therefore add significantly to double ionization. In addition, ionization-excitation is included in their double ionization estimates, whereas it is excluded in our cross sections and in the cross sections obtained by Colgan and Pindzola[13]. Other recent time-dependent calculations[14] have obtained cross sections in even closer agreement with the present ones.

Conclusions

We have given an overview of our recent progress in the application of the R-matrix Floquet approach for multiphoton processes. By combining R-matrix Floquet theory with B-spline basis sets, we have been able to simplify calculations for Ca significantly while simultaneously retaining a high degree of accuracy. In addition, the combination has enabled us to study multi-photon double ionization processes. These latter results will assist experimentalists in assessing the feasibility of carrying out experiments at 4GLS facilities.

Acknowledgement

LF was supported by the Engineering and Physical Sciences Research Council under grant ref. no. GR/N26241. C McKenna acknowledges the receipt of a postgraduate research studentship from the Department of Employment and Learning, Northern Ireland.

References

1. J S Parker *et al*, J. Phys. B 34, L69 (2001).
2. A Becker and F H M Faisal, J. Phys. B 29, L197 (1996).
3. P G Burke *et al*, J. Phys. B 24, 761 (1991).
4. J E Hansen *et al*, J. Phys. B 32, 2099 (1999).
5. H Bachau *et al*, Rep. Prog. Phys. 64, 1815 (2001).
6. H W van der Hart and L Feng, J. Phys. B 34, L601 (2001).
7. C McKenna and H W van der Hart, J. Phys. B 36, 1627 (2003).
8. J Sugar and C Corliss, J. Phys. Chem. Ref. Data 8, 865 (1979).
9. C H Greene and L Kim, Phys. Rev. A 36, 2706 (1987).
10. U Griesmann *et al*, J. Phys. B 21, L83 (1988).
11. O Latinne *et al*, Phys. Rev. Lett. 74, 46 (1995).
12. L Feng and H W van der Hart, J Phys. B 36, L1 (2003).
13. J Colgan and M S Pindzola, Phys. Rev. Lett. 88, 173002 (2002).
14. L A A Nikolopoulos and P Lambropoulos, J. Phys. B 34, 545 (2001).
15. B Piraux and H Bachau, private communication (2002).

Target rear surface effects in high intensity laser plasma experiments

R G Evans

Plasma Physics Dept, AWE Aldermaston, Reading, RG7 4PR, UK

L O Silva, J R Davies

GoLP, Instituto Superior Tecnico, 1049-001 Lisboa, Portugal

W B Mori

Department of Physics and Astronomy, University of California, Los Angeles, California, 90095, USA

Main contact email address: *r.g.evans@physics.org*

Introduction

Intense ($I > 10^{18}$ Wcm^{-2}) pulses of visible laser light interacting with solid targets generate high current relativistic electron beams propagating broadly in the laser direction. The beams typically carry 1 - 100 MAmp of current with electron energies in the range 1 - 10 MeV. The beam currents are vastly greater than the Alfven limit ($I_A = 17\beta\gamma$ kAmp) and can only propagate if very closely current neutralised by a return current of "cold" electrons. Considerations of the magnetic field energy require the return current to be spatially co-located with the forward beam to within a collisionless skin depth c/ω_p. The forward propagating relativistic electron beam co-located with the return current is unstable to the Weibel instability which grows on the time scale of the plasma period of the electron beam ($\omega_{pb}^2 = 4\pi n_b e^2/\gamma m_e$). There is an extensive literature describing the Weibel instability both in the linear regime[1,2] and through simulations in two[3] and three[4] space dimensions.

Recent experiments by the Imperial College group of Krushelnick et al[5] have prompted us to examine the electron beam transport in the presence of rear surface plasmas and for differing target geometries.

Simulations

Our simulations are carried out with the OSIRIS code[6] developed at UCLA which is a collisionless relativistic electro-magnetic PIC model. The calculations reported here were carried out in 2-1/2D geometry on a small Linux cluster.

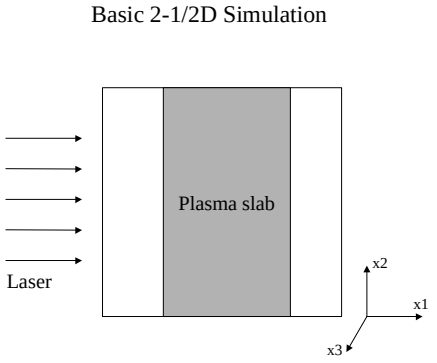

Figure 1. Schematic of the 2-1/2 PIC simulations.

Our reference calculation is summarised in Figure 1. The laser is incident in the x1 direction with its **E** vector in the x2 direction (p-polarised) and in this first simulation **E** is uniform across the grid. The laser intensity is given by the normalised vector potential a0 = 2.8 and rises to its steady value in about four laser periods.

Figure 2 shows a time sequence of the magnetic field component B3, ie out of the simulation plane, which is the signature of the current filaments generated by the Weibel instability. At early times the instability grows fastest for modes with $k \sim c/\omega_{pb}$ and at later times these filaments merge and according to simulations by Honda et al[7] give rise to an increase in transverse beam temperature. Our simulations show that at later times the magnetic field of the Weibel instability is confined to the front part of the target and at greater depths the Weibel modes appear to be stabilised.

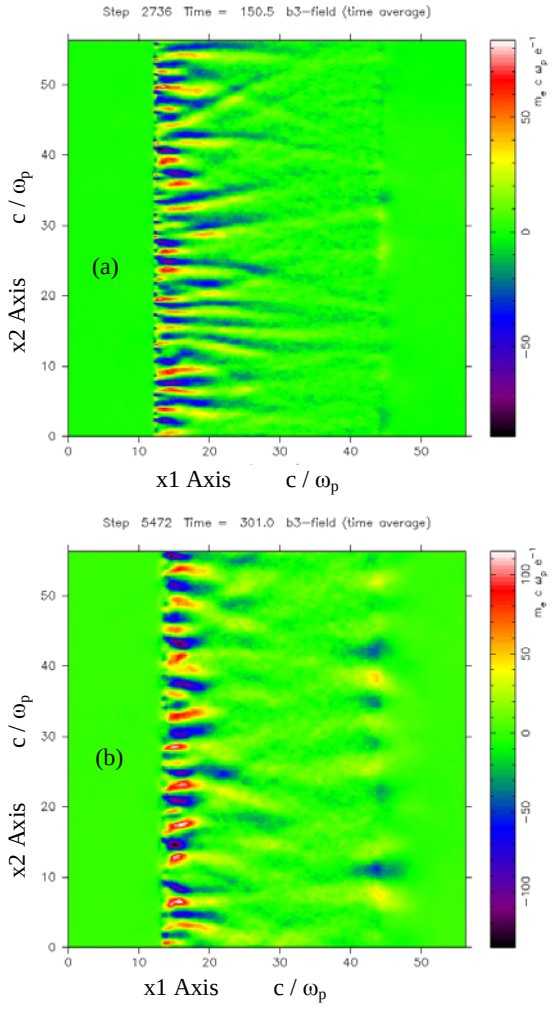

Figure 2. Magnetic field of the Weibel instability at (a) $t = 150\ c/\omega_p$ and (b) $t = 300\ c/\omega_p$.

This is explained by the results of Silva et al[2] who show that for simple velocity distributions the threshold of the Weibel instability is given by $\alpha > \gamma(\beta_\perp/\beta_{//})^2$ where $\alpha = n_b/n_e$ is the ratio of beam density to background electron density, γ and $\beta_{//}$ are the Lorentz factors of the beam electrons and $\beta_\perp$ is a measure of the transverse beam temperature. The combination of the longitudinal velocity spread of the laser accelerated electrons and their deflection in the large magnetic fields generated by the Weibel instability gives rise to a an increase in transverse momentum spread $\beta_\perp$ with depth and eventually this is large enough to stabilise the instability.

With the addition of a linear density ramp at the rear of the target we see a dramatic change in the above picture. Figure 3 shows the magnetic field at time 300 ω_p^{-1} and there is clearly a second region of Weibel instability in the rear density tail. The second region of instability shows growth at smaller values of k than for the front surface instability. For a 1μm wavelength laser, the peak value of the magnetic field on the rear of the target is about 100 MGauss and the wavelength of the rear surface instability is about 3μm.

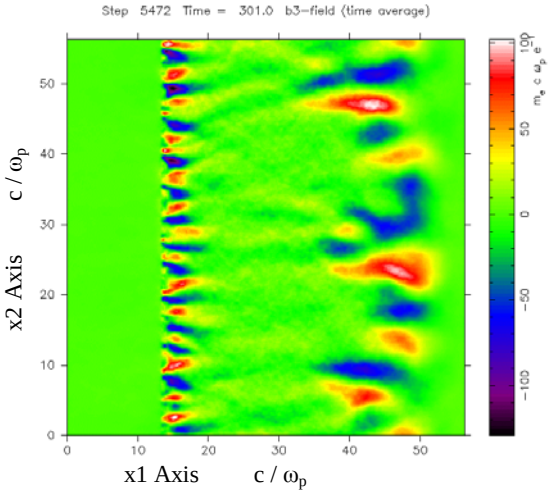

Figure 3. Magnetic field in the presence of a density tail on the rear surface of the plasma slab.

The explanation for the recurrence of the Weibel instability is straightforward. The instability initially occurs because the laser generated electron beam has a low transverse temperature and the threshold for Weibel growth is exceeded even though the ratio n_b/n_e of beam density to background density is small (about 0.1 in our simulation). Deeper in the target the transverse temperature increases and eventually the Weibel instability drops below threshold. As the electron beam encounters the rear density tail the ratio $\alpha = n_b/n_e$ increases to 1 and the threshold is again exceeded despite the larger transverse temperature. The larger transverse temperature causes the maximum growth rate on the rear surface to be at smaller values of k than on the front part of the target as in the theory of Silva et al[2].

This recurrence of the Weibel instability suggests a possible explanation for the fine spatial structure observed in some electron detectors[5]. As the electron beam propagates from target to detector its radius will increase from perhaps 100μm to several mm and its transverse temperature will cool due to the adiabatic expansion of the electron cloud. The residual gas pressure in the experiments is typically 10^{-4} mBar and singly ionised background gas atoms would give an electron density of about $3x10^{15}$ cm^{-3} and a collisionless skin depth of 0.5mm. The density of the laser generated electron beam would match the background over some part of the propagation path and there would be a third region of Weibel instability due to the plasma formed by ionising the background gas. This would give rise to spatial structure on the scale 1 - 5 c/ω_p ie 0.5 - 2.5mm which is exactly what is observed.

Finite Laser Spot Simulations

We have also carried out several simulations with focal spot sizes of 5μm FWHM and laser intensity of $10^{20}Wcm^{-2}$. The behaviour of the Weibel instability is somewhat different since modes with a transverse wavelength greater than the focal spot diameter are not strongly driven. Figure 4 shows the eventual configuration of a single current filament with its surrounding magnetic field.

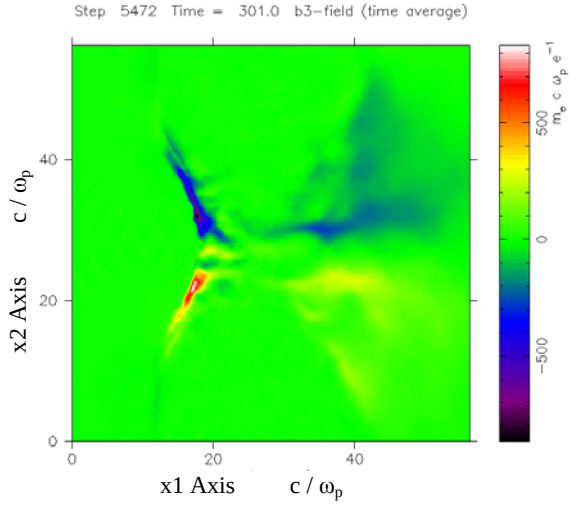

Figure 4 . The magnetic field configuration at time t = 300 c/ω_p for a finite width laser pulse on a plasma with rear density ramp.

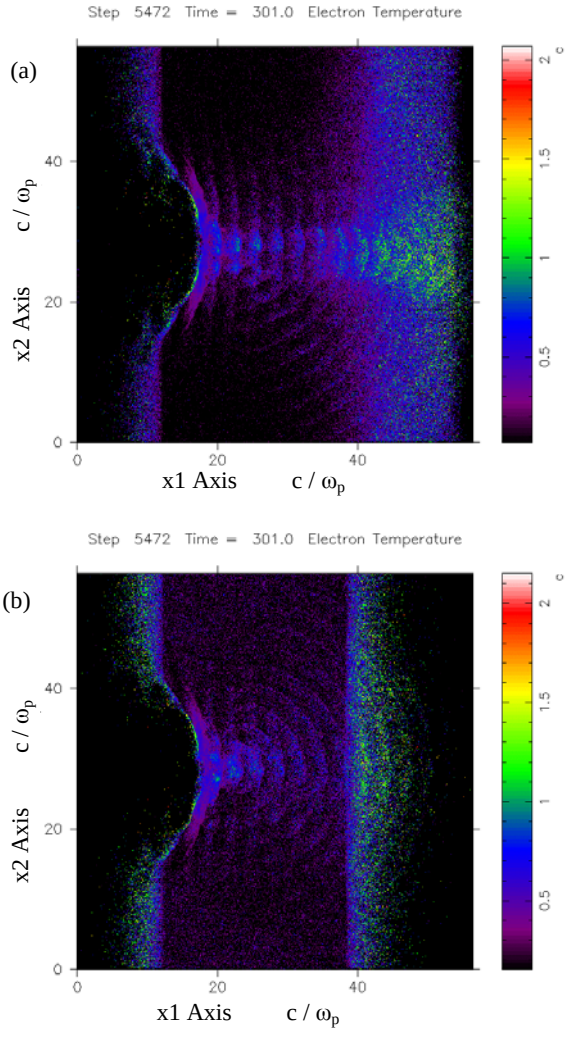

Figure 5. The RMS dispersion of electron velocities in each cell of the simulation a) with a rear surface plasma and b) without the rear plasma.

The magnetic field inside the target foil strongly influences the transport of the relativistic electrons and Figure 5 shows a comparison of the electron transport with and without the rear surface plasma. The "temperature" shown in Figure 5 is the RMS dispersion of momentum for the electrons within each cell of the simulation. It is a convenient way to show the spatial distribution of the relativistic electrons which make the

dominant contribution to the "temperature". With the rear surface plasma present the internal electron beam is much more compact, due to the additional focusing of the magnetic field, and the heated region of rear surface plasma is also smaller. The cause of this change of magnetic field configuration appears to be due to the inhibition of the "cold" return current by the MGauss magnetic fields of the rear surface Weibel instability and a consequent increase in the magnetic field of the forward relativistic beam.

Electron beam pointing and wedged target effects

There is experimental evidence[8] that the γ ray bremsstrahlung radiation, and by implication the relativistic electron beam, in a wedged target may show two angular peaks from the same laser shot. We have simulated a wedged target with an angle of about 20 degrees with the laser incident normally on the front surface. This simulation has a rear density tail and the development of the magnetic field at a time 200 ω_p^{-1} is shown in Figure 6(a). The magnetic field has retained some internal structure rather than decaying to a single 'filament' as in the case of normal incidence.

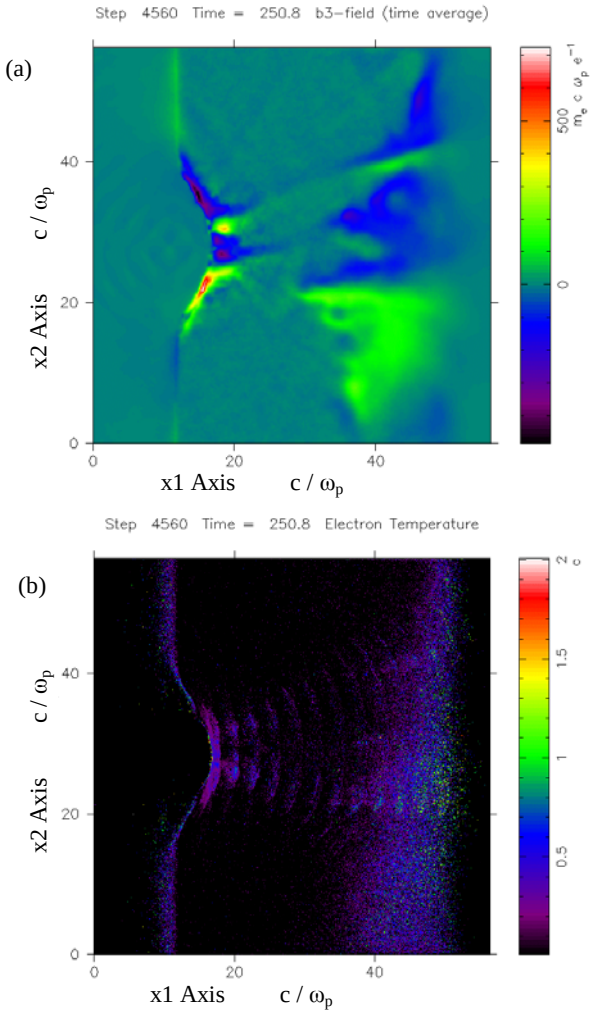

Figure 6. a) The magnetic field at time 250 c/ω_p for a wedged target with a rear density ramp and b) the RMS dispersion of electron velocities at the same time.

The most striking result from the wedged target is that the internal electron beam, as evidenced by the "temperature" plot shown in Figure 6 (b) at 250 ω_p^{-1}, has now split into two beams one of which is deflected so as to be approximately normal to the rear surface. If we replace the wedged rear surface with a 'bi-wedge' with the laser spot aligned with the apex then we again see two internal electron beams as shown in Figure 7 .

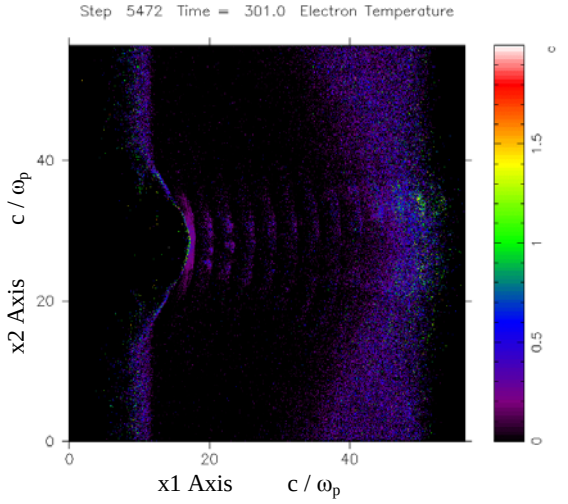

Figure 7. The 'temperature' of the electrons in a simulation with a bi-wedge target .

If we perform the simulation without the rear density ramp then the split beam is only observed at late times ($t > 400\ c/\omega_p$)after a rear surface plasma has evolved due to the reflected beam electrons.

Conclusion

The rear surface conditions can play an important part in electron beam transport and initially sharp surfaces can develop a plasma tail over the laser pulse duration.

References

1. F Califano, F Pegoraro and S V Bulanov
Phys Rev E 56, 1, 963 (1997)

2. L O Silva, R A Fonseca, J W Tonge, W B Mori and J M Dawson
Physics of Plasmas 9, 6, 2458 (2002)

3. Y Sentoku, K Mima, S Kajima and H Ruhl
Physics of Plasmas 7, 2, 685 (2000)

4. Y Sentoku, K Mima, Z M Sheng, P Kaw, K Nishihara and K Nishikawa
Phys Rev E 65, 046408 (2002)

5. See for instance the Vulcan experiments by Krushelnick *et al*, this report, pp 5 -23

6. R G Hemker
PhD Thesis UCLA (2000)

7. M Honda, L Meyer-ter-Vehn and A Pukhov
Phys Rev Lett 85 5055 (2001)

8. M I K Santala, M Zepf, I Watts, F N Beg, E Clark, M Tatarakis, K Krushelnick, A E Dangor, T McCanny, I Spencer, R P Singhal, K W D Ledingham, S C Wilks, A C Machacek, J S Wark, R Allott, R J Clarke and P A Norreys
Phys Rev Lett 84, 7, 1459 (2000)

Non-local magnetic field generation in laser-plasmas with isotropic pressure

R J Kingham, A R Bell

Plasma Physics Group, Imperial College London, Blackett Laboratory, Prince Consort Road, London, SW7 2BZ, UK

J Boisson

ENS Lyon, France

Main contact email address: *rj.kingham@imperial.ac.uk*

Introduction

The "$\nabla n \times \nabla T$" or thermoelectric mechanism is a well known source of B-fields in laser-plasmas under collisional conditions[1,2]. It is responsible for the B-fields observed in the plasma ablated from the surface of solid targets and foils when illuminated by an intense laser pulse. These fields have been shown to affect expansion of the ablated plasma[3]. Additionally, strong thermoelectric magnetic fields are believed to be responsible for the hot spots measured in the (ionized) gas fill of hohlraums[4] since they suppress thermal transport.

The thermoelectric B-field mechanism originates from the curl of the "ambipolar" electric field that maintains quasineutrality, i.e., $E = -\nabla P_e/(en_e)$, where $P_e=n_eT_e$, n_e, T_e are the electron pressure, density and temperature respectively. The pressure gradient is one term appearing in Ohm's law, which describes momentum balance of the electron fluid. The *local approximation* is conventionally made when obtaining the versions of Ohm's law (e.g. Braginskii's version) from the Vlasov-Fokker-Planck equation which are then used to derive $\partial B/\partial t = -(k_b/en_e)\nabla n_e \times \nabla T_e$.

By solving the Vlasov-Fokker-Planck equation directly and thereby dispensing with the local approximation we have found new B-field source terms which are non-local analogues of the $\nabla n \times \nabla T$ mechanism. It is well known that non-local effects lead to a severe reduction of heat flow compared to the Spitzer-Härm value (which uses the local approximation) when the temperature gradient is steep. This necessitates the use of "flux limiters" in hydro codes. We have found that non-local effects are also important for magnetic field generation. In particular the non-local sources do not need density gradients or anisotropic electron pressure (which drives the Weibel instability) and can be powered by crossed gradients in electron temperature and ionization number Z or simply by a non-symmetrical hot spot. These effects become important when the characteristic temperature and Z scale-lengths become small, approaching the collisional mean-free-path.

Fokker-Planck simulation

The 2D Vlasov-Fokker-Planck (VFP) code IMPACT[5,6] was used to look at strong, localized, thermal heating of a uniform density plasma with the spatially varying ionization state shown in Figure 1.

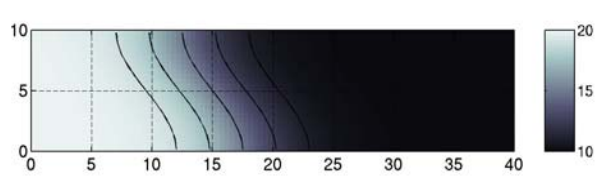

Figure 1. Non-uniform spatial ionization profile Z(x,y) used in FP simulation. Lengths are in mean-free-path units.

The density and ionization profiles were non-evolving. Note that effects due to anisotropic pressure were not considered. Also the Lorentz approximation was used, i.e., there are no e-e collisions in the $\underline{f}_1$ equation (see below) which is valid for high Z plasma. The effect of the heating was to energize f_0, the isotropic part of the electron distribution function, and did not involve momentum transfer to the plasma – beams of fast electrons were not injected (which would require anisotropic pressure to describe). The spatial heating was applied to a strip of plasma on the very left side of the computational box with the heating rate described by a "1 - tanh[(x-x_0)/L]" profile centred on x_0=15 and with a scale parameter of L=5. The size of the plasma was $10\lambda_{ei}$ high by $60\lambda_{ei}$ deep (where λ_{ei} is the mean-free-path for scattering of an electron moving at the (initial) thermal speed $v_t = \sqrt{(2k_bT_e/m_e)}$ by collisions with ions). A time step of τ_{ei} /2 was used. The ratio of λ_{ei} to the collisionless skin depth was taken to be 32 which corresponds to a plasma with T_e= 6keV and $n_e=3\times10^{23}$cm^{-3} in which case λ_{ei}=0.3μm and τ_{ei}=7fs. It could equally well correspond to T_e = 1.5keV and $n_e=10^{21}$cm^{-3} whence λ_{ei}=5μm and τ_{ei}=70fs.

IMPACT solves the Vlasov-Fokker-Planck equation together with Maxwell's equations in two spatial dimensions. It is the first VFP code to self-consistently include magnetic field in 2D. IMPACT uses a reduced description of the electron velocity distribution

$$f(\underline{v},\underline{r},t) \approx f_0(v,\underline{r},t) + \underline{f}_1(v,\underline{r},t)\cdot\hat{\underline{v}}$$

which is appropriate when collisions are important. This is effectively the leading two terms in a spherical harmonic expansion of *f* in velocity space angles. Doing this splits the full VFP equation into coupled equations for f_0 and $\underline{f}_1$,

$$\frac{\partial f_0}{\partial t} + \frac{v}{3}\nabla\cdot\underline{f}_1 - \frac{e}{3v^2m_e}\frac{\partial}{\partial v}\left(v^2\underline{E}\cdot\underline{f}_1\right) = \frac{\nu'_{ee}}{v^2}\frac{\partial}{\partial v}\left[Cf_0 + D\frac{\partial f_0}{\partial v}\right]$$

$$\frac{\partial \underline{f}_1}{\partial t} + v\nabla f_0 - \frac{e\underline{E}}{m_e}\frac{\partial f_0}{\partial v} - \frac{e\underline{B}}{m_e}\times\underline{f}_1 = -\frac{\nu'_{ei}Z^2n_i}{v^3}\underline{f}_1 + \left(\frac{\delta \underline{f}_1}{\delta t}\right)_{ee}$$

where C and D are the Rosenbluth coefficients. Note that f_0 the isotropic part of the distribution 'contains' the electron density and temperature while $\underline{f}_1$ describes heat flow and electrical current. These macroscopic quantities are obtained via moments/velocity-integrals over the distribution functions; e.g., $n_e=4\pi\int f_0v^2dv$ and $\underline{j} = -e(4\pi/3)\int\underline{f}_1v^3dv$. Ohm's law:-

$$en_e\underline{E} = -\nabla P_e + \underline{j}\times\underline{B} + en_e\underline{\underline{\alpha}}\cdot\underline{j} - n_e\underline{\underline{\beta}}\cdot\nabla T_e - \nabla\cdot\underline{\underline{\Pi}}_e$$

is obtained from the equation for $\underline{f}_1$ by setting f_0 to a Maxwellian f_M (i.e. the local approximation) and then taking a moment of the resulting equation. The term involving the stress tensor Π_e appears if $\underline{\underline{f}}_2$ is retained in the expansion of the electron distribution function. The form above neglects electron inertia and is valid in a frame where there is no bulk ion motion. Non-local effects distort f_0 away from Maxwellian which changes the values of the transport coefficients/tensors α (resistivity) and β (thermoelectric), as well as the value of κ (thermal conductivity).

Figure 2 shows the magnetic field at 1 and 200 collision times into the simulation. At $t=1\tau_{ei}$ B_z, the B-field component calculated by IMPACT, is relatively small and the plasma is not yet magnetized because the Hall parameter $\omega\tau \propto BT_e^{3/2} / Z^2n_i$ is much less than unity. It peaks where the Z and T_e gradients are greatest and where there is maximum shear in the Z profile. However by $t=200\tau_{ei}$ the plasma has become magnetized in places ($\omega\tau>1$), has convected to the right with the heat flow (i.e. the Nernst effect), and has assumed a complex profile. The appearance of any magnetic field is surprising since the usual

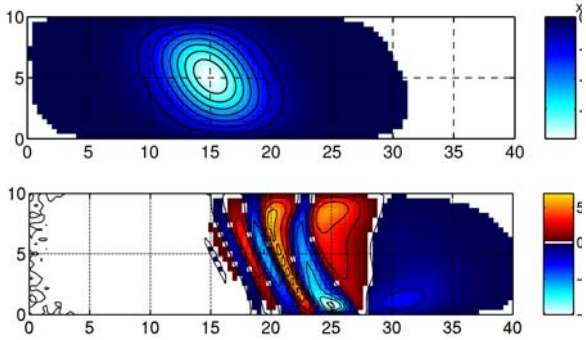

Figure 2. Non-local magnetic field profiles after 1 and 200 collision times (upper and lower plots, respectively). The colour scale shows the intensity of B_z in 'units' of the Hall parameter $\omega\tau$. Lengths are in mean-free-path units.

(i.e. local) theory would predict no magnetic field generation for the configuration used because neither anisotropic pressure nor electron-electron collisions in the equation for $\underline{f}_1$ are present in the simulation. Anisotropic pressure could, in principle, result in some B-field production while it has been noted that in the local approximation, non-uniform Z can cause B-field generation but only if e-e collisions are included in the $\underline{f}_1$ equation. But since neither of these effects are included in the simulations, then clearly the fields in Figure 2 cannot be explained by the local theory. Instead they are generated by a new mechanism which is a non-local effect. Importantly the strong B-field occurring towards the end of the simulation affects thermal transport from the heated region into the bulk plasma as shown by the temperature profile in Figure 3. This in turn occurs because the heat flow is severely deflected by the magnetic field (see Figure 3, lower part). Details of non-local B-fields for a different case (non-uniform heating and $\nabla Z=0$) were published recently [5].

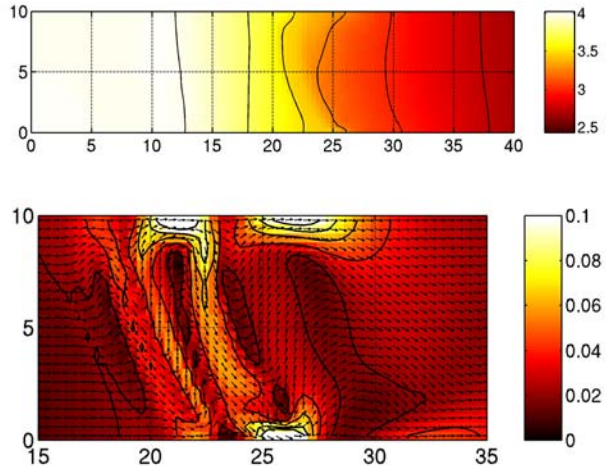

Figure 3. Fractional electron temperature increase (upper figure) and heat flow (lower figure) 200 τ_{ei} into the simulation. Heat flow has been normalized to the free streaming value.

Explanation of the non-local mechanism

The non-local origin of the fields presented in Figure 2 can be understood by obtaining a more general version of Ohm's law that does away with the local approximation. Under the assumptions/simplifications used in the simulations (i.e. to neglect f_2 and e-e collisions in the $\underline{f}_1$ equation) Ohm's law becomes $e\underline{E}/m_e = -\nabla(n_e\langle v^5\rangle)/(n_e\langle v^3\rangle)$ when the current and magnetic field are negligible (as occurs at the beginning of the simulation). This is valid for arbitrary f_0 and the moments are defined as $n_e\langle v^m\rangle = 4\pi\int f_0 v^{2+m} dv$. The curl of the electric field therefore involves the cross product $\nabla(n_e\langle v^3\rangle)\times\nabla(n_e\langle v^5\rangle)$. When $f_0 \rightarrow f_M$ the moments become $\langle v^m\rangle \propto T_e^{m/2}$ and $\nabla\times\underline{E}$ yields the familiar result: $\nabla n \times \nabla T$. But if f_0 is not Maxwellian a B-field can be generated even when $\nabla n=0$ if the gradients in the $\langle v^3\rangle$ and $\langle v^5\rangle$ moments are not parallel. Non-local transport can do this. Appearance of an angle between $\nabla\langle v^3\rangle$ and $\nabla\langle v^5\rangle$ can be understood by considering diffusion of different velocity groups of electrons and how this distorts f_0 away from Maxwellian. Because $\lambda_{mfp} \propto v^4/Z$ (at constant n_e) and therefore the spatial diffusion coefficient $D \propto v^5/Z$, energetic/hot electrons (in the tail of the distribution) can move through the plasma more readily than cold ones. Also electrons diffuse more readily through low Z plasma. When the temperature and Z scale lengths become comparable to 10 —100 λ_{mfp} the hot and cold portions of f_0 can form different spatial profiles because e-e collisions are not rapid enough to Maxwellianize f_0 (which would then make the profiles of hot and cold electrons the same). Because $\langle v^5\rangle$ is biased more towards the hot electron profile and $\langle v^3\rangle$ more the profile of colds, non-parallel $\nabla\langle v^3\rangle$ and $\nabla\langle v^5\rangle$ can then occur. Having ∇Z and ∇T non-parallel or $\nabla Z=0$ but T non-symmetrical, can cause this to happen. Figure 4 shows the angle between $\nabla\langle v^3\rangle$ and $\nabla\langle v^5\rangle$ at 1 and 100τ_{ei} into the simulation, while Figure 5 shows that the non-local distortion of f_0 at x=30, y=5 becomes large by t= 100τ_{ei}.

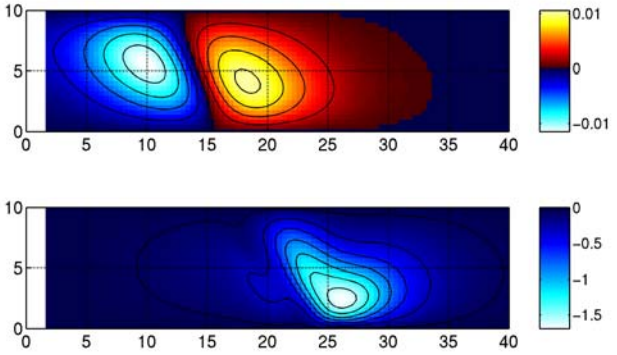

Figure 4. Angle (in degrees) between $\nabla\langle v^3\rangle$ and $\nabla\langle v^5\rangle$ at 1 (upper) and 100τ_{ei} (lower) into the Fokker-Planck simulation.

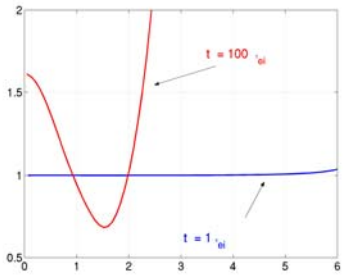

Figure 5. f_0/f_M versus v/v_{th} at x=30, y=5 at t=τ_{ei} (blue) and t=100τ_{ei} (red).

Analytical prediction of non-local B-field

We have developed an analytical expression for the non-local magnetic field that is generated at early times by prescribed, initial, electron temperature, density and ionization-state profiles. The formula assumes that f_0 starts out as Maxwellian (with the relevant local density and temperature) at t=0 and essentially predicts the ensuing perturbation to f_0 brought about by non-local transport of electrons. It is derived from the VFP equations for f_0 and $\underline{f}_1$ neglecting time dependent ionization, hydrodynamic effects, electron inertia and e-e collisions in the limit when B and j are negligibly small. Its range of validity extends over the first few collision times only, primarily because of the neglect of e-e collisions and because it does not accurately follow relaxation of the temperature profile.

Nevertheless it gives a good indication of which configurations can generate B-field by non-local effects and elucidates how the growth of these fields scales with temperature, density and Z scale-lengths. A detailed derivation will be given elsewhere. Here, it suffices to say that it is obtained by taking moments of the f_0 and $\underline{f}1$ equations and using the zero current condition. When only temperature gradients are present, we find that the magnetic field grows according to :-

$$\frac{e\dot{\underline{B}}}{m_e} = -\left(\frac{\lambda^4}{\tau^3}\right)\frac{\nabla T}{T}\times\left[154\frac{\nabla(\nabla^2 T)}{T} + 620\frac{\nabla(|\nabla T|^2)}{T^2}\right]$$

where $\lambda=(4\pi\varepsilon_0 m_e/e^2)^2 v_t^4/(4\pi Z^2 n_i \ln\Lambda)$ is the mean-free-path for scattering of a thermal electron with $v_t=\sqrt{(2k_B T_e/m_e)}$ by ions and $\tau=\lambda/v_t$ the corresponding collision time. The second term is a nonlinear correction that essentially accounts for the temperature dependence of the transport coefficients. This equation shows that a non-symmetrical temperature profile is required to generate B when the density and Z are uniform. For instance a planar or circularly symmetric profile cannot produce non-local B-field whereas, e.g. an elliptically symmetric could. Including the effect of non-uniform Z we find *extra* non-local source terms:-

$$\frac{e\dot{\underline{B}}}{m_e} = -\left(\frac{\lambda^4}{\tau^3}\right)\frac{\nabla Z}{Z}\times\frac{\nabla T}{T}\left[154\frac{\nabla^2 T}{T} + 620\frac{|\nabla T|^2}{T^2} - 310\frac{\nabla Z\cdot\nabla T)}{ZT}\right] + 154\left(\frac{\lambda^4}{\tau^3}\right)\frac{\nabla T}{T}\times\frac{\nabla(\nabla Z\cdot\nabla T)}{ZT}$$

(Note that the numerical constants appearing in this and the previous equations are given to 3s.f.) The first term is the most significant one (under most conditions) and confirms that a non-local magnetic field can indeed be produced under the conditions used to obtain Figure 2 with IMPACT. Early on in the simulation, a planar temperature profile (invariant in y) appears due to the heating and this in turn powers a $\nabla Z \times \nabla T$ source. Finally, introducing a density gradient introduces terms like $(\nabla n\times\nabla T)\nabla^2 T$, $(\nabla n\times\nabla Z)\nabla^2 T$, and $\nabla n\times\nabla(\nabla^2 T)$, amongst others. In total, there are 20 terms. It is possible to derive an expression for $\partial^2 B/\partial t^2$ in the local approximation by taking the time derivative of $\partial B/\partial t = -(k_b/en_e)\nabla n_e\times\nabla T_e$, assuming n_e is constant, and then using the temperature/energy equation $(3/2)n_e\partial T_e/\partial t=\nabla\cdot(\kappa\nabla T_e)$ for the case of no Ohmic heating where $\kappa=\kappa_0 T^{5/2}/Z$ (and κ_0 is a constant). This equation for $\partial^2 B/\partial t^2$ describes the instantaneous change in the B-field growth rate due to decay of the temperature profile by thermal conduction and has nine terms including $(\nabla n\times\nabla T)\nabla^2 T$, $(\nabla n\times\nabla Z)\nabla^2 T$, and $\nabla n\times\nabla(\nabla^2 T)$. However, all of these nine terms involve $\nabla n\times$ and there are no terms in $\nabla T\times$ and $\nabla Z\times$. Also, the numerical coefficients are 4—15 times larger in the non-local case.

Figure 6 compares the B-field predicted by the analytical expression (upper figure) with the equivalent result from IMPACT (lower figure) after $1/5^{th}$ of a collision time for initial temperature and Z perturbations of $\delta T=(To/10)\cos(2\pi x/100)$ and $\delta Z=(Z_o/10)\cos(2\pi y/100)$. They are both in very good qualitative agreement. We expect that a more accurate simulation, achieved using finer meshes, should see better quantitative agreement too.

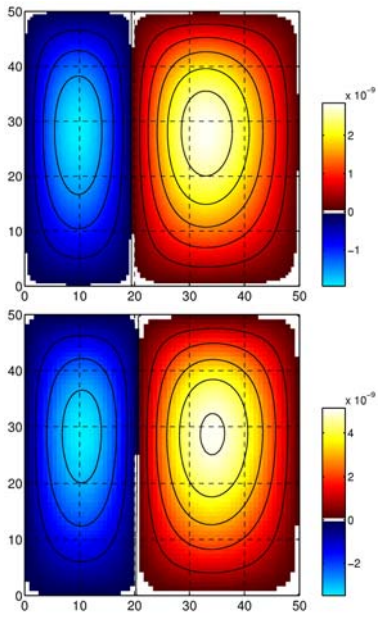

Figure 6. Comparison of analytic (upper) and VFP-simulation (lower) predictions of non-local B-field for crossed T and Z perturbations, after $1/5^{th}$ of a collision time.

Conclusions

We have demonstrated via Vlasov-Fokker-Planck simulations and via analytical treatment of the VFP equation that non-local effects can generate magnetic-fields under conditions where local theories would predict no field generation is possible in a collisional laser-plasma: no density gradients and no anisotropic electron pressure. According to local theory, the field growth shown here due to crossed gradients in Z and electron temperature should not be possible in the Lorentz approximation (no e-e collisions in the electron momentum equation) which was actually used. Several non-local source terms for B-field generation have been identified and are non-local analogues of the well known $\nabla n \times \nabla T$ mechanism. These are missed by local theories which 'clamp' f_0, the isotropic component of the electron distribution, to Maxwellian. When $L>>\lambda$ does not hold (where L is the density, Z, or T scale-length and λ the collisional mean-free-path) non-local transport can significantly distort f_0 away from Maxwellian and thereby generate B-fields strong enough to affect thermal transport.

References

1. J. A. Stamper *et al.*
Phys. Rev. Lett. 26, 1012 (1971)

2. M. G. Haines
Can. J. Phys. 64, 912 (1986)

3. M. Borghesi *et al.*
Phys. Rev. Lett. 81, 112 (1998)

4. S. H. Glenzer *et al.*
Phys. Plasmas 6, 2117 (1999)

5. R. J. Kingham and A. R. Bell
Phys. Rev. Lett. 88, 045004 (2002)

6. R. J. Kingham and A. R. Bell,
"An implicit Vlasov-Fokker-Planck code to model non-local electron transport in 2-D with magnetic fields",
Accepted by J. Comput. Phys.

Atoms, molecules and clusters in intense laser fields

D Dundas

Department of Applied Mathematics and Theoretical Physics, Queen's University Belfast, University Road, Belfast, BT7 1NN, UK

Main contact email address: *d.dundas@qub.ac.uk*

Introduction

The interaction of atoms, molecules and clusters with intense, ultra-short laser pulses is of fundamental importance in physics[1]. Not only does the study of these systems allow for the mechanisms underpinning basic physical processes to be understood, but the processes observed when the interaction occurs can also be exploited in a number of applications. In dealing with these systems three regimes of matter can be defined.

At one extreme, few-electron atoms and diatomic molecules act as the prototype for other more complex atoms and molecules. In particular helium represents the fundamental multi-electron atom while H_2 represents the fundamental multi-electron molecule. Understanding electron correlation effects in these two systems, together with the coupling between the electronic and ionic degrees of freedom in H_2 is crucial in the development of many-body theories of more complex systems. Much work has already been carried out on the laser-driven treatment of these systems [2,3].

At the other extreme are clusters, an intermediate form of matter between gases and solids. The laser heating of clusters gives rise to fascinating phenomena not occurring in atomic and molecular gases exposed to the same pulses. For instance, pulsed, coherent x-ray radiation with conversion efficiencies several orders of magnitude greater than those found in gases has been observed[4]. Highly charged atomic ions[5] and electrons emitted with extremely large energies[6] have also been observed. In contrast to these experimental findings, the theory — and therefore the physical understanding — of these processes is still modest and many unresolved questions exist about the exact mechanisms underlying the observations. The challenge comes about through the diversity of time-scales that occur in the problem. These time-scales range from a plasmon cycle (~1.5 femtoseconds) for direct electron emission through 10s of fs for excitation processes to 100s of fs characterizing the ionic motion. All these processes need to be described within a consistent dynamical picture.

Bridging these two extremes are polyatomic molecules, which are of fundamental importance in chemistry. The availability of ultra-short (femtosecond) laser pulses allows for the possibility of analyzing ultra-fast chemical reactions and in devising schemes for coherently controlling these reactions through the use of tailored light sources.

The goal of this work is the development of a theoretical approach that will be able to describe all of the systems discussed above with particular emphasis placed on the treatment of laser-heated clusters. In the next section we describe our approach, namely a non-adiabatic quantum molecular dynamics approach. Illustrative results are then presented.

Method of Solution

In clusters one encounters a real, many-body situation that places a full-dimensional quantum description beyond the scope of computer technologies and methodologies for the foreseeable future. A non-adiabatic quantum molecular dynamics (NA-QMD) approach is therefore being developed in order to study both the electron and nuclear dynamics. This approach consists of a time-dependent density functional theory (TDDFT) treatment of the electronic dynamics and a classical treatment of the nuclear dynamics. This TDDFT treatment is also applicable to the treatment of atoms while the NA-QMD approach is applicable to the treatment of molecules.

The TDDFT method provides the most detailed, practical and feasible ab initio approach for tackling many-body problems. Density functional theory (DFT), as first introduced by Hohenberg and Kohn[7] and Kohn and Sham[8] describes a system of interacting particles in terms of its density. The theory is based on the existence of an exact mapping between densities and external potentials and leads to the density of the interacting system being obtained from the density of an auxiliary system of non-interacting particles moving in an effective local single particle potential, i.e. the particle interactions are treated in an averaged-over manner. Runge and Gross[9] provided a time-dependent formalism of DFT (TDDFT) by showing that the time-dependent density could be obtained from the response of non-interacting particles to a time-dependent local effective potential. In principle the averaged-over many-body effects can be included exactly through the exchange-correlation term in the local effective potential, but in practice these effects have to be approximated.

Our numerical implementation of TDDFT uses a cylindrical grid treatment of the electronic Kohn-Sham orbitals similar to that used previously in a full dimensional treatment of laser-driven H_2^+ [11], namely a finite difference treatment of the z-coordinate, a Lagrange mesh treatment of the ρ-coordinate based upon Laguerre polynomials and a Lagrange mesh treatment of the azimuthal angle, ϕ, based upon Chebyshev polynomials. Time propagation is performed using a high-order unitary, explicit Arnoldi propagator [2]. The resulting code is parallelized to run on massively parallel processors meaning that grid sizes can readily be altered to handle large spatial extents and/or a large number of orbitals coming into play in a calculation.

In the case of molecules and clusters the nuclear motion is treated classically through the time-integration of Newton's equations of motion. In general a calculation proceeds as follows. Firstly, some arbitrary configuration of positions and velocities of the ions is chosen. This allows us to obtain the local effective potential for the TDDFT calculation and thus calculate the electronic density self-consistently. The electronic density is input into Newton's equations to obtain a new configuration of ion positions and velocities that are fed back into the TDDFT equations. Calculation of the initial state involves replacing the Kohn-Sham wave equations with a set of diffusion equations so that the density relaxes to the ground state. In the same way Newton's equations are solved with the addition of a damping force so that the ionic configuration relaxes to its ground state configuration.

Results

The results presented in this section serve to illustrate the accuracy of both parts of the NA-QMD approach, namely the quantum description of the electronic structure and the classical description of the nuclear motion. We begin by calculating the electronic ground state energies of the first ten atoms in the periodic table using the exchange-only local density approximation (xLDA) to the exchange-correlation functional. These results, which are compared with previously published results that use a different numerical method[12], are presented in Table 1. In our calculation a finite difference mesh having a spacing of 0.02 a.u. and a Lagrange-Laguerre mesh having 50 mesh points was used. These mesh parameters were chosen to

obtain fully converged results for the neon atom. The same mesh was then used to calculate the energies for all lighter atoms. In this way the accuracy of the mesh could be tested over a range of atoms since we can use coarser meshes for lighter atoms. For example, the mesh required for giving fully converged energies of the hydrogen atom requires mesh spacings ten times larger than the mesh spacings required for the neon atom. We find good agreement between the two sets of results. Slight differences are mainly due to inaccuracies in our calculation of the Hartree potential in the local effective potential. In our case this was calculated from the integral expression of the Hartree potential. This inaccuracy, arising from the azimuthal integration, can be overcome by calculating the Hartree potential through the solution of a Poisson equation. Such an approach is currently being implemented.

Species	Ground State Energy (a.u.)	
	Present	Previous
H	-0.4567	-0.4571
He	-2.7267	-2.7236
Li	-7.1771	-7.1934
Be	-14.2074	-14.2233
B	-24.0436	-24.0636
C	-37.0023	-37.1119
N	-53.5558	-53.7093
O	-73.9070	-73.9919
F	-98.4712	-98.4740
Ne	-127.4883	-127.4907

Table 1. Electronic ground state energies for the first ten atoms in the periodic table. Present results are compared with previous results of Grabo et al[12].

In Figures 1 and 2 we present results from the classical treatment of the nuclear dynamics in diatomic molecules. In both figures we calculate the ground state energies and internuclear separations obtained by replacing the Kohn-Sham equations with diffusion-like equations and incorporating a damping force into Newton's equations of motion. In general we find that only certain discrete energies and internuclear separations are obtained. Figure 1 presents results for H_2^+. In this case we are dealing with a one electron molecular ion and so the TDDFT description of the electronic dynamics is replaced with the solution of the Schrödinger equation. We see that the energies and internuclear separations correspond roughly to the outer turning points of vibrational states of the molecular ion. While it is possible to also obtain separations corresponding to the inner turning points, this is less probable since the force gradient is much larger at the inner turning points. In Figure 2 we present the results for H_2. In this case the exchange-correlation potential is approximated using xLDA. In this case it can be seen how the xLDA gives a poor representation of the ground state potential energy surface. As in Figure 1 we find that using the NA-QMD approach only discrete energies and internuclear separations are obtained which again seem to correspond to the turning points of the vibrational levels of this potential.

Conclusions

We have presented details of an NA-QMD method that allows the dynamics of atoms and molecules to be treated. At present the method is only applicable to atoms and diatomic molecules. Extensions to the method which will allow general polyatomic molecules and clusters to be considered are already in progress. This involves extending the Kohn-Sham orbitals to a full 3-dimensional description and performing a pseudopotential description of the electron-ion potentials.

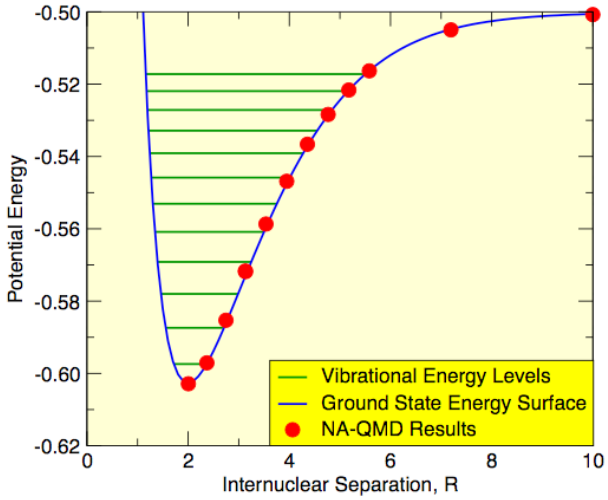

Figure 1. Initial state energies and internuclear separations obtained from the NA-QMD approach for H_2^+ compared with the vibrational energy levels of the ground state potential energy curve.

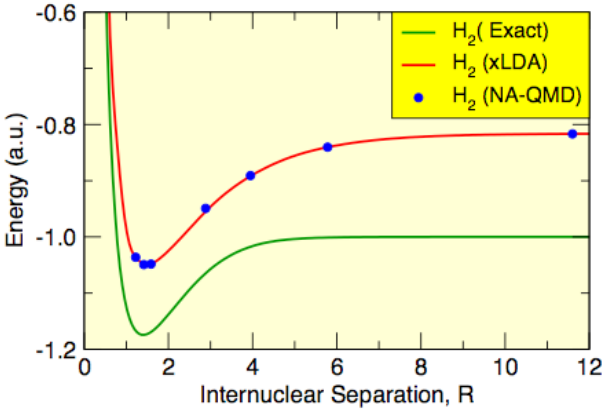

Figure 2. Initial state energies and internuclear separations obtained from the NA-QMD approach for the ground state potential energy curve of H_2. The exact H_2 potential energy surface is shown for comparison.

References

1. Molecules and Clusters in Intense Laser Fields, Ed. Posthumus J H, (Cambridge University Press) 2001.
2. Smyth E S, Parker J S and Taylor K T, Comp. Phys. Comm. 114, 1, 1998.
3. Dundas D, Meharg K J, McCann J F and Taylor K T, Euro. Phys. J. D, 2003. In press.
4. Donnelly T *et al* (1996), Phys. Rev. Lett. 76, 2472, 1996.
5. McPherson A *et al*, Nature 370, 631, 1994.
6. Ditmire T *et al*, Nature 386, 54, 1997.
7. Hohenberg P and Kohn W, Phys. Rev. 136, B864, 1964.
8. Kohn W and Sham L J, Phys. Rev. 140 , A1133, 1965.
9. Runge E and Gross J F, Phys. Rev. Lett. 52 , 997, 1984.
10. Dundas D, Phys. Rev. A 65 , 023408, 2002.
11. Grabo T, Kreibich T, Kurth S and Gross E K U, in Strong Coulomb Correlations in Electronic Structure Calculations: Beyond the Local Density Approximation, ed. Anisimov V I, (Gordon and Breach), 2000.

High magnetic field generation with a Helmholtz coil

C Courtois, A D Ash, D Chamber, R A D Grundy, N C Woolsey

Department of Physics, University of York, Heslington, York, YO10 5DD, UK

M M Notley, N Prior, M Tolley

Central Laser Facility, CCLRC Rutherford Appleton Laboratory, Chilton, Didcot, Oxon, OX11 QX, UK

Main contact email address: *cc20@york.ac.uk*

Introduction

In a recent experiment in Target Area East of the Vulcan facility, the use of high-energy, high-power lasers to address questions associated with collisionless shocks formation in magnetised plasmas was studied[1]. In this experiment, a 1 mm diameter exploding plasma is immersed in a magnetic field. This magnetic field is produced with a mm-scale Helmholtz coil driven by an intense laser to produce a large (tens of Tesla), homogeneous and mainly longitudinal magnetic field in the plasma area. In this paper, a simple model of the coil is used to study the properties of the magnetic field.

Description of the Helmholtz coil

The Helmholtz coil, based on Daido et al. one turn coil [2], is illustrated in Figure 1, with a) a side view, and b) a front view.

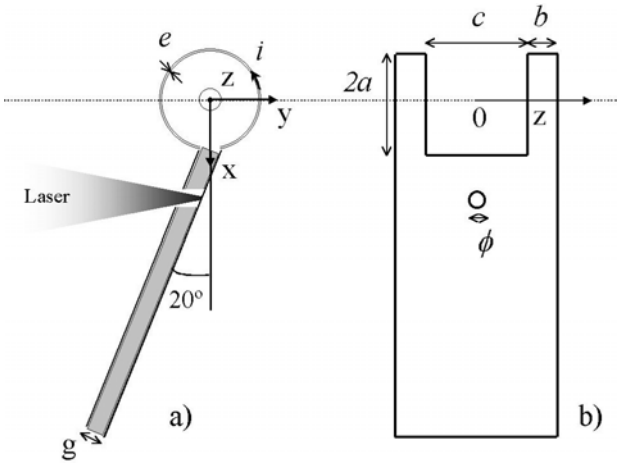

Figure 1. a) side view and b) front view of the Helmholtz coil and definition of the geometric parameters.

The Helmholtz coil is constructed from a photo-etched single copper sheet that is bent to form two parallel plates connected by 2 concentric loops. The thickness of the copper, *e*, is 50 μm, the diameter and the width of the loops, *2a* and *b*, are respectively 2.5 mm and 0.75 mm, the distance between the loops, *c*, is 2.5 mm, the gap between the two parallel plates, *g*, can be varied between 250 and 750 μm. A plastic insulator placed between the two parallel plates sets the plate spacing. The magnetic field is generated by the circulation of an intense reverse current *i* in the loops by the large potential difference between the front and the rear plates (left and right hand plates in Figure 1a). A laser, focused to $I\lambda^2 \sim 10^{16}$ W.cm^{-2}.μm^2 on the back plate, passes through a 500 μm diameter hole in the front plate and 1.2 mm diameter hole in the plastic insulator to produce on the rear plate, by resonant absorption, a hot electron population. The hot electrons preferentially move down the plasma density gradient, and charge the front plate to create the potential difference. The angle between the plate normal and the laser axis is fixed to 20° to maximize resonant absorption.

Assumptions used in the model

In the model the current in the loops creates the magnetic field, and the 2 loops are treated independently. The current is treated in the low frequency approximation with a uniform current density throughout a cross section of the loops. These assumptions will be discussed later. The equations describing the spatial distribution of the magnetic field are based on the Biot-Savart law, the calculated field components are resolved into 3 orthogonal components; $B_x(x,y,z)$, $B_y(x,y,z)$, and $B_z(x,y,z)$ following the convention shown in Figure 1.

The temporal evolution of the magnetic field is proportional to the current *i(t)*, and is obtained by solving the following equation :-

$$L\frac{\partial i(t)}{\partial t} + Ri(t) = V_o f(t) \qquad (1)$$

where *L* and *R* are respectively the self-inductance and the resistance of one loop, V_o is the maximum electric potential between the plates and $f(t)$ is the normalised temporal envelope of the potential difference which is assumed to be identical to the laser pulse. Here the laser pulse is assumed Gaussian with a full width at half maximum of τ_{fwhm}.

Results

Figure 2 represents the amplitude of the components B_z (top curves) and B_x (bottom curves) of the magnetic field along z axis for y = 0 and three positions along the x axis, x = -0.5 mm, x = 0 mm (dotted lines) and x = 0.5 mm. This corresponds to the vertical diameter across the loops and the initial extension of the 1 mm plasma. The grey area represents the region occupied by the plasma of interest. For this calculation, the peak current per loop is *i* = 50 kA [2].

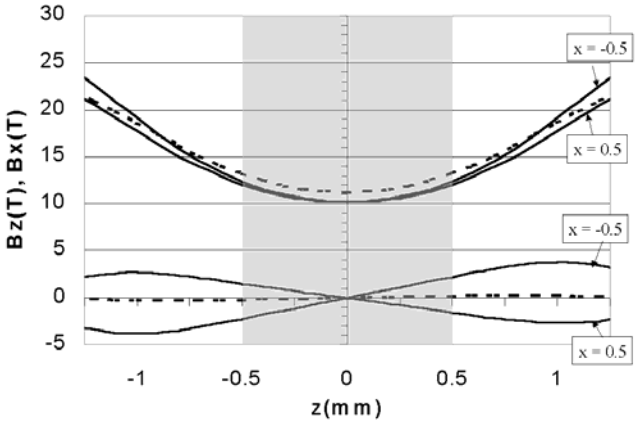

Figure 2. Amplitude of the components B_z (top curves) and B_x (low curves) of the magnetic field along z-axis at three positions on the vertical diameter, x = -0.5 mm, x = 0 mm, x = 0.5 mm. The grey area represents the area occupied by the plasma of interest.

Figure 2 clearly indicates the magnetic field in the central 1 mm region (i.e. -0.5 mm < z < 0.5 mm) is;

- around 10 T, this is consistent with the field measured in Reference 1;
- sufficiently homogeneous for experiments described in Reference 1, and that the maximal amplitude variation is 30 % of the field amplitude at the loop centre;
- dominated by the longitudinal magnetic field, i.e. $|B_z|$ is at least 5 times the transverse component $|B_x|$.

The gap at the lower portion of the loops, where the parallel plates join the two loops, introduces an asymmetry in the magnetic field structure; this asymmetry is small and not significant; it reduces the field amplitude by a few percent.

The Helmholtz coil is modelled using a low frequency approximation with a constant current density through the loop cross-section. The problem can be treated in the high frequency regime with a current pulse travelling in the loop within a skin depth of the conductor surface. Results show this effect to be negligible reducing the magnetic field amplitude by a few %.

The Helmholtz coil self-inductance is obtained via the calculation of the magnetic field flux through one loop, and is $L = 3.5\ 10^{-9}$ H. This exceeds the estimated mutual inductance of $1\ 10^{-10}$ H, and justifies the assumption that the 2 loops are independent.

As the plasma generated at the back plate reaches the front plate a short circuit occurs and the circulating current i decays with a characteristic time $t = L/R$. An estimated resistance of a single loop is $R = 0.14\ \Omega$ [3] giving a characteristic time equal to 25 ns, which is consistent with the results in Reference 1.

In Figure 3 the behaviour of different loop diameters for fixed loop width (b = 0.75 mm) and separation (c = 2.5 mm) is illustrated. Here the amplitude of B_z at the centre of the Helmholtz coil is plotted as a function of the loop radius a. Note the current i varies with radius a, the calculations are scaled from i = 50 kA for a = 1.25 mm and τ_{fwhm} = 350 ps, and there are also resistive and impedance dependences, i.e. $R(a)$ and $L(a)$ c.f. Equation (1).

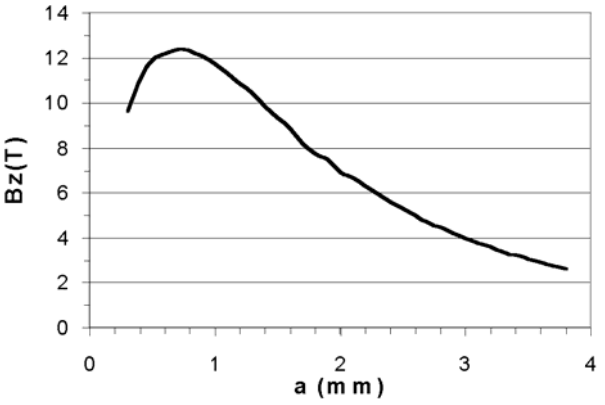

Figure 3. Variation of the amplitude of B_z at the Helmholtz coil centre with radius a. Current i varies with radius a ($i(a)$ is scaled to i = 50 kA for a = 1.25 mm), b = 0.75 mm, c = 2.5 mm and τ_{fwhm} = 350 ps.

As $i(a)$ decrease with a, Figure 3 shows that B_z is maximum at a = 0.7 mm. For a given constant current i, the magnetic field amplitude depends geometrically on the loop radius a and is maximum for a = 2.3 mm.

Magnetic field measurement

In their article [2], Daido et al. estimates the magnetic field time evolution and amplitude at the centre of a one turn coil, $B_z(t)$, by measuring the temporal variation of the magnetic field flux through a search coil placed at a distance r and at an angle θ to the z axis. $B_z(t)$ is related to the voltage v(t) recorded at the search coil by :-

$$B_z(t) = r^3 \int \frac{v(t)dt}{\pi a^3 b^2 (\cos^2\theta - 0.5\sin^2\theta)} \qquad (2)$$

where b is the radius of the circular search coil. This equation can be used to estimate the magnetic field amplitude at the centre of the Helmholtz coil on incorporating three minor modifications. First, Equation (1) assumes a dipole field - errors below 10% are expected when the ratio $r/a > 10$. For example, the search coils must be placed at least 15 mm from the centre of the Helmholtz coil if the loop radius is 1.25 mm. Second, Equation (1) must be multiplied by a factor 0.5 to account for the current separation between the two loops. Third, the factor $k(a,b,c,e)$ accounts for the different geometry between the one turn coil and the Helmholtz coil. Here, for the Helmholtz coil geometry of Reference 1, k = 0.48.

Measurement of the magnetic field spatial distribution $B_z(x,y,z)$ around a position z_o is possible by determining the Faraday rotation $\alpha(x,y,z_o)$, of a probe laser beam as it propagates through a piece of glass l thick. If $V(\lambda_o)$ is the Verdet number and λ_o the laser wavelength then[4] :-

$$\alpha(x, y, z_0) = V.B_z(x, y, z_0).l \qquad (3)$$

A prediction of the polarisation rotation in a Helmholtz coil with central B_z = 10 T is shown in Figure 4. Rotation at positions along the vertical and horizontal diagonals is shown by the solid line and squares respectively.

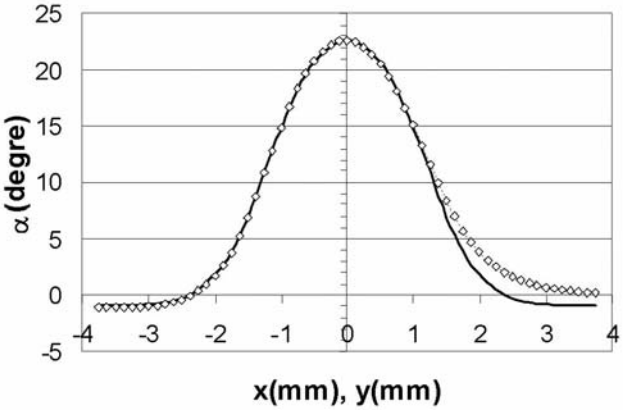

Figure 4. Predicted polarisation rotation with a 1 mm thick SF57 piece of glass (V = 1900 °.T^{-1}.m^{-1} at λ_o = 526 nm) centred in a = 1.25 mm Helmholtz coil (B_z = 10 T) along a the vertical diameter (square line) and horizontal diameter (solid line).

These calculations assume a 1 mm thick piece of SF57glass [4] probed with the second harmonic of Vulcan; at λ_o = 526 nm SF57 has a Verdet number of V = 1900 °.T^{-1}.m^{-1}. These calculations indicate readily measurable rotations of ~ 20° at the centre of the Helmholtz coil. Differences in the two curves are due to the gap where the parallel plates join the loops (see Figure 1).

Conclusions

This simple model indicates mm-scale laser driven Helmholtz coils can produce intense (10 T), homogeneous and longitudinal magnetic fields over a 1 mm^3 volume. These numerical results will be compared with future experimental results.

References

1. N. C. Woolsey, *et al*
Phy. Plasmas, 8 2439 (2001)

2. H. Daido, *et al*
Phy. Rev. Lett. 56, 846 (1986)

3. F. W. Grover
Inductance calculations: working formulas and tables
Dover, NY (1946)

4. Technical Information
Optical Glass Schott Glaswerke, 17, (1985)

Relativistic filamentation of ultra-intense laser light in plasma

L J Hill, H C Barr

Department of Physics, University of York, Heslington, York, YO10 5DD, UK

Main contact email address: *ljh12@york.ac.uk*

Introduction

The self-focusing and filamentation of laser light can be due to a variety of mechanisms: Joule heating in collisional plasma, the ponderomotive expulsion of electrons and ions in collisionless plasma, induced ionization, or relativistic corrections. The latter predominate for short ultra-intense pulses where the plasma is collisionless and the ions effectively immobile. This is the Relativistic Filamentation Instability (RFI), which has been analysed in detail in weakly relativistic cases[1]. Transverse perturbations in the relativistic mass modify the refractive index creating regions into which the light refracts. The increase in laser intensity in these regions further modifies the refractive index closing the feedback loop and making parametric instability possible. Also, electrons (but not ions on these timescales) are ponderomotively driven from regions of high intensity. RFI is therefore an amalgam of zero frequency fluctuations in relativistic mass and electron density perpendicular to the laser propagation direction**.**

In this report we extend the theory to the deeply relativistic limit in which the electrons in the field of ultra-intense laser light attain velocities close to the speed of light. Circularly polarized light is assumed so that plasma electrons move in circular orbits with constant relativistic mass increase. A general dispersion relation[2] which describes all parametric instabilities (including stimulated Raman scattering and stimulated harmonic generation among others) and based on a cold relativistic electron plasma description is applied to the case of RFI. This is in the form of a 4th order difference equation[3]. In the case of rarefied plasma an explicit solution can be found.

The general dispersion relation

We reprise the main forms from which the RFI results are extracted. The general form is the difference equation for Φ, the fluctuation in the ratio of number density to mass increase:

$$\sum_{n=-2}^{n=2} \alpha_n(\omega, \mathbf{k})\,\Phi(\omega + n, \mathbf{k} + n\mathbf{k}_0) = 0$$

where $\omega_n = \omega + n$, $k_n = k + nk_0$ and $s = k_\perp v_0$,

$$\alpha_0(\omega,\mathbf{k}) = \frac{\Delta(\omega,\mathbf{k})}{D(\omega,\mathbf{k})} + \left(\frac{v_0^2\omega_{pr}^2}{2} + \frac{s^2}{4}\right)\left(\frac{1}{D(\omega_{+1},\mathbf{k}_{+1})} + \frac{1}{D(\omega_{-1},\mathbf{k}_{-1})}\right)$$

$$\alpha_{\pm1}(\omega,\mathbf{k}) = -\frac{s}{2}\left(\frac{\omega}{D(\omega,\mathbf{k})} + \frac{\omega_{\pm1}}{D(\omega_{\pm1},\mathbf{k}_{\pm1})}\right)$$

$$\alpha_{\pm2}(\omega,\mathbf{k}) = \frac{s^2}{4D(\omega_{\pm1},\mathbf{k}_{\pm1})}$$

$D(\omega,\boldsymbol{k})$ and $\Delta(\omega,\boldsymbol{k})$ are the familiar dispersion relations for light waves and electron plasma waves. Here v_0 is the electron oscillation velocity, related to the laser strength parameter q (the normalized peak vector potential $e\mathbf{A}_0/m_0c^2$), by $v_0 = q/\gamma_q$ ($\gamma_q = (1+q^2)^{1/2}$ is the laser-induced relativistic electron mass increase). This also lowers the effective ('relativistic') plasma frequency such that $\omega_{pr}^2 = \omega_p^2/\gamma_q$. Times are normalized to the inverse of the laser driver frequency, ω_0^{-1}, velocities to c and lengths to c/ω_0. $k_\perp$ is the wavenumber perpendicular to the laser propagation direction and hence, in the context of this report, the filament wavenumber.

Low density approximation (LDA)

The difference equation can be solved in the limit where the relativistic plasma frequency is small in relation to the laser frequency, i.e. that the density is low in relation to the relativistic critical density to which the light can propagate due to the self-induced transparency allowed by the electron mass increase: $n/n_{cr} = \omega_{pr}^2 << 1$, namely that $n/n_c << \gamma_q$. Letting $\omega_l = \Omega + l$, $k_l = k + lk_0$ and $D_l = D(\omega_l,k_l)$ the dispersion relation becomes

$$1 + \frac{\omega_{pr}^2 D_0}{\Omega^2}\sum \frac{F_l}{D_l} = 0$$

where

$$F_l = \frac{v_0^2}{2}\left[J_{l+1}^2(s) + J_{l-1}^2(s)\right] - J_l^2(s)$$

The function F_l is identical to that met in the theory of synchrotron emission from a single relativistic electron in a circular orbit.

Weakly relativistic RFI at low density

For weakly relativistic intensities (such that $s << 1$) in low density plasma either of the above forms can be used to obtain analytic expressions for the growth rate. RFI is characterized by a four-wave interaction between a non-resonant, purely growing transverse fluctuation of density and mass increase, the laser driver and its Stokes and anti-Stokes sidebands. Assuming $D_{\pm1}$ are simultaneously resonant, $D_{\pm1} \approx 0$, while $D_{l\neq\pm1} >> 1$ we isolate the resonant denominators and neglect other terms in the summation. The maximum growth rate is:-

$$\Gamma^{\max} = \frac{\omega_{pr}^2 v_0^2}{4\sqrt{1 - v_0^2}}$$

at the filament wavenumber given by:-

$$k_\perp^2 = \frac{\omega_{pr}^2 v_0^2}{2\sqrt{1 - v_0^2}}$$

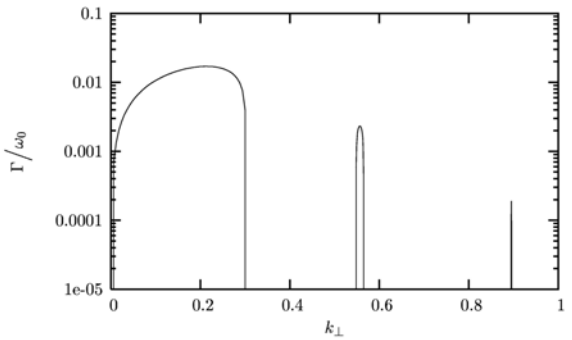

Figure 1. Numerically calculated growth rates of standard RFI along with theoretical values for three values of the laser intensity for low density plasma ($\omega_{pr}^2 = 0.1$).

Growth rates of the RFI, calculated numerically from the difference equation, are plotted for three weakly relativistic values of the laser strength parameter, q, in Figure 1. These show classic RFI behaviour and accord accurately with the above analytic expressions. Agreement fails when s << 1 can no longer be justified. As the intensity rises the spectrum of

unstable modes broadens, the peak growth increases but moves to shorter scale-length filaments.

Strongly relativistic RFI at low density

As $v_0 \rightarrow 1$ and $s >> 1$, the qualitative behaviour of the growth rates remain unchanged. However, the detailed picture is substantially different; there is strong coupling to higher order modes as the difference equation implies. The oscillation of electrons across the filament 'grating' is a source of strong nonlinear conversion into harmonics. These are then subject to filamentation in the same way as the fundamental. One could term this instability Relativistic Harmonic Filamentation (RHF).

Phase matching indicates that growth from RHF would be expected where both $D_{\pm N} \approx 0$ are simultaneously resonant; this predicts instability when

$$k_\perp^2 = \omega_{pr}^2 (N^2 - 1)$$

Figure 2 shows the emergence of this growth for conversion into 2nd and 3rd harmonics for a moderately strong strength parameter of $q = 1$. RFI is still dominant and RHF for each harmonic occurs at well-separated wavenumbers. At still higher intensities, the spectrum of RFI growth broadens to envelop, or merge with, RHF. Figure 3 shows this for a range of strongly relativistic strength parameters; growth occurs down to fine-scale filaments narrower than the laser wavelength yet still much wider than the wavelength of the relevant harmonic. For this case where $\omega_{pr}^2 \approx 0.1$, the growth curve saturates ($v_0 \rightarrow 1$) with maximum growth corresponding to filamentation into the 3rd harmonic.

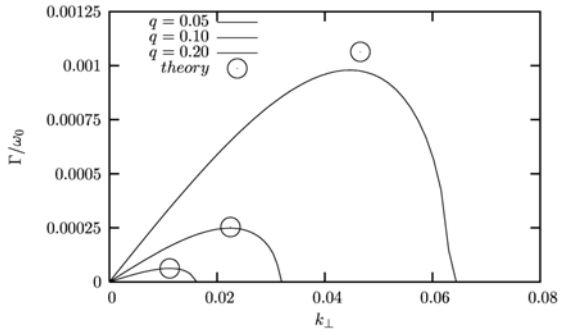

Figure 2. Semi-log plot of growth from RFI along with 2nd/3rd harmonic RHF for $q = 1.0$, $\omega_{pr}^2 = 0.1$.

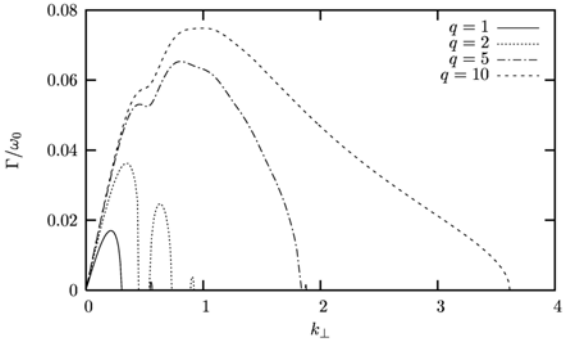

Figure 3. RFI/RHF growth curves for $\omega_{pr}^2 = 0.1$ for $q=1, 2, 5$ and 10.

Strongly relativistic RFI at high densities

As the relativistic plasma frequency is increased so the wavenumber spacing between harmonics widens to the extent that the RFI spectrum can no longer encompass the regions of RHF even at the highest intensities. The spectrum remains discrete as shown in Figure 4. Growth rates are comparable over a wide range of harmonics and corresponding filament

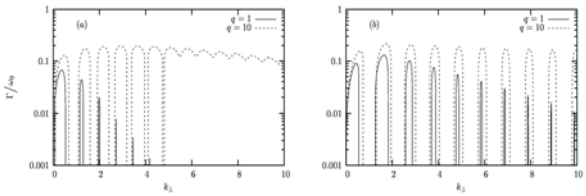

Figure 4. Growth profiles for relativistic ($q = 1$) and ultra-relativistic ($q = 10$) laser intensities at (a) half critical density ($\omega_{pr}^2 = 0.5$) and (b) critical density ($\omega_{pr}^2 = 1.0$).

width, falling off slowly with harmonic number. For low q, RFI is always strongly dominant whereas in the ultra-intense case RHF at some harmonic number is dominant but only weakly so. Figure 4 shows $q = 1$ and $q = 10$ growth curves for half critical ($\omega_{pr}^2 = 0.5$) and critical ($\omega_{pr}^2 = 1.0$) density plasma. For the ultra-intense cases we see fast growth ($\Gamma \approx 0.2\omega_0$; a significant fraction of the laser fundamental) into high harmonics across a large range of $k_\perp$.

We might expect the original beam to produce fine-scale harmonic filaments with transverse scale lengths much shorter than the vacuum laser wavelength, $\lambda_0 = 2\pi c/\omega_0$

$$\frac{\lambda_\perp}{\lambda_0} = \frac{1}{k_\perp}$$

This is in contrast to standard RFI where incident laser light filaments into scales larger than the vacuum laser wavelength.

Conclusions

The Relativistic Filamentation Instability has been studied for strongly relativistic intensities in both underdense and classically overdense plasmas. Classic RFI merges with a higher order filamentation mechanism at laser harmonics to form a hybrid instability at low densities; the strong peak in growth moves from RFI at the fundamental to higher harmonics as the density increases. At yet higher densities, the growth regimes remain distinct with broadly comparable growth rates over a wide range of harmonics corresponding to finer and finer filaments. These results need to be put in the context of other parametric instabilities (stimulated Raman scattering, stimulated harmonic generation, etc.), which have faster growth. At the highest intensities there is instability over a wide range of scales all of which are in competition. It is not clear, in the context for example of a short tightly-focused ultra-intense laser pulse, how these growth rates might be modified and which mechanism is predominant.

References

1. C E Max and J Arons
Phys. Rev. Lett., 33, 209 (1974)

2. H C Barr and L J Hill
Phys. Plasmas., 10 1135, (2003)

3. B Quesnel, P Mora, J C Adams, S Guérin, A Héron and A Laval
Phys. Rev. Lett., 78 2132, (1997)

Scaling of resonant laser wakefield acceleration

A J W Reitsma, D A Jaroszynski

Department of Physics, University of Strathclyde, John Anderson Building, 107 Rottenrow, Glasgow, G4 0NG, UK

Main contact email address: *a.reitsma@phys.strath.ac.uk*

Introduction

The laser wakefield accelerator[1] (LWFA) is a leading candidate for plasma-based, high gradient electron accelerators. Most experiments to date[2,3] have been in the so-called self-modulated regime, which is characterized by the condition that the laser pulse length z_l is much longer than the plasma wavelength λ_p. In the self-modulated regime the laser pulse can propagate over several Rayleigh lengths due to relativistic self-focusing effects, but further propagation is hindered by the development of self-modulation and Raman forward scattering instabilities. If the laser pulse is sufficiently intense, a large number of electrons from the background plasma can be trapped and accelerated, but the resulting electron beam is usually of poor quality with a large energy spread.

In the resonant LWFA regime[1], for which the laser pulse length is of the order of the plasma wavelength, stable laser pulse propagation over many Rayleigh lengths can be obtained if some form of optical guiding of the laser pulse can be provided. A preformed plasma channel with a density minimum on axis can produce such guiding and offers the possibility of substantially enhancing the energy gain. The beam quality can be improved if electrons are injected into the wakefield from a suitable external source (an RF gun, for example) rather than trapped from the background plasma in an uncontrolled way. Alternatively, one may consider methods of trapping the background electrons in a more controlled manner with additional laser pulses (all-optical injection).

In this article we discuss the analytical scaling of the performance of a channel-guided resonant laser wakefield accelerator with an injected electron bunch. This work is an extension of the analysis given by Hubbard et al[4]. In their article, Hubbard et al. characterize the LWFA performance with three parameters, namely the peak accelerating gradient E_m, the dephasing-limited acceleration length L_d, and the single-stage energy gain W_d. The value of these parameters are derived from six elementary experimental parameters, namely the peak laser power P_0, the laser pulse length z_l, the laser wavelength λ_0, the resonance ratio $\alpha \equiv z_l/\lambda_p$, the channel radius r_{ch} and the relative channel density modulation $\Delta n/n_0$, assuming a parabolic channel density $n(r) = n_0 + \Delta n\, r^2/r_{ch}^2$. Other quantities, such as the on-axis density n_0, the plasma wavelength λ_p, the matched spot size r_M, and the laser strength parameter a_0 are derived from the elementary parameters. In their conclusions, they point out that the scaling laws for E_m, L_d and W_d clearly illustrate the trade-offs in choosing laser and channel parameters. In our work, we discuss some additional figures of merit, namely the electron bunch charge Q, the total bunch energy U_b, the emittance ε and the relative energy spread $\delta E/E$, which are relevant to many applications. This will illustrate the trade-offs in the parameters of the injected electron bunch.

Wakefield model

All wakefield quantities are derived from the dimensionless wakefield potential $\Psi = e(\varphi - A_z)/mc^2$, which is a function of the comoving longitudinal coordinate $\zeta = z - v_g t$ and the transverse coordinates in the quasi-static approximation[1]. The wakefield is excited by the ponderomotive force of the laser pulse, as described by the envelope a of the dimensionless transverse vector potential $eA_\perp/mc^2$ and by the Coulomb force due to a finite density n_b of injected bunch electrons. For a plasma with density n_0, the linearized wakefield equation is :-

$$\left(k_p^2 + \frac{\partial^2}{\partial \zeta^2}\right)\left(k_p^2 - \nabla_\perp^2\right)\Psi = k_p^2\left(k_p^2 - \nabla_\perp^2\right)\frac{|a|^2}{4} + k_p^4\frac{n_b}{n_0}, \quad (1)$$

where $k_p = \lambda_p/2\pi = (4\pi n_0 e^2/mc^2)^{1/2}$ denotes the plasma wave number. Note that equation (1) does not describe the effect of the radial channel density profile on the shape of the wakefield. This effect can be calculated, but it is not relevant for our analysis, at least as long as the channel is not too narrow (i.e. $r_M \geq \lambda_p$). The linearization is valid as long as $|\Psi| \ll 1$ and allows us to conveniently write the wakefield potential $\Psi = \Psi_l + \Psi_b$ as a sum of separate contributions from the laser pulse and from the electron bunch.

Laser wakefield

For the laser pulse envelope, we take :-

$$|a|^2 = a_0^2 \cos^2(\pi\zeta/z_l)\exp(-r^2/r_M^2) \quad (2)$$

if $|\zeta| \leq z_l/2$, and *0* otherwise. From equation (2), the laser pulse peak power $P_0 = \pi^2 a_0^2 r_M^2 m^2 c^5/2e^2\lambda_0^2$ and total energy $U_l = \pi^2 a_0^2 z_l r_M^2 m^2 c^4/4e^2\lambda_0^2$ are found. In the rest of this article, we choose a laser pulse with λ_0 = 800 nm, z_l/c = 60 fs and P_0 = 30 TW, which gives $a_0 r_M \approx 21.1$ μm and a total energy of 900 mJ. By combining (1) and (2) we find that the wakefield in the region behind the laser pulse ($\zeta < -z_l/2$) is given by :-

$$\Psi_l = -\frac{a_0^2}{4}\frac{\sin(\pi z_l/\lambda_p)}{1 - z_l^2/\lambda_p^2}\sin(k_p\zeta)\exp(-r^2/r_M^2), \quad (3)$$

from which the peak accelerating gradient is found to be $E_m = k_p\Psi_0 mc^2/e$, where Ψ_0 denotes the amplitude of Ψ_l. For the laser parameters given above, a maximum of E_m as a function of n_0 is found at n_0 = 4.4 x 10^{18} cm^{-3} ($\lambda_p \approx 20\ \lambda_0$), with E_m = 36 GVm^{-1} at r_M = 30 μm.

The single-stage energy gain is limited by dephasing, i.e. the effect that an electron moving at axial velocity $v_z \approx c$ eventually slips out of the accelerating and focusing region of the wakefield that moves with phase velocity $v_\varphi < c$. The phase velocity is equal to the group velocity v_g of the laser pulse, given by :-

$$\frac{v_g}{c} = \sqrt{1 - \frac{\lambda_0^2}{\lambda_p^2}\left(1 + \frac{2}{k_p^2 r_M^2}\right)}, \quad (4)$$

from which we calculate the acceleration length :-

$$L_d = \frac{\lambda_p^3}{2\lambda_0^2}\frac{1}{1 + 2/k_p^2 r_M^2} \quad (5)$$

and the single-stage energy gain $W_d = 2eE_m L_d/\pi$. For our parameters we find W_d = 71 MeV, L_d = 3.1 mm at n_0 = 4.4 x 10^{18} cm^{-3}. Higher values of W_d are found at lower density, for example W_d = 500 MeV, E_m = 6.6 GVm^{-1}, L_d = 12 cm at n_0 = 3.5 x 10^{17} cm^{-3}. This illustrates the point (also made by Hubbard et al.) that at high plasma density, although the gradient can be very large, dephasing severely limits the energy gain.

Bunch wakefield

The amount of charge of the electron bunch is limited by beam loading[5], i.e. the effect that the electrons in the front part of the

bunch produce a wakefield that decelerates the electrons in the tail part of the bunch. The beam loading factor η is commonly defined as the ratio of the on-axis amplitudes of Ψ_b and Ψ_l and the maximum charge is determined by the condition $\eta \leq 1$. With the axisymmetric bunch distribution :-

$$n_b = n_{b0}(1 - r^2 / r_b^2) \quad (6)$$

if $|\zeta| < z_b$, $r < r_b$ and 0 otherwise, the on-axis bunch wakefield in the region behind the bunch ($\zeta < -z_b$) is found to be :-

$$\Psi_b = \frac{2n_{b0}}{n_0}\sin(k_p z_b)\left(1 - \frac{4}{k_p^2 r_b^2} + 2K_2(k_p r_b)\right)\sin(k_p \zeta). \quad (7)$$

By comparing equations (7) and (3) one finds the maximum value of the charge $Q = \pi z_b r_b^2 n_{b0} e$. With the assumptions $k_p z_l \ll 1$, $k_p z_b \ll 1$, $k_p r_M \gg 1$, $k_p r_b \gg 1$ this results in the following scaling:-

$$Q \leq \frac{eU_l}{mc^2}\left(\frac{r_b}{r_M}\right)^2\left(\frac{\lambda_0}{\lambda_p}\right)^2. \quad (8)$$

Equation (8) implies that the maximum charge scales linearly with n_0. Under the same assumptions, we derive from equations (3) and (5) that W_d scales with $n_0^{-1/2}$, so we find that the total bunch energy U_b, which is proportional to the product QW_d, scales with $n_0^{1/2}$. These scalings do not hold if the assumptions $k_p z_l \ll 1$, $k_p z_b \ll 1$, $k_p r_M \gg 1$, $k_p r_b \gg 1$ are violated. In particular, for a laser pulse with a given length z_l, increasing the density will eventually give $k_p z_l \gg 1$ (pulse length far off resonance) so that E_m drops to 0. Therefore the value of the bunch energy U_b as a function of n_0 has a local maximum, i.e. it should be possible to maximize the bunch energy by choosing the proper plasma density. For the laser parameters given above, a maximum occurs at $n_0 = 1.1 \times 10^{18}$ cm^{-3} (for which $k_p r_l \approx 18$, $k_p z_l \approx 3.5$ and $Q \leq 1.1$ nC at $r_b = r_M$).

Acceleration dynamics

Equation (8) shows that the maximum charge depends on the bunch width r_b. During the acceleration, the bunch width decreases with increasing energy[6] γ roughly as $\gamma^{-1/4}$. This means that the charge limit is set by the final rather than the initial bunch width. Using Hamiltonian theory[7], we find that the energy gain W_d scales with $\lambda_p^2/(\lambda_0^2\gamma_b)$, where γ_b denotes the initial energy (Lorentz factor). This implies that the final bunch width r_f scales with $(\gamma_b\lambda_0/\lambda_p)^{1/2}$, the charge Q with $\gamma_b(\lambda_0/\lambda_p)^3$ and the final bunch energy U_b with λ_0/λ_p, which is a scaling with $n_0^{1/2}$ independent of γ_b (as found above). The scalings of Q and W_d reveal a trade-off between the energy and the charge: by choosing a lower injection energy, one can reach a higher final energy at the expense of bunch charge. The lower limit for the injection energy γ_b is set by the threshold for trapping of the electrons in the wakefield potential, given by :-

$$\gamma_b \geq \frac{1}{2}\left(\Psi_0 + \frac{1}{\Psi_0}\right). \quad (9)$$

Assuming that the bunch distribution is constant on betatron orbits, the emittance ε is calculated from the bunch width r_b, the energy γ_b and the magnitude of the focusing force: $\varepsilon / mc = (2\Psi_0\gamma_b)^{1/2} r_b^2/r_M$. Using equation (9), this results in a lower limit for the emittance :-

$$\frac{\varepsilon}{mc} \geq \sqrt{1+\Psi_0^2}\,\frac{r_b^2}{r_M}. \quad (10)$$

We find that there is a trade-off between charge and emittance: in order to maximize the charge Q, equation (8) shows us that a large bunch width r_b is required. On the other hand, we find from equation (10) that a large value of r_b corresponds to a large emittance ε. If a bunch is injected into the wakefield with a value of r_b larger than indicated by equation (10), then the emittance would grow rapidly during the acceleration process due to phase mixing.

The evolution of the energy spread is determined mostly by the length and the charge of the bunch[8]. There is a contribution to the energy spread from the beam loading effect, i.e. the deceleration of electrons in the bunch wakefield that is excited by all the preceding electrons. This contribution is (partly) cancelled, because typically the accelerating laser wakefield increases from the front of the bunch towards the tail. In fact, if the accelerating laser wakefield increases by such an amount that it exactly compensates the decelerating bunch wakefield, then the accelerating force on all the electrons is the same, so that no energy spread is induced at all. However, due to phase slippage this ideal situation cannot be maintained during the whole acceleration process and the two contributions can cancel out only 'on average'. The residual energy spread remaining after such a cancellation is depicted in Figure 1, which shows the bunch energy U_b, the bunch length z_b, and the relative energy spread $\delta E/E$ as functions of the beam loading factor η (which is proportional to the charge Q). As expected from the beam loading effect, the plot shows that there is a limit on the amount of charge that can be effectively accelerated (U_b as a function of Q has a local maximum). Figure 1 also clearly shows two trade-offs: lower energy spread comes at the expense of bunch energy and requires a shorter bunch length.

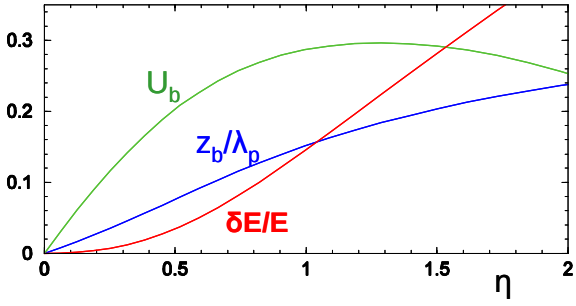

Figure 1. Bunch energy U_b (in arb. units), bunch length z_b, and relative energy spread $\delta E/E$, as functions of beam loading factor η.

Conclusion

We have discussed the scaling of some relevant figures of merit for the performance of a resonant laser wakefield accelerator. Extending previous work, in which the scalings of the accelerating gradient, the dephasing length, and the single-particle energy gain are derived, we have determined the maximum charge, the total bunch energy, the minimum emittance, and the energy spread of the electron bunch. We found that the bunch energy has a maximum as a function of the plasma density n_0 for a laser pulse with fixed energy and pulse length. We found a trade-off between the charge and the emittance which both scale with the square of the bunch width. We also found trade-offs between the energy spread and the bunch energy and between energy spread and bunch length.

References

1. E. Esarey *et al*, IEEE Trans. Plasma Sci. 24, 252 (1996)
2. W.P. Leemans *et al*, Phys. Plasmas 8, 2510 (2001)
3. R.F. Hubbard *et al*, Phys. Rev. E 63, 036502 (2001)
4. V. Malka *et al*, Phys. Plasmas 8, 2605 (2001)
5. T. Katsouleas *et al*, Part. Accel. 22, 81 (1987)
6. A. Reitsma *et al*, Phys. Rev. E 63, 046502 (2001)
7. R.D. Ruth and A.W. Chao, AIP Conf. Proc. 91, p. 94 (1981)
8. A. Reitsma *et al*, IEEE Trans. Plasma Sci. 28, 1165 (2000)

Simulation of electromagnetically induced transparency in plasma

B Ersfeld, D A Jaroszynski

Strathclyde Terahertz to Optical Pulse Source (TOPS), Department of Physics, University of Strathclyde, Glasgow, G4 0NG, UK

Main contact email address: *bernhard.ersfeld@strath.ac.uk*

Introduction

Electromagnetically induced transparency (EIT) means that an electromagnetic wave is enabled to propagate through an otherwise opaque medium by the interaction with a second wave. In plasma, the coupling mechanism is a modulation of the plasma frequency, which determines the refractive properties of the plasma. This can be due to a relativistic increase of the electron mass, or due to a variation in electron density caused by longitudinal plasma oscillations driven by the ponderomotive force associated with the beat of the waves.

The original study of EIT by Harris [1] employs a three-wave model, incorporating two transverse electromagnetic waves – with frequencies $\omega_0 > \omega_p$, $\omega_s < \omega_p$, where ω_p is the plasma frequency – and a longitudinal plasma wave at the difference frequency $\omega_- = \omega_0 - \omega_s$. It predicts transparency if the latter is slightly lower than ω_p. More recent investigations of EIT have addressed three issues:

1. Matsko et al.[2], and Gordon et al.[3] found that the conditions for EIT are affected by plasma oscillations at the anti-Stokes frequency $\omega_a = \omega_0 + \omega_-$ as well, whereas, in the original model, scattering of the wave at ω_0 occurs only into the Stokes wave at ω_s.
2. Gordon et al.[3] also studied the possibility of achieving transparency in finite plasma; it proved difficult to establish the crucial phase relations between the waves starting from a surface.
3. While References 1 - 3 assume that the amplitude of the wave at the lower frequency is small, we have started to explore the conditions of EIT for **two** waves of **comparable**, weakly relativistic amplitudes [4].

Coupled Propagation in Plasma

Relativistic Fluid Equations

We start from a description of the plasma as cold electron fluid. We take the relativistic corrections to the electron mass into account since they are of the same order of magnitude as the ponderomotive coupling. In one dimension the relevant equations read (see *e.g.* Reference 5):

$$\left(\partial^2/\partial z^2 - \partial^2/\partial t^2 - n/\gamma\right)\vec{a} = \vec{0} \qquad (1)$$

$$\partial E/\partial t = np/\gamma \qquad (2)$$

$$\partial E/\partial z = 1 - n \qquad (3)$$

$$\partial p/\partial t = -E - \partial\gamma/\partial z \qquad (4)$$

where $\vec{a}$ is the transverse vector potential, scaled by mc^2/e, E is the longitudinal electric field, scaled by $\omega_p mc^2/e$, p is the longitudinal momentum, scaled by mc, n is the electron density, scaled by the unperturbed density n_0, and $\gamma = \sqrt{1+\vec{a}^2 + p^2}$ is the Lorentz factor.

Time is scaled by $1/\omega_p$, and length by c/ω_p, where the plasma frequency is given by $\omega_p = \sqrt{4\pi n_0 e^2/m}$, m and e are the electron mass and charge, and c is the vacuum speed of light.

We assume a vector potential consisting of three waves, the pump $\vec{a}_0$, and Stokes / Anti-Stokes waves $\vec{a}_{s,a}$, respectively:

$$\vec{a} = \vec{a}_0 + \vec{a}_s + \vec{a}_a \qquad (5a)$$

$$\vec{a}_j = a_j\left[\cos(\theta_j)\vec{e}_x + \sin(\theta_j)\vec{e}_y\right] \qquad (5b)$$

$$\theta_j = k_j z - \omega_j t + \varphi_j \qquad (5c)$$

We choose circularly polarized waves in order to avoid harmonics of their frequencies, and to restrict the beat wave to the difference frequency and wave number (for co-rotating waves):

$$\omega_- \equiv \omega_a - \omega_0 = \omega_0 - \omega_s \qquad (6a)$$

$$k_- \equiv k_a - k_0 = k_0 - k_s \qquad (6b)$$

Frequencies ω_j are scaled by ω_p, and wave numbers k_j by ω_p/c.

Expansion in Powers of the Vector Potential

We expand the quantities *E*, *p*, and *n* corresponding to longitudinal plasma waves up to second order in the vector potential *a*. To this order, we find that the density modulations are driven by the relativistic ponderomotive force:

$$\left(\partial^2/\partial t^2 + 1\right)(n-1) \approx \partial^2\gamma/\partial z^2 \qquad (7a)$$

$$\gamma \approx \sqrt{1+\vec{a}^2} \approx 1 + \vec{a}^2/2 \qquad (7b)$$

For the vector potential given in equations (5) we find, neglecting terms of second order in $a_{s,a}$, which are assumed small compared to the pump:

$$\vec{a}^2 \approx a_0^2 + 2a_0(a_s + a_a)\cos(\theta_-) \qquad (8)$$

$$n = 1 + a_0(a_s + a_a)\cos(\theta_-)k_-^2/(\omega_-^2 - 1) \qquad (9)$$

Dispersion Relations

Substituting the expressions (7b), (8) and (9) for γ and *n* into equation (1), and retaining only terms up to first order in $a_{s,a}$, we arrive at dispersion relations for the three transverse waves:

$$D_0 = 0 \qquad (10a)$$

$$D_s a_s = Q(a_s + a_a) \qquad (10b)$$

$$D_a a_a = Q(a_s + a_a) \qquad (10c)$$

with $D_j = k_j^2 - \omega_j^2 + 1 - \alpha$, $Q = \alpha\dfrac{k_-^2 - \omega_-^2 + 1}{1 - \omega_-^2}$ and $\alpha = \dfrac{a_0^2}{2}$.

The factors D_j contain the reduction of the plasma frequency due to the relativistic mass increase, while Q accounts for the modifications of the refractive properties due to the beat wave. The solvability of the equation system for $a_{s,a}$ requires $(D_s - Q)(D_a - Q) - Q^2 = D_s D_a - Q(D_s + D_a) = 0$:

$$\left(1-\omega_-^2\right)\left[\left(k_-^2-\omega_-^2\right)^2-4\left(k_0k_--\omega_0\omega_-\right)^2\right] - 2\alpha\left(k_-^2-\omega_-^2\right)\left(k_-^2-\omega_-^2+1\right)=0 \qquad (11)$$

For given ω_0, α ($\Rightarrow k_0$), and ω_-, this is a fourth-order equation for k_-. For transparency, at least one of the roots must be real (for real frequencies).

For comparison, if the Anti-Stokes wave can be neglected, the dispersion relation becomes $D_s - Q = 0$:

$$\left(1-\omega_-^2\right)\left[\left(k_-^2-\omega_-^2\right)-2\left(k_0k_--\omega_0\omega_-\right)\right]-\alpha\left(k_-^2-\omega_-^2+1\right)=0 \qquad (12)$$

which is a quadratic equation for k_- and can be solved analytically. Close to the plasma resonance, $\omega_- = 1+\delta$, $|\delta| << 1$, this equation predicts a transparency band for $\delta < 0$. However, Gordon et al. [3] pointed out that in the vicinity of the resonance the Stokes and Anti-Stokes amplitudes are of comparable magnitude, so that the simplified dispersion relation cannot be used there.

The fourth-order equation (11) has approximate solutions

$$k_- = \begin{cases} \pm 1 \mp \delta\left[2(\omega_0 \mp k_0)^2/\alpha + 1\right] \\ \pm\sqrt{-\delta\left[\left(4\omega_0^2-1\right)/\alpha - 2\right]} \end{cases} \qquad (13)$$

in this regime. Note that the second pair is real for negative δ.

Numerical Simulation

Hydrodynamic Code

In order to check the assumptions and approximations made in the analytical theory, we performed numerical simulations, using a code implementing the fully relativistic hydrodynamic equations for the plasma motion, and solving the electric field propagation in a leapfrog scheme. Compared to Particle-in-Cell simulations, results from a hydrodynamic simulation should contain less noise, while a one-dimensional system does not yet require excessive computation times.

Boundary Conditions

In the simulations, the plasma was set up using two different boundary conditions:

a) Either the plasma region was bounded by short regions of (almost) zero density, so that electromagnetic waves incident from vacuum could be simulated.

b) Or the plasma region extended over the entire simulation range; at both ends the physical quantities outside this range were assumed to be mirror images of those inside. This allowed to treat the hypothetical case where the electromagnetic waves are generated inside the plasma, and effects of the vacuum-plasma interface can be neglected.

In either case, the initial electron density was homogeneous (inside the plasma for a)), and equal to the (constant) ion density. The electromagnetic fields were applied as boundary values, typically as superposition of oscillations at two (or three) distinct frequencies.

Results and Conclusions

In general, our simulations confirmed the findings of Gordon et al. [3]: although theoretically possible in infinite plasma, EIT in a bounded system appears to be very hard or impossible to achieve. Typically, close to the surface or source of the waves, plasma oscillations upshift part of the Stokes wave to the pump or Anti-Stokes frequencies, which can freely propagate, so that the corresponding energy is carried away. This can be seen in Figure 2.

In Reference 3, the argument is given that the Stokes wave cannot effectively generate the necessary density modulations. We tried to use a short intense pulse to generate a wake and thus pre-form the plasma; this should provide the approximate modulations for the case $k_- \approx 1 \approx \omega_-$. The results were, however, not decisively different from the case without wake. It may be possible to improve the matching of the beat wave and the wake.

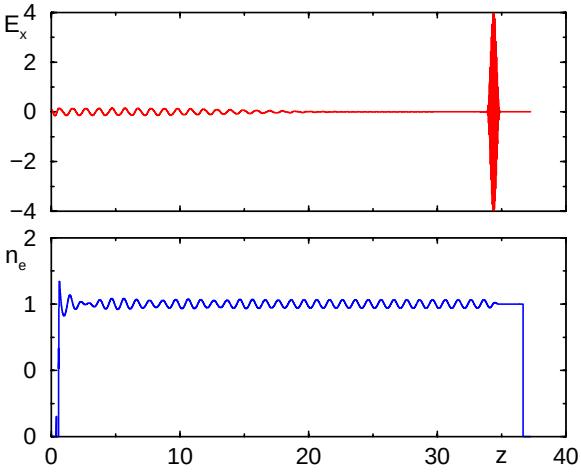

Figure 1. Snapshots of transverse electric field, propagating from left to right (top), and electron density (bottom). Note the short pulse generating the wake.

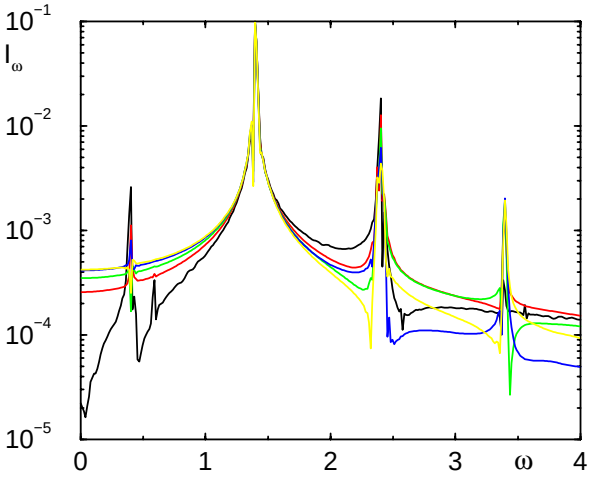

Figure 2. Spectral intensity of the transverse electric field at equidistant positions from the surface; the order is black=0, red=d, green=2d, blue=3d, yellow=4d; d=3.66 c/ω_p .

References

1. S.E. Harris, Phys. Rev. Lett. 77, 5357 (1996)
2. A.B. Matsko, Y.V. Rostovtsev, Phys. Rev. E 58, 7846 (1998)
3. D.F. Gordon, W.B. Mori, C. Joshi, Phys. Plasmas 7, 3145 and 3156 (2000)
4. B. Ersfeld, D.A. Jaroszynski, J. Mod. Optics 49, 889-896 (2002)
5. H.C. Barr, P. Mason, D.M. Parr, Phys. Plasmas 7, 2604 (2000)

Recent developments in the Belfast approach for laser-driven helium

K J Meharg, B J S Doherty, J S Parker, K T Taylor

DAMTP, David Bates Building, Queen's University Belfast, Belfast, BT7 1NN, Northern Ireland, UK

Main contact email address: *k.taylor@qub.ac.uk*

Introduction

The Belfast approach[1,2] for laser-driven helium goes after the time-dependent Schrödinger equation (TDSE) for this system, directly, in full-dimensionality. Since the laser light is considered to be linearly polarized there is a residual spatial symmetry of the overall two-electron system about the laser polarization axis. This allows the full-dimensionality TDSE to be written as a partial differential equation in 5 spatial dimensions and the time.

Recently we have made two significant developments in the approach taken and these will be described briefly below.

The first development has been a computational one, re-engineering our HELIUM code so as to fully exploit the power of the new IBM regatta supercomputer recently installed at CCLRC Daresbury Laboratory. This will allow us to extend our approach so as to obtain accurate and reliable results for both single- and double-ionization of helium exposed to high-intensity Ti:Sapphire laser light with wavelengths around 780 nm. The second development is a theoretical one which we term the Essential States Approximation. This allows us considerably more insight into the mechanisms underlying energy absorption from the laser light and its subsequent sharing between the two electrons, resulting in one or both ionizing.

Re-engineering of the HELIUM code

The new IBM regatta system recently installed at CCLRC Daresbury Laboratory has in its initial configuration 40 nodes each containing 32 processors. The processors are grouped 8 to a board with 8 Gigabytes of memory per chip. Thus there are 1280 Gigabytes of addressable memory over the whole machine.

The re-engineering of HELIUM is straightforward to summarize. We continue to write our wavefunction as an expansion over coupled spherical harmonics (partial waves) which handle the angular degrees of freedom. The two radial co-ordinates and the time are treated by finite-difference techniques. In the old HELIUM code we distributed the wavefunction over processors so that one (or more) partial waves was the responsibility of each processor. In the new, re-engineered HELIUM code we now make a sub-region of the two-dimensional radial finite-difference grid the responsibility of each processor. Most importantly, and of crucial importance to an effective exploitation of the IBM regatta architecture, the only inter-processor communication demanded with this re-engineered code is between nearest neighbours.

The new code has already been developed to the point of generating reliably accurate results and the first such results for double-ionization of helium by high-intensity Ti:Sapphire light are presently being obtained.

The Essential States Approximation

The essential states approximation (ESA) attempts to model the two-electron dynamics of laser-driven helium by retaining only the 'essential' partial waves for representing the angular degrees of freedom. What states are essential can only be determined through knowing in advance what are the true results in bench-mark cases where the full expansion over partial waves has been retained in the HELIUM code.

Initial investigations with the ESA model have concentrated on the choice of essential states necessary in order to generate reliable single ionization rates. Figure 1 illustrates our findings at a laser wavelength of 130 nm and intensity of 10^{15} W/cm^2. In this case there are 91 partial waves in the full basis but one can observe from the figure that perfect convergence to this result is obtained with retention of just 33 partial waves.

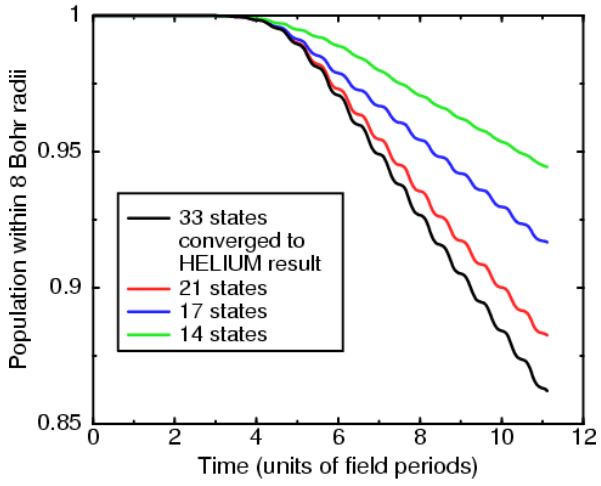

Figure 1. Laser-driven helium electronic population within eight Bohr radii of nucleus evolving in time.

Of course it is the *particular* partial waves that are retained that is of crucial importance. With just 14 (the green curve in the figure) only one of the two electrons is allowed to have an orbital angular momentum greater than zero (except when the total angular momentum of the system is zero). This would be an adequate approximation if only one of the electrons was interacting with the laser and *not* sharing angular momentum and energy with the other. Since the corresponding result does not agree with that from the full HELIUM calculation (black curve) we see such a simple process does not prevail. The 33 partial waves yielding the converged result bring in additional partial waves where the angular momenta of *both* electrons differ from zero but still remain markedly different for high overall angular momentum of the system. This indicates certainly in single ionization at this wavelength and intensity that both electrons are *not* behaving on an equal footing in their interactions with the laser light but that, through electronic interaction, a marked exchange of angular momentum and energy is nevertheless taking place between them.

Conclusions

The two developments outlined above are crucial not only to determining accurate, reliable single- and double-ionization rates for laser-driven helium at Ti:Sapphire wavelengths but also for insight into the physics that prevails.

References

1. E S Smyth, J S Parker and K T Taylor, Comput. Phys. Commun., 114 1, (1998)

2. J S Parker, L R Moore, K J Meharg, D Dundas and K T Taylor, J. Phys. B: At. Mol. Opt. Phys. 34 L69, (2001)

Preliminary design study for a magnetic transport channel

S Karsch, C D Murphy, P A Norreys

Central Laser Facility, CCLRC Rutherford Appleton Laboratory, Chilton, Didcot, Oxon, OX1 0QX, UK

Main contact email address: *S.Karsch@rl.ac.uk*

Introduction

As part of the efforts for the ALPHA-X basic technology programme to develop a laser-driven all optical injector for a table-top X-ray FEL, we consider three different approaches to transporting a bunch of electrons from one laser (wakefield) accelerator to the next. The structure should provide energy discrimination to cut out electrons of a desired energy from the (usually broad) spectrum emitted by the self-modulated wakefield accelerator and propagate and focus these electrons into a second wakefield for post-acceleration. Ultimately, we want to propagate a subset of the laser-accelerated electrons with a total charge on the order of 1 nC with an energy of approximately 10 MeV and an energy spread of approx. 1-10%, amounting to 10^7 particles.

In order to achieve phase matching of the electron bunch with the plasma wave, its temporal dispersion from TOF differences through the transport structure must be kept smaller than one plasma oscillation period (on the order of 20-50 fs). Additionally, the time-of-flight dispersion Δt introduced by the energy spread $\Delta\gamma$ must be considered and can be expressed as:-

$$\Delta t = \frac{dt}{d\gamma}\Delta\gamma = -\frac{x}{c}\cdot\frac{1}{\left(\gamma^2-1\right)^{3/2}}\cdot\Delta\gamma \qquad (1)$$

with x being the distance travelled by the electron in a time t, c is the speed of light, and γ is the electron's relativistic γ-factor. Equation 1 amounts to a TOF dispersion of 10 fs/cm for 10 MeV electrons and 10% energy spread. This immediately shows that the transport structure has to be kept as short as possible to minimize the temporal spread.

The simulations shown below were done with the SIMION 7.0 [1)] code, which tracks particles in three dimensions through a given geometry of electromagnetic fields.

It has some limitations in treating magnetic fields correctly, because instead of solving Poisson's equation it treats magnetic fields in much the same way as electric fields from a quasi-magnetic potential. The simulations all assume the electron bunch energy to be 10 MeV, and two beams with a divergence angle of 5° (box-shaped angular distribution) in horizontal and vertical orientation, respectively.

The simulations show that regardless of what configuration is used, electrons at 10% energy spread are not focused anymore into the second wakefield, whereas 1% energy spread electrons are still within the wakefield's diameter. The first configuration investigated was a structure consisting of a focusing quadrupole doublet and a dipole monochromator (2Q1D).

2Q1D-monochromator and focuser

The electron-optical length of this system amounts to 10 cm, which is almost the most compact design that can be achieved with field strengths limited by the saturation flux in iron. A sketch of the magnet geometry and the electron trajectories is shown in Figure 1(a). It immediately becomes clear that the large lateral spread of the electrons in the horizontal (dipole's deflection) plane causes a large temporal spread between electrons on axis and those at an angle to it. It can be quantified by monitoring the electrons' time-of-flight before they hit the detector. The results are shown in Figure 1(b,c) for both planes. The TOF spread for monoenergetic electrons is 340 fs and 26 ps, far too much for phase-controlled injection into the wakefield, which renders this simple approach useless.

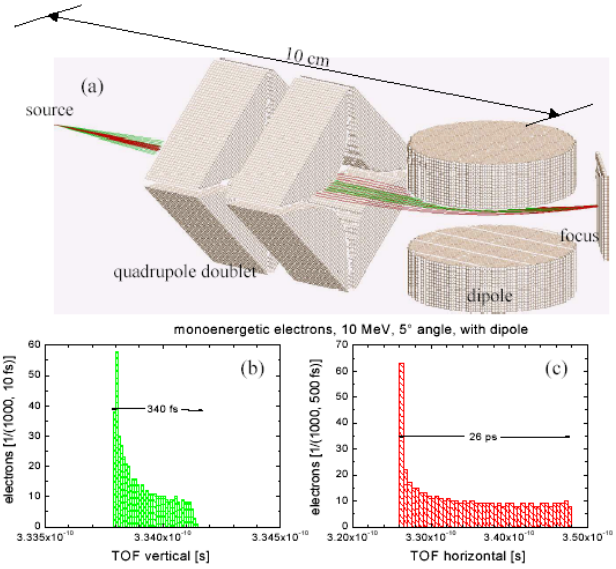

Figure 1. 2Q1D setup (a) and corresponding electron TOF spectra in the vertical (b) and horizontal plane (c).

2Q-monochromator and focuser

A first order approach for improving the situation is leaving out the dipole bending magnet as a source for large temporal spread. The energy selection is now performed by the chromatic aberration of the doublet, i.e. electrons of different energy focus at different points along the axis. For energy discrimination to ±1%, this method is sufficient. The optical path length is now 11 cm, and the laser generating the second wakefield can be sent down the quadrupole axis. While removing the dipole leads to a substantial reduction in TOF dispersion, unfortunately the results are still not satisfying. Figure 2 illustrates this case.

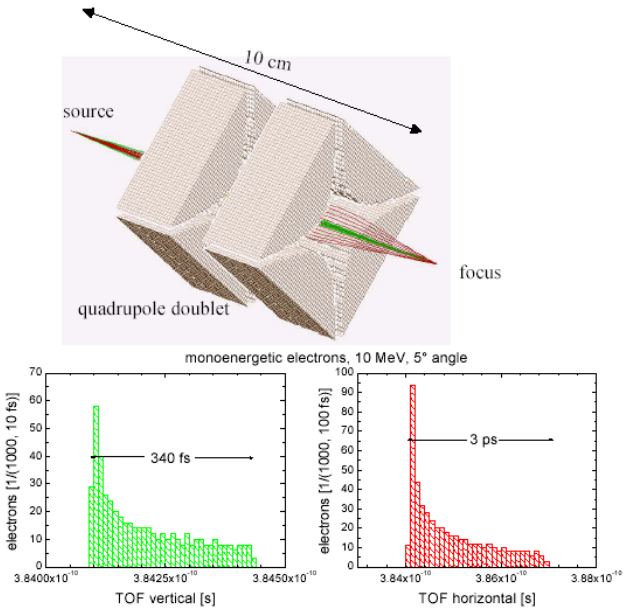

Figure 2. 2Q setup (a) and corresponding electron TOF spectra in the vertical (b) and horizontal plane (c).

Now the TOF spread is 340 fs and 3 ps in the vertical and horizontal plane, respectively, still far too much for our purpose. Obviously, focusing a beam with 5° opening angle using quadrupole magnets leads to large deviations from the optical axis and consequently to large path differences between electrons on axis and electrons at an angle to it.

Longitudinal field in a solenoid

Passing an electron beam along the axis of a solenoid (and therefore parallel to the magnetic field lines) leads to zero force on the electrons. However, if the electrons are emitted at an angle to the solenoid axis, the Lorentz force sends them spiralling around the field lines. An electron starting on axis at an angle α to it comes back after one revolution. The time T_c needed for one revolution is given by the inverse of the cyclotron frequency ω_c :-

$$T_c = \frac{2\pi}{\omega_c} \quad ; \quad \omega_c = \frac{eB}{m\gamma} \tag{2}$$

which is independent of the transverse velocity $v_t = v \sin \alpha$ of the electron and therefore independent of α. It only depends on the electron energy $E \propto \gamma$. $v = \beta c \approx c$ is the electron velocity. The longitudinal velocity v_l is given by $v_l = v \cos \alpha$. The distance x travelled by the electron in axial direction after one full circle thus can be written as:-

$$x = v_l \cdot T_c = v \cdot \cos\alpha \frac{2m\gamma\pi}{eB} \tag{3}$$

and is maximal for $\alpha = 0$. $\alpha = 0$ defines the small-angle focal length x_0. If $\alpha \neq 0$, x is shorter than x_0 and the time needed by an electron to reach x is longer by the delay time Δt:-

$$\Delta t = \frac{x_0}{v_l} - \frac{x_0}{v} = \frac{x_0}{v}\left(\frac{1}{\cos\alpha} - 1\right) = \frac{2\pi}{\omega_c}\left(\frac{1}{\cos\alpha} - 1\right) \tag{4}$$

Equation 2 gives the electron TOF to the focus for a small angular spread and Equation 3 gives the focal length of the solenoid. Equation 4 gives the TOF dispersion of an electron beam in dependence of the divergence angle α. The factor γ in the expression for the cyclotron frequency ensures the energy selectivity of the setup. This view holds only if the electrons travel in a homogeneous magnetic field for at least one revolution.

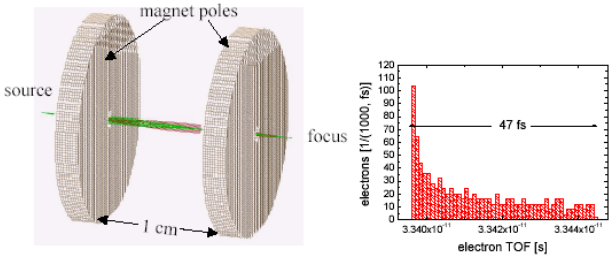

Figure 3. Solenoid set-up and corresponding electron TOF spectra in the vertical and horizontal plane. Note that the awkward magnetic field treatment of SIMION requires pole surfaces in order to model the magnetic field. The model here is therefore equivalent to a solenoid coil in terms of magnetic field configuration.

If the electrons are emitted in a field-free region and enter the solenoid after a certain distance, they will not enter it on axis anymore. The mechanism described above is then not efficient for focusing anymore, since it leaves the transverse position of the particle unchanged. However, it is possible to find a configuration where the electron can be focused in this case, essentially when it undergoes a quarter revolution and then leaves the field in a plane perpendicular to the one it entered. This case can be modelled with a particle tracking code and is shown in Figures 3 and 4.

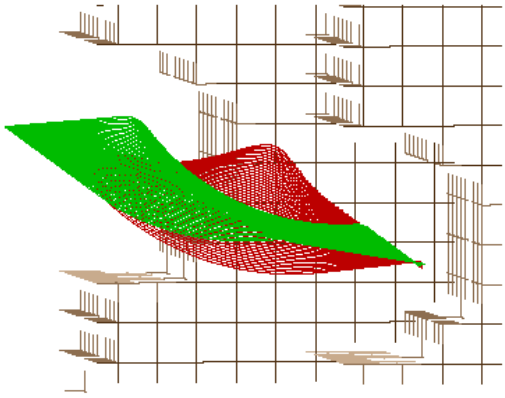

Figure 4. Enlargement of the electron trajectories in Figure 3.

In order to minimize the TOF dispersion, the dimensions of the solenoid are downscaled to a length of 1 cm. To focus electrons at 10 MeV, these dimensions require a magnetic field of 25 T, which can be produced by pulsing the solenoid.

The simulation shown here again assumes the same electron beam parameters as above, and at a field of 25 T, the electrons are focused in a spot size of < 20μm.

The TOF dispersion is only 47 fs, and since the TOF spectrum is peaked, cutting out an even narrower TOF window would result in only a moderate loss of particles. This configuration therefore is a very promising approach.

Conclusion and things to do

While a magnetic transport structure based on conventional focusing quadrupoles does not seem appropriate for achieving the goal of transporting the electron bunch from one wakefield accelerator to the other with minimal temporal spread, a solenoid with a longitudinal magnetic field seems to do the job.

However, a number of questions concerning space charge is still unsolved. A simulation run with a total of 100 pC charge in a broad spectrum completely blows the beam up due to space charge. No focusing is observed anymore.

A self-generated magnetic field pinching the electrons should not be present in vacuum, since in a co-moving frame the electrons see only their repelling electric field. Only a sufficiently dense, cold background plasma can shield the space charge, or generate a focusing magnetic field (in the comoving frame). So it may be necessary to fill the magnet system with a pregenerated plasma in order to eliminate space charge effects. However, SIMION does not treat transient shielding effects. The dynamics and dephasing effects of electrons with different energies comoving in the field cannot be modelled by this code either. The synchrotron radiation of the electron emitted during the focusing, on the other hand, is negligible. Nevertheless, it is necessary to repeat the calculation with a full 3-D PIC code that is able to treat all these effects.

References

1. SIMION-3D 7.0: http://www.sisweb.com

Lasers for Science Facility Programme

1) Chemistry

2) Biology

3) Physics

Transient absorption and Kerr gated TR^3 study of DMABN and its derivatives

W M Kwok, C Ma, D Phillips

Department of Chemistry, Imperial College, London, SW7 2AY, UK

P Matousek, A W Parker, M Towrie

Central Laser Facility, CCLRC Rutherford Appleton Laboratory, Chilton, Didcot, Oxon, OX11 0QX, UK

W T Toner

Department of Physics, Clarendon Laboratory, Parks Road, Oxford, OX1 3PU, UK

Main contact email address: *macs@hkucc.hku.hk*

Introduction

The structure of the intramolecular charge transfer (ICT) state of DMABN (4-dimethylaminobenzonitrile) continues to be of much theoretical interest and a challenge for experimental observation. Two possibilities are presently being considered. That is, whether the dimethylamino group lies perpendicular (twisted, TICT state[1,2]) or in plane (planar, PICT state[3]) to the benzene ring. This has been widely studied using time resolved vibrational spectroscopy by ourselves[4-6] and other groups[7-9] with our findings supporting the TICT model. Most theoretical works[10,11] favor the TICT model as well. However, the PICT model cannot be conclusively ruled out. Additional evidence is required to further clarify the ICT structure. We have therefore extended our previous transient absorption (TA) and Kerr gated-TR^3 (K-TR^3) work on DMABN to a series of its derivatives, the specially designed model compounds closely related to the two models. Molecular structures of these compounds are shown in Scheme 1. The twist angle, in the ground state, between the plane of the dimethylamino group and phenyl ring has been found to be 0, ~21, ~37, ~60 and 90°, respectively, in the sequence of DMABN, DEABN, DIABN, TMABN and CBQ.[12,13] Based mainly on steady state and time-resolved fluorescence studies, TMABN and CBQ have been taken as the TICT model compounds with DEABN and DIABN as model compounds for the PICT model[1-3]. We believe that the TA and K-TR^3 spectra presented here provide convincing evidence for the ICT state structure of DMABN and related fluorescence family molecules.

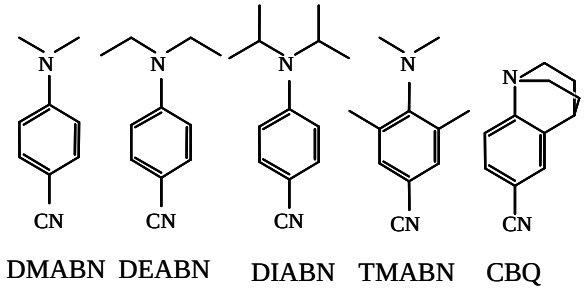

Scheme 1. Molecular structures of the studied compounds.

Experimental arrangements

The experiments were carried out using the sub-picosecond TA and K-TR^3 systems based on optical parametric amplifiers (OPAs), as described elsewhere[14,15]. The pump wavelength was 267 nm for both the TA and K-TR^3 experiments. Probe wavelengths of 400 and 330 nm were used for the K-TR^3 measurements in resonance with two different electronic transitions of the ICT state. All the spectra shown here are recorded at 50 ps time delay. Spectroscopic grade acetonitrile is used for all the experiments. Sample concentrations were 1 to 3 x 10^{-3} mol dm^{-3}.

Results and discussion

TA spectra of the ICT state of DMABN, DEABN, DIABN, TMABN and CBQ in acetonitrile are displayed in Figure 1. It is clear that the spectra show close resemblance and all peak at ~ 420 nm. This implies a similarity in the electronic properties of the ICT and upper S_n states. We infer from this that the same chromophore will be resonantly enhanced for the TR^3 measurements with probe wavelength falling into the absorption band.

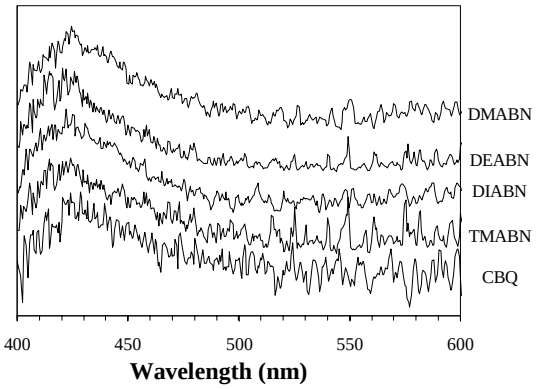

Figure 1. Transient absorption spectra of the ICT state for DMABN, DEABN, DIABN, TMABN and CBQ obtained with 267 nm excitation wavelength in acetonitrile at 50 ps time delays.

This is confirmed by the K-TR^3 spectra (Figure 2) obtained in this solvent at 400 nm probe wavelength. Again, there are obvious similarities across the TR^3 spectra of the five compounds. All the spectra show a strong feature at ~1580 cm^{-1} corresponding to phenyl ring central C=C stretching vibration. Two more weak features appear at similar positions, ~1170 and 950 cm^{-1}, for DMABN, DEABM and DIABN. The bands can be assigned to the ring C-H bending (9a) (~1170 cm^{-1}) and ring C-C stretch (12) (950 cm^{-1}), respectively.[5,6] Rather than these two, three weak features, 1288, 1148 and 1097 cm^{-1}, are observed for the TMABN spectra. The bands can be attributed to vibrations related to the two ring substituted methyl groups.[6] Due to relative poor S/N ratio, no additional weak feature can be assigned for the CBQ spectra.

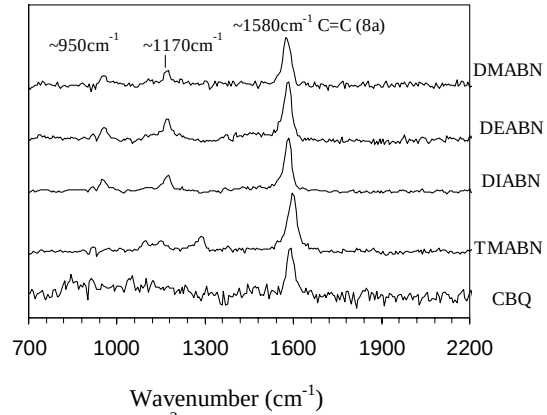

Figure 2. Kerr-gate TR^3 spectra of the ICT state for DMABN, DEABN, DIABN, TMABN and CBQ obtained with 267 nm pump and 400 nm probe wavelength in acetonitrile at 50 ps time delay.

A TA study with detection range down to ~300 nm finds DMABN ICT state has another strong absorption band peaking at ~310 nm[16]. Based on the similar spectral characteristics observed in the above TA and 400 nm K-TR^3 measurements, we expect the same ICT absorption for DEABN, DIABN TMABN and CBQ at ~310 nm. This expectation is supported by K-TR^3 spectra of the ICT state we have obtained for these compounds at 330 nm probe wavelength with exception of TMABN due to strong ground state absorption at this wavelength. For example, TR^3 spectra of DMABN, DIABN and CBQ are shown in Figure 3. The spectra show noticeable similarity and all have three strong features at ~2100, 1580 and 750 cm^{-1}. The ~1580 cm^{-1} band corresponds to the strongest band observed in the 400 nm spectra. The ~2100 cm^{-1} bands are due to the C≡N stretch and the ~750 cm^{-1} bands are attributed to the Wilson 1 ring breathing mode[5]. Several weak bands, though not well resolved, can be seen for the three compounds in the 800-1300 cm^{-1} region.

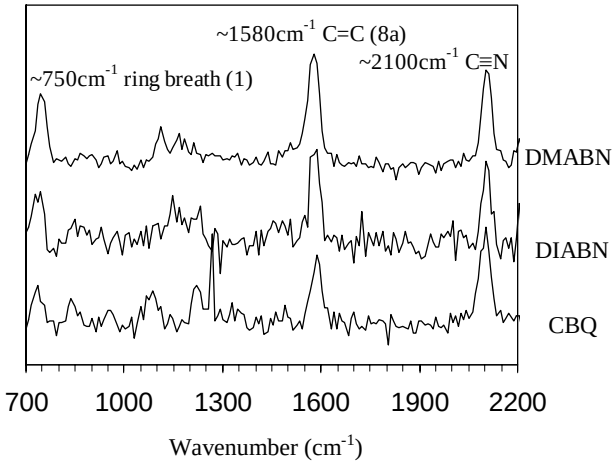

Figure 3. Kerr-gate TR^3 spectra of the ICT state for DMABN, DIABN and CBQ obtained by 267 nm pump and 330 nm probe wavelength in acetonitrile at 50 ps time delay.

Previous DMABN ICT state studies have shown that the ICT absorption spectrum has its band positions (the two bands peaking at ~420 and ~310 nm) and their relative intensities resemble the absorption spectrum of benzonitrile radical anion[6,16]. Moreover, several characteristic modes observed in the DMABN ICT state TR^3 spectra have been found to appear in comparable positions to the corresponding modes observed for the benzonitrile radical anion[4-6,17]. For example, the above mentioned C≡N stretch (~2100 cm^{-1}), the Wilson 8a (~1580 cm^{-1}) and 1 (~750 cm^{-1}) modes have their counterparts in the benzonitrile anion at 2093, 1592 and 760 cm^{-1}, respectively[17]. This has been taken as convincing experimental evidence for the full charge transfer from the amino to benzonitrile subgroup in the ICT state. The fact that such a spectral resemblance remains for the series of DMABN derivatives studied here indicates that all these compounds share a similar electronic structure and the full charge transfer character. We note that the donor (the amino subgroup) ability increases from DMABN to DEABN to DIABN, and the acceptor ability for TMABN is weaker than for the others. Our observation that the ICT state absorption and Raman spectra show almost identical character independent of the donor and acceptor ability implies that the interaction between the donor and acceptor is weak in the ICT state. This is in full agreement with the electronically decoupled concept proposed in the TICT model in contrast with the electronically coupled PICT model.

Through amino N^{15} isotopic substitution, our previous K-TR^3 study with 330 nm probe wavelength has identified the spectroscopic signature of the amino N-C_{ring} stretching, $\nu(C_{ring}$-N), at ~1280 cm^{-1} corresponding to ~100 cm^{-1} downshift ongoing from its ground state frequency[5]. This result has been taken as crucial evidence to support the TICT model[5]. However, due to the extensive vibrational coupling character of the $\nu(C_{ring}$-N) mode, it has been pointed out that the inference is not conclusive[18]. The ~1280 cm^{-1} band, though weak, can still be seen in the 330 nm TR^3 spectra of DMABN (Figure 3). Due to its weak intensity, we do not attempt here to identify this mode for the other compounds but we believe that it could appear at the similar position. We conclude that, irrespective to ground state twisting angle, the ICT Raman spectra of the compounds investigated show distinctly similar character. This, together with the fact that the twisting angle in CBQ is fixed to 90^o, due to the rigid double bridge amino substitution, we believe provides further support to the twisted geometry of the ICT state (the TICT model). This also indicates that such a structure is general and also applicable to DMABN derivatives.

Acknowledgements

We thank Dr. K A Zachariasse for providing DIABN and CBQ samples and helpful discussion.

References

1. K. Rotkiewicz, K. H. Grellmann, Z. R. Grabowski Chem. Phys. Lett., 19 315, (1973).
2. W. Rettig, B. Bliss, K. Dirnberger, Chem. Phys. Lett., 8 305, (1999).
3. W. Schuddeboom, S. A. Jonker, J. M. Warman, U. Leinhos, W. Kuhnle, K. A. Zachariasse J. Phys. Chem., 96, 10809, (1992).
4. W. M. Kwok, C. Ma, P. Matousek, A. W. Parker, D. Phillips, M. Towrie J. Phys. Chem. A, 104 , 4188, (2000)
5. W. M. Kwok, C. Ma, P. Matousek, A. W. Parker, D. Phillips, W. T. Toner, M. Towrie, S. Umapathy J. Phys. Chem. A., 105, 984, (2001).
6. W. M. Kwok, C. Ma, M. W. George, D. C. Grill, P. Matousek, A. W. Parker, D. Phillips, W. T. Toner, M. Towrie, Phys. Chem. Chem. Phys. 5 1043, (2003).
7. M. Hashimoto, H. Hamaguchi, J. Phys. Chem., 99 7875, (1995).
8. C. Chudoba, A. Kummrow, J. Dreyer, J. Stenger, E.T.J. Nibbering, T. Elsaesser, K.A. Zachariasse Chem. Phys. Lett., 309 357, (1999)
9. H. Okamoto, J. Phys. Chem. A, 104 4182, (2000).
10. L. Serrano-Andres, M. Merchan, B. O. Roos, R. Lindh J. Am. Chem. Soc., 117 3189, (1995)
11. J. Dreyer, A. Kummrow J. Am. Chem. Soc., 122 2577, (2000).
12. A. Heine, R. H. Irmer, D. Stalke, W. Kuhnle, K. A. Zachariasse, Acta. Crystallogr., B50, 363, (1994).
13. A. B. J. Parusel, G. Köhler, Intern. J. Quant. Chem., 149 84, (2001).
14. M. Towrie, A. W. Parker, W. Shaikh, P. Matousek Meas. Sci. Technol., 9 816, (1998)
15. P. Matousek, M. Towrie, A. Stanley, A. W. Parker Appl. Spectrosc., 53 1485, (1999)
16. T. Okada, M. Uesugi, G. Kohler, K. Rechthaler, K. Rotkiewicz, W. Rettig, G. Grabner Chem. Phys., 241 327, (1999).
17. I. Juchnovski, C. Tsvetanov, I. Panayotov Monatsh. Chem., 100 1980, (1969).
18. H. Okamoto, M. Kinoshita, S. Kohtani, R. Nakagaki, K. A. Zachariasse, Bull. Chem. Soc. Jpn., 75 957, (2002).

Dynamics of metal to ligand charge transfer states in $[Re(Cl)(MQ^+)_2(CO)_3]^{2+}$ and $[Re(Cl)(PQ^+)_2(CO)_3]^{2+}$; An ultrafast time-resolved visible, IR absorption, resonance Raman, and emission study (MQ = *N*-methyl-4,4'-bipyridinium, PQ^+ = *N*-phenyl-4,4'-bipyridinium)

M Busby, A Vlček Jr.

Department of Chemistry, Queen Mary, University of London, Mile End Road, London, E1 4NS, U K

P Matousek, M Towrie

Central Laser Facility, CCLRC Rutherford Appleton Laboratory, Chilton, Didcot, Oxon, OX11 0QX, UK

Main contact email address: *A.Vlcek@qmul.ac.uk*

Introduction

Viologen-type ligands *N*-methyl-4,4'-bipyridinium (MQ^+) and *N*-phenyl-4,4'-bipyridinium (PQ^+) are strong electron acceptors whose presence in the coordination sphere of a transition metal gives rise to very rich electrochemical, spectroscopic and photochemical behaviour. Herein we investigate and characterise the photophysical properties of $[Re(Cl)(MQ^+)_2(CO)_3]^{2+} \equiv Re(MQ^+)_2$ and $[Re(Cl)(PQ^+)2(CO)^3]^{2+} \equiv Re(PQ^+)_2$, Figure 1, using a plethora of ultrafast time-resolved spectroscopic techniques.

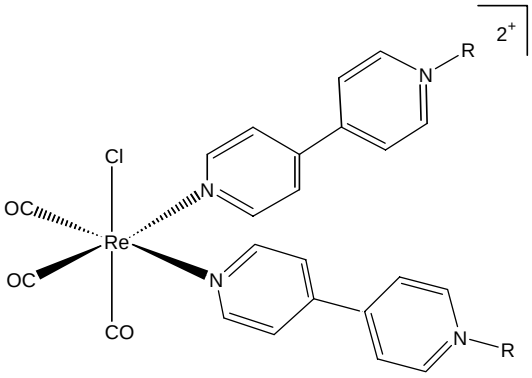

Figure 1. Schematic structures of $[Re(Cl)(MQ^+)_2(CO)_3]^{2+}$; R=Me and $[Re(Cl)(PQ^+)_2(CO)_3]^{2+}$; R=Ph.

Results and Discussion

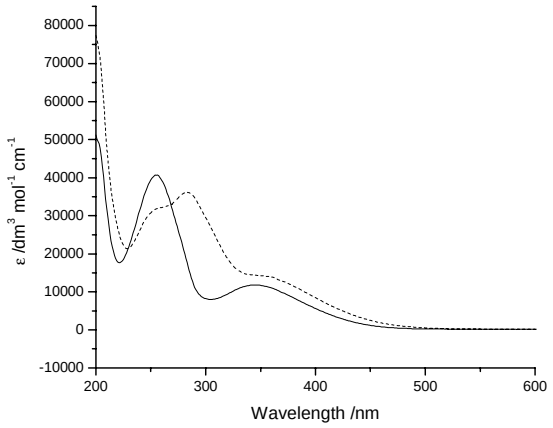

Figure 2. UV/VIS spectrum, of $[Re(Cl)(MQ^+)_2(CO)_3]^{2+}$ in acetonitrile (solid line) and $[Re(Cl)(PQ^+)_2(CO)_3]^{2+}$in acetonitrile (dashed line).

The UV/VIS spectra of both complexes, were measured in acetonitrile and are shown in Figure 2. $Re(MQ^+)_2$ has a broad absorption with a maximum at 345 nm, assigned to a $Re\rightarrow MQ^+$(MLCT) transition. At higher energies there is a more intense and sharper band at 255 nm. This transition is present in the UV/VIS spectrum of the free ligand and is thought to be of a $\pi\rightarrow\pi^*$ character, localised on the MQ^+ ligand. The $Re(PQ^+)_2$ complex has a similar UV/VIS spectrum. The $Re\rightarrow PQ^+$(MLCT) transition is just seen as a shoulder that stretches to longer wavelengths than for $Re(MQ^+)_2$. $Re(PQ^+)_2$ has a similar $\pi\rightarrow\pi^*$ transition in the UV region, as well as an extra transition at 283 nm, which is thought to be localised on the phenyl group of the ligand.

The resonance Raman spectrum of the $Re(MQ^+)_2$ has been previously reported in the literature with 406.7 nm excitation[1]. We have repeated with longer wavelength excitation, resulting in no significant difference. The most prominent bands are the A'(2) carbonyl mode at 2029 cm^{-1} and ligand localised C-C and C-N modes between 1648-733 cm^{-1}. The enhancement of both CO and MQ^+/PQ^+ modes, indicates that the excitation wavelength is pre-resonant with the MLCT transition at 345 nm. For the PQ^+ complex the Raman bands are strongly obscured by emission, though the carbonyl mode at 2030 cm^{-1} and lower energy C-C and C-N modes at 1642, 1617, 1302, 1235, 1074, and 1021 cm^{-1} can be clearly made out (see Figure 3). Both complexes have near identical resonance Raman spectra indicating that the excited state is localised primarily on the bipyridinium moiety of the MQ^+ and PQ^+ ligand.

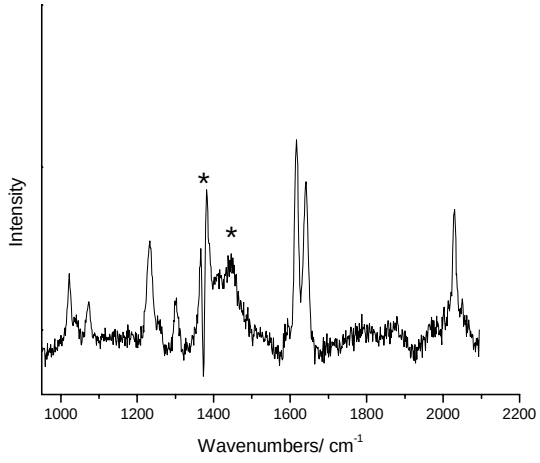

Figure 3. Resonance Raman spectrum of $[Re(Cl)(PQ^+)_2(CO)_3]^{2+}$ measured after excitation at 457.9 nm in acetonitrile.* indicates solvent subtraction residue. Baseline was corrected for emission.

The emission that obscures the resonance Raman spectral measurements for the $Re(PQ^+)_2$ complex has been subsequently studied in acetonitrile and shows a broad band centred at 550 nm (see Figure 4). The $Re(MQ^+)_2$ complex shows no detectable steady state emission.

Transient absorption (TA) experiments were performed in acetonitrile, between 0-1000 ps, pumping into the $Re\rightarrow MQ^+/PQ^+$(MLCT) transition with a 400 nm excitation wavelength. Both complexes show a very broad, intense

transient signal that covers the entire visible region, to beyond 700 nm. The band maximum for both complexes is at 620 nm (see Figure 5). The broad transient is due to an electronic transition originating from a $MQ^{\bullet}$ moiety [2], formed through population of the $Re \rightarrow MQ^{+}$(MLCT). Similar TA spectra have been observed for the complex $[Re(MQ^{+})(CO)_3(dmb)]^{+}$.

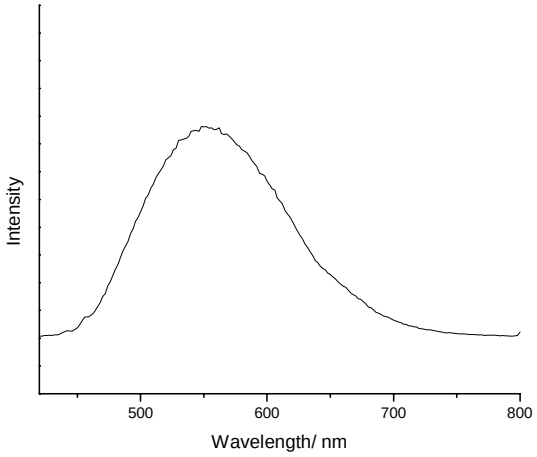

Figure 4. Emission spectrum of $[Re(Cl)(PQ^{+})_2(CO)_3]^{2+}$ measured after excitation at 400 nm in acetonitrile. The spectrum has not been corrected.

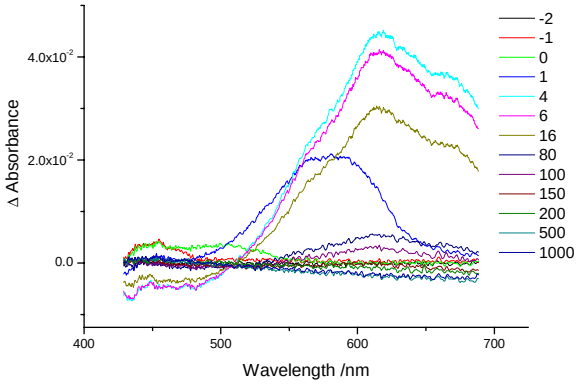

Figure 5. ps-Time-resolved visible absorption spectrum, measured after excitation at 400 nm, of $[Re(Cl)(PQ^{+})_2(CO)_3]^{2+}$ in acetonitrile.

Time resolved emission studies of both $Re(MQ^{+})_2$ and $Re(PQ^{+})_2$ show ultrafast emissions centered around 530 nm (see Figure 6). The emission lifetime is within the instrumental time resolution of the Kerr-gate apparatus and can be estimated to be less than 4 ps. $Re(PQ^{+})_2$ has a second, much weaker longer lived component with a maxima at ca. 550 nm. This emission has a lifetime of more than 1 ns and corresponds to the emission seen on the steady state apparatus.

TR^3 experiments were performed on both complexes in acetonitrile with a pump wavelength of 400 nm, and a probe beam exciting into the band maximum of the transient absorption at 610 nm. Only bands pertaining to the $MQ^{\bullet}/PQ^{\bullet}$ chromophore are seen to be resonantly enhanced, ratifying that the transient absorption is localised on the $MQ^{\bullet}/PQ^{\bullet}$ (see Figure 7). As with the ground state resonance Raman studies, there are no significant differences between the $Re(MQ^{+})_2$ and $Re(PQ^{+})_2$. Both complexes show ν(CO) bands in the FTIR spectra that are typical of $[Re(CO)_3(X)(L)_2]$ systems, consisting of a singlet at 2028 cm^{-1} and at lower energies a well resolved doublet 1925,1899 cm^{-1}. The bands can be assigned to A'(1), A'(2) and A" ν(CO) vibrations respectively. The resolved splitting of the A'(2) and A" ν(CO) modes is attributed to the local C_s symmetry induced by the halide and the MQ^{+}/PQ^{+}on the metal centre.

(a)

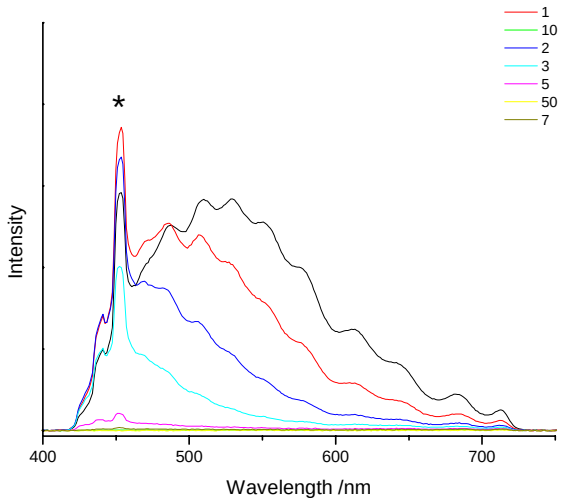

(b)

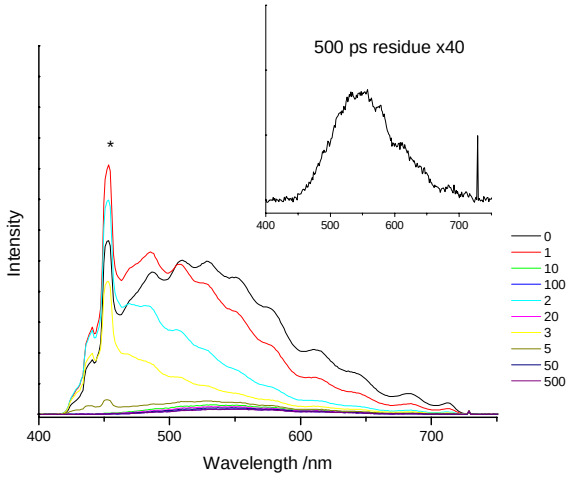

Figure 6. ps-Kerr-gate time-resolved emission spectrum, measured after excitation at 400nm (a) of: $[Re(Cl)(MQ^{+})_2(CO)_3]^{2+}$ in acetonitrile and (b) $[Re(Cl)(PQ^{+})_2(CO)_3]^{2+}$in acetonitrile.* indicates solvent Raman scatter.

The ps TRIR spectra of $Re(MQ^{+})_2$ and $Re(PQ^{+})_2$ are shown in Figure 8. The negative peaks in the spectrum arise from the depletion of the ground-state population; whereas the positive peaks represent the photo-generated excited state. All GS bleach bands are seen to shift to higher energies in the excited state. Such behaviour is indicative of an MLCT excited state, where the ν(CO) bond is weakened as a result of a decrease in $Re \rightarrow CO$ π back-donation and increased $OC \rightarrow Re$ σ donation. The difference in wavenumbers between the bleach and the maxima of the fundamental transient after it has undergone vibrational cooling is indicative of the magnitude of charge transfer. Values are typically between 65-90 cm^{-1} , which indicates a significant charge separation (see Table 1).

From the asymmetrical shapes of the 2090 cm^{-1} transient, it can be seen that the band comprises of both a fundamental and a hot-band absorption. Such transients have been seen on $[Pt(4,4'\text{-}CO_2Et)2\text{-}2,2'\text{-}bpy)(Cl)_2]$ [3]. To rigorously characterize the transient, it must be fitted to multiple Lorentzian functions, comprising of the fundamental at 2092 cm^{-1}, and a hot-band at 2078 cm^{-1} (see Figure 9). It is important to note that in these systems both depopulation of hot-bands and vibrational cooling are contributing to the temporal evolution of the transient band shape at early time delays.

Vibrational cooling of carbonyls typically occurs on a time scale of 10 ps, and is manifested by the narrowing and blue shift

of transients. Such data is difficult to extract precisely from the high energy transient due to the complexity of the spectra. For the lower energy carbonyl transients, only one peak is fitted for each mode, so it is not possible to differentiate between the processes of hot-band decay and vibrational cooling, though it is evident that narrowing and blueshifting do occur. Both $Re(MQ^+)_2$ and $Re(PQ^+)_2$ have very nearly identical behaviour in the early time delays between 0-10 ps. From the fits the decay in intensity for the high energy transient hot-band in $Re(PQ^+)_2$ occurs with a time constant of ca 2.6 ±0.14 ps. This decay is consistent with the growth in intensity of the fundamental transient. Both decay of hotband and growth and fundamental occur concurrently with the overall decay of the excited state.

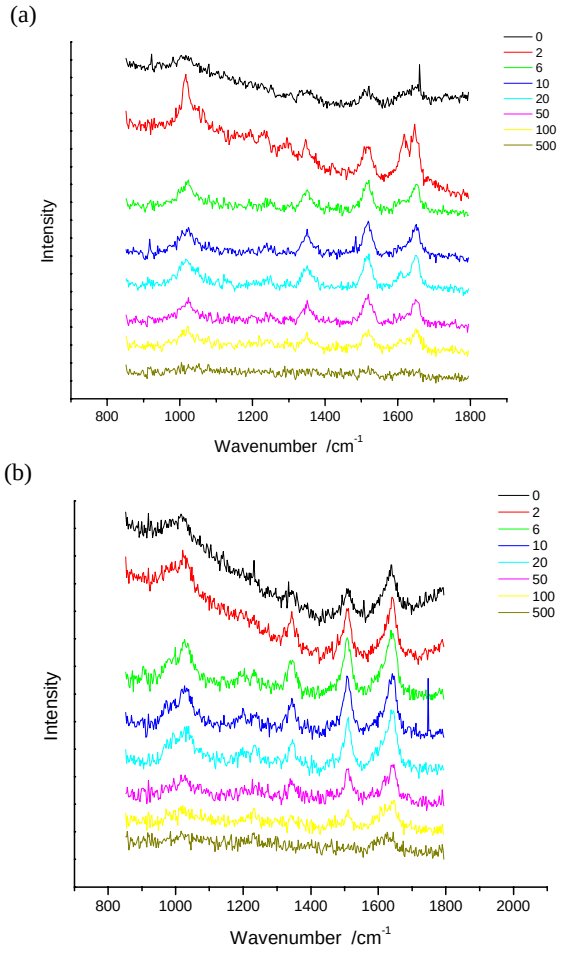

Figure 7. ps-Kerr-gate time-resolved resonance Raman spectrum, measured after excitation at 400 nm and probing at 610 nm, of (a) $[Re(Cl)(MQ^+)_2(CO)_3]^{2+}$ in acetonitrile and (b) $[Re(Cl)(PQ^+)_2(CO)_3]^{2+}$ in acetonitrile.

This study has combined several time-resolved experiments to investigate the photophysical dynamics of novel organometallic complexes. We have employed visible and IR absorption, Kerr-gate TR[3] and Kerr-gate emission spectroscopies, that are available at the Ultrafast Spectroscopy Laboratory at RAL.

Acknowledgments

Financial support from EPSRC and beam time allocation by the CCLRC are gratefully appreciated.

References

1. J. R. Schoonover, P. Chen, D. Bates, R. B. Dyer, and T. J. Meyer, Inorg. Chem., 33, 793(1994).
2. D. J. Liard and A. Vlcek, Inorg. Chem., 39, 485, (2000).
3. J. A. Weinstein, D. C. Grills, M. Towrie, P. Matousek, A. W. Parker, and M. W. George, J. Chem. Soc., Chem. Commun. 382,(2002).

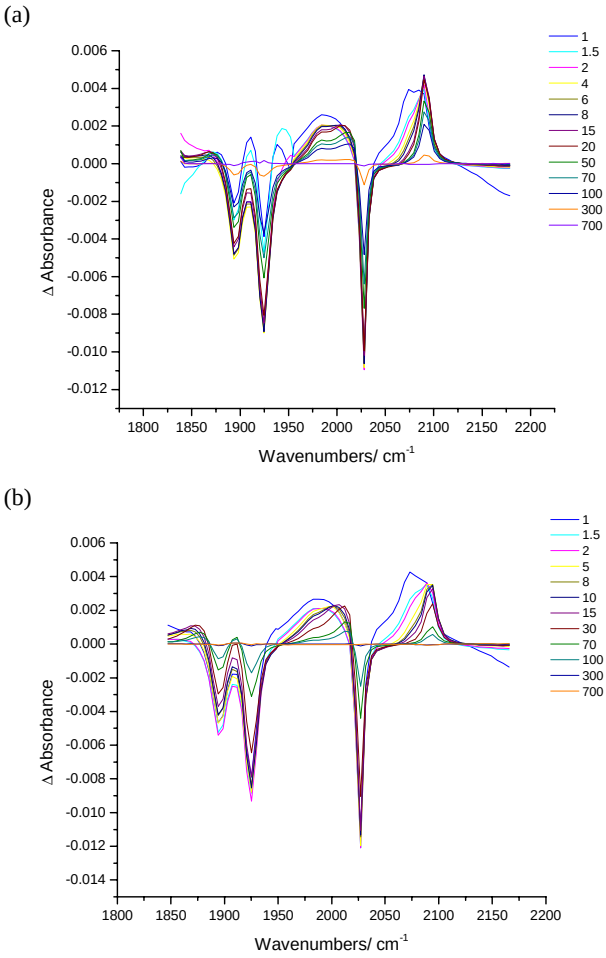

Figure 8. Time-resolved infrared spectrum, measured after excitation at 400 nm (a) $[Re(Cl)(MQ^+)_2(CO)_3]^{2+}$ in acetonitrile and (b) $[Re(Cl)(PQ^+)_2(CO)_3]^{2+}$ in acetonitrile.

$[Re(Cl)(MQ^+)_2(CO)_3]^{2+}$			$[Re(Cl)(PQ^+)_2(CO)_3]^{2+}$		
Bleach	Transient	Δν	Bleach	Transient	Δν
1896.2	1986.5	+90.3	1897.0b	1990.0	+93.0
1925.9	2015.6	+89.7	1927.2b	2015.7	+88.5
2027.8	2091.8	+67.0	2026.6	2092.4	+65.3

Table 1. Positions of infrared ground state bleach and excited state transients for $[Re(Cl)(MQ^+)_2(CO)_3]^{2+}$ and $[Re(Cl)(PQ^+)_2(CO)_3]^{2+}$.

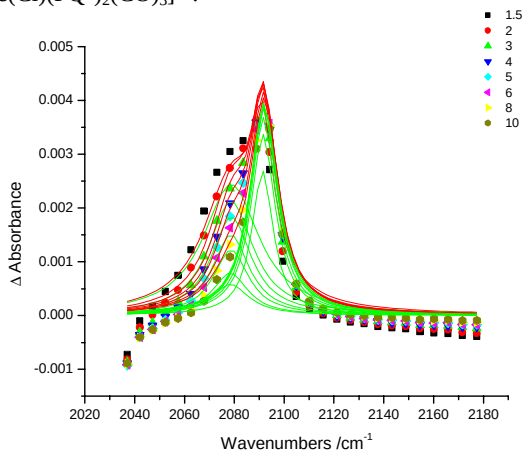

Figure 9. Time-resolved infra red spectrum of: $[Re(Cl)(MQ^+)_2(CO)_3]^{2+}$ showing the excited state A'(1) ν(CO) region. Transients are fitted to two Lorentzian functions describing the fundamental and the hot-band.

Using picosecond time-resolved infrared spectroscopy to study excited states of Re(I) Carbonyl complexes

M K Kuimova, D C Grills, X-Z Sun, M W George

School of Chemistry, University of Nottingham, University Park, Nottingham, NG7 2RD, UK

P Matousek, M Towrie, A W Parker

Central Laser Facility, CCLRC Rutherford Appleton Laboratory, Chilton, Didcot, Oxon, OX11 0QX, UK

Main contact email address: *Mike.George@nottingham.ac.uk*

Introduction

There has been considerable interest in the interactions of substitution-inert transition metal complexes with DNA[1]. Ru^{II} and Os^{II} *α-diimine* complexes containing the strong intercalator dppz (dipyrido[3,2a:2',3'c]phenazine) and its derivatives are at the forefront of such investigations. The photophysics of these complexes is very sensitive to the properties of the environment such as solvent polarity or the ability to hydrogen bond. They are well-known to show the 'light switch effect'[2] and therefore provide a spectroscopic handle for the presence of double-helical DNA in solution and DNA mediated electron transfer. However, there is an increasing interest in Re^{I} carbonyl complexes containing dppz[3]. These complexes possess the light switch properties but they could also provide additional structural information on the excited state dynamics in different solvents and DNA if studied by vibrational spectroscopy, since they possess CO groups, which are strong infrared reporters.

TRIR spectroscopy is a powerful tool for studying the excited states and short-lived reaction intermediates of coordination compounds containing infrared reporters with high oscillator strength such as CO or CN [4]. The PIRATE (Picosecond Infrared Absorption and Transient Excitation) facility in the Ultrafast Spectroscopy Laboratory provides a tunable source of ultrashort pulses in the mid-infrared region (1000-3000 cm^{-1}) synchronised with UV/vis excitation[5]. In this paper we report an investigation into the photophysics of the series of complexes, *fac*-$[Re(CO)_3(dppz\text{-}Cl_2)(R)]^{n+}$ (dppz-Cl_2 = 10,11-dichloro-dipyrido[3,2a:2',3'c]phenazine; R = py (n = 1) (**I**), (4-dimethylamino)pyridine (n = 1) (**II**) and Cl^- (n = 0) (**III**)) using PIRATE.

Photophysics of Re^{I} complexes in CH_3CN

The interest in complexes of the type *fac*-$[Re(CO)_3(dppz\text{-}XX')(R)]^{n+}$ is induced by their potential to act as DNA probes. However, prior to the studies of DNA-mediated electron transfer it is necessary to elucidate their photophysics in solution, which remains somewhat ambiguous. The complexity of the photophysics is partially due to the electronic structure of the dppz ligand.

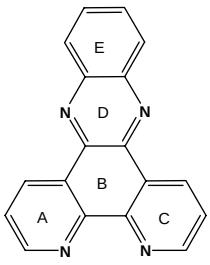

Figure 1. Schematic diagram of the dppz ligand.

DFT calculations and electrochemical and photophysical studies[2, 7] have demonstrated that this ligand is best described as a combination of two independent parts – phenanthroline ('phen') (Figure 1, rings A, B, C) and phenazine ('phz') (Figure 1, rings B, D, E) with independent π* acceptor orbitals localised on each part. This could lead to at least four excited states of different orbital nature which are close in energy – two intraligand (IL) ππ* states and two metal-to-ligand charge transfer (MLCT) states with charge transfer to either the 'phen' or 'phz' moiety of dppz. The relative ordering of these four states can be tuned by donor/acceptor substituents on the intercalating or ancillary ligands and also is expected to be sensitive to the solvent environment.

ps-TRIR spectroscopy was utilised to study complexes **I**, **II** and **III** in CH_3CN solution at room temperature. Figure 2 shows the spectra obtained in the ν(CO) region 20 ps after 400 nm excitation. All three complexes show depletion of the ground state ν(CO) bands and the formation of new transient bands. It is clear that the excited state spectra for the three complexes under study are very different.

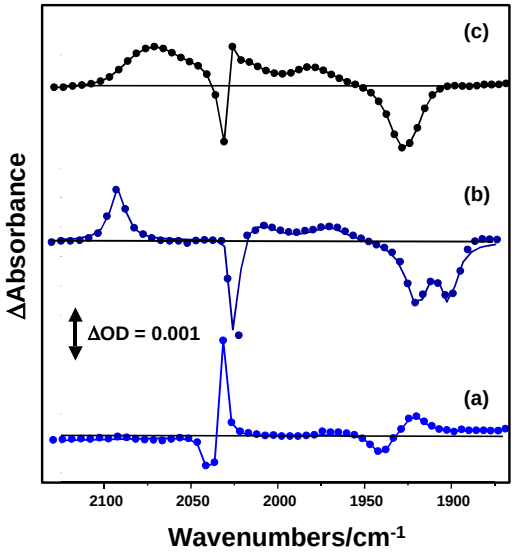

Figure 2. TRIR spectra of $[Re(dppz\text{-}Cl_2)(CO)_3L]^{n+}$ in CH_3CN obtained 20 ps after 400 nm excitation, (a) L = py, n = 1 (**I**); (b) L = Cl-, n = 0 (**III**); (c) L = 4-Me_2N-py, n =1 (**II**).

Excitation of **I** leads to a small negative shift of the ν(CO) bands which is characteristic[4] of an IL ππ* excited state (Figure 2, a). Population of the π* orbital results in stronger donor properties of the dppz ligand and therefore in a slightly higher electron density on the Re centre. Thus the backbonding to the π* orbitals of the CO ligands is slightly increased and a small negative shift of the ν(CO) is observed. The ground state bleaches and the transient absorptions do not show decay on the timescale of the ps-TRIR experiment, which is consistent with the 7 ns lifetime obtained for **I** in CH_3CN at room temperature. However, within the first 50 ps of the TRIR experiment the transient ν(CO) bands narrow and shift to higher wavenumber. These spectral changes could correspond to either vibrational cooling[8] or the interconversion of ^{3}IL ππ* 'phen'- and 'phz'-based states.[7] Both processes might occur on this timescale and might contribute to the observed spectral change. The ps-TRIR data alone do not allow us to distinguish between these two processes. The characteristic rate of collective vibrational cooling and interconversion between IL ππ* states is *ca.* 20 ps.

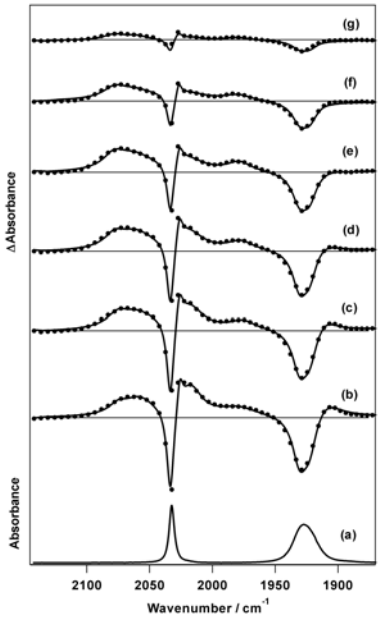

Figure 3. (a) FTIR spectrum of *fac*-[Re(CO)$_3$(dppz-Cl$_2$)(4-Me$_2$N-py)](PF$_6$) (**II**) in CH$_3$CN at room temperature. (b-g) Series of TRIR spectra obtained between 2 and 2000 ps after 400 nm excitation of this solution: 2 ps (b), 7.5 ps (c), 15 ps (d), 40 ps (e), 500 ps (f), 2000 ps (g).

Contrary to **I**, excitation of **II** leads to the instant formation of two sets of excited state bands (Figure 2, c and Figure 3). One set of transient ν(CO) bands is shifted to slightly lower wavenumber and therefore can be assigned to absorptions of an IL ππ* state formed upon excitation, analogous to **I**. The other set of ν(CO) bands is shifted to higher wavenumber compared to the parent bleaches. This shift is characteristic of the formation of an MLCT excited state[4], since this leads to a decrease in the electron density on the metal centre and therefore reduced back-bonding to the π* orbitals of the CO ligands. A comparison of the magnitude of the positive shift of the ν(CO) bands with the ν(CO) band shift in the ns-TRIR spectrum of the MLCT state of [ReCl(CO)$_3$(phen)][4] (phen = 1,10-phenanthroline) allows the MLCT state formed upon excitation of **II** to be described more precisely as a dπ(Re) → π*(phen) ^{3}MLCT state. The formation of a 'phz' based MLCT state would result in further reduction of the electron density on the metal and therefore a larger ν(CO) shift. Both sets of bands are present in the *ps*-TRIR spectra from 2 ps to 2.5 ns and therefore we tentatively conclude that the IL ππ* and 'phen'-based MLCT states formed after 400 nm excitation of **II** are in equilibrium. The rate of the excited state decay is 1.0 (± 0.2) ns and this value is similar to the fluorescence lifetime obtained for **II**.

It is noteworthy that only the MLCT state was revealed in a steady-state emission study of **II** in CH$_3$CN solution. This result indicates that the MLCT state is probably the lowest-lying state for **II**.

The *ps*-TRIR investigation is particularly valuable for **III** since it is not emissive in fluid solution at room temperature. A previous TR^3 investigation into the nature of the lowest excited state of this complex also did not provide a clear assignment of the lowest excited state[9]. Upon 400 nm excitation the ground state ν(CO) bands are bleached and new transient bands are formed, shifted to higher energy (Figure 2, b). This shift is consistent with the formation of an MLCT excited state similar to **II**. However in the case of **III** the shift of the ν(CO) bands is much larger than that for **II**. Also this shift is analogous to the shift observed for [Re(CO)$_3$(dppz)(py)]$^+$ in *ns*-TRIR experiments where we tentatively assigned it to a 'phz'-based MLCT state[7]. These data allow us to assign the excited state species observed for **III** after 400 nm excitation to a dπ(Re) → π*(phz) ^{3}MLCT state. The bleached parent ν(CO) bands recover with a time constant of 150 (± 20) ps. Such a short excited state lifetime is consistent with no emission being observed for a fluid solution of the complex. The transient bands for complex **III** first narrow and shift to higher wavenumber, which is consistent with vibrational cooling of the excited state species and then decay with the same lifetime as the parent bleaches recover. The kinetic decay traces for the areas of the high-energy parent ν(CO) band and the 'cool' and 'hot' transient bands allow the characteristic time for the vibrational cooling process to be estimated (*ca* 20 ps).

Conclusions

The present study shows that *ps*-TRIR is a powerful tool for studying the photophysics of metal complexes containing IR reporters with high oscillator strengths. In the series of complexes of *fac*-[Re(CO)$_3$(dppz-Cl$_2$)(R)]$^{n+}$, modification of ligand R was shown to induce substantial changes in the nature of the lowest excited state. In CH$_3$CN solution at room temperature, changing from the neutral *fac*-[Re(CO)$_3$(dppz-Cl$_2$)(R)] (R= Cl$^-$), which possesses a phz-based MLCT state, to R = py or 4-Me$_2$N-py leads to charged complexes with low-lying IL ππ*(dppz) states. The introduction of a donor substituent on the pyridine moiety results in an equilibrium between the MLCT (phen) and IL ππ*(dppz) excited states. The proximity of the various excited states also potentially offers the possibility of tuning the nature of the lowest excited state with changes in the environment polarity or hydrogen bonding, which highlights the use of such metal complexes as DNA probes.

References

1. K E Erkkila, D T Odom and J K Barton
Chem. Rev., 99 2777, (1999)

2. A E Friedman, J C Chambron, J P Sauvage, N J Turro and J K Barton
J. Am. Chem. Soc., 112 4960, (1990)

3. H D Stoeffler, N B Thornton, S L Temkin and K S Schanze,
J. Am. Chem. Soc., 117 7119, (1995)

4. M W George and J J Turner
Coord. Chem. Rev., 177 201, (1998)

5. M Towrie, D C Grills, J Dyer, J A Weinstein, P Matousek, R Barton, P D Bailey, N Subramaniam, W M Kwok, C Ma, D Phillips, A W Parker and M W George,
Appl. Spectrosc., 57 367, (2003)

6. J Fees, W Kaim, M Moscherosch, W Matheis, J Klima, M Krejcik and S Zalis,
Inorg. Chem., 32 166, 1993.

7. J Dyer, W J Blau, C G Coates, C M Creely, J D Gavey, M W George, D C Grills, S Hudson, J M Kelly, P Matousek, J J McGarvey, J McMaster, A W Parker, M Towrie and J A Weinstein,
Photochem. Photobiol. Sci., 2 542, (2003)

8. T P Dougherty and E J Heilweil
Chem. Phys. Lett., 227 19, (1994)

9. M R Waterland, K C Gordon, J J McGarvey and P M Jayaweera,
J. Chem. Soc., Dalton Trans., 609, (1998)

Photolysis of $Fe(CO)_5$ studied by picosecond time-resolved infrared spectroscopy in conventional and supercritical fluids

J Yang, P Portius, X-Z Sun, D C Grills, M W George

School of Chemistry, University of Nottingham, University Park, Nottingham, NG7 2RD, UK

M Towrie, P Matousek, A W Parker

Central Laser Facility, CCLRC Rutherford Appleton Laboratory, Chilton, Didcot, Oxon, OX11 0QX, UK

Main contact email address: *Mike.George@nottingham.ac.uk*

Introduction

The photochemistry of $Fe(CO)_5$ has been studied extensively due to its numerous applications ranging from photocatalysis and synthesis[1,2] to coherent control of gas phase reactions[3]. Many techniques have been employed to elucidate the mechanisms of $Fe(CO)_5$ photolysis, including matrix isolation, flash photolysis, time-resolved infrared spectroscopy, and time-resolved electron diffraction[4].

Poliakoff and Turner showed that photolysis of $Fe(CO)_5$ in low temperature (12 K) matrices generated $^3Fe(CO)_4$, which has C_{2v} symmetry[5-7]. Triplet ground state coordinatively unsaturated species are very unusual for 16 VE organometallics. Furthermore, upon near IR irradiation or annealing the matrix they observed the conversion from $^3Fe(CO)_4$ to $^1Fe(CO)_4(L)$ (L = matrix) in Xe and CH_4 matrices but not in Ne and Ar matrices[6]. Time-resolved infrared spectroscopy (TRIR) has been used to probe the photochemistry of $Fe(CO)_5$ at room temperature, characterising $^3Fe(CO)_4$ in the gas phase[8,9]. Higher resolution TRIR experiments showed the photon energy dependence of the dissociation of $Fe(CO)_5$, as well as the detection of $^1Fe(CO)_4$ at low buffer gas pressures. In solution, $^1Fe(CO)_4$(cyclohexane) was characterised by Grevels using μs-TRIR[10]. Grevels has recently shown that $Fe(CO)_3$(solvent) is formed as a primary photoproduct on the microsecond timescale[11]. Another ps-TRIR study in *n*-heptane showed that $^3Fe(CO)_4$ is formed within 33 ps following excitation and is long-lived (up to 660 ps)[12]. However, these data were not recorded in the region of the $Fe(CO)_3$ ν(CO) band and no information can be obtained as to the formation dynamics of $Fe(CO)_3$. There are some key questions remaining unanswered regarding the photochemistry of $Fe(CO)_5$ in solution on the picosecond time scale, *e.g.* the intersystem crossing from $^1Fe(CO)_4$ to $^3Fe(CO)_4$ and the formation of $Fe(CO)_3$(solvent).

In this report we use the ps-TRIR PIRATE facility[13] to examine the photochemistry of $Fe(CO)_5$ in *n*-heptane and several supercritical fluids as solvents.

Results and Discussion

Figure 1(a) shows the FTIR spectrum of $Fe(CO)_5$ dissolved in *n*-heptane in the presence of 1 atmosphere of CO. Figure 1 (b) shows the picosecond TRIR spectra of this solution at a series of time delays after 267 nm UV excitation. The two parent $Fe(CO)_5$ bands are bleached instantaneously a broad band appears at early time. This broad vibrational feature then narrows and blue-shifts to produce three main transient ν(CO) bands at 1988, 1967 and 1926 cm^{-1}. The shift of the ν(CO) bands over the first 50 ps is consistent with a vibrational cooling of the newly formed species. The ν(CO) bands at 1988 and 1967 cm^{-1} can readily be assigned to $^3Fe(CO)_4$ by comparison to the previous matrix isolation[6] and ps-TRIR results[12]. The kinetic information shown in this work can further be compared to the photolysis of $Fe(CO)_5$ in the gas phase. Analogous to the gas phase study, ground state $^3Fe(CO)_4$ is formed vibrationally excited, showing "hot" bands in the IR spectrum.

The band at 1926 cm^{-1} can be assigned to $Fe(CO)_3$(heptane) by comparison with the previous matrix isolation[14] and μs-TRIR results[11]. It is the first time that this species has been observed on the picosecond time scale. In principle, there should be an A_1 ν(CO) mode of this species around 2040 cm^{-1}, but it might be too weak to be detected in this work.

The observation of $Fe(CO)_3$(heptane) within 5 ps raises a debate about multiple CO ejection by single photon irradiation in the solution phase, since this type of process is usually restricted to the gas phase[15]. In order to resolve this issue, we have performed additional experiments to investigate the laser energy dependence of the $Fe(CO)_3$ band intensity. The results strongly suggest that $Fe(CO)_5$ loses two CO ligands in a one photon process to generate $Fe(CO)_3$ within the first 5 ps. We can draw a tentative conclusion: after the formation of $^1Fe(CO)_4$, which is presumably in a highly vibrationally excited state, it can experience a further dissociation by loss of another CO ligand in addition to its quenching to $^3Fe(CO)_4$. Therefore, it is more likely that the singlet dissociation pathway of $Fe(CO)_5$ is applicable to the photolysis in the condensed phase.

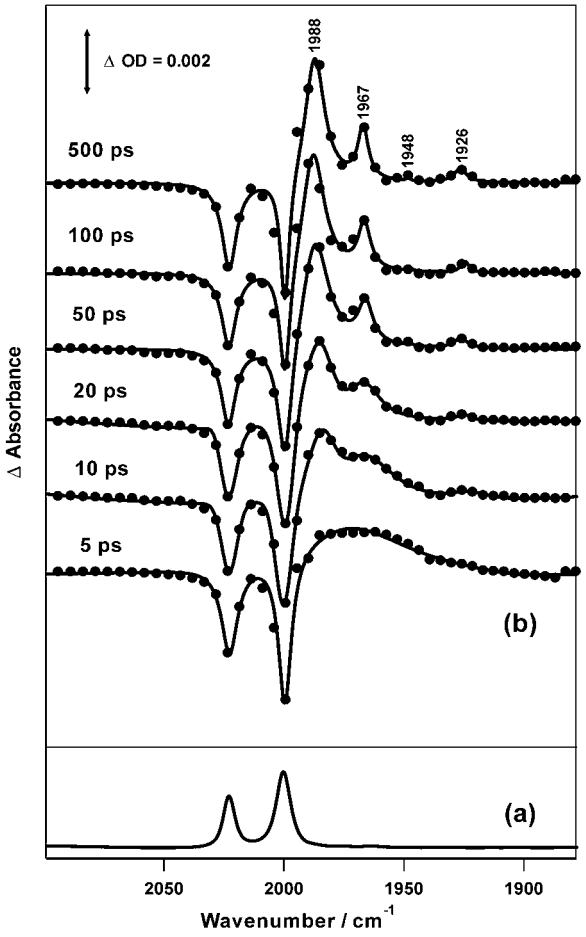

Figure 1. (a) FTIR spectrum of $Fe(CO)_5$ in n-heptane (0.5 mM, CO-saturated); (b) ps-TRIR spectra following 267 nm excitation of the same solution at room temperature. The time on each spectrum is the pump-probe delay time.

A close inspection of Figure 1 reveals a very weak band at 1948 cm^{-1}, which cannot be neglected. Considering a previous report[11] we tentatively assign this vibration to be $^1Fe(CO)_4$(heptane) resulting from the direct solvation of $^1Fe(CO)_4$ on the picosecond timescale. This indicates another pathway for the decay of $^1Fe(CO)_4$ besides recombination with CO and intersystem crossing to $^3Fe(CO)_4$. However, the solvation of $^1Fe(CO)_4$ is a relatively minor decay route compared with the formation of $^3Fe(CO)_4$.

We performed similar ps-TRIR experiments in $scCH_4$, scXe and scAr to compare the vibrational lifetimes and band intensities of $^3Fe(CO)_4$ and $Fe(CO)_3$(solv) in different solvent media. For a given solvent there is no significant difference between the vibrational relaxation time of $Fe(CO)_4$ and $Fe(CO)_3$(solv). The vibrational relaxation time increases in the order *n*-heptane < $scCH_4$ < scXe < scAr. It is interesting to note that there is relatively less $Fe(CO)_3$ produced in *n*-heptane, Table 1. The ratio of $^3Fe(CO)_4$:$Fe(CO)_3$ is 17:1 in heptane whereas it is only 5:1 in scXe, 4:1 in $scCH_4$, and 3:1 in scAr. Furthermore, we have performed additional ps-TRIR experiments in the more polar $scCO_2$, CH_3CN, and $scCHF_3$. However, there is no spectral evidence for the $Fe(CO)_3$ species in these solutions. Therefore, changes in polarity and/or density substantially influence the photochemistry of $Fe(CO)_5$.

solvent	Vibrational relaxation rate (s^{-1})	$Fe(CO)_4$: $Fe(CO)_3$
heptane	$1.0 \pm (0.2) \times 10^{11}$	17:1
scXe	$4.2 \pm (0.2) \times 10^{10}$	5:1
scAr	$1.5 \pm (0.2) \times 10^{10}$	3:1
$scCH_4$	$6.9 \pm (0.2) \times 10^{10}$	4:1

Table 1. Vibrational relaxation rates and intensity ratio of $Fe(CO)_4$: $Fe(CO)_3$ (at 100 ps) in the four solvents used in this paper. The ratio was calculated by the sum of two $^3Fe(CO)_4$ band intensities to the band intensity of $Fe(CO)_3$(solv).

We have also found that the lifetime of $Fe(CO)_3$(solv) in scAr (~ 300 ps) is at least one order of magnitude shorter than in the other three solvents. A simple assumption for such a phenomenon is that $Fe(CO)_3$ is coordinated to the solvent and the strength of the Fe-solvent bond increases in the order Ar << Xe/CH_4 < heptane. The long lifetime of $Fe(CO)_3$ in *n*-heptane, scXe, or $scCH_4$ strongly supports this assignment of $^1Fe(CO)_3$(heptane), $^1Fe(CO)_3$(Xe) and $^1Fe(CO)_3(CH_4)$. However, there is much less evidence for the coordination of Ar to $Fe(CO)_3$. The diffusion controlled rate in scAr under the conditions of this experiment is calculated to be 1.8×10^{11} $dm^3mol^{-1}s^{-1}$. The rate of decay of $Fe(CO)_3$ in scAr (k_{obs} = 3.8×10^9 s^{-1}) is x4 slower than the effect diffusion controlled rate given the concentration of CO used in these experiments. Therefore, it is more likely that the Ar has a weak coordination to naked $Fe(CO)_3$ in scAr solution.

Conclusions

The ps-TRIR study on the photochemistry of $Fe(CO)_5$ has offered valuable information on the formation and nature of the primary photoproducts, $^3Fe(CO)_4$ and $Fe(CO)_3$(heptane). By investigating the vibrational cooling and band intensities in conventional and supercritical solutions, we have found a significant effect from the solvent environment on the transient species.

References

1. F Asinger and O Berg
Chem. Ber., 88 445, (1955)
2. M S Sigman and B E Eaton
J. Am. Chem. Soc., 118 11783, (1996)
3. M Bergt, T Brixner, B Kiefer, M Strehle and G Gerber
J. Phys. Chem. A, 103 10381, (1999)
4. M Poliakoff and J J Turner
Angew. Chem., Int. Ed., 40 2809, (2001) and refs. therein
5. M Poliakoff and J J Turner
J. Chem. Soc., Dalton Trans., 1351, (1973)
6. M Poliakoff and J J Turner
J. Chem. Soc., Dalton Trans., 2276, (1974)
7. T J Barton, R Grinter, A J Thomson, B Davies and M Poliakoff
J. Chem. Soc., Chem. Commun., 841, (1977)
8. A J Ouderkirk, P Wermer, N L Schultz and E Weitz
J. Am. Chem. Soc., 105 3354, (1983)
9. T A Seder, A J Ouderkirk and E Weitz
J. Chem. Phys., 85 1977, (1986)
10. F W Grevels
NATO ASI Ser., Ser. C, 376 141, (1992)
11. V Bachler, F W Grevels, K Kerpen, G Olbrich and K Schaffner
Organometallics, 22 1696, (2003)
12. P T Snee, C K Payne, K T Kotz, H Yang and C B Harris
J. Am. Chem. Soc., 123 2255, (2001)
13. M Towrie, D C Grills, J Dyer, J A Weinstein, P Matousek, R Barton, P D Bailey, N Subramaniam, W M Kwok, C Ma,
D Phillips, A W Parker and M W George
Appl. Spectrosc., 57 367, (2003)
14. M Poliakoff
J. Chem. Soc., Dalton Trans., 210, (1974)
15. E Weitz
J. Phys. Chem., 91 3945, (1987)

Kerr gated fluorescence rejection to obtain *in-situ* resonance Raman spectra from charge transfer materials in light emitting polymer devices and from drugs of abuse

W E Smith, R E Littleford

Department of Pure and Applied Chemistry, University of Strathclyde, 295 Cathedral Street, Glasgow, G1 1XL, UK

G Dent

Avecia Ltd. Hexagon House, Blackley, Manchester, M9 8ZS, UK

P Matousek, M Towrie, A W Parker

Central Laser Facility, CCLRC Rutherford Appleton Laboratory, Chilton, Didcot, Oxon, OX11 0QX, UK

Main contact email address: *w.e.smith@strath.ac.uk*

Introduction

Light emitting polymers (LEPs) now form a key component of some projected new technology platforms. Examples include their use in flexible television screens and in large displays. One key problem that is not properly understood is the way in which these devices transfer electrons from the activating electrode through the charge transfer (CT) material to the LEP material. It is known that the transfer occurs through a coloured radical, but the mechanism for transfer through a thick film of polymer, which can either contain the material as part of the polymer structure or as crystal inclusions, is difficult to study *in-situ*. A schematic diagram of a typical LEP device is shown in Figure 1.

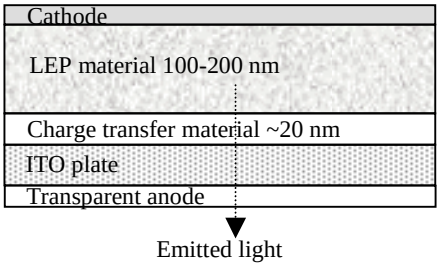

Figure 1. Cross section of a multilayer light emitting polymer device.

Initial studies of CT materials have been carried out using theoretical methods[1)]. Additionally, strong Raman scattering can be obtained from the radical generated in an OTTLE cell, indicating that the Raman spectrum of the radicals can be picked out from the matrix at very low concentrations due to the very large resonance enhancement[2)]. Further, the combination of the theoretical understanding with the informative Raman spectra provides information on the nature of the radicals present.

However, a major problem arises in detecting Raman scattering in the LEP device. In order to achieve resonance enhancement and therefore pick out the layers of material and the radical in-situ, it is necessary to use visible excitation. Although this is effective in solution, in the device the fluorescence from the LEP material masks the Raman spectrum from the radical and it is not possible to determine in-situ the properties of the CT material. This prevents visible Raman studies of the LEP material directly. With Kerr gated Raman fluorescence rejection, a completely unique and ideal probe to determine the nature and amount of the charge carriers is created, enabling all stages in the electron transfer in the functional device to be probed. In this initial study we concentrated on obtaining spectra from fluorescent black dyes and from the assembled device. The generation and detection of the radicals in the spectrometer will require further study using control circuitry.

During preliminary familiarization experiments, we were fortunate to be able to obtain street samples of drugs of abuse cut with various common cutting agents from the Police Scientific Development Branch of the Home Office. Since these samples are extremely difficult to obtain a short study was carried out and the samples immediately destroyed.

Results and Discussion

Two black dyes which fluoresce strongly were studied initially. The Kerr gating procedure removed the fluorescence and allowed the direct measurement of resonance Raman spectra from the double azo chromophores using different excitation frequencies. An example of the advantage of the Kerr gating technique is given in Figure 2.

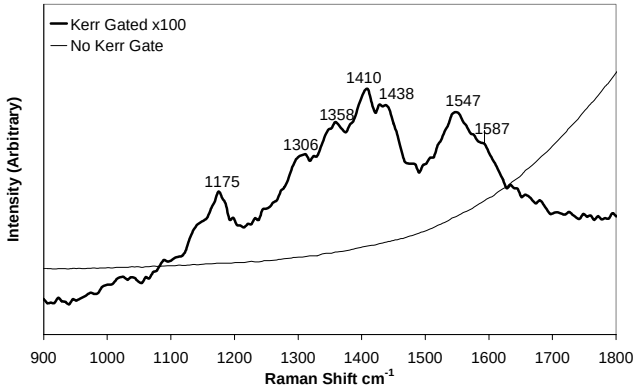

Figure 2. Comparison of Kerr gated and ungated Raman spectra from a black diazo inkjet dye.

This procedure enables the electronic nature of the chromophore to be probed. It was found that the chromophore involved an interaction between the two azos, and that one azo group was present in the azo and one in the hydrazo form. A previous attempt to investigate this by surface enhanced resonance Raman scattering (SERRS) had led to similar general conclusions[3)]. However, this method only detects molecules directly attached to a SERRS active surface such as aggregated silver colloid, and there are concerns that this will not give a true reflection of the nature of the chromophore. It was discovered that there were differences in the relative contributions of the two azos between the two techniques and the observation that the chromophores are linked requires the use of the Kerr gating technique. Thus, the Kerr gating study validates the qualitative use of SERRS but indicates that there are differences created by the nature of the SERRS procedure.

Some of the individual components of the LEP do not fluoresce strongly and consequently good spectra can be obtained both with and without Kerr gating. However, the device does fluoresce strongly and consequently no effective Raman spectra can be obtained, even with 785 nm excitation. Using Kerr gating and an excitation frequency of 400 nm clear Raman scattering, which was identified as arising from the charge transfer layer, was obtained. Figure 3 shows the difference between the normal Raman and the Kerr gated Raman spectra with this excitation frequency. This indicates that Kerr gating can be used to study these devices *in-situ*. It has the advantage that the technique is non-invasive, and with 400 nm excitation the coloured radicals which may form when the device is switched on should provide good resonance spectra, making the detection of small concentrations possible. However, the spectra show some evidence of sample burning. Further, in one widely used form of this device an additional dye coating is added. Attempts to run the spectra of this material were inhibited by additional burning of the sample. For full use of Kerr gating to study these devices, a spinning sample or rastered beam will be required together with control circuitry for the LEP.

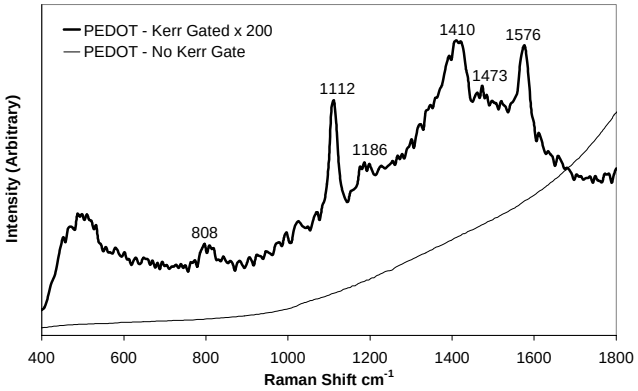

Figure 3. Comparison of Kerr gated and ungated Raman spectra from a charge transfer material *in-situ* in an LEP device.

Raman spectroscopy is known to be very effective for the identification of drugs of abuse since it provides sharp spectra from which specific molecules can be identified *in-situ* without separation procedures or sample contact or manipulation. However, while this has been clearly demonstrated on pure samples, the cutting agents in street samples usually cause extremely strong fluorescence preventing Raman spectra from being recorded. Kerr gated fluorescence rejection provides high quality signals, and Figure 4 shows the difference achieved with Kerr gating for a street sample of cocaine. These preliminary experiments show that Kerr gating could be of value for forensic analysis of 'real' samples of drugs.

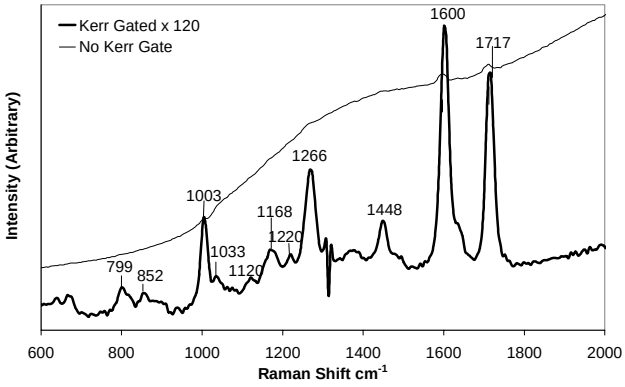

Figure 4. Comparison of Kerr gated and ungated Raman spectra from a street sample of cocaine hydrochloride.

Conclusions

Kerr gating proved extremely effective for the range of samples studied. It enables direct measurement of Raman spectra using frequencies which directly probe electronic transitions in fluorescing molecules, and provides an effective method for the study of *in-situ* properties of materials in a complete LEP device which has a high fluorescent background. The main disadvantages encountered are the high power and relatively long accumulation time. The sample burning which results from this in some cases is not too severe for most of the samples studied, indicating that it could be overcome by spinning the sample or rastering the beam. Additionally Kerr gating is effective in enabling the measurement of cocaine and amphetamine in street samples.

References

1. D. Tackley, University of Strathclyde, PhD Thesis, (2000)
2. R. E. Littleford, University of Strathclyde, Unpublished work, (2002)
3. R. E. Littleford, D. Tackely, M. P. Hughes, G. Dent and W. E. Smith, Applied Spectroscopy, Accepted for publication, (2003)

Photophysical primary processes of anhydrotetracycline in aqueous solution

S Schneider, M Schmitt, G Brehm, N Fritz

Institut für Physikalische und Theoretische Chemie, Friedrich-Alexander-Universität Erlangen-Nürnberg, D-91058 Erlangen, Germany

P Matousek, M Towrie

Central Laser Facility, CCLRC Rutherford Appleton Laboratory, Chilton, Didcot, Oxon, OX11 0QX, UK

Main contact email address: *schneider@chemie.uni-erlangen.de*

Introduction

Anhydrotetracycline (Scheme 1) is a common degradation product of the antibiotic tetracycline. Since it is hepatotoxic and phototoxic *in vivo*, it seems worthwhile to study its photophysics[1]. Anhydrotetracycline must be considered a three-protic acid with acidity constants $pK_{a1} \approx 3.93$ (O3H), $pK_{a2} \approx 5.94$ (O12H) and $pK_{a3} \approx 8.48$ ($CN4^+H$) (Scheme 2).

The UV/vis absorption spectra exhibit only moderate changes upon changing the state of protonation (Figure 1). The most pronounced change is observed upon deprotonation of the BCD chromophore ($AtcH_2^{\pm} \rightarrow AtcH^-$), whereas deprotonation of the groups connected to the A-ring chromophore cause only minor changes.

The fluorescence spectra of all four forms exhibit an unusually large Stokes shift (Figure 2) indicating either a large structural change in the first excited state (including excited state intramolecular proton transfer ESIPT) or even emission from a deprotonated species (just as in the "normal" tetracyclines [2]). Since in contrast to the red absorption maxima, the fluorescence maxima vary with the state of protonation, different relaxation processes should be dominating at different pH.

Because at intermediate pH, anhydrotetracycline exists as a mixture of differently protonated forms, we restricted our time-resolved measurements to pH 2 and pH 11, where only one tautomeric form should prevail.

Materials and Methods

Anhydrotetracycline (Acros, Belgium) and solvents were used as supplied by the manufacturers. After dissolution in H_2O, 0.1M HCl or 0.1M NaOH were added until pH 2 or pH 11 was reached.

The experimental setup employed for monitoring the time- resolved emission spectra and the transient absorption spectra is described in detail elsewhere[3,4]. The concentration of anhydrotetracycline was about $1\text{-}3 \cdot 10^{-4}$M for fluorescence and absorption measurements.

In order to improve the S/N ratio of the displayed Optical Density Change (ΔOD) spectra, we employed the technique of single value decomposition (SVD) [5].

Results and Discussion

The fluorescence spectrum of $AtcH_3^+$ appears quasi instantaneously and seems to decay without much change of the spectral distribution in a biphasic manner (Figure 3). The fast decay time is on the order of 60ps, the slower one about 550ps.

In contrast to the time-resolved emission spectra, the spectral distribution of the transient absorption spectra changes extensively with the delay time of the probe light and with the pump wavelength chosen (Figures 4,5).

With λ_{pu} = 266 nm several isosbestic points are observed thus indicating that the spectral distributions of the absorbing and emitting species do not change in time (Figure 4). Noteworthy is the negative ΔOD for $\lambda_{pr} \geq 600$ nm, which must be due to stimulated emission (note that the steady state fluorescence spectrum extends beyond 700 nm). Taking into consideration

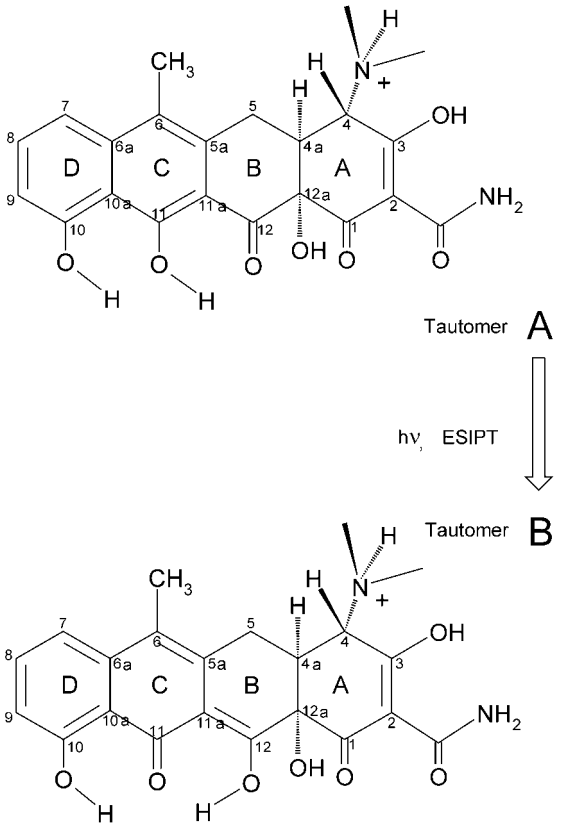

Scheme 1. Chemical structures and numbering of atoms of possible tautomers of protonated anhydrotetracycline ($AtcH_3^+$).

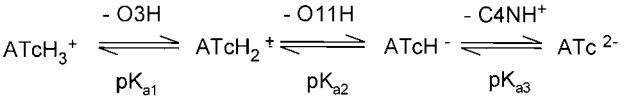

Scheme 2. Protonation / deprotonation eqilibria.

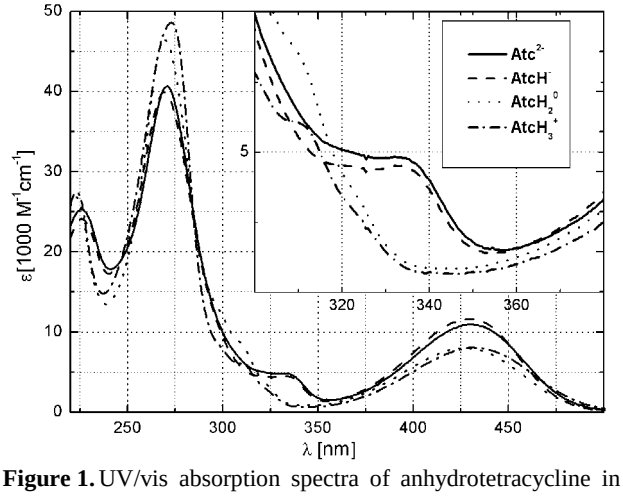

Figure 1. UV/vis absorption spectra of anhydrotetracycline in different states of protonation (see also Scheme 2).

that the emission maximum is found around 580 nm, one must conclude that there is a very strong excited state absorption between 525 and 625 nm. At first glance it is also surprising that one does not observe a significant bleaching for wavelength $\lambda \leq 470$ nm where the "red" absorption band of $AtcH_3^+$ starts. According to an analysis of absorption pH titration experiments, one must assume that with λ_{ex} = 266 nm, the A-chromophore is excited in addition. If its excited state absorption cross section is higher than that of the ground state around 440 nm, then a positive ΔOD will be generated. Also, one must conclude that relaxation of the excited A-chromophore leads, within our experimental time resolution, to one and only one species.

The expected bleaching of the ground state absorption is observed with λ_{pu} = 400 nm implying that the excited state absorption of the BCD chromophore is lower than that of the S0 → S1 transition (Figure 5). The bleaching around 450 nm indicates excited state reaction(s) by which one (or more) species are generated with an absorption cross section similar to that of the electronic ground state. The photolytically created species must possess a high absorption cross section in the wavelength range from 500 nm to 600 nm, because the contribution of stimulated emission is overcompensated. The negative ΔOD above $\lambda \approx 600$ nm can again be attributed to stimulated emission as discussed above for λ_{pu} = 266 nm. It is interesting to note that for longer delay times, there seems to exist an isosbestic point around 595 nm. This could mean that due to excited state relaxation, the same emitting species is formed as upon excitation at λ_{pu} = 266 nm. The signal around 650 nm decays approximately monoexponentially with decay times of 39 ± 10 ps (λ_{pu} = 400 nm) and 48 ± 1 ps (λ_{pu} = 266 nm).

The latter decay time is also derived from the monoexponential fits of the fluorescence signals recorded between 550 nm and 650 nm thus providing additional evidence that the transient absorption monitored there originates exclusively from the emitting species.

Relaxation of the excited BCD-chromophore leads obviously to two different product states. One is the same as that observed for λ_{pu} = 266 nm, the decay times derived from both fluorescence and transient absorption being roughly 50 ps. The long-lived component in the fluorescence decay is in accordance with the fact that there is a non-negligible ΔOD for delay times greater than 150 ps.

As in the case of pH 2, we find fundamentally different ΔOD spectra at pH 11 for pump wavelength λ_{pu} = 266 nm and λ_{pu} = 400 nm (Figures 6 and 7). Again, a significant bleaching of the ground state absorption is observed for λ_{pu} = 400 nm only. However, no isosbestic points are found for either pump wavelength.

Another immediately apparent difference of the ΔOD spectra recorded for the anhydrotetracycline dianion, Atc^{2-}, versus those of $AtcH_3^+$ is the shift of the minimum around 600 nm with delay time. As a consequence, the signal decay time varies between 100 and 110 ps (for both pump wavelengths) but matches roughly the dominant decay time found for signals around 500 nm. Common to both sets of spectra is the shift of the zero crossing to longer wavelength which is in accord with the assumption that the spectral distribution of the induced absorption is fairly independent of delay time, whereas the fluorescence profile shifts in time.

It is generally assumed that tautomer A corresponds to the predominant form of $AtcH_3^+$ (and $AtcH_2^0$). In the lowest excited state (excitation of the BCD-chromophore) intramolecular proton transfer could yield the excited state of tautomer B (Scheme 1). Alternatively, the compound could release either O11H or O10H (deprotonation).

In the dianion, the only proton left to undergo a transfer in the electronically excited state is O10H. This, together with the postulated change in conformation of the dianion, could explain, why the Stokes shift of the dianion is so different and also the lifetime of the predominant emitting state.

Further evidence for the proposed relaxation processes is expected from quantum chemical calculations which proved quite informative in case of "normal" tetracycline[2].

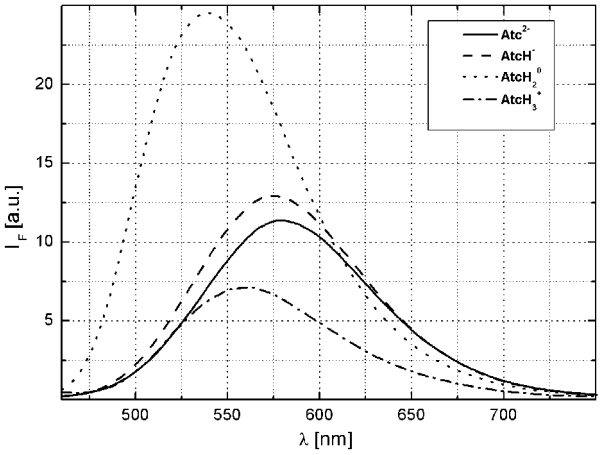

Figure 2. Steady state fluorescence spectra of anhydrotetracycline in different states of protonation (λ_{ex} = 440 nm).

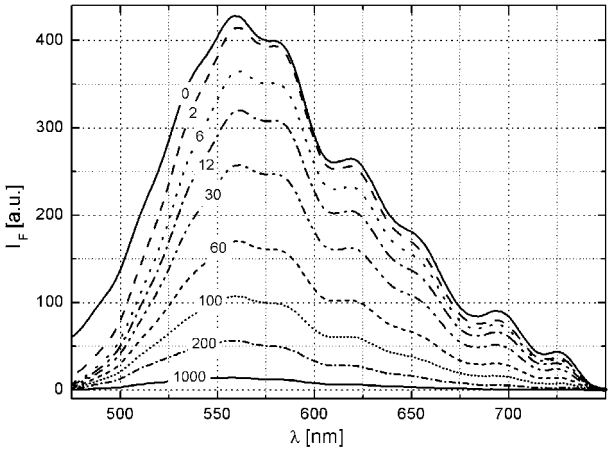

Figure 3. Time-resolved emission spectra of anhydrotetracycline in acidified H_2O (pH 2: $AtcH_3^+$); λ_{ex} = 390 nm, delay times in ps.

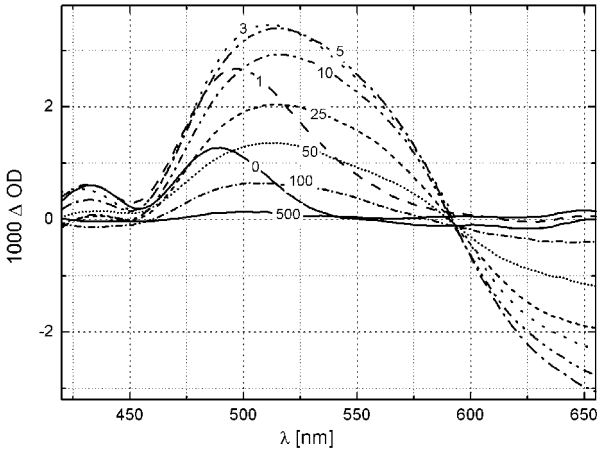

Figure 4. Transient absorption spectra of anhydrotetracycline in acidified H_2O (pH 2: $AtcH_3^+$); λ_{pu} = 266 nm, delay times in ps.

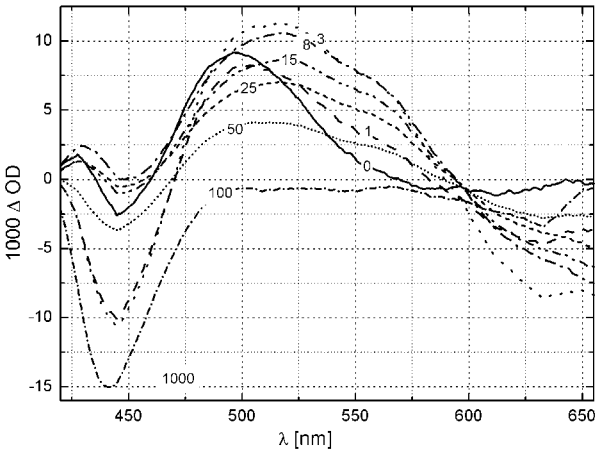

Figure 5. Transient absorption spectra of anhydrotetracycline in acidified H_2O (pH 2: $AtcH_3^+$); λ_{pu} = 400 nm, delay times in ps.

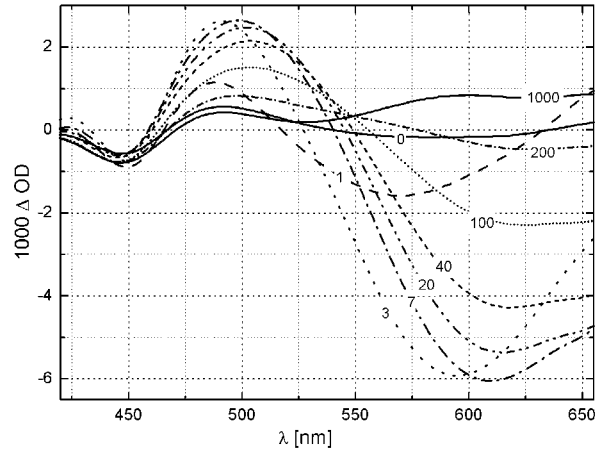

Figure 6. Transient absorption spectra of anhydrotetracycline in alkaline H_2O (pH 11: $AtcH^{2-}$); λ_{pu} = 266 nm, delay times in ps.

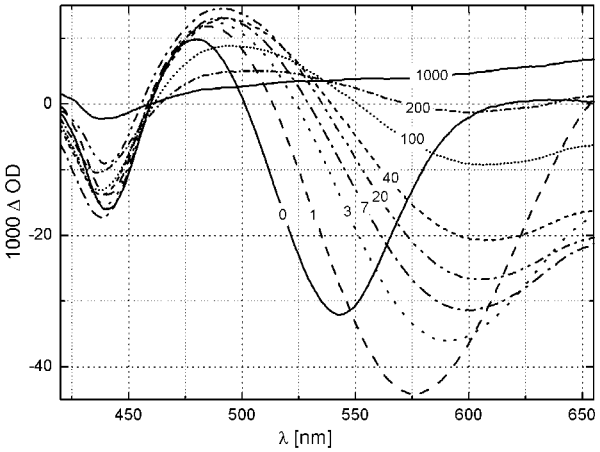

Figure 7. Transient absorption spectra of anhydrotetracycline in alkaline H_2O (pH 11: $AtcH^{2-}$); λ_{pu} = 400 nm, delay times in ps.

References

1. Tetracyclines in Biology, Chemistry and Medicine, ed. R.A. Greenwald, W. Hillen and M. Nelson, Birkhäuser, Basel, Switzerland, 2001.
2. S. Schneider, G. Brehm, P. Matousek, M. Reiher, M.O. Schmitt and M. Towrie, Fluorescence kinetics of aqueous solutions of tetracycline and its complexes with Mg2+ and Ca2+, Photochem. Photobiol. Sciences, submitted for publication.
3. P.Matousek, M.Towrie, C.Ma, W.M.Kwok, D.Phillips, W.T.Toner, A.W.Parker, J. Raman Spectrosc., 32 983 (2001).
4. M.Towrie, P.Matousek, A.W.Parker, S.Jackson, Dual Diode Array System for Transient Absorption Spectroscopy, Annual Report of the Central Laser Facility, RAL-TR-1998-080, 183, (1998).
5. H. Gampp, M. Maeder, C.J. Meyer and A.D. Zuberbühler, Talanta,, 33, 943 (1986).

Studies of the S_1 state in a prototypical molecular wire using picosecond time-resolved spectroscopies

A Beeby, K Findlay, P J Low, T B Marder, S R Rutter

Department of Chemistry, University of Durham, South Road, Durham, DH1 3LE, UK

P Matousek, A W Parker, M Towrie

Central Laser Facility, CCLRC, Rutherford Appleton Laboratory, Chilton, Didcot, Oxon, OX11 0QX, UK

Main contact e-mail address: *andrew.beeby@durham.ac.uk*

Introduction

Materials based upon the phenylene(ethynylene) skeleton are currently of great interest[1]. The fluorescent and electroluminescent properties of both molecular and polymeric systems has prompted speculation about the suitability of these materials as the emitting layer in electroluminescent-devices[2], while the conjugated π-system has led to the development of molecular wire-like architectures[3] , and materials which display negative differential resistance[4]. STM experiments on derivatives of 1,4-bis(phenylethynyl)benzene, **1**, embedded in an alkyl thiol self-assembled monolayer are consistent with the concept of substantial "through molecule" conductance which can be influenced by the potential applied by the STM tip[5,6] .

The origin of many of these fascinating properties can be attributed to their extended linear π-systems, and consequently to the relative intramolecular orientation of the aromatic rings. However, the barrier to rotation about the alkyne-arene single bond in the ground state is low, leading to relatively free rotation about this bond, unless the molecular motion is restricted by environment such as in an ordered monolayer or polymer matrix[7]. Thus, engineering control over the molecular conformation in materials derived from **1** is a formidable challenge. Photo-excitation may offer one avenue for *transient* control over the confirmation of the molecular skeleton, although there is little information available regarding the nature of the molecular and electronic structure of the excited states of these materials[8,9].

The excited states of oligoaryleneethynylenes are not well modelled by the 2-ring system, diphenylacetylene, DPA which is unusual in that the S_1 and S_2 excited states are very close lying, with fluorescence occurring only from the higher state. Picosecond-CARS studies reveal that the S_1 and S_2 states of DPA have markedly different structures, with the higher state having a linear, acetylenic type structure, and the lower state a bent conformation with a substantially weakened C≡C link. In contrast, **1** behaves in a similar manner to the oligomers and is chosen as a model system to study the excited state behaviour of this family of materials. The compound has strong absorption bands in the UV region arising from π-π* transitions, is highly fluorescent, and offers characteristic vibrational modes with which to probe the molecular structure in detail. We have recently established that **1** behaves according to Kasha's rule, undergoing excitation to a vibrationally excited Franck-Condon state, before rapid relaxation to the lowest vibrational level of the S_1 state and subsequent emission and/or non-radiative decay[10]. Based upon quantum mechanical calculations, it has been stated that the electronic and molecular structure of the S_1 states of poly (phenyleneethynylene)s are strongly influenced by quinoidal and cumulenic contributions[8]. However, we are unaware of any conclusive experimental evidence to support this hypothesis.

We have carried out time-resolved fluorescence, transient absorption and vibrational spectroscopic studies on the picosecond timescale in order to characterise more fully the S_1 state of **1**, and related aryleneethynylenes **2** and **3**, see Figure 1. Importantly, our results demonstrate that there is no significant cumulenic or quinoidal character in the S_1 state of these compounds, but that the excited state still shows triple-bond character.

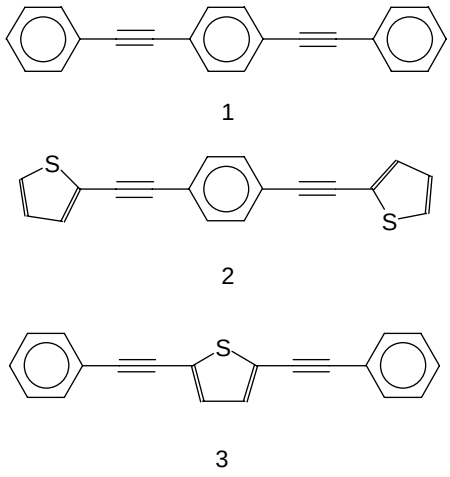

Figure 1. Molecular structures of interest.

Results and Discussion

The time-resolved emission spectrum of **1** in cyclohexane solution was recorded using a Kerr-gate fluorescence spectrometer with a time resolution of 2 ps FWHM[11]. A number of emission spectra were recorded over a range of time delays following excitation at 267 nm. Intriguingly there is a subtle change in the emission spectra, which is particularly pronounced at the blue edge of the spectrum at short time intervals, <50 ps. At longer time intervals, the spectral profile remains constant, decaying with a fluorescence lifetime of 530 ps. The changes in the spectra are more pronounced when the spectra are normalised in the range 370-450 nm as illustrated in Figure 2.

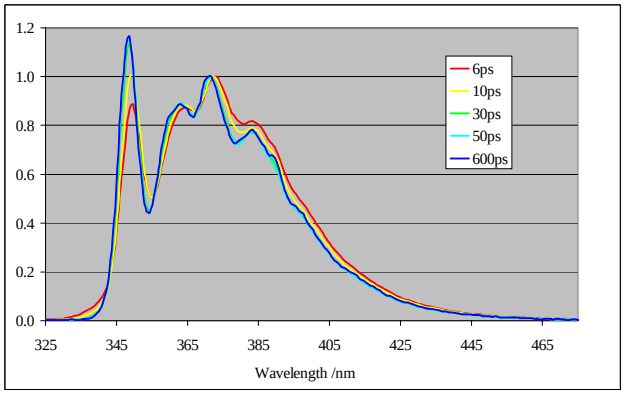

Figure 2. Normalised time-resolved emission spectra of 1 in cyclohexane, λ_{ex} = 267nm, recorded using Kerr-gate spectrometer.

In fluid solution at ambient temperature **1** exists as a continuous distribution of rotational isomers due to free rotation about the sp^2-sp bonds[10,11]. The changes in the emission spectra at short time intervals are attributed to the reorientation and relaxation of the Franck-Condon states to the lowest energy vibrational

and torsional levels of the S_1 state, which has a more static molecular geometry than the ground state at ambient temperature, over tens of picoseconds. Similar observations have been reported for the time resolved emission spectra of oligoarylenethynylenes[8]. However, whilst the fluorescence data supports the concept of re-orientation of the Franck-Condon states, they yield no detailed structural information relating to the bond-order of the arylene-ethynylene skeleton in the excited state. Resonance Raman spectroscopy yields structural information about the chromophore and, coupled with time-resolved techniques, allows a more detailed investigation of the structure of the excited singlet state.

In order to establish the optimum wavelength for time-resolved resonance Raman spectra the $S_n \leftarrow S_1$ transient absorption spectra of **1** in cyclohexane solution were recorded by ultra-fast pump-probe spectroscopy[12]. The spectra were collected from samples excited at 267 nm and probed in the range 450-700 nm. At early time intervals after excitation the transient absorption shows a strong band centred at 625 nm, which increased in intensity by ca. 20% and shifted to 620 nm over a 50 ps period, after which the absorption band decayed with a lifetime similar to the fluorescence lifetime.

The ps time resolved resonance Raman spectra of the S_1 state of **1, 2** and **3** were obtained by pumping at 267nm and probing at 588 nm, i.e. to the blue of the transient absorption band. Fluorescence from the samples was rejected using the Kerr-gate[13]. The TR^3 spectra also showed subtle, but distinct, changes during the first 50 ps following excitation. The resonance Raman spectrum of the S_1 state of **1** shows distinct bands at 2128, 1588, 1138 and 999 cm^{-1} (Figure 3). The intensity of all of the bands increased by ca. 20-25% over the first 50 ps. This observation may be due to reorientation within the excited state changing the electronic structure and Raman excitation profiles. Hence, the Raman cross-sections may be dynamic shortly after excitation. After this initial rapid change the TR^3 signal decayed with a lifetime matching that of the singlet excited state.

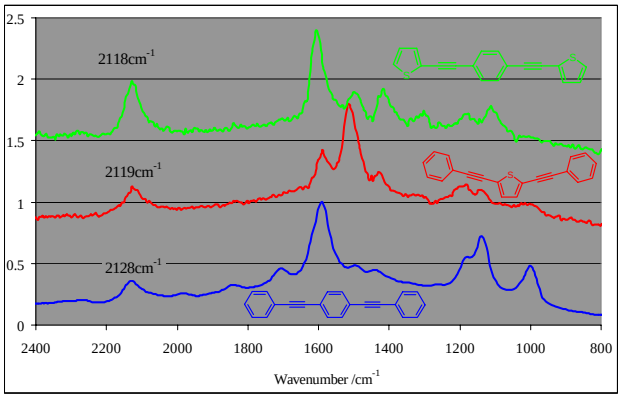

Figure 3. The resonance Raman spectrum of the S_1 state of **1**, **2** and **3** 50ps after pump =267nm, probe =588nm.

It is interesting to note that both compounds **1** and **2**, which have a common 1,4-bis(ethynyl)benzene core show similar bands at 1598cm^{-1}.

The non-resonance Raman spectrum of the ground electronic state of **1**, in dilute cyclohexane solution, shows the presence of three major bands centred at 2217, 1598 and 1132 cm^{-1}. The highest wavenumber band is clearly associated with the localised vibrational motion of the acetylene groups, whilst that at ca. 1600 cm^{-1} is assigned to the symmetric stretch of all three aromatic rings along the molecule's long axis[14]. In the excited state, the S_1 chromophore shows similar vibrational bands, indicating that there is little change in the bonding upon electronic excitation. The decrease in the frequency of the ν(C≡C) band to 2128 cm^{-1} is indicative of a small reduction in the bond strength of the acetylene moiety in the ground state. The shift of the acetylene band by ca. 90 cm^{-1} upon excitation is consistent with observations made by Ishibashi and Hamaguchi who determined the Raman bands for the ground and S_2 excited states of DPA to be 2217 and 2099 cm^{-1} respectively.[9] Whilst this 118 cm^{-1} shift to lower wavenumber represents a weakening of the C≡C central bond in the S_2 state the authors concluded that the bond order was still "triple" and that the excited molecule is linear.

Significantly the spectrum of the S_1 state of these compounds does not indicate the presence of a cumulenic/quinoidal structure, which would be expected[15] to show a strong band near 2000 cm^{-1}. Butatriene derivatives exhibit intense Raman bands at ca. 2040 cm^{-1} assigned to the symmetrical stretching vibration of the >C=C=C=C< linkage[15]. Furthermore, it was found that extended conjugation leads to a further lowering of ν(C=C=C=C) in the Raman spectrum[15] .

Conclusions

The observation of significant acetylenic character in the S_1 state is not inconsistent with the molecular orbital structure of **1** and related compounds [6c]. The HOMO in **1**, whilst sensitive to the precise molecular geometry, is calculated to be essentially delocalised over the molecule, with bonding character between the carbon atoms of the acetylenes, and anti-bonding with respect to the C(sp)-C(sp^2) bonds, whilst the reverse is true of the LUMO. Given the large number of lower lying occupied orbitals which contribute to the acetylenic and aromatic sub-structure of the molecule, it is perhaps not surprising that promotion of a single electron from the HOMO to LUMO does not bring about a significant change in the bond order of the acetylene. Work with conformationally restricted systems, and those containing electron donors and acceptors, is currently underway to further investigate the electronic structure and properties of this intriguing class of compounds.

References

1. (a) U.H.F. Bunz, Chem. Rev., 100, 1605, 2000; (b) U.H.F. Bunz, Y. Rubin, Y. Tobe, Chem. Soc. Rev., 28, 107, 1999; (c) P.F.H. Schwab, M.D. Levin, J. Michl, Chem. Rev., 99, 1863, 1999.

2. I.K. Spiliopoulos and J.A. Mikroyannisis, J. Polym. Sci. A, Polym. Chem., 40, 2591, 2002; S. Anderson, Chem. Eur. J., 7, 4706, 2001; E. Arias-Marin, J.C. Arnault, D. Guillon, T. Maillou, J. Le Moigne, B. Geffroy and J.M. Nunzi, Langmuir, 16, 4309, 2000.

3. C. Hortholary and C. Coudret, J. Org. Chem., 68, 2167, 2003; J.-S. Yang and T.J. Swager, J. Am. Chem. Soc., 120, 11864, 1998; C.R. Hess, G.A. Juda, D.M. Dooley, R.N. Amii, M.G. Hill, J.R. Winkler and M.B. Grey, J. Am. Chem. Soc., 125, 7156, 2003.

4. K. Stokbro, J. Taylor and M. Brandbyge, J. Am. Chem. Soc., 125, 3674, 2003; J. Cornil, Y. Karzazi and J.L. Bredas, J. Am. Chem. Soc., 124, 3516, 2002.

5. L.A. Bumm, J.J. Arnold, M.T. Cygan, T.D. Dunbar, T.P. Burgin, L. Jones, D.L. Allara, J.M. Tour and P.S. Weiss, Science, 271, 1705, 1996.

6. J.M. Seminario, P.A. Derosa and J. L. Bastos, J. Am. Chem. Soc, 124, 10266., 2002; Z.J. Donhauser, B.A. Mantooth, K.F. Kelly, L.A. Bumm, J.D. Monnell, J.J. Stapleton, D.W. Price Jr., A.M. Rawlett, D.L. Allara, J.M. Tour and P.S. Weiss, Science, 292, 2303, 2001.

7. J. Kim, I.A. Levitsky, D.T. McQuade and T.M. Swager, J. Am. Chem. Soc, 124, 7710., 2002; J. Kim and T.M. Swager, Nature, 411, 1030, 2001; W.A. Reinerth, L. Jones II, T.P. Burgin, C. Zhou, C.J. Muller, M.R. Deshpande, M.A. Reed and J.M. Tour, Nanotechnology, 9, 246, 1998.

8. M.I. Sluch, A. Godt, U.H.F. Bunz and M.A. Berg, J. Am. Chem. Soc, 123, 6447., 2001.

9. S.A. McFarland and N.S. Finney, J. Am. Chem. Soc, 124, 1178., 2002; T.Ishibashi and H. Hamaguchi, J. Phys. Chem. A, 102, 2263, 1998; T. Ishibashi, H. Okamoto and H. Hamaguchi, Chem. Phys. Lett., 325, 212, 2000; Y. Hirata, Bull. Chem. Soc. Jpn., 72, 1647, 1999.

10. A. Beeby, K. Findlay, P.J. Low and T.B. Marder, J. Am. Chem. Soc., 124, 8280, 2002.

11. M. Levitus, K. Schmieder,H. Ricks, K.D. Shimizu, U.H.F. Bunz and M. Garcia-Garibay, J. Am. Chem. Soc, 124, 8181, 2002.

12. C. Ma, W. M. Kwok, P. Matousek, A.W. Parker, D. Phillips, W.T. Toner and M. Towrie, J. Phys. Chem. A, 106, 3294, 2002.

13. P. Matousek, M. Towrie, C. Ma, W. M. Kwok, D. Phillips, W. T. Toner and A. W. Parker, J.Raman Spectroscopy, 32, 983, 2001.

14. Z. Chenia, T. Livneh, I. Pro-Bar, and J.E. Koresh, Vibr. Spectrosc., 25, 119, 2001.

15. M. Kijima, I. Kinohita and H. Shirakawa, Synth. Metals, 101, 145, 1999.

Mapping vibrational relaxation in a Donor-Acceptor complex

A C Benniston

Molecular Photonics Laboratory, School of Natural Sciences (Chemistry), University of Newcastle, Newcastle upon Tyne, NE1 7RU, UK

P Matousek, A W Parker, M Towrie

Central Laser Facility, CCLRC Rutherford Appleton Laboratory, Chilton, Didcot, Oxon, OX11 0QX, UK

Main contact email address: *A.C.Benniston@ncl.ac.uk*

Introduction

Supramolecular and molecular-scale model systems have been vital in testing parameters associated with electron transfer[1]. There have been numerous elegant model systems prepared to test, for example, superexchange theory[2], quantify through-space electronic coupling[3], parameterize electron transfer distance dependence[4], and quantify solvent contributions to electron migration[5] . One pertinent parameter associated with charge migration is the vibrational reorganization of molecular components as they distort to support charge separation and redistribute excess energy. Resonance Raman (rR) spectroscopy has been shown to be a powerful tool in enumerating this parameter and has been widely applied to many systems. In all cases it is worth noting that vibrational reorganization analysis has been applied to ground-state rR spectra for a charge-transfer transition. Time-resolved rR spectroscopy on the other hand offers the opportunity of 'watching' directly where energy is distributed within a system, and more importantly mapping precisely structural reorganization and environmental effects[6] . Hence, we have attempted to quantify structural reorganization using picosecond time-resolved rR spectroscopy, which allows the collection of vibrational information on fast time scales. An intimate cyclophane-based electron donor-acceptor (EDA) complex has been identified as candidate to follow structural reorganization, since excitation is accompanied by charge-separation and molecular rearrangement. The results collected on an EDA complex (Figure 1) are reported as our first attempt to map vibrational relaxation.

Picosecond Time-Resolved Resonance Raman Studies

ps-TR^3 experiments were performed on equimolar solutions of **DBC8** and $\mathbf{MV^{2+}}$ at a total concentration of *ca* 30 mmols. At this concentration the complex exists in the 1:1 form, which simplifies interpretation of the spectroscopic data. Direct selective illumination into the CT absorption band of **1** with a 1ps (fwhm) laser pulse at λ_{exc} = 400 nm resulted in the creation of an intimate radical ion pair (RIP) in unitary quantum yield. This highly energetic and unstable species is created by injection of an electron from the polycycle catecholate group into the π-orbital of an adjacent N,N'-bipyridinium unit. Comparable behavior has been documented in analogous CT complexes fashioned using the more rigid N,N'-bipyridinium-based cyclophane first prepared by Stoddart et al. and 1,4-disubstituted electron-donor aromatics. The transient rR signals of the RIP were monitored at λ_{prob} = 610nm where an absorption profile is located, which is unique to the mono-reduced bipyridinium π-radical cation. Illustrated in Figure 2 are the transient rR bands collected for the complex in acetone at two different time delays. At the very early time delay four distinctive rR signals are visible and are unequivocally assigned to vibrational bands associated with the $MV^{+\cdot}$ radical cation. The disappearance of the main vibrational band (1528 cm^{-1}) was fitted to two exponentials affording decay lifetimes of τ_1 = 3(±1) ps and τ_2 = 69 (±1) ps, respectively. By comparison with related systems studied to date the fast component is attributed to the rate of direct charge recombination within a highly compact RIP, whereas the slower component, which constitutes *ca.* 7% to the overall decay, is charge recombination/separation from a different RIP conformer. Considering the flexibility of the crown polycycle this second conformer is presumably more open, with the mono-reduced N,N'-bipyridinium group emerged from the cavity.

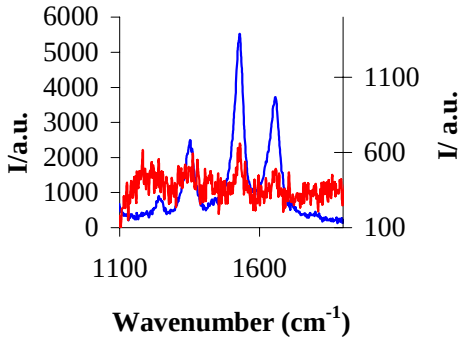

Figure 2. Time-resolved resonance Raman bands collected on 1 in acetone at (a) 1ps and (b) 100ps.

Vibrational cooling of the initially generated RIP was clearly evident by monitoring the change with time of the half-height peak width for the band located at 1528cm^{-1}. Illustrated in Figure 3 (next page) is the relevant plot for data collected in acetone and the highly polar solvent mixture of CH_3CN/H_2O (1:1). In this later solvent mixture vibrational cooling mirrors closely the rate of decay of the RIP. In contrast, in acetone the half width remains relatively constant over ~20ps and it is

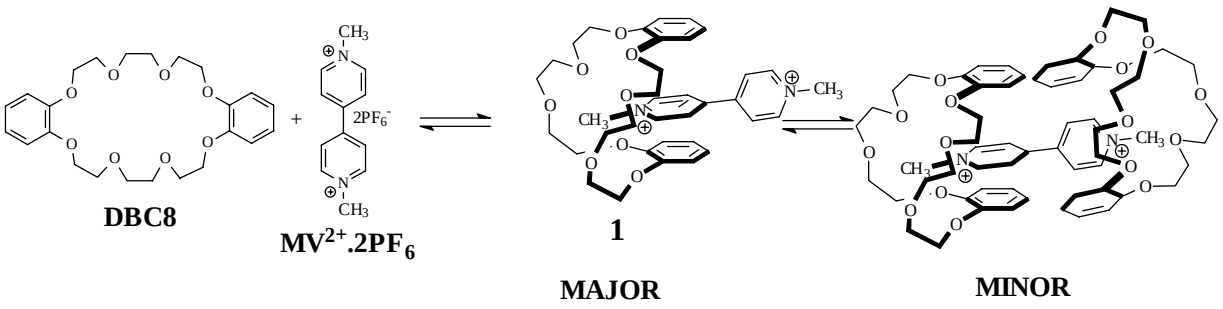

Figure 1. Illustration of the CT complex studied by ps-TR^3 spectroscopy.

hypothesized that this is indicative of $MV^{+\cdot}$ still trapped in the crown ether cage. At the much longer time scale the peak width is dramatically reduced, and corresponds to the solvated radical ion cation generated following its escape from the crown polycycle. A reasonable reason for this difference in behavior of **1** in these two solvents is that the structure of the EDA complex is different.

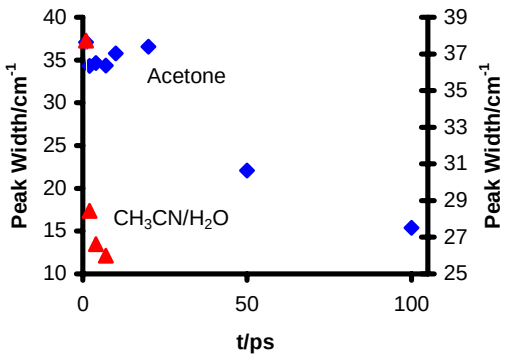

Figure 3. Change in half-height peak width of the resonance Raman band (1538cm^{-1}) with time following excitation.

Conclusions

Picosecond time-resolved resonance Raman spectroscopy is a powerful tool for probing vibrational bands associated with compact EDA complexes. From the onset we were particularly trying to see if Raman bands for $MV^{+\cdot}$ would be sensitive to the local environment. However, for the EDA system **1** there were no observable shifts in Raman bands for $MV^{+\cdot}$ when in the complex or when free in solution. This is somewhat disappointing since in other studies using DNA intercalator complexes Raman bands have been shown to be sensitive to the surrounding medium. It is noted that complex **1** is not as compact as one would like, since the structure is fairly open, and is one feasible reason why we do not see any shifts in the Raman bands. Because of the high quality and simplicity of the Raman spectrum obtained for $MV^{+\cdot}$ we have been able to map environmental effects by monitoring line-narrowing over time. Future work will concentrate on more structurally rigid and highly compact EDA complexes where π-overlap is enhanced and compression between donor-acceptor groups is greatly increased. These results will be reported at a later date where more comparisons will be possible and a clearer picture in this electron transfer topic will unfold.

Acknowledgements

This work was supported by the University of Newcastle and the EPSRC (GR/29109).

References

1. M. R. Wasielewski, Chem. Rev. 92, 435, (1992).
2. A. S. Lukas, P. J. Bushard, and M. R. Wasielewski, J. Am. Chem. Soc. 106, 2074, (2002).
3. D. Gostztola, B. Wang, and M. R. Wasielewski, J. Photochem. Photobiol. A., 102, 71, (1996).
4. J-P Launay, Chem. Soc. Rev. 386, (2001).
5. S. M. Napper, I. Read, R. Kaplan, M. B. Zimmt and D. H. Waldeck, J. Phys. Chem. A. 123, 5684, (2001).
6. S. Nakashima, S. Taniguchi, T. Okada, A. Osuka, Y. Mizutani, T. Kitagawa, J. Phys. Chem. 103, 9184, (1999).

Picosecond TR^3 and TRL studies on homoleptic Ru(II) Polypyridyl Species: Isotope dependence of early excited state processes

C G Coates, C Brady, J J McGarvey, W R Browne

School of Chemistry, The Queen's University Belfast, Belfast, BT9 5AG, Northern Ireland, UK

J G Vos

National Centre for Sensor Research, School of Chemical Sciences, Dublin City University, Dublin 9, Ireland

M Towrie, S W Botchway, A W Parker

Central Laser Facility, CCLRC Rutherford Appleton Laboratory, Chilton, Didcot, Oxon, OX11 0QX, UK

Main email contact address: *j.mcgarvey@qub.ac.uk*

Detailed investigations by picosecond time-resolved resonance Raman spectroscopy of ruthenium complexes containing the DNA-intercalating ligand, dipyridophenazine (dppz, Figure 1) have been carried out during previous visits to the Ultrafast Spectroscopy Laboratory[1)]. As a complement to these, the excited state properties of the transition metal complexes tris(2,2'-bipyridine) ruthenium(II) and tris(4,7-diphenyl-1,10-phenanthroline) ruthenium(II) and of their predeuteriated analogues were examined using picosecond time resolved luminescence spectroscopy (ps-trl). As is well known, these compounds emit at room temperature from a long-lived triplet metal-to-ligand-charge transfer state (^{3}MLCT) that is populated from higher energy excited states. The photophysical behaviour of the emitting triplet state is well understood, but much less is known about the events which lead to its formation.

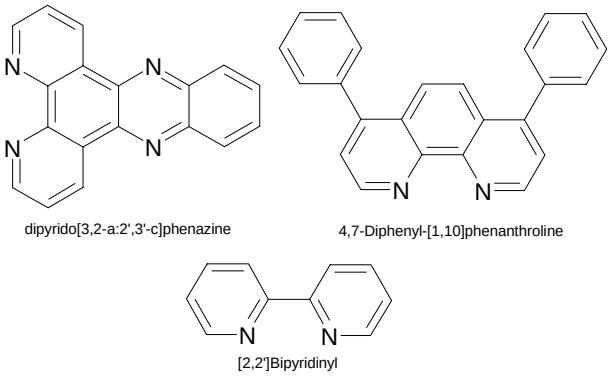

Figure 1. Ligand Structures.

Picosecond TRL Spectroscopic studies of Ru(II) Polypyridyl complexes

For both complexes, direct observation of a short-lived 520 nm emission with a lifetime of less than 4 ps was observed. Upon deuteriation of the complexes the lifetime of the 520 nm emission showed a marked increase with a biexponential decay (~20 ps and ~300 ps components, as exemplified for the tris(2,2'-bipyridine) ruthenium(II) complex in Figure 2).

The decays are clearly non-exponential and although the number of data points available precludes an accurate fitting, estimates of emission lifetimes can still be made. The emission signal decays in < 4 ps for the perprotio complex, but for $[Ru([D_8\text{-bpy})_3]^{2+}$ a process with a time constant of some 15 ps is followed by a slower process (τ > 200 ps). Analogous results were obtained for the H_{16} and D_{14} isotopologues of tris(4,7-diphenyl-1,10-phenanthroline) ruthenium(II) and for both sets of complexes, the findings were confirmed from a parallel range of studies on their respective hexafluorophosphate salts in acetonitrile. It is interesting to consider the significant effect of deuteriation on the decay rate of the 520 nm emission alongside the recent studies of Bhasikuttan et al.[2)] using fluorescence upconversion spectroscopy who also reported a very weak emission from $[Ru([H_8\text{-bpy})_3]^{2+}$ at 520 nm which they discussed in terms of fast ISC from ^{1}MLCT states to a vibrationally hot, emissive ^{3}MLCT state, followed by vibrational cooling of the latter on a timescale of 600 fs to 1 ps. However, the increase in emission lifetime from less than 3 ps to over 200 ps upon deuteriation, reported in the present work does not seem to support this hypothesis. Instead, we suggest that the 520 nm emission may be assigned, tentatively, as ^{1}MLCT in origin rather than being from vibrationally hot triplet states.

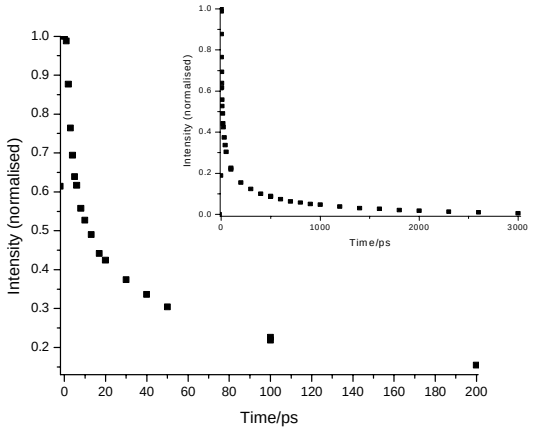

Figure 2. Normalized luminescence decay trace of $[Ru([D_8]\text{-bpy})_3]^{2+}$ in H_2O between 0 and 210 ps. λ_{exc} 410 nm, λ_{em} 510 to 545 nm (inset 0 to 3000 ps).

Picosecond TR^3 Spectroscopic studies of Ru(II) Polypyridyl complexes

To try to provide additional insight, picosecond time resolved resonance Raman (ps-TR^3) investigations of the various systems are also being carried out and some of the initial findings are presented here. For $[Ru([H_8\text{-bpy})_3]^{2+}$ the grow-in of the ^{3}MLCT state can be monitored by the prominent feature at 1506 cm^{-1} (Figure 3), readily assignable to a skeletal mode of the bpy ligand on the basis of the well-known excited state resonance Raman studies of Kincaid et al[3)] . It is evident that the risetime lies within the cross-correlation time of the laser pulse. For the perdeuterio complex, the grow-in of the counterpart feature[3)] at 1472 cm^{-1} of the ^{3}MLCT state (Figure 4) occurs over 10-20 ps. Notably, there is evidence in these traces also of what appears to be a parallel decay on the same 10-20 ps timescale of a distinct feature near 1400 cm^{-1}, (marked by an asterisk in Figure 4). This appears to correspond to the shorter component observed in the ps-trl studies and we provisionally ascribe it to ^{1}MLCT decay. However the longer-lived component observed in the ps-trl studies (τ > 200 ps) is not easily identified in the TR^3 data. Nevertheless, any model proposed to explain our observations must involve the

possibility of a second electronic [singlet] state, which is strongly affected by deuteriation of the molecule.

Although this state is not immediately observable in the TR[3] data available, this is not too surprising, given that its population is likely to be less than 10 % compared with the population of the ^{3}MLCT state. While the photophysical picture is incomplete, it does appear that deuteriation may influence the efficiency of ISC between the lowest excited states in these complexes and a reassessment is warranted of previous models used to describe the earliest processes which occur in trishomoleptic Ru(II) polypyridyl complexes. Further work is required to fully understand the novel photophysics involved[4)].

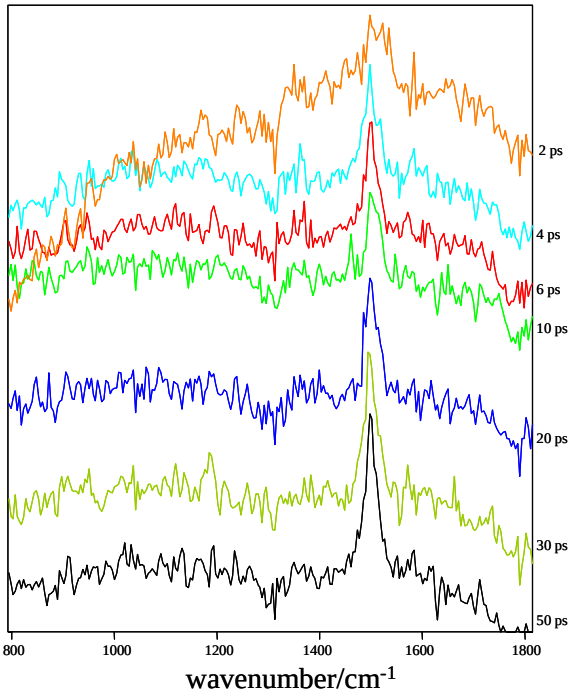

.

Figure 3. Time resolved resonance Raman spectra of [Ru([H_8]-bpy)$_3$]$^{2+}$ in H_2O between 2 and 50 ps following excitation. Steady state spectra have been subtracted. Pump = 410 nm; probe = 470 nm. Spectra offset on the vertical axis for clarity.

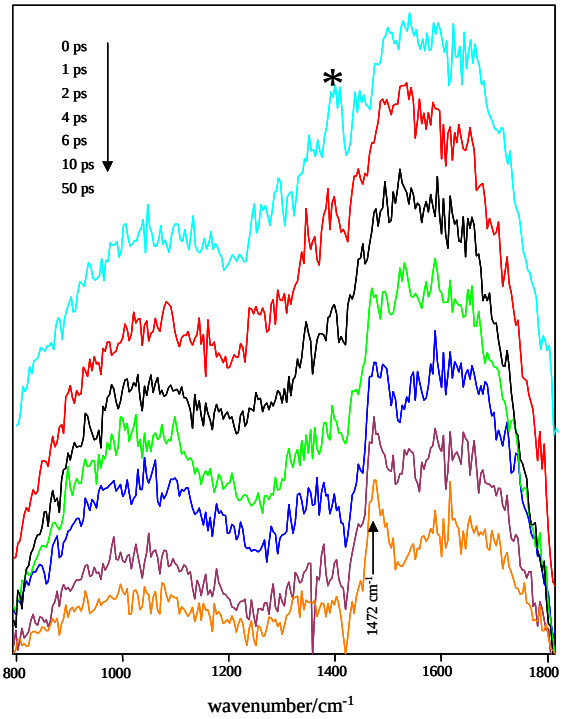

Figure 4. Time resolved resonance Raman spectra of [Ru([D_8]-bpy)$_3$]$^{2+}$ between 0 and 50 ps following excitation in H_2O. Steady state spectra have been subtracted. Pump = 410 nm; probe = 470 nm. Spectra are offset on the vertical axis for clarity.

Acknowledgement. We thank the EPSRC (GR/M45696) for access to USL.

References

1. C. G. Coates, J. Olofsson, M. Coletti, J. J. McGarvey, B. Önfelt, P. Lincoln, B. Norden, E. Tuite, P. Matousek, and A. W. Parker, J. Phys. Chem., 105, 12653 (2001)

2. A. C. Bhasikuttan, M. Suzuki, S. Nakashima, T. Okada, J. Am. Chem. Soc., 124, 8398, (2002)

3. D. P. Strommen, P.K. Mallick, G. D. Danzer, R. S. Lumpkin, J. R. Kincaid, J. Phys. Chem., 94, 1357,(1990)

4. W. R. Browne, C. G. Coates, C. Brady, P. Matousek, M. Towrie, S. W. Botchway, A. W. Parker, J. G.; Vos, J. J. McGarvey, J. Am. Chem. Soc., 125, 1706, (2003).

Excited states of metal (bis)thiolates: The formation of a sulfur-sulfur bond?

J A Weinstein

School of Chemistry, University of Nottingham, University Park, Nottingham, NG7 2RD, UK

M Ya Mel'nikov

Department of Chemistry, Moscow Lomonosov State University, Moscow, 119899 Russia

S W Botchway, P Matousek, A W Parker, M Towrie

Central Laser Facility, CCLRC Rutherford Appleton Laboratory, Chilton, Didcot, Oxon, OX11 0QX, UK

Main contact email address: *Julia.Weinstein@Nottingham.ac.uk*

Introduction

Most photophysical devices include a Donor-Spacer-Acceptor (D-sp-A) unit as the component responsible for the photoinduced-electron transfer step, with a long-lived charge-separated excited state, $[D^+\text{-sp-}A^-]^*$ being a key transient[1]. The problem with *artificial* systems is that the $[D^+\text{-sp-}A^-]^*$ state is often too short-lived to be chemically useful, *due to a facile back electron transfer*. The issue of vital importance is how to block back electron transfer before the chemical event occurs. One of the approaches to this fundamental issue is to use *structural reorganization in the excited state* to control back electron transfer. Over the last few years, we have been developing this approach to controlling the lifetime of the charge-separated excited state in *metal chromophores*. A new type of structural reorganization – namely, the formation of a transient three-electron sulfur-sulfur bond (S∴S) which is well-established in organic chemistry[2], has been applied to metal chromophores. The Pt(II) diimine (bis)thiolates, Pt(bpy)(4-X-PhS)$_2$ (bpy=2,2'-bipyridine) have been chosen as model compounds to probe the plausibility of this approach since:

- Their lowest excited state has a Charge-Transfer[3,4] nature, as shown by UV/Vis absorption, emission, resonance Raman and (spectro)electrochemical techniques. The HOMO has a mixed Pt(d)/thiolate(π)/S(LonePair) origin, while the LUMO is mainly localized on the diimine ligand.
- This charge-transfer transition gives rise to an intense solvatochromic absorption centred at 450 – 600 nm, the energy of which is both thiolate and diimine dependent.
- The metal ***d***-orbitals involvement in the frontier orbitals provides a non-dissociative excited state.

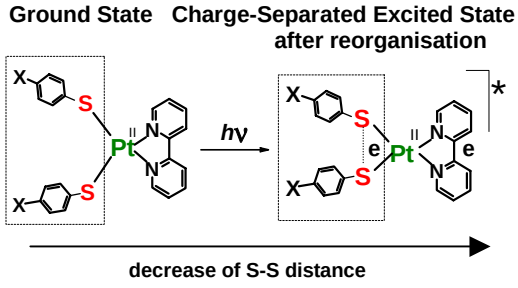

Figure 1. A schematic representation of the formation of the three-electron sulfur-sulfur bond with a concomitant shortening of the S-S distance in the excited state of a metal (bis)thiolate.

In Pt(bpy)(4-X-PhS)$_2$ (Figure 1) light induces electron transfer from the thiolate moiety to the diimine, forming a system with a coordinated thiolate anion and thiyl radical, which can interact with each other via the metal centre. This interaction decreases the sulfur-sulfur distance in the excited state compared to the ground state. In effect, a new three-electron bond, S∴S, which provides an energetic barrier to back electron transfer and stabilises the charge-separated state, could be formed. Generally, the disulfide radical-anion, $[RS\therefore SR]^-$ has a doubly-occupied bonding, and a singly-occupied antibonding orbital, SHOMO[2] (this bonding situation is denoted as "∴").

Should the S∴S bond be formed in the excited state of a *metal chromophore*, such a bonding situation would offer a tool to tune the lifetime of this excited state via changes in the population of the antibonding SHOMO through variations in the thiolate. Therefore, direct information on excited state dynamics of Pt(bpy)bis(thiolate)s as a function of the thiolate ligand is vital for elucidating the possibility of the structural reorganisation in their excited state. To address this issue, the present study has explored a combination of picosecond time-resolved emission (time-correlated single-photon counting (TCSPC) and Kerr-gate set-up) and time-resolved resonance Raman (TR^3) spectroscopic techniques. The application of TR^3 has also allowed us to probe *directly* the sulfur-sulfur interaction in the excited state of Pt(bpy)(4-X-PhS)$_2$.

Results and Discussion

Excited state lifetimes as a function of thiolate

The lifetimes of the excited states of [Pt(bpy)(4-X-PhS)$_2$] (Figure 1), with systematic variation of the thiolate donor capability achieved via X = NO_2, H, MeO, and thiolate = 4,6-dimethyl-2-mercaptopyrimidine (tpym) measured in fluid solution at room temperature, are summarised in Table 1. When time-correlated single photon counting was used, the excited state lifetime was determined from an emission decay curve, such as the one presented in Figure 2 for the case of a triimine monothiolate analogue, [Pt(tpy)(4-NO_2-PhS)][BF_4][5]. The emission kinetic traces obtained for all the compounds studied show biexponential decay, with the short component following the instrument response. The contribution of this short component is wavelength dependent and decreases towards the red side of the spectrum. The overall kinetic profile and the values of the lifetimes obtained do not depend on either the excitation/registration wavelength or the solvent used. In agreement with this result, the gradual red shift of the emission spectrum with time has been observed when emission studies have been performed on the Kerr-gate apparatus.

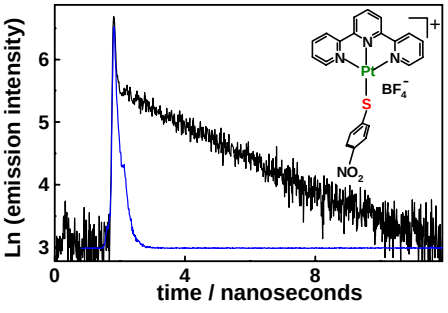

Figure 2. The kinetic trace of emission decay of [Pt(tpy)(4-NO_2-PhS)][BF_4] (DMF solution, 293 K, 400 nm excitation, 640 nm registration, black line), and the instrument response function (blue line) of the TCSPC apparatus used.

These findings can be tentatively explained by occurrence of an ultrafast intersystem crossing (ISC) from the initially formed singlet excited state, ^{1}[Pt(bpy)(4-X-PhS)$_2$]*, to the ^{3}[Pt(bpy)(4-XPhS)$_2$]*. The fact that the ISC in the Pt(II) complexes studied occurs on the sub-picosecond time scale is not surprising, as 40 fs has been recently reported for the ISC in [Ru(bpy)$_3$]$^{2+}$[6]. It is thus likely that it is the lowest triplet state that represents the structure of the reorganized [Pt(bpy)(4-X-PhS)$_2$]*, and which is responsible for the photoreactivity of the complexes.

Photoreactivity as a function of thiolate The bimolecular photo-oxidation of Pt(bpy)(4-X-PhS)$_2$ by an electron acceptor, 4,4'-dibenzyl-4,4'-bipyridine dication (viologen, Bv^{2+}) was used as a model process to estimate photoreactivity (Table 1)[7]. The photo-oxidation occurs via electron transfer from the excited state of Pt(bpy)(4-X-PhS)$_2$ to Bv^{2+}, leading to the formation of a radical cation $Bv^{+\bullet}$, and was monitored by following the $Bv^{+\bullet}$ absorption as a function of time.

Thiolate	E_p^{ox} / V	Photo-reactivity	Lifetime / ps	Methods	Energy of S∴S in [RS-SR]$^{\bullet}$
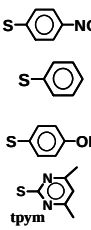	+0.58	Decreases	840 ± 12	Emission / TR^3	Decreases
	+0.22		470 ± 9	Emission	
	-0.04		ca. 40	TR^3 / TA	
	+0.60		33 ± 3	TR^3	

Table 1. A correlation between the lifetimes, electrochemical potentials, photoreactivites and stabilities of the S∴S bond in the Pt(bpy)(bis)thiolates studied.

The following conclusions can be drawn from the data in Table 1: (i) The trend in the excited state lifetimes obtained does not follow the electrochemical potentials of the complexes; (ii) the photoreactivity correlates with the trend in the lifetimes, while no correlation has been observed with the electrochemical potentials. This is highlighted by a comparison between Pt(bpy)(NO$_2$-PhS)$_2$ and Pt(bpy)(tpym)$_2$, which possess very similar electrochemical potentials, but exhibit very different lifetimes and photoreactivities; (iii) We are currently in the process of obtaining the bond dissociation energies (BDE) for the corresponding disulfide radical anions, [RS∴SR]$^{-\bullet}$. The trend obtained for the BDEs is in a good agreement with the trend for both the lifetimes and photoreactivities, and predicts a BDE that is at least 30 kJ/mol higher for R=4-NO$_2$-PhS- vs. R=tpym. These data have provided significant indirect support for the formation of the transient S∴S bond in the excited state of the metal thiolates.

Direct probing of the sulfur-sulfur interaction in the excited state of Pt(bpy)(RS)$_2$ by Time-Resolved Resonance Raman

The ps-TR^3 technique is a widely used powerful tool for obtaining structural information on the excited states of metal chromophores[8]. The application of ps-TR^3 to Pt(II) diimine (bis)thiolates opens up an ideal route to test the S∴S hypothesis, by probing the sulfur-sulfur interaction directly in the excited state. This is possible since: **(i)** ν(SS) is strongly Raman active; **(ii)** For disulfides, RSSR, the ν(SS) energy is strongly dependent on "R", changing from 545 to 470 cm^{-1} for R=Ph[9] vs. *H$_2$N*-Ph; **(iii)** The ν(SS) in disulfide radical anions, [RSSR]$^{\bullet}$, occurs at energies lower than in disulfides, due to a single-occupied antibonding character of the HOMO in the S∴S species (e.g. 218 for $(SCN)_2^{-\bullet}$ *vs.* 450 cm^{-1} for $(SCN)_2$)[10]; **(iv)** The ν(S∴S) of a transient S∴S can be anticipated to occur at higher energies in Pt(bpy)(RS)$_2$ than in [RSSR]$^{-\bullet}$, due to delocalisation over the Pt *d*-orbitals.

The transient absorption[11] spectrum of Pt(bpy)(4-MeO-PhS)$_2$ in DMF (Figure 3), shows the lowest absorption band of the excited state at ca. 490 nm. The ground state Raman spectrum and the TR^3 spectra obtained under 400 nm and 493 nm probes are presented in Figure 4 a, b and c, respectively. Although a detailed analysis of the data obtained is currently under way, some preliminary conclusions can be drawn. The ground state Raman spectrum (Figure 4, a) corresponds to the one observed in our previous resonance Raman investigation[3], and exhibits features characteristic of the coordinated bpy-ligand, and a band at ca. 820 cm^{-1}, typical for a vibration with a significant ν(CS) contribution. The TR^3 spectra obtained under 400 nm and 493 nm probe both exhibit vibrations in the bpy region, as could be anticipated as both wavelengths are in resonance with the absorptions of the coordinated bpy^{-3}, present in the {charge-transfer-to-diimine} excited state, [(bpy$^-$)(Pt(4-MeO-PhS)$_2$)$^+$]*. However, these TR^3 spectra are strikingly different in the low energy region. The spectrum obtained under 493 nm probe, exhibits a band at ca. 850 cm^{-1} which is present in the ground state Raman spectrum, and also a band at ca. 390 cm^{-1}, which is not present in either the ground state spectrum or the spectrum of a *higher energy* transition of the excited state (400 nm probe) and lies in the region where, as has been discussed above, ν(S∴S) can be anticipated. This result is the first direct indication of formation of a new transient S-S bond in the reorganised excited state of Pt(II) diimine (bis)thiolates.

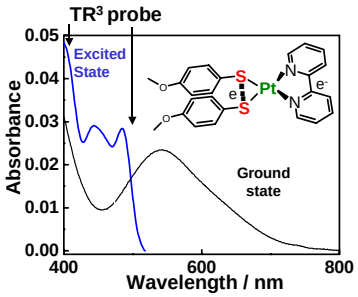

Figure 3. The ground state UV/Vis (black line) and transient absorption (blue line) spectra of Pt(bpy)(4-MeO-PhS)$_2$ at 10 ps time delay (DMF, 298 K, excitation 616 nm, 15 fs pulse)[12].

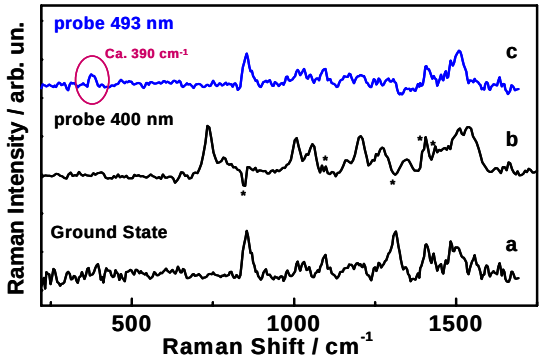

Figure 4. The Raman spectra obtained under 400 nm pump of (a) Ground state, (b) excited state under 400 nm probe and (c) excited state under 493 nm probe of Pt(bpy)(4-MeO-PhS)$_2$ at 10 ps time delay (DMF, 298 K).

Conclusions

(i) A combined application of picosecond emission and TR^3 spectroscopies at RAL allowed, for the first time, an evaluation of the lifetime of the excited state of a series of Pt(II) diimine (bis)thiolates. These data have provided considerable support for the formation of a transient sulfur-sulfur bond in the lowest excited state of these chromophores.

(ii) The resonance Raman spectrum of the lowest excited state of $Pt(bpy)(4\text{-}MeO\text{-}PhS)_2$ is indicative of the presence of the transient sulfur-sulfur bond in this excited state.

Experimental arrangements

For time-correlated single-photon counting measurements performed in the Confocal Microscopy Laboratory, samples were excited at 380-420 nm, achieved through a frequency doubling, using a BBO crystal, of the output of a titanium sapphire laser (Spectra-Physics) operating at 710–850 nm, 81 MHz with 120 fs pulse. The fluorescence was re-imaged at the slit of a monochromator (IBH Ltd). Emission was detected with a single-photon counting micro-channel plate photomultiplier (Hamamatsu R3809-U) with a response time of 35 ps. Lifetime measurements were performed using a Becker and Hickl (GmbH) time-correlated single photon counting PCI module (SPC-700) with a time resolution of 830 fs per channel. All the usual functions of the SPC set up such as TAC and CFD were computer controlled with software supplied with the SPC-700 module. The measurements were performed in DMF, dichloromethane and acetonitrile.

The ps emission experiments and the ps-TR^3 experiments on the Kerr gate apparatus described in detail in[13)] were performed in DMF, under a vertically flowing open jet sample arrangement. The 400 nm pump and 400 nm or 493 nm probe wavelengths were used, with typical pulse energies of ca. 10 μJ (pump) and 3 μJ (probe), and both beam diameters being ca. 300 μm at the sample. Acetonitrile Raman bands were used for calibration of the spectra, with an estimated accuracy of the absolute frequency ± 10 cm^{-1}. Approximately 500 s integration time was used for each time delay. The ground state Raman spectrum was obtained from the spectrum at –50 ps time delay in a single-color 400 nm experiment after scaled subtraction of the solvent spectrum. From the TR^3 experiments, the lifetime of the excited state was obtained from the bleach recovery of the Raman bands resonant with the ground state. All the TR^3 spectra were first corrected for the solvent absorptions by a scaled subtraction of the solvent spectrum. The pure excited state spectra were then obtained by a scaled subtraction of the spectrum at a negative time delay from the spectrum at the time delay of interest.

Acknowledgements

We wish to gratefully acknowledge the on-going collaboration with Prof. P.M.W. Gill and Mr. S.-H. Cheng on quantum mechanical calculations. We are grateful to Profs. M.W. George and R.H. Bisby for fruitful discussions, and EPSRC, Russian Fund of Basic Research and University of Nottingham for funding.

References

1. R Ballardini, V Balzani, A Credi, M T Gandolfi and M Venturi
Acc. Chem. Res., 34 445, (2001)

2. S-Centered Radicals, Ed. by Z B Alfassi
J.Wiley & Sons, Ch.1,2, (1999)

3. J A Weinstein, N N Zheligovskaya, M Ya Mel'nikov and F Hartl
J. Chem. Soc. Dalton Trans., 2459, (1998)

4. S Huertas, M Hissler, J E McGarrah, R J Lachicotte and R Eisenberg
Inorg. Chem., 40 1183, (2001);
J A Zuleta, J M Bevilacqua, D M Prosperio, P D Harvey and R Eisenberg
Inorg. Chem., 31 2396, (1992)

5. This report is focused on the Pt(diimine)(bis)thiolates, in which the formation of a transient sulfur-sulfur bond is possible. We have also performed the same set of studies on their monothiolate analogs, $[Pt(trpy)(4\text{-}X\text{-}PhS)][BF_4]$, in which the formation of such a bond is not possible (trpy=2,2';6',6''-terpyridine).

6. A C Bhasikuttan, M Suzuki, S Nakasima and T Okada
J. Amer. Chem. Soc., 124 8398, (2002)

7. I V Lileev, Master Thesis, Moscow State University, (2000)

8. J R Schonoover and J F Strouse
Chem. Rev., 98 1335, (1998)

9. C A Szafranski, W Tanner, P E Laibinis and R L Garrell
Langmuir, 14 3570, (1998)

10. R Wilbrandt, N H Jensen, P Pagsberg, A H Sillesen, K B Hansen and R E Hester
Chem. Phys. Lett., 60 315 (1979)

11. S A Antipin, A N Petrukhin, F E Gostev, V S Marevtsev, A A Titov, V A Barachevsky, Yu P Strokach and O M Sarkisov
Chem. Phys. Lett., 331 378, (2000)

12. J A Weinstein, M Ya Melnikov, F E Gostev, D Tovbin and O M Sarkisov, unpublished results

13. P Matousek, M Towrie, C Ma, W M Kwok, D Phillips, W T Toner, A W Parker, J. Raman Spectrosc., 32 983, (2001).

Nanosecond time-resolved resonance Raman spectroscopy of functional (diimine)Re(CO)$_3$(L) complexes: Novel Alkynyl- and Stryryl-Azacrown systems

J D Lewis, J N Moore

Department of Chemistry, The University of York, Heslington, York, YO10 5DD, UK

I P Clark

Central Laser Facility, CCLRC Rutherford Appleton Laboratory, Chilton, Didcot, Oxon, OX11 0QX, UK

Main contact email address: *jnm2@york.ac.uk*

Introduction

The design and study of light-controlled ion-switches, where light can be used to release cations such as Ca^{2+} into solution, is of interest because of potential applications that range from mimicking natural ion-signalling to optical computing. Our recent interest in such systems has centred on (bpy)Re(CO)$_3$L$^+$ complexes[1,2], where L is a functionalized pyridine ligand with a pendant azacrown ether, and where light-induced changes within the chromophore change the cation-binding properties of the azacrown and result in cation release.

Previously, we have studied **1** (Scheme 1)[1] using time-resolved UV-visible absorption (TRVIS) and time-resolved resonance Raman (TR^3) spectroscopy. We have demonstrated that when an alkali or alkaline-earth cation is bound to the azacrown, excitation of **1**-M^{n+} to the metal-to-ligand charge-transfer (MLCT) state results in cation release on a timescale of 6-100 ns, depending on the identity of the cation, with subsequent rebinding from bulk solution in <1 ms. We have shown that TR^3 spectroscopy is an excellent technique for studying this type of complex because an appropriate choice of probe wavelength for resonance enhancement enables the various excited states to be studied with high selectivity. In addition, the vibrational bands of the excited states provide key structural information that is not obtainable from TRVIS spectra.

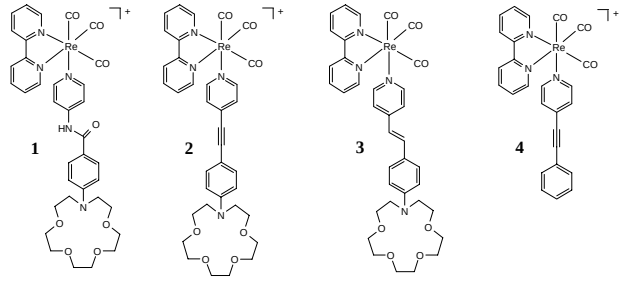

Scheme 1.

We have synthesised new complexes **2**-**4**, where **4** is a model for **2**. Complexes **1**-**3** are closely similar but the "spacer" between the Re centre and the azacrown is changed from an amido to an alkynyl (C≡C) or a styryl (C=C) group, thus providing greater electronic communication between the Re centre and the azacrown, as well as providing strong vibrational marker bands due to ν(C≡C) and ν(C=C) modes. TRVIS studies at York have established that 355 nm excitation of **2**–M^{n+} or **3**–M^{n+} results in cation release on a timescale of ≤50 ns, and that subsequent cation rebinding from bulk solution restores the initial equilibrium on a timescale of <1 ms. However, establishing the detailed photochemical mechanisms that underlie these observations is not straightforward because the MLCT absorption bands overlap with strong intraligand charge-transfer (ILCT) (**2**-**3**) or ππ* (**4**) absorption bands, and so the identities of the excited states driving cation release are not obvious. Thus, the aims of our recent nanosecond TR^3 studies at RAL were to use vibrational marker bands: (i) to identify the key excited states populated on excitation of **2**-**4**, and thereby to obtain information on structure and bonding; and (ii) to obtain clear evidence of the cation release mechanism by monitoring changes in marker bands that report on cation binding.

Single-colour experiments: 355 nm

Single-colour pulsed laser experiments using 355 nm as both pump and probe wavelengths enabled ground- and excited-state Raman bands of **2**-**4** to be observed. Ground-state bands were identified by comparison with cw spectra recorded with 350.6 nm excitation in York. Excited-state bands were identified by their increase in relative intensity with pulse energy.

Ground-state resonance Raman bands of model compound **4** (Figure 1) are assigned to bpy modes, L-ligand modes, and a ν(CO) mode, consistent with the excitation being in resonance with both MLCT and intraligand transitions. The excited-state bands are assigned to (bpy•-) modes of the MLCT state[1,3].

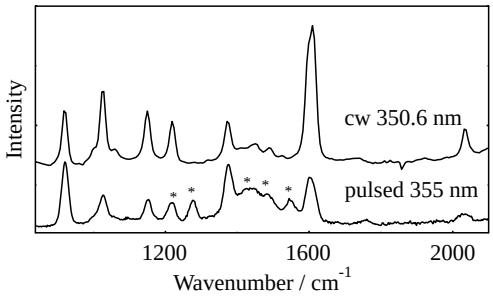

Figure 1. Resonance Raman spectra of **4** from cw 350.6 nm and pulsed 355 nm excitation; excited state bands (*).

The strong ground-state resonance Raman bands of **2** (Figure 2) are assigned to L-centred modes, consistent with resonance with the intense ILCT band. Excited-state bands of **2** observed in the single-colour experiment are attributed to resonance with an ultrashort-lived TRVIS band at 400 nm[4]. One excited-state Raman band at 1567 cm^{-1} is assigned to a mixed mode comprising in-plane stretching of phenyl and pyridyl rings, shifted down from the ground-state band at 1594 cm^{-1}; another band at 2154 cm^{-1} is assigned to the ν(C≡C) band, shifted down from the ground-state band at 2210 cm^{-1}. These shifts are consistent with weaker bonding at the central (C≡C) group and

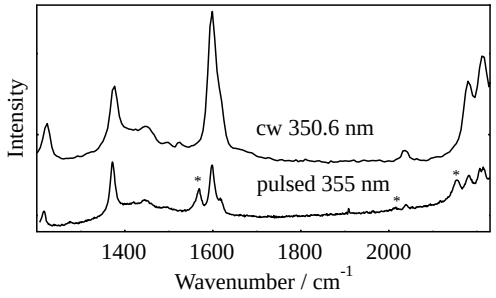

Figure 2. Resonance Raman spectra of **2** from cw 350.6 nm and pulsed 355 nm excitation; excited-state bands (*).

within the phenyl and pyridyl rings, due to the formation of an ultrashort-lived charge-transfer (CT) state in which electron density is transferred from the azacrown towards the Re centre[5]. An excited-state band at 2012 cm^{-1}, assigned to a down-shifted ν(CO) band, is consistent with this interpretation.

A single-colour experiment on **2**-Ba^{2+} resulted in excited-state Raman bands which were very similar in position to those from **2**, but in which the excited-state ν(C≡C) band had a markedly higher relative intensity. The increased intensity indicates that Ba^{2+} must be associated with **2** on the timescale of the experiment, while the very similar band positions indicate that its association in the probed state of **2**-Ba^{2+} may be relatively "loose", with only a weak interaction between Ba^{2+} and the azacrown nitrogen atom. This may indicate a species in which the cation and azacrown are separated by solvent[6].

Two-colour experiments: 355 and 660 nm

Two-colour pulsed laser experiments, pumping at 355 nm and probing at 660 nm, were carried out in resonance with strong excited-state TRVIS bands of **2** and **3**[4].

No excited-state Raman bands were observed from **2** or **2**-Ba^{2+}, attributable to the ultrashort lifetime of this state in each case. However, similar experiments on **3** and **3**-Ba^{2+}, for which the analogous state is longer-lived[4], resulted in excited-state Raman bands (Figure 3) that are assigned to L-centred modes of a charge-transfer excited state that may be similar to that observed for **2** and **2**-Ba^{2+} in the single-colour experiments. The observation of more bands in the spectrum of the charge-transfer excited-state of **3** than that of **2** may arise from the different resonance conditions. Small differences were observed between the excited-state band positions from **3** and **3**-Ba^{2+}: for example, bands of **3** at 1534 and 1614 cm^{-1} were observed at 1536 and 1611 cm^{-1}, respectively, for **3**-Ba^{2+}. This observation suggests that the cation is still associated with the azacrown in the charge-transfer state of **3**-Ba^{2+} but, as for **2**-Ba^{2+}, that its association with the azacrown in the probed state of **3**-Ba^{2+} may be relatively "loose".

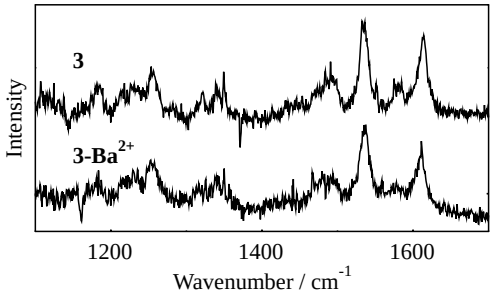

Figure 3. Resonance Raman spectra from coincident (Δt = 0 ns) 355 nm pumping and 660 nm probing of **3** and **3**-Ba^{2+}.

Two-colour experiments: 355 and 425 nm

Two-colour pulsed laser experiments, pumping at 355 nm and probing at 425 nm, were carried out in resonance with long-lived TRVIS bands that are markers for cation release from **2**-Ba^{2+} and **3**-Ba^{2+}. These TRVIS bands correspond to the ground state with the cation completely dissociated from the azacrown.

In the cw resonance Raman spectra of **2** and **2**-Ba^{2+} recorded with 350.6 nm excitation, two L-centred bands shift up ca. 7 cm^{-1} on cation complexation: a ν(ring) band at 1594 cm^{-1} shifts to 1600 cm^{-1}, and the ν(C≡C) band at 2210 cm^{-1} shifts to 2218 cm^{-1}. Similar but larger changes were observed between **3** and **3**-Ba^{2+}: in particular, a band at 1589 cm^{-1} shifts to 1602 cm^{-1}.

In TR^3 studies of **2**-Ba^{2+}, the spectra at early times showed a band at 1600 cm^{-1} from **2**-Ba^{2+}, with a shoulder at 1594 cm^{-1} from "free" **2**, whereas those at >500 ns showed only the band at 1600 cm^{-1} from **2**-Ba^{2+}. Similarly, the TR^3 spectra of **3**-Ba^{2+} (Figure 4) at ca. 50 ns showed a band at 1602 cm^{-1} from **3**-Ba^{2+}, with a shoulder at 1589 cm^{-1} from "free" **3**, whereas only the band from **3**-Ba^{2+} was present at 600 ns. For both **2**-Ba^{2+} and **3**-Ba^{2+}, plots of the intensity of the "free" **2** or **3** Raman marker bands versus time were very similar to TRVIS kinetics recorded under comparable conditions. The "cation-free" band observed on excitation of **2**-Ba^{2+} showed a risetime of <10 ns, whereas that from **3**-Ba^{2+} showed a risetime of ca. 50 ns, indicating that "full" cation release is slower for **3**-Ba^{2+}. The recovery of the "cation-bound" band on a time scale of ca. 200 ns arises from rebinding from bulk solution, consistent with the high Ba^{2+} concentrations used in these experiments.

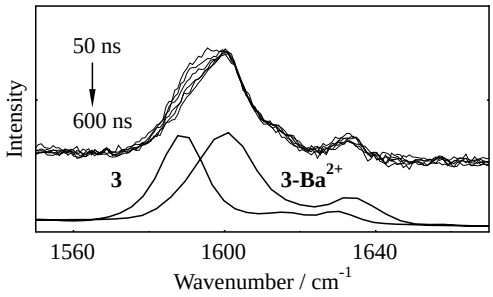

Figure 4. TR^3 spectra of **3**-Ba^{2+} from 355 nm pumping and 425 nm probing, normalised to the intensity of the 1600 cm^{-1} band. Resonance Raman spectra of **3** and **3**-Ba^{2+} from cw 350.6 nm excitation.

Conclusions

Time-resolved resonance Raman spectroscopy has been used to study a series of (bpy)Re(CO)L^+ complexes. The Raman spectra have enabled the natures of the excited states present on the nanosecond timescale to be determined: an MLCT state is present on excitation of **4**, whereas charge-transfer states associated with the azacrown ligands are present on excitation of **2** or **3**. On excitation of **2**-Ba^{2+} or **3**-Ba^{2+}, the Raman spectra indicate that a similar but longer-lived charge-transfer excited state is formed initially in each case, in which the cation may only be loosely associated with the azacrown. The time dependence of the Raman marker bands for full cation release show that the decay of this "loosely-associated" species to give "full" cation release occurs in <10 ns for **2**-Ba^{2+} and in ca. 50 ns for **3**-Ba^{2+}. This study demonstrates that time-resolved vibrational studies are essential to develop an understanding of the key excited states and mechanisms that drive light-controlled cation release in these systems.

References

1. D B MacQueen and K S Schanze, J. Am. Chem. Soc., 113 6108, (1991); J D Lewis, J N Moore and I P Clark Central Laser Facility Annual Report, RAL-TR-2002-013 108, (2002); J D Lewis L Bussotti, P Foggi, R N Perutz and J N Moore J. Phys. Chem. A, 106 12202, (2002)
2. J D Lewis, R N Perutz and J N Moore Chem. Commun., 1865, (2001)
3. W K Smothers and M S Wrighton J. Am. Chem. Soc., 105 1067, (1983)
4. J D Lewis, L Bussotti, P Foggi and J N Moore unpublished results
5. W M Kwok, C Ma, P Matousek, A W Parker, D Phillips, W T Toner and M Towrie, Chem. Phys. Lett., 322 395, (2000)
6. P Dumon, G Jonusauskas, F Dupuy, Ph. Pee, C Rulliere J-F Letard and R Lapouyade J. Phys. Chem., 98 10391, (1994)

Laser temperature jump experiments with micrometre space resolution using Rhodamine 101 anti-Stokes fluorescence from nanoseconds to milliseconds

J F Holzwarth, S Couderc

Fritz-Haber-Institute, MPG, D-14195 Berlin, Germany

A Beeby

Department of Chemistry, University of Durham, Durham, DH1 3LE, UK

A W Parker, I P Clark

Central Laser Facility, CCLRC Rutherford Appleton Laboratory, Chilton, Didcot, Oxon, OX11 0QX, UK

Main contact email address: *Holzwarth@fhi-berlin.mpg.de*

Introduction

The investigation of dynamic changes in solutions is very important in learning about reaction mechanisms. The laser temperature jump technique, which uses the solvent as energy absorber allows the observation of kinetic events over a time scale from 100 ps to 1s [1a,,b)], and offers the possibility to produce temperature changes in volumes of a microlitre or less.

The absorption spectrum of water shown in Figure 1 demonstrates that for convenient laser energy absorption a wavelength of 1.31 µm is most suitable because the absorption coefficient is around 1 cm^{-1}; this avoids strong temperature gradients and therefore shockwaves [1a,,b)].

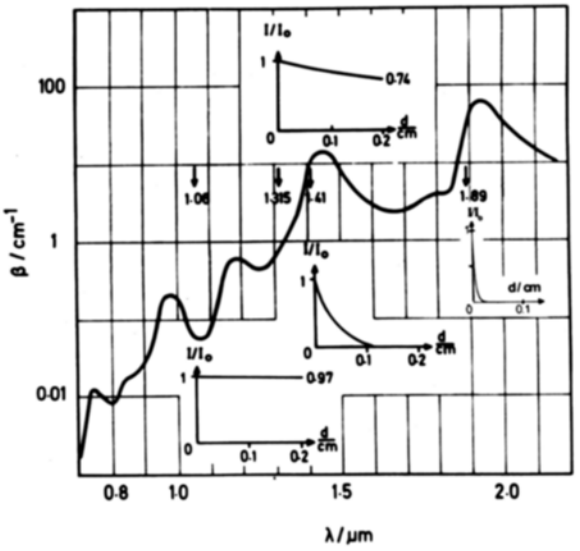

Figure 1. Absorption of H_2O in the overtone region at 303K.

The measurement of fast temperature changes produced by lasers in micro- to nano-litre volumes is a serious problem, especially if both high precision and nano-second time resolution is required.

Rhodamine 101 (Rh101) is a water soluble fluorescent dye, whose solutions have been shown to present Anti-Stokes fluorescence with a quantum field of 1 [2)]; this offers a convenient solution to the above problem. Figure 2 contains the absorption and emission spectrum of Rh101 in ethanol. The emission spectrum was measured applying an excitation range of 610-630 nm, at the long wavelength edge of the absorption spectrum. A similar type of excitation and Anti-Stokes fluorescence observation was used for time resolved measurements of small temperature changes in solutions.

Experimental

We used three types of lasers. A continuous wave He-Ne laser (632.8 nm) for steady state excitation measurements, a pulsed dye laser (632.8 nm, 10-15 ns) for time resolved fluorescence experiments, and an H_2-Raman shifted Nd:YAG laser (1.9 µm ,

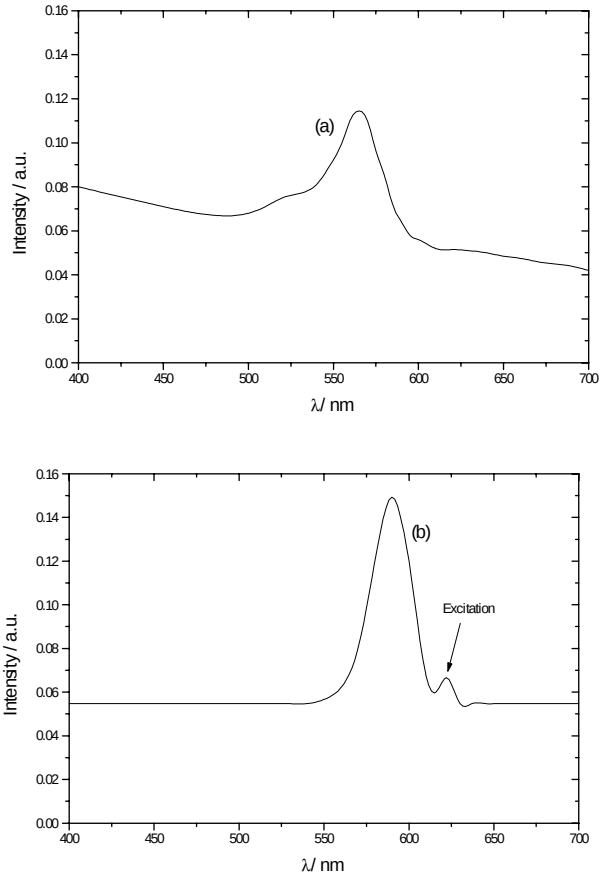

Figure 2. Absorption (a) and emission (b) spectrum of Rhodamine 101 10^{-6} M in ethanol at 25°C.

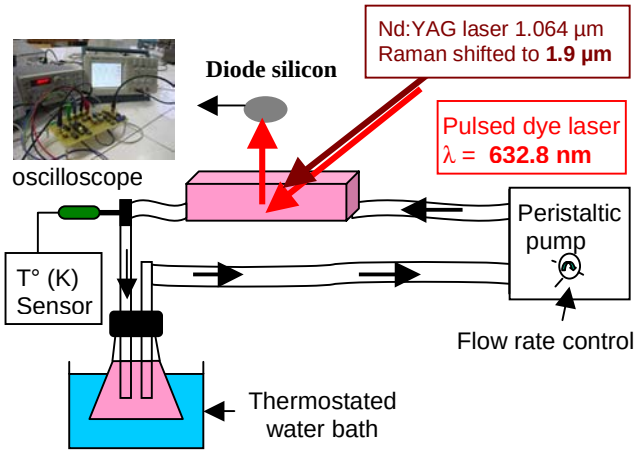

Figure 3. Experimental arrangement.

7-10 ns) to produce the temperature jumps in ethanolic solutions with some water added as energy absorber for producing the temperature jumps and to control the absorption at 1.9 µm to be 1-2. The absorption around 1 cm^{-1} for the T-jump laser is important to achieve a useful balance between good energy absorption and small temperature gradients. Figure 1 shows this for some wavelengths and details are given in the literature[1a,b]. The experimental set up is given in Figure 3.

During the experiments a solution is pumped through a measuring cell of 2 mm cross section and 2 cm length. All lasers can be focused into the same spot of 1 µm and a water bath allows for temperature control.

Results and Discussion

We measured the Anti-Stokes fluorescence in an ethanolic solution of Rh101 after an excitation with the continuous wave He-Ne laser at 632.8 nm. Figure 4 demonstrates the drastic increase with temperature of fluorescence intensity measured for T = 293 K and 315 K. The dip at 635 nm is caused by the blocking of the excitation laser in the emission detector. The maximum of Anti-Stokes fluorescence appears around 595 nm, 30 nm away from the excitation laser. Such experiments with the continuous wave laser were performed for temperature calibration of fluorescence intensity.

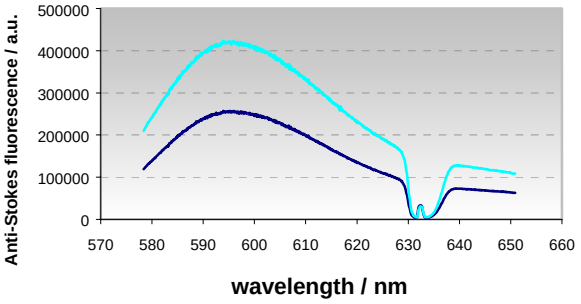

Figure 4. Anti-Stokes fluorescence of Rhodamine 101 in ethanol at two temperatures : T=293 K for the lower curve and T=315 K for the upper curve.

The calibration experiments were followed by time resolved investigations using the pulsed dye laser for Rh101 excitation at 632.8 nm (~10 ns half width) as well as the Raman shifted Nd:YAG laser for temperature jumps with emission at 1.9 µm and a half width of 10 ns. We added 2-4% water to achieve an absorption of 1-3 cm^{-1} for the temperature jump laser.

Figure 5 shows the relative Anti-Stokes fluorescence intensity changes measured in the case of continuous excitation and time resolved measurements. Both sets of data follow the same temperature dependence, if the repetition rate in the pulse experiments did not exceed 1 Hz. The time delay between the T-jump laser (1.9 µm) and the pulsed excitation laser at 632.8 nm could be varied between 10 ns and 100 ms. In this way, it was possible to follow changes of temperature in the time range from 10^{-8} to 10^{-1} s.

Measurements with delay times between 30 ns and 500 ns gave similar and reproducible results of fluorescence intensity change with temperature. Delay times in the range of 1-10 µs showed big deviations, if inhomogeneous heating was applied; this is caused by shockwaves as expected and explained in the literature[1a,b]. In the fluorescence detection delay range 10 µs-10 ms, fluorescence results were reliable again. At longer delay times, the start of temperature decrease because of thermo-diffusion into the unheated surrounding was observed. After several seconds, the temperature prior to the temperature jump was reached again. All these effects have to be taken into consideration for reliable measurements of temperature changes.

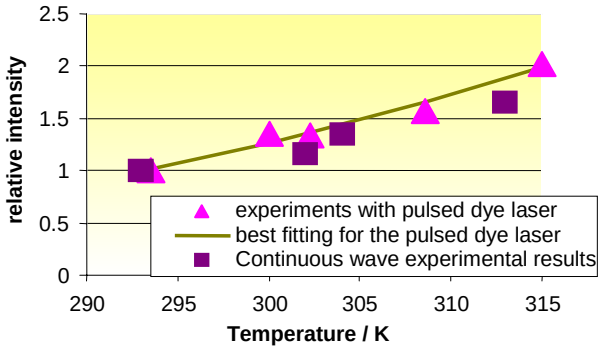

Figure 5. Relative Anti-Stokes fluorescence intensity (ratio between intensity at T and intensity at 293 K) of ethanolic solutions of Rhodamine 101 vs temperature.

Results in Figure 5 (excitation delay 30 ns) can be explained by an increasing population of the first vibrational state of the singlet ground state of Rh101 following the equation [3]:

$$I / I_o = A\exp\left(-\frac{\Delta E}{kT}\right) \quad (1)$$

Both sets of experiments follow the same temperature dependence resulting in an activation energy of ~3.7 ± 0.3 x 10^{-20} J. By variation of the delay time between the T-jump laser and excitation laser as well as the water content in the Rh101 solution we could control the temperature gradient in the solutions and measure time resolved temperature changes with a precision better than 0.5 K.

Conclusions

This new technique of time resolved Anti-Stokes fluorescence measurements using Rh101 provides a convenient and precise tool to observe small temperature changes in nano-volumes of liquid samples between 10 ns and 1 s under many different experimental conditions. In summary Rh101 offers a precise probe to follow the size, space and time dependence of temperature changes after a nanosecond temperature increase. This will be useful especially in complex biological systems like enzymes and membranes as well as nano-aggregates from surfactants or polymers.

Outlook

Rhodamine 101 is one of the few water soluble molecules with a fluorescence quantum yield near one. This is a perfect basis to link Rh101 to big organic molecules like enzymes and proteins and observe local temperature changes in nano-space and characterize temperature dependent molecular changes from nanoseconds to minutes.

Acknowledgements

JFH and SC want to thank the "European Union" for a travel and experiment grant: NLEV 32 C1/02 and the "Deutsche Forschungsgemeinschaft" DFG for grant No 696/11-2.

References

1. a) J F Holzwarth in: Techniques and Applications of Fast Reactions in Solution, Eds W J Gettins and E Wyn-Jones, Reidel Publishing Company, pp 47-59 (1979)

   b) J F Holzwarth, A Schmidt, h Wolff and R Volk J. Phys. Chem., 81 2300, (1977)

2. L E Erikson, J. Luminescence, 5 1, (1972)

3. J L Clark, P F Miller and G. Rumbles J. Phys. Chem. A, 102 4428, (1998)

Protonated neurotransmitters in the gas-phase

P Butz, P Carcabal, R A Jockusch, N A Macleod, L C Snoek, F O Talbot, J P Simons

Physical and Theoretical Chemistry Laboratory, University of Oxford, South Parks Road, Oxford, OX1 3QZ, UK

Main contact email address: *jpsimons@chem.ox.ac.uk*

Introduction

Gas-phase spectroscopy of small biomolecules is a rapidly maturing area of research. A combination of experimental techniques (resonant 2-photon ionisation, laser-induced fluorescence, etc.) with state of the art quantum chemical calculations allows the conformational landscape of neutral molecules to be fully unravelled[1,2].

However, biology is predominately a solution based discipline with water providing the ubiquitous solvent. Stepwise studies of hydration in the gas-phase provide a stepping stone to an understanding of the effects of the bulk solvent. A more fundamental problem is found in the presence of basic groups (e.g. NH_2) in a wide variety of natural and synthetic biomolecules. A good example is the ephedra series of pharmaceuticals (see Figure 1) whose neutral and hydrated species have been extensively studied in recent years[3,4].

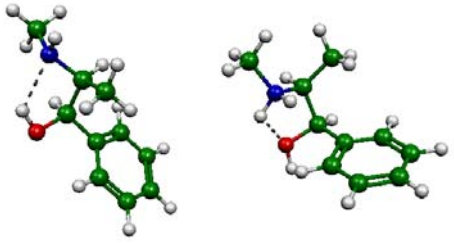

Eph. (AGa) **Eph-H$^+$. (GGa)**

Figure 1. Computed structures of neutral and protonated ephedrine (B3LYP/6-31+G*).

In the parent molecule (ephedrine), the neutral conformational landscape is dominated by a solitary conformer with an extended side chain geometry (AGa) and an intramolecular hydrogen bond between the functional groups of the type OH → N. Quantum chemical calculations indicate that protonation reverses the hydrogen bonding (NH → O) and, perhaps more significantly, alters the side-chain geometry (in the energetically favourable species) to a folded arrangement (GGa).

The aim of the current work is to produce protonated neurotransmitters in the gas-phase by photochemical means. Recent work on clusters of phenol and ammonia have found protonated ammonia clusters ($(NH_3)_nH^+$) following excitation of the phenol chromophore. The mechanism involves the transfer of an H-atom (from phenol to ammonia) and subsequent ionisation of the hydrogenated cluster[5]. The relatively high proton affinities of ephedrine and its fellow ethanolamines make them ideal candidates for such studies. An initial starting point is to cluster phenol with the simplest ethanolamine, namely 2-aminoethanol.

Results

Resonant 2-photon ionisation (R2PI) of phenol clustered with 2-aminoethanol are shown in Figure 2. A large number of features are observed: UV-UV holeburn spectra (also shown in Figure 2) allow the majority of features to be assigned to vibronic bands based on three principal origins (denoted A, B and C).

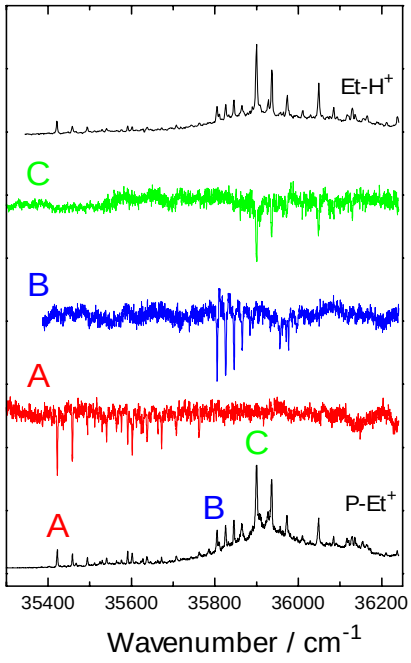

Figure 2. R2PI and UV-UV holeburn spectra of clusters of phenol with 2-aminoethanol.

Each origin displays an identical mass-spectrum (see Figure 3) with significant intensity in the parent mass-channel (phenol-(2-aminoethanol)$^+$ (m / z = 155)) and in a channel with m / z = 62 corresponding to *protonated* 2-aminoethanol. Little or no resonant signal is observed in the phenol$^+$ channel (m / z = 94).

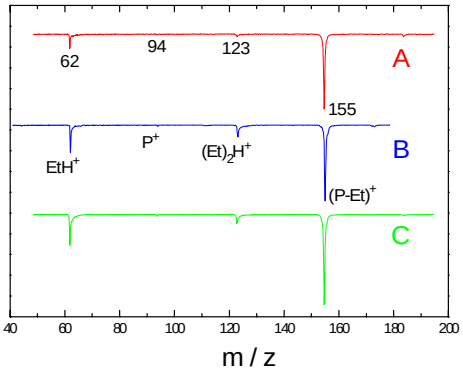

Figure 3. Time-of-flight mass spectra of features A, B and C.

Infra–red ion-dip spectra associated with the UV features A, B and C are shown in Figure 4. Also shown are calculated (B3LYP/6-31+G*) spectra for the energetically low-lying 1:1 clusters of phenol and 2-aminoethanol. Computed structures are shown in Figure 5. Comparison of the calculated and experimental spectra favour the assignment of feature A to an insertion type cluster and B and C to addition type geometries.

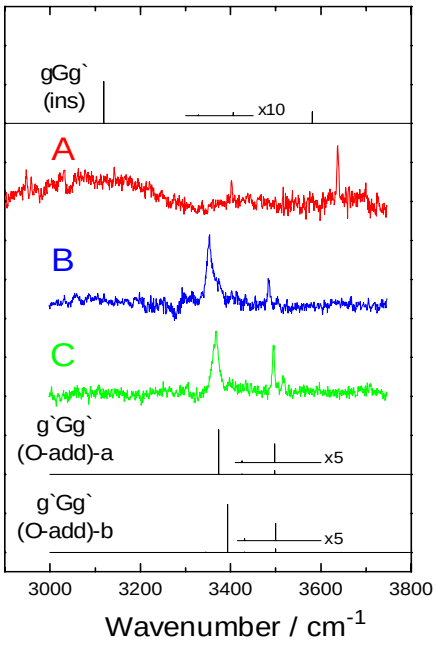

Figure 4. Infra-red ion-dip spectra of clusters of phenol with 2-aminoethanol. Also shown are calculated spectra (B3LYP/6-31+G* with scaling factors of 0.976 (OH) and 0.956 (NH_2)) for the energetically low-lying clusters.

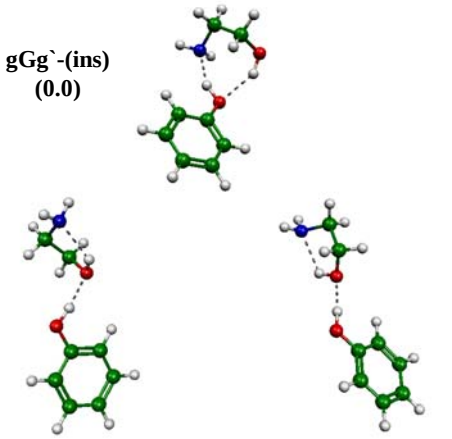

Figure 5. Computed structures (B3LYP/6-31+G*) of clusters of phenol with 2-aminoethanol. Relative energies ($kJmol^{-1}$) are from MP2/6-311+G** single point calculations and include the B3LYP/6-31+G* zero-point energies.

Discussion

Two points of interest arise from the present work. Firstly, clustering of 2-aminoethanol with phenol results in a change of conformation of the ethanolamine group from g`Gg` to a gGg` structure through a distortion of the amino group. This allows two, geometrically favourable, intermolecular H-bonds to be made with phenol with little or no re-arrangement of the OCCN backbone. In contrast the favoured conformation of the uncomplexed species (g`Gg`) requires the OCCN dihedral angle to open by ca. 20°. A similar effect has been noted for hydrated clusters of 2-amino-1-phenylethanol[6].

For all three observed clusters of phenol and 2-aminoethanol, proton transfer *is* observed. The distinct asymmetry (denoting the decay of a metastable state during the flight time) of the 2-aminoethanol-H^+ mass peak in combination with *ab-initio* computation (see Figure 6) indicate that proton transfer occurs after ionisation (for the binary cluster at least). Future work will focus on 2-colour R2PI in an effort to elucidate the precise mechanism.

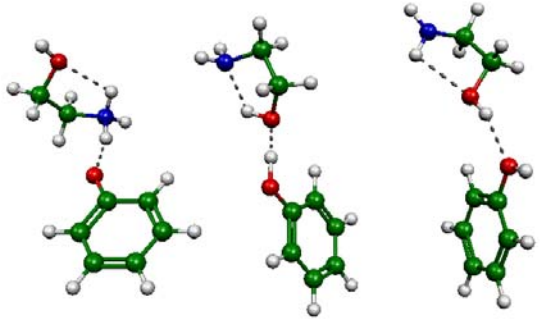

Figure 6. Computed structures for phenol-(2-aminoethanol) clusters following ionisation. Relative energies ($kJmol^{-1}$) are from B3LYP/6-31+G* and include zero-point energies.

Conclusion

A combination of experimental techniques (R2PI, UV-UV hole-burning and IR ion-dip spectroscopy) with high level quantum chemical computation has explored the conformational landscape of clusters of phenol and 2-aminoethanol. Three binary clusters are observed, one of which has an insertion type configuration and two in which phenol adds to the alcohol oxygen leaving the intramolecular hydrogen bond intact. Insertion prompts a significant change in the arrangement of the ethanolamine group.

The appearance of proton transfer (most likely in the ionised state) provides a means of (selectively) producing protonated biomolecules in the gas-phase. Future work will extend the work to more relevant species (e.g. ephedrine) and attempt to produce cold protonated clusters which can be probed by infra-red photodissociation.

References

1. E.G. Robertson and J.P. Simons, Phys.Chem.Chem.Phys., 3, 1, (2001).
2. T.S. Zwier, J.Phys.Chem.A., 105, 8827, (2001).
3. P. Butz, R.T. Kroemer, N.A. Macleod and J.P. Simons, J.Phys.Chem.A., 105, 544, (2001).
4. P. Butz, R.T. Kroemer, N.A. Macleod and J.P. Simons, Phys.Chem.Chem.Phys. 4, 3566, (2002).
5. A.L. Sobolewski, W. Domcke, C. Dedonder-Lardeux and C. Jouvet, Phys.Chem.Chem.Phys., 4, 1093, (2002).
6. N.A. Macleod, E.G. Robertson and J.P. Simons, Mol. Phys., in press.

Sugars in the gas phase: a step-by-step investigation of glycosides

F O Talbot, L C Snoek, N A Macleod, P Butz, J P Simons

Physical and Theoretical Chemistry Laboratory, South Parks Road, Oxford, OX1 3QZ, UK

R T Kroemer

Molecular Modelling & Design, Discovery Research Oncology, Pharmacia, Viale Pasteur 10, 20114 Nerviano, (MI) Italy

Main contact email address: *jpsimons@chem.ox.ac.uk*

Introduction

Carbohydrates are of key importance in all biological systems. They are found with an enormous range of complexity, from simple monosaccharides to megadalton polysaccharide structures; they may exist as free molecules, or bound to proteins and lipids, or incorporated in nucleotide units[1]. This wide range of forms is a reflection of their biological versatility and the great diversity of their biological functions – including structural, protective, metabolic and recognition roles. Such diverse functionalities must have a structural basis. In the last decade, a reductionist approach has been consistently applied to better understand the conformational landscape of complex biological systems by first characterizing their building blocks. This approach was successfully utilized to study polypeptides and DNA via the characterization of amino-acids and DNA bases.

We report here on the extension of this approach to the study of the structural and conformational preferences of carbohydrates. The first step in this methodology was to characterize the monosaccharides glucose and galactose by studying their models phenyl-β-D-glucopyranoside[2] and phenyl-β-D-galactopyranoside[3]. Knowing the conformational landscape of the subunits will then facilitate the study of bigger, more complex sugars and their derivatives.

The combination of gas-phase spectroscopic techniques (like UV/UV and IR/UV ion-dip) with ab initio computations has proven very useful in studying flexible biological molecules[4,5]. These techniques allow the separation (UV/UV ion-dip) and individual characterization (IR/UV ion-dip) of the various conformers present in the gas phase by comparison with ab initio predictions.

Monosaccharides

1. Phenyl-β-D-glucopyranoside (PheβGlc)

The UV R2PI and UV/UV ion-dip spectra of the model monosaccharides phenyl-β-D-glucopyranoside (PheβGlc) were recorded (Figure 1). The UV/UV ion dip spectra reveal the presence of three different conformers in the gas phase, which differ by the orientation of their hydroxymethyl groups. The two most abundant conformers (`A` and `B`) adopt a *gauche* orientation while the least abundant has a *trans* orientation. These assignments follow the comparison of the measured IR spectra to the ones predicted ab initio (see Figure 1). The presence, in the gas phase, of the *trans* conformer contrasts with the aqueous phase NMR data that report only the two *gauche* conformers. In order to better understand the solvation effects, we also investigated the singly hydrated complex of the PheβGlc molecule in the gas phase. The R2PI and UV/UV ion-dip spectra (not shown) revealed the presence of just two conformers, one of which is largely predominant. Comparison with the calculated IR spectra (Figure 2), though extremely delicate, seems to favour assignments of the experimentally observed species to two *gauche* conformers with the water inserting in position 2 (most abundant in panel `b`) and in position 6 (panel `a`) of the sugar ring.

2. Phenyl-β-D-galactopyranoside (PheβGal)

In contrast to glucose, where all the ring-hydroxyl groups are equatorial, galactose has an axial hydroxyl at C4. This results in the OH4···O3 H-bonds being somewhat shorter (~2.2 Å) and slightly more linear in phe-β-D-gal than in the corresponding phe-β-D-glc conformers. The same is also true for the hydrogen-bonded interactions with the hydroxy methyl group,

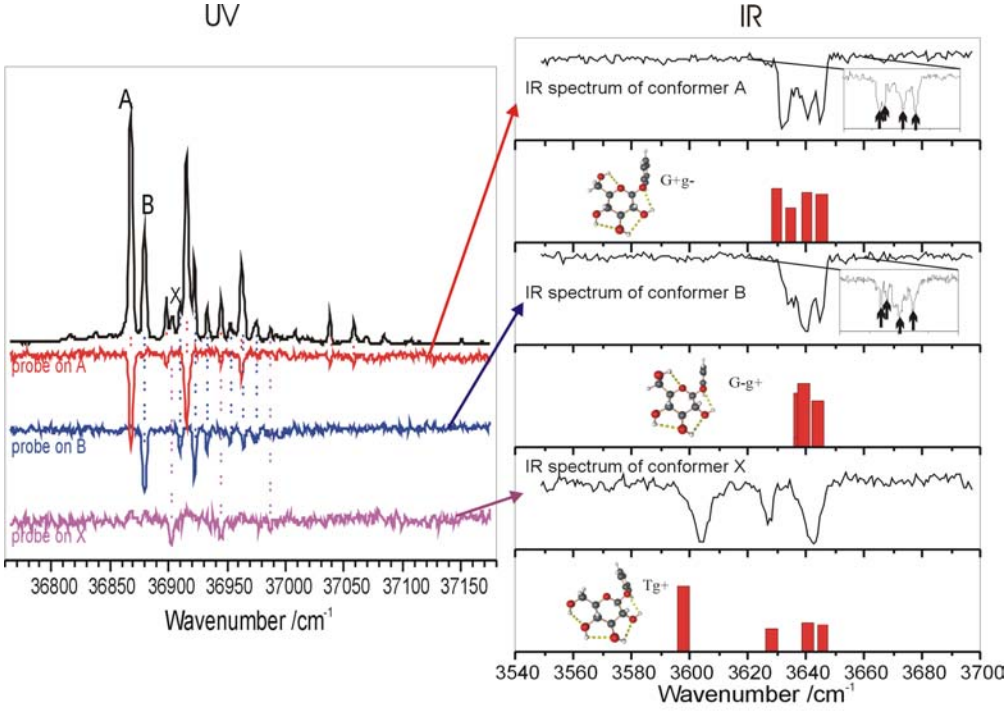

Figure 1. R2PI and UV/UV ion-dip spectra of PheβGlc (*left*) and the corresponding IR spectra (*right*).

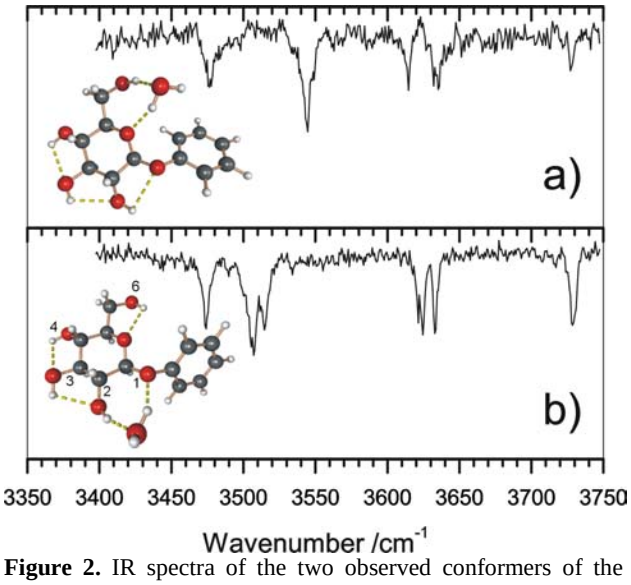

Figure 2. IR spectra of the two observed conformers of the PheβGlc–(H_2O) complex.

OH6···O4 and OH4···O6 in the tttG-g- and gggG-g+ conformers: the O—H stretching modes involving these stronger interactions should appear shifted somewhat to the red of the corresponding modes in phe-β-D-glc.

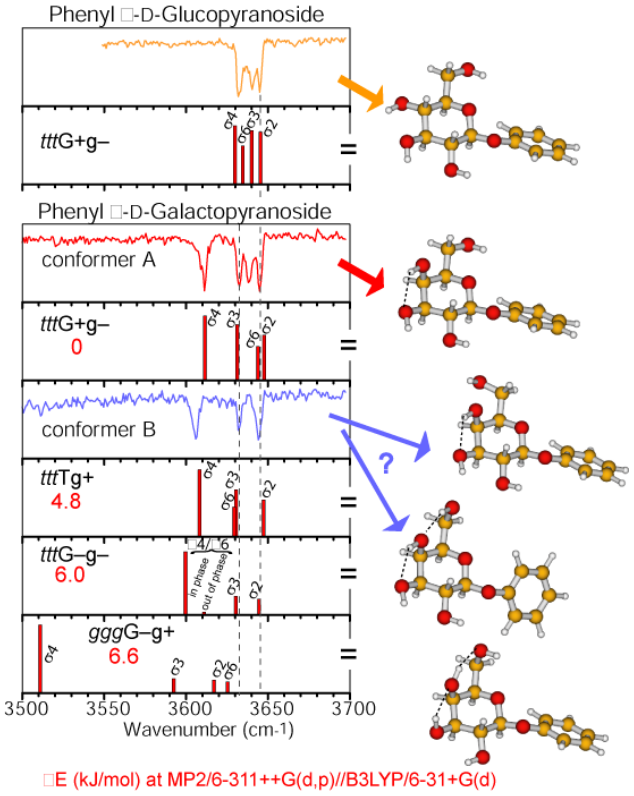

Figure 3. Experimental and calculated infrared spectra of the PheβGal galactoside.

The UV spectra (not shown) reveal one main conformer accompanied with a minor one. The comparison of the experimental and calculated infrared spectra shown in Figure 3 suggests the assignment of the main conformer to the *gauche* conformer G+g–. The minor conformer could either be the other gauche conformer (G–g–) or the *trans*, as both infrared spectra are calculated to be quite similar.

The infrared spectra in the OH stretching region provide distinct fingerprints for the glucose and galactose sugar rings, confirming the high sensitivity of the technique to very subtle structural changes.

Sugar amino-acids (carbopeptoids)

The combination of carbohydrate and amino acid moieties is a route to increased polyfunctionality and is of great interest in peptidomimetics. The relative ease of synthesis of carbopeptoids (compared to oligosaccharides) makes their use especially attractive. The first experimental proof of secondary structure in carbopeptoids was reported by Fleet and co-workers who reported that four repeating tetrahydrofuran amino acid moieties form β-turns in solution[6]. The β-turns are stabilized by the formation of intramolecular hydrogen bonds (Scheme 1). Our IR/UV ion dip spectroscopic technique is especially well suited for identification of such hydrogen bonds.

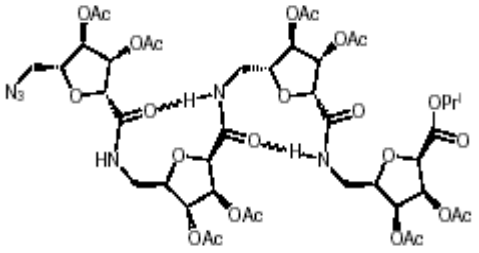

Scheme 1. A carbopeptoid tetramer based on β-D-arabino-furanose which exhibits hydrogen bonding in solution.

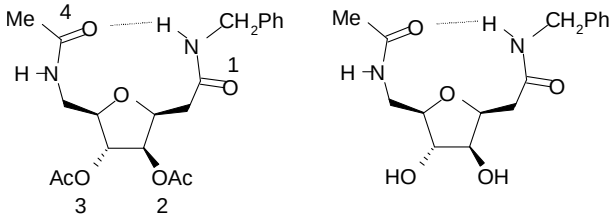

Scheme 2. Protected and un-protected monomer units of the carbopeptoid, showing the `expected` internal H-bond.

The first step of our investigation consisted of checking whether the predicted NH···O=C hydrogen bonds already occurs in the monomer units shown in Scheme 2. The acetylated (protected) monomer does not have OH stretching vibrations, which should allow a straightforward assignment/identification of the two NH stretches.

Protected monomer

The IR/UV ion-dip spectrum (Figure 4, top frame) reveals two NH stretches: one unperturbed at 3456 cm^{-1} while the other is red-shifted (at 3349 cm^{-1}) indicating H-bonding. The ab initio calculations predict however the NH---O=C hydrogen bond to occur, not with the carbonyl at position 4 but with that of the acetate group in position 2 (see computed structure in Figure 4). The proposed structure in Scheme 2 is not a minimum of the Hartree-Fock (HF)/sto-3G hypersurface and all attempts to optimize it led to the global minimum with the NH---O=C(acetate) hydrogen bond. It appears the acetate groups, which replace the hydroxyl in order to simplify the infrared spectra, prevent the formation of the desired inter-chain internal H-bond. Note however that the measured infrared spectra would probably fit either of these conformations.

Unprotected monomer

The IR/UV ion-dip spectrum of the unprotected monomer unit (Figure 4, bottom frame) shows two additional bands associated with the two hydroxyl groups that are no longer blocked. One immediately notices that only *one* band is visible in the 3650 cm^{-1} region, where free OH stretches are expected. This tells us that one of the two OH is involved in a hydrogen bond, which rules out the possibility of a structure like the one

proposed in Scheme 2, which would have two free OHs. The lowest-energy structure calculated ab initio (Figure 4, bottom frame) exhibits an $N_4H^{\cdots}O_2H^{\cdots}O_1$=C internal chain of H-bonds that shifts the frequency of the O2H hydroxyl to the red, in agreement with the experimental spectra.

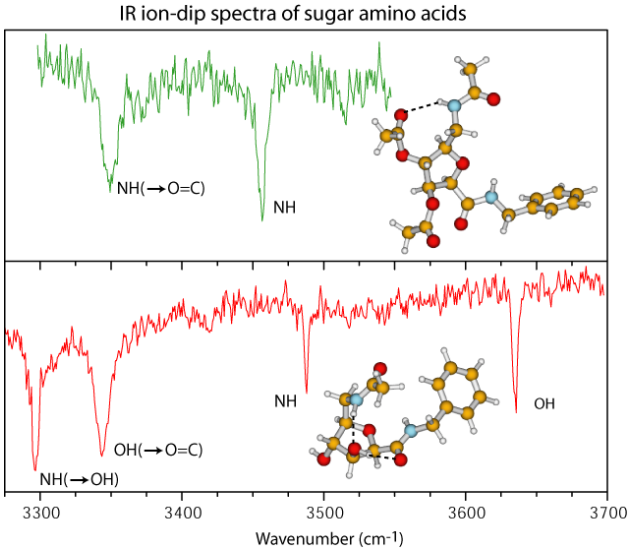

Figure 4. IR spectra of the protected (top) and unprotected (bottom) monomer units, alongside the calculated structures.

Imino-sugars

Inhibition of glycosidases, enzymes which cleave oligosaccharides, promises to have important medical applications including antiviral and antidiabetic uses[7-13]. Imino sugars, saccharide analogs in which the ring oxygen is replaced by a nitrogen, mimic the natural substrate of many glycosidases and have been shown to inhibit their activity. Thus, they are of great interest in the medical community. For example, clinical trials of the imino sugar N-Butyl-deoxynogirimycin (NB-DNJ) have shown benefits against Gaucher disease, a glycolipid lysosomal storage disorder[14]. Understanding the molecular details of the inhibitory activities should lead to the design of better therapeutic agents. As a starting point, we investigated the gas-phase conformations of N-benzyl DNJ, a close relative of NB-DNJ.

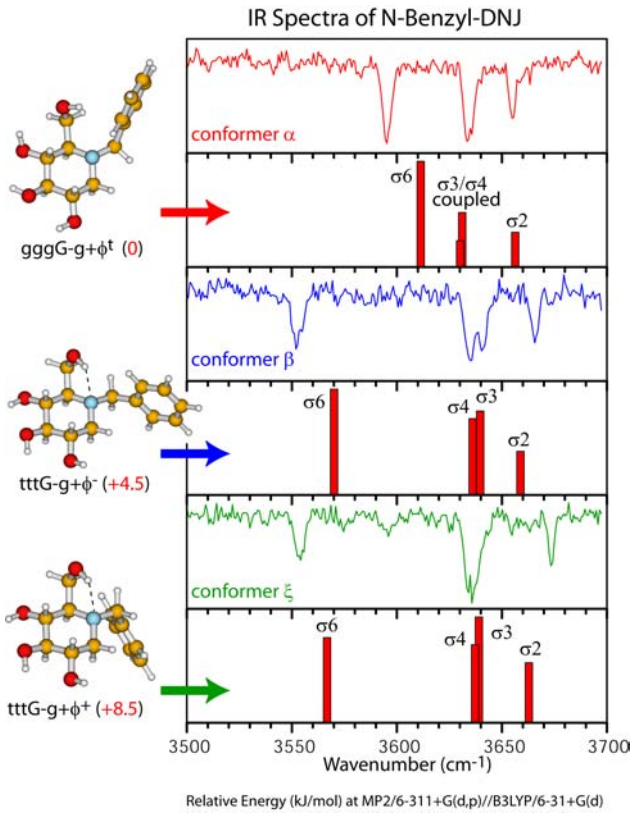

Figure 5. Experimental and calculated infrared spectra of N-benzyl-DNJ.

The R2PI spectra of N-benzyl-DNJ showed the presence of three distinct conformers, two of which have almost degenerate UV spectra. The infrared spectra corresponding to the three conformers are shown in Figure 5, alongside three of the lower-energy calculated conformers that best match the experimental frequencies. In all conformers, the hydroxymethyl group adopts a G–g+ orientation. The fact that only three of the lowest six calculated conformers are observed suggests there might be some conformational relaxation during the cooling process of the supersonic expansion.

Conclusions

These results constitute the first gas phase experimental investigations of carbohydrate building blocks. The infrared spectroscopy in the OH/NH stretching region provides a remarkably sensitive fingerprint of the examined monosaccharide. The investigation of these model monosaccharides has allowed us to study confidently more biologically relevant molecules and opens the doors to the investigation of larger (and more complex) carbohydrates.

Acknowledgments

We wish to thank the EPSRC (NAM, FOT) and the Royal Society (RAJ, LCS) for grant support. We also thank the Lasers for Science Facility at the Rutherford Appleton Laboratory for the loan of a YAG/dye laser combination.

References

1. Stryer, L., Biochemistry. 4th ed. 1995, New York, NY: W.H. Freeman and Company. xxxiv, 1064.
2. Talbot, F.O. and J.P. Simons, Physical Chemistry Chemical Physics, 2002. 4 (15): p. 3562-3565.
3. Jockusch, R.A., F.O. Talbot, and J.P. Simons, Physical Chemistry Chemical Physics, 2003. 5 (8): p. 1502-1507.
4. Robertson, E.G. and J.P. Simons, Physical Chemistry Chemical Physics, 2001. 3 (1): p. 1-18.
5. Zwier, T.S., Journal of Physical Chemistry A, 2001. 105 (39): p. 8827-8839.
6. Smith, M.D., *et al.*, Chemical Communications, 1998(18): p. 2041-2042.
7. Asano, N., *et al.*, Tetrahedron-Asymmetry, 2000. 11 (8): p. 1645-1680.
8. Butters, T.D., R.A. Dwek, and F.M. Platt, Chemical Reviews, 2000. 100 (12): p. 4683-4696.
9. Fleet, G.W.J., *et al.*, Febs Letters, 1988. 237 (1-2): p. 128-132.
10. Gruters, R.A., *et al.*, Nature, 1987. 330 (6143): p. 74-77.
11. Robinson, K.M., E.W. Heineke, and M.E. Begovic, Journal of Nutrition, 1990. 120 (1): p. 105-111.
12. Winchester, B. and G.W.J. Fleet, Glycobiology, 1992. 2 (3): p. 199-210.
13. Winchester, B. and G.W.J. Fleet, Journal of Carbohydrate Chemistry, 2000. 19 (4-5): p. 471-483.
14. Cox, T., *et al.*, Lancet, 2000. 355(9214): p. 1481-1485.

Rate coefficients for removal of CN($X^2\Sigma^+$, v = 2) from selected rotational levels between N_i = 0 and 57 in collisions with N_2 and C_2H_2

K M Hickson, C M Sadowski, I W M Smith

School of Chemical Sciences, The University of Birmingham, Edgbaston, Birmingham, B15 2TT, UK

Main contact email address: *i.w.m.smith@bham.ac.uk*

Introduction

Double resonance (DR) methods provide a powerful technique for investigating energy transfer in molecular collisions[1]. Here we report the results of infrared-visible double resonance (IR-VIS DR) experiments on the total transfer of CN($X^2\Sigma^+$, v = 2, N_i) from several different initial rotational levels between N_i = 0 and 57 in collisions with N_2 and C_2H_2. N_2 does not react with CN, but C_2H_2 is known to react rapidly [2] (k_{reac}(298 K) = 2.8 × 10^{-10} cm^3 $molecule^{-1}$ s^{-1}). In addition to examining how the rate coefficients for collisional removal from specific rotational levels (N_i) depend on N_i in these two systems, we have demonstrated that DR experiments can be used to determine rate coefficients for reaction of radicals in specific rovibronic levels, when reaction is fast enough to compete with rotational relaxation. To obtain this information, both *total* removal rates and *state-to-state* rates from a particular N_i must be measured. The total rate constant ($k_{tot,i}$) is the sum of rate coefficients for loss through both reactive ($k_{reac,i}$) and rotationally inelastic collisions ($k_{ret,i}$); *i.e.*, $k_{tot,i} = k_{reac,i} + k_{ret,i}$.[#] However, the sum over final states (N_f) of the state-to-state rate coefficients ($\Sigma_f k_{i\to f}$) corresponds to $k_{ret,i}$ alone, so that $k_{reac,i}$ for a particular initial state can be determined since $k_{reac,i} = k_{tot,i} - \Sigma_f k_{i\to f}$.

To demonstrate this method, we have measured values of $k_{tot,i}$ and $k_{i\to f}$ for collisions between CN($X^2\Sigma^+$, v = 2, N_i = 0 and 1) and C_2H_2. To verify the argument that the difference between $k_{tot,i}$ and $\Sigma_f k_{i\to f}$ corresponds to the rate constant for removal by reaction, we have also carried out some experiments with N_2. In this case, $k_{tot,i}$ and $\Sigma_f k_{i\to f}$ should be. We are unaware of any previous studies in which the competition between rotational energy transfer and reaction has been studied in this way.

Experimental Method and Analysis

Full details of the experimental method have been reported elsewhere[3]. In brief, CN radicals were generated by photolysis of a small fraction of ICN in mixtures with N_2 or C_2H_2, using the frequency-quadrupled output from a Nd:YAG laser at 266 nm. A small fraction of these radicals was promoted to a specific rovibrational level by absorption of pulsed IR laser radiation tuned to a line in the (2, 0) vibrational overtone band. The evolution of this excited population was then followed using laser-induced fluorescence (LIF), the probe laser being tuned to lines in the (0,2) band of the $B^2\Sigma^+$–$X^2\Sigma^+$ system of CN.

Two kinds of experiment were performed. In *kinetic* experiments, the delay between pulses from the photolysis and IR pump lasers was set to be *ca*. 50 ns and, the delay between pulses from the IR pump and VIS probe lasers was varied and the decay of the LIF signals was fitted to single exponentials. The short delay between the photolysis and pump lasers ensured that the rotationally 'hot' distribution of CN($X^2\Sigma^+$, v = 0) produced from the photolysis of ICN [4] was essentially unrelaxed when the IR pump laser fired, allowing high rotational levels in the $X^2\Sigma^+$, v = 2 level to be accessed. Moreover, it should be appreciated that the CN radicals are formed with a considerable translational velocity[4] (see below)[#].

In *spectroscopic* experiments, the delay between pulses from the IR pump and VIS probe lasers was fixed to correspond to a collisional probability of < 0.2, and the frequency of the probe laser was scanned to record a double resonance spectrum. The relative intensities of lines in this spectrum then yield the state-to-state rate coefficients for transfer from N_i to different final levels N_f.

[#] We assume here that vibrational energy transfer is negligible.

Results and Discussion

Total removal rate coefficients

Rate coefficients for the total removal of CN from specified N_i in ($X^2\Sigma^+$, v = 2) were measured in kinetic experiments. The pressure of the sample was chosen to ensure that the LIF signals decayed to a steady final value within 1 μs and was varied between 50 mTorr for low values of N_i to 5 Torr at the highest N_i excited in the present experiments. Each decay trace gave a first-order rate coefficients, $k'_{tot,i}$, for a known gas density of N_2 or C_2H_2. Values of $k'_{tot,i}$ obtained at different pressures were subsequently plotted against [N_2] or [C_2H_2], yielding the second-order rate coefficients, denoted by $k_{tot,I}$, that are shown in Figure 1.

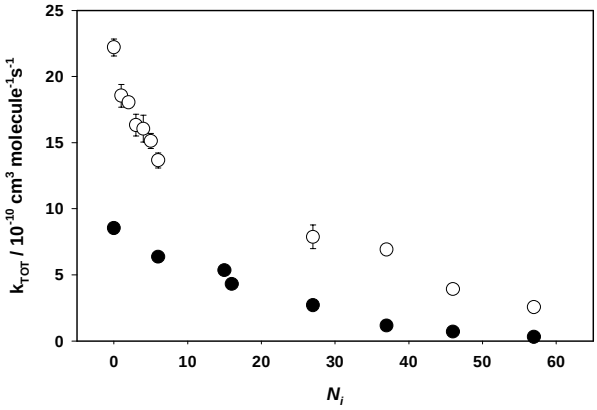

Figure 1. Second-order rate coefficients ($k'_{tot,i}$) for total removal of CN from specific rotational levels $X^2\Sigma^+$, v = 2, N_i, with N_i between 0 and 57, by collisions with: ●, N_2; ○, C_2H_2.

CN($X^2\Sigma^+$, v = 0, N_i = 1) radicals generated by photolysis of ICN at 266 nm are created with a laboratory speed of 2.96 × 10^3 m s^{-1} [4] and the great majority of the radicals promoted to ($X^2\Sigma^+$, v = 2, N_i = 0) were excited before undergoing a collision. Likewise, CN($X^2\Sigma^+$, v = 0, N_i =56) radicals were created with a laboratory speed of 2.04 × 10^3 m s^{-1}. As removal from the initially prepared state occurs at essentially every collision, the reported rate coefficients are properly viewed as phenomenological rate coefficients appropriate to the initial collision energies. For the first collisions between CN($X^2\Sigma^+$, v = 0, N_i = 1) and stationary N_2 molecules, the collision energy would be equivalent to 4940 cm^{-1}, whilst for CN($X^2\Sigma^+$, v = 0, N_i = 57) and stationary N_2, the collision energy would be equivalent to 2345 cm^{-1}. The energies of collisions between CN in a particular rovibrational state and N_2 and C_2H_2 should be very similar and direct comparisons between the results for the two species are valid.

State-to-state rate coefficients for the transfer of CN radicals from $X^2\Sigma^+$, v = 2, N_i = 0 and 1

In these experiments, the time delay (δt) between pulses from the IR pump laser and the VIS probe laser was fixed at < 65 ns

and a pressure of < 100 mTorr was maintained in the cell. These conditions ensured that the probability of a CN radical undergoing a collision before the probe laser fired was < 0.2.

At short delays (δt), the population in any level N_f populated by collisional transfer from N_i is given by:

$$\mathbf{N}_f = k_{i\rightarrow f}\,\mathbf{N}_i\,[M]\,\delta t \qquad (1)$$

The relative populations, $\mathbf{N}_f$ and $\mathbf{N}_i$, were related to the measured integrated line areas, I_i and I_f, using the respective line strength factors for *saturated* P- and R-branch LIF transitions[5]. In practice, only R-branch transitions were used to measure the relative populations. Each of the energy levels is split into doublets so we can substitute N for j as $j = (N + 1/2)$ and $j = (N - 1/2)$ for the upper and lower spin components, respectively. The exception to this rule occurs when $N_i = 0$, where $j = N + ½$ only[5]. As an infrared R-branch transition was used to populate CN($X^2\Sigma^+$, v = 2, N_i = 1), only the j = 3/2 spin component was initially populated.

The observed line intensities directly reflect the rates of collisional transfer from the initially populated level. These line intensities were converted to population ratios using the appropriate form of the line strength factors for the CN $B^2\Sigma^+$–$X^2\Sigma^+$ probe transition, and finally converted to state-to-state rate coefficients by dividing by the product of [M] and δt. The individual state-to-state rate coefficients, $k_{i\rightarrow f}$, obtained for collisions of CN with both N_2 and C_2H_2 are listed in Table 1.

$N_f - N_i$	CN($X^2\Sigma^+$,v=2, N_i=0) + N_2	CN($X^2\Sigma^+$,v=2, N_i=0) + C_2H_2	CN($X^2\Sigma^+$,v=2, N_i=1) + C_2H_2
-1			3.3 ± 0.4
0			
1	4.1 ± 0.4	8.2 ± 1.0	5.9 ± 0.7
2	2.2 ± 0.3	3.4 ± 07	2.4 ± 0.4
3	1.16 ± 0.44	2.3 ± 0.4	1.52 ± 0.21
4	0.89 ± 0.33	1.31 ± 0.45	1.22 ± 0.19
5	0.65 ± 0.23	0.91 ± 0.43	0.80 ± 0.22
6			0.54 ± 0.21
$\Sigma\, k_{i\rightarrow f}$ [a]	9.0 ± 0.8	16.1 ± 1.4	15.7 ± 1.0
k_{Ni} [b]	8.5 ± 0.4	22.2 ± 0.7	18.5 ± 0.9
$k_{react,i}$ [c]		6.1 ± 1.5	2.9 ± 1.3

Table 1. State-to-state rate coefficients ($k_{i\rightarrow f}$ / 10^{-10} cm^3 $molecule^{-1}$ s^{-1}) for collisional transfer of population from the initially populated level, N_i to final level N_f.

[a] the individual values of $k_{i\rightarrow f}$ have been added to obtain $\Sigma_f\, k_{i\rightarrow f}$.
[b] k_{Ni} values shown here are derived from the kinetic experiments described in the text. For collisions of CN with C_2H_2, $k_{tot,i} \equiv k_{Ni}$. The values for $k_{tot,i}$ are shown in Figure 1.
[c] The rate coefficient for reactive loss of CN, $k_{reac} = k_{Ni} - \Sigma_f\, k_{i\rightarrow f}$.

Discussion

In comparison with the data for radicals in $^2\Pi$ states colliding with N_2, the rate coefficients k_{N_i} for total removal of CN($X^2\Sigma^+$) from specific levels N_i in collisions with N_2 fall more steeply with N_i. In part, this steep fall of k_{N_i} with N_i may be due to the fact that the collision frequency decreases at higher N_i because the translational energy associated with the formation of CN in higher rotational levels is less. However, the major reason may be connected with the fact that the interaction of a species in a $^2\Sigma^+$ state with a closed shell species gives rise to only a single doublet potential energy surface. On the other hand, two potential energy surfaces ($^2A'$ + $^2A''$) arise when a species in a $^2\Pi$ state interacts with a closed shell species. In the latter case, collisions can lead to rotational energy transfer both within the same spin-orbit manifold and between the two spin-orbit manifolds. The former occurs under the influence of the sum potential $V_{sum} = {}^1/_2(^2A' + {}^2A'')$, the latter under the influence of the difference potential $V_{diff} = {}^1/_2(^2A' - {}^2A'')$[6]. The latter can become more important at high N_i and might counteract the tendency for the rate coefficients to decrease as N_i increases.

The very large values of k_{N_i} for low N_i result in part from the high speed of the photolytically generated CN radicals and hence the large relative velocity in collisions between these radicals and the molecular partner. Nevertheless, the corresponding collision cross-sections for total removal, calculated by dividing the rate coefficients shown in Figure 1 by the initial speed of the CN radicals given earlier, are very large: 29 Å^2 for CN($X^2\Sigma^+$, v = 2, N_i = 0) + N_2 and 75 Å^2 for CN($X^2\Sigma^+$, v = 2, N_i = 0) + C_2H_2. Between both pairs of collision partners, the dominant attractive force at long-range should be that between the electric dipole moment of CN (1.74 D) and the quadrupole moment of N_2 and C_2H_2. The reaction between CN and C_2H_2 is known to occur on a potential energy surface without a barrier[2], so it is possible that, in this case, the potential at long-range is even more attractive than that due to purely electrostatic forces because of the onset of attractive chemical forces. The state-to-state rate coefficients for CN($X^2\Sigma^+$, v = 2, N_i = 0) with N_2 show the expected decrease with increased ΔN. For N_2, the agreement between the values of $k_{tot,i}$ and $\Sigma_f\, k_{i\rightarrow f}$ is as expected.

We attribute the difference in the values of $k_{tot,i}$ and $\Sigma_f\, k_{i\rightarrow f}$ for collisions of CN($X^2\Sigma^+$, v = 2, N_i = 0 and 1) with C_2H_2 to rotationally state-specific reaction and believe that our experiments are the first to demonstrate that DR methods can be used to measure such rate coefficients in systems where reaction is sufficiently rapid to compete with rotational relaxation. The state-selected rate coefficients for reaction given in Table 1 show that CN in N_i = 0 reacts more rapidly than a thermal distribution of CN over rotational states, as is present in a standard kinetics experiment[2]. We intend to extend the present work by making similar measurements to those reported here for CN($X^2\Sigma^+$, v = 2, N_i = 0 and 1) for a wide range of initial rotational levels in order to determine the influence of the rotational state of CN on the value of the reaction rate constant and its dependence with temperature.

References

1. P.J. Dagdigian in The Chemical Dynamics and Kinetics of Small Radicals, eds K. Liu and A.F. Wagner (World Scientific, Singapore, 1995) chap. 8, p. 315.
2. I.R. Sims, J-L. Queffelec, D. Travers, B.R. Rowe, L.B. Herbert, J. Karthauser and I.W.M. Smith, Chem. Phys Lett. 211 (1993) 461.
3. K.M. Hickson, C.M. Sadowski and I.W.M. Smith, Chem. Phys. Lett. 372/3-4, (2002) 443.
4. Nadler, D. Mahgerefteh , H. Reisler and C. Wittig, J. Chem. Phys. 82 (1985) 3885.
5. G. Herzberg, Molecular Spectra and Molecular Structure. I. Spectra of Diatomic Molecules (van Nostrand Co., Princeton and New York, 1950).
6. M.H. Alexander, J. Chem. Phys. 76 (1982) 5974.

Detection of visible emissions from Rare Earth doped Yttria phosphors under UV excitation

R Withnall, J Silver, E Barrett

Centre for Phosphors and Display Materials, School of Chemical and Life Sciences, University of Greenwich, Central Avenue, Chatham Maritime Campus, Chatham, Kent, ME4 4TB, UK

Main contact email address: *R.Withnall@gre.ac.uk*

Introduction

Among the processes converting light to higher energy, frequency conversion in non-linear optical crystals is the best known. This requires coherent light of high intensity, whereas up-conversion is a non-linear process with a completely different physical basis which occurs mainly in the rare earth compounds. We have recently studied up-conversion emission from Y_2O_3:Er^{3+}, Y_2O_3:Eu^{3+}, Y_2O_3:Tm^{3+} and Y_2O_3:Ho^{3+} under 632.8 nm excitation[1-5]. The reason that up-conversion luminescence is obtained from these phosphors is that the activator ions contain a large number of low-lying Russell-Saunders *LSJ* states having lifetimes on the microsecond to millisecond scales. These long lifetimes are due, in large part, to the weak electron-phonon coupling between the 4*f* electrons of the lanthanide cations and the Y_2O_3 host lattice, and they facilitate up-conversion via the excited states absorption (ESA) mechanism. An alternative mechanism involves a co-activator ion which transfers energy to the activator, i.e. energy transfer up-conversion (ETU). There was evidence to suggest that both the ESA and ETU up-conversion mechanisms can occur in Y_2O_3:Tm^{3+} and Y_2O_3:Ho^{3+} phosphors[4,5]. The interest of the present work was to investigate complementary down-conversion luminescence processes in Y_2O_3:M^{3+} phosphors when exciting them with ultraviolet light. Our ultimate aim is to obtain quantum cutting in oxide lattices which are doped with two different rare earth ions, whereby more than one visible photon is emitted for each ultraviolet photon that is absorbed.

Experimental

Samples of Y_2O_3:M^{3+} phosphors (where M^{3+} is a trivalent rare earth cation) were prepared via a homogeneous precipitation route prior to firing, as described previously[1-5]. The emission spectra were collected with a Spex 1877 Triplemate Raman spectrometer equipped with a Peltier-cooled open-electrode CCD detector (Wright instruments). Excitation of wavelength equal to 244 nm was provided by an intracavity frequency-doubled argon ion laser (Coherent Ltd.) which was a loan pool laser (CWL3) from the Central Laser Facility.

Results and Discussion

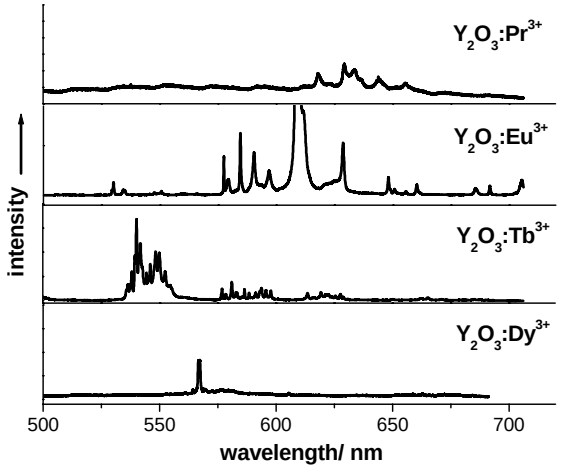

Figure 1. Visible emission spectra obtained from Y_2O_3:M^{3+} (M^{3+} = Pr^{3+}, Eu^{3+}, Tb^{3+}, Dy^{3+}) phosphors under 244 nm excitation.

Strong visible luminescence was observed from Y_2O_3:Eu^{3+} under 244 nm excitation as can be seen in Figure 1. This result was expected as Y_2O_3:Eu^{3+} is a red photoluminescent phosphor that is used in fluorescent light tubes, the phosphors being excited by the light emission from mercury vapour. The Y_2O_3:Eu^{3+} phosphor has a strong absorption around 244 nm due to charge transfer transition between the Eu^{3+} and O^{2-} ions. Light emissions are also shown in Figure 1 for Y_2O_3:Pr^{3+}, Y_2O_3:Tb^{3+}, and Y_2O_3:Dy^{3+} in the red, green and yellow regions, respectively.

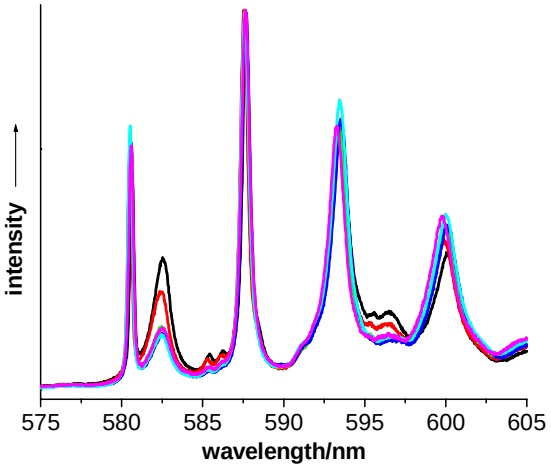

Figure 2. Visible emission spectra obtained from Y_2O_3:Eu^{3+} phosphors under 244 nm excitation for Eu^{3+} concentrations of 1, 2, 3, 4, 5 and 7 mol % shown by the black, red, green, blue, cyan and magenta traces, respectively.

As can be seen from Figure 2, an emission band at 582.5 nm decreases in intensity on increasing the Eu^{3+} concentration from 1 to 3 mol %, but its intensity remains approximately constant on increasing the Eu^{3+} concentration from 3 to 7 mol %. This behaviour is explained by energy transfer from Eu^{3+} on S_6 sites to Eu^{3+} on C_2 sites which is less efficient for the lower Eu^{3+} concentrations where the activator ions are more separated from each other.

References

1. J Silver, M I Martinez-Rubio, T G Ireland, G R Fern and R Withnall, J. Phys. Chem. B, 105 948, (2001)
2. J Silver, M I Martinez-Rubio, T G Ireland and R Withnall J. Phys. Chem. B, 105 7200, (2001)
3. J Silver, M I Martinez-Rubio, T G Ireland, G R Fern and R Withnall, J. Phys. Chem. B, 105 9107, (2001)
4. J Silver, M I Martinez-Rubio, T G Ireland, G R Fern and R Withnall, J. Phys. Chem. B, 107 1548, (2003)
5. J Silver, M I Martinez-Rubio, T G Ireland and R Withnall J. Phys. Chem. B, accepted for publication, (2003)

Detection of visible emissions from Rare Earth doped Yttrium Vanadate phosphors under UV excitation

R Withnall, M P Rebollo-Pedruelo, J Silver, E Barrett

Centre for Phosphors and Display Materials, School of Chemical and Life Sciences, University of Greenwich, Central Avenue, Chatham Maritime Campus, Chatham, Kent, ME4 4TB, UK

R Janes

Department of Chemistry, Open University, Walton Hall, Milton Keynes, MK7 6AA, UK

Main contact email address: *R.Withnall@gre.ac.uk*

Introduction

In the past yttrium vanadate (YVO_4) has been shown to be a useful host lattice for phosphors containing rare earth cations. Indeed, YVO_4:Eu^{3+} was developed in 1964 as a red phosphor for colour television and it was used for over 20 years in cathode ray tubes. However, another Eu^{3+} activated phosphor, Y_2O_2S:Eu^{3+}, was developed a short time later and it is currently in use due to its superior luminescence efficiency. Furthermore YVO_4:Eu^{3+} is known to be efficiently excited by near ultraviolet light, making it useful as the red phosphor in high pressure mercury lamps.

Experimental

Samples of YVO_4:M^{3+} phosphors (where M^{3+} is a trivalent rare earth cation) were prepared by both precipitation and combustion methods. For the precipitation method, aliquots of an aqueous solution of the nitrates of yttrium and the dopant rare earth were added to an aqueous solution of ammonium metavanadate and EDTA. Then, following the addition of urea, the whole mixture was heated to boiling until 2 h after precipitation[1]. A literature method was followed for the synthesis of YVO_4:M^{3+} phosphors via the combustion method[2].

The emission spectra were collected with a Spex 1877 Triplemate Raman spectrometer equipped with a Peltier-cooled open-electrode CCD detector (Wright instruments). Excitation of wavelength equal to 244 nm was provided by an intracavity frequency-doubled argon ion laser (Coherent Ltd.) which was a loan pool laser (CWL3) from the Central Laser Facility.

Results and Discussion

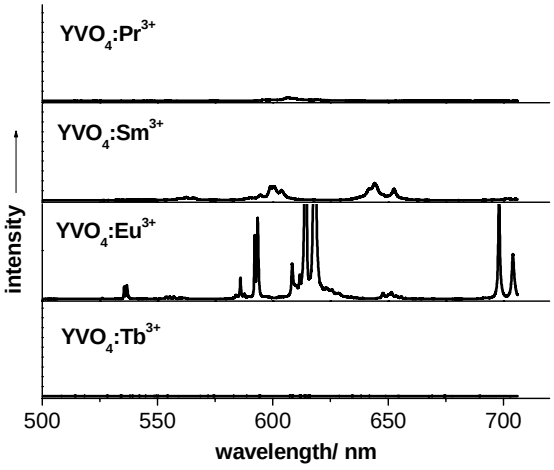

Figure 1. Visible emission spectra obtained from YVO_4:M^{3+} (M^{3+} = Pr^{3+}, Sm^{3+}, Eu^{3+}, Tb^{3+}) phosphors under 244 nm excitation.

As can be seen from Figures 1 and 2, YVO_4 provides a good host for the trivalent rare earth cations. However, it is interesting that no visible emission is observed from the YVO_4:Tb^{3+} phosphor under 244 nm excitation. This observation is in contrast to that observed for the Y_2O_3:Tb^{3+} phosphor which exhibits a green emission under 244 nm excitation[3]. It appears that quenching can occur in YVO_4:Tb^{3+} via a low-lying charge transfer state of the type Tb^{4+} - V^{4+} which provides a non-radiative decay pathway.

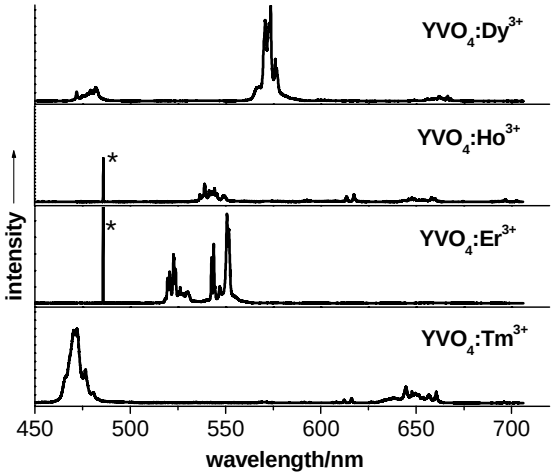

Figure 2. Visible emission spectra obtained from YVO_4:M^{3+} (M^{3+} = Dy^{3+}, Ho^{3+}, Er^{3+}, Tm^{3+}) phosphors under 244 nm excitation. The asterisk denotes a line at 488 nm due to the second order diffraction of the 244 nm laser line.

The strong red emission observed from YVO_4:Eu^{3+} is dominated by the doublet at *ca.* 615 nm which is due to the $^5D_0 \rightarrow {}^7F_2$ transition. This $\Delta J = 2$ transition is a so-called hypersensitive transition as it gives rise to an emission which is strongly influenced by the surroundings of the rare earth ion. Likewise the strong emission observed from YVO_4:Dy^{3+} at *ca.* 570 nm is due to the $^4F_{9/2} \rightarrow {}^6H_{13/2}$ transition which is also a hypersensitive $\Delta J = 2$ transition. Both of these hypersensitive transitions give rise to strong emissions because the Eu^{3+} and Dy^{3+} ions are located on D_{2d} sites of the tetragonal YVO_4 lattice which do not have a centre of symmetry.

Conclusions

YVO_4 is a good host lattice for the Pr^{3+}, Sm^{3+}, Eu^{3+}, Dy^{3+}, Ho^{3+}, Er^{3+} and Tm^{3+} rare earth cations when using 244 nm excitation. However, YVO_4 is not a good host lattice for Tb^{3+} since the emission from this cation is quenched by the low-lying charge transfer state of the type Tb^{4+} - V^{4+} which provides a non-radiative decay pathway.

References

1. A Newport, J Silver and A Vecht
J. Electrochem. Soc., 147 3944 (2000)

2. S Ekambaram and K C Patil
J. Alloys and Compounds, 217 104 (1995)

3. R Withnall, J Silver and E. Barrett, this report,
CLF Annual Report RAL-TR-2003-018, 140, (2003)

Laser ablation and photocrystallographic development work on Organic and Organometallic complexes

K F Bowes, J M Cole, S L G Husheer

Department of Chemistry, University of Cambridge, Lensfield Road, Cambridge, CB2 1EW, UK

P R Raithby

Department of Chemistry, University of Bath, Claverton Down, Bath, BA2 7AY, UK

S J Teat

Synchrotron Radiation Source, CCLRC Daresbury Laboratory, Daresbury, Warrington, Cheshire, WA4 4AD,UK

I P Clark, M Gourlay, A W Parker, M Towrie

Central Laser Facility, CCLRC Rutherford Appleton Laboratory, Chilton, Didcot, Oxon, OX11 0QX, UK

Main contact email address: *jmc61@cam.ac.uk*

Introduction

Since its development in the early part of the last century, single crystal X-ray crystallography has played an essential role in the characterization of compounds, but until recently has been a purely static technique, determining the ground state structures of crystalline materials. Now, a new and exciting field known as time-resolved crystallography is developing, with huge potential, which allows the structure of transient species in a single crystal to be ascertained. If the transient species of interest are generated by photo-excitation, then the technique is commonly referred to as 'photocrystallography' [1,2].

In a 'photocrystallographic' experiment, the crystal sample is irradiated with a laser, and depending on the lifetime of the excited state, a strategy is employed to probe the geometry changes, using X-ray diffraction. For lifetimes that are longer than the laser repetition rate, a pseudo-steady-state of the excited state can be generated, and a continuous pump-probe method employed. This means that the laser continues to irradiate the crystal throughout the X-ray data collection. If the lifetimes are of the order of milliseconds or microseconds, a mechanical chopper can be used to create X-ray pulses that are synchronised with the laser acting on the crystal. For very short lifetimes (micro- or pico- second), X-ray pulses can be created by employing the inherent time structure of a synchrotron, which are then time-gated to a pulsed laser with nano- or femto-second bandwidth.

To acquire the desired information about the excited state structure, the photoexcited and ground state crystal are compared in both real and reciprocal space, by the generation of a photodifference electron density map.

The work reported here describes the preliminary laser testing carried out before a 'pseudo-steady-state photocrystallographic' experiment on terpyridine, **1**, the 'excited state' experiment itself, and laser ablation studies on organometallic compounds in preparation for future photocrystallographic experiments.

1 was chosen as the sample for the experiment due to its long phosphorescence lifetime, reported as 2.1 seconds in frozen ethanol at 77 K [3], allowing the continuous pump-probe method to be employed. Technically this type of photocrystallographic experiment is relatively straightforward, as it does not require synchronization of the laser and X-ray beams. **1** is commonly used as a ligand in transition metal and lanthanide complexes, which are of interest due to their potential application as light harvesting materials, and in the analysis of biomedical materials[4].

The photophysics of **1** in solution are well known[4]. However, it could not be assumed that **1** will exhibit the same properties in the crystalline form. This is particularly true since a different polymorph of **1** is being utilized in these experiments compared with that on which the photophysical experiments were carried out, and polymorphs of a compound frequently display different physical properties. Therefore, the solid state UV/Vis absorption spectrum was obtained, the fluorescence UV/Vis emission spectrum of a single crystal was measured at room temperature and at 104 K, and the fluorescence lifetime was measured at 100 K. However, for the photocrystallography experiment, it is the phosphorescence properties that are of greater interest and, therefore, the phosphorescence lifetime (τ_p) and pseudo-steady-state of phosphorescence were measured as a function of temperature, using laser radiation of wavelength 355 nm. Laser ablation studies were also undertaken to see whether or not the crystal would survive constant laser irradiation during X-ray data collection.

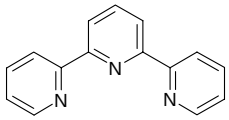

Figure 1. Structure of **1**.

Preliminary Laser Testing

Methods

The preliminary experiments were carried out at the Nanosecond Laser Laboratory at the CLF. A Nd:YAG laser was used to excite the crystal at 355 nm, 10Hz repetition rate and a spectrometer with monochromator, fronted with a 355 nm filter to remove incident beam, was used to probe the emissive spectrum of the fluorescent state. Variable temperature measurements of the phosphorescent state were achieved using an open-flow nitrogen flow from an Oxford Cryosystems Cryostream cooling apparatus. Associated lifetime measurements were measured via a photomultiplier tube placed on the exit to the monochromator housing and recorded on an ns-based two-channel oscilloscope.

During the ablation studies, the wavelength was changed to 395nm. The diffraction grating was used to tune the wavelength.

Laser ablation testing was initially carried out at 100 K with a laser wavelength of 355 nm. The laser (rep rate 10 Hz) was focused on the crystal for 10 minutes and the difference in intensity between the ground state and the excited state was monitored during that time using an oscilloscope, to give an indication of crystal damage. This procedure was carried out for laser energies 0.5 mJ/mm^2, 1 mJ/mm^2 and 2 mJ/mm^2, and repeated with a laser wavelength of 395 nm, as the absorption spectrum showed that this was the optimal wavelength for photoexcitation of terpy. The wavelength was changed using a laser dye, PBBO, dissolved in dioxane (range of 386-420 nm). The dye laser was a Lambda Physik FL3002, pumped by a Lumonics Pulsemaster 848 excimer laser (XeCl, 308 nm).

Results and Discussion

The solid state UV/vis absorption spectrum (Figure 2) shows that at wavelengths lower than 340nm the sample of **1** is saturated, at 355 nm the absorbance is 0.57 and at wavelengths greater than 390 nm the absorbance is less than 0.2. In order for the laser beam to pass through the sample, and not cause localised heating within the crystal, the absorption has to be fairly low (but not zero, otherwise no molecules will be excited), and thus wavelengths longer than 355 nm but less than 532 nm are favoured for the photoexcitation of **1**.

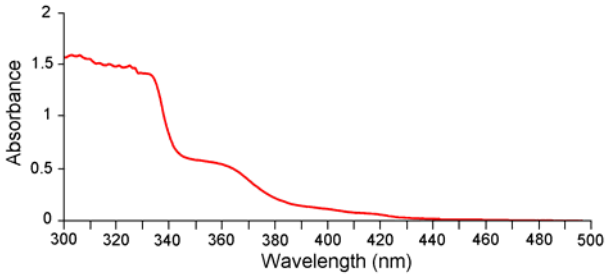

Figure 2. Solid state absorption spectrum of **1**.

The fluorescence emission spectrum shows that the intensity of the peak at 530 nm at 104 K is more than double that which it is at room temperature (Figure 3). Figure 4 shows the fluorescence profile at 104 K from which the fluorescence lifetime was determined as 18 ns.

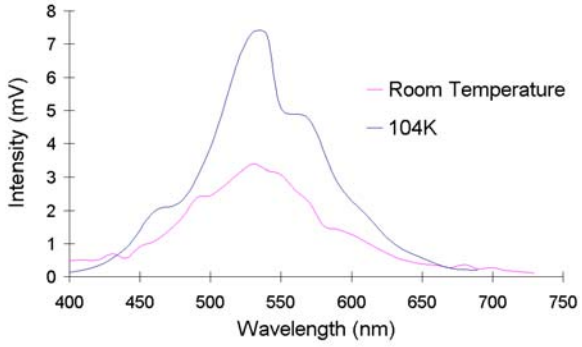

Figure 3. Fluorescence emission spectrum of **1** at 104 K and room temperature.

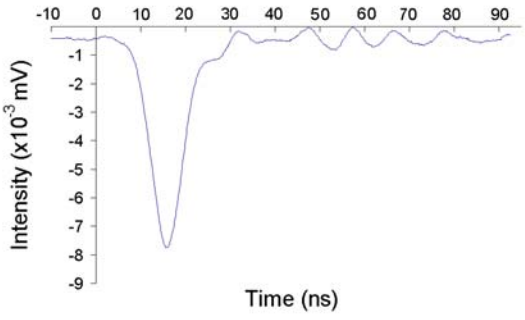

Figure 4. Fluorescence profile of **1** at 104 K.

The phosphorescence lifetime of the sample decreased as the temperature increased, as shown in Figure 4. From 100K (when τ_p = 0.91 s) to 240 K, the decrease is very small, but this is followed by a sharp drop as the temperature rises to 280 K.

These results show that a pseudo-steady-state of photo-excited molecules in a crystal of **1** can be achieved with a laser, and that it is imperative to carry out the photocrystallography experiment at as low a temperature as possible. Moreover, the photophysics measurements on this new polymorph of **1** are of value in their own right.

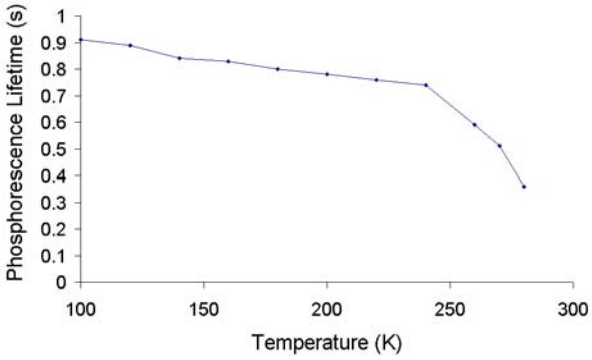

Figure 5. Graph to show phosphorescence lifetime of **1** as a function of temperature.

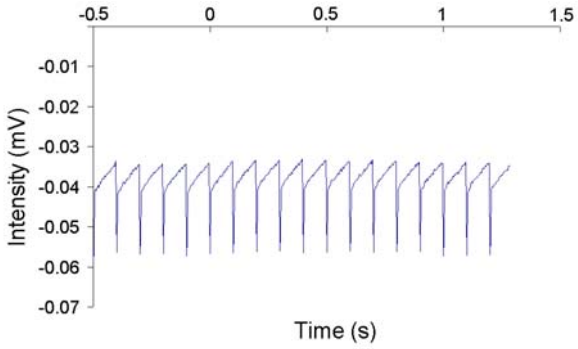

Figure 6. Pseudo-steady-state of 1 at 100 K, achieved by laser irradiation at 355 nm, 10 Hz rep rate.

Photocrystallography Experiment

Methods

The photocrystallography experiment was carried out at Station 9.8, SRS, Daresbury. The lasers employed in this experiment were a Nd:YAG laser, and a dye laser – the dye used was Excalite 411 (0.30 g/litre of *p*-dioxane). An Oxford Cryosystems Cryostream cooling apparatus was used to cool the sample.

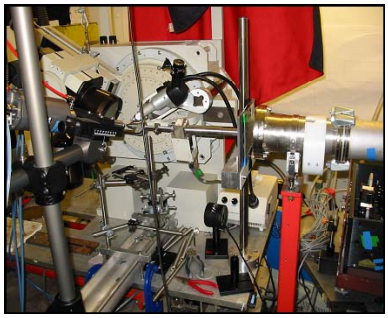

Figure 7. Experimental set-up at Station 9.8 at SRS, Daresbury.

The X-ray wavelength was 0.6928 Å with the synchrotron accelerator in multibunch mode. Data was collected at 150 K, as the insertion of the crystal into the gas flow in the range 90 – 150 K caused the crystal to fracture.

Two full sets of data were collected: a ground state set (7141 reflections collected, $4.40^0 < 2\theta < 58.857^0$) and a set when the laser was irradiating the crystal (8568 reflections, $4.401^0 < 2\theta < 58.880^0$).

Software was developed [5] to interleave frames of diffraction data with the laser on and laser off, which would allow time dependent variations in the experiment to be accounted for. The software was successful in its aim, but the crystal only survived about 3 h of an 11 h data collection, and therefore the data could not be analysed.

Results and Discussion

The unit cell parameters of the ground state and laser irradiated crystals are almost identical, although in successful photocrystallography experiments one rarely sees a discernible difference in cell parameters. There is little, if any, observable difference between the ground state and excited state data that was collected. There are several possible reasons for this: first, there is in fact no perceptible change in molecular geometry when the molecules are excited; second, the population of the excited state in the crystal was too low for any change in geometry to be detected. Calculations estimated the population to be about 2 %. If the true population were less than 2 %, observing any geometry difference in between the ground state and the lased sample would be very difficult. Thirdly, thermal libration may have entirely masked the changes in molecular geometry. It was therefore unfortunate that we were unable to carry out the experiment at a much lower temperature.

Although a pseudo-steady-state of the excited state population could be obtained with **1**, and it withstood laser irradiation for short periods during testing at the CLF, with hindsight it was not an ideal sample. The quality of the crystals obtained by recrystallisation was not high enough, considering the subtlety of the structural changes sought, and during the experiment **1** was far more sensitive to temperature and heating and cooling effects than our preliminary results suggested.

For future photocrystallographic experiments the sample must be robust, form high quality crystals, and undergo an observable structural change upon excitation. Despite being unsuccessful in the ultimate goal of obtaining structural information of the excited state of **1**, the experience gained through this experiment, in particular, successfully setting up the complex experimental arrangement, will no doubt prove invaluable for further work.

Laser Ablation Studies on Organometallics

Methods

A Nd:YAG laser from the Laser Loan Pool was used to undertake laser ablation studies on iridium complexes (**2** to **5**) and gold acetylides (**6** to **8**), which are compounds of interest for future photocrystallographic experiments.

Each sample was irradiated for 1 h at a known laser power with 10Hz rep rate, and any resulting physical damage observed by optical inspection. The sample was rotated by 90^0 to check for anisotropy of laser absorption. If the sample appeared to be intact, the laser power was increased and the procedure repeated.

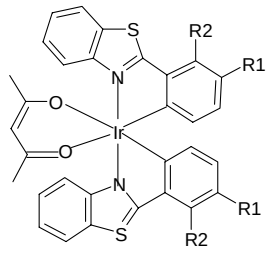

Cpd	R1	R2
2	CF_3	H
3	Me	H
4	OMe	H
5	H	F

Figure 8. Structure of **2** to **5**.

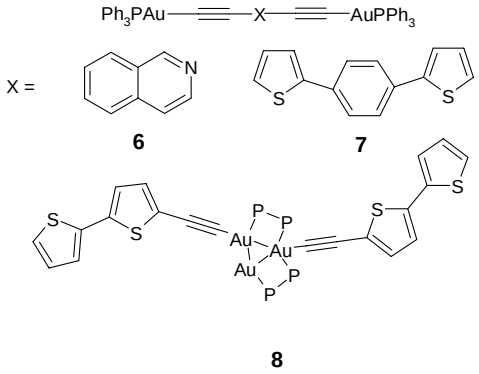

Figure 9. Structures of **6** to **8**.

Results and Discussion

Sample	Maximum Power (mJ/mm^2/pulse) with laser at 10Hz	Maximum Energy (mJ/mm^2/pulse) with laser at 1Hz
2	1.2	-
3	1.6	-
4	1.2	-
5	0.5	-
6	0.7	1.6
7	0.4	1.6
8	< 0.4	1.6

Table 1. Maximum laser energy that samples could withstand.

The iridium complexes gave encouraging results, withstanding long term (hrs) laser irradiation. The exception was compound **5**, but the crystals were of poorer quality. The gold acetylides could only withstand laser irradiation when the laser had a low rep rate, and it is unlikely that they will be suitable for a monochromatic photocrystallographic experiment.

Acknowledgements

The authors wish to thank Inamur Laskar, Department of Applied Chemistry, NCTU, University of Taiwan, Hsimchu, Taiwan, ROC for provision of the Ir complexes, Ms Li-ling Ooi, University of Bath, for providing the terpy crystals, SRS for beam time and CLF for the laser loan. KFB and SLGH are grateful for PhD funding: KFB from the EPSRC and CMSD (CCLRC), SLGH from the Cambridge Commonwealth Trust, SRS, Daresbury Laboratories, UK, and the Foundation for Research Science and Technology, New Zealand. JMC also wishes to thank the Royal Society for a University Research Fellowship and St. Catharine's College, Cambridge, for a Bibby Research Fellowship.

References

1. P. Coppens, D. V. Formitchev, M. D. Carducci and K. Culp, J. Chem. Soc., Dalton Trans., 865, (1998)
2. P. Coppens Chem. Commun., 1317, (2003).
3. Saskar and S. Chakravorti J. Luminescence, 63, 143, (1995)
4. H. R. Murner, E. Chassat, R. P. Thummel and J. G. Bunzli, J. Chem. Soc., Dalton Trans., 2809, (2000)
5. S. L. G. Husheer, J. M. Cole, S. J. Teat, M. Towrie, P. R.Raithby, J. Appl. Cryst., in prep, (2003)

Characterisation of DNA damage induced by near infrared multiphoton absorption

E L Davis, T J Jenner, P O'Neill

MRC Radiation and Genome Stability Unit, Harwell, Didcot, Oxon, OX11 0RD, UK

S W Botchway, E Conein, A W Parker

Central Laser Facility, CCLRC Rutherford Appleton Laboratory, Chilton, Didcot, Oxon, OX11 0QX, UK

Main contact email address: *p.oneill@har.mrc.ac.uk*

Introduction

When cells are exposed to ionising irradiation lesions are introduced into the DNA. Such lesions include single strand breaks (SSBs), double strand breaks (DSBs) and base damage resulting in multiple or clustered damage sites, a specific feature of radiation induced DNA damage. It is known that DNA bases absorb maximally in the UVC wavelength range (~260nm), resulting in the formation of cyclobutane pyrimidine dimers (CPDs) and 6-4 photoproducts (6-4pps).

We have undertaken some preliminary studies to characterise the DNA damage induced in mammalian cells by near infrared multiphoton processes. One of the aims is to irradiate the cell nucleus through focused multiphoton processes to simulate the effects of ionising radiation. For multiphoton processes to occur a molecule must absorbs a photon whilst still in an excited state following the absorption of a previous photon, further increasing the level of the excited state of the molecule. As wavelength increases the energy of each photon at a wavelength decreases (Table 1), for example the energy of a single photon from a 750nm source is a third of the energy of a photon from a 250nm source. If 3 photons are therefore absorbed by a molecule in a stepwise fashion from a 750nm source (NIR) it is equivalent in energy to that molecule absorbing a single photon from a 250nm source (UV).

Energy/Photon (eV)	λ/nm	Two photon λ/nm equivalent	Three photon λ/nm equivalent
1.73	715	359	238
1.70	730	365	243
1.65	*750*	*376*	*250*
1.59	780	390	260
1.55	800	400	267

Table 1. Multiphoton irradiation wavelength and photon equivalents.

The alkali comet assay or single cell gel electrophoresis assay is an electrophoresis technique adapted from earlier nucleoid sedimentation and halo assays. The Comet assay is commonly used for the direct visualisation of alkali labile sites and SSBs in individual eukaryotic cells. An early step in the response of mammalian cells to DSBs is the substantial phosphorylation of the histone H2AX at sites of DNA DSBs (Burma et al, 2001). H2AX, a 14kDa protein, is one of three conserved H2A histones and comprises 2-10% of the H2A complement in mammalian tissues (Rogakou et al, 1998). It differs from the other two by the presence of a conserved motif SQ(E/D)-(I/L/Y) at the carboxy terminus. Phosphorylation of the serine 139 residue of this motif in response to DNA damage yields the modified γ-H2AX protein, which can be visualised by immunofluorescence as an indicator of DSBs in individual cells.

In this preliminary study we set out to investigate the induction DNA strand breaks (SSBs and DSBs) induced in individual mammalian cells by multiphoton near infrared irradiation by different wavelengths of the infrared photons. Further we report on the efforts taken to optimise the irradiation conditions.

Material and Methods

Cell Culture

Mammalian cells (V79-4 cells) were maintained in DMEM supplemented with 200mM L-glutamine, 10U/ml penicillin/streptomycin, 10% FCS and grown at 37°C in a humidified incubator under 5% CO_2, exhibiting doubling times of ~12 hours. Cultures of cells were maintained in exponential growth by routine passage. 2 x 10^5 cells were seeded into 2.5μM hostaphan dishes 40 hours prior to irradiation.

Multiphoton Irradiation

Exponentially growing cells (47% S-phase, 45% G0/G1-phase) plated on hostaphan dishes were placed into a cooling rig. A 1cm x 1cm area at the centre of the dish was irradiated by raster scanning using a femtosecond pulsed Tsuanami Titanium:Sapphire (Ti:S) laser. The near infrared (pseudo UV) light was focused in the cell nucleus and generated by multiphoton reactions. Following irradiation the medium was removed, the cells rinsed with 1X PBS and analysed for DNA damage.

γ-Irradiation

Exponentially growing cells (47% S-phase, 45% G0/G1-phase) plated on hostaphan dishes were exposed to 10 Gy γ-irradiation (Cobalt ^{60}) at a dose rate of 2.9 Gy/min. Following irradiation the medium was removed, the cells rinsed with 1X PBS and analysed for DNA damage.

Hydrogen Peroxide Treatment

The medium from exponentially growing cells (47% S-phase, 45% G0/G1-phase) plated on hostaphan dishes was removed and replaced with medium containing 10μM hydrogen peroxide. The dishes were placed into an incubator for 10 mins. Following incubation the medium was removed, the cells rinsed with 1X PBS and analysed for DNA damage.

Comet Assay

Following irradiation or treatment cells were harvested using 1X trypsin-EDTA and pelleted through centrifugation at 1750rpm for 10 mins at 10°C. Part frosted microscope slides were coated with a layer of 1% low melting point agarose (LMPA) and allowed to dry. An initial layer of 170μl of 2% LMPA was placed onto the slide. The pelleted were mixed 1:1 with 2% LMPA and a second layer (170μl) containing the cells was added to the slide covered by a final layer of 200μl 1% LMPA. 2 slides were prepared per sample. The slides were placed into lysis buffer for 1 hour then rinsed in ice cold 1X PBS for 15min. A horizontal electrophoresis tank was filled with 2 litres of ice cold alkali buffer. The slides were placed into the alkali buffer for 30min prior to electrophoresis to allow the DNA to unwind. The slides were electrophoresed at a constant voltage of 22V (500mA) for 30mins. The slides were finally placed in 500ml ice cold neutralising buffer for 10min and rinsed in ice cold PBS. The DNA was stained with 1ml of 10μg/ml of EtBr. Comets were visualised by confocal microscopy and scored manually.

γ-H2AX Assay

Following irradiation the dishes were placed in an incubator at 37°C for 8 minutes. Cells were fixed for 30 minutes in 3% paraformaldehyde dissolved in 1X PBS at 4°C. Fixed cells were rinsed in 1X PBS and permeabilised with ice cold 0.1% Triton X-100 in 1X PBS for 4 minutes at room temperature. Cells were blocked for 1 hour in 0.2% fish skin gelatin (vol/vol) in 1X PBS, rinsed and incubated with the primary antibody (anti-phospho H2AX ser139 rabbit monoclonal antibody, 5µg/ml) raised against γ-H2AX for 1 hour at room temperature. Cells were then rinsed in 1X PBS, blocked for 1 hour in 0.2% fish skin gelatin (vol/vol) in 1X PBS and incubated with the secondary antibody (fluorescein conjugated $F(ab')_2$ fragment goat anti-rabbit IgG, 7.5µg/ml) for a further 1 hour at room temperature. The cells were finally rinsed in 1X PBS before being mounted with vectashield and a coverslip added. Foci were visualised by confocal microscopy and scored manually.

Results

The experimental set up was optimised by evaluating (1) temperature of irradiation to minimise DNA damage repair and (2) changing the raster steps of the irradiation stage to optimise the number of cells irradiated.

We investigated the feasibility of using near infrared multiphoton irradiation to induce DNA damage in individual mammalian cells in the wavelength range 720-750nm of the primary photons. The Comet assay, a generally applied technique that allows visualisation of SSBs (Davis et al, 2001), was used to analyse induced DNA damage in mammalian cell populations. Hydrogen peroxide (10µM) treated cells were used as positive controls with non-exposed cells as negative controls.

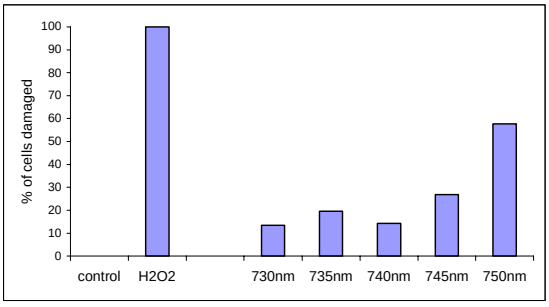

Figure 1. Percentage of cells showing DNA damage as a function of wavelength as visualised by the Comet assay.

The results shown in Figure 1 indicate that DNA damage, in the form of SSBs, was induced by near infrared multiphoton irradiation in individual mammalian cells. The results indicate that the percentage of cells irradiated which show damage increases with wavelength in the range tested, with a maximum at 750nm (3 photon equivalent to 250nm).

We further investigated the effect of temperature on repair of DNA strand breaks, to ensure that any SSBs produced by multiphoton excitation were not repaired during the irradiation period. Mammalian cells were exposed to γ-irradiation (10Gy) and allowed to repair for varying time periods at 18°C, the temperature to which the multiphoton laser room can be cooled. It was found that SSBs, as visualised by the Comet assay, could be repaired at 18°C over a 60 minute period (Figure 2). During subsequent experiment the dishes containing the cells were cooled to 10°C using a cooling rig.

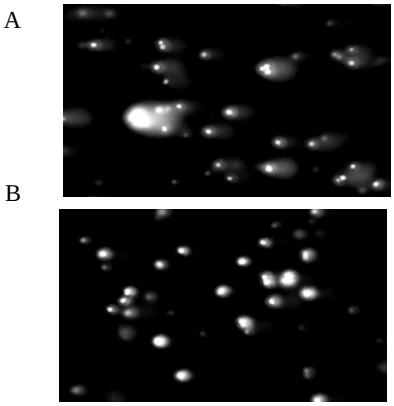

Figure 2. DNA damage present in a mammalian cell population after 10 Gy γ-irradiation and (A) 0 minutes and (B) 60 minutes repair time at 18°C respectively as visualised by the Comet assay.

Having optimised the temperature and established that SSBs were indeed induced in mammalian cells by near infrared multiphoton irradiation we carried out a small side study to detect whether DSBs were also induced. In this study the raster step size (5, 12 and 25µm) was investigated to determine the conditions which would allow the majority of the cells in a population to be irradiated with a single pass of the laser whilst limiting the number of cells receiving multiple exposures to the multiphoton processes. Figure 3 shows an exponentially growing mammalian cell population covered by both a 5µm and a 25µm grid.

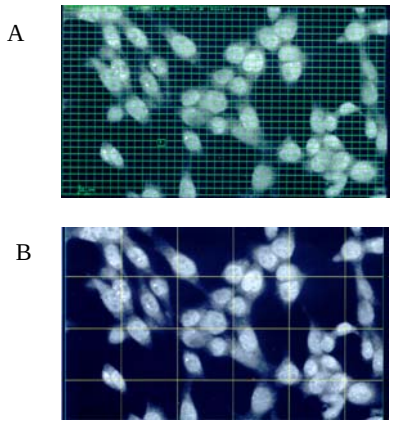

Figure 3. A shows a cell population covered by a 5µm raster grid, whereas **B** shows a cell population covered by a 25µm raster grid.

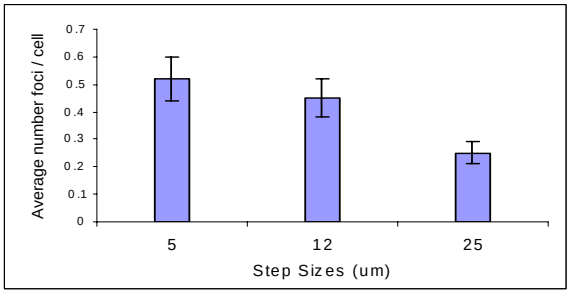

Figure 4. Formation of DSBs in a mammalian cell population (phosphorylated H2AX histones) induced by 740nm multiphoton irradiation at various raster step sizes.

The γ-H2AX assay, an immunofluorescence assay capable of detecting DSBs was used to determine DSB induction at 5, 12 and 25μm raster step sizes. Figure 4 shows that DSBs were indeed induced by multiphoton irradiation based on the number of foci formed per cell. The number of DSBs (foci) per cell were also seen to increase as the raster step size decreases. It was deemed that a raster step size of 12μm was optimal as this allows the majority of cells in a population to be exposed to the multiphoton laser without being irradiated multiple times through additional passes.

Conclusions

From these preliminary studies carried out thus far using the multiphoton processes it is very encouraging that we have observed the induction of both single and double strand breaks in individual mammalian cells. During these experiments we were able to optimise a number of conditions including irradiation temperature and raster step size. From the wavelength studies carried out to date we have observed an increase in DNA damage with wavelength in the range 720-750nm. These studies are currently on-going so that future studies will enable us to investigate the repair processes involved in DNA damage induction using immunofluorescence assays and various repair deficient mutant cells.

References

1. S. Burma, B.P. Chen, M. Murphy, A. Kurimasa and D.J. Chen. The Journal of Biological Chemistry. (2001), 276 (45), 42462.
2. E.L. Davis, A.K. Daly & F.M. Williams. Toxicology. (2001). 168(1), 95.
3. C.L. Limoli, E. Giedzinski, W.M. Bonner & J.E. Cleaver. PNAS. (2002) 99, 233.
4. T. Melvin, S.W. Botchway, A.W. Parker and P. O'Neill. J. Am. Chem. Soc. (1996), 118, 10031.
5. T. Melvin, S.M. Cunniffe, P. O' Neill, A.W. Parker and T. Roldan-Arjona. Nucleic Acid Research. (1998), 26, 4935.
6. S.K. Mohanty, A. Rapp, S. Monajembashi, P.K. Gupta & K.O. Greulich. Radiat. Res. (2002) 157, 378.
7. T.T. Paull, E.P. Rogakou, V. Yamazaki, C.U. Kirchgessner, M. Gellert. W.M. Bonner. Curr. Biol. (2000) 10 (15), 886.
8. E.P. Rogakou, D.R. Pilch, A.H. Orr, V.S. Ivanova & W.M. Bonner. J.Biol. Chem. (1998) 273 (10), 5858.
9. C. von Sonntag. (1987) The chemical basis of radiation biology. Taylor and Francis, London, UK.

Localised induction of UV damage in cellular DNA for the study of DNA repair dynamics. Comparison of the methods using a focused near infra-red laser beam and a focused 248nm UV beam

W Shaikh, G J Hirst, D N Winter, S W Botchway, E Conein, R Meldrum

Central Laser Facility, CCLRC Rutherford Appleton Laboratory, Chilton, Didcot, Oxon, OX110QX, UK

Main contact email address: *r.meldrum@rl.ac.uk and r.meldrum@bham.ac.uk*

Introduction.

Localised induction of DNA damage is a major goal of cell biologists who wish to study the molecular dynamics of DNA repair [1)], intra-cellular signalling process and cell-cell communication [2)].

We have illustrated how a focused 750nm laser beam can be used to induce DNA photoproducts with nanometre three-dimensional resolution in cell nuclei in a defined geometrical pattern [2)]. Cyclobutane pyrimidine dimers (CPDs) have been induced by the focused NIR beam tuned to wavelengths 720, 730, 750, 770, 790, 810, and 830 (complete data not shown). Three photon absorption from these wavelengths would correspond to single photon absorption in the wavelength range 240nm – 280nm. The levels of CPDs induced by the different NIR wavelengths when the mean power of the laser was 10mW, is very similar and corresponds to the mode of lesion induction by 240 to 280nm single photon UV irradiation.

We have now developed methods to focus a 248nm UV laser beam onto cell nuclei to induce the DNA photoproducts in a defined pattern by single photon absorption. The different properties of the laser irradiation are likely to give rise to some different small side effects in the quality of the damage induced in the cells.

The UV irradiation is delivered in nanosecond pulses while the infra-red is delivered in femtosecond pulses. We previously observed that DNA strand breaks, under certain conditions, are induced by 248nm UV nanosecond pulses [3-6)]. Collateral one and two photon effects from the focused NIR beam are unlikely to be of significance [2)]. The intensity of the radiation used is not likely to be high enough to give rise to a significant amount of 4-photon absorption which would lead to single strand breaks.

The different distributions of damage in the cell nucleus formed by the absorption of single photon UV or 3-photon NIR are shown below (Figure 5).

It remains to be established if light scattering of UV from a single photon source is more of a problem than when 3-photon NIR is used.

Fabrication of chrome mask

The patterned mask was fabricated by removing portions of the metal layer from a commercial chrome-on-silica mask blank (see Figure 1). The 10 µm holes were made using electron beam lithography in the CCLRC Central Microstructure Facility. The broad ring was generated by excimer laser ablation using contact masking. The tube lens and microscope objective reduce the pattern size by a factor of 100 in the sample/image plane, so in the geometric optics approximation the 10µm holes are reduced to 100nm diameter.

Figure 2 . Preliminary Image of UV ‘ring’, reduced by 100x, produced in homogeneous Gafchromic film – the outer ring is 10µm in diameter and 1.2µm in width.

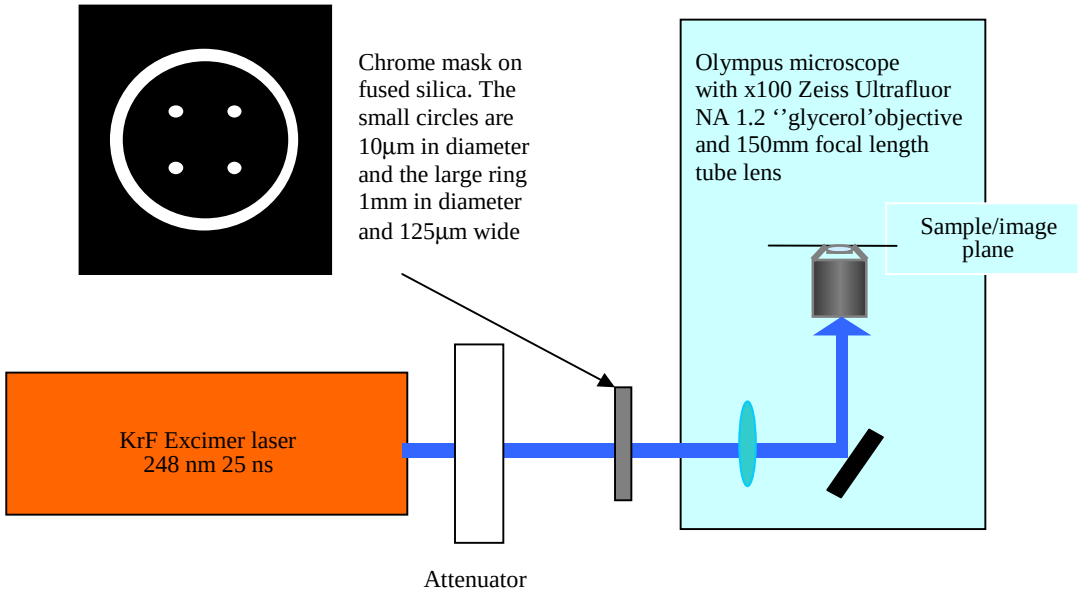

Figure 1. Schematic of UV set-up.

The active layer of this film medium is 6.5 microns – it was placed directly above a 200µm cover slip (with glycerol between the objective and cover slip) and produced using five laser shots at of 0.1mJ/cm^2.

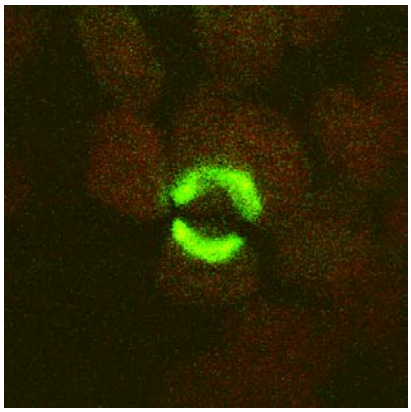

Figure 3. Pattern of DNA photoproducts induced in V79 chinese hamster ovary cells and stained with specific antibody.

Cells were grown on quartz cover-slips and irradiated as shown in the schematic diagram (Figure 1). The dose used here was a large dose (5mJ/cm^2). This overexposure has created a broadened image of the 1µm ring. The maximum width of the ring shown here is ca. 4µm. Although the cells could be viewed through the microscope eyepieces or by projection on a TV monitor, the cover-slip had to be placed manually because of a lack of a mechanical device to do this. Thus the ring covers the nuclei of two or three cells and the image is missing where there is no DNA in the path of the irradiation. Work is in progress to reduce dose levels and acquire a more faithful reproduction of the mask pattern in cellular DNA.

The important result here is that we have shown that DNA damage can be created in a defined pattern in single cell nuclei by single photon UV irradiation of cells through a microscope objective. Previously we have shown that this is possible by 3 photon absorption from a focused near infra-red laser beam tuned to a wavelength between 720 – 850nm, (Figure 4).

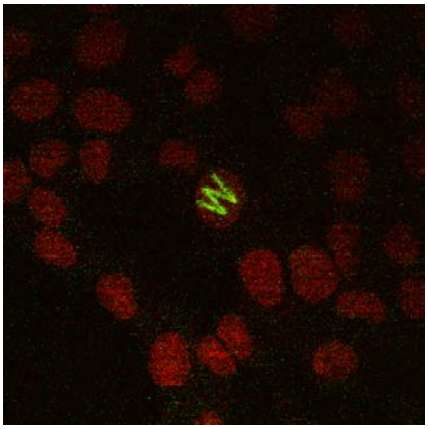

Figure 4. The W pattern outlines cyclobutane pyrimidine dimers induced by a focused 730nm NIR laser beam and stained by a specific antibody.

Distribution of DNA damage induced in the cell nucleus by single photon UV or 3-photon NIR absorption

Figure 5A shows cells which were irradiated under a mercury lamp at 254nm. The image is created by making a series of confocal scans through the depth of the cell. This is known as the z-plane image and it runs parallel to the axial direction of the incident light. The DNA damage, again detected by staining with antibody, is distributed fairly evenly through the depth of the cell with perhaps some more intense areas lying closer to the side of the nucleus on which the light first impinges.

Figure 5B illustrates how UV photoproducts which are induced in DNA by 3-photon NIR absorption are confined to the central section of the nucleus.

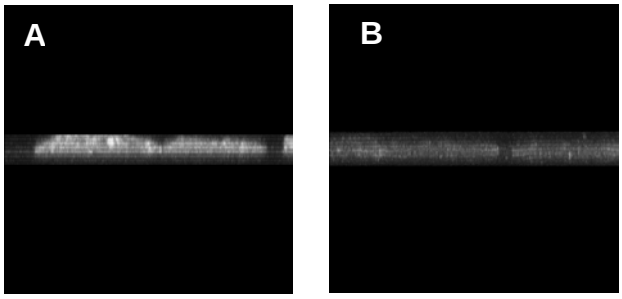

Figure 5. Z-plane images of DNA photoproducts produced in cells by single photon UV irradiation [A] and focused NIR irradiation [B].

The functions which take place in the cell nucleus, such as replication and transcription, are non-randomly distributed and their position can change throughout the cell cycle from the nuclear periphery to the centre [7]. The different distributions of damage created by the different methods used to induce the damage will have implications for the interpretation of results of biological experiments carried out using the alternative methods.

The greater challenge of increasing the resolution of the induction and imaging of the DNA damage to dimensions (ie. 200-300nm) that enable the tracking of fine movements of DNA and proteins to be studied, still remains.

Images were recorded using a Biorad Radiance 2000 laser scanning system (School of Biosciences, University of Birmingham) and a Plan Apo 60 x, 1.4 NA oil immersion lens with a working distance of 0.21mm. Z-plane scans were taken at steps of 500nm.

References

1. R.A. Meldrum, G.O. Edwards, J.K. Chipman, C.W. Wharton, S.W. Botchway, G.J. Hirst, W. Shaikh (2001) Multiphoton UV and X-ray micro-irradation to track intra- and inter-cellular dynamics. CLF Annual Report , RAL-TR-2001-030, 117 (2001)

2. R.A.Meldrum, C.W.Wharton, S.W.Botchway, G.J.Hirst, S.Topley (2002) Induction of localized UV photoproducts in cell nuclear DNA by 3-photon near infrared absorption. CLF Annual Report, RAL-TR-2002-013, 139 (2002))

3. W.Meaking, R.A.Meldrum, J.Edgerton, S.Ward & C.W.Wharton Kinetics and mechanism of DNA repair: The nature of the UV-laser damage-induced "panic' phase DNA synthesis. Ann. Rep. CLF SERC 189-191, (1993)

4. K.M.Prise, B.D.Michael, R.A.Meldrum & C.Wharton Studies of damage to plasmid DNA using 248nm laser pulses. Ann. Rep. CLF DRAL 163, (1995)

5. K.M.Prise, B.D.Michael, R.A.Meldrum and C.W.Wharton Yields of SSB and DSB in plasmid irradiated with 248nm photons: role of hydration. Ann. Rep. CLF DRAL, (1996)

6. W. Meaking (1994) PhD Thesis, Birmingham University.

7. J.B. Lawrence and G.L.Hager (2003) Nucleus and gene expression: motion meets architecture. Current Opinion in Cell Biology, 15, 255-259.

Amorphous Chalcogenide/Metal bilayers – A new X-ray mask material

A G Fitzgerald, N Nusbar, S Persheyev

Division of Electronic Engineering and Physics, University of Dundee, Dundee, DD1 4HN, UK

Main contact email address: *A.G.Fitzgerald@dundee.ac.uk*

Introduction

Arsenic and germanium based chalcogenides such as As_2Se_3 and GeS are semiconductor materials with structural and optical properties that change upon light and electron beam irradiation. It has been shown by McHardy et al[1)] that when thin amorphous chalcogenide/metal bilayers are exposed to a scanned electron beam in a scanning transmission electron microscope, that metal deficient lines are formed. The width of these lines depends on the size of the electron source. This property has potential applications in the formation of X-ray masks for the fabrication of silicon chips with structures at the nanometer level. Figure 1 shows a dark field scanning transmission electron micrograph of an a-GeSe/Ag bilayer with metal-free lines produced by scanning the electron beam.

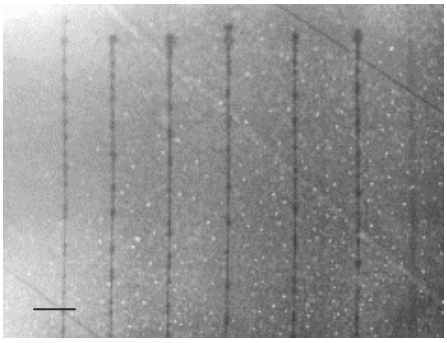

Figure 1. TEM annular dark field electron micrograph showing silver-free lines generated in a free-standing Ag/$GeSe_2$ bilayer. Scale mark 1µm.

Figure 2 shows an atomic force micrograph of a simple pattern of copper deficient lines that has been formed in an a-As_2Se_3/Cu bilayer supported on a thin silicon nitride membrane. In addition to these trough-like lines, under certain conditions of electron beam accelerating voltage and film thickness, protruding metal-rich lines form in the area scanned by the electron beam.

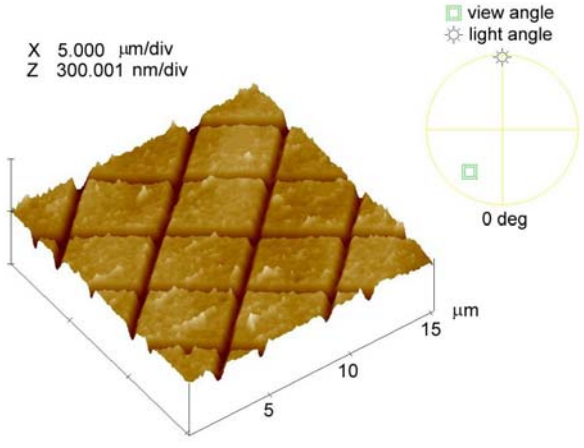

Figure 2. Atomic force micrograph showing a grid of copper-free lines in an As_2Se_3/Cu bilayer.

The objective of the research project described here was to examine the possible application of electron beam generated patterns in these metal/chalcogenide bilayers as X-ray masks for the fabrication of silicon chips using the Cu Lα and C K X-ray sources at the X-ray and UV Laboratory at the Rutherford Appleton Laboratory, Central Laser Facility.

Experimental Methods

A transparent silicon nitride membrane (Si_3N_4) in the form of TEM and SEM compatible silicon wafer frames was used in the X-ray mask fabrication. The frames which consist of a thin film window with membrane of 100 nm thickness and 1 mm^2 of membrane size were supplied by Silson Ltd. Arsenic triselenide (As_2Se_3) and silver were the chalcogenide and metal used in these experiments.

The metal/chalcogenide bilayers were prepared by sequential evaporation of an As_2Se_3 film followed by a silver film. The As_2Se_3 films ranged in thickness from 147 nm to 530 nm and the silver films ranged in thickness from 12 nm to 118 nm. The vacuum depositions were carried out at a pressure of 10^{-6} torr onto silicon nitride membrane substrates of 100 nm thickness. These bilayers were then patterned using an electron beam writer system consisting of a JEOL T220 scanning electron microscope which had been modified to put the electron beam under computer control using ELPHY Quantum software for nanolithography. A JEOL 120C scanning transmission electron microscope was also used to pattern the As_2Se_3/Ag bilayers.

Preliminary work was required using the copper Lα and carbon K X-ray sources before the masks generated by the electron beam writing equipment could be exposed to the X-ray beam to generate a pattern on a photoresist.

A calculation was first made to determine the optimum thickness of the chalcogenide and metal films for soft X-ray transmission. Figure 3 shows the plots of X-ray transmission versus Cu Lα X-ray photon energy for films of each of the materials that the X-rays were to be transmitted through.

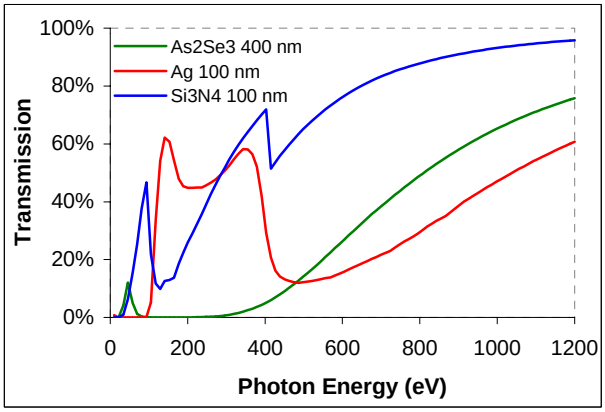

Figure 3. Cu Lα X-ray transmission curves for a 100 nm thick silicon nitride film, a 100 nm silver film and a 400 nm a- As_2Se_3 film.

The final step in the research programme was to demonstrate the applicability of these patterns as X-ray masks. The soft X-ray sources at the Central Laser Facility of the Rutherford Appleton Laboratory were used in these experiments. Initial experiments were carried out with the copper Lα X-ray source to characterise the PN114 photoresist that was to be used in fabricating patterns from the X-ray masks formed by the electron beam. The first experiment used simple non-electron beam generated masks that consisted only of an area of a-As_2Se_3 film. For the second experiment a similar mask was

prepared with a silver film as the absorbing layer. The third experiment involved the X-ray exposure of a-As_2Se_3/Ag films with large features. These three experiments enable the optimum exposure time to be calculated for the electron beam fabricated X-ray masks in a-As_2Se_3/Ag films.

The final experiments involved the testing of masks with nanometer dimension metal-free features.

Results and Discussion

Transferred images were first obtained using Cu Lα X-rays. Two types of mask were tested, masks in which protruding structures had been formed and X-rays are transmitted between these structures and masks with trough-like structures where X-ray transmission was through the trough. Transferred images from the protruding mask only were observed but these were not of good quality (Figure 4). The main problem was due to photoresist uniformity after image transfer using the soft X-rays. Even after using new, fresh photoresist the developed photoresist surface was found to be uneven. This photoresist uniformity problem may have been caused by debris in the chamber which is generated from the plasma during X-ray emission. The 3μm of aluminium foil that was used as a filter to pass the X-rays was also observed to be contaminated with copper debris. The identity of the contaminant was confirmed as copper by x-ray microanalysis in a scanning electron microscope.

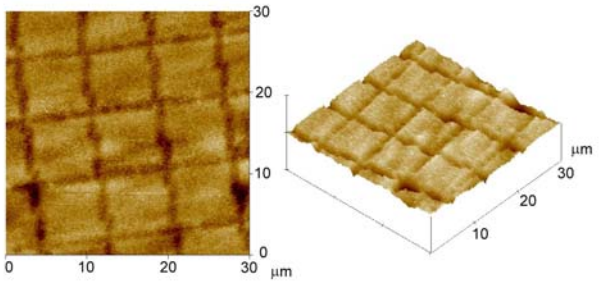

Figure 4. Atomic force micrograph of pattern produced on the PN114 photoresist with Cu Lα X-rays.

To overcome the photoresist uniformity problem and also improve the quality of the images the carbon K X-ray source was used to transfer the image of the mask to the photoresist. Masks with a trough-like structure were used in these experiments. The masks were patterned manually in the JEOL 120C transmission electron microscope by removing the condenser lens aperture, focusing the electron beam and moving it to produce a series of metal-free high X-ray transmitting lines. On examining this pattern at high resolution in the transmission electron microscope it was found that under these conditions of mask fabrication the metal as well as the chalcogenide along the scanned line had been removed. An improved photoresist uniformity for transferred images was achieved when this mask was exposed to carbon K X-rays. The pattern transferred to the photoresist was of micrometer dimensions.

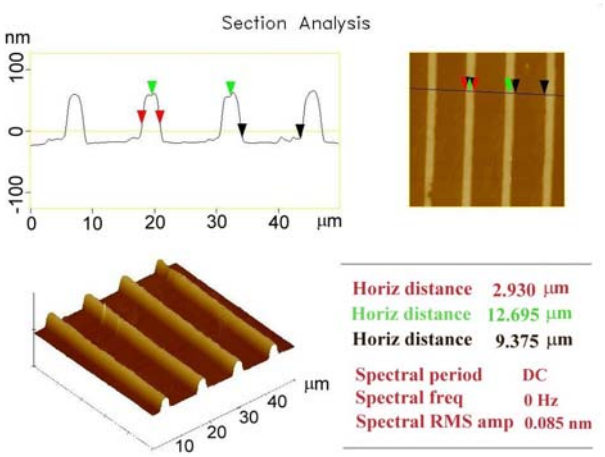

Figure 5. Image formed in the PN114 photoresist from transmission of C K X-rays through an a-As_2Se_3/Ag mask.

Conclusions

It has been demonstrated that X-ray masks can be fabricated by scanning an electron beam across metal/chalcogenide bilayers to form linear patterns that can be metal-free, metal rich or are completely free of metal and chalcogenide.

Due to the higher absorption of the C K X-rays in the photoresist material and the higher sensitivity of the resist to C K X-rays, improved contrast was obtained in the images of the mask obtained with this X-radiation.

Future experiments should involve computer control of the electron beam scan in the TEM and optimization of the electron beam diameter to produce nanometre scale patterns in the photoresist.

Acknowledgements

We wish to thank EPSRC for the award of a research grant GR/N1462 to support this project.

References

1. C.P. McHardy, A.G. Fitzgerald, P.A. Moir and M. Flynn, J. Phys. C: Solid State Phys., 20: 4055-4075, 1987.

Excimer laser crystallisation of Silicon films deposited on metal layers

S Summers, H S Reehal

Faculty of Engineering, Science and Technology, South Bank University, 103 Borough Road, London, SE1 0AA, UK

G J Hirst

Central Laser Facility, CCLRC Rutherford Appleton Laboratory, Chilton, Didcot, Oxon, OX11 0QX, UK

C Jeynes

University of Surrey Ion Beam Centre, Guildford, GU2 7XH, UK

Main contact email address: *reehalhs@sbu.ac.uk*

Introduction

The growth of polycrystalline Si films on low cost substrates such as glass is important for thin film solar cells. However the formation of these films, with the required thickness and electronic properties, is difficult due to temperature constraints. Very thin (~up to a few 100 nm) Si films can be formed on glass by a number of techniques including excimer laser crystallisation (ELC). These could possibly serve as seeding layers for the growth of thicker crystalline films using low temperature epitaxial growth techniques. We have previously reported on the ELC of Si films on glass substrates for seed layer preparation[1)]. In this work we present initial results on the ELC of Si films deposited on a variety of metal-coated glass surfaces. This is important because practical device structures require the efficient extraction of generated charge carriers and, hence, need to be fabricated on substrates equipped with contact layers.

Experimental

A variety of metal coated Corning 1737 glass substrates were prepared for Si film growth. Ni, Al and Cr layers were deposited by thermal evaporation. The layers were between 200 and 300nm thick. Mo layers were deposited by RF magnetron sputtering, again on CG1737, and were ~300nm thick. A commercial transparent conducting oxide (TCO) coated float glass was also investigated. The TCO was determined to be polycrystalline SnO_2 by X-ray diffraction analysis. The Si films were deposited to thicknesses of ~200-400 nm on the metal layers by electron cyclotron resonance (ECR) plasma-enhanced chemical vapour deposition (PECVD). Silane and hydrogen were used as the deposition gases. The growth system has been described previously[1,2)].

The Si films were crystallized using a KrF excimer laser and an Excitech laser beam homogenizer. This system has also been described previously[1)]. Single shot irradiations at different fluences were undertaken. The laser anneals were carried out at room temperature in an Ar atmosphere.

The irradiated samples were analysed by SEM, X-ray diffraction (XRD) and Raman spectroscopy at South Bank and by Rutherford backscattering (RBS) at Surrey University.

XRD Results

Figure 1 presents post ELC XRD spectra of Si films on Al, Mo and Cr backing films. The XRD spectrum for Al shows no alloying: all peaks are separately identifiable as Si or Al peaks. The Si peaks are indicated while all the other peaks correspond to Al peaks. In order from low 2θ they are (with approximate positions): (111) at 38.5º, (200) at 44.8º, (220) at 65º and (311) at 78.5º. Si and Al do not readily form alloys and have not done so at a detectable level here although RBS measurements indicate gross intermixing.

The bottom spectrum in Figure 1 is for the Si/Cr binary layers. The peaks not corresponding to Si are attributable to Cr peaks at 44.4º and 81.8º. This is consistent with no alloying between the two materials after laser irradiation.

The Si/Mo spectrum is very different. While the Si peaks are all still present, the other features in the spectrum are more reminiscent of a disordered or fine grained material. The broad humps could result from the Mo film acting to reflect X-rays to the detector, although the low-incidence angle arrangement for the measurements would seem to physically preclude this possibility. The features coincide with peaks attributable to Mo silicides; namely Mo_3Si (200) at ≈37º and (420) at ≈89º. A number of single crystal $MoSi_2$ peaks are scattered around 45º, but none coincide with the 43º feature present. Whilst the coincident features mentioned here do not prove the existence of silicidation there are no elemental Mo peaks present, in contrast to the cases of Si/Al and Si/Cr.

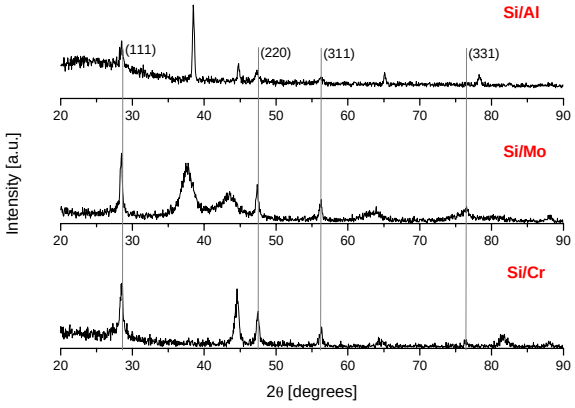

Figure 1. XRD spectra of ELC Si films on Al, Mo and Cr coated CG. The Si peaks are marked.

RBS Results

RBS was used to determine macroscopic intermixing between layers; the RBS measurements are accurate to within 1% and therefore cannot indicate levels of intermixing less than this. The raw RBS data was fitted and the resultant depth profiles of the films' materials were derived using the simulated annealing Data Furnace package developed at Surrey University. The depth profiles show the relative amounts of the major observed constituents of the films as a function of depth into the surface, in the form of plots. The surface/air interface corresponds to a film thickness of zero.

Transparent Conducting Oxides

Results of silicon films deposited on the tin oxide (SnO_2) are shown in Figure 2 for a sample as-deposited (A) and a series of identically grown films irradiated using the ELC scheme with a single shot at varying fluence (B-C). The as-deposited film, deposited at 400°C, shows some intermixing within about 20nm of the interface but is generally a sharp interface indicating no gross mixing throughout the film. Even with a low fluence shot the interface begins to become more complex. The data shows that while the intermixing is considerable, and that the contact material has moved through ~80% of the Si film, it is not simply a migration of SnO_2 as a single material but rather only

the Sn component moving through the Si, while the oxygen component retains a sharp interface at the film/contact interface.

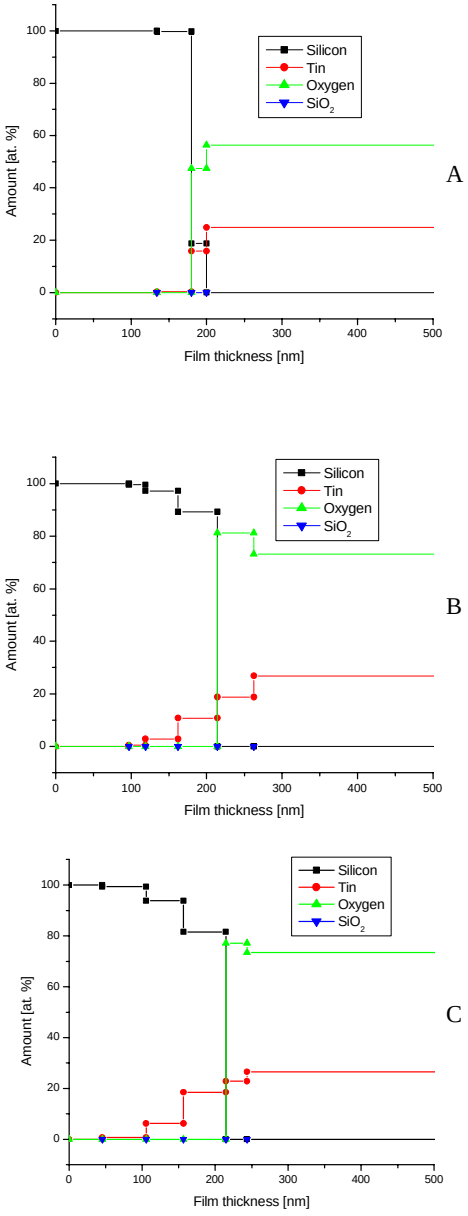

Figure 2. RBS depth profiles for Si/SnO_2/Glass systems irradiated by A) 0mJcm^{-2}, B)121mJcm^{-2} and C) 255mJcm^{-2}.

Metal Contacts

The RBS results obtained for the films deposited on metals show a variety of results. Materials such as Si and Cr form silicide layers on contact. Si-Ni silicides require thermal processes for deep silicide formation. RBS measurements made of Ni/Si and Cr/Si bilayers irradiated by XeCl excimer lasers were interpreted as being evidence of the formation of crystalline $NiSi_2$ and $CrSi_2$ layers, respectively[3]. These layers were formed by 50nm of evaporated metal on silicon substrates irradiated by 100 laser pulses over the fluence range 0.5 to 1.5 Jcm^{-2}. The layers were reported to be in the range 400 – 500nm thick.

Results of RBS depth profiling both before and after laser irradiation are shown for Si/Cr, Si/Ni and for post-ELC of Si/Mo only in Figures 3-5, respectively. Those for Si/Cr indicate no intermixing with the Si film before ELC and a relatively low level of mixing after. Around 1% Chromium exists over a range of 80nm into the Si film. There is apparently substantial mixing of the underlying glass and the Cr although this is not likely to be the case and that oxidation of the Cr film before the deposition of Si may have caused this observation.

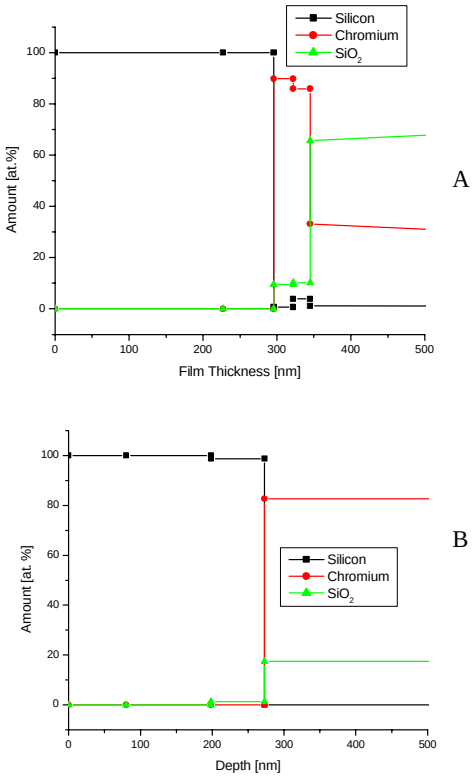

Figure 3. RBS depth profiles of Silicon films on Cr before (A) and after (B) ELC.

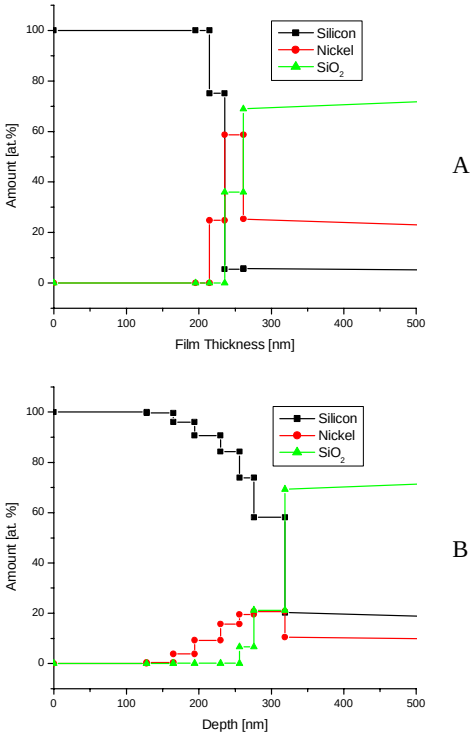

Figure 4. RBS depth profiles of Silicon on Ni before (A) and after (B) ELC.

The RBS spectrum for the Si/Ni bilayer (Figure 4) indicates the formation of nickel silicides over ~50nm of the Si/Ni interface during deposition. The stoichiometry of nickel silicides can take a number of combinations under the deposition conditions, particularly with the heated substrate. The first in the phase sequence of the Ni-Si system is Ni_2Si. A transformation occurs over time during thermal treatments to NiSi and finally $NiSi_2$.

After laser irradiation, the Ni moves into the Si and a graded interface is produced. It is not realistic to infer the stoichiometry of the products. There may be regions of metal-rich and silicon-rich silicides.

Figure 5 presents the depth profile of the Si/Mo bilayer. Substantial intermixing has occurred during deposition with a layer of more than 250nm of $MoSi_x$ formed. A further layer 200nm thick exists where Si makes up 81% of the material.

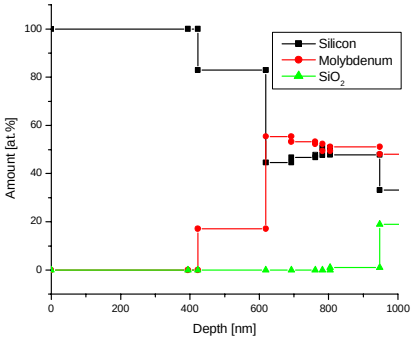

Figure 5. RBS depth profile of Silicon on Molybdenum after ELC.

Discussion

Al mixes readily with Si and this has been confirmed by RBS measurements. As expected, no alloy formation between the two has been observed. The melting point of Ni (1453 °C) is below that of c-Si and approximately the same as that of a-Si (supercooled). The RBS profile after irradiation shows the depth of mixing to be ≈175nm from the glass substrate into the film. The XRD data presented supports the RBS results in as much as the Si/Cr system shows distinct XRD peak patterns corresponding to the elemental constituents and the RBS shows no intermixing. We can conclude that no alloying has occurred. In the case of Si/Mo the XRD spectrum shows Si elemental peaks as well as broad features that coincide with some Mo silicide peaks, while no elemental Mo peaks are displayed. The RBS implies considerable mixing between the two materials at their interface. We can conclude that gross silicidation has occurred between the two materials.

While the work done on excimer laser crystallisation of silicon films is contributing to an ever-expanding published record in the literature, data on any interfacial mixing between film and substrate during ELC has not been widely offered. Where it has appeared it has generally been incidental or cursory. A paper by Yi et al.[4)] was published containing data on the intermixing of silicon films on Cr or MoW substrates. They found little in the way of gross intermixing. The paper concludes that the intermixing is of the silicon entering the substrate and not the other way around.

Conclusions

Thin Si films have been deposited on various metallic layers on glass substrates and crystallised using excimer laser irradiation. This is a rapid and non-equilibrium physical action. The results show varying amounts of intermixing between the Si film and the underlying metal, depending on the metal used. The overall material profiles do not match typical silicide stoichiometry for the materials used. While there may well be localised silicide formation, the type of intermixing is dependant on the metal used. More details will be presented elsewhere.

References

1. S Summers, H S Reehal and G J Hirst
J. Mat. Sci.: Materials in Electronics, 11, 557 (2000)

2. S Summers, H S Reehal and G H Shirkoohi
J Phys. D, 34, 2782 (2001)

3. C J Barbero, C Deng, T W Sigmon, S W Russell and T L Alford
J. Crystal Growth, 165, 57 (1996)

4. C Yi, S-W Rhee, J-H Ju, S-K Yim and H Min
J.Mat.Sci.: Materials in Electronics, 12, 697 (2001)

Rydberg electron wave packet dynamics in molecules

R S Minns, R Patel, R A L Smith, J R R Verlet, H H Fielding

Department of Chemistry, King's College London, Strand, London, WC2R 2LS,UK

Main contact email address: *helen.fielding@kcl.ac.uk*

Introduction

Rydberg wave packets are important non-stationary quantum states, bordering on the classical limit of high principal quantum number. Molecular Rydberg wave packets are much more complicated than their atomic counterparts and exhibit many of the dynamical complications shown by larger, more chemical, systems. The interplay between molecular and electronic phase has important implications in coherent control strategies. This report describes a series of experiments that unravel the role of molecular phase on the dynamics of a molecular electron wave packet, and exploit this phase to control either the autoionisiation/predissociation branching ratio.

Section 1 - The influence of a rotating core on electron wave packet dynamics

We reported the first experimental observation of a Rydberg wave packet in a molecule just over three years ago[1)], but the role of electronic and molecular phase on the wave packet dynamics has only recently been understood[2)]. Electron wave packets are created in NO using resonance-enhanced multiphoton excitation via a well-defined rotational level of the A-state, allowing some control over the core rotational angular momentum and the electronic angular momentum of the Rydberg wave packet system.

Specific rovibrational levels of the intermediate, $A^2\Sigma^+(\upsilon'=1,N',J') \leftarrow X^2\Pi_{3/2}(\upsilon''=0,J'')$, were excited using the narrow bandwidth output of a nanosecond laser. Superpositions of vibrationally autoionising Rydberg states, $NO^+X^1\Sigma^+(\upsilon^+=1)nl(N^+)$ were then excited using the broad bandwidth output of a picosecond laser.

In order to monitor the dynamics of a wavepacket created from autoionising Rydberg states, it is necessary to distinguish ions that have been generated by autoionisation from those that have been excited directly. The optical Ramsey method is ideally suited to this kind of problem and was employed in these experiments. Briefly, two identical wave packets are created and the interference between the two is measured. If the first wave packet has returned to the core at the time when the second wavepacket is excited, we see Ramsey interference fringes in the total Rydberg population as we scan through the optical wavelength. If the first wave packet is not at the core, there is no interference. The interference is measured by field-ionising the final Rydberg state population, and gives a measure of how much of the first wavepacket has returned to its original state i.e. its autocorrelation.

As a result of the variety of orbital angular momenta and rotational states of the ion core in the superposition, when the measured orbit periods are plotted as a function of the excitation energy it becomes apparent that there are deviations from hydrogenic behaviour. These deviations may be explained in terms of interferences between the various electronic and molecular motions within the molecule.

The picture is as follows. Consider exciting two electron wave packets in a system where each wave packet is associated with a differerent rotational state of the molecular ion core. These two wave packets (a) and (b) are allowed to propagate. At a later time both wave packets return to the core, if they overlap spatially (i.e. $t \approx t_{cl}^a \approx t_{cl}^b$, which is true for $2\nu_a^2 \Delta E_{Rot} << 1$) they will interfere with one another. For constructive interference to occur the phase-difference must be $2\pi k$ (where k is an integer). The resulting interference pattern consists of maxima and minima in the Rydberg population whose temporal spacing is inversely proportional to the energy difference between the two rotational states. The spatial position of the fringes depends on the quantum defects of the two series.

These observations are illustrated in Figure 1, which is a plot of the measured electronic period of a wave packet composed predominantly of $np(0)$ and $nf(2)$ Rydberg series in NO, using the nomenclature $nl(N^+)$ where N^+ is the rotational quantum number of the molecular ion core. The hydrogenic curves represent the periods of motion of a classical electron in a single unperturbed Rydberg series converging to each rotational ionization limit, plotted as a function of the average principal quantum number of the lower Rydberg series, $\bar{n}_0 = (-2\bar{\varepsilon}_0)^{-1/2}$.

In an atom, the electronic period scales as n^3, but in NO, clear plateaus are observed in plots of the period of motion of the molecular Rydberg wave packets as a function of average principal quantum number. These plateaus appear at multiples of the rotational beat period but they are offset by the quantum-defect difference, i.e. they appear at times corresponding to:-

$$T_S = T_{Rot}(k + \Delta\mu) \,. \qquad (1)$$

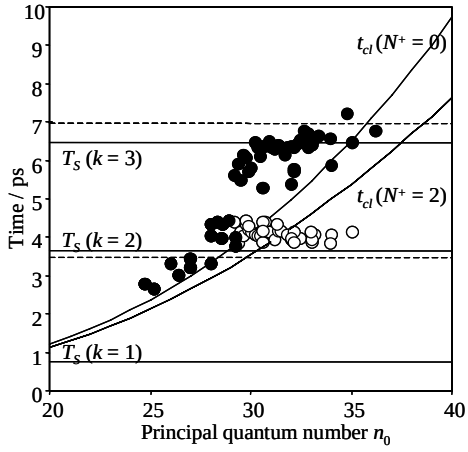

Figure 1. A plot of the measured orbit period (filled circles = most intense peak; open circle = less intense but still prominent peak) as a function of average excitation energy expressed in terms of the average principal quantum number $\bar{n}_0$, in the superposition. The wave packets are composed predominantly of $np(0)$ and $nf(2)$ Rydberg states with $\nu^+ = 1$. Trend lines mark the hydrogenic orbit periods $t_{cl} = 2\pi\bar{n}^3$; solid horizontal lines mark the stroboscopic periods defined in the text.

Section 2 - Observation and control of a predissociating Rydberg electron wave packet

In the classical picture of autoionisation, the electron scatters off the ion core. During the scattering event, the ion core has a non-zero probability of imparting electronic, vibrational or rotational energy to the electron, which acquires this excess energy as kinetic energy. Vibrational or rotational autoionisation is unique to molecules, but autoionisation is not. Spin-orbit or electronic autoionisation are processes which may occur in both atoms and molecules. An alternative decay route, which *is* totally unique to molecules, is predissociation. In principle, predissociation is similar to autoionisation and occurs

when a Rydberg state is degenerate and overlapping (in the internuclear coordinate) with a continuum associated with the dissociated molecule. From a classical viewpoint, the electron crashes into the molecular core and may exchange energy with the molecule. In this case, the energy of the electron is imparted to the internuclear bond. As the predissociating state lies above the dissociation limit the bond has too much energy and breaks, leaving the atomic products.

The dynamics of the predissociating electron wave packet may, like an autoionising wave packet, be measured using the optical Ramsey method. In this case, instead of field-ionising the Rydberg state population, the dissociation product is photoionised. As for autoionising states, two broad bandwidth picosecond optical pulses excite Rydberg states in the weak field limit. Their temporal delay allows one to probe the dynamics at different times, whereas the phase relation between the two optical pulses introduces interference fringes in the population of the Rydberg states. For predissociating wave packets, the fringes in the Rydberg population are transferred to fringes in the population of the dissociation product. Therefore, to detect the predissociating Rydberg states, the population or yield of the fragment atoms can be monitored by ionizing one of the atoms. In these experiments, we have achieved this by ionising the N (^2D) atoms by a 2 + 1 REMPI process.

Figure 2 represents a plot of the time of the first experimentally observed peak in the dissociating wave packet spectrum as a function of the average principal quantum number, following excitation of a predissociating wave packet via the $v' = 1, N' = 0$ level of the intermediate[3]. Overall, the points follow the classically expected orbit periods for single series excitation of *np*(0) states, which is plotted on the graph as $t_{cl} = 2\pi n_0^3$. The horizontal lines represent the stroboscopic periods for interference between *np*(0) and *nf*(2) series (solid) and for the *np*(0) and *np*(2) series (dashed) calculated using Equation (1). We do not consider the effect of interference between the *np*(2) and *nf*(2) series since for the predissociating Rydberg states the *np*(0) series is by far the most intense. There is some scatter of the measured recurrence times and evidence of very weak plateaus at the stroboscopic periods, indicating that there is a very weak contribution to the wave packet dynamics from the *f*(2) series.

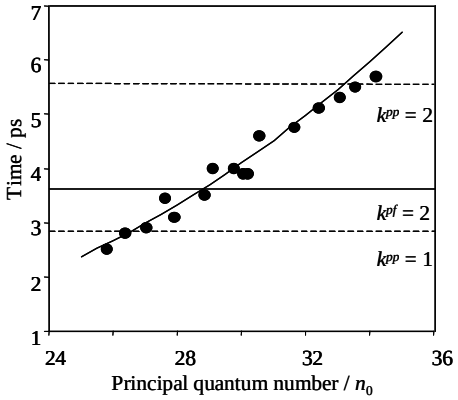

Figure 2. A plot showing how the experimentally measured orbit period of a predissociating electron wave packet changes with increasing average principal quantum number (circles). The expected classical period for an atomic wave packet, with respect to the $N^+ = 0$ ionisation limit is plotted as a curve. The horizontal lines indicate the relevant stroboscopic periods.

The plateaus or stroboscopic periods arise as a result of interferences between different Rydberg components of the wave packet, i.e. their origin is the phase that is inherent in the Rydberg molecule. The optical Ramsey method employed to observe the wave packet dynamics is based on interferences between oscillations in the Rydberg population induced by the optical field, i.e. the origin of the interference fringes in the population is the optical phase. We now show how it is possible to exploit the internal phase of the Rydberg molecule together with the optical phase inherent in the optical Ramsey method to control the composition of the wave packet in an intuitive way.

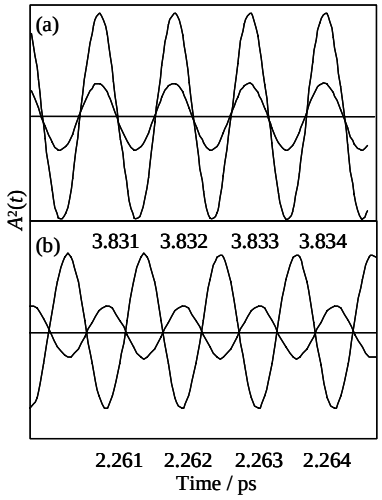

Figure 3. Ramsey fringes in the Rydberg population $A_i^2(t)$ for a wave packet excited around n_0 = 30 (a) and 25 (b), and measured after one orbit period. The larger amplitude fringes belong to the *p* Rydberg population whilst the lower amplitude fringes belong to the *f* Rydberg population.

The phase-dependent populations $A_i^2(t)$ for a wave packet excited around n_0 = 30 (a) and 25 (b) are calculated and plotted in Figure 4[3]. In each of these plots, the larger amplitude oscillation represents the Ramsey fringes of the *p* Rydberg population whilst the lower amplitude oscillation represents the Ramsey fringes of the *f* population. For excitation around n_0 = 30, the Ramsey fringes of the two angular momentum components after one orbit period $t = t_{cl}$, are in phase with one another. This is understood by noting that n_0 = 30 lies in the middle of the k = 2 stroboscopic plateau, observed in Figure 1. In contrast, for excitation around n_0 = 25, the Ramsey fringes of the two angular momentum components are out of phase with one another after one orbit period. This is also readily understood by reference to Figure 1: n_0 = 25 lies midway between the k = 1 and k = 2 stroboscopic plateaus. The evolution of the phase difference with excitation energy manifests itself in the amplitude of the Ramsey fringes in the *total* Rydberg population. The explanation is as follows. The first wave packet is excited and allowed to evolve for one classical period t_{cl}. During this time, it acquires a phase difference between the two angular momentum components, ϕ_M. At $t = t_{cl}$, the second wave packet is launched and allowed to interfere with the first. The angular momentum components within the second wave packet are in phase with one another at the moment of its creation. If ϕ_M = 0, the amplitude of the Ramsey fringes in the total Rydberg population will obviously be larger than if $\phi_M = \pi$. This effect is illustrated in the inset of Figure 4. Ramsey fringes recorded around the time of the first recurrence in the autoionising wave packet spectrum are plotted for excitation around (a) n_0 = 25.1 ($\phi_M \approx \pi$) and (b) n_0 = 29.6 ($\phi_M \approx 0$) under identical experimental conditions. The amplitude of the fringes in (b) is significantly larger than those in (a). In contrast, the amplitude of equivalent sets of fringes recorded around the time of the first recurrence in the predissociating wave packet spectrum changes less dramatically with phase.

It is now possible to exploit this phase evolution to control the ratio of autoionisation to predissociation in an intuitive way. At n = 25, where $\phi_M = \pi$, the p and f components are out of phase with each other after one orbit period. The amplitude of the autoionising Ramsey fringes is therefore $\left(\pm\{A_p - A_f\} + \{A_p + A_f\}\right)^2 = 4A_p^2$ or $4A_f^2$, where A_l is the fringe amplitude for an individual l component of the wave packet. The first set of curly brackets refers to the first wave packet, which has evolved for one classical orbit period, and the second set refers to the second wave packet, which is created at $t = t_{cl}$. The ± depends on whether the Rabi oscillations induced by the second laser pulse are in phase with the Rabi oscillations of the p component of the initial wavepacket (+) or with the f component of the initial wavepacktet (-). The predissociating Ramsey fringes have amplitude of $\left(\{A_p\} + \{A_p\}\right)^2 = 4A_p^2$, assuming the f Rydberg states have negligible contribution.

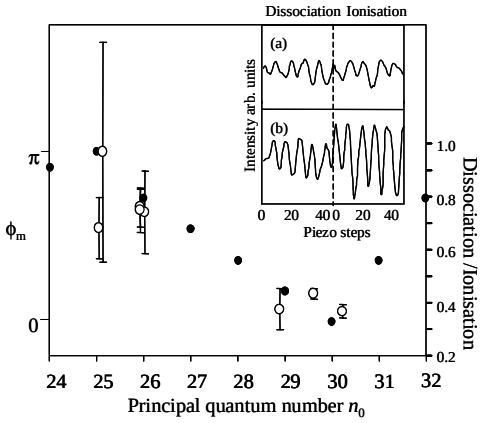

Figure 4. A plot of the phase difference between the $p(0)$ and $f(2)$ series at $t = t_{cl}$, as a function of average principal quantum number n_0 (filled circles), together with a plot of the ratio of the experimentally recorded Ramsey fringes in the dissociating and autoionising Rydberg spectra, at the time of the first recurrence (hollow circles). The inset compares representative sets of Ramsey fringes from dissociating and autoionising spectra recorded at n_0 = 25.1 (a) and 29.6 (b). Ramsey fringes were collected over 50 piezo steps, each corresponding to 0.15 fs.

At n = 30, where ϕ_M = 0, the p and f components are in phase with each other and the amplitude of the autoionising fringes is now $\left(\{A_p + A_f\} + \{A_p + A_f\}\right)^2 = 4A_p^2 + 4A_f^2$ (assuming no cross terms) whilst the amplitude of the predissociating fringes remains $4A_p^2$. Thus, the ratio of the amplitudes of the observed Ramsey fringes in the predissociating and autoionising wave packet spectra, at the time of the first recurrence, varies as a function of the phase-difference between the dominant angular momentum components at this time. This is illustrated in Figure 4. The phase difference between the $p(0)$ and $f(2)$ series at $t = t_{cl}$ is plotted as a function of average principal quantum number n_0 (filled circles). It is determined directly from the experimental frequency spectrum, using Equation (2) to calculate the Ramsey fringes of the separate angular momentum components. The phase difference oscillates between 0 and π, passing through a minimum around n_0 = 30. On the same graph, we plot the ratio of the experimentally recorded Ramsey fringes in the dissociating and autoionising Rydberg spectra, at the time of the first recurrence (hollow circles). The actual value on this scale (right hand vertical axis) is arbitrary since the NO^+ ion signal recorded for an autoionising wave packet spectrum is orders of magnitude larger than the N^+ ion signal recorded for a dissociating wave packet spectrum. However, all the data contributing to Figure 5 were recorded using consistent experimental conditions. What is important is the variation in the ratio of the dissociating and ionising fringe amplitudes with excitation energy. Representative pairs of Ramsey fringes are plotted in the inset. The dissociation/ionisation ratios were measured at excitation energies around n_0 = 25 where $\phi_M = \pi$ and around n_0 = 30 where ϕ_M = 0. Although there is scatter in the data, it is quite clear that there is a correlation between the phase ϕ_M and the dissociation/ionization ratio.

Section 3 - Controlling the rotational angular momentum of a Rydberg wave packet in a molecule

In this final section we exploit the interference effects mentioned above to control the rotational angular momentum of the ion core in a Rydberg molecule and characterize its behavior by looking at the resulting population distribution[4]. A wave packet excited around n = 33 has a classical orbit period of 5.04 ps. After one classical orbit period $\phi_M = \pi$. If a second pulse is introduced at around t_2 = 5.04 ps, it can be chosen to be either in phase with the p component of the wave packet or the f component. Keeping the p component and pumping down the f states leaves a core in the stationary state with N^+ = 0, whilst keeping the f component and pumping down the p states leaves a core in the N^+ = 2 state. i.e. the rotational quantum number of the molecular ion core can be controlled.

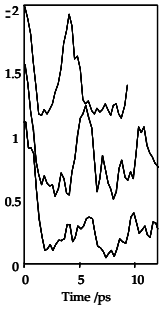

Figure 5. Recurrence spectra of a wave packet excited around n_0 = 33 following single pulse excitation (lower) and two pulse excitation eliminating the N^+ = 2 states (middle) and N^+ = 0 states (upper).

Summary

These investigations of electron wave packets in molecules were intended to understand and exploit the electronic and molecular phases of these 'classical' systems that test the limits of the correspondence principle. The concept of phase in wave packet dynamics is of interest in its own right, but it is also important because of its link to coherent control[5,6]. Understanding the sources of phase in a molecular system and how they can be manipulated by optical phase is central to the design of intuitive coherent control schemes. Because it is relatively straightforward to understand where the phase comes from in a Rydberg system, and it is possible to model the system using time-dependent MQDT methods, Rydberg molecules make ideal laboratories for developing and testing new coherent control scenarios.

References

1. V.G. Stavros *et al.* Phys. Rev. Lett. 83 2252 (1999); 84 1847 (2000)
2. R.A.L. Smith *et al.* J. Chem. Phys. 119 000 (2003)
3. R.S. Minns *et al.* J. Chem. Phys. submitted (2003)
4. R.S. Minns *et al.* Phys. Rev. Lett. in preparation (2003)
5. J.R.R. Verlet *et al.* Phys. Rev. Lett. 89 263004 (2002)
6. J.R.R. Verlet *et al.* Phys. Rev. A. 65 2504 (2002)

Aspects of laser-generated acoustic shock waves in air

K Attenborough, Q Qin

Acoustics Research Centre, University of Hull, Cottingham Road, Hull, HU6 7RX, UK

Main contact email address: *k.attenborough@hull.ac.uk*

Introduction

Although the use of pulsed lasers to generate acoustic pulses in both solid and liquid media is well known[1], research into laser-generated acoustic pulses in air has not been reported to the same extent. Laser users usually try to avoid a breakdown in air, since the laser energy is absorbed and heat is produced when charged particles such as electrons stripped from atoms are generated[2]. Nevertheless it remains a fact that strong sparks can be produced in air when a light intensity, of the order of 10^{11} W cm^{-2}, is applied to a small volume. This requires that the light beam from a laser has a peak power of the order of 10 MW or more and that this beam is focused through a lens. In the focal area, the air absorbs energy from the light by means of the cascade process. The energy gain causes local heating of the gas, which expands outwards as a propagating shock wave with a rarefaction or suction region behind the shock front. Thus a powerful acoustic source is produced in air and it can be located so as to avoid unwanted reflections from the associated equipment. Given the similarity between the laser-induced acoustic shock waveform and that associated with a blast-wave[4], acoustic pulses associated with laser-induced sparks could be used to simulate blast sounds from explosions or sonic booms in the laboratory and to investigate the associated propagation effects. Measurements made near the laser sparks show that the free field sound pressures obtained within a source-receiver distance of less than 1.5m are at levels sufficient to result in nonlinear effects and are highly repeatable. Therefore, laser-generated acoustic shocks can be used for laboratory-based research into nonlinear acoustics. Results of laboratory measurements illustrating the effects of surface roughness on nonlinear propagation are presented here. The high-frequency content and high-amplitudes of laser-generated acoustic shocks makes them useful also for measurements of acoustic transmission through porous materials. Preliminary results of measurements on three materials are presented here.

Laser and Measurement System

The laser used to generate the sparks was a Q-switch Surelite III-10 Nd: YAG laser with a 1064 nm wavelength and a power of 800 mJ per pulse. If the duration of the pulse is between 4 and 6 nanoseconds[2], the pulse power of the III-10 Nd: YAG laser at 1064 nm wavelength is between 133 and 200 MW. Without focusing, the laser beam has a beam diameter of 9 mm and the intensity of the laser pulse is between 2.07 and 3.14 $\times 10^{8}$ W cm^{-2}. This intensity is much lower than the threshold of 10^{11} Wcm^{-2} required to break down the air. In the experiments reported here, the laser beam was focused using a convex lens with a focal length of 10cm to a spot of diameter of about 0.3mm so that the light intensity in the focused spot is between 1.88 and 2.83 Wcm^{-2}. The sensing and analysis system that was used for measurements of laser-induced acoustic shock waves consisted of high-pressure and high frequency microphones, B&K Types 4138 (1/8″) and 4939 (1/4″); a high frequency amplifier, B&K Type 2636, a National Instruments 5911 data acquisition card and LabView software. The peak pressure, duration and stability of the laser-induced acoustic shocks have been investigated.

Characteristics of the laser-induced acoustic shocks

A measured waveform at 3cm from the spark source, using a 1/8″ microphone, is shown in Figure 1(a). The peak pressure at this distance is found to be 181dB re 20 μPa (22,683 Pa). Since

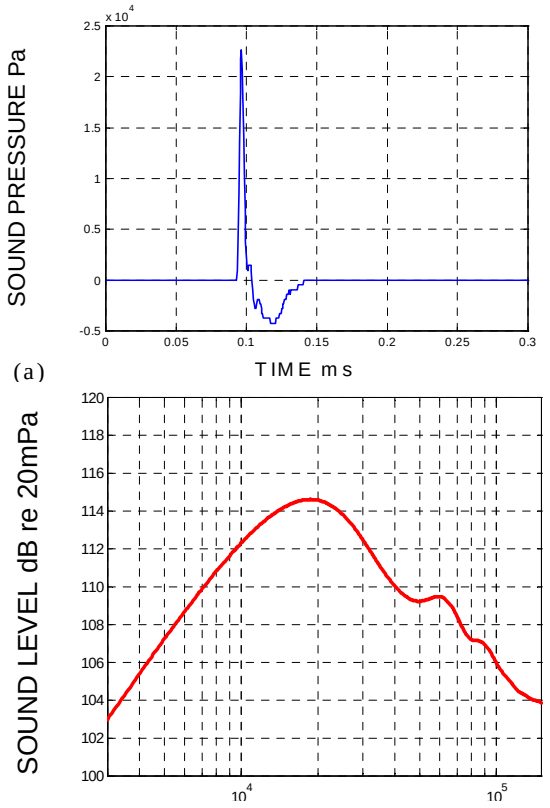

Figure 1. (a) Acoustic waveform (b) Spectrum obtained at 3 cm from the laser-generated spark using an 1/8″ microphone.

nonlinear convective effects, in contrast with dissipative effects (such as viscosity and thermal conductivity), become apparent at sound pressure levels of around 140 dB[3], the measured laser-induced spark source is useful for research into non-linear acoustics. Even at a source-receiver distance of 150cm, the peak pressure of the received pulse is higher than 140 dB. The spectrum of the laser-induced acoustic shock is broadband and high frequency (Figure 1(b)). The sound energy spectrum is between 3 kHz and 150 kHz and peaks at 20 kHz.

The peak pressures due to the laser-generated shocks measured with 1/8″ microphone are shown as a function of source-receiver distance in Figure 2. The decay with distance becomes logarithmic beyond about 10 cm from the source. Figure 2 shows that there is increasing departure from inverse square law with distance. This is associated with air absorption and with nonlinear hydrodynamic loss in air. The calculated effect of air absorption[4] on the peak pressure of the laser spark as the source-receiver distance is changed from 3 cm to 153 cm is 1.57 dB. Estimates of hydrodynamic nonlinear effects in air as a function of distance x may be made by approximating the laser-generated pulses as triangular waveforms with amplitude p and duration T and using Equations (1) and (2)[5].

$$p = \frac{p_0}{\sqrt{1+\frac{\varepsilon p_0 x}{c_0^3 \rho_0 T_0}}} \qquad (1)$$

$$T = T_0\sqrt{1+\frac{\varepsilon p_0 x}{c_0^3 \rho_0 T_0}} \qquad (2)$$

where $p_0 = p(x=0)$, $T_0 = T(x=0)$, ρ_0 is the density of air, c_0 is adiabatic sound speed in air, $\varepsilon = (\gamma+1)/2 \approx 1.2$ and γ is the adiabatic constant.

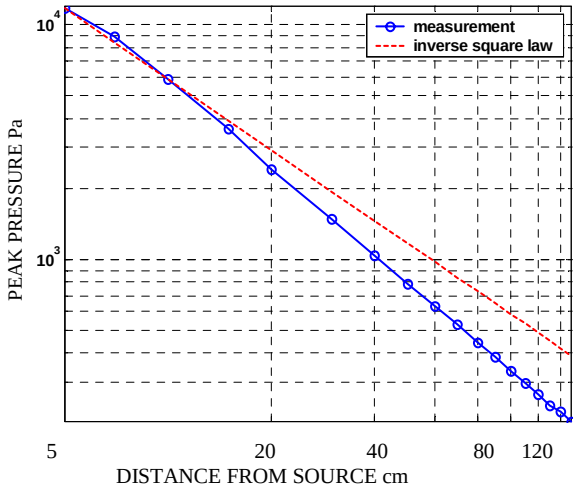

Figure 2. Measured reduction in peak pressure with distance in the free-field compared with spherical spreading; 1/8″ microphone receiver.

Assuming a peak pressure of 22.163 kPa, and assuming a duration (t_0) of either 12 μs (the positive duration) or 48 μs (the total duration) which are the measured characteristics of the waveform at 0.03m from the spark, the effects of hydrodynamic nonlinearity are predicted to be between 3.5 and 7.8 dB. In particular, for the given peak pressure, a reduction due to hydrodynamic nonlinearity in air of 5.2 dB is predicted to correspond to a (triangular) pulse duration of 26 μs at 3cm from the spark. From the data and calculations it may be concluded that, although the spark itself is asymmetric and elongated in the direction of the incoming light beam[6], the associated acoustic pulse behaves essentially as though from a point source at distances beyond 10 cm but with additional nonlinear hydrodynamic losses and air absorption. Hydrodynamic nonlinearity in air is predicted also to cause gradual elongation of the pulse with distance resulting in an increased duration at a distance of 1.5m from the spark of between 150% and 250% of that at 3cm from the spark. The peak pressures in 50 shocks have been measured at fourteen source-receiver distances between 20 cm and 150 cm. The results from using a ¼″ microphone are shown in Figure 3. The ¼″ receiving system has a frequency response only up to 100 KHz. Consequently, the use of a 1/4″ microphone results in lower peak pressures and less apparent absorption but preserves the overall trend of the variation with distance. The error bars present the standard deviations of the measured peak pressures. The standard deviations are found to vary between only 1.5% and 3.0% of the peak pressures, which indicates that the laser-induced acoustic pulses are very repeatable.

Nonlinear propagation over rough hard surfaces

Measurements have been carried out using a ¼″ microphone over six different rigid rough surfaces consisting of single layers of randomly-distributed but uniformly-sized grains fixed to smooth glass plates. The grains were fixed to the glass base by epoxy adhesive. The grains, the glass base plate and the dried epoxy adhesive are acoustically rigid. The grain sizes on the six rough surfaces varied between 0.2mm and 5.0mm i.e. between 1/65 and 1/3 of the wavelength at the peak energy frequency (20 KHz).

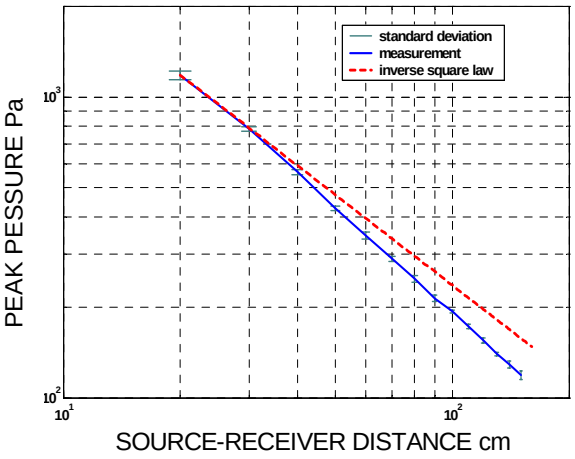

Figure 3. Measured reduction in peak pressure with distance in the free-field compared with spherical spreading; 1/4″ microphone receiver, 50 shocks. Error bars represent standard deviations of data at each range.

The distances between the source and the receiver were set at 20.0, 22.5, 25.0, 27.5, and 30.0cm respectively. The source and the receiver heights were kept constant at 0.75 cm, corresponding to grazing angles of 4.29, 3.81, 3.43, 3.12, and 2.86 degrees respectively. The data in Figure 4 show a large variation in the measured sound peak pressures at the same source receiver distance as a function of the surface roughness. The difference in peak pressure over the smooth rigid surface and the 5mm cubic glass grain surface was found to be as much as 1,400 Pa (9.4dB level difference) at 20 cm from the laser spark source (see Figure 4).

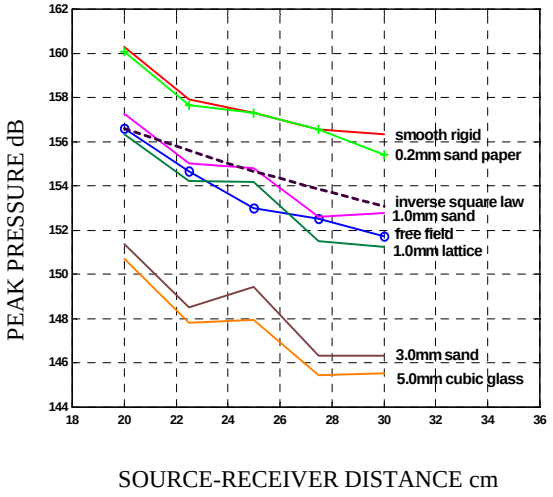

Figure 4. Measured peak pressures (dB) as a function of distance in free field, over a smooth acoustically rigid surface and over 5 different rough surfaces. Inverse square law decay is shown also.

Over the range of surface roughness used, the sound attenuation at a given distance was found to increase with increasing roughness size. For the data shown, the path length differences between the direct and the scattered signals of the geometry of the measurements are between 0.056 and 0.037 cm. This implies time delays of between 1.6 and 1.1 μs at the receiver points. These time differences are less than 2% of the pulse duration, which is between 64.5 and 108.0 μs, as shown in Table 1 and may account for the interference effects observed in Figure 4. Without the ground surface, the peak pressures

decreases monotonically with increasing distance, as shown by the free field data in Figures 2 and 3. Surface roughness is found also to cause elongation of the waveforms beyond that expected from nonlinear hydrodynamic effects. Figure 5 compared waveforms received at 30 cm from the laser-generated sparks over smooth glass and the surface formed from 5mm cubic glass grains. As well as reduction in amplitude and elongation, the waveform received over the rough surface shows evidence of a surface wave similar to that observed at lower amplitudes[7].

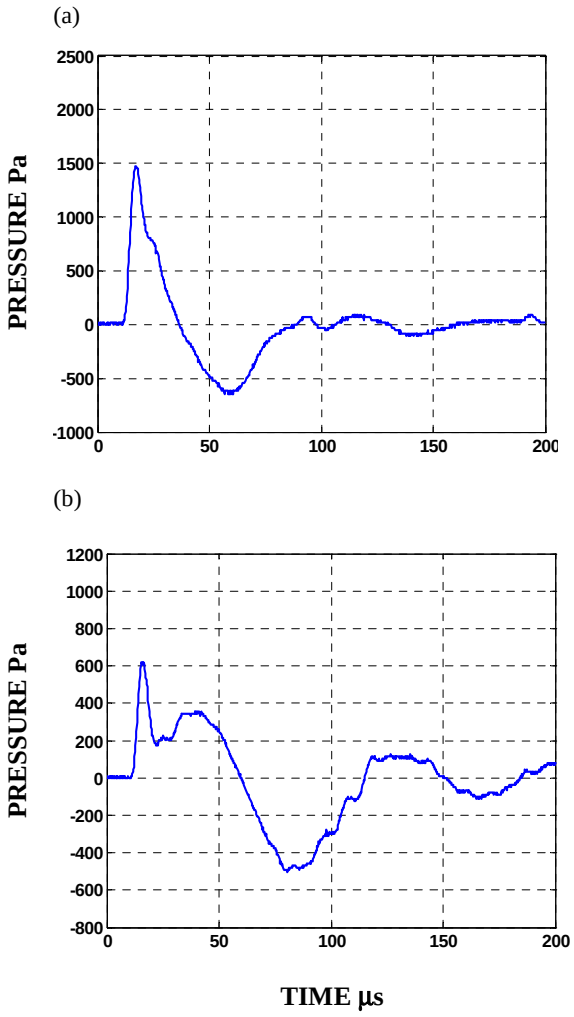

Figure 5. Comparison of measured waveforms at 20 cm (a) over a smooth glass surface (b) over a rough surface (5mm cubic glass) with the spark source at 1.7 cm height and microphone at 1.5 cm height.

Use of laser-induced acoustic pulses for tortuosity measurements

The high frequency content and high amplitudes of laser-generated acoustic pulses makes them suitable for an ultrasonic measurement of the tortuosity in porous materials[8] but on larger samples than used in typical ultrasonic experiments. An exploratory deduction of the tortuosity of a 15 cm long cylindrical sample of porous aluminium with 5cm diameter has been made by measuring the speed of propagation of laser-generated acoustic pulses through the sample. Two transducers were placed 15cm apart inside and outside a metal cylinder without and with the material sample respectively. The distance between the lens and the first transducer was about 20 cm. The propagation time of the front edge of the pulse in air without the sample was 0.447 ms. In the presence of the porous aluminium sample it was 0.462 ms. Using Equation (3), this implies a value of tortuosity of 1.068.

$$tortuosity = \left(\frac{Sound\ \ Speed\ \ in\ \ air}{Sound\ \ Speed\ \ in\ \ material} \right)^2 \quad (3)$$

This tortuosity value is very close to the average value 1.067 deduced by fitting data for the acoustic characteristic impedance that have been obtained independently. Similar data and deductions have been obtained with samples of gravel and porous concrete. The results are summarised in Table 1 together with values deduced from fitting impedance tube data and the measured flow resistivities. Not surprisingly, there is evidence that timing the front end of shock becomes a less accurate method for tortuosity deduction as the flow resistivity of the porous material increases. Further work is needed to investigate possible nonlinear and dispersive effects. However, it appears that laser-generated acoustic pulses offer an alternative to the conventional ultrasonic cell method for measurement of tortuosity.

Material	**Measured Flow resistivity Pasm^{-2}**	**Tortuosity from laser-induced acoustic shock data**	**Tortuosity from fitting impedance tube data**
Porous aluminium	204.6	1.07	1.067
8mm gravel	846	1.5	1.46
Porous concrete	3619	1.57	1.8

Table 1. Results from tortuosity measurements.

Conclusions

a. The characteristics of laser-generated acoustic pulses are useful for laboratory research into nonlinear acoustic effects.

b. Small-scale measurements made over a series of ground surfaces have shown that the propagation of laser-induced acoustic shocks near to the ground is sensitive to small-scale ground roughness.

c. Preliminary measurements of the speed of laser-induced acoustic pulses through thick samples of material suggest the possibility for developing a novel ultrasonic method for determining the tortuosity of rigid-porous materials.

References

1. R J Dewhurst, D A Hutchins, and S B Palmer, J. Appl. Phys. 53 (6), 4064-4071, (1982).
2. J F Ready, Industrial applications of lasers, 2nd edition, Academic Press, (1997).
3. D A Webster, and D T Blackstock, J. Acoust. Soc. Am., 62, 518-523, (1977)
4. D T Blackstock, Fundamentals of Physical Acoustics, University of Texas, Austin, Texas, JOHN WILEY & SONS, INC, (2000).
5. L D Landau, and E M Lifshitz, Fluid mechanics, Pergamon Press, Oxford, London, Paris, Frankfurt, (1963).
6. J F Ready, Effects of High-Power Laser Radiation, , Academic Press, (1971).
7. J P Chambers and Y H Berthelot, J.Acoust. Soc. Am., 102 (2) 707 - 714 (1997)
8. J F Allard, B Castagnede, M Henry, W Lauriks, Rev. Sci. Instrum. 65, 754–5 (1994).

Simulating space weathering using a pulsed laser

M S Bentley, I P Wright, J C Zarnecki

Planetary and Space Sciences Research Institute, The Open University, Walton Hall, Milton Keynes, MK7 6AA, UK

N J Mason

Dept Physics and Astronomy, The Open University, Walton Hall, Milton Keynes, MK7 6AA, UK

Main contact email address: *M.S.Bentley@open.ac.uk*

Introduction

Space weathering is defined as the collection of processes that modify the surface of an airless planetary body over time. These processes include micrometeorite bombardment and solar wind sputtering. The effects include changes to both the Vis-NIR reflectance spectrum and magnetic properties of the surface regolith[1)].

This study builds on previous work[2)] by examining the effects of temperature on the rate of weathering (of particular interest to the surface of the planet Mercury) and by using a suite of analytical techniques designed to examine the number and size distribution of submicroscopic iron spherules produced in the process.

Experimental procedure

In order to simulate the first of these processes, we have used the Loan Pool's Spectra-Physics Quanta Ray Pro 230 laser to provide an "impact like" impulsive input of energy to a powdered sample placed under high vacuum. The energy, spot size and timescale are designed to be comparable to a typical hypervelocity dust grain impact[3)]. Work performed previously by other researchers has shown this method to be a good analogue of real impact events, causing melting and vaporization followed by subsequent re-condensation. During this process, FeO in the regolith is believed to be reduced to nanometre sized spheres of metallic iron (commonly called SMFe, or submicroscopic metallic iron). The porous nature of the sample is essential to allow the vapour to become trapped and not immediately lost.

A range of sample materials has been prepared to evaluate the effects of mineralogy and FeO concentration on the space weathering process. These include NASA's JSC-1 lunar regolith stimulant (a basaltic ash with elemental abundance and chemical composition similar to the lunar soil) and a range of minerals found on the Moon and in asteroids, including olivines, pyroxenes and ilmenite. These have been ground to a fine powder and dry sieved to extract the sub 63 micron fraction. In the lunar case it is this fine element that dominates the space weathering effect, presumably due to its large surface area on which vapour can condense. Some samples have been pressed into pellets under approximately 10-15 Tonnes per square inch pressure.

The fundamental 1064nm output of the laser is passed through a beam delivery system consisting of two computer controlled mirrors and a lens, allowing uniform scanning of the sample surface through an optical window on top of the vacuum chamber. Spot size on the sample is approximately 500 microns. This equipment is placed in an interlocked cabinet to ensure user safety. Once pumped down to approximately 10^{-7} mbar, the sample is baked out to remove excess water and volatiles and then brought to the correct experimental temperature, controlled by a PID controller and nichrome heater.

The laser energy is measured at the output of the beam delivery system before irradiation. Beam and mirror control are synchronised via a computer while temperature and pressure can be monitored throughout the experiment. During irradiation, the vacuum chamber pressure is seen to increase, indicative of sample heating and potentially vapourisation. After the programmed number of irradiation cycles, the laser is made safe and the sample allowed to cool to room temperature before being removed from the vacuum chamber for analysis.

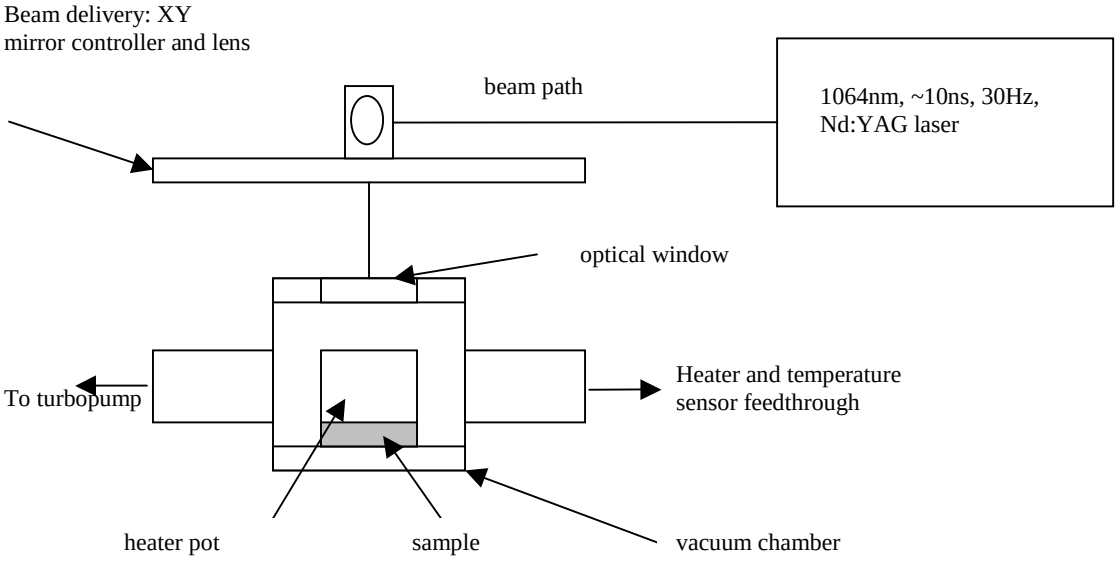

Figure 1. Schematic of the equipment used to irradiate the sample.

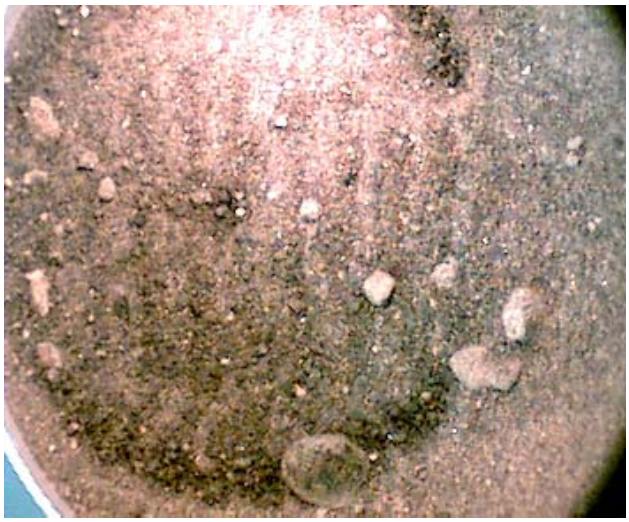

Figure 2. Irradiated sample showing striations due to beam scanning.

Analysis and results

Initial analysis can be made using a magnetic susceptibility meter, in this case a Bartington MS-2 meter with MS-2B dual frequency bench top sensor. This works by placing the sample in an energized coil, the frequency of oscillation of which changes according to the magnetic permeability, and hence susceptibility, of the sample. This should readily show even small changes in the metallic iron content of the sample.

In the first analysis this has not, however, been observed. Powdered samples show darkened striations where the beam has scanned (see Figure 2). If the beam is left in one spot for longer a black, amorphous, glassy substance is seen, resembling lunar agglutinates (Figure 3).

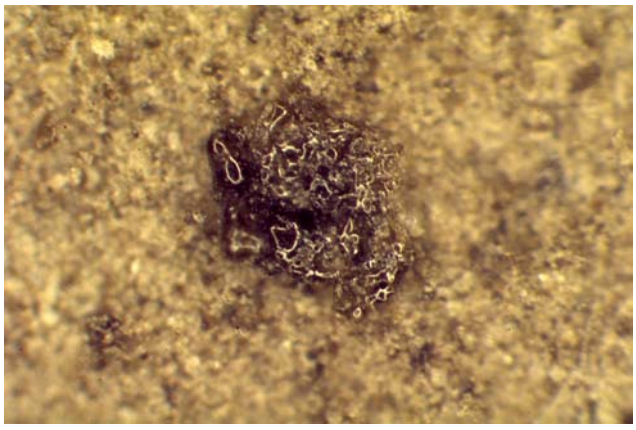

Figure 3. A glassy, agglutinate-like, grain.

An attempt was made to measure the electron spin resonance spectra of both pre and post irradiated materials, but no change was observed. Current work is ongoing to resolve whether or not the sample is actually undergoing vapourisation. To this end a quadrupole mass spectrometer has been added to a customized chamber in which the filament is held a few mm from the sample. Although a clear signature is seen during irradiation, the only obvious components observed are water, CO_2 and other adsorbed gases. This might be expected as the samples cannot be heated in the alternate chamber housing the mass spectrometer. A modification is currently being performed so that spectra can be acquired in the main experimental chamber after a high temperature bakeout.

Conclusions

It has not yet been possible to reproduce the experiments performed previously at Tokyo University, although experiment parameters are now almost identical. This could be due to the sensitivity of the analytical equipment in use, or because the desired simulation is not actually taking place.

The laser irradiation technique is certainly simulating some aspects of micrometeorite impacts, in particular melting and formation of agglutinate like materials. It is hoped that further study will verify the production of silicate mineral vapour and of submicroscopic metallic iron.

References

1. B Hapke
J. Geophys. Res., 105 10039, (2001)

2. S Sasaki *et al*.
Nature 410 555, (2001)

3. H J Melosh
Impact Cratering: A Geologic Process. Oxford, Oxford University Press, (1989)

Laser Science and Development

1) **Vulcan Petawatt**
2) **Vulcan**
3) **Lasers for Science Facility**
4) **Instrumentation**
5) **Laser Research and Development**

Vulcan Petawatt Upgrade Overview

C N Danson, D Neely, B E Wyborn

Central Laser Facility, CCLRC Rutherford Appleton Laboratory, Chilton, Didcot, Oxon, OX11 0QX, UK

Main contact email address: *c.n.danson@rl.ac.uk*

Introduction

The reporting year has seen the most important phases of the Petawatt upgrade project – its evolution following the installation phase, through commissioning and finally delivery to users for an ultra-high field interaction experiment.

The project to upgrade the ultra-short pulse CPA beam capability of Vulcan to the Petawatt regime began in April 1999. The upgrade was funded through an EPSRC grant, GR/M48383, to deliver 500J in 500fs to target giving a focused intensity of 10^{21}Wcm^{-2}. Further EPSRC funding was provided through a grant GR/S06875/01 covering the commissioning of the interaction area.

Laser Commissioning

The commissioning of the laser was a process of bringing on-line the many systems that had been individually commissioned and integrating them into a working facility. These systems included:

- 100fs optical pulse generator and stretcher
- OPCPA preamplifier
- Vulcan amplifier chain upgrade to 208mm
- Adaptive optics
- Optical pulse compressor
- Focusing to target

The commissioning of the beamline was complex due to the newly developed systems used , the optical handling required in the compressor and the need to develop new alignment techniques. All of this came together during the year with demonstrations of the required pulse duration; the delivery of laser energy and the required beam quality.

Target Commissioning

Before users could be given access to the newly commissioned facility, a radiological survey had to be conducted to validate the shielding effectiveness and the performance of the focused beam on-target. Radiological dosimetry data demonstrated that the shielding was operating as required. The measurements were approved by the site RPA (Radiation Protection Advisor) for facility delivery to users. The focal profile was measured at low energies delivering a spot size of ~7 microns. At high energies it was impossible to directly measure the optical spot but x-ray images gave a FWHM spot size of 11 microns indicating a smaller optical spot. This was consistent with our most optimistic predictions. During this experiment significant operational experience was gained in order that the first user experiment could be conducted with a high degree of confidence in the facility performance.

First user experiment

The first user experiment on the Petawatt facility was conducted by Dr Karl Krushelnick of Imperial College, London to investigate advanced particle acceleration schemes. The laser performed very well with 39 shots requested and no failures recorded. 36 of these shots were requested at the 300J level (~300TW to target) and were all delivered within 20% of that energy. The experiment produced some exciting data achieving world leading electron acceleration results as detailed elsewhere in this report.

Project Management

The project has been managed according to the CCLRC's Corporate Project Management procedures. The Project Management Committee, which oversaw the project, was chaired by Dr AD Taylor, Deputy CE CCLRC, Director ISIS.

Figure 1. CLF staff gather to celebrate the completion of the commissioning of the Vulcan Petawatt project.

Vulcan Petawatt – Compressor and system commissioning

J L Collier, C Hernandez-Gomez, S J Hawkes, J Smith, T B Winstone, C N Danson, R J Clarke, D Neely, Ch Ziener, T Strange, A J Frackiewicz

Central Laser Facility, CCLRC Rutherford Appleton Laboratory, Chilton, Didcot, Oxon., OX11 0QX, UK

Main contact email address: *j.l.collier@rl.ac.uk*

Introduction

This article describes the process that was undertaken over a 15 month period to commission the Vulcan Petawatt system. In general the approximate chronological steps that were followed were as follows:

1. LA4 forward going and retro diagnostics commissioning and adaptive optics verification
2. Surveying of each mount and large optic into position
3. Vacuum Spatial Filter (VSF) commissioning, normalization and output collimation
4. Wave front and surface quality tests of each large optic individually
5. Approximate geometrical alignment of the large optics and compressor gratings – setting of the incidence angle
6. Precision compressor alignment procedure
7. Commissioning of the diagnostics channel and diagnostics suite
8. OPCPA temporal compression optimisation and stretcher conjugation
9. Low energy shot series – energy stability verification
10. Parabola installation, optimisation and on target far field characterization
11. Energy ramp and optics inspection sequence
12. Energy ramped operations / radiological commissioning

For clarity, the definitions that are used throughout for the optics, in the order that the propagating beam would see, are shown in Figure 1 and are as follows:

L1 - Output VSF Lens

M1 - Input turning mirror in North Tank

G1 - 1st grating located in South Tank

G2 - 2nd grating located in North tank

M2 - Output Turning Mirror in South Tank

M3 - Turning Mirror in Interaction Chamber

DM1 - First diagnostic turning mirror – South Tank

DM2 - Second diagnostic turning mirror – South Tank

L2 - Diagnostic down collimating lens – South Tank

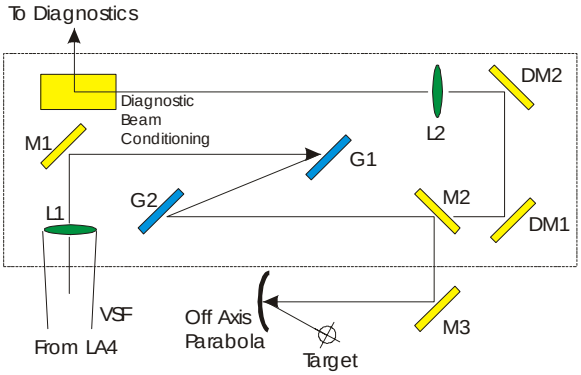

Figure 1. Schematic Layout of the PW Compressor.

Each of the optics had between 3 and 5 linear and angular degrees of freedom that were electronically and precisely controllable by PC external to the chamber. This enabled alignment under vacuum. For the motions of the optics the axis definitions used are:

TILT – Rotation of the optic about a vertical axis lying in the plane of the optic surface

TIP – Rotation of the optic about a horizontal axis lying in the plane of the optic surface

ROTATION – Rotation of the optic about a horizontal axis lying perpendicular to the plane of the optic surface

X - horizontal motion, across beam

Y - vertical motion, across beam

Z - longitudinal motion, along beam

LA4 System

A key element to the alignment of the compressor system was a suite of systems housed in LA4. These are described in detail in the CLF Annual Report 2001/2002. The systems were:

- A forward going set of diagnostics comprising a near field monitor, a narrow angle far field monitor and a self referencing radial shear interferometer.
- A set of diagnostics capable of analysing a beam propagating back from the compressor or target chamber. This consisted of both a wide and narrow field far-field monitor and an interferometer. This retro system was used extensively for the commissioning of the Petawatt system.
- A 200 mm diameter λ/10 diffraction limited 1053 nm or 1047 nm alignment beam of "top hat" intensity profile that could easily be injected into the VSF. This beam was near-field stabilised through the use of a permanent aperture and far-field stabilised through the use of very tight spatial filtering. The absolute collimation of this system was set by observing its propagation over ~ 60 m distance. Once the collimation was established, a set of forward going references were recorded – the far-field for example is shown in Figure 2(a). This alignment beam also served as the reference beam for the adaptive optic system. Furthermore, by utilising a reference flat located immediately after its output a retro-reflective reference wavefront was also recorded for later comparative use. This is shown in Figure 2(b).

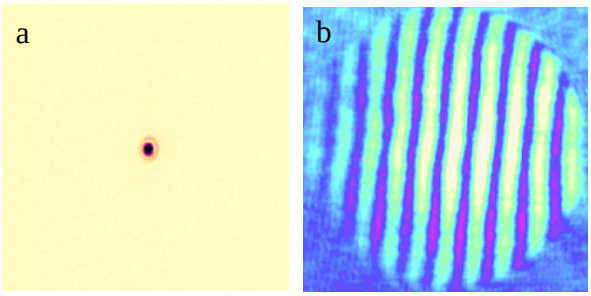

Figure 2. Forward Far Field in LA4 (a) and Retro Wavefront (b) of the alignment (AO reference) laser.

Surveying

Each mount, minus its large optic, was surveyed into the correct floor plan position initially with a positional accuracy of the order of ~3 mm. All mounts were installed in the compressor chamber prior to the installation of the large aperture optics. The mounts were electrically commissioned at this stage. The large optics were installed on a sequential basis excluding initially the VSF output lens (L1) to enable a pencil alignment beam propagating along the centre line of the VSF to be used as an alignment aid. At this time, the central beam height was set and a subsequent horizontal plane that we term the reference, or diffraction, plane of operation was also defined. A finer positioning occurred towards the end of the precision alignment sequence described later to finely adjust the exact near field position of each optic to be central with respect to the propagating beam.

VSF Commissioning

The VSF input and output lenses were installed. The input lens formed a direct vacuum seal to the VSF tube. Therefore it was not possible to adjust the lens normalisation. This meant that great care was required in the specification, surveying and installation of the VSF mechanical systems to ensure appropriate orthogonality to the reference pencil beam.

The output lens (L1) normalisation was accomplished by attaching a small mirror to a flat steel bar positioned across the mounting bezel of L1 and utilising the retro-reflection pencil alignment beam from LA4. Normalisation to the 1 mrad level was possible using this technique which is well within specification.

The VSF collimation was set by utilising M1 in a retro-reflective mode and observing the reflected wavefront in the LA4 retro interferometer in comparison with the stored reference wavefront. The longitudinal position of L1 was adjusted for a net zero defocus utilising a Zernike analysis. It should be noted here that there was a slight difference in defocus between air and vacuum and the collimation was set for vacuum operation.

With M1 in retro arrangement also enabled a measurement of the general stability of the optical component mounting system in the compressor chamber in passing from air to vacuum.

Figure 3 shows a retro far-field comparison between air and vacuum for this arrangement. The “line” nature of the far field is illustrative of the slight astigmatism present on M1. The stability is excellent, with a relative movement of approximately 4 µrad between air and vacuum.

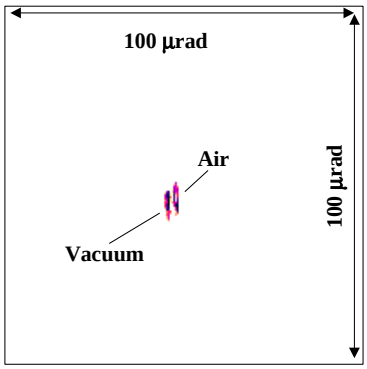

Figure 3. Retro far-field off M1 illustrating the stability of the air – vacuum stability of the compressor optical mounts.

Large Optic Wavefront Quality

Sequentially, each large optic was positioned in retro reflective mode to check the wave front quality of each optic. Interferograms were recorded for each optic and processed to remove the contributions of preceding optics. It was important to undertake the measurements under vacuum because of the significant wavefront errors that are introduced by thermal gradients and air flow in the compressor. Generally each optic was measured to be within λ/2 peak-valley except M1. The wavefront quality of mirror M1 is shown in Figure 4(a), and that of M1 and G1 is shown in Figure 4(b). In this way it was also possible to measure the wavefront quality of the beam leaving the final mirror M2. This is shown in Figure 4(c), illustrating that there was approximately one wave of peak-valley distortion in a predominately astigmatic mode. This astigmatism, arising primarily from M1, should be finally correctable by operating the off-axis parabola slightly away from normal incidence.

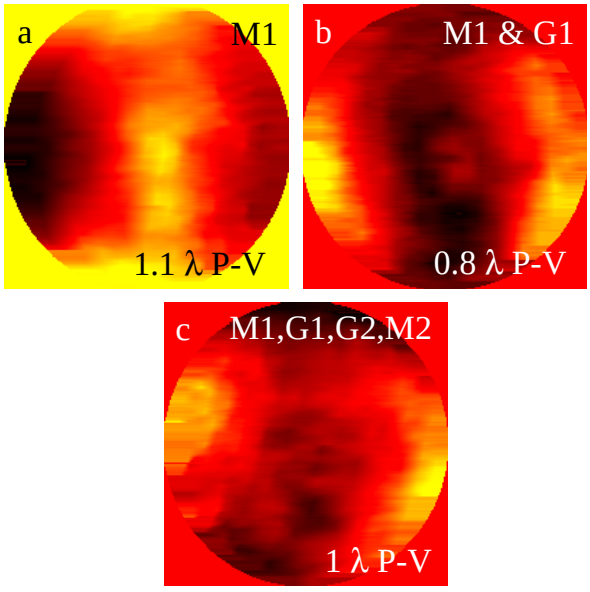

Figure 4. Wavefront recorded in the LA4 retro interferometer from various places in the compressor system.

Orthogonality of TILT Axis and Reference Plane

For every optic, whilst each of the three angular axes are orthogonal to one another, it is not necessarily the case that the reference plane lies orthogonal to the TILT axis. This arises because at the surveying stage it is difficult to set the orthogonality of this axis to the reference plane to better than several mrad given the adjustments available on the mount bases. This means that there is a coupling between TILT and TIP with respect to the reference plane when the optics are adjusted. For example, in TILTing M1 from its retro position to its 45 degree operating position, a beam deviation on Grating G1 of several centimetres with respect to the reference plane was observed. For the mirrors M1 and M2, its correction is relatively trivial given only reflection is involved. However, for the gratings it is complicated by the diffraction process. Access to the zero order (diffraction free) from the gratings to set the TILT was restricted by the walls of the chamber so the accuracy in setting this was limited to about 1 mrad for each grating.

Following this, the diffracted pencil beam was set to the reference plane height by grating ROTATION. Thus, the grating grove parallelisms are set through this geometrical method to within 1 mrad or ten times specification. Fine tuning required the dichroic alignment system. This procedure also ensured that the grating surface parallelism in the non

dispersion plane of the gratings was within ~ 2 mrad - also within specification.

The incidence angle matching of the compressor to the stretcher was set in a geometric manner using the reduced aperture alignment beam. The pencil beam was propagated from M1 to G1 and from G1 to G2. The included angle between the incident and diffracted beam from G2 was geometrically set to be 6.83 degrees as required. However, there is a setting error which, in this case, arises from the fact that different alignment lasers are used in setting the stretcher and the compressor. This means that even though both alignment lasers are narrow band Nd:YLF based, there is a centre wavelength error of possibly 0.2 to 0.3 nm between the two systems. This in turn translates to an input angle setting error and therefore consumes a large amount of the input angle matching tolerance budget for setting this parameter.

Dichroic Precision Grating Alignment Sequence

Having followed the above procedures, the near-field position of the optics should be within a few millimetres and the far-field position within a mrad. The precision alignment technique that follows was iterative until an optimum situation was reached.

M2 was set such that the full aperture 1053 nm alignment beam propagated back through the compressor system and into LA4. The position of the retro far-field was recorded as a nominal reference.

The alignment beam was then switched in wavelength to 1047 nm, but crucially had its near-field and in particular its far-field defined by the same system as for the 1053 nm beam. The 1047 nm retro far-field will be in a different position with respect to the 1053 nm. This dichroic far-field difference can only be due to a diffractive error. To first order, a horizontal (i.e. in the reference, or dispersion, plane) angular dichroic difference is due to a misalignment of grating surface parallelism and requires a relative grating TILT to correct. A vertical difference (i.e. perpendicular to reference plane) is a grove parallelism error and requires a relative grating ROTATION to correct. This is illustrated in Figure 5. Some care however is required in making any correction. G1 is left at all times unchanged and all adjustments are to G2 (and M2).

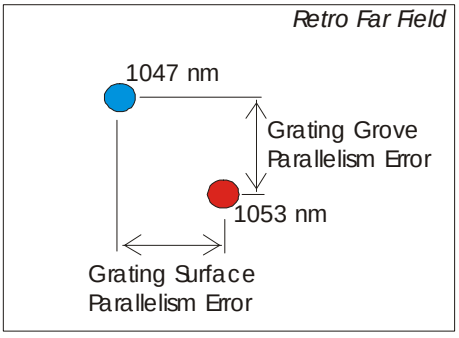

Figure 5. Explanation of retro far field di-chroic alignment technique.

To set the reference (or dispersion) plane grating surface parallelism, small adjustments were made to G2 TILT, whilst always returning the 1053 nm far-field to the retro reference position using a corresponding M2 TILT adjustment. The dichroic far-field separation was measured and this was repeated until the horizontal dichroic retro far-field displacement, as determined by a centroiding algorithm, was less than about one third of a focal spot diameter.

To set the grating grove parallelism small adjustments to G2 ROTATION were made, whilst always returning the 1053 nm far-field to the retro reference using a corresponding G2 TIP adjustment (not M2 as before). This was repeated until the vertical dichroic retro far-field displacement, as determined by a centroiding algorithm, was also less than one third of a focal spot diameter.

This double pass process will have established that the gratings and their groves are sufficiently parallel such that in single pass operation there is no residual dispersion across the expected bandwidth that is outside the monochromatic diffraction limit. For this bandwidth, this corresponds to a temporal compression error of no more than 50 fs.

Diagnostics Suite

Following the precision alignment of the gratings the diagnostics beam line was commissioned. Great care was taken in the optical design of the diagnostics system that true imaging was maintained throughout the various measurement devices and its commissioning was appropriately careful to implement this design. The source image plane chosen was the plane immediately in front of grating G2. A photograph of the diagnostics suite undergoing commissioning is shown in Figure 6.

Figure 6. Diagnostics Suite undergoing commissioning.

The diagnostics suite will be described in detail in next years CLF Annual Report so in summary form, at the time of laser commissioning the systems that were available were:

- **Beam Conditioning Optics**: incorporating a design to provide appropriate image relaying whilst ensuring that the propagation of the diagnostics beam out of the tank was at large aperture to minimise B-Integral.
- **Beam Energy Dump**: an externally switchable beam dumping optical arrangement to enable operation at either CW / OPCPA level or at full shot energy.
- **Near and Far-Field**: A high resolution near-field image of the beam leaving G2 and an approximate equivalent plane far field. Figure 7 is an example of the output of the near-field monitor for a low energy OPCPA beam at air and under vacuum. The shadow at air is a deliberate obscuration structure placed in the beam at the G2 plane position. The differences between the two arise from a spatial change in the transmission properties of the M2 optical coating. The “popes nose”, a feature of the manufacturing process of the gratings, is clearly visible.

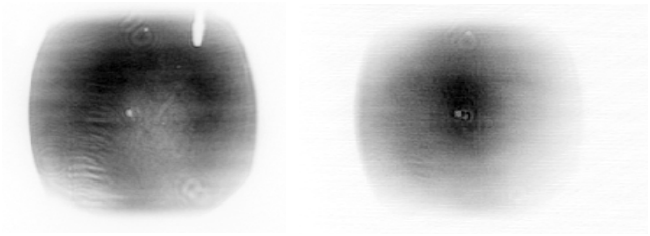

Air Vacuum

Figure 7. Diagnostic near field output under air and vacuum.

- **Dispersion Plane Autocorrelator**: providing a pulse length measurement integrated in the vertical beam direction (perpendicular to the reference plane) – this provides an estimation of the pulse length deriving from a combination of the stretcher-compressor conjugation and residual groove non-parallelism.
- **Non Dispersion Plane Autocorrelator**: providing a pulse length measurement integrated in the horizontal beam direction (parallel to the reference plane) giving an additional estimation of the pulse length driving from a combination of the stretcher-compressor conjugation and the residual grating non-parallelism.
- **Spectrometer**: for spectral shape and bandwidth.

Temporal Optimisation

Following the commissioning of the diagnostics suite, the exact conjugation of the stretcher compressor system was performed. This was done by injecting the 10 Hz output of the OPCPA front end system all the way through the Vulcan chain into the PW system. The diagnostics system is capable of operating with this very low (relative) energy OPCPA pulse when M2 is in a near retro, and thus non HR position.

Initially, as a measure of pulse compression the diagnostics beam output was focussed into a second harmonic crystal. The output of this was maximised by adjusting the longitudinal position of the stretcher grating. Through this method it was possible to determine an approximate position for optimum compression and to bring the pulselength into the window of operation of the two autocorrelators.

Finally, there was a carefully optimisation of the pulse length by adjusting the stretcher whilst recording the autocorrelator outputs. Given the 10 Hz operation of the OPCPA system it was possible to do this in real time and a typical output from this OPCPA operation is shown in Figure 8.

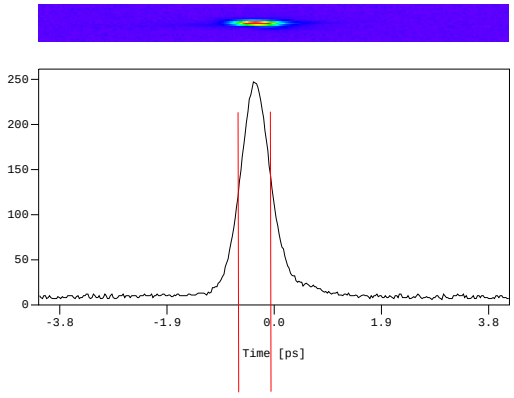

Duration 430 fs FWHM

Figure 8. Broad band OPCPA compression to a transform limited pulse indicating good conjugation of the stretcher – compressor system.

The compressed pulse duration is consistent with the transform limit of the available bandwidth. This was a major achievement illustrating that CPA conjugation had been achieved. It also meant that a scan of input angle was not required to optimise the compression. A later development to occur during 2003/04 will be the installation of a SPIDER spectral phase measurement device to verify this situation.

Low Energy Shots and Silicate Chain

Following the temporal compression optimisation, a series of low energy (2 minute shots) were performed to characterise the performance of the system under the combined action of the OPCPA system and the Vulcan rod amplifiers. At this stage the silicate rod system was not available for use and thus all the rod gain was in phosphate glass. A large number of shots were fired at this level in order to measure the stability of the OPCPA / Rod system arrangement and verify its safe use with the disk amplifier chain. Pulse lengths were typically in the 600 –700 fs range.

At the time of laser commissioning the silicate glass rod chain was still under construction. It is now fully installed but as yet has not been used in conjunction with the Petawatt scheme – this is planned for late 2003/04. A photograph of the silicate chain is shown in Figure 9.

Figure 9. Commissioning of the silicate rod chain in LA1.

Parabola Installation and Optimisation

Following the low energy shot series, the off axis parabola was installed in the target chamber and this process is described elsewhere in this annual report. This was a critical moment because following its optimisation it was the first time that we would be able to verify that the focal spot would meet the design specification under pulsed operation. Figure 10 illustrates this. A series of images are shown where a camera system has been placed at the focal plane of the parabola to record the spot under a variety of different conditions. The adaptive optic system is in operation at all times.

As can be seen, the series shows the CW alignment beam from LA4, (i.e. very low bandwidth and the reference for the adaptive optics) that is focussed to a 5 μm spot diameter by the F# 3.2 parabola (figure10(a)). The CW alignment beam from

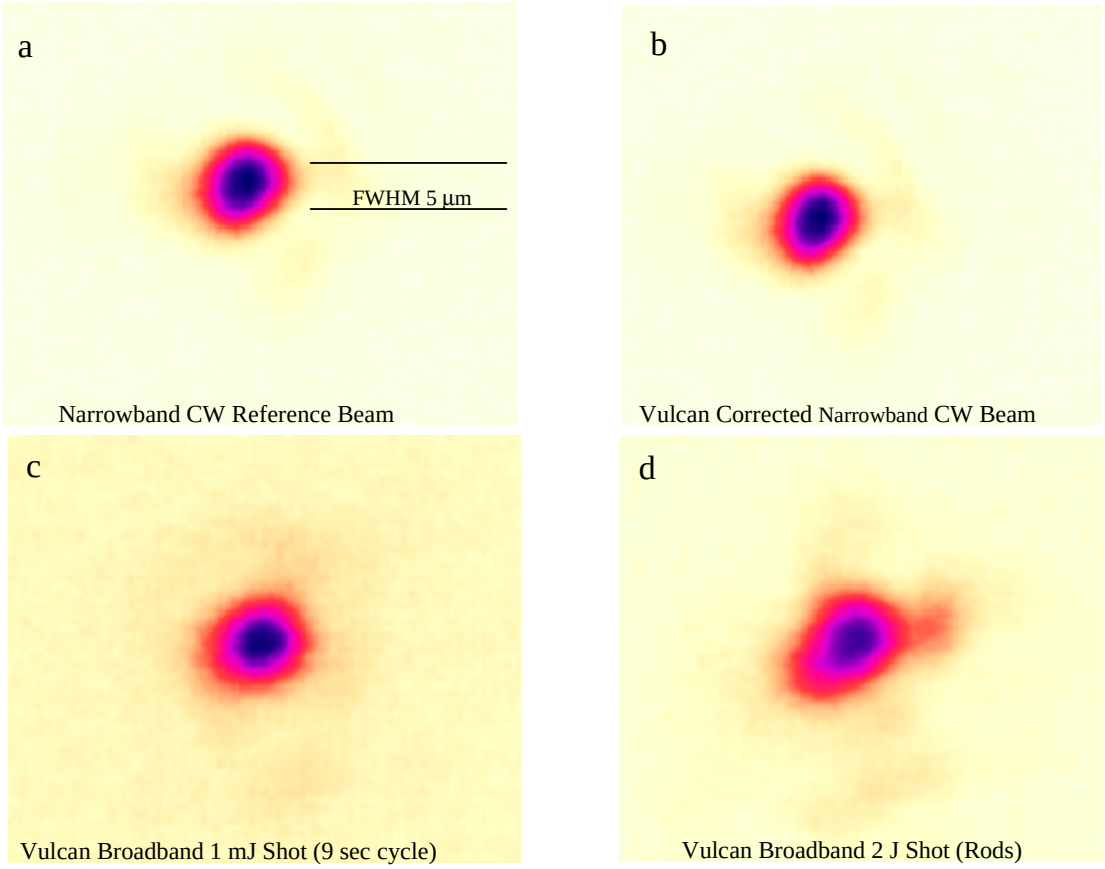

Figure 10. A series of images recorded directly at the target plane of the PW system under a variety of conditions. Importantly they show that a high quality 5 µm focal spot is produced that can be maintained for shots by the adaptive optics system with the compressor in broadband operation. This is a key result for the project.

Vulcan that has passed through the whole chain and is dynamically corrected by the adaptive optics is also shown to be focusable to 5 µm (figure10(b)). Critically, the broadband (and thus dispersion sensitive) OPCPA image (figure 10(c)), also passing through the whole system with dynamic AO correction, is shown to also be focussable to 5 µm. Finally a combined OPCPA / rod shot is shown showing also a 5µm spot with only slight degradation to the lateral wings (figure10(d)).

This was again a very important result because it demonstrated that the system overall was capable of operating to specification in a virtually diffraction limited manner. An approximate radial integration of Figures 10 (a-d) is shown in Figure 11 illustrating the high quality nature of the focussing.

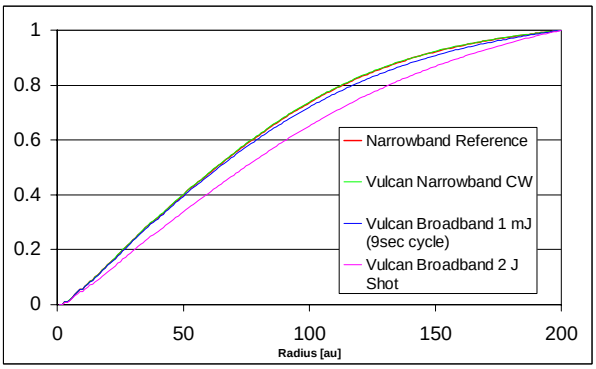

Figure 11. Approximate radial integrations of the spots in Figure 10 – there is a 13 % reduction in 80% encircled energy between the reference beam and a 2 J broadband shot.

High Energy Ramp and Inspection Sequence

The 208 mm amplifiers in LA4 had been previously commissioned and characterised in a controlled and ramped manner as described in a previous annual report. There was an energy cross-calibration using several measurement devices in order to accurately calibrate the permanent calorimeters located in LA4.

To escalate the energy through the compressor and to enable the high energy commissioning of the compressor and Petawatt system it was important that this proceeded in a careful and controlled manner. An energy ramped series of shots was planned with an inspection of each optic occurring after every high energy shot.

The first high energy shot into the system (at about the 50J level) was onto a large piece of laminated “burn” paper located in front of grating G1. Previous experience on Vulcan had shown this technique to be a clean, dust free and vacuum compatible method of producing a beam “burn”. This was undertaken to verify that no strange near-field effects were occurring at the VSF pinhole causing a self focussing or filamentation action on the beam that by the time of propagation to G1 or G2 could have caused damage.

Following this, the first shot was fired through the compressor at the ~100 J level. Subsequent inspection of the gratings following this showed minor damage to grating G2, although the beam fluence was significantly below the design fluence. A photograph of this damage is shown in Figure 12. However, subsequent shots at the same level and higher level have produced no additional damage or, indeed no growth of the existing damage. No damage has ever been observed on G1. The pulse lengths recorded during this series of disk shots in moving from the 100 J level to the 300 J level have been

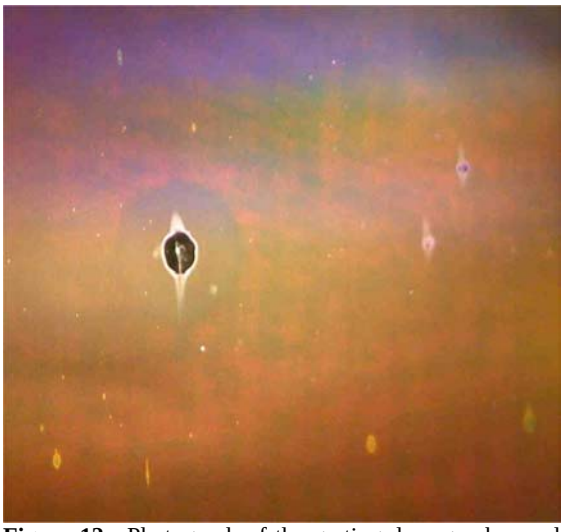

Figure 12. Photograph of the grating damage observed on G2 following the first high energy shot. The size of the central feature is about 8 mm. No subsequent degradation or growth of this feature has been observed.

typically in the range 600 to 800 fs. This pulse length is longer than the design specification of 500 fs. There are two factors that are preventing the achievement of this.

The first is that for operational reasons the bandwidth in the OPCPA front end systems is limited to 8 nm and not the 16 nm as intended. This will be addressed later this year by a slight re-design of the system to enable 16 nm operation.

Secondly, the silicate glass rod chain, whilst commissioned has not yet been used in full operation. This means that there is a net output bandwidth reduction due to increased gain narrowing. The reason for this is that without the OPCPA bandwidth increase there is basically little point in using it and thus the increased operational complexity that arises from it is not justified. Again this situation will be addressed later in 2003/04.

Operational Ramp and Radiological Commissioning

Throughout the course of the commissioning stage and also the operational phase there has been a gradual increase in the energy injected into the compressor system. This has been undertaken commensurate with the radiological commissioning described elsewhere in this Annual Report.

Following each energy increase there has been a grating inspection and to date no additional damage has been observed at up to 600 J into the compressor, only 70 J short of the nominal design specification. The system has been routinely operational in a reliable manner for several user experiments to date. Figure 13, for example, shows the energy performance of the system over the second user experiment. It is generally both controllable and stable.

Future

The highest energy shot to date has been 602 J, with 400 J on target. On that shot a pulse length of 840 fs was recorded yielding a ~ 0.5 PW power.

The commissioning process so far has therefore seen the Vulcan system deliver up to 0.5 PW shots on a routine basis. Clearly, there is still a little way to go to realise 1 PW performance. Issues associated with the pulse length have already been identified above and will go some way to address this. There are however, several other issues associated with energy transport that also need to be addressed. Currently the overall energy transport efficiency from LA4 to target has been measured at approximately 67%, short of the design specification of 75%. This is principally due to mirrors M1 (96%), M3 (92%) and the parabola (96%) that are not perfectly reflecting. M1 and M3 are scheduled to be replaced later this year with 99% coatings should will bring the overall efficiency to 77%. The parabola will remain with the 96% silver coating for operational reasons.

Conclusion

The Vulcan Petawatt system has been successfully commissioned and is now operating in a reliable and stable manner at the 0.5 PW level, with excellent beam focussability. All aspects and systems have so far met the design expectation. It is anticipated that the final commissioning activities scheduled for the 2003/04 reporting period should see the Vulcan system successfully deliver a 1 PW pulse.

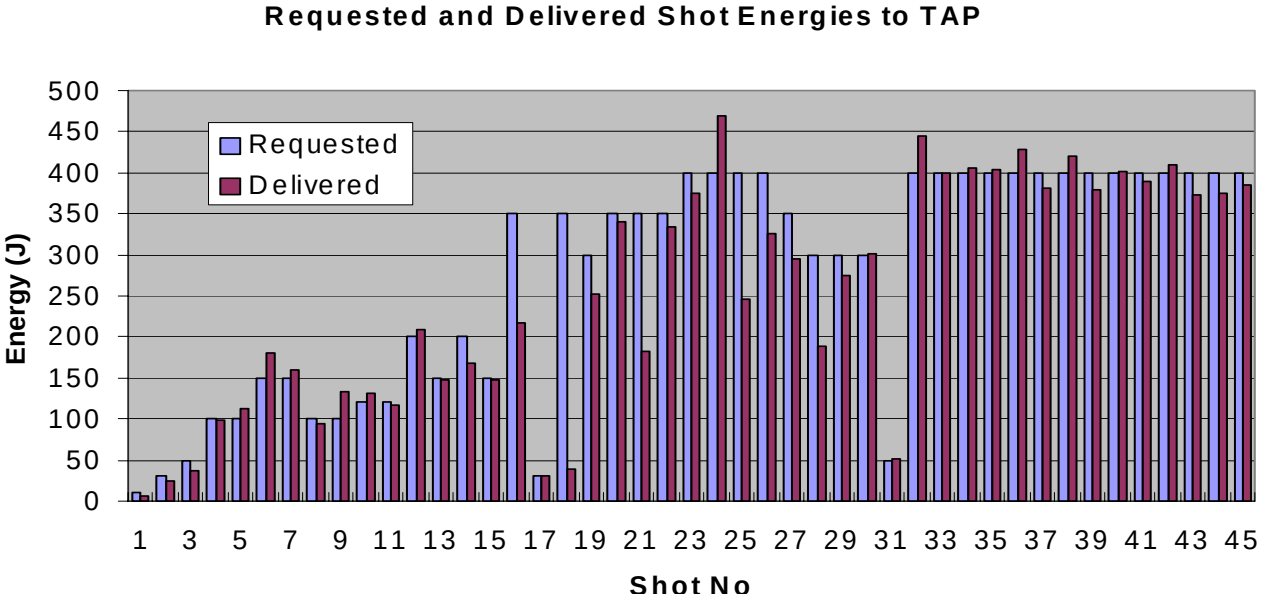

Figure 13. Energy performance over a user experiment.

208mm Amplifier wavefront characterization

S J Hawkes, J L Collier

Central Laser Facility, CCLRC Rutherford Appleton Laboratory, Chilton, Didcot, Oxon, OX11 0QX, UK

Main contact email address: *s.j.hawkes@rl.ac.uk*

Introduction

An integral part of the Petawatt upgrade was the installation of an additional 208 mm amplifier chain to boost the CPA output energy from 100 Joules to the 600 Joule level [1]. It comprises three Nova style 208mm clear aperture Nd: glass slab amplifiers each containing three laser discs. The amplifiers have been modified from the original Nova design to incorporate a different pumping geometry. The discs are pumped using eight large bore flash lamps, as used in the 150mm disc amplifiers in the Vulcan system. It is important to characterise how these new amplifiers affect the wavefront of the laser. This can happen in two ways; the static aberrations caused by the glass itself, and the dynamic post shot wavefront recovery, caused by flash lamp induced thermal loading in the glass. It is important to fully characterise the post-shot wavefront recovery to determine the shot turn round time for TAP (Target Area Petawatt) and also to highlight any complications regarding wavefront correction of the Petawatt beam.

The post disc shot wavefront recovery has been previously studied on Vulcan [2] using the beam 8 amplifier chain and has been shown to support a 20 minute shot turn around. It was anticipated that the increased size and volumes of glass involved in the larger Nova amplifiers would however impact on the wavefront recovery.

Results

Post shot thermal recovery was also characterised using the Vulcan CW YLF and measurements taken using a radial shear interferometer [3]. The static aberration was measured, then the 208mm amplifier chain was fired and the subsequent effects of the thermal loading were recorded using a video cassette recorder. The magnitude and nature of the aberrations are expressed using Zernike analysis in Figure 1.

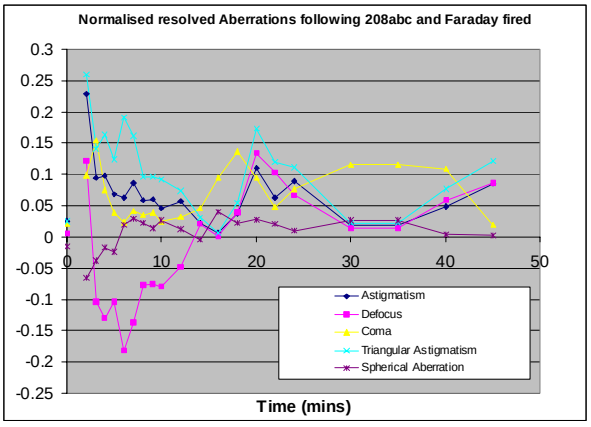

Figure 1. 208mm amplifier chain temporal aberrations.

Clearly there is notable thermal loading in the 208 mm amplifiers which results in a dramatic increase in the magnitude of post-shot aberrations. Cold air blowers are run for 15 minutes following the firing of the amplifiers and one can clearly see a thermal shock effect from the switching off of these cooling systems. The gradually reducing aberrations are seen to rise again after 15 minutes. It is interesting to note the behaviour of certain aberrations following the 20-minute mark. All aberrations, except classical coma, are seen to gradually reduce to their nominal start values and hold these values for over 5 minutes. There is then an unusual increase in the magnitude of the aberrations defocus astigmatism and triangular astigmatism, whereas at the same time coma is seen to recover to the start value. What causes the increase in aberration magnitude is not known, however it is interesting to compare this result with that when the entire Petawatt beam line is fired, which includes the existing beam 8, 150mm and 108mm amplifiers, see Figure 2.

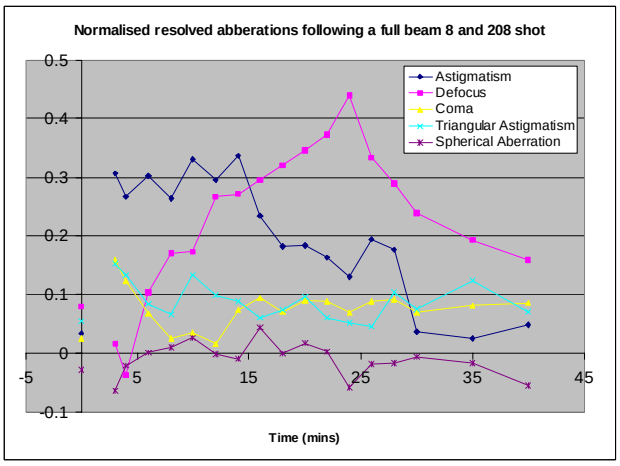

Figure 2. Amplifier Recovery including full amplifier chain.

There is a marked increase in the defocus of the beam following a shot, which requires over 40 minutes to recover to its original value. This was observed during the Petawatt MOD (Ministry of Defence) experiment which required a rapid shot rate. It was observed that when the adaptive optics were run, only half an hour following a Petawatt shot, then some difficulty was experienced in correcting the wavefront of the laser. This was due to the fact that the current adaptive mirror has an inherent amount of defocus, for which the mirror is using some proportion of its corrective power to flatten out. This combined with a large residual defocus after 30 minutes caused the problem. It is noted that the MOD experiment was not typical, in that a rotating target wheel was employed. TAP shot turn around time is usually around the hour mark and therefore this problem would not normally be encountered.

Conclusions

We have demonstrated that the post shot recovery of the 208mm amplifiers does not produce any major wavefront problems. We have shown that when fired in conjunction with the beam 8 amplifiers that a significant residual defocus remains after 30 minutes, which may impact on the higher repetition rate Petawatt experiments.

References

1. Gain Measurements on the Petawatt 208 mm Amplifier Chain, D. Pepler *et al*, 2001/2002, RAL-TR-2002-013, 35 (2002)

2. Wavefront analysis of the Vulcan glass laser system, C Hernandez-Gomes *et al*, CLF annual report 1997/98, RAL-TR-1998-080, 150, (1998)

3. A radial sheer interferometer, C Hernandez-Gomez *et al*, CLF annual report 1997/98, RAL-TR-1998-080, 165, (1998)

System cleanliness in Vulcan Petawatt interaction and compression chambers

P A Brummitt, A J Frackiewicz, R Wellstood, T B Winstone

Central Laser Facility, CCLRC Rutherford Appleton Laboratory, Chilton, Didcot, Oxon, OX11 0QX, UK

Main contact email address: *p.a.brummitt@rl.ac.uk*

Introduction

When the concept of Target Area Petawatt (TAP) was conceived, there was a stringent requirement set down that the system must have a very high standard of cleanliness. This was mainly due to the nature and cost of the optics involved. There was an obvious requirement for the target area and all associated equipment to be clean as well as the chambers.

Design considerations

When the chambers were designed, a material had to be chosen which was not only vacuum friendly but also easy to clean. Many options were considered but the decision mainly came down to two options. These were Stainless Steel or Mild Steel with plating on the top surface. Due to the size of the chambers it was decided that the cost of stainless steel would be prohibitive. The final choice then came down to Mild Steel with plating. The plating, which was used on the Mild Steel, Nickel, was chosen on the basis of vacuum compatibility i.e. low outgassing rate, good corrosion resistance as well as longevity of life in service.

Cleaning

Once the chambers had been installed into the target area and all of the welding on the chambers had been finished, the initial cleaning could be carried out. The chambers were initially cleaned using a preparatory solvent. The chambers were very dirty initially after their manufacturing processes. They were cleaned several times with the solvent cleaner to remove the initial layer of dirt. Once the chambers had been cleaned the target area itself was also thoroughly cleaned so as not to re-contaminate the chambers.

Once the initial dirt was removed from the chamber walls final cleaning could begin. This involved removing all of the flanges from the chambers and meticulously cleaning all of the areas in the chamber. The cleaning process included cleaning all of the walls with alcohol, cleaning out all of the holes in the chamber, right down to the base of the holes to remove any risk of swarf from the cutting process getting into the chamber once the optics had been installed. Once all of the cleaning had been completed, the system was ready for its first vacuum test.

Vacuum testing

The chamber was first pumped down to test the vacuum system but also so a residual gas analysis (RGA) scan could be taken to determine the level of cleanliness within the chambers. The first scans of the chamber showed that the chamber was still contaminated with some hydrocarbons, so a re-clean was carried out and the scan taken again. The results were much improved and showed that the chamber was in a state to start installing the optical mounts and their optics. Figures 1 and 2 show the results of RGA scans taken from both the compression chamber and interaction chamber respectively. From the scans it can be seen that the interaction chamber is slightly cleaner. An ion current level was set for the chambers of $1x10^{-10}$Amps or better for hydrocarbons on the RGA scan. This level was set after testing of other systems within Vulcan and testing of dry, hydrocarbon free pumping systems. The above level was set at a level, which exceeded cleanliness in Target Area West, which also has expensive optics. The results show that both chambers met these criteria.

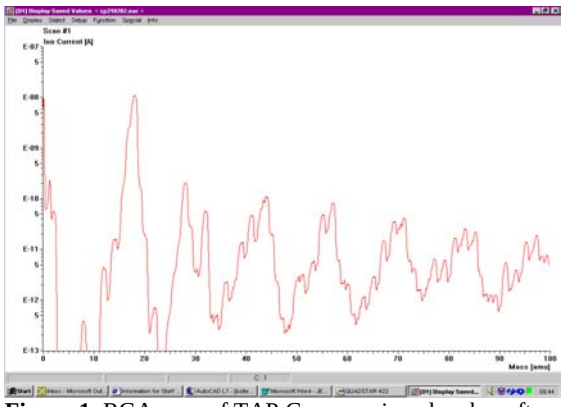

Figure 1. RGA scan of TAP Compression chamber after cleaning.

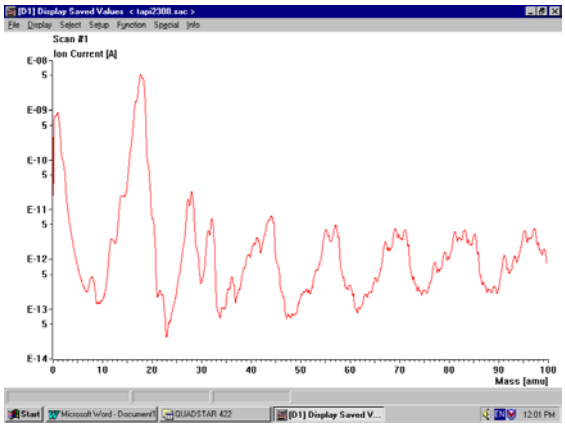

Figure 2. RGA scan of TAP Interaction chamber after cleaning.

Optical mount and optics installation

Once the chambers were at an acceptable cleanliness level, the optical mounts could be installed. The mounts were pre-cleaned before arriving in the target area, so were relatively clean. They underwent final cleaning before being installed into the chamber. Again the cleaning on these was very meticulous and great care was taken to make sure there was nothing on the mounts, which could contaminate the chamber and therefore the optics. When the mounts were cleaned and had passed final inspection, they were installed into the chamber. Once the installation was complete, the system was then placed under vacuum and the system checked for cleanliness using the residual gas analyser. The results showed no deterioration from the initial tests and hence the system was in a state to install the optics.

Before the optics were installed the target area was given a final clean. This was to make sure of not contaminating the optics with dust. The optics were installed into the chamber and then vacuum tested.

Conclusion

The cleaning process for Target Area Petawatt had to be carried out in a thorough manner to produce a quality environment for the system components to be housed in. This cleaning took a very large effort but in the end it produced an excellent environment for experiments to be carried out.

Operational experience of Petawatt gratings on Vulcan

T B Winstone, C N Danson, A J Frackiewicz, J L Collier, C B Edwards*

Central Laser Facility, CCLRC Rutherford Appleton Laboratory, Chilton, Didcot, Oxon, OX11 0QX, UK

* *now at AWE, Aldermaston, Reading, Berks, RG7 4PR*

Main contact email address: *t.b.winstone@rl.ac.uk*

Introduction

Gold coated gratings suitable for the compression of high power laser pulses using the chirped pulse amplification technique are generally both expensive and delicate. They are the highest cost items and yet they have the lowest damage threshold of any item in the system. We report on the marking on the gratings prior to any shots, the damage observed in the early stages of operation and how the damage has evolved since.

Grating marks prior to shots

The 940 mm diameter gratings, supplied by Lawrence Livermore National Laboratory (LLNL)[1], were installed into the compressor chamber in April 2002 (See Figure 1).

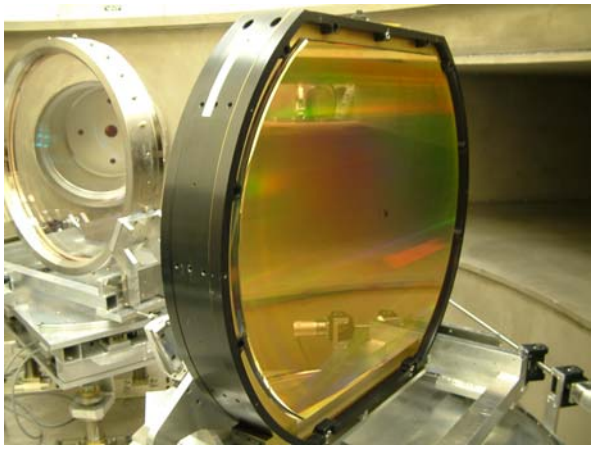

Figure 1. Overall view of the first of the 940 mm diameter compression gratings.

Initial inspection revealed the so-called 'parson's nose' (see Figure 2). This is an artifact of the manufacturing process where ghosts from the imaging system appear on the photo-sensitive resist during the exposure of the gratings. For small aperture gratings it is possible to displace this outside the grating area. We estimate the diameter of the larger circle of the parson's nose to be approximately 50 mm giving an overall width of about 80 mm.

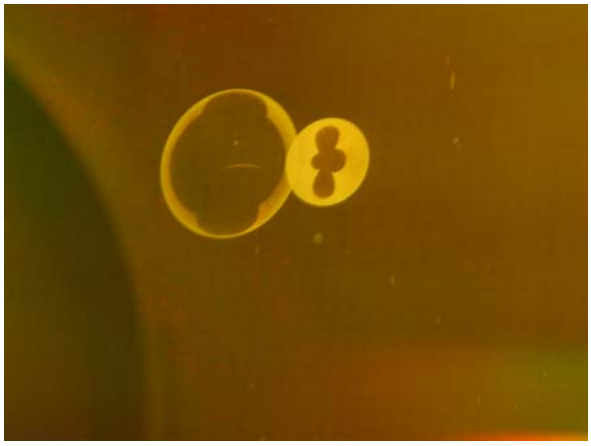

Figure 2. The parson's nose, an artifact of the grating manufacturing process.

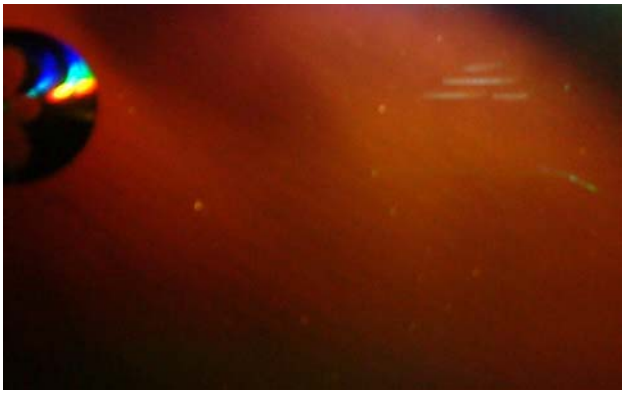

Figure 3. Three parallel lines on south grating in a triangular formation.

As can also be seen from Figure 2 the gratings have a faint lattice structure visible on the surface, although it is thought that this has no effect on the overall performance of the grating.

The first grating in the system (the south grating) has a mark near to the parson's nose which consists of three parallel lines forming the shape of a triangle (Figure 3). This is believed to be mechanical damage that occurred during the manufacturing process.

The second compression grating (the north grating) in the system has what appears to be a drying mark composed of many small spots. This is not of concern as the mark is outside the beam footprint. There is also a mark towards the centre at the top of the north grating which looks like a drying mark in the shape of an inverted teardrop (see Figure 4).

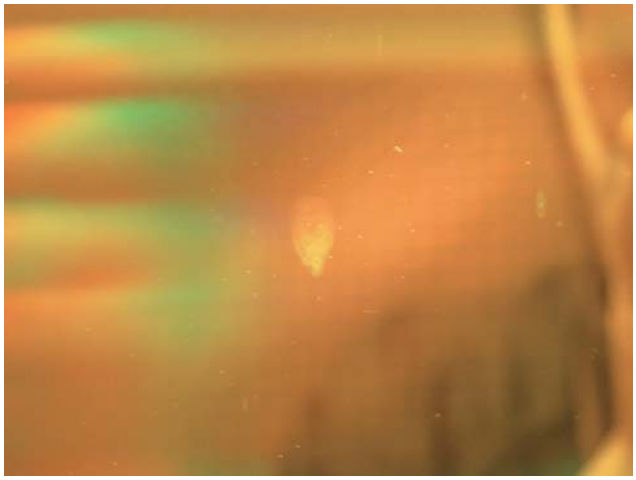

Figure 4. Drying type stain high and central on the north grating.

Both gratings also exhibited some vertical marks along the grating grooves. The south grating has a short vertical line as seen in Figure 5a estimated at 20 mm, while the vertical line in Figure 5b on the north grating has the longer line at 30 mm.

a)


b)


Figure 5. a) The vertical mark on the south grating
b) The longer vertical mark on the north grating.

Grating damage evolution

Following the first few shots through the petawatt system at energies up to 260 J an inspection was called of all the petawatt optics. There was concern on discovering a large damage mark which was not recorded before. This mark was found on the second of the two gratings (north) which interacts with the compressed pulse. Upon closer inspection it seems as if there is a small fissure in either the substrate material or the photoresist layer, which can be seen as a bright vertical line in the centre of the damage site (see Figure 6a). There appears to be a patch of non diffractive gold around this site to a diameter of about 3-4 mm, and a larger plume which is less obvious to a diameter of about 12-14 mm.

It is possible to see the fissure in either the substrate or the photoresist from behind, although when a torch is shone through no light can be seen in transmission. This seems to indicate that the fissure existed prior to the gold coating of the photoresist.

As well as the large spot a number of small sites of damage were detected. Their growth in the horizontal direction has been negligible, although LLNL experience indicates that over a period of time they are likely to grow slowly in the vertical direction i.e. along the direction of the ruling grooves. It is believed that these sites are due to small particles of dust being on the gratings and being burnt into the photoresist layer.

Upon closer inspection of the two gratings, by shining a light through from the back of each grating, pinholes were observed. The south grating shows few pinhole features whereas the north grating exhibits many pinholes across the entire grating surface.

Following the discovery of the grating damage regular inspections of the gratings were conducted. Up to the end of April 2003 there had been in excess of 100 high power laser shots. The north grating has seen initial damage, which seems to have stabilised: there being no significant growth in the size or type of damage as can be seen in Figure 6b. The south grating has shown no damage during this period of petawatt operations.

Conclusion

During the first commissioning period the gratings were inspected after every shot. As no significant growth in the damage was observed, and due to the concern that inspection could cause contamination, these gratings are now inspected at the beginning and end of each experimental run.

Acknowledgement

The authors would like to gratefully acknowledge the help of Deanna Pennington, LLNL, USA whose working knowledge of this type of grating was invaluable.

References

1. Lawrence Livermore National Laboratory, Livermore, CA94550, USA

a)
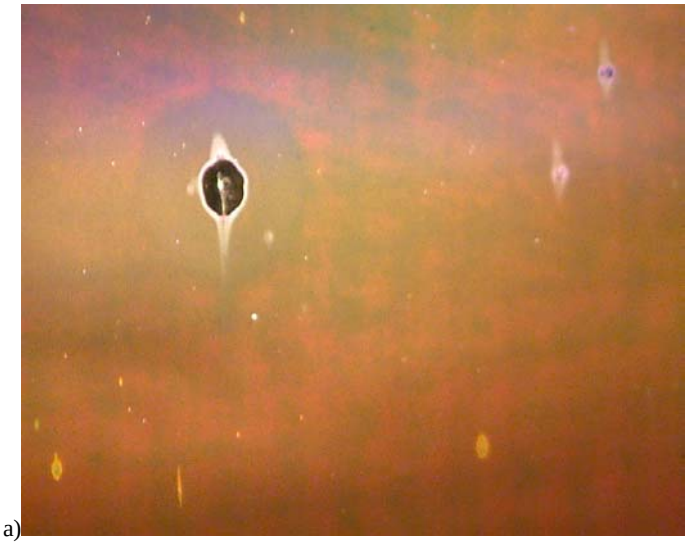

b)
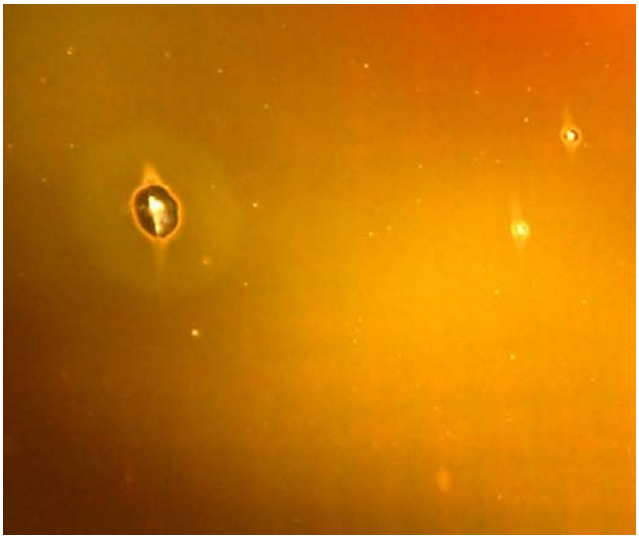

Figure 6. a) Main damage mark on the North Grating discovered in October 2002
b) Main damage mark on the North Grating on 30th April 2003 following a further 100 plus high power shots to target.

Radiological commissioning of the Vulcan Petawatt facility

D Neely, R J Clarke, P A Brummitt, J L Collier, C N Danson, A J Frackiewicz, J A C Govans, S Hancock, P E Hatton, S J Hawkes, R Heathcote, C Hernandez-Gomez, P Holligan, C J Hooker, M H R Hutchinson, A K Kidd, W J Lester, D McAllister, J McLaughlan, D R Neville, P A Norreys, D A Pepler, M R Pitts, C J Reason, I N Ross, R Wellstood, B E Wyborn, T B Winstone, P N M Wright, R W W Wyatt, Ch Ziener

Central Laser Facility, CCLRC Rutherford Appleton Laboratory, Chilton, Didcot, Oxon, OX11 0QX, UK

C B Edwards, R D Edwards

AWE plc, Aldermaston, Reading, RG7 4PR, UK

Main contact email address: *d.neely@rl.ac.uk*

Introduction

Vulcan is established as a world leading user facility for studies of ultra-high intensity laser interactions with matter. The Petawatt (PW) Upgrade project will deliver an order of magnitude increase in laser power to target, delivering interaction intensities of 10^{21} Wcm^{-2}. This upgrade was funded by EPSRC through grant GR/M48383 and was completed in early 2002. A further commissioning grant GR/S06875/01, enabled access to the newly constructed Petawatt facility. The objectives of the commissioning grant and investigation were:

- To perform radiological surveys of the facility in anticipated target configurations and to install additional shielding for high-Z interactions as required.
- To measure the target irradiance and the X-ray spot size.
- To investigate the effects of electromagnetic noise produced on the chamber and target area equipment.
- To determine the level of debris produced from the target and to devise a suitable operating scheme to protect chamber optics from damage.
- Installation of an optical probe.
- Contrast measurement of the laser pulses.

This report will review the experimental and radiological data obtained from the thirteen solid target interaction shots fired during the commissioning run in the newly constructed PW interaction facility[1]. Commissioning of the PW laser and compressor chain is reported in separate articles, as is the commissioning of the large aperture gratings at high laser fluences[2].

Introduction

The shielding requirement against radiation (γ-rays, X-rays, neutrons and activation) produced by Petawatt laser shots on a range of target materials was calculated[3] using experimental electron energy flux distributions and cross checked by scaling data from the earlier experiments on Vulcan and other facilities at intensities approaching 10^{20} Wcm^{-2}. For medium and high Z targets, a shield blanket of 15cm lead and 10 cm of high density polyethylene and a shielded fire escape door were required.

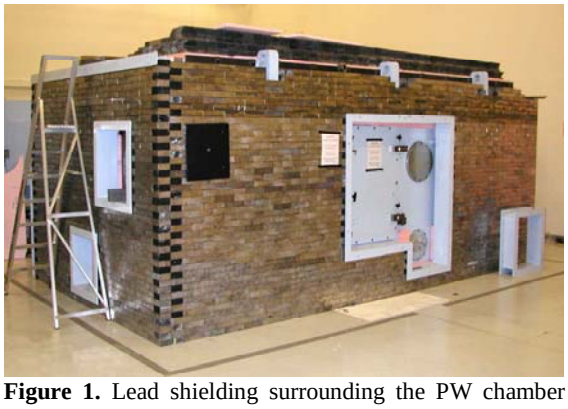

Figure 1. Lead shielding surrounding the PW chamber required for high atomic number target experimental investigations.

Figure 1 shows the 70 ton lead shield wall in place surrounding the interaction chamber with gaps for access to the diagnostic ports. External blocker-frames covering these gaps were installed before any radiological measurements were made. For the initial commissioning experiment only a limited number of diagnostic ports were opened. As more experiments are scheduled on the facility the additional ports will be opened as required.

The 15 cm thick lead shield wall surrounding the chamber provides high γ-ray absorption and in combination with the 60 cm thick concrete walls surrounding the interaction area gives an attenuation of γ-rays as shown in Figure 2 with a minimum direct transmission of 50,000 at 6 MeV .

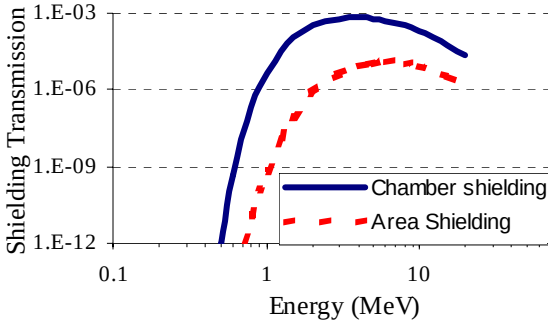

Figure 2. Attenuation of a Gamma ray emission as a function of photon energy.

In addition to the γ–ray shielding, a neutron absorbing and moderating blanket is required. A 10 cm thick high density polyethylene shroud was added to the chamber to fulfil this requirement. A 7 ton lead shielded fire escape door, which was bought through the commissioning grant, was also installed in the target area. This interlocked door must be closed prior to locking up the area for a full energy shot and opened by the first people returning into the area after a shot.

A complete radiological survey of gamma and neutron doses was conducted with measurements being made inside the interaction chamber, in the surrounding target area, immediately outside the target area and in the surrounding buildings. Measurements were also made to confirm the shielding effectiveness of the new radiation shielded fire door, which forms an integral part of the environmental radiation certification.

In accordance with recommended safe working practices, initial measurements were made at energies and fluences where existing dosimetry measurements exist. Low atomic mass plastic targets were used to minimise the possibility of unexpected radiation escape. Shots were repeated on such targets and when sufficient data was available to indicate that all emission was within safe limits and no unexpected dose

present, the target atomic mass was increased to copper and the radiological characterisation process repeated. This method was continued until shots with gold targets were taken, as such targets will produce the hardest and most penetrating radiation possible from such interactions.

The dose in the forward cone and lateral directions from a 1 mm thick gold target backed with a 1 mm thick Aluminium converter irradiated at an intensity of $3x10^{20}$ Wcm^{-2} is shown in Figure 3. This dose was measured using Thermo Luminescent Dosimetry (TLD) detectors in a similar fashion to earlier experiments on Vulcan [3]. The peak forward dose is 43 mSv @ 1m which is larger than any dose previously generated in a laser plasma interaction. The primary emission is in the forward direction of the laser beam emitted in a 35 degree cone in the direction of the forward going laser beam.

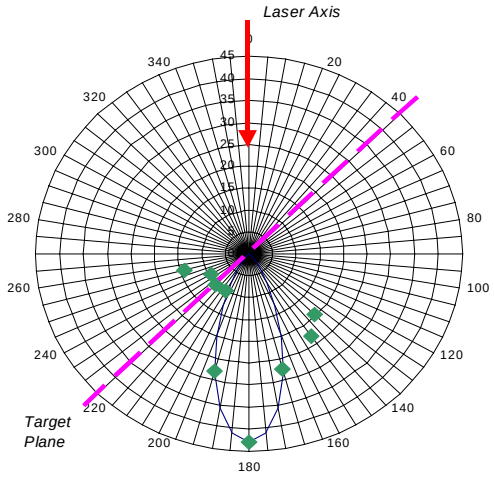

Figure 3. Dose Measurement of X-ray and Gamma ray emission from a Gold target.

The plastic and copper shots all produced a forward directed γ-ray emission peak of FWHM 35±15 degrees. The gold target shots tended to produce a forward directed peak but also a subsidiary peak normal to the target surface and another at 60 degrees to the forward direction was observable on some shots.

In most cases the X-ray and γ-ray beams emitted from the target coincided. However, on one shot, the X-ray component is at 60 degrees to the γ-ray beam, which lies along the laser beam direction. It is believed this difference arises from the dominance of different interaction mechanisms with the target surface and will require further study to understand the relative contributions from the different mechanisms.

Previous high intensity laser matter interaction studies[3] have demonstrated a variation of emission direction when a pre-plasma is present[4] and significant enhancement of the γ-ray emission[3] when the laser beam interacts first with a low density gas target placed immediately prior to a high Z converter. It is anticipated that a target design incorporating a lower density pre-target will produce higher flux levels. However, to optimize such a target would require a separate experimental campaign which was considered to be outside the scope of this initial study. It was decided to try a pre-pulse shot on a gold target to look at the emission intensity and direction. Figure 4 is a summary of all the 1.5 MeV filtered TLD dosimetry data at tight focus on target for different target types and at varying energies. The dosimetry data shows a strong correlation with incident energy on target and surprisingly, much less correlation with the target type. For the plastic targets the forward directed 1.5 MeV data was not taken as a commercially available TLD was run in that position for the first few shots to check on the absolute detector calibration. However, data at ±15 degrees to the laser direction was available for the plastic target shots and is plotted in Figure 4.

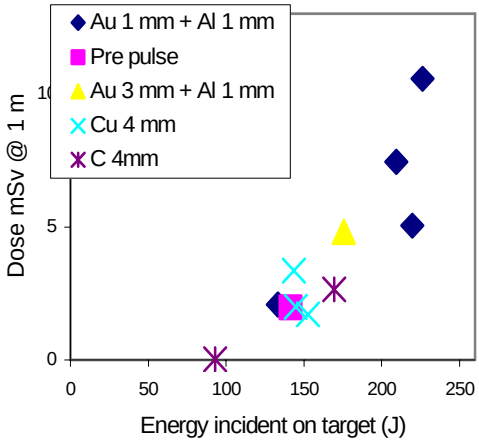

Figure 4. TLD dosimetry data on the 1.5 MeV channel for a variety of targets types all shot at best focus. 1.1 ps pulses were used on the plastic and Copper targets and 0.6 ps pulses on the gold.

Activation of mechanical hardware components within the interaction chamber was observed as anticipated. Peak activated component dose rates of greater than 50 μSv/hr were observed for mechanical apparatus in the locality of the interaction point. This level of activation is above recommended handling/working limits and personnel access was restricted until the level of activity had fallen to below recommended levels as laid out in the Radiological local rules. Investigation of this process showed that the activation was derived from high-energy ion bombardment emitted primarily in a direction normal to the target surface. Steel and brass were particularly susceptible to activation and will be replaced with aluminium or alternative materials before the first user experiment. The nuclear activation thresholds for protons and γ-ray activation are similar. However, as Figure 5 shows, the likelihood of a proton being stopped in thin material, or much closer to the surface, is significantly higher than for a γ-ray. Hence, the likelihood of a decay from a daughter product escaping is much higher for protons and as a significant amount of the laser energy can be deposited into the proton flux[5] they form the dominant accessible activation mode within the interaction chamber.

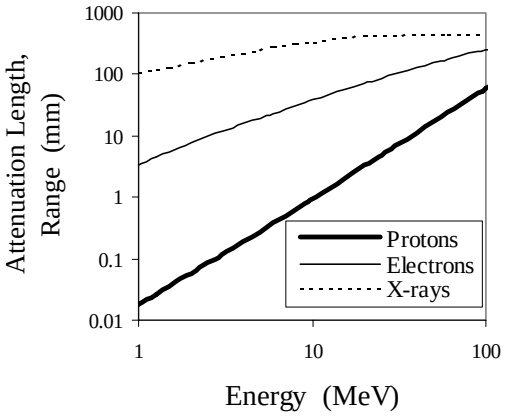

Figure 5. Attenuation length for γ-rays and range for electrons and protons in plastic.

Neutron detectors were situated in the target area outside the neutron absorbing and moderating blanket surrounding the interaction chamber. The neutron detectors did not measure any radiologically significant doses during the series of shots.

Radiological dosimetry data demonstrated that the shielding was operating as anticipated and preventing the escape of γ, and hard X-rays from the interaction area. The site Radiological

Protection Advisor reviewed the measurements and has given authorisation for shots to be delivered for external users using the present facilities and working practices.

Focal spot and target positioning

The focused laser spot size was initially measured using the Vulcan CW alignment beam and oscillator pulses by directly magnifying the focal plane onto a CCD detector. Spot sizes of Full Width at Half Maximum (FWHM) 4.6-6 microns diameter were recorded. A retro focus system to accurately set the target at the optimum focal plane was also set-up and tested. The system injects a 200mm diameter 1054nm beam into the chain just after the final amplifiers and the beam is then propagated to target and returns back to this point in the system before entering a telescope. Tests demonstrated that this system was capable of positioning a target surface with an accuracy of ±7 μm w.r.t. the optimum focal plane.

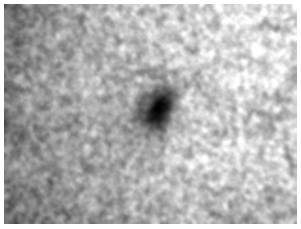

Figure 6. X-ray image of emission from a thin target.

By using a combination of suitable optics it was possible to produce 2 J shots, filter the output energy and still record the focal plane intensity distribution. The intensity distribution remains excellent under these conditions, having a slightly larger FWHM of 7 μm. It is not practically possible to maintain this filtering when full energy shots are fired and the alternative technique of X-ray imaging was used to measure the emission from the focal region. Figure 6 shows a 20 KeV X-ray image was taken which has a FWHM of 11 μm. Full shot laser far field measurements were not possible due to optical imperfections in the laser diagnostic chain. An optical compensator has now been designed and ordered and will be installed in the system in 2003 to allow far-field measurements to take place.

EM noise

The interaction of the laser pulse with a solid target can generate very high electric and magnetic fields. One objective of the investigation was to ensure that the computer controlled motor drive system, vacuum system, interlock system and diagnostic systems were not susceptible to the electromagnetic noise generated. During the installation and design of potentially susceptible systems, care was taken to install measures to minimise the impact of such laser-plasma shot generated noise. During full shots all systems functioned normally. The only system to display problems was a vacuum pump controller that failed after a few full shots and was replaced. The replaced controller worked without fault for the remainder of the experiment. A number of sensitive detectors were placed outside the interaction chamber and only observed low level noise spikes of less than 10 mV, which is considered acceptable. A CCD detector was placed within 200 mm of the interaction point and no detectable degradation of the CCD detector electronics occurred.

Experience with earlier short pulse interaction experiments is that the level of electromagnetic noise generated will depend on the exact experimental geometry and can increase substantially as the laser interaction pulse intensity or energy is increased. The data obtained during the commissioning run demonstrates that the current system design is adequate for external experimenters to commence work on the facility. However, as the delivered energy to target is increased to the 500 J level the situation will be monitored closely.

Debris

During a laser matter interaction, only a small volume of material is directly ablated from the target. However, the energy that is deposited in the target by the laser is capable of vaporising and sending a significant cloud of debris of many cubic mm in volume from the interaction target after the laser has switched off. The particle size and angular distribution of the material emitted from the interaction target was measured using sampling plates situated at 100-200 mm from the target. The debris is emitted from the target primarily in a direction centred on the target normal. Significant amounts of debris in the 5-50 micron diameter range were detected at angles of up to 35 degrees from the target normal. For future experiments it is therefore recommended that no solid target be irradiated at an angle of incidence of less than 35 degrees to the laser axis to minimise the risk of damaging the Off-axis parabola.

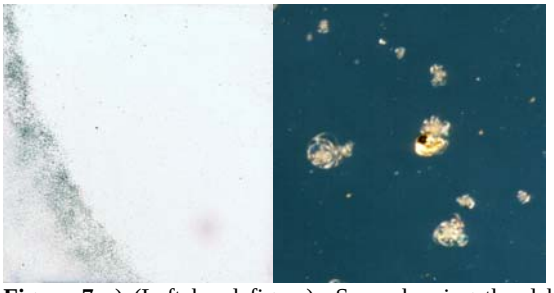

Figure 7 a) (Left hand figure) Scan showing the debris distribution on a 10 cm square glass plate situated in the blow-off direction b) (Right hand figure) Magnified image of 1 mm portion of the debris plate showing craters and gold deposit.

Optical systems

A short pulse optical probe capable of delivering 50 mJ of frequency doubled light was designed, purchased, constructed and installed in the interaction chamber. Due to a lack of time the probe was not finalised during the commissioning period but will be available for future experiments. Pulse durations were measured using two orthogonal auto-correlators during the run demonstrating high energy pulses of 0.6 ps on target. Pulse contrast measurements using a third order cross-correlator will be undertaken at a later stage.

Conclusions

During the commissioning period, radiological shielding was bought and installed in the Vulcan Petawatt target area and a commissioning experiment conducted on this new interaction facility. The necessary radiological characterisation has now taken place and the area is ready for interaction experiments producing high radiation yields to take place. As new target geometries are studied, dosimetry data will be taken to ensure safe working conditions are maintained. Significant operational experience was gained and the facility is now in a position to proceed with the first user experiments.

References

1. C Zeiner *et al*, CLF Annual report RAL-TR-2000-034, , 177, (2000) and RAL-TR-2001-030, 150, (2001)
2. This report: C N Danson *et al*, PetaWatt overview, 167 J Collier *et al* , Compressor system commissioning, 168, S Hawkes *et al* , 208mm Amplifier characterisation, 174, P Brummitt *et al* , System cleanliness, 175, T Winstone *et al*, Petawatt Gratings on Vulcan, 176
3. R Allott *et al*, CLF Annual report RAL-TR-2000-034, 177, (2000)
4. R D Edwards *et al*, Appl Phys Letts 80 (12) 2129-31 (2002)
5. M Santalla *et al*, Phys. Rev. Letts 84 (7) 1459-1462 (2000)
6. McKenna *et al*. Rev. Sci. Inst. 73, 4176 (2002)

Petawatt phase plate development

B T Parry, D A Pepler, C N Danson, T B Winstone

Central Laser Facility, CCLRC Rutherford Appleton Laboratory, Chilton, Didcot, Oxon, OX11 0QX, UK

Main contact email address: *c.n.danson@rl.ac.uk*

Phase Plate Background

Random Phase Plates[1)] and Phase Zone Plates[2)] have, for a number of years, been successfully utilised on the Vulcan high power laser system for the purpose of focal spot manipulation and smoothing. These are fabricated[3)] 'in house' using lithographic techniques to create diffractive elements of PMMA photoresist on commercially available substrates[4)].

Until now, phase plates have been used on beamlines up to intensities of ~10^{10} Wcm^{-2}. The recent multi-million pound Petawatt upgrade to Vulcan has made possible access to new regimes of high energy in ultra-short pulse lengths, derived using standard chirped pulse amplification (CPA) techniques.

The extreme intensity of the laser and the physical restrictions imposed by the configuration of the new target area have imposed additional design considerations that must be taken into account when producing phase plates for Petawatt laser operation.

The phase plates described here were requested for the first external user experiment in the new facility, on laser wakefield electron acceleration, to produce a focal spot 300 µm in diameter.

Petawatt Considerations

It was deemed impractical to manufacture phase plates at diameters in excess of 600 mm diameter, which would be required if they were to be used in the collimated beam of the Vulcan Petawatt Facility. Instead the plates were designed to be placed following the final parabolic mirror, 345 mm from focus.

This figure was decided upon for two main reasons. The most important was the limitation imposed by the set-up of the optical arrangement inside the interaction chamber. The phase plate had to be located so that it would not obscure the beam incident on the parabola, shown in Figure 1. The other consideration was the size of plate which could be easily manufactured on site, which was 150 mm diameter. At a distance of 345 mm from focus the beam diameter is 115 mm, which also satisfied this condition.

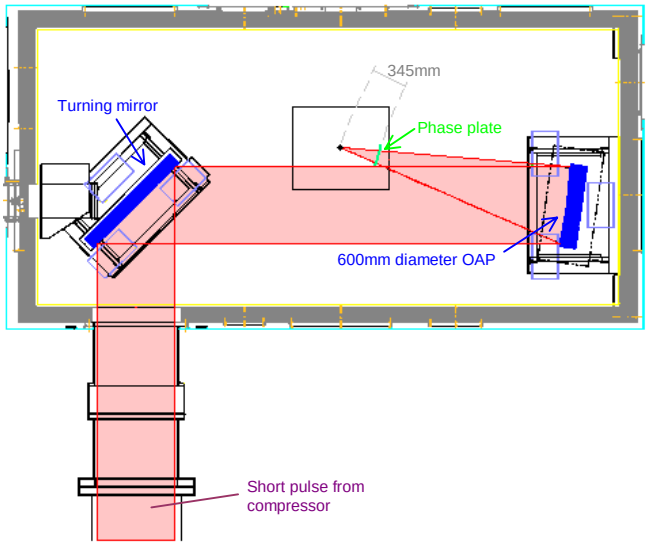

Figure 1. Layout of the target chamber showing the position of the phase plate.

The phase plate could have been placed closer to target to avoid the incoming beam, with the limit in this case being around 170 mm from target, at which point the intensity would be sufficient (~10^{13} Wcm^{-2}) to form a plasma on the front surface. If this were allowed to happen then the plasma would absorb or reflect some of the pulse energy; absorption would reduce the ultimate energy on target; reflection would potentially damage optics back inside the laser.

It is well known from previous studies[5)] that passing high power laser pulses through a medium such as glass can result in non-linear effects such as self-focusing and self phase modulation. For this reason, to avoid degradation of the spatial beam profile, the phase plates were made on the thinnest available substrate, in this case 625 µm thick artificial quartz (fused silica).

Another new consideration for the Petawatt phase plates arises from the high intensity at the point where they are positioned. At only 345 mm from focus the beam is 103.9 cm^2 and the CPA pulse has been re-compressed to an ultra-short pulse, for the experiment in question 700 fs on average. From Figure 2 it can be seen that the damage threshold of quartz[6)] for this pulse length is 2.3 Jcm^{-2}, and simple calculation indicates that energies greater than 239 J on target will exceed this limit.

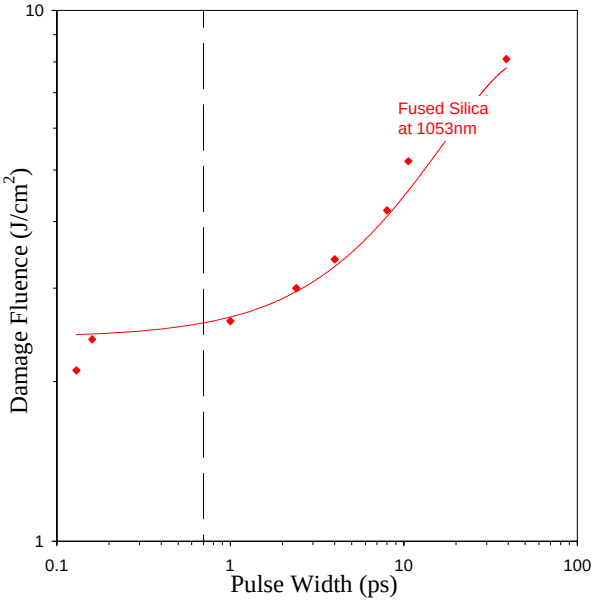

Figure 2. Damage threshold of quartz for changing pulse lengths.

For radiological reasons, the energy limit for the experiment in question was set at 350J from the output of the laser, with 69% transmission through the compressor gratings and non-optimum mirror reflectivities. This gives a maximum of 242 J on target. This figure almost exactly matches the damage threshold of the phase plate substrate, and although no similar research has been carried out on damage thresholds in photoresist, it could be expected to be lower than that for fused silica.

For these reasons the Petawatt phase plates are not expected to maintain their usefulness beyond one or two shots, and are essentially a 'disposable' optic.

Possible Problems

Because of the way in which energy is absorbed in a short pulse, a full energy shot would cause material to be ablated from the substrate, rather than just localised melting. This poses a possible hazard for the focusing optic if fragments of material are thrown back towards it. For this reason, when using phase plates at high intensities it is suggested that some sort of debris shield be employed.

Additional Notes

In the past, phase plates to be used in Vulcan have normally been made on glass substrates. In this case quartz was chosen because it was available in a wider range of thicknesses and finished to a better quality of surface flatness.

An interesting by-product of using very thin quartz plates was the edge effects produced during the spin coating process. When being spun the plates are held at the centre by a vacuum chuck, so the effects were attributed to turbulence around the rim due to inadequate support at the plate edges. This can be seen in Figure 3 of a finished phase plate along with the diffractive element pattern. The rippled effect could only be seen in a 2-3 mm wide strip around the circumference of the plate, and since the beam diameter was 10 mm less than that of the plate at the point it was being used, the beam passing through would not be affected.

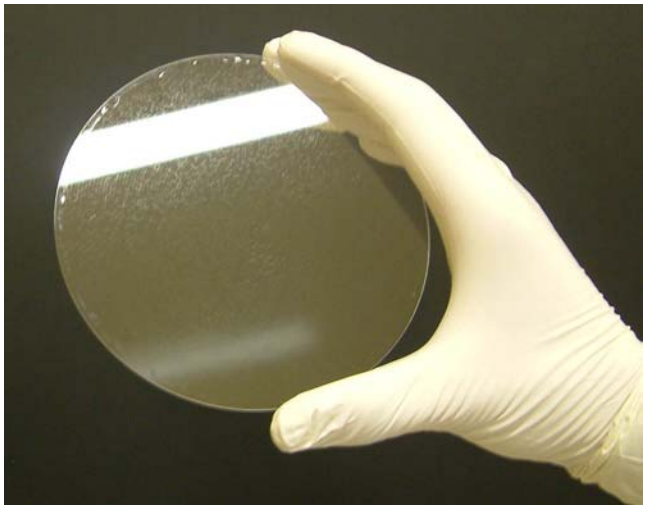

Figure 3. A random phase plate for the Petawatt experiment.

Conclusions

The phase plates requested for the first user experiment in the Vulcan Petawatt Facility were designed and manufactured on site, taking into account the extra limitations imposed by the very high intensities involved. The thickness of the photoresist layer was tested and found to be within ±2% of the specified value.

The short pulse length poses potential problems for the use of phase plates on a quartz substrate. Ablation caused by higher intensities could damage focusing optics if measures are not put in place to prevent this.

References

1. Y Kato, K Mima, N Miyanaga, S Arinaga, Y Kitagawa, MNakatsuka and C Yamanaka, Phys Rev Lett. 53, 1057-1060 (1984)
2. T H Bett, R M Stevenson, M J Norman, C N Danson, D A Pepler, I N Ross, Proceedings-of-the-SPIE-The-International-Society-for-Optical-Engineering., 1870: 76-87, (1993)
3. T Boland, D A Pepler, T B Winstone, C N Danson, CLF Annual Report 2001/2002, RAL-TR-2002-013, 185, (2002)
4. Hoya Corporation Europe, London W5 2ST
5. Hecht, Optics (3rd edition) p634-644
6. B C Stuart, M D Feit, A M Rubenchik, B W Shore and M D Perry, Phys Rev Lett 74 , 12, 2248-2251 (1995)

The design of a long pulse stretcher for synchronous CPA/long pulse interactions

S J Hawkes, C Hernandez-Gomez

Central Laser Facility, CCLRC Rutherford Appleton Laboratory, Chilton, Didcot, Oxon, OX11 0QX, UK

Main contact email address: *s.j.hawkes@rl.ac.uk*

During the September/October 2002 TAW experiment there was a requirement for highly synchronised use of the six long pulse beams on Vulcan in conjunction with the ultra high intensity Chirped Pulse Amplification (CPA) beam line. The normal operating mode for this type of experiment would be to use the Single Longitudinal Mode (SLM) laser oscillator to generate the long pulses. The pulse slicing for the long pulse oscillators is done using the inner track Pockels cell chain which generates ~150 ps of jitter in the timing between the long and short pulses. However this particular experiment [1)] required a much higher degree of synchronicity between the long and short pulses. The implications of running with the higher level of jitter would effectively be to increase by a factor of four the number of successful shots required in order to demonstrate the physics.

The normal operating practice when this degree of synchronicity has been requested is to use the uncompressed pulses generated by the short pulse CPA oscillator. This effectively eliminates any jitter, as both pulses are now derived from the same source. These pulses when uncompressed are of 300 ps in length. The experiment in question specified pulses to be longer, i.e. of the order of 1 ns.

To meet the experimental requirements an additional stretcher on the inner track, to increase the normal stretched pulse length from 300 ps to 900 ps, was designed. A double pass stretcher configuration was used with a 1470 line per millimetre grating and a 600 m focal length lens shown in the bottom grey block in Figure 1. The high line density was needed to provide the additional stretch. The stretcher needed to be switched in and out on a shot to shot basis to accommodate parallel operations in the other interaction area. This was achieved using polarising beamsplitter cubes and pneumatically driven waveplates and beam blocks.

It was decided that as extensive work was being conducted on the CPA beams lines at the pre-amplifier stages that the opportunity would be taken to improve the CPA and long pulse (LP) beams into Vulcan. As with the stretcher injection changes, polarising beamplitter cubes and pneumatically driven waveplates and beam blocks were used. This is shown in the upper grey block in Figure 1. When commissioning the arrangement, care was taken in orientating the beamsplitters in order to avoid self-lasing or pre-pulse generation.

This configuration was used in the successful September/October 2002 TAW experiment. The pulse length was measured in TAW to be of the order of 850 ns. This pulse length was routinely delivered to target at the 150 Joule level, highly synchronised to the 100TW high intensity beam.

References

1. Advanced fast ignition studies on the Vulcan laser – cone/shell implosions, P. Norreys *et al*, CLF annual report 2002/03 (this report), 35, (2003)

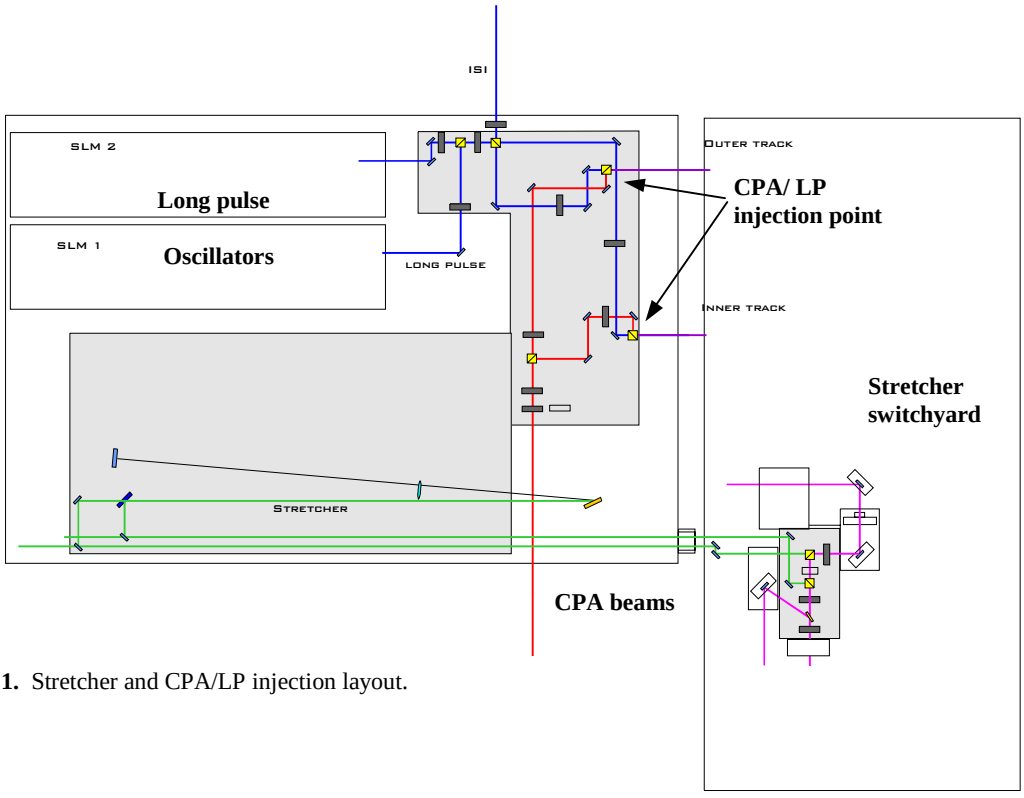

Figure 1. Stretcher and CPA/LP injection layout.

An automatic timing corrector for the X-ray laboratory excimer lasers

D N Winter, W Shaikh, G J Hirst

Central Laser Facility, CCLRC Rutherford Appleton Laboratory, Chilton, Didcot, Oxon, OX11 0QX, UK

Main contact e-mail address: *david.winter3@student.shu.ac.uk*

Introduction

The LSF X-ray laboratory houses a 2 ps laser system used to generate the high peak powers required for X-ray production. Low energy pulses from a 746 nm Ti:sapphire oscillator are amplified in two dye cells pumped by 308 nm radiation from a XeCl excimer laser. The amplified 746 nm light is frequency doubled and mixed to 249 nm. This beam is then double-passed through a KrF excimer laser amplifier either as single picosecond pulses or as a nanosecond train of pulses from an optical multiplexer. The excimer lasers must be timed to fire when the picosecond pulses pass through the amplifiers. This requires careful control of the trigger pulses to the excimers to compensate for problems described below. The trigger pulses are produced by a Stanford Research Systems DG535 digital delay/pulse generator. The laser outputs are displayed on oscilloscopes connected to vacuum photodiodes which monitor the lasers' scattered ASE.

Problem

The excimer laser discharges are powered through thyratron switches, which change their timing delay as a result of changes in their temperature. There is a "warm-up" effect because the thyratron is slightly inefficient as a switch, so each time it operates a small amount of heat is dissipated in it. In the first few minutes after switch-on the thyratron temperature rises until the extra heat loss (due to increased radiation and conduction) balances the extra heat input. The temperature and timing then stabilize. This warm-up effect must be corrected to maintain optimum timing performance when starting the lasers "from cold" or when changing the pulse repetition rate of the system. In addition the thyratrons' internal heaters are powered directly from the transformed mains supply which causes 100 Hz timing fluctuations. Correction of the warm-up effect was initially provided by a commercial Questek controller, but this could not accommodate the 100 Hz fluctuations and it also introduced unwelcome levels of shot-to-shot jitter.

Solution

The 100 Hz effect has been obviated by synchronising, in hardware, the whole laser system to twice the mains frequency (or a submultiple thereof). In addition, a computer program, written in LabVIEW, has been developed to monitor and correct any slower variations, including changes due to warm-up. The program takes the traces from the monitor oscilloscopes and finds their peaks to establish the actual timings of both excimer lasers. It then calculates the necessary corrections to the DG535 delays and implements these to restore the lasers to their correct timings.

The program operates through a GPIB interface card in the computer which is connected to the oscilloscopes and the DG535. The computer exchanges both instructions and data with the oscilloscopes but only sends instructions to the DG535.

The program reads and deals with one laser at a time, alternating between them until it is halted by the laser operator or until the laser(s) are switched off. The program detects switch-off automatically, thus avoiding the DG535 settings being shifted far from their optimum positions or even reaching the end of their ranges.

Information exchange with the instruments is handled through a driver sub-program [1]. This step limits how quickly the process can run, with the oscilloscopes taking ~1 second to transfer each trace. Once in the computer the data is converted into an appropriate format using another sub-program[1]. The peak amplitude and timing are then located and a check is carried out that the laser is still running by comparing the amplitude to a minimum value, set just above the noise floor. The peak timing is compared to a reference value and the necessary correction is calculated. The appropriate command to the DG535 is then constructed. A typical command [2] might be:

DL 1,0,0;CS 0;SC 17;IC 1

telling the DG535 which display line in its menu to select, to select cursor mode, to move the cursor to column 17 and to increment by one. All of the DG535 command lines are similar, differing only in the display line menu selection, the column selection and whether to increment or decrement the setting.

The program can operate with both excimer lasers running or with just one. It has two operating modes: Automatic (adjusting in either 100 ps or 1 ns steps, depending on how large a correction is needed) or Manual (allowing the laser operator to choose from 4 different step sizes). The Manual mode can deliver very rapid changes of the timings, needed when the lasers are first fired, or very fine adjustments when the thyratron has reach an equilibrium state and high stability is called for.

The image below shows the "front panel" of the user interface. The two oscilloscope traces are displayed as are the instrument settings and the manual program controls.

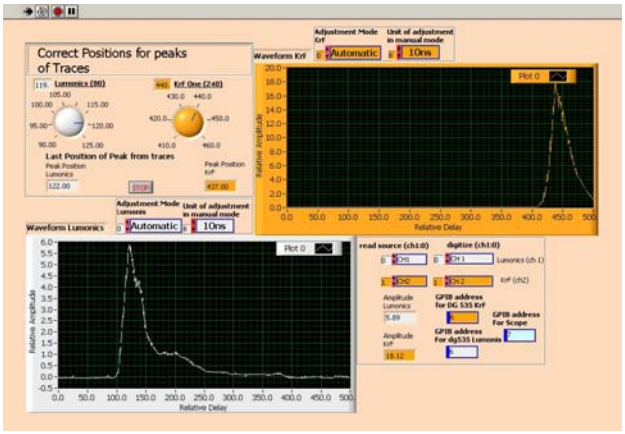

The program runs constantly while the excimer lasers are in use, correcting for any slow drifts in their timings. Although the largest of these are due to thyratron warm-up other factors include changes in the room temperature, the laser cooling water temperature and the mains voltage (which has small effects on the thyratron heater and HT voltages).

References

1. Software elements obtained from the National Instruments Driver Download www site at: http://www.ni.com/devzone/idnet/default.htm

2. Stanford Research Systems DG535 manual (1987)

Neutron spectroscopy using the LaNSA detector on the Vulcan laser facility

H Habara, K L Lancaster, P A Norreys

Central Laser Facility, CCLRC Rutherford Appleton Laboratory, Chilton, Didcot, Oxon, OX11 0QX, UK

Main contact email address: *h.habara@rl.ac.uk*

Introduction

Recent developments in intense laser systems have enabled the study of new regimes of laser-matter interactions that are particularly relevant to fusion energy research[1,2]. In this context, the 'fast ignitor' (FI) scheme[3] significantly relaxes the strict symmetry conditions required to generate the hot spark. The energy needed to produce the spark is created externally using a Petawatt laser. Fast electrons and ions slow down in the dense material and heat the fuel to thermonuclear temperatures before it has time to disassemble. It is therefore extremely important to understand how high-energy particles are generated and their propagation into the super-critical region of the compressed plasma. These energetic particles also have important applications in astrophysics[4] and nuclear physics[5].

Neutron spectroscopy is one of the most fascinating methods to investigate the ion acceleration generated by ultra-intense laser-plasma interactions (via beam-fusion neutron spectroscopy) [6, 7]. For this purpose, we have re-constructed the multi-channel neutron spectrometer, LaNSA [8,9]. The system records the timing when the neutrons are detected at each scintillator in the array. These timings are converted into neutron spectra via the time-of-flight (TOF) method. Neutron energy spectra taken at several different directions can then be used to determine the momentum distribution of the accelerated ions by taking into account the Doppler shifts of neutron spectra from 2.45MeV for each viewing angle. Here, we report the re-commissioning of the LaNSA system in the Vulcan TAW and TAP target areas and also preliminary results obtained in the TAW experiment earlier this year.

Large Area Neutron Spectroscopy Array (LaNSA)

The LaNSA system originally consisted of 960 channels of scintillator-photomultiplier detectors. In order to measure the neutron angular distribution, these modules were divided into three separate units, each of which has about 240 channels. The neutron detectors consist of an array of Thorn-EMI9902KB05 photo-multipliers coupled to BC505 liquid scintillators. The signal from each PMT is digitized at the discriminators according to the pre-set voltage threshold for each module. The electrical signals are delivered to a Time-Digital-Converter (TDC), which records the arrival time of the signal via the discriminator. These timings are collected and converted into a neutron spectrum through the time-of-flight (TOF) method. The data acquisition of the system is based on a PC used to control all CAMAC and Fastbus modules.

Figure 1. One of the two LaNSA array for PW experiments, which consists of 16 modules, each of which includes 16 scintillator / PMT detectors, corresponding to 256 detectors.

These three modules are positioned in Target Area Petawatt (TAP) and Target Area West (TAW) of the Vulcan laser facility at the Rutherford Appleton Laboratory. Figure 1 shows a schematic image of the neutron array for one spectrometer in TAP together with an overview of the setup for PW laser and the neutron spectrometers. An image of chamber and the module at TAW is also shown in Figure 2. The distances between the two modules and the chamber centre in TAP are about 12m and 5m. The distance of the array in TAW is about 8m from the chamber centre.

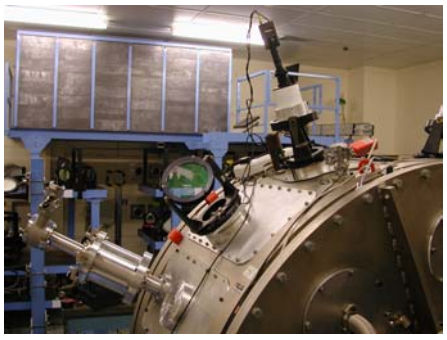

Figure 2. LaNSA detector (up) and the target chamber (bottom) at TAW. The unit has 18 modules, corresponding to 288 detector channels.

The energy resolution for each module as a function of distance from the target is shown in Figure 3 for different neutron energies. For example, at 6m distance, the module has 300keV of energy resolution for 2.45MeV neutrons, whereas there is only 800keV resolution for 14MeV neutrons. On the other hand, at 12m distances, the energy resolution of the module becomes much smaller (100keV for 2.45MeV neutron and 350keV for 14MeV neutron). By adjusting the target rotation and the incident laser direction, the energy resolution of both modules can remain at a comparably low level. The dynamic range for detecting the neutrons can be controlled by a factor of two by adjusting the voltage of the photo-multipliers and the discriminator threshold.

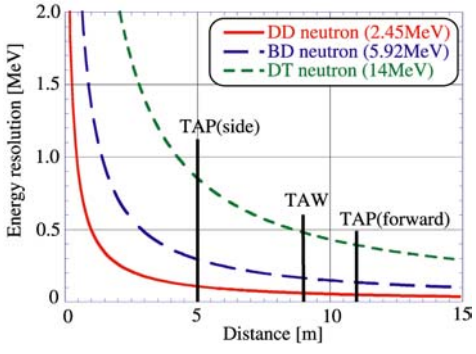

Figure 3. Energy resolutions for different neutron energies as a function of the detector distance.

The LaNSA system is operated by a newly commissioned PC via a CAMAC and Fastbus control unit. To make data acquisition procedure easy and routine, as well as being compatible with other control software on Vulcan, we have written the control software in DELPHI, an object-oriented Pascal language.

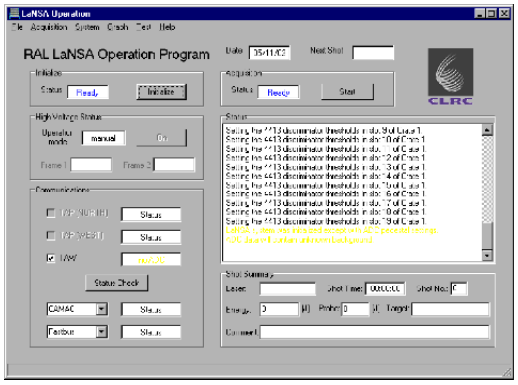

Figure 4. Main window of the LaNSA operation software. After the data acquisition, a data window is opened to show the temporal spectrum.

The software, run on Windows NT4, provides a wide range of operational options and test procedures to check the controller status. The software consists of multithread processes to protect the acquired data. The detailed operation procedure has been written in the operations manual that will soon be published as a RAL report.

Neutron spectrum

We observed a neutron signal using the LaNSA system at the TAW experiment on February / March 2003 as shown in Figure 5. The laser irradiated the deuterated plastic (CD) target with 100μm thickness focused about 600μm in front of the target, corresponding to an intensity of 10^{18}W/cm^2. The target has also a CD catcher approximately 35mm behind the target. The LaNSA module was set at about 6.2m from the chamber center and viewed angles ranged from about 60 to 90 degrees from the target normal direction.

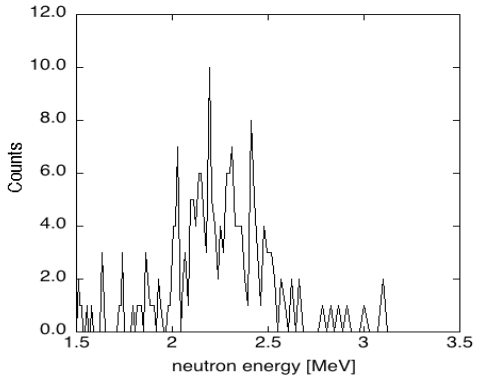

Figure 5. Neutron spectrum observed with the LaNSA system at the TAW experiment.

The neutron energy in Figure 5 shows a slight Doppler shift to the lower energy side from the thermal neutron energy of 2.45MeV for the deuteron-deuteron reaction. The spectrum suggests that the ions are accelerated at the target surface and the neutrons are generated immediately after the laser irradiation. However, there are several other possibilities of where the ions are accelerated, such as at front or back of the target, at the catcher target, and initial ion distribution. We are now analyzing the spectrum using a 3-dimensional Monte-Carlo simulation and comparing these with particle-in-cell simulation.

On the other hand, the count in each energy bin was always less than 10. This count is much smaller than the saturation level, about 200 channel, derived from the decrease of neutron detection sensitivity of the system at the high counting number.

Summary

We have reconstructed a multi-channel neutron spectrometer to measure the plasma temperature and estimate the ion acceleration. One of the detector units was built in TAW and the other two are now being installed in the TAP target area. The operation of the system is controlled from the host PC using newly established control software. Using these neutron spectrometers, we have obtained the first neutron spectrum for a TAW experiment. Detailed analysis is now being carried out. We also plan experiments to measure the ion acceleration distribution for incident intensities up to 10^{21} Wcm^{-2} using the Vulcan PW system to change a plasma density in order to determine the effect of scale-length on the ion acceleration mechanisms. Measurement of neutron spectra generated by a number of different nuclear fusion reactions has other interesting applications. In particular, B-D and Li-D reactions generate higher energy neutrons and have higher energy cross sections than those of the DD reaction - this may lead to the simultaneous observation of the high energy part of the ion momentum distribution.

Acknowledgements

The work is supported by the UK Engineering and Physical Science Research Council. The LaNSA array is on loan from the U.S. Department of Energy to the UK Ministry of Defense.

References

1. J Nuckolls, L Wood, Z Thiessen, and G Zimmerman
Nature, 239 139, (1972)
2. J. Lindl, R. L. McCrory, and E. M. Campbell
Phys. Today, 45 32, (1992)
3. M Tabak *et al.*,
Phys. Plasmas, 1 1626, (1994)
4. B A Remington, D Arnet, R P Drake and H Takabe
Science, 284 1488, (1999)
5. E P Liang, S C Wilks and M Tabak
Phys. Rev. Lett., 81 4887, (1998)
6. P A Norreys *et al.*
Plasma Phys. Control. Fusion, 40 175, (1998)
7. H Habara *et al*
Proceedings of SPIE, 3886 513, (2000)
8. M D Cable, S P Hatchett and M B Nelson
Rev. Sci. Instrum., 63 4823, (1992)
9. M B.Nelson and M D Cable,
Rev. Sci. Instrum., 63 4874, (1992)

Construction and testing of an optical parametric amplifier correlator

E J Divall, I N Ross

Central Laser Facility, CCLRC Rutherford Appleton Laboratory, Chilton, Didcot, Oxon, OX11 0QX, UK

Main contact email address: *e.j.divall@rl.ac.uk*

Introduction

This work was undertaken through the SHARP program. SHARP is a European program working to improve the contrast of short pulse high intensity laser systems and develop higher dynamic range contrast measuring techniques. This article details work on Astra to demonstrate a new design of high contrast correlator using optical parametric amplifier (OPA) technology.

The work has shown the ability to measure contrast below the 10^{-10} level. Measurements taken in Astra TA1 could not use the full range as they were limited by the actual ASE background level at the $10^{-6} – 10^{-7}$ level.

Technique

Conventional high contrast correlators use 3rd harmonic generation. The input beam is split in two. One half is frequency doubled to produce the probe pulse. The second pulse is then probed by mixing the two in a 3rd harmonic crystal. By measuring the 3rd harmonic generated and changing the relative path lengths on the 2 pulses a scan of the input pulse can be built up.

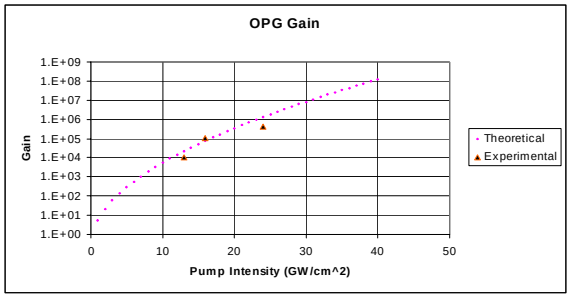

Figure 1. OPA gain rises exponentially with pump intensity.

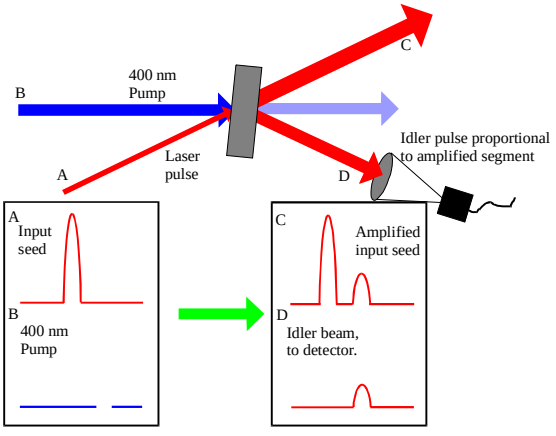

Figure 2. Operation of OPA Correlator (OPAC) Pump amplifies short segment of seed pulse and a copy is generated on the idler channel.

The OPA correlator built for this project uses a very similar set-up except the 3rd harmonic stage is replaced by an OPA. The probe pulse becomes pump and the fundamental the signal pulse. The gain of an OPA is exponentially dependent on the pump intensity and gains in excess of 1 million can easily be achieved. (Figure 1).

The correlator is set so the pump pulse amplifies one short time segment of the signal pulse 1 million times (Figure 2). The OPA process creates a copy of this amplified segment in the idler direction, which can be measured. This technique has a number of advantages:

1. It reduces background noise since the measured signal is switched into a completely different direction.
2. Unlike the conventional correlator the signal is greatly amplified giving a bigger detectable signal, so the signal is no longer limited by detector noise.

However since the OPA is used at degeneracy in this case, the idler is at the same wavelength as the signal, so scattered signal light especially from the OPA itself could limit the overall performance. This scattered light is minimised by increasing the non-collinear angle (10^{o} (internal) in our case).

Experimental Set-up

The experimental layout is shown in Figure 3. The 10 mJ, 50 fs beam in Astra TA1 was used. The input beam was split into 2 using an uncoated (+ AR) wedge (Wedged to reduce post pulses). The OPA pump pulse was made by frequency doubling the undeviated beam using a 2mm BBO crystal. A half waveplate before the doubling crystal gave control of the pump energy up to 1.2 mJ. The pump pulse length was measured as 200 fs. To generate the necessary pump intensity for the OPA process whilst maintaining the beam quality the pump beam was telescoped down by a factor 3 and imaged through a helium filled relay tube. This gave a pump intensity of 20 GW / cm^2 in a 4 mm diameter beam at the OPA crystal. The signal arm was reduced to 1 mm diameter by placing the OPA crystal near the focus of a 300mm lens. This beam could also be delayed / advanced with respect to the pump by a computer controlled Newport translation stage with 25mm of movement.

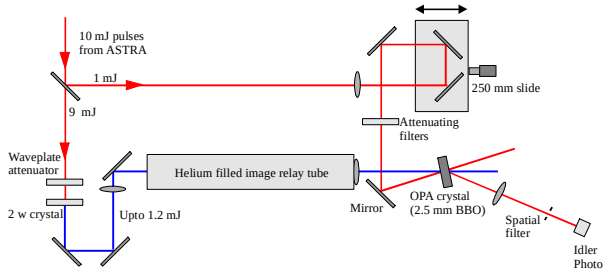

Figure 3. Setup of OPA correlator.

Due to the non-collinear geometry in the OPA, the phase matching condition required the pump and idler to propagate in the OPA crystal at an angle of 10 degrees. A large area photodiode was used to monitor the idler beam. The diode and delay stage were linked to a PC. Software was written in LabVIEW to move the translation stage to scan the pump pulse relative to the signal. The computer recorded an averaged idler

intensity at each point to build up a profile of the signal pulse. To measure the full contrast it was necessary to take several scans with increasing the attenuation of the signal arm until the diode signal was not saturated.

Results

Initial measurements showed that only 5 nm bandwidth of the signal was amplified. This was found to be due to poor phase matching in the OPA across the bandwidth. By using a 200 line / mm grating to spectrally disperse the signal before the OPA the amplified bandwidth was doubled to 10 nm. Figure 4.

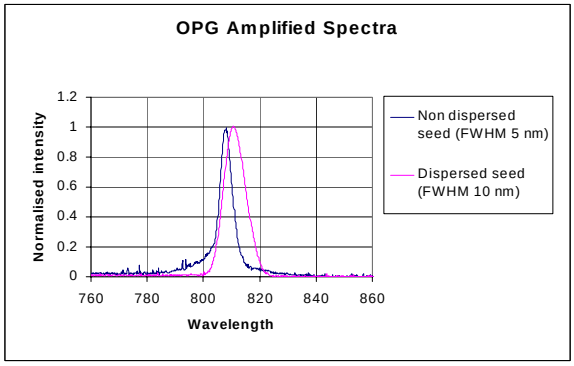

Figure 4. Bandwidth limited by phase matching condition.

Typical nearfields for the signal and idler are shown in Figure 5. They appear elliptical since the beam is still dispersed. The vertical stripes have not been explained.

SIGNAL IDLER

Figure 5. Typical pulse nearfields after the OPA.

By blocking either the pump to leave just the scattered signal, or the signal to leave only the pump-induced ASE and comparing with the maximum amplified idler signal with both pump and signal temporally coincident, it was possible to assess the maximum contrast measurable with the set-up used. Both the scattered red from the signal and ASE from the pump were measured at below the 10^{-10} level with the scattered signal being

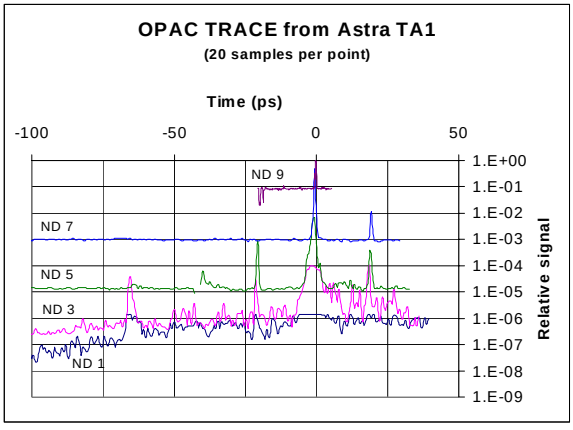

Figure 6. OPAC scan with varying attenuations signal beam before OPA.

the dominant term. This implies that the maximum measurable contrast could have been increased by increasing the pump since this would have increased the gain and hence the maximum signal without significantly increasing the background. Initial correlation traces of the recompressed fundamental pulses from the Astra laser were made by scanning the relative timing of the two arms and are shown in Figure 6.

Five traces were taken with increasing attenuation of this test beam, five being needed as the photodiode / ADC card combination only had a dynamic range of just over two orders of magnitude. These scans show a background at the few times 10^{-7} level, which is well above the 10^{-10} minimum level of the detector. Probing the pulse up to 1ns early gave the same background indicating that the compressed pulse from Astra itself has a long ASE plateau. These results agree with earlier third order correlator measurements.

These results are promising for a first trial of the design. Considerable improvements are possible by:

1. Increasing pump intensity
2. Matching pump and signal sizes
3. Repolishing OPA crystal to reduce scatter
4. Improving the detector shielding from 800nm light
5. Spatial filtering the idler beam
6. Normalising to pre-amplified 800 nm and 400 nm pump energies to reduce the shot-to-shot noise
7. Improving the phase matching in the OPA
8. Increasing the signal by using blazed grating or prism
9. Modifying the OPAC so the input pulse is automatically attenuated so that the whole trace can be taken in one scan.
10. Looking further into the pulse wings by increasing its temporal scan range.

With these improvements in mind a proposed design for the new OPA correlator is shown in Figure 7.

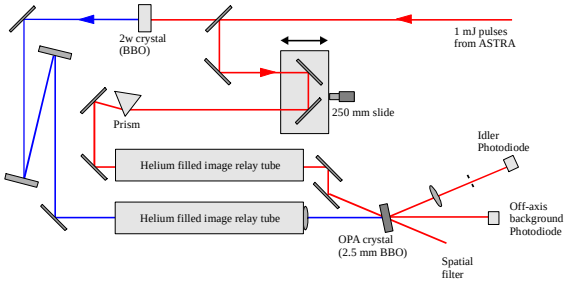

Figure 7. Proposed layout for improved correlator.

Conclusions

A simple OPA correlator was set up and demonstrated the potential to measure a contrast ratio of 10^{10}. Tests on the Astra laser showed the compressed pulse had a contrast of just over 10^{6}.

Ultrafast time resolved emission spectroscopy using a Kerr gate

A P Monkman, B Lyons

OEM Research Group, Department of Physics, University of Durham, South Road, Durham, DH1 3LE

Main contact email address: *a.p.monkman@durham.ac.uk*

Introduction

Our intention for this initial one week project was to follow up on recent reports from Japan indicating that it was possible to use thin quartz or glass plates as Kerr media instead of the more typical CS2 or benzene. This then allows Kerr gates to be made with opening times down to as low as 250 fs as opposed to the more usual 1-4 ps. If we could replicate this in a useable spectrometer at RAL we were then going to study early time photophysics and energy migration processes in luminescent polymers.

The main difference between the ultrafast Kerr gate and the more standard CS_2 one currently used at RAL is the need to replace the large volume calcite polariser before the Kerr gate with a much thinner plastic sheet polariser so that the minimum amount of dispersion was then introduced into the sample emission. With the polarisers available to us this meant that between 1.5 and 2 orders of magnitude of polarisation were lost as compared to the calcite polariser. What this implies is that the rejection of scattered light passing through the crossed polarisers astride the Kerr cell is much worse.

Initial experiments proved rather difficult, especially in achieving proper alignment of the optics. However using excitation pulse scatter it was possible to change the Kerr medium step wise from CS_2 (4 ps response) to a thin cell of benzene (1 ps response) to a 0.5 mm quartz plate giving a response (autocorrelation) of 390 fs, shown in Figure 1. Thus we were able to demonstrate significant improvements to the temporal response of the RAL Kerr gate system.

We next tried to use this ultrafast gate to time resolve the emission from polyfluorene, the archetypical blue emitting luminescent polymer. From previous studies it is known that this polymer has a fluorescence lifetime of 350 ps in solution at room temperature. This however proved to be too long for the system as the amount of stray light passing the Kerr gate in the 'off' state during the long emission lifetime swamped the emission actually time gated. In an attempt to shorten the lifetime of the polyfluorene, TPP was added to the solution. This efficiently de-excites the polyfluorene by Forster transfer, reducing the polymers lifetime to 30 ps or less. This does though drastically reduce the amount of emission from the polymer and we were not able to clearly resolve a fast emission from the polymer. We also encountered another problem here. As the RAL system runs at 1 kHz repetition rate to obtain a useable signal to noise ratio the solution or film sample has to be excited at high intensities which rapidly degrades the samples even if used in a flowing jet.

Thus, we succeeded in producing an ultrafast Kerr gate and have been able to put limitations on its use. Only samples with very fast luminescence lifetimes can be studied, typically very much less than 300 ps. Secondly, the sample must be able to withstand high excitation intensities and have low singlet-singlet annihilation thresholds.

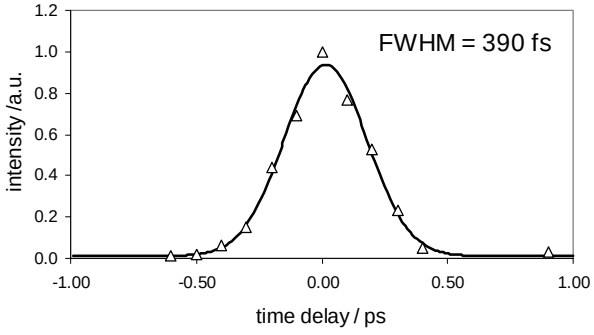

Figure 1. Gaussian fit of the 'autocorrelation' function of a 0.5 mm quartz plate Kerr gate.

Vulcan OPCPA – Results from the first experiment

I N Ross, J L Collier, O Chekhlov, M M Notley, C Hernandez-Gomez, C N Danson, D Neely, P Matousek, S Hancock
Central Laser Facility, CCLRC Rutherford Appleton Laboratory, Chilton, Didcot, Oxon, OX11 0QX, UK

L Cardoso
Centro de Fisica de Plasmas, Instituto Superior Tecnico, Av. Rovisco Pais, 1049-001, Lisbon, Portugal

Main contact email address: *i.n.ross@rl.ac.uk*

Introduction

The technique of optical parametric chirped pulse amplification[1)] (OPCPA) offers the possibility of generating powers and intensities much higher than is feasible with current CPA systems and provides a route to possible future upgrades for the Vulcan laser. Earlier work[2)] demonstrated feasibility up to the TW level. The current programme, supported by an EPSRC grant, is aimed at fully assessing the technique to much higher powers with a view to including it in future upgrade plans for Vulcan. The grant programme includes three experimental runs on Vulcan and the purpose of this article is to report on the results from the first of these.

Design and arrangement

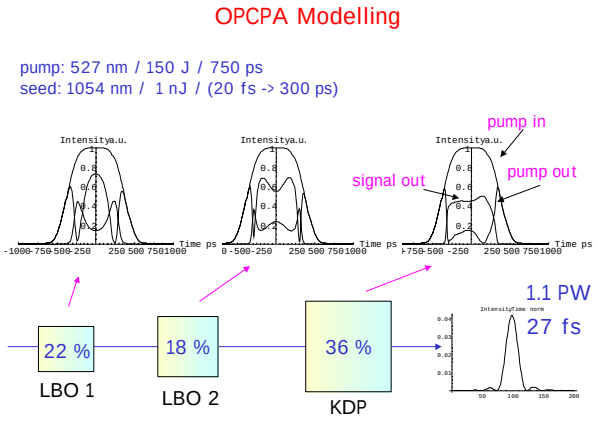

Figure 1. Optimised performance of Vulcan OPCPA scheme.

The design was based on the optimisation of an OPCPA system pumped using a single 150mm beam from Vulcan and is illustrated in Figure 1. This shows the result of simulations and optimisation and predicts a potential performance of close to 1PW. An OPA pump beam of 150J at 527nm was available leading to an amplified signal energy of about 50J at 1050nm.

The signal beam was derived from a 150fs 1050nm Ti:sapphire oscillator followed by self-phase-modulation in an optical fibre, to increase the spectral width to 40nm, and stretch to 400ps. The Layout of the OPCPA system for the first experiment is shown in Figure 2. It is a 3-stage amplifier scheme using LBO for stage 1 and 2 and a 110mm aperture KDP for stage 3. The geometry is slightly non-collinear to allow spatial separation of pump, signal and idler beams after each amplifier and is fully image relayed to ensure best uniformity of the pump beam and best optical quality of the signal beam. The aim was to have a 'super-Gaussian' pump beam temporal profile with an adjustable duration using the Vulcan fast optical gate and a circuit to increase the rise and fall times of this gate.

The goals of this first experiment were to demonstrate:
a) saturated amplification with high conversion efficiency
b) amplification over the full oscillator spectrum
c) high near and far-field quality in the amplified beam

Amplification and extraction efficiency

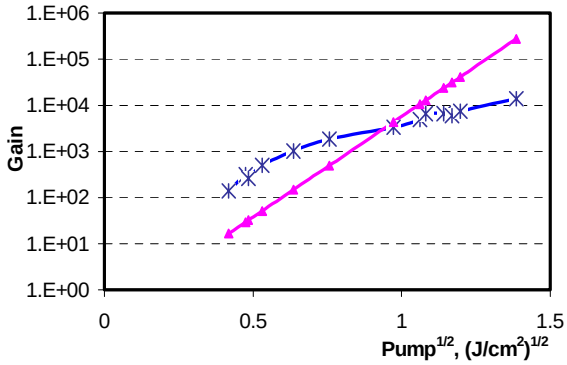

Figure 3. Dependence of gain OPA1/OPA2 stages on square root of pump fluence. Straight line is an estimated gain for a pump pulse 0.7ns pulsewidth.

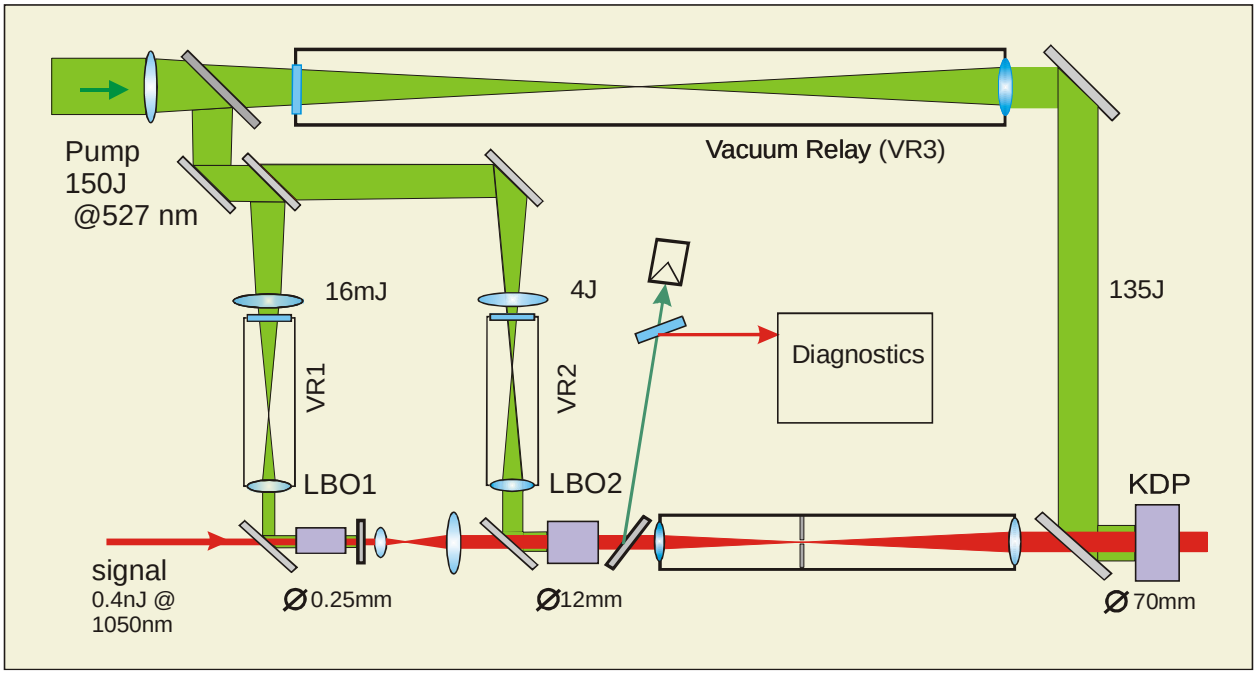

Figure 2. OPCPA Experimental setup.

Measurements of the small and large signal gain were made for individual amplifiers and for combinations of amplifiers. A curve of measured small signal gain for the first two amplifiers (OPA1 and OPA2) individually is shown in Figure 3 against the expected straight line of logG against (pump intensity)$^{0.5}$. A general conclusion was that the expected gains were achieved but other factor suppressed this gain at the higher pump levels. Further comments on this anomalous result will be given below.

Strong gain saturation was achieved in both OPA2 and OPA3 and, with the 3 amplifiers together, input signal levels of 0.4nJ could be amplified to greater than 10J indicating a saturated gain well in excess of 10^{10}.

Figure 4 plots the measured extraction efficiency in the final KDP power amplifier and shows a maximum of 24%. This represents an excellent result although somewhat less than the optimised design result due to non-optimisation of the amplifier gain distribution and limitations to the spectrum. Both these effects will be discussed later.

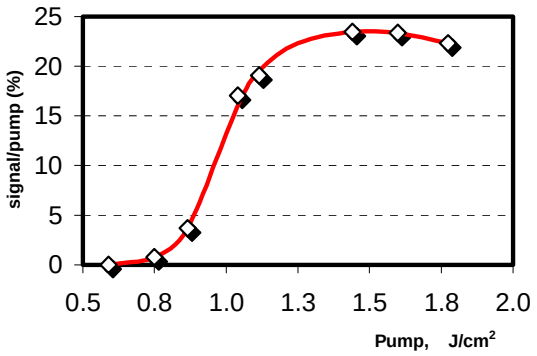

Figure 4 . Conversion efficiency of a signal pulse on pump fluence at OPA3 stage.

Spectral Measurements

A spectrometer was set up to record either the transmitted and un-amplified seed signal spectrum or simultaneously the amplified signal spectrum after OPA2 and OPA3 respectively. Examples of these spectra are shown in Figure 5.

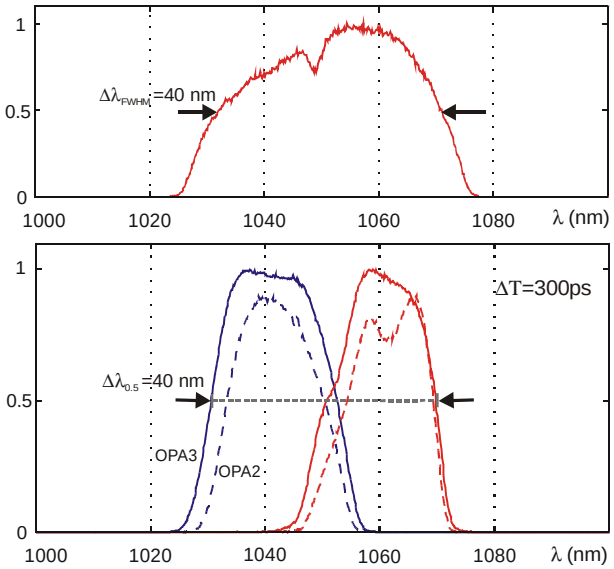

Figure 5. Spectrum of SPM and stretched pulse from a mode-locked Ti:Sapphire laser (top picture). The bandwidth corresponds to a 40fs pulsewidth. Amplified spectra after OPA2 (lower lines) and OPA3 stages at different relative timing of the pump pulse, ΔT= 300ps.

The seed signal spectral width is seen to be 40nm and corresponds to a transform-limited pulse duration of about 40fs. Two pairs of amplified spectra are also shown with a relative pump timing difference of 300ps, demonstrating that the optical parametric amplifiers had a gain bandwidth larger than 40nm but that the pulse bandwidth is significantly narrowed by the amplification process.

This spectral narrowing has been shown to result from the far from ideal temporal shape of the pump pulse. There were three contributing effects which biased the pump intensity strongly towards the leading edge of the pulse reducing the effective pulse duration. Subsequent tests on the Vulcan gate in the configuration used pointed to a double pulse transmission rather than a flat top; at the higher energies gain saturation in Vulcan increases the leading edge intensity relative to the trailing edge intensity by a factor of 2 to 3; and the second harmonic process will enhance any intensity differences in the fundamental.

The ability to tailor the amplified spectral shape is indicated by the red curves in Figure 5. OPA2 is over-driven in this case causing a dip in the centre of the spectrum but this dip is 'filled in' by the amplification process in OPA3. This ability needs to be exploited to achieve the maximum amplified bandwidth with the optimum shape.

Amplified noise

Problems were encountered with excessive amplified noise principally from OPA2. This appeared to be a parasitic which was able to extract significant energy from OPA2 at a pump beam intensity much lower than anticipated. There is not yet an adequate explanation for this but some properties of the generated beam were measured. It is close to being collinear with the amplified signal and could be suppressed by reducing the pump area in OPA2. Spectra were recorded and examples are shown in Figure 6. Curve 1 is the spectrum without a signal beam in the amplifier and indicates a generation of mainly shorter wavelengths than the signal but with a strong enhancement at the signal wavelength. As expected the noise spectrum is suppressed by saturated amplification of the signal but there still remains a significant component at still shorter wavelengths.

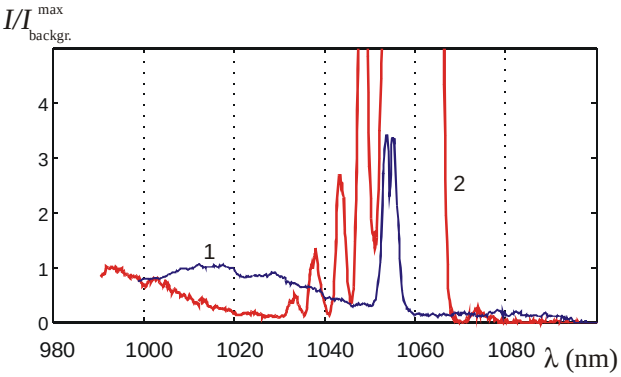

Figure 6. Examples of amplified spectra after OPA 2 stage, with (2) and without (1) input signal. (Amplified signal is modulated due to mode-beating on the pump). Pump for (1) - 3.2J/cm^2, for (2) - 4.1 J/cm^2.

Output beam near and far-field profiles

The measured output amplified signal beam near field profile is shown in Figure 7 under conditions of high extraction efficiency. This is close to a flat top distribution with a diameter of 70mm, less than the design diameter of 100mm due to the need to restrict the beam aperture in OPA2 to suppress the amplified noise. This flat top profile allows good extraction efficiency from the final amplifier (OPA3).

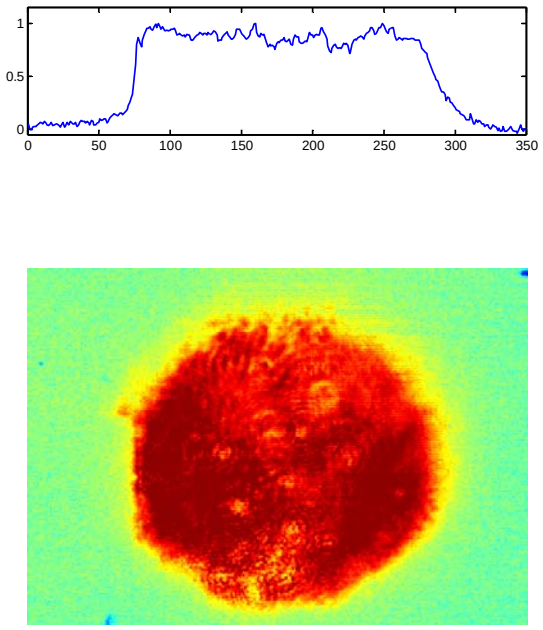

Figure 7. Profile and near field image of amplified signal after OPA3.

To assess the wavefront quality and focusability the far-field distribution was recorded in the focal plane of a m focal length lens and compared with the diffraction-limited Airy distribution characteristic of a flat top beam of diameter 70mm. Figure 8 shows a measured profile along a diameter of the far-field given alongside a calculated Airy distribution for a top-hat 70mm near field profile. The ratio of the two peak values gives a Strehl Ratio of 0.72 and indicates an rms wavefront error of 0.084λ, since, for small phase errors (φ),:

$$\phi^2_{rms} = 1 - \text{Strehl Ratio with } \varphi \text{ in radians}$$

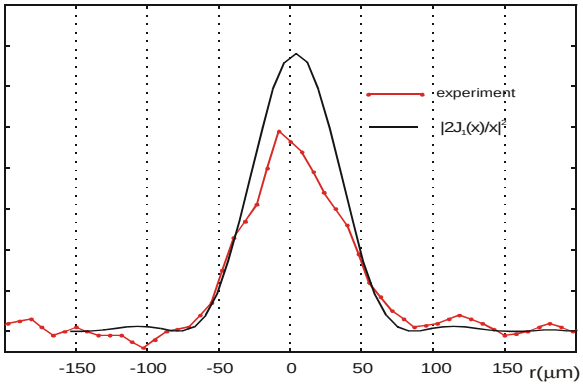

Figure 8. Far-field intensity distribution of an amplified signal beam (f~449cm) and theoretical profile for a flat-top intensity of the beam.

Summary and future programme

The aims of this experiment were largely achieved. A 3-stage OPCPA system was set up and the amplification properties fully tested using one of the Vulcan 150mm beams to generate up to 150J pulses for pumping the OPAs.

The ability to achieve sufficient gain to fully saturate the amplifier gain confirmed the predictions. Gains in excess of 10^{10} enabled amplification from 0.4nJ up to more than 15J in spite of the necessity of restricting the area by a factor 2 to suppress the amplified noise. Extraction efficiencies of 24% were measured, the somewhat lower than expected values being well explained as a result of some spectral narrowing in the amplifiers together with imperfections in the amplifier staging.

The OPAs demonstrated gain spectral bandwidths greater than the 40nm input signal bandwidth and expected saturation effects were observed providing data to help with future optimisation. The amplified spectrum was adversely affected in both profile and duration by the limited uniformity in time of the pump beam intensity, showing this to be a critical issue in an OPCPA system.

Both the amplitude and phase integrity of the amplified output signal pulse were tested and demonstrated that, as expected, OPCPA systems can operate with low aberration at high output energy. A Strehl Ratio of 0.72 was measured.

Difficulties with the pump beam profile have been noted. The other major, and in this case unexpected, problem was the presence of a parasitic or very high level of amplified noise appearing after the second amplifier (OPA2). This was largely suppressed by reducing the gain of this amplifier and by limiting the pumped area of crystal. This noise occurred at a wavelength significantly shorter than the 1050nm signal wavelength.

The second experiment of the campaign is planned for early 2004 with the aim of optimising the performance of the amplifier system and demonstrating maximum power in re-compressed pulses. Optimisation will require us to re-stage the first two OPAs by increasing the gain in OPA1 to increase its level of saturation and reducing the gain in OPA2 to enable the full aperture to be used while suppressing the amplified noise. A new driver for the Vulcan fast optical gate together with better electrical coupling will provide a more optimised pump temporal profile and is expected to increase the conversion efficiency in the OPCPA as well as increase the amplified bandwidth. We would like to instal as the signal source a new ultra-short pulse oscillator which is currently under development.

References

1. I.N.Ross *et al.* Opt. Comm. 144 125 (1997)
2. I.N.Ross *et al.* App. Opt. 39 2422 (2000)

Design and implementation of an oscillator for OPCPA

L Cardoso

GoLP – Centro de Fisica de Plasmas, Universidade Tecnica de Lisboa, Av. Rovisco Pais, 1049-001 Lisboa, Portugal

I N Ross, J L Collier, O Chekhlov

Central Laser Facility, CCLRC Rutherford Appleton Laboratory, Chilton, Didcot, Oxon., OX11 0QX, UK

Main contact email address: *luis.cardoso@ist.utl.pt*

Optical Parametrical Chirped Pulse Amplification, OPCPA, is a promising technique to achieve higher powers due to its broadband acceptance and absence of energy deposition in the amplifier media. Given a 526 nm pump pulse, efficient amplification is calculated to occur in the range 1030-1050 nm, supporting bandwidths in excess of 100 nm. To provide seed pulses at this wavelength an oscillator is being constructed. The active medium is Ti:sapphire for its well known characteristics, namely a broadband spectrum. However, working so far from its centre line, the gain is 10 times smaller than at maximum, vanishing at around 1100 nm. Therefore cavity losses must be kept as low as possible while giving the crystal good amplifying conditions. On the other hand, to achieve short pulses, group velocity dispersion, GVD, must also be controlled. These two requirements drive us to short, 4 and 6 mm long, and highly doped crystals, with an α=6.2. The set up, Figure 1, can be pumped from both sides, to maximize energy deposition while preventing damage.

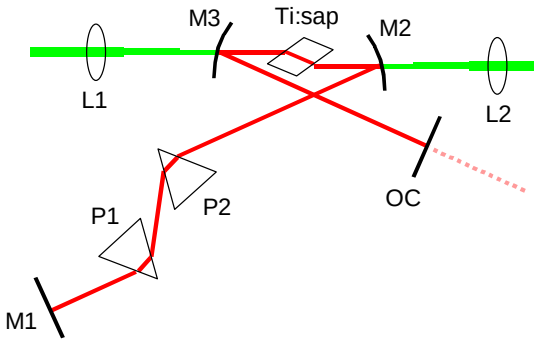

Figure 1. Oscillator setup scheme.

Besides avoiding reaching the damage threshold, two side pumping has the ability to improve the inverted media channel profile, used as a soft aperture for Kerr lens mode locking.

M1 to M3 are 99.8% reflecting mirrors with GVD<20 fs^2. M2 and M3 have a radius of curvature of 100 mm, although a 50 mm set is also available should we wish to increase intensity in the crystal. OC is the output coupler, with reflectivity ranging 97-99%, GVD<20 fs^2.

In order to keep losses low, instead of chirped mirrors we use the prisms P1 and P2 made of a suitable glass. Plotting the difference between the $(\partial^2\phi/\partial\omega^2)/(\partial^3\phi/\partial\omega^3)$ ratio for material and prism dispersion it is possible to check if both 2nd and 3rd order GVD can be compensated at the same time. Figure 3 shows the results for six types of glass. Other common glasses, such as BK7 and fused silica, returned much worse results, out of the range shown. From the tested glass types, LaSF32 is one which accomplishes the task with a practical insertion amount. Calculated prism separation for a zero cavity round trip GVD is about 40mm.

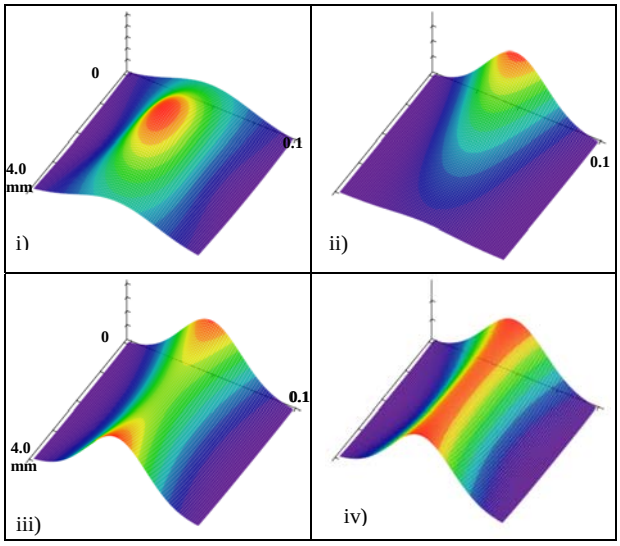

Figure 2. Intensity plots along the sagittal plane in a 4mm long, α=6.2, Ti:sapphire rod: i) 18µm waist 1050nm beam; ii) 18µm waist 514nm single side beam; iii) double side 514nm beams, 18µm centred waists; iv) double side 514nm beams, 16µm waists overlapping by 1,2 mm.

With a 6mm crystal and the higher output coupler, the cavity is tuneable in the range 950-1080 nm, with one prism only, and 950-1050 nm with both prisms and a tuning slit; shorter wavelengths are not available with these mirrors as they are made to suppress them. An additional care has been taken to correct the crystal c-axis orientation due to imperfect crystal cut and to achieve tuning over broad spectral region.

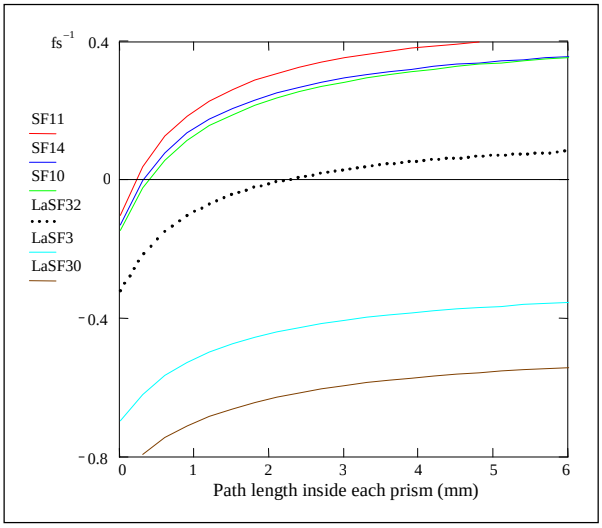

Figure 3. Crossing at zero shows how much glass makes both 2nd and 3rd order GVD null for a 3 m round trip cavity and a 4 mm long Ti:sapphire rod, at 1050 nm.

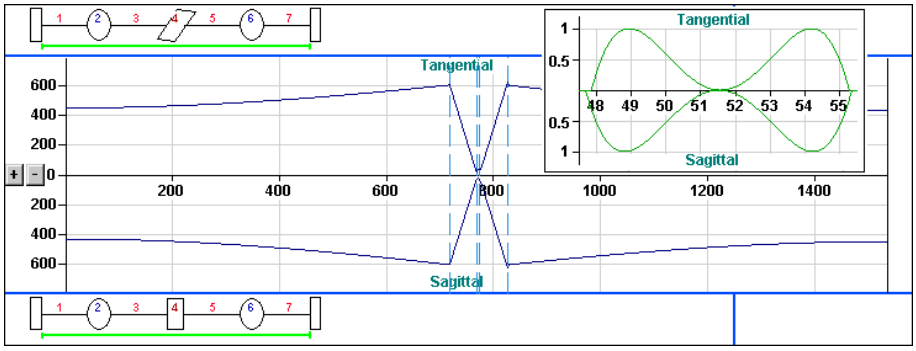

Figure 4. Cavity simulation in Winlase. Main: gaussian beam propagation inside cavity. Inset: stability as a function of mirror-crystal separation.

Apart from that, there was also a problem of too high absorption in the infra-red, which is usually assigned to a higher concentration of Ti^{4+} ions and vacancy clusters at high doping levels. The absorption losses in the crystals available for the experiment were accounted for the majority of the total loss of the system and severely affect the overall performance, and future plans include trying a different, lower doped crystal. At the time of the experiment the optimum was a 4 mm crystal. It shows lower absorption and better beam shape, while the 6 mm one introduces too much astigmatism which could not be fully compensated for due to geometrical constraints.

In order to achieve mode-locking we have to characterize the cavity and know its operating properties. We are also interested in matching our results to theoretical simulations of the system.

Figure 5 shows a few sampling points where the size of the bubble represents the output power (in a.u.), and the axes represent the distance between each curved mirror and the crystal. Here, the cavity is 154 cm long, symmetric, without any prisms or tuning device, so the laser is free running at about 960 nm. The dashed areas correspond to stable cavity conditions, as simulated by software. The shadowed band shows for which configurations the beam waist remains inside the crystal.

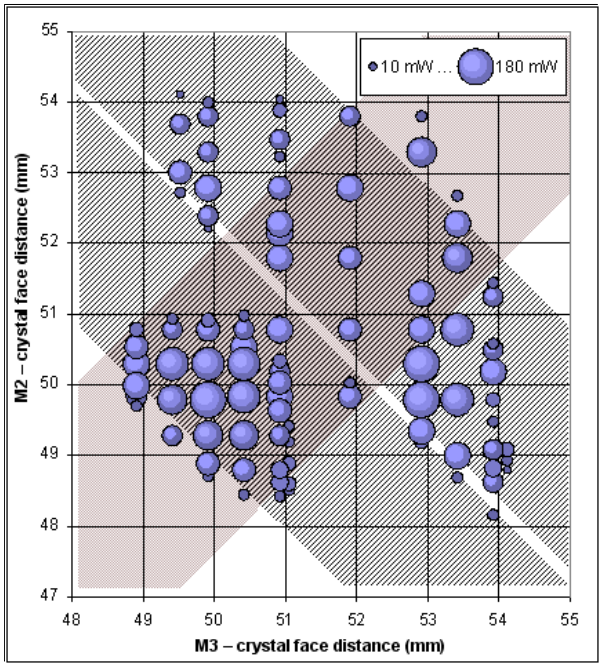

Figure 5. Output power for 4 mm crystal, pumped at 11 W, over different mirror separation.

The power asymmetry on the upper zone is just due to off centre pumping. Overall, there is a good agreement between experiment and theory.

To increase power and make mode locking easier, we replace the 1 µm mirror set for a 800 nm one. Soft-aperture is the mode locking mechanism, which is the best for wider bandwidth support. The cavity length is 150 cm, with an arm length ratio close to 1:2, shorter on the output coupler side. For tuning purposes the prisms are separated about 4 times more than the optimum separation calculated for both 2nd and 3rd order GVD compensation. In fact, at 800 nm, LaSF32 is unable to completely remove 3rd order term. Because so much negative dispersion is introduced, the prisms are inserted a long way in, to add glass for a positive dispersion contribution. The pump level used is about 3.5-4 W, single side only, although double sided pumping has also been demonstrated to work. The starting mechanism is a strong push on the output coupler which is mounted on a sliding stage.

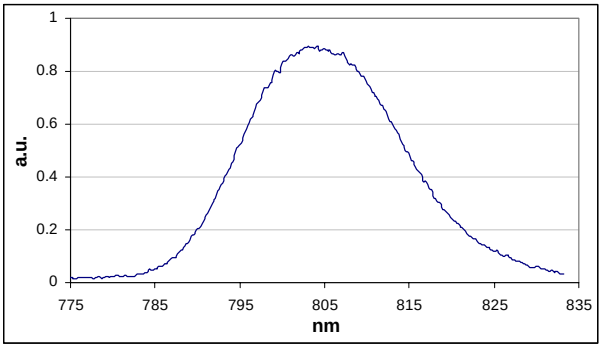

Figure 6. Mode locked spectrum.

The centre wavelength for mode locking tends to shift up to a few tens of nm from CW line. In Figure 6 one can see that the bandwidth reaches 22 nm, and may correspond to a pulse length less than 55 fs, which is a good result given that with the described configuration we cannot control 3rd order GVD.

Figure 7 (next page) shows the laser activity for this cavity, along with the mode locked configurations circled red. Note that M2 could not be set closer than 50 mm from crystal due to geometrical constraints. Two very interesting features are shown: the cavity is still able to oscillate even if the geometry isn't stable, according to computer simulation and the mode locking active band confirms the correct prediction of the boundaries of the stability zone, as it is in its inner edge that the mode locked regime is usually reported to be most easily achieved. Mode locking in the upper stability zone, the most usual for soft aperturing, is currently under study as it requires further changes in the layout.

With mode locking occurring with 2 to 3 W intracavity beam power, bringing it to the 1040 nm range could be possible with pump power as low as 11 W, based on previous experience with the 6 mm long crystal.

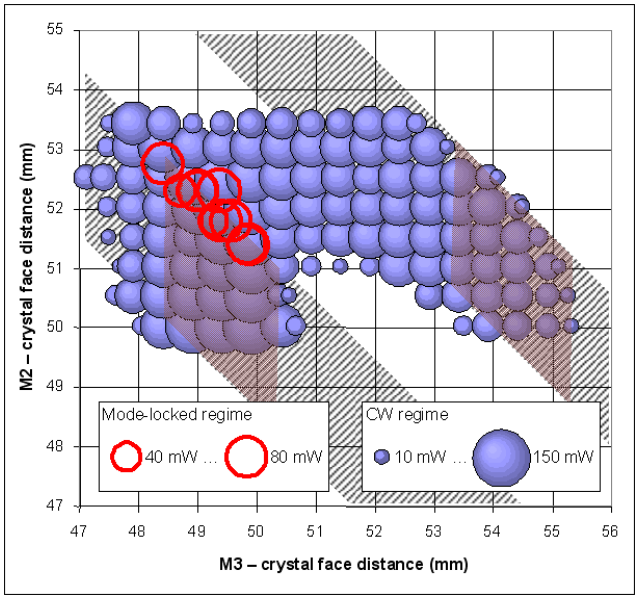

Figure 7. Output power for 4 mm crystal, for CW and mode locked modes, over different mirror separation.

Conclusion

As a future seed source for OPCPA, a Ti:sapphire oscillator has been built that is capable of CW operation up to 1080nm, and femtosecond mode locking at 800nm, with 22 nm bandwidth. Current work deals with extending the mode locking regime both to other zones and longer wavelengths.

A diode-pumped photoinjector laser system for the CERN linear collider (CLIC)

M Csatari

Department of Optics and Quantum Electronics, University of Szeged, Dóm tér 9, H-6701 Szeged, P.O.Box 406, Hungary

I N Ross

Central Laser Facility, CCLRC Rutherford Appleton Laboratory, Chilton, Didcot, Oxon, OX11 0QX, UK

Main contact email address: *i.n.ross@rl.ac.uk*

Introduction

Photo injectors have been under development over the past decade promising high brightness electron beams for linear colliders (LINACs) as well as for Free Electron Lasers. Photo-injector systems typically generate a train of electron bunches from a photocathode illuminated by a train of laser pulses. This technique makes it possible to produce the complex electron bunch structure required by LINACs. The laser system described below is designed to satisfy the requirements for the PILOT (Photo Injector LOng Train) test programme for the proposed CERN LINAC (CLIC).

System description

The values indicated in Table 1 show both the CLIC, and the PILOT photoinjector specifications. The PILOT laser system was designed to be a realistic scaled down version of design for CLIC, to enable testing of the critical parameters such as gain and saturation properties, thermal aberration in the amplifier, harmonic generation efficiencies and stability.

	CLIC	PILOT		
Parameters (units)		***Worst case***	***Nom***	***Best case***
Charge / pulse (nC)	**750000**	**0.072**	**0.15**	**0.36**
Number of pulses	**45000**	**350**		
Distance between pulses (ns)	**2.13**	**4**		
Macro-pulse width (μs)	**96**	**1.4**		
Pulse length (ps)	**10**			
QEmin (%)	**5**	**4**	**5**	**6**
Wavelength (nm)	**262**			
W cathode / pulse (nJ)	**5000**	**18**	**30**	**60**
IR/UV conversion eff. (%)	**5**	**3**	**5**	**10**
Wout / pulse (amplifier) (μJ)	**100**	**1.5**		
Wout / pulse (oscillator) (nJ)	**?**	**0.4**		
RMS Stability of micropulse energy long term	**<0.5%**			
Repetition rate (Hz)	**100**	**5**		

Table 1. Laser/ photo cathode specifications.

After careful studies and analysis of the possible configurations [1-3] the injection laser system for PILOT with the given master oscillator characteristics are shown in Figure 1. The laser is composed of an additive pulse mode-locked oscillator, a multi-pass pulsed amplifier, a feedback stabilization system and a fourth harmonic generation stage. The Nd:YLF diode-pumped laser built and developed at RAL provides an up to 20μs long train of ~10ps pulses at 262 nm, and 0.15 μJ micropulse energy.

The oscillator. A commercial (Coherent DMP 1000) additive pulse mode-locked Nd:YLF oscillator delivers 5 ps pulses at 120 MHz with up to 1.5 W output power at 1047 nm. However for the PILOT tests at CERN an existing oscillator at CERN was used, with 250 MHz, 100 mW output, so for realistic tests at RAL we attenuated the output of the DMP 1000 oscillator to ~50 mW (~0.42 nJ/pulse). The oscillator is protected against feedback from the amplifier by a Faraday isolator.

The amplifier material and pump source (Figure 2.). Nd:YLF satisfies most of the requirements, such as high gain, natural birefringence, long upper laser level lifetime (480 μs), low saturation fluence, low thermal distortion, and ideal absorption wavelength for efficient pumping. The low fracture limit of the material does limit the maximum extracted power per unit length to about 50W/cm. 5 x 1kW stacked diode arrays provide the QCW pumping of the amplifier rod. The same water circuit cools the diodes and the rod, and allows temperature control of the wavelength. The emitted light of the diodes is efficiently coupled into the crystal using a lens and a cylindrical cavity containing the rod. For high coupling efficiency this cavity has reflecting areas to couple transmitted light back into the rod.

A 100V, 100A stabilised supply drives the diodes in series providing a square pump pulse with adjustable duration and repetition frequency. The pump duration was normally 400 μs, long enough to allow the amplifier to reach steady state. At the 5 Hz repetition rate used the thermal effects in the rod are negligible.

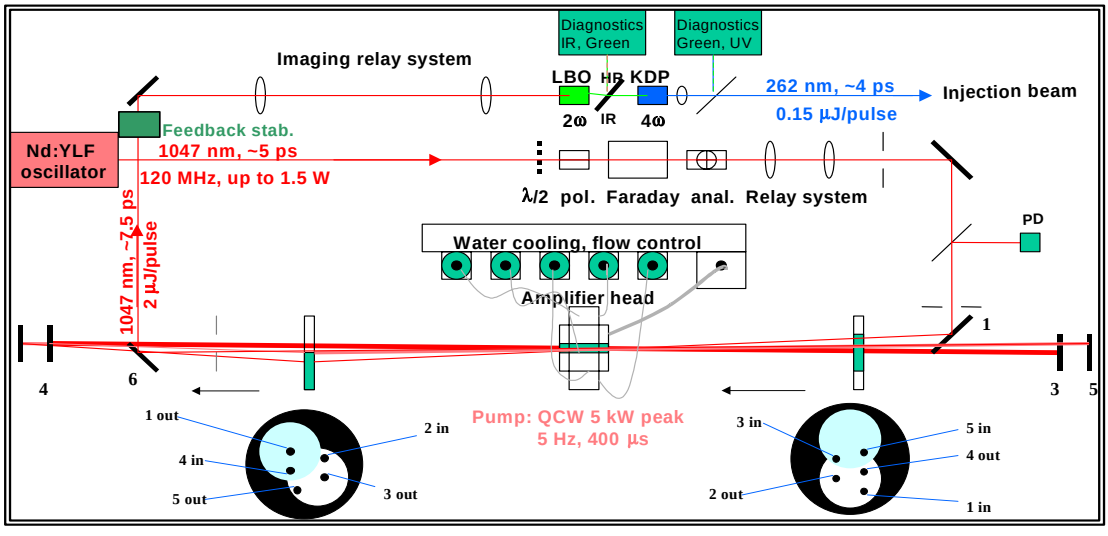

Figure 1. Layout of the photoinjector laser system.

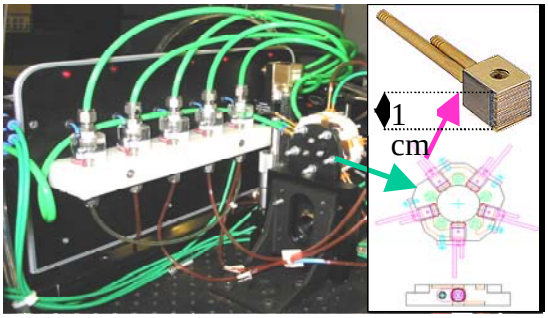

Figure 2. Amplifier Head with cooling system "in-situ" Head design and picture of stacked diode array.

The amplifier geometry and gain. A 5 cm long, 0.5 mm diameter wedged, deep etched rod is used with an effective pump length of ~ 2cm With the configuration given on Figure 1, we can reach ~x12 small signal gain/pass. The tests used 50 mW input from the oscillator, giving 30 mW at the amplifier due to losses in the waveplate, Faraday rotator, polarizers, and relay lenses. A 5-pass arrangement using two 4^o wedges enabled steady state operation to be reached after a relatively short pumping time and a relay system optimised the beam sizes over the entire length of the 5-pass arrangement. The beam diameter was comparable with the size of the crystal aperture in the last pass to deplete the energy left in the rod, but small enough to avoid edge diffraction in the beam, which could cause a less efficient conversion to UV.

Feedback stabilization requirement. The feedback stabilization requirement is 0.5% as shown in Table 1. The oscillator instability is a potential problem, however by working in steady-state mode and saturating the harmonic generation stages this effect can be suppressed. Both the water temperature and diode current stability of the system are excellent. In the infrared, 0.27% long term stability was demonstrated. However, for the final system, feedback stabilization will be required. The basic layout of the feedback system is given on Figure 3. A part of the beam is coupled out and measured with a photodiode. An offset bias is applied to the photodiode signal to enable control over a chosen region of signal voltage. This signal when amplified and inverted is fed to a Pockels-cell to stabilise the transmitted power of an optical gate. The speed of the current system is ~2 μs, which is probably acceptable for CLIC with 100 μs pulse-train length.

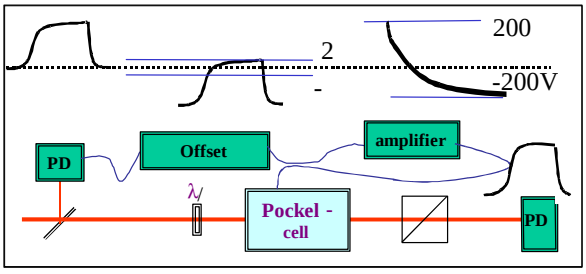

Figure 3. Basic layout of the feedback stabilisation system.

The conversion stages. The 2^{nd} harmonic of 1047 nm is generated by a 2cm long x 0.5 x 0.5cm LBO crystal (cut to $\varphi=13^o$ $\theta=90^o$). A 2cm long x1 x1 cm KDP crystal (cut to $\varphi=90^o$ $\theta=81^o$) produces the 4^{th} harmonic. The end surface of the amplifier rod is relay-imaged to a plane in between the crystals, to get both small divergence and the ideal beamsize and beam profile. We note that the Gaussian beam profile is slightly flattened due to saturation in the amplifier.

The efficiencies are shown in Figure 4. Further analysis was carried out to estimate the change of the diffraction pattern during propagation. Because of the two nonlinear processes, the modulation in the intensity beam-profile will be significantly larger in the fourth harmonic.

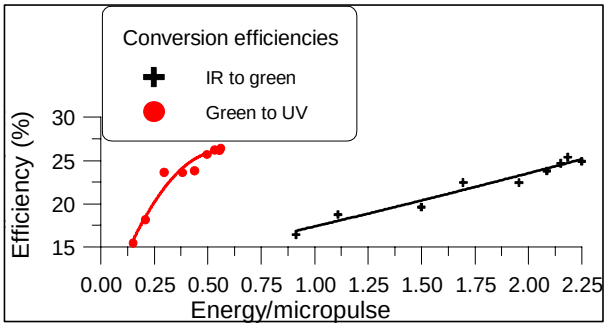

Figure 4. Harmonic generation efficiencies.

It is interesting to determine for a particular beam size how far from the image plane the level of modulation is still acceptable. In Figure 5 measured and calculated patterns are shown for a Fresnel-number ($N=r^2/(\lambda z)$, where r: the radius of the aperture, λ: wavelength, z: distance from the aperture) of 7.8. The calculations also show that with high saturation of the amplifier, when the beamprofile becomes super-gaussian, the propagation properties are much better. We concluded that we could use one imaging relay system for the two crystals as long as we minimized the distance between them to ~3 cm.

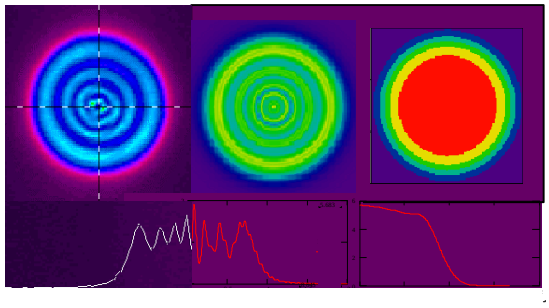

Figure 5. Measured (left) and calculated (middle, right) diffraction patterns for N = 7.8.

Conclusion

The Photo Injector Laser for PILOT test meets most of the specifications. The feedback stabilization system requires further improvements in speed. The output beam-profile and pulse-trains are shown on Figure 6. The laser system is currently under test as part of the PILOT experiments at CERN.

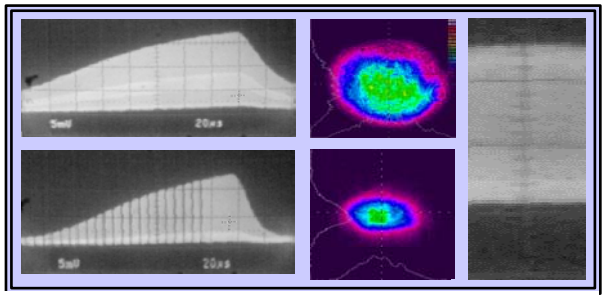

Figure 6. IR (top) and UV (bottom) train and beam profile for a 5 μs slice of the UV train.

References

1. I N Ross and S Hutchins RAL-TR-2001-082, 184-187 (2001)
2. I.N.Ross and M. Csatari RAL-TR-2002-098 202-205 (2002)
3. I.N.Ross, M Csatari and S. Hutchins, Appl. Opt., Vol. 42, No. 6. 1040-1047 (2003)

Design of a laser and optical system for the proposed γ-γ collider

I N Ross

Central Laser Facility, CCLRC Rutherford Appleton Laboratory, Chilton, Didcot, Oxon, OX11 0QX, UK

Main contact email address: *i.n.ross@rl.ac.uk*

Introduction

A number of exciting fundamental physics investigations are possible if the proposed future electron-positron linear collider can be extended to provide a gamma-gamma collider. This would be achieved by Compton scattering a high intensity laser pulse from the TeV electron and positron bunches. Such a scheme is being investigated for the TESLA superconducting LINAC.

The requirement for a workable number of gamma photons from the Compton scattering process has led to the following specification on the optical pulse train arriving at the interaction point:-

Specification		
Individual pulse energy	-	5 joules
Individual pulse duration	-	1 picosecond
Wavelength	-	about 1 micron
DL focal spot diameter	-	10 microns
Pulse train	-	3000 pulses in 1 ms
Pulse train repetition rate	-	5 Hertz

This looks to be a challenging specification since, in addition to the high peak power of 5 TW and high focused intensity of 5.10^{18} W/cm^2 , there is also the requirement for a pulse train average power of 15MW and a long term average power of 75kW.

A laser system to meet this specification looks to be very large and very expensive. However an important feature of the collider has been pointed out, namely that there will only be a loss of less than 1% from each laser pulse at the Compton scattering event. Consequently, if the pulses are re-circulated, then the energy needs only to be topped up and the power requirements are reduced by a factor of at least 100.

An elegant scheme has been suggested by MBI in which a laser generating the pulse train requirements at low pulse energy is coupled to a high-Q 100m cavity such that the internal re-circulating pulses have an energy magnified by perhaps a factor of 100. This cavity has the correct round-trip time to match the time between electron bunches, and includes a top-up amplifier and adaptive optics to ensure maintenance of the correct energy and wavefront. This is difficult in view of the tight specification and the length of the cavity and a second scheme, first suggested by Valerie Telnov, looks more tractable. It requires a laser providing one 5J, 1ps pulse at 5Hz. This pulse is switched into a 100m cavity using a Pockels' cell, and is re-circulated for 1ms the pulse energy being maintained with an internal top-up amplifier, as in the high-Q cavity scheme. In this scheme a) the input laser system requires less development, b) the laser amplifier is required to provide a feasible average power and gain and c) the optical requirement on the cavity does not include interferometric stability.

This article suggests a possible design and presents conclusions on its performance. The system can be considered in three parts, the input laser, the re-circulating cavity and the top-up amplifier, and these will be presented separately in the following sections.

The Input Laser

This laser is to provide 5 J, 1 ps pulses at a repetition frequency of 5 Hz. This will require chirped pulse amplification (CPA) and we propose to use diode-pumping for maximum efficiency, minimum heat deposition and maximum stability. Best efficiency is also obtained by operating at a neodymium wavelength. The amplifiers will need to have high gain as well as high efficiency, and a gain bandwidth capable of maintaining a 1 ps pulse. We suggest at this stage to use Nd:glass but it may be useful to look at other media such as neodymium in other hosts and ytterbium in a crystal host. The pulse source or oscillator may be neodymium or Ti:sapphire. A schematic of an all-Nd:glass amplifier system is shown in Figure 1. An alternative architecture using a mixed OPA/Nd:glass system is also possible. Although less conventional the latter offers significant advantages, having a greatly reduced material path length, higher gain bandwidth, reduced thermal effects and less wavefront distortion. In either case the final amplification stage is the same and is the critical component. A feasible design for this amplifier is as follows:-

We choose a rod amplifier of diameter 16mm and length 150mm, although the more complex and expensive slab geometry may be better if the average power leads to a serious thermal problem in the glass. Output energy is taken as 10 J to allow for losses in the pulse compressor and other optics. Let the stored energy be 20 J, giving a small signal gain of:-

$$G = \exp\left(F_{st}/F_{sat}\right) = 9.1$$

Use of the saturated gain equation (Franz-Nodvik) enables us to calculate the required input energy to the final amplifier. If we use the final amplifier in double pass this equation predicts an input energy of ~0.25J (a saturated gain of 40) after allowing for some loss between passes.

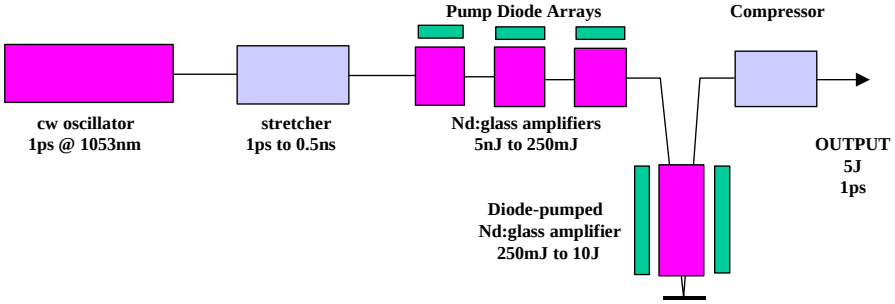

Figure 1. Possible design of input laser. Some advantages would be obtained by replacing the initial set of Nd:glass amplifiers with optical parametric amplifiers.

The pulse emitted by the oscillator is chirped and stretched for CPA operation of the amplifiers. A maximum stretched pulse duration is chosen to minimise the non-linear effects in the amplifiers while keeping within reason the necessary size of the stretcher and compressor gratings (their length is proportional to the stretched pulse duration). For a grating length of 300mm the stretched pulse duration must be restricted to approximately 0.5 ns. With this pulse duration the B-integral in the final double-pass amplifier is estimated to be 1.6, and is about at the limit of acceptability for a CPA system.

For the diode pump power requirement for the final amplifier we assume a pump duration of 0.5ms and a diode-to-absorbed efficiency of 70%. Given the fluorescence lifetime of 0.35ms a pump power of 160kW is needed to give a stored energy of 20 J. This pump pulse leads to a heat deposition in the amplifier rod of 18 J, giving an average heat load of 90 W at 5 Hz. For a 150mm rod this is 6 W/cm, an acceptable value for Nd:glass. The current cost of the diode pump is estimated to be about $5 per watt or a total of $800k. This could be reduced by pumping for a longer duration but this would lead to a greater heat load. For example an increase in the pump duration to 1 ms would reduce the cost of the diodes by 22% but increase the heat load by 56%. The estimated thermally induced focal length of this amplifier with a thermal load of 90 W is over 10 m and can be compensated very effectively using a subsidiary lens. Thermal stress-induced birefringence is likely to be more difficult to compensate and would need to be properly assessed.

The Re-circulating Cavity

The requirements for the re-circulating cavity are as follows:

a) Round trip time to be 100m (or a sub-multiple of 100m).

b) Laser pulse to be input through a polariser and Pockels' cell, the latter giving an initial 90 degree polarisation rotation which is switched off during the first round trip of the cavity.

c) A thin slab amplifier to be included, probably at one of the flat cavity mirrors, giving a total gain of about 10% during the interval between electron bunches.

d) F/10 focusing optics to be included to focus the pulses onto the electron bunches with a 10 micron spot with Rayleigh length 0.4mm for the wavelength of 1 micron.

e) Cavity to contain spatial filtering to counteract the effect of distortions, scattering and non-linear optical effects (self-focusing).

f) If possible the cavity to have an odd total number of beam reflections + beam focus inversions. This ensures improved stability to misalignments.

g) The entire cavity to be in vacuum to eliminate beam distortion and the growth of non-linear optical effects in the air.

h) The passive beam losses need to be kept down to a minimum with a total loss less than about 1%. The cost of any intra-cavity loss is high since it results in an increased pump requirement to, and an increased heat load in, the top-up amplifier. For our example an additional loss of 1% requires a 33% increase in required pump power.

Many designs of cavity are possible and we illustrate the features by the one shown schematically in Figure 2. This has two spatial filters using off-axis paraboloidal mirrors as focusing elements. The collimated beam diameter in the cavity is 300mm and the cavity overall dimensions are ~16m x 12m. For a 300mm beam the beam intensity is approximately 7 GW/cm^2 and a total length of transmissive optics in the cavity (Pockels' cell, amplifier and focusing lenses) of 100mm would imply a non-linear B-integral of 1.4, a value which can be supported if there is effective spatial filtering within the cavity. Replacement of the focusing lenses by mirrors would reduce the non-linear effects but would probably lead to a more complex cavity.

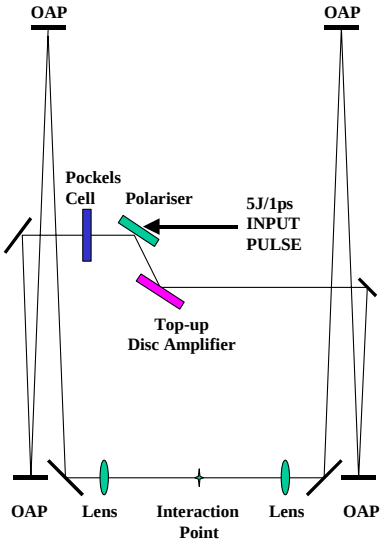

Figure 2. Design of re-circulating cavities.

It is important to keep the spatial vignetting of the beam at optical components to an absolute minimum. The best beam profile is probably one with a uniform flat-top profile in the collimated regions of the cavity and with a relatively fast intensity roll-off at the edges. Good image relaying throughout the cavity will help to maintain a clean square profile at the most restrictive optical elements.

Top-up Amplifier

A possible design of a face-pumped Nd:glass disc amplifier is proposed (Figure 3) for which the technology is available and its operating characteristics are quite well known.

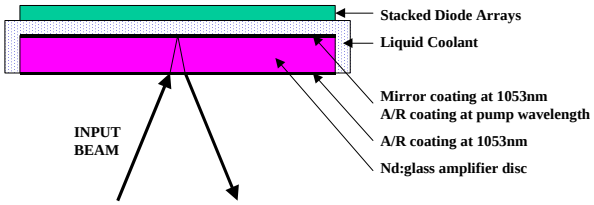

Figure 3. Schematic of top-up amplifier.

An alternative would be to use Brewster angle incidence. This gives less B-integral but requires a longer disc and more diode pump power.

The incident pulse fluence for a 5J 300mm beam is 7.1mJ/cm^2, and as this is small compared to the saturation fluence of 4.5J/cm^2 the amplifier will be operating in the small signal regime. The required gain of 1.02 in double pass is then given by:-

$$G = [\exp(F_{st}/F_{sat})]^2 = 1.02$$

from which the stored energy is calculated to be 30J.

For a stored energy of 30J the rate of loss of stored energy due to fluorescence is 30 / fluorescence lifetime = 86kW.

This must be maintained by an additional pump power of 160kW, assuming a coupling and absorption efficiency of 80% and the fraction of absorbed energy reaching the upper laser level of 68%. This is in addition to the power needed to top-up the beam. The requirement for this is for a stored power of 300kW (0.1J every 0.33 μs) or a pump power of :-

$$300/0.8x0.68 = 560kW.$$

Thus the total pump power requirement during the 1ms is 720kW (~$3.6M at current prices). The long term average pump power at 5Hz would be 4kW.

The fraction of the pump power appearing as heat within the laser medium is given by:-

$$0.8x(1-0.68)x \text{ pump power} = 0.224x4 = 0.9kW.$$

This is well within the fracture limit for Nd:glass with the proposed geometry.

A feedback system will be required to maintain constant pulse energy within the cavity. We would propose detection of the circulating energy through one of the cavity mirrors and a feedback loop controlling the diode pump power to the top-up amplifier.

One challenge with this scheme is to maintain the spatial wavefront quality and it is probable that an adaptive optic mirror will be required within the re-circulating cavity to offset the average distortion of the reflecting amplifier.

Conclusions

The above considerations suggest that the proposed laser and re-circulating cavity scheme is potentially viable, given that the extrapolation from the existing state-of-the-art has a reasonable expectation of success and does not depend on new technology. New developments in diode-pumping and diode-pumped amplifiers are likely to significantly improve the performance and reduce the cost. To date only one type of laser system and top-up amplifier has been considered and the cavity design is just one of an infinite set of possible geometries. Consequently further consideration can be expected to lead to further improvements.

Schedules and Operational Statistics

1) **Vulcan**
2) **Astra**
3) **Lasers for Science Facility**

Vulcan Operational Statistics

A K Kidd, C N Danson

Central Laser Facility, CCLRC Rutherford Appleton Laboratory, Chilton, Didcot, Oxon, OX11 0QX, UK

Main contact email address: *a.k.kidd@rl.ac.uk*

Vulcan has completed an active experimental year, with 9 full experiments taking place in target areas TAW and TAE between April 2002 and March 2003. Significantly during this period, the Petawatt target area (TAP) was commissioned and the first user experiment completed.

Table 1 below shows the operational schedule for the year, and illustrates the shot rate statistics for each experiment. Numbers in parentheses indicate the total number of full energy laser shots delivered to target, followed by the number of these that failed.

The total number of full disc amplifier shots that have been fired to target this year is 852 with 172 of these failing to meet user requirements. The overall shot success rate to target for the year is 80%. This is lower than in recent years. Figure 1 shows the improvement in reliability as the year progressed to nearer 90%. Analysis of the reasons for failure of the individual shots enables a breakdown of these causes into specific categories. This is discussed below.

The EPSRC Facility Access Agreement (FAA) requires that the laser system be available, during the four week periods of experimental data collection, from 09:00 to 17:00 hours, Monday to Thursday, and from 09:00 to 16:00 hours on Fridays (a total of 156 hours). The laser has not always met the startup target of 9:00 am but it has been common practice to operate the laser well beyond the standard contracted finish time on several days during the week and to operate during some weekends.

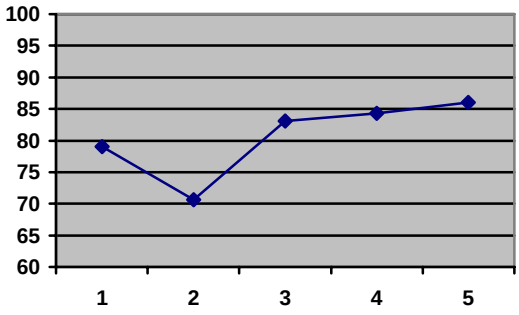

Figure 1. Shot reliability (percent) for each experimental period.

On average, Vulcan has been available for each experiment for approximately 113 hours during contracted hours and 164 hours overall. However, each experiment has also experienced an average of 5 hours of laser downtime.

PERIOD	TAE	TAW	TAP
15 Apr – 26 May	N36806 – *C Lewis* X-ray laser studies (118, 25)	EV16 – *B Cros* Particle acceleration (39, 8)	
10 Jun – 21 Jul	R12626 – *N Woolsey* Supernova remnant studies (116, 29)	N33188 – *K Ledingham* Nuclear laser solid interactions (105, 36)	
29 Jul – 8 Sep			PW commissioning (N/A)
16 Sep – 27 Oct	R25699 – *J Wark* Stacking fault measurements (102, 16)	LLNL (46, 9)	
28 Oct – 17 Nov			PW commissioning (N/A)
25 Nov – 2 Feb	R31768 – *I Ross* OPCPA trials (158, 31)		R23909 – *K Krushelnick* Relativistic particle acceleration (39, 0)
10 Feb – 23 Mar	R05062 – *M Haines* Hohlraum studies (51, 10)	R16778 – *P Norreys* Electron heating measurements (78, 8)	

Table 1. Experimental schedule for the period April 2002 – March 2003.

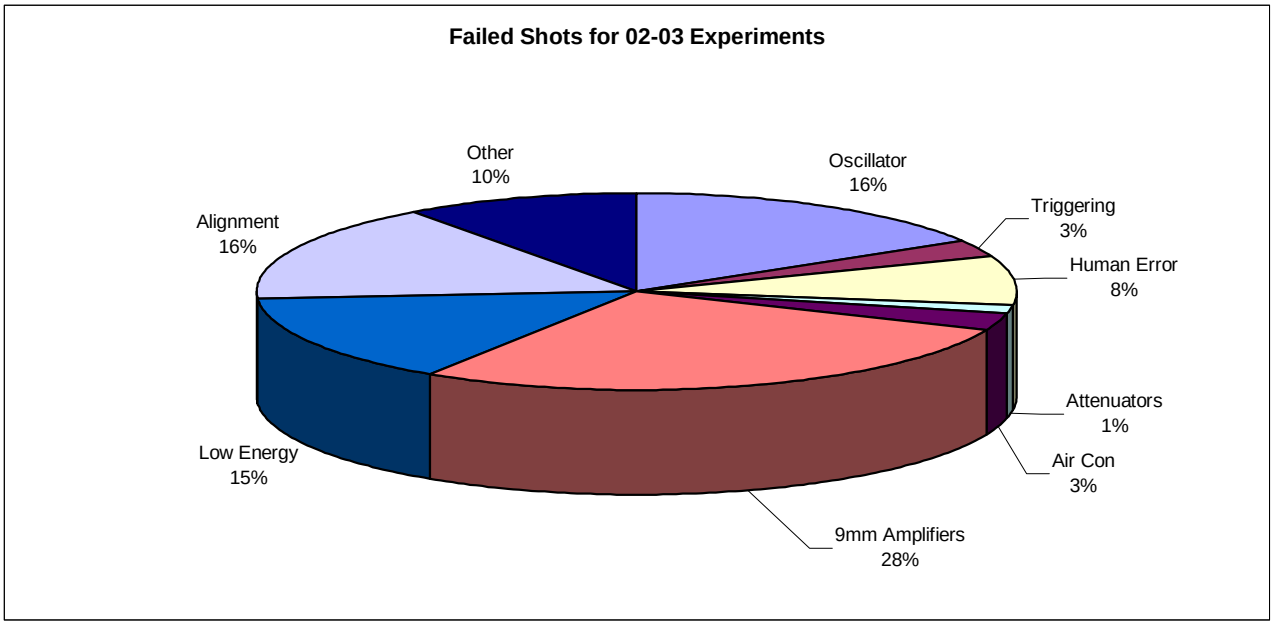

Figure 2. Analysis of Vulcan failure modes.

Figure 2 shows the identified failure modes and their individual failure rates. This information enables servicing and equipment refurbishment to be focused on the most serious sources of system downtime. Figure 2 shows the most serious cause of failed shots to be the 9mm amplifiers (48 failed shots, or 28%). This compares with 34 failed shots due to the 9mm amplifiers during 2001-2002, when this was again the primary cause of failures. A grant has been awarded to improve the infrastructure of the Vulcan laser and this area will be targeted.

Figure 3 shows the requested and delivered energies to TAP for the first user experiment (December 2002 – January 2003). A total of 39 shots were delivered to target with no failures. This was a very satisfying performance following the 3.5 years of design, installation and commissioning of the Petawatt facility.

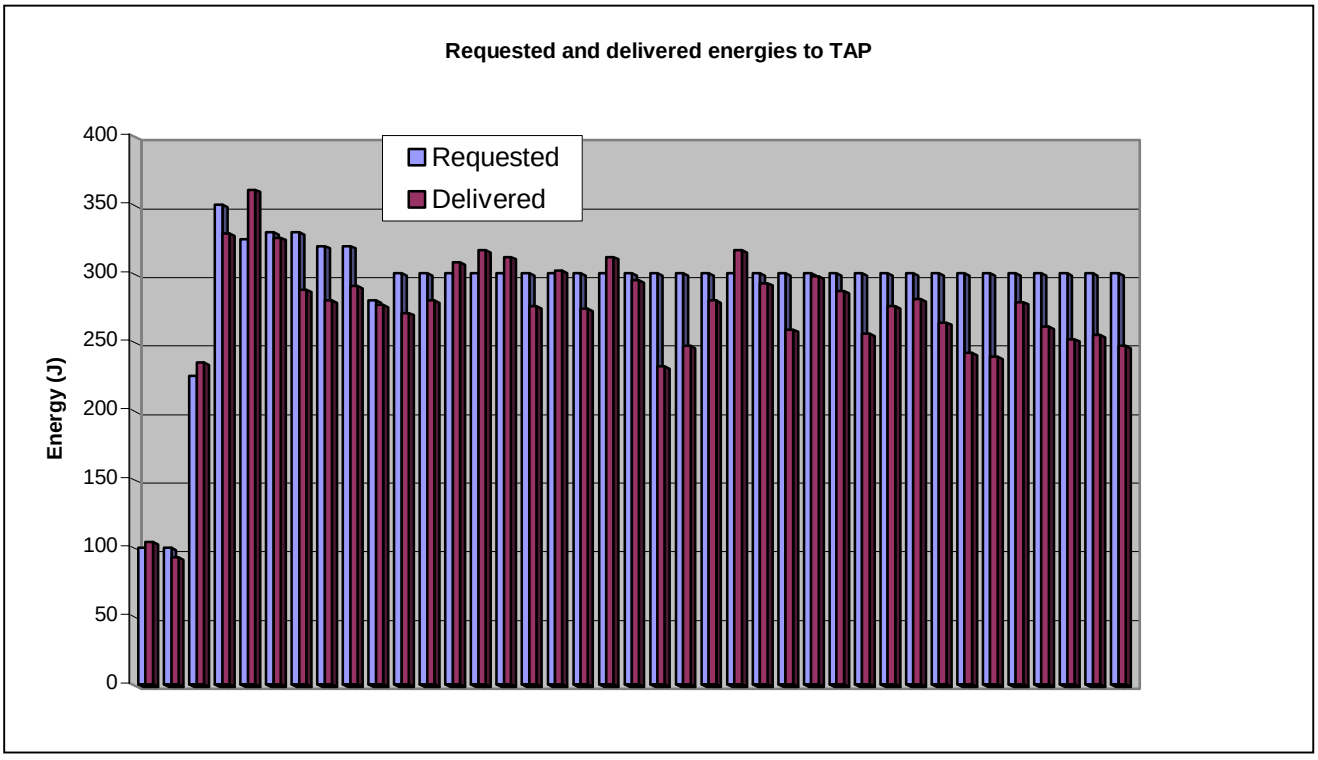

Figure 3. Requested and delivered energies to TAP for the first user experiment (December 2002 – January 2003).

Astra Operational Statistics

A J Langley

Central Laser Facility, CCLRC Rutherford Appleton Laboratory, Chilton, Didcot, Oxon, OX11 0QX, UK

Main contact email address: *a.j.langley@rl.ac.uk*

A total of 31 scheduled experiment weeks were carried out with the Astra laser during the reporting period April 2002 to April 2003. The EPSRC sponsored 74% of the experiments whilst the remainder were sponsored by the EU. All of the experiments were physics based.

For five out of the total of six experiments the Astra laser was available to researchers for an average of 89% of the time in normal daytime hours during scheduled experiments and 94% of daytime down-time was made up in out-of-hours working.

The laser reliability, defined as the time the laser was available as a percentage of the total time provided, was 93%. In one additional experiment, however, the laser was available for only one third of the time due to a serious breakdown of the Nd:YAG laser that pumps the third TiS amplifier.

We have had the opportunity to carry out 10 weeks of laser optimisation this year. The details of the upgrades implemented in this time are described in detail elsewhere in this report.

Date	Target Area 1 (ATA1)	Target Area 2 (ATA2)
1 Apr–6 May		System optimisation
13 May		
20 May		
27 May		**Krushelnick** Magnetic field studies of laser generated plasma IC
3 Jun	**SHARP** OPCPA studies	
10 Jun		
17 Jun		
24 Jun		
1 Jul		
8 Jul		
15 Jul		
22 Jul		**Riley** Femtosecond X-ray scattering QUB
29 Jul		
5 Aug		
12 Aug		
19 Aug		Maintenance
26 Aug		
2 Sep		
9 Sep		**Riley**
16 Sep		
23 Sep		
30 Sep		**Malka** Short pulse laser wakefield experiments LOA
7 Oct		
14 Oct		
21 Oct		
28 Oct		
5 Nov		
11 Nov		
18 Nov		**Zepf** Contrast measurements using plasma mirrors QUB
25 Nov		
2 Dec		
9 Dec		
16 Dec		
23/30 Dec		
6 Jan	System optimisation	Maintenance
13 Jan		
20 Jan		
27 Jan		
3 Feb	**Newell / Williams** Laser interactions with ions and TOF studies UCL / QUB	**Ledingham** Proton acceleration experiments Strathclyde
10 Feb		
17 Feb		
24 Feb		
3 Mar		
10 Mar		
18 Mar		
23 Mar		

Table 1. Astra Experiment Schedule 2002/2003.

LSF Operational Statistics

S M Tavender, M Towrie, A W Parker

Central Laser Facility, CCLRC Rutherford Appleton Laboratory, Chilton, Didcot, Oxon, OX11 0QX, UK

Main contact email address: *s.m.tavender@rl.ac.uk*

RAL-based experiments

In the reporting period (April 2002 to March 2003), 29 different User groups performed a total of 59 experiments in the LSF laboratories at RAL. A total of 4236 hours laser time was scheduled throughout the year and 4905 hours delivered with only 76 hours downtime. Across the funding Councils, the weeks scheduled were 79 to EPSRC, 3 to the MRC, 17 to BBSRC, 10 to European Users and 4 to Commercial Users and other Research Councils giving 113 weeks delivered to the User community overall. Once again, a wide spread of disciplines was covered and a breakdown is shown in Figure 1 with the RAL-Based schedule Table 1. 27 papers, 5 theses and 25 conference proceedings were published during the reporting year.

Laser Loan Pool

The Loan Pool delivered 465 weeks of laser time in the reporting period. Downtime was 17 weeks and was mainly due to teething problems and misalignment of the new laser systems. In the laser loans there were 7 groups new to the Loan Pool. The chemistry community was once again the biggest user with 70% of allocated time but this year engineering was also featured. The breakdown is shown in Figure 2. The Loan Pool schedule is shown in Table 2. There was a total of 29 publications, 12 conference proceedings and 2 PhDs during the reporting year.

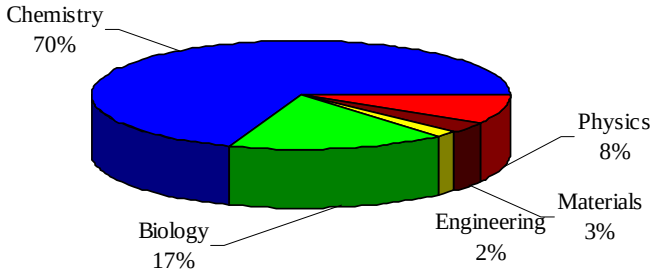

Figure 1. RAL-based experiments by subject group.

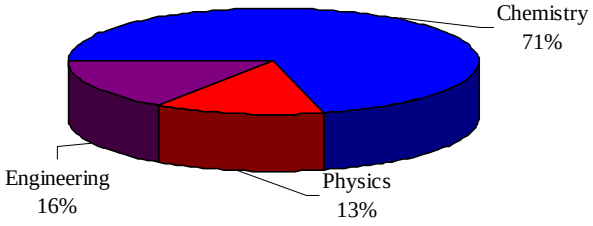

Figure 2. Loan Pool experiments by subject group.

Table 1. LASERS *for* SCIENCE FACILITY RAL-BASED SCHEDULE: 2002-03

Date	Laser Microscope Laboratory	Nanosecond Science Laboratory	Ultrafast Spectroscopy Laboratory	X-Ray and UV Laboratory
01-Apr-02			**MAINTENANCE**	
08-Apr-02	**CLF 25th ANNIVERSARY**			
15-Apr-02	**MAINTENANCE**		**A BENNISTON** (Newcastle)	
22-Apr-02		**MAINTENANCE**	*Excited-state structure of MC540 in a biomembrane mimic*	
29-Apr-02			US1C1/02 GR/R29109	
06-May-02	**LSF USER MEETING AND WORKSHOP**			
13-May-02			**D PHILLIPS** (Imperial College)	
20-May-02			*Intramolecular charge transfer states of DMABM*	COMMERCIAL
27-May-02			*derivatives* US3C1/02 GR/R29062/01	
03-Jun-02			**MAINTENANCE**	
10-Jun-02			**J J McGARVEY** (QUB) *DNA Interactions at*	
17-Jun-02			*colloidal surfaces* GR/M45696 US6C1/02	
24-Jun-02	**A WARD** (CLF) *Individual DNA polymer detection*	**D PHILLIPS** (IC) *Intramolecular charge transfer*	**K REID** (Nottingham)	**A MICHETTE** (Kings)
01-Jul-02	*using optical entrapment with colloidal silver particles*	*of DMABN derivatives* GR/R29062/01 NL1C1/01	*Time-resolved photoelectron spectra and photoelectron*	*Development of the scanning x-ray microscope*
08-Jul-02	*to enhance fluorescence CM01C1/02 BBSRC DA*		*angular distributions* GR/M83759 US04C1/02	GR/N28061/01 XU01P1/02
15-Jul-02	**A BEEBY** (Durham) *Are there metastable rotamers*	**J HOLZWORTH** (Germany) *Quantitative measurement of*	**M GEORGE** (Nottingham)	
22-Jul-02	*of phenylethynylbenzene in solution?* US9C1/02 EPSRC DA	*temperature jump* NLEV32C1/02	P.I.R.A.T.E.	
29-Jul-02	**N QUIRKE** (IC) *Carbon nanotubes* CM7C2/02		GR/M40486 US08C1/02	

Date	Laser Microscope Laboratory	Nanosecond Science Laboratory	Ultrafast Spectroscopy Laboratory	X-Ray and UV Laboratory
05-Aug-02	**J McGARVEY** (QUB) CM9C2/02 GR/M45696			
12-Aug-02	**C WHARTON** (Birmingham) *Gap Junction EPSRC DA*	**MAINTENANCE**	**A VLCEK** (QMWC) US7C1/02 GR/N11414	**C WHARTON** (Birmingham) XU3C2/02 EPSRC DA
19-Aug-02	**MAINTENANCE**		**D PHILLIPS** (IC) US3C1/02 GR/R29062/01	**MAINTENANCE**
26-Aug-02			**MAINTENANCE**	
02-Sep-02	**J SANDERSON** (Durham)		**BRYCE/BEEBY** (Durham) *Optical properties of new*	
09-Sep-02	*Optical Tweezing of liposomes as a Tool for*		*phthalocyanines* US10C1/01 GR/M95745/01	
16-Sep-02	*Membrane Research* CM2B2/02 EPSRC DA	**M CHESTERS** (Nottingham)	**D PHILLIPS** (Imperial College)	
23-Sep-02		*UV Resonance Raman Studies of*	*DMABM derivatives* US3C1/02 GR/R29062/01	
30-Sep-02	**N QUIRKE** (Imperial College) *Capillary flow in carbon*	*Adsorbates on Metal Surfaces*	**M GEORGE** (Nottingham)	
07-Oct-02	*nanotubes* CM7C2/02 EPSRC DA	NL02C1/02 EPSRC DA		
14-Oct-02	**S HILL** (Queens Medical Centre, Nottingham) *Ligand*	**J CALLOW** (Birmingham) BBSRC 6/13596		
21-Oct-02	*binding to GPRC Receptors* CM3B2/02 BBSRC DA		P.I.R.A.T.E.	**A FITZGERALD** (Dundee) *Structures in Metal Chalcogenide*
28-Oct-02	**O'NEILL** (MRC) *Characteristics of DNA*	**C BAIN** (Oxford) *Coalescence between*		*Bilayers* GR/N14682 EPSRC ABT XU4M3/02
04-Nov-02	*damage induced by IR multi-photon ionisation-relation*	*oil emulsion droplets CM5C2/02 GR/M83797*	GR/M40486 US08C1/02	
11-Nov-02	*to DNA ionisation* CM6B2/02 MRC		**A VLCEK** (QMWC) *Early photochemical*	**A MICHETTE** (Kings)
18-Nov-02	**J CALLOW** *Marine spores* CM4/B2/02 BBSRC 6/13596	**E TUITE** (Newcastle) *Luminescence and Raman*	*dynamics of organometallics* US7C1/02 GR/N11414	*Development of the scanning x-ray microscope*
25-Nov-02		*of Quantum Dots NL4C2/02 BBSRC DA*	**J KELLY** (DCU, Ireland)	GR/N28061/01 XU2P2/02
02-Dec-02	**R MELDRUM** (CCLRC) CM11C3/02 GR/S13217	**MAINTENANCE**	*Photoxidation of DNA by rhenium carbonyl*	COMMERCIAL (Q 01/0042s)
09-Dec-02	**C BAIN** (Oxford) *Coalescence between oil*	**M JASPARS** (Aberdeen) *Cu(II) fluorosensors for applications*	*and other metallo-polypyridyl complexes*	**H REEHAL** (SBU) *Crystalline Silicon Thin Films on Glass*
16-Dec-02	*emulsion droplets CM12C3/02 GR/M83797*	*in environmental and medical research* 1/E12737 NL08B3/02	USEV23C1/02	*for Solar Cells* GR/R50783/1 XU5E3/02
23-Dec-02	**CHRISTMAS and NEW YEAR**			
30-Dec-02				
06-Jan-03	**MAINTENANCE**	**MAINTENANCE**	**MAINTENANCE**	**MAINTENANCE**
13-Jan-03	**A MACROBERT** (UCL) *Fluorescence lifetime imaging*		**A VLCEK** (QMWC) *Early photochemical*	
20-Jan-03	**K BRINDLE** (Cambridge) 8/E11895 CM10B3/02	**M BIETTI** (Italy) *Reactivity of Alkoxyl radicals*	*dynamics of organometallics* US7C1/02 GR/N11414	**A FITZGERALD** (Dundee) *Structures in Metal Chalcogenide*
27-Jan-03	**A MACROBERT** (UCL) *Fluorescence lifetime imaging*	*generated by laser photolysis* NLEV8C3/00	CLRC/MRC *Feasibility of Kerr gated Raman Microscopy*	*Bilayers* GR/N14682 EPSRC ABT XU4M3/02
03-Feb-03	*mTHPC* CM15B3/02 BBSRC DA	**J MOORE** (York) *Temperature jump studies*	**MAINTENANCE**	
10-Feb-03	**C BAIN** (Oxford) *Coalescence between oil emulsion*	*of azo dyes* EPSRC DA NL6C3/02	**S SCHNEIDER** *Raman of* tetracyclines USEV12C3/02	
17-Feb-03	*droplets EPSRC ABT* CM12C3/02 GR/M83797	**S SCHNEIDER** (Germany) *Tetracyclines* NLEV12C3/02	**M JASPARS** (Aberdeen) *Cu(II) fluorosensors for applications*	
24-Feb-03	**P O'NEILL** (MRC)	**MAINTENANCE**	*in environmental and medical research* 1/E12737 US5B1/02	
03-Mar-03	**J WEINSTEIN** (N'ham) *Excited state metal thiolates*	**J MOORE** (York)	**M BRYCE** (Durham) US10C1/01 GR/M95745/01	
10-Mar-03	**R MELDRUM** (CCLRC) CM11C3/02 GR/S13217	*Ns TR^3 spectroscopy of functional*	**W E SMITH** (Strathclyde) *Light Emitting Polymers*US13C3/02	
17-Mar-03	**J CALLOW** *(B'ham)* BBSRC *Marine spores* CM16B3/02	*(diimine) Re (CO)$_3$ complexes*	**J WEINSTEIN** (N'ham) *Excited state metal thiolates* US15C3/02	
24-Mar-03	**R MELDRUM** (CCLRC) CM11C3/02 GR/S13217	GR/R01316/01 NL7C3/02	**A MONKMAN** (Durham) *fs Kerr gate* US14C3/02	

Table 2. LASERS *for* SCIENCE FACILITY LOAN POOL SCHEDULE: 2002-03

Date	NSL1 POWERLITE/ SIRAH + DFG	NSL2 SURELITE III-10/SIRAH	NSL3 SURELITE III-10/ SIRAH		NSL4 Continuum 8010/ND6000	NSL5 Fluoride Excimer	NSL6 Nd:YAG/ Dye/SHG	CWL2 VERDI/MIRA + SHG & THG	CW3 FreD Argon Ion	Millenia/ Tsunami
Apr 01	**McKENDRICK**	**STACE**	**FROST**		**SMITH**	**CRANTON**	**SIMONS**	**DEVONSHI RE**	**LEGGATT**	**LINFIELD**
08	**Herriot-Watt**	**Sussex**	**Herriot-Watt**		**Birmingham**	**NTU**	**Oxford**	**Sheffield**	**UMIST**	**Cambridge**
15					State-Selected					
22	LP18C3/01		REMPI-LIF		and	Laser	Protonated	LP23C3/01		
29			studies of simple		State-to -State	processing	neurotransmitters		LP21C2/01	
May 06	SERVICE	LP22C3/01	ion-molecule		Rate	of thin film	In the			
13	at		Reactions		Constants for	phosphors for	Gas phase	**DEVONSHIRE**		
20	PHOTONIC				Inelastic and	flat		**Sheffield**	**SHEN**	
27	SOLUTIONS	**STACE**	LP14C2/01		Reactive	screen displays		Femtosecond	**Salford**	
June 03		**Sussex**			Collisions			non-linear	A Brillouin	
10					of		LP06C1/01	Raman techniques:	light	
17	**FIELDING**		**ATTENB'H**	**McGARVEY**	CN X2sigma			development and	scattering	Development
24	**Kings**		**Hull**	**Keele**	And OH X2pi	LP20C3/01		applications and	investigation	of an
July 01			YAG	Dye			**SIMONS**	interferometric	of	all-optical
08		LIF studies of	Lab'tory	Photo-	LP07C1/02		**Oxford**	measurements	Ultra-thin	high power
15		Molecules	Simu-	physical		**CRANTON**		of fs pulse	epitaxial	terahertz
22	Molecular	trapped	lation	properties		**NTU**		propagation	Fe films grown	source
29	Electron	in helium	of sonic	of			Sugars in the gas	in technological	on Singular	
Aug 5	Wavepackets	nanodroplets	booms	prophyrin		Laser	phase:	devices	and vicinal	
12				fullerene	**UNALLOCATED**	Processing	spectroscopy	And fluids	GaAs	
19				dyads		of Transparent	and structure of	LP09C1/02	substrates	
26						Conductive	model mono-and		LP02P1/02	
Sep 2		LP05C1/02				Coatings	disaccharides.			
9								**BEEBY**		
16								**Durham**	**CHESTERS**	
23	LP10C1/02	**STACE**	LP11E1	LP212C2					**RAL/N'ham**	
30		**Sussex**							Adsorbates on	
Oct 7							LP15C2/02	Time-	surfaces LP8C1	
14	**FIELDING**		**ATTENBOROUGH**		**COLE**			Resolved		
21	**Kings**	Gas Phase	**Hull**		**Bath**	LP14E2/02		Fluorescence		
28		Ligand Field	(YAG)				**SIMONS**	Spectroscopy		
Nov 4		Spectroscopy					**(Oxford)**			
11	Controlling		Laboratory		Photo-	**CRANTON**				
18	Molecular		simulation		crystallographic	**(NTU)**				**WILKINSON**
25	Electron		of sonic		study of	Effect of	Biologically			**(ORC)**
Dec 2	Wavepackets		booms		terpyridine	Environment	Relevant Sugar		**UNALLOCATED**	
9						on	Derivatives in			
16						the Laser	the			Gallium/
23						Processing	Gas Phase:			Titanium
30						of Inkjet	Structural	LP22C2/02		Co-Diffused
Jan 06						Printed	Investigation			Waveguide
13		LP19C2/02				Transparent	of Imino Sugars			Lasers in
20						Conducting	and	**LINFIELD**		Sapphire
27	LP18C2/02					Thin	Carobpeptoids	**(Cambridge)**	**WITHNALL**	
Feb 03		**STACE**				Films			**(Greenwich)**	
10		**(Sussex)**	LP20E2/02		LP16C2/02			The development	Visible	
17	**SIMS**							of	Emissions	
24	**(Birmingham)**							Applications	for Phosphors	
Mar 03	Astrochemistry	Gas Phase	**ATTENBOROUGH**		**MASON**	LP25E3/02	LP28C3/02	Of all optical	under UV	
10	Collisional	Ligand	**(Hull)**		**(Open University)**			High power	excitation	LP24P3/00
17	energy:	Field	(YAG)		Space			Terahertz source		**DISPOSAL**
24	transfer	Spectroscopy			Weathering on					**Dr S Matcher**
31	LP32C3/02	LP27C3/02			Mercury			LP33C3/02	LP35P3/02	**Exeter**

Publications

1) **Vulcan Laser Programme**
2) **Astra Laser Programme**
3) **Lasers for Science Facility Programme**
4) **Laser Science and Development**

Vulcan Laser Programme

JOURNAL PUBLICATIONS, BOOKS AND PUBLISHED PROCEEDINGS

Y Abou-Ali, G J Tallents, M Edwards, R E King, G J Pert, S J Pestehe, F Strati, R Keenan, C L S Lewis, S Topping, O Guilbaud, A Klisnick, D Ros, R Clarke, D Neely, M Notley, A Demir
Measurement of the duration of X-ray lasing pumped by an optical laser pulse of picosecond duration
Opt Comms 215 (4-6) 397-406 (2003)

M Borghesi, S Bulanov, D H Campbell, R J Clarke, T Z Esirkepov, M Galimberti, L A Gizzi, A J MacKinnon, N M Naumova, F Pegoraro, H Ruhl, A Schiavi, O Willi
Macroscopic evidence of soliton formation in multiterawatt laser-plasma interaction
Phys Rev Letts 88 (13) 135002 (2002)

M Borghesi, D H Campbell, R J Clarke, M Galimberti, L A Gizzi, M Haines, A J MacKinnon, A Schiavi, O Willi
Imaging of plasmas using proton beams generated by ultra-intense laser pulses
In "Advanced Diagnostics for Inertial and Magnetic Fusion" eds P E Stott, A Wootton, G Gorini, E Sindoni, D Batani, publ Kluwer (2002)

M Borghesi, D H Campbell, A Schiavi, M G Haines, O Willi, A J MacKinnon, P Patel, L A Gizzi, M Galimberti, R J Clarke, F Pegoraro, H Ruhl, S Bulanov
Electric field detection in laser-plasma interaction experiments via the proton imaging technique
Physics of Plasmas 9 (5) 2214-2220 (2002)

M Borghesi, D H Campbell, A Schiavi, O Willi, A J Mackinnon, D Hicks, P Patel, L A Gizzi, M Galimberti, R J Clarke
Laser-produced protons and their application as a particle probe
Laser and Particle Beams 20 (2) 269-275 (2002)

M Borghesi, L Romagnani, A Schiavi, D H Campbell, M G Haines, O Willi, A J Mackinnon, M Galimberti, L Gizzi, R J Clarke, S Hawkes
Measurement of highly transient electrical charging following high-intensity laser-solid interaction
Appl Phys Letts 82 (10) 1529-1531 (2003)

A C Cefalas, E Sarantopoulou, Z Kollia, P Argitis, E Tegou, T W Ford, A D Stead, C N Danson, D Neely, S Kobe
Nanostructured imaging of biological specimens in vivo with laser plasma X-ray contact microscopy
Mat Sci & Eng C 23 (1-2) 105-108 (2003)

D M Chambers, P A Pinto, J Hawreliak, I R Al'Miev, A Gouveia, P Sondhauss, E Wolfrum, J S Wark, S H Glenzer, R W Lee, P E Young, O Renner, R S Marjoribanks, S Topping
K-shell spectroscopy of an independently diagnosed uniaxially expanding laser-produced aluminum plasma
Phys Rev E 66 (2) 026410 (2002)

S Fritzler, Z Najmudin, V Malka, K Krushelnick, C Marle, B Walton, M S Wei, R J Clarke, A E Dangor
Ion heating and thermonuclear neutron production from high-intensity subpicosecond laser pulses interacting with underdense plasmas
Phys Rev Letts 89 (16) 165004 (2002)

D H Kalantar, A M Allen, F Gregori, B Kad, M Kumar, K T Lorenz, A Loveridge, M A Meyers, S Pollaine, B A Remington, J S Wark
Laser driven, high pressure, high strain-rate materials experiments
AIP Conf Proc 620 (1) 615-618 (2002)

D H Kalantar, E Bringa, M Caturla, J Colvin, K T Lorenz, M Kumar, J Stolken, A M Allen, K Rosolankova, J S Wark, M A Meyers, M Schneider, T R Boehly
Multiple film plane diagnostic for shocked lattice measurements
Rev Sci Instr 74 (3) 1929-1934 (2003)

R Keenan, C L S Lewis, S J Topping, J S Wark, E Wolfrum
Development of X-ray lasers for radiographic and other applications
AIP Conf Proc 641 (1) 160-165 (2002)

R Keenan, C L S Lewis, J S Wark, E Wolfrum
Measurements of the XUV transmission of aluminium with a soft X-ray laser
J Phys B 35 (20) L447-L451 (2002)

R Kodama, K A Tanaka, S Fujioka, H Fujita, H Habara, Y Izawa, T Jitsuno, Y Kitagawa, K Krushelnick, K Mima, N Miyanaga, K Nagai, P Norreys, T Norimatsu, K Shigemori, H Shiraga, Y Toyama, M Zepf, T Yamanaka
Fast heating of super-solid density plasmas towards laser fusion ignition
Plasma Physics & Controlled Fusion 44 (12B) B109-B119 (2002)

R Kodama, H Shiraga, Y Toyama, S Fujioka, H Azechi, T Jitsuno, Y Kitagawa, K Krushelnick, K L Lancaster, K Mima, K Nagai, M Nakai, H Nishimura, T Norimatsu, P A Norreys, S Sakabe, K A Tanaka, A Youssef, M Zepf, T Yamanaka
Fast heating scalable to laser fusion ignition
Nature 418, 933 (2002)

K Krushelnick, M I K Santala, K W D Ledingham, F N Beg, E L Clark, R J Clarke, A E Dangor, T McCanny, P A Norreys, I Spencer, M Tatarakis, I Watts, M S Wei, M Zepf
Nuclear diagnostics of high intensity laser plasma interactions
AIP Conf Proc 611 (1) 253-263 (2002)

K Krushelnick, I Watts, M Tatarakis, A Gopal, U Wagner, F N Beg, E L Clark, R J Clarke, A E Dangor, P A Norreys, M S Wei, M Zepf
Using self-generated harmonics as a diagnostic of high intensity laser-produced plasmas
Plasma Physics and Controlled Fusion 44 (12B) B233-B245 (2002)

Z Najmudin, K Krushelnick, E L Clark, D J Colling, M Tatarakis, A Modena, A E Dangor, J Faure, V Malka, D Gordon, C Joshi
The production of high-energy electrons from the interaction of an intense laser pulse with an underdense plasma
J Mod Opt 50 (3-4) 673-681 (2003)

Z Najmudin, K Krushelnick, M Tatarakis, E L Clark, C N Danson, V Malka, D Neely, M I K Santala, A E Dangor
The effect of high intensity laser propagation instabilities on channel formation in underdense plasmas
Physics of Plasmas 10 (2) 438-442 (2003)

P Norreys
Physics with petawatt lasers
Physics World 15 (9) 39-44 (2002)

F Pegoraro, M Borghesi, S V Bulanov, F Califano, T Z Esirkepov, A V Kuznetsov
Some recent developments in nonlinear relativistic plasma dynamics
AIP Conf Proc 634 79-86 (2002)

D Riley, I Weaver, D McSherry, M Dunne, D Neely, M Notley, E Nardi
Direct observation of strong coupling in a dense plasma
Phys Rev E 66 (4) 046408 (2002)

I Spencer, K W D Ledingham, R P Singhal, T McCanny, P McKenna, E L Clark, K Krushelnick , M Zepf, F N Beg, M Tatarakis, A E Dangor, R D Edwards, M A Sinclair, P A Norreys, R J Clarke, R M Allott
A nearly real-time high temperature laser-plasma diagnostic using photonuclear reactions in tantalum
Rev Sci Instr 73 (11) 3801-3805 (2002)

G J Tallents, Y Abou-Ali, M Edwards, R King, G J Pert, S J Pestehe, F Strati, C L S Lewis, R Keenan, S Topping, A Klisnick, O Guilbaud, D Ros, R Clarke, M Notley, D Neely
A review of X-ray laser development at Rutherford Appleton Laboratory
Laser and Particle Beams 20 (2) 201-209 (2002)

M Tatarakis, A Gopal, I Watts, F N Beg, A E Dangor, K Krushelnick, U Wagner, P A Norreys, E L Clark, M Zepf, R G Evans
Measurements of ultrastrong magnetic fields during relativistic laser-plasma interactions
Physics of Plasmas 9 (5) 2244-2250 (2002)

B Walton, Z Najmudin, M S Wei, C Marle, R J Kingham, K Krushelnick, A E Dangor, R J Clarke, M J Poulter, C Hernandez-Gomez, S Hawkes, D Neely, J L Collier, C N Danson, S Fritzler, V Malka
Large-amplitude plasma wave generation with a high-intensity short-pulse beat wave
Opt Letts 27 24 2203-2205 (2002)

I Watts, M Zepf, E L Clark, M Tatarakis, K Krushelnick, A E Dangor, R M Allott, R J Clarke, D Neely, P A Norreys
Dynamics of the critical surface in high-intensity laser-solid interactions: Modulation of the XUV harmonic spectra
Phys Rev Letts 88 (15) 155001 (2002)

I Watts, M Zepf, E L Clark, M Tatarakis, K Krushelnick, A E Dangor, R Allott, R J Clarke, D Neely, P A Norreys
Measurements of relativistic self-phase-modulation in plasma
Phys Rev E 66 (3) 036409 (2002)

M Zepf, E L Clark, F N Beg, R J Clarke, A E Dangor, A Gopal, K Krushelnick, P A Norreys, M Tatarakis, U Wagner, M S Wei
Proton acceleration from high-intensity laser interactions with thin foil targets
Phys Rev Letts 90 (6) 064801 (2003)

PUBLISHED DURING 2001/2002

T J Goldsack, T F Bryant, P F Beech, S G Clough, G M Cooper, R Davitt, R D Edwards, N Kenna, J McLean, A G Pearce, M J Phillips, K P Pullinger, D J Short, M A Sinclair, K J Thomas, J R Threadgold, M C Williamson, K Krushelnick
Multimegavolt multiaxis high-resolution flash X-ray source development for a new hydrodynamics research facility at AWE Aldermaston
IEEE Trans Plasma Sci 30 (1 Pt2) 239-253 (2002)

Z Najmudin, M Tatarakis, K Krushelnick, E L Clark, V Malka, J Faure, A E Dangor
Ultra-high-intensity laser propagation through underdense plasma
IEEE Trans Plasma Sci 30 (1 Pt1) 44-45 (2002)

S J Pestehe, G J Tallents
Escape factors for laser plasmas
J Quant Spectr Rad Trans 72 (6) 853-878 (2002)

IN PRESS AT END OF 2002/2003

K W D Ledingham, P McKenna, R P Singhal
Applications for nuclear phenomena generated by ultra-intense lasers
Science 300 (5622) 1107-1111 (2003)

Z Najmudin, K Krushelnick, E L Clark, S P D Mangles, B Walton, A E Dangor, S Fritzler, V Malka, E Lefebvre, D Gordon, F S Tsung, C Joshi
Self-modulated wakefield and forced laser wakefield acceleration of electrons
Physics of Plasmas 10 (5Pt2) 2071-2077 (2003)

K A Tanaka, R Kodama, K Mima, Y Kitagawa, H Fujita, N Miyanaga, K Nagai, T Norimatsu, T Sato, Y Sentoku, K Shigemori, A Sunahara, T Shozaki, M Tanpo, S Tohyama, T Yabuuchi, J Zheng, T Yamanaka, P A Norreys, R Evans, M Zepf, K Krushelnick, A Dangor, R Stephens, S Hatchett, M Tabak, R Turner
Basic and integrated studies for fast ignition
Physics of Plasmas 10 (5Pt2) 1925-1930 (2003)

M Tatarakis, F N Beg, E L Clark, A E Dangor, R D Edwards, R G Evans, T J Goldsack, K W D Ledingham, P A Norreys, M A Sinclair, M S Wei, M Zepf, K Krushelnick
Propagation instabilities of high-intensity laser-produced electron beams
Phys Rev Letts 90 (17) 175001 (2003)

CONFERENCE PRESENTATIONS

IEEE International Conference on Plasma Science, Banff, Canada (May 2002)

D Riley
X-ray Thomson scattering

Workshop on Advanced Accelerator Concepts, Oxnard, USA (Jun 2002)

A MacKinnon
Energetic ion emission from solid targets irradiated by laser pulses

International Conference on Warm Dense Matter, Hamburg, Germany (Jun 2002)

D Riley
X-ray scattering from plasmas

14th Topical Conference on High-Temperature Plasma Diagnostics, Madison, USA (Jul 2002)

M Borghesi
Proton imaging detection of transient electromagnetic fields in laser-plasma interactions

11th International Conference on Plasma Physics, Sydney, Australia (Jul 2002)

O Willi
Progress and issues in the fast ignition approach to ICF

29th EPS Conference on Plasma Physics and Controlled Fusion, Montreux, Switerland (Jul 2002)

R Kodama, K A Tanaka, S Fujioka et al
Fast heating of super-solid density plasmas towards laser fusion ignition

K Krushelnick, I Watts, M Tatarakis et al
Using self-generated harmonics as a diagnostic of high intensity laser-produced plasmas

M S Wei, F N Beg, E L Clark, A E Dangor, A Gopal, K W D Ledingham, P McKenna, P A Norreys, I Spencer, M Tatarakis, M Zepf, K Krushelnick
Experimental observations of the Weibel instability in laser solid interactions

11th International Conference on Emerging Nuclear Energy Systems, Albuquerque, USA (Oct 2002)

P McKenna
Experiments in laser-induced nuclear physics

High Speed Photography Conference, Beaune, France (Sept 2002)

C B Edwards, C J Aldis, R Allott, P A Brummitt, J Collier, R J Clark, C N Danson, R Day, M Dominey, B C Eltham, A J Frackiewicz, J A C Govans, B J Gray, S Hancock, P E Hatton, S Hawkes, C R Heathcote, C Hernandez-Gomez, P Holligan, C Hooker, M H R Hutchinson, A R Jackson, A Kidd, T Knott, W J Lester, J M A Loose, A J MacPhee, J Monk, Z A Miljus, D Neely, D R Neville, P Norreys, M Notley, J O'Dell, D A Pepler, M R Pitts, C J Reason, D Robinson, K J Rodgers, D A Rodkiss, D Rose, S J Rose, I N Ross, A J Ryder, M R Selley, T Strange, G P Warner, R Wellstood, G N Wiggins, T B Winstone, P N M Wright, R W W Wyatt, B E Wyborn, C Ziener
The Vulcan petawatt interaction facility

International Conference on New Directions in Laser-Matter Interactions, Brussels, Belgium (Sept 2002)

P McKenna
Experiments in laser-induced nuclear physics

44th Annual Meeting of the Division of Plasma Physics of the American Physical Society, Orlando, USA (Nov 2002)

Z Najmudin
High intensity laser interactions with underdense plasma: a source of energetic electrons, ions, neutrons and gamma rays

K A Tanaka
Basic and integrated studies for fast ignition

M Zepf, E L Clark, F N Beg, R J Clarke, M Tatarakis, M S Wei, U Wagner, A E Dangor, A Gopal, P A Norreys, K Krushelnick
Proton acceleration from high intensity laser interactions with thin foil targets

International Conference on Frontiers of Plasma Physics and Technology, Bangalore, India (Dec 2002)

M Lontano, M Borghesi, S V Bulanov, T Z Esirkepov, D Farina, N Naumova, K Nishihara, M Passoni, F Pegoraro, H Ruhl, A S Sakharov, O Willi
Non-drifting relativistic electromagnetic solitons in plasmas

F Pegoraro, S Atzeni, M Borghesi, S V Bulanov, T Z Esirkepov, J J Honrubia, Y Kato, V S Khoroshkov, K Nishihara, T Tajima, M Temporal, O Willi
Production of ion beams in high power laser plasma interaction and their applications

DESY Workshop on Plasma Physics with X-Rays, Hamburg, Germany (Mar 2003)

D Riley
Thomson scattering principles and first applications

THESES

E Breschi
Analisi dello spettro energetico di protoni generati da interazione ultraintensa laser-plasma
Laurea Thesis, University of Pisa

Astra Laser Programme

JOURNAL PUBLICATIONS, BOOKS AND PUBLISHED PROCEEDINGS

J B Greenwood, I M G Johnston, P McKenna, I D Williams, T R J Goodworth, J H Sanderson, W A Bryan, A A A El-Zein, W R Newell, A J Langley, E J Divall
Suppression of multiple ionization of atomic ions in intense ultrafast laser pulses
Phys Rev Letts 88 (23) 233001 (2002)

P McKenna, K W D Ledingham, I Spencer, T McCany, R P Singhal, C Ziener, P S Foster, E J Divall, C J Hooker, D Neely, A J Langley, R J Clarke, P A Norreys, K Krushelnick, E L Clark
Characterization of multiterawatt laser-solid interactions for proton acceleration
Rev Sci Instr 73 (12) 4176-4184 (2002)

J H Sanderson, T R J Goodworth, A El-Zein, W A Bryan, W R Newell, A J Langley, P F Taday
Coulombic and pre-Coulombic geometry evolution of carbonyl sulfide in an intense femtosecond laser pulse, determined by momentum imaging
Phys Rev A 65 (4) 043403 pt B (2002)

C Ziener, P S Foster, E J Divall, C J Hooker, M H R Hutchinson, A J Langley, D Neely
Specular reflectivity of plasma mirrors as a function of intensity, pulse duration, and angle of incidence
J Appl Phys 93 (1) 768-770 (2003)

IN PRESS AT END OF 2002/2003

I Spencer, K W D Ledingham, P McKenna, T McCanny, R P Singhal, P S Foster, D Neely, A J Langley, E J Divall, C J Hooker, R J Clarke, P A Norreys, E L Clark, K Krushelnick, J R Davies
Experimental study of proton emission from 60-fs, 200-mJ high-repetition-rate tabletop-laser pulses interacting with solid targets
Phys Rev E 67 (4) 046402 (2003)

Lasers for Science Facility Programme

JOURNAL PUBLICATIONS, BOOKS AND PUBLISHED PROCEEDINGS

R Aveyard, B P Binks, J H Clint, P D I Fletcher, T S Horozov, B Neumann, V N Paunov, J Annesley, S W Botchway, D Nees, A W Parker, A D Ward, A N Burgess
Measurement of long-range repulsive forces between charged particles at an oil-water interface
Phys Rev Letts 88 (24) 246102 (2002)

R Aveyard, B P Binks, J H Clint, P D I Fletcher, B Neumann, V N Paunov, J Annesley, S W Botchway, A W Parker, A D Ward, A N Burgess
Drag forces on a stationary particle in flowing two-dimensional ordered particle monolayers:simulation and measurement using optical tweezers
Langmuir 18 (24) 9587-9593 (2002)

R H Bisby, M Arvanitidis, S Botchway, I P Clark, A W Parker, D Tobin
Investigation of multiphoton-induced fluorescence from solutions of 5-hydroxytryptophan
Photochem Photobiol Sci 2 157-162 (2003)

W R Browne, C G Coates, C Brady, P Matousek, M Towrie, S W Botchway, A W Parker, J G Vos, J J McGarvey
Isotope effects on the picosecond time-resolved emission spectroscopy of Tris(2,2'-bipyridine)ruthenium (II)
J Am Chem Soc 125 (7) 1706-1707 (2003)

D C Clary, E Buonomo, I R Sims, I W M Smith, W D Geppert
C + C_2H_2: a key reaction in interstellar chemistry
J Phys Chem A 106 (23) 5541-5552 (2002)

J M Cole, P R Raithby, M Wulff, F Schotte, A Plech, S J Teat, G Bushnell-Wye
Nanosecond time-resolved crystallography of photo-induced species:case study and instrument development for high-resolution excited-state single-crystal structure determination
Faraday Discuss 122 119-129 (2002)

C S Colley, D C Grills, N A Besley, S Jockusch, P Matousek, A W Parker, M Towrie, N J Turro, P M W Gill, M W George
Probing the reactivity of photoinitiators for free radical polymerization: time-resolved infrared spectroscopic study of benzoyl radicals
J Am Chem Soc 124 (50) 14952-14958 (2002)

A G Davies, E H Linfield, M B Johnston
The development of terahertz sources and their applications
Phys Med Biol 47 (21) 3679-3689 (2002)

J A Davies, K L Reid, M Towrie, P Matousek
Picosecond pump-probe photoelectron spectroscopy as a probe of intramolecular dynamics in S_1 para-fluorotoluene
J Chem Phys 117 (20) 9099-9102 (2002)

J Dyer, D C Grills, P Matousek, A W Parker, M Towrie, J A Weinstein, M W George
Revealing the photophysics of fac-[(dppz-12-NO_2)Re(CO)$_3$(4-Me_2Npy)]$^+$: a picosecond time-resolved IR study
Chem Comms 8 872-873 (2002)

I R Farrell, P Matousek, M Towrie, A W Parker, D C Grills, M W George, A Vlcek
Direct observation of competitive ultrafast CO dissociation and relaxation of an MLCT excited state: picosecond time-resolved infrared spectroscopic study of [Cr(CO)$_{(4)}$(2,2'-bipyridine)]
Inorg Chem 41 (17) 4318-4323 (2002)

K M Hickson, C M Sadowski, I W M Smith
Collisional transfer between Λ-doublet levels of OH($X^2\Pi_{3/2}$, v=1, j=3.5, and 6.5) in collisions with He, Ar, N_2 and HNO_3
J Phys Chem A 106 (36) 8442-8449 (2002)

K M Hickson, C M Sadowski, I W M Smith
Rate coefficients for rotational energy transfer from the levels OH($X^2\Pi_{3/2}$, v=1, ji=1.5, 3.5-8.5) in collisions with He, Ar, N2 and HNO3
Phys Chem Chem Phys 4 (22) 5613-5621 (2002)

M A Hill, D L Stevens, S J Marsden, R Allott, I C E Turcu, D T Goodhead
Is the increased relative biological effectiveness of high LET particles due to spatial or temporal effects ? Characterisation and OER in V79-4 cells
Phys Med Biol 47 (19) 3543-3555 (2002)

W M Kwok, C Ma, M W George, D C Grills, P Matousek, A W Parker, D Phillips, W T Toner, M Towrie
Further time-resolved spectroscopic investigations on the intramolecular charge transfer state of 4-dimethylaminobenzonitrile (DMABN) and its derivatives, 4-diethylaminobenzonitrile (DEABN) and 4-dimethylamino-3,5 dimethylbenzonitrile (TMABN)
Phys Chem Chem Phys 5 (6) 1043-1050 (2003)

M B Johnston, D M Whittaker, A Corchia, A G Davies, E H Linfield
Simulation of terahertz generation at semiconductor surfaces
Phys Rev B 65 165301 (2002)

M B Johnston, D M Whittaker, A Dowd, A G Davies, E H Linfield, X Li, D A Ritchie
Generation of high-power terahertz pulses in a prism
Opt Letts 27 (21) 1935-1937 (2002)

C F Leypold, M Reiher, G Brehm, M O Schmitt, S Schneider, P Matousek, M Towrie
Tetracycline and derivatives - assignment of IR and Raman spectra via DFT calculations
Phys Chem Chem Phys 5 (6) 1149-1157 (2003)

C Ma, W M Kwok, P Matousek, A W Parker, D Phillips, W T Toner, M Towrie
Excited states of 4-aminobenzonitrile (ABN) and 4-dimethylaminobenzonitrile (DMABN): time-resolved resonance Raman, transient absorption, fluorescence and ab initio calculations
J Phys Chem A 106 (14) 3294-3305 (2002)

P Matousek, A-M Saariaho
Kerr-portti vaimentaa häiritsevän fluoresenssin - resonanssiramanspektroskopialle uutta käyttöä
Kemia Kemi 29 (7) 22-23 (2002)

C S McCaw, K M Murdoch, R G Denning
Energy levels of terbium(III) in the elpasolite $Cs_2NaTbBr_6$ I luminescence and two-photon excitation spectroscopy
Mol Phys 101 (3) 427-438 (2003)

C S McCaw, R G Denning
Energy levels of terbium(III) in the elpasolite $Cs_2NaTbBr_6$ II a correlation crystal field analysis
Mol Phys 101 (3) 439-447 (2003)

R A Meldrum, G O Edwards, J K Chipman, C W Wharton, S W Botchway, G J Hirst, W Shaikh
A pulsed laser generated soft X-ray source for the study of gap junction communication and 'bystander' effects in irradiated cells
Radiation and Homeostasis International Congress Series 1236 289-294 (2002)

A G Michette, S J Pfauntsch, A K Powell, T Graf, D Losinski, C D McFaul, A Ma, G J Hirst, W Shaikh
Progress with the King's College Laboratory scanning X-ray microscope
J de Phys IV 104 123-126 (2003)

P Mojzes, P Praus, V Baumruk, P-Y Turpin, P Matousek, M Towrie
Structural features of two distinct molecular complexes of copper(II) cationic porphyrin and deoxyribonucleotides
Biopolymers 67 (4-5) 278-281 (2002)

J Olofsson, B Onfelt, P Lincoln, B Nordén, P Matousek, A W Parker, E Tuite
Picosecond Kerr-gated time-resolved resonance Raman spectroscopy of the $[Ru(phen)_2dppz]^{2+}$ interaction with DNA
J Inorg Biochem 91 (1) 286-297 (2002)

S J Pestehe, G J Tallents, I C E Turcu, Y Abou Ali, G Hirst, M Powers, W Shaikh
Efficiency of 1.5-4.5 keV X-ray production from 2 ps duration KrF laser pulses incident onto solid targets
J Phys D 35 (11) 1117-1122 (2002)

P A Shields, R J Nicholas, K Takashina, N Grandjean, J Massies
Observation of magnetophotoluminescence from a $GaN/Al_xGa_{1-x}N$ heterojunction
Phys Rev B 65 (19) 195320 (2002)

L C Snoek, R T Kroemer, J P Simons
A spectroscopic and computational exploration of trytophan-water cluster strctures in the gas phase
Phys Chem Chem Phys 4 (11) 2130-2139 (2002)

F O Talbot, J P Simons
Sugars in the gas phase: the spectroscopy and structure of jet-cooled phenyl β-D-glucopyranoside
Phys Chem Chem Phys 4 (15) 3562-3565 (2002)

F W Vergeer, F Hartl, P Matousek, D J Stufkens, M Towrie
First direct observation of a CO-bridged primary photoproduct of $[Ru_3(CO)_{12}]$ by picosecond time-resolved IR spectroscopy
Chem Comms 11 1220-1221 (2002)

S Zalis, A Vlcek, C Daniel
The character of low-lying excited states of mixed-ligand metal carbonyls: TD-DFT and CASSCF/CASPT2 study of $[W(CO)_4L]$ (L=ethylenediamine,N,N'-dialkyl-1,4-diazabutadiene) and $[W(CO)_5L]$ (L=pyridine,4-cyanopyridine)
Collect Czech Chem Commun 68 (1) 89-104 (2003)

PUBLISHED DURING 2001/2002

D Carty, V Le Page, I R Sims, I W M Smith
Low temperature rate coefficients for the reactions of CN and C_2H radicals with allene ($CH_2=C=CH_2$) and methyl acetylene (CH3CCH)
Chem Phys Letts 344 (3-4) 310-316 (2001)

M B Johnston, A Corchia, A Dowd, E H Linfield, A G Davies, R McLaughlin, D D Arnone, M Pepper
Magnetic-field-induced enhancement of terahertz emission from III-V semiconductor surfaces
Physica E 13 (2-4) 896-899 (2002)

M B Johnston, D M Whittaker, A Corchia, A G Davies, E H Linfield
Theory of magnetic-field enhancement of surface-field terahertz emission
J Appl Phys 91 (4) 2104-2106 (2002)

S Sun, K S L Chong, G J Leggett
Nanoscale molecular patterns fabricated by using scanning near-field optical lithography
J Am Chem Soc 124 (11) 2414-5 (2002)

A Wellner, R E Palmer, J G Zheng, C J Kiely, K W Kolasinski
Mechanisms of visible photoluminescence from nanoscale silicon cones
J Appl Phys 91 (5) 3294-3298 (2002)

IN PRESS AT END OF 2002/2003

A C Benniston, P Matousek, I E McCulloch, A W Parker, M Towrie
Detailed picosecond Kerr-gated time-resolved resonance Raman spectroscopy and time-resolved emission studies of merocyanine 540 in various solvents
J Phys Chem A 107 (22) 4347-4353 (2003)

J Dyer, W J Blau, C G Coates, C M Creely, J D Gavey, M W George, D C Grills, S Hudson, J M Kelly, P Matousek, J J McGarvey, J McMaster, A W Parker, M Towrie, J A Weinstein
The photophysics of fac-$[Re(CO)_3(dppz)(py)]^+$ in CH_3CN: a comparative picosecond flash photolysis, transient infrared, transient resonance Raman and density functional theoretical study
Photochem Photobiol Sci 5 542-554 (2003)

W M Kwok, M W George, D C Grills, C S Ma, P Matousek, A W Parker, D Phillips, W T Toner, M Towrie
Direct observation of a hydrogen-bonded charge-transfer state of 4-dimethylaminobenzonitrile in methanol by time-resolved IR spectroscopy
Angew Chem Int Edit 42 (16) 1826-1830 (2003)

W M Kwok, C S Ma, A W Parker, D Phillips, M Towrie, P Matousek, D L Phillips
Picosecond time-resolved resonance Raman study of CH_2I-I produced after ultraviolet photolysis of CH_2I_2 in CH_3OH, CH_3CN/H_2O and CH_3OH/H_2O solutions
J Phys Chem A 107 (15) 2624-2628 (2003)

C A T Laia, S M B Costa, D Phillips, A W Parker
Spectroscopy of photoinduced charge-transfer reactions between tetrasulfonated aluminium phthalocyanine and methyl viologen
Photochem Photobiol Sci 5 555-562 (2003)

CONFERENCE PRESENTATIONS

PITTCON 2002, New Orleans, USA (Mar 2002)

P Matousek, M Towrie, A W Parker
Fluorescence suppression in resonance Raman spectroscopy by optical Kerr gating

BBSRC Meeting on Biological Applications of Nanotechnology, London, UK (May 2002)

G Leggett
Photopatterned self-assembled monolayers: versatile templates for the control of biological organisation

Informal Conference on Photochemistry, Miami, USA (Jun 2002)

I W M Smith
State-selected and state-to-state rate constants for inelastic and reactive collisions of CN(X2Σ) and OH(X2Π)

Euresco Conference, Wilbad Kreuth, Germany (Jul 2002)

N A Macleod, P Butz, F O Talbot
Biological molecules in the gas phase

30th Annual Meeting of the American Society for Photobiology, Quebec, Canada (Jul 2002)

R Meldrum, S Botchway, G Hirst
Writing on the genome - focused indiction of UV photoproducts in cell nuclear DNA by 3-photon infra-red radiation

Fast Reactions in Solution, Istanbul, Turkey (Jul 2002)

J F Holzwarth, S Couderc, A Beeby, I P Clark, A W Parker
T-jump experiment with micrometre space resolution applying rhodamine 101 anti-Stokes fluorescence

International Gas Kinetics Symposium, Essen, Germany (Aug 2002)

I W M Smith
State-selected and state-to-state rate constants for inelastic and reactive collisions of CN(X2Σ) and OH(X2Π)

Seventh International Conference on X-Ray Microscopy, Grenoble, France (Aug 2002)

A G Michette, A K Powell, T Graf, D Losinski, C D McFaul, A Ma, G J Hirst, W Shaikh
Progress with the King's College laboratory scanning X-ray microscope

International Conference on Raman Spectroscopy, Budapest, Hungary (Aug 2002)

A W Parker
Efficient rejection of fluorescence from Raman and time-resolved Raman spectra using picosecond Kerr gating

26th European Conference on Molecular Spectroscopy, Lille, France (Sept 2002)

A W Parker
Time-resolved vibrational spectroscopy of an intramolecular charge transfer reaction

ISD Workshop, Grasmere, UK (Sept 2002)

W Cranton
Printing of electronic material

Photon02, Cardiff, UK (Sept 2002)

G Hirst
Laser plasma X-ray sources

S Pal, J Mandal, T Sun, K T V Grattan
High temperature sensor potential of Bragg gratings fabricated in different photosensitive fibres

THz 2002: 10th IEEE International Conference on Terahertz Electronics, Cambridge, UK (Sept 2002)

M B Johnston, A Dowd, D M Whittaker, A Corchia, A G Davies, E H Linfield
Enhancement of THz emission from semiconductor surfaces

IOP Meeting on Advanced Sensors and Instrumentation Systems for Combustion Processes, London, UK (Oct 2002)

S Pal, J Mandal, T Sun, K T V Grattan, M A Fokine, F Carlsson, P Y Fonjallaz
High temperature performance of Bragg grating devices for potential sensor applications

African Laser Conference Workshop, Pretoria, South Africa (Oct 2002)

A W Parker
Lasers in microscopy - biological applications

FACSS 2002, Providence, USA (Oct 2002)

P Matousek, M Towrie, C Ma, W M Kwok, D Phillips, W T Toner, A W Parker
Fluorescence-suppressed steady-state and picosecond time-resolved resonance Raman spectroscopy in solutions

Atoms, Molecules and Radiation, Gif-sur-Yvette, France (Nov 2002)

J P Simons
Sugars in the gas phase: spectroscopy and structure of model mono- and disaccharides

1st International Conference on Optical and Laser Diagnostics, London, UK (Dec 2002)

T Sun, D I Forsyth, S A Wade, S Pal, J Mandal, K T V Grattan
Fibre Bragg grating coupled fluorescent optical fibre sensors

225th ACS National Meeting, New Orleans, USA (Mar 2003)

J F Holzwarth, S Couderc, A Beeby, I P Clark, A W Parker
Laser temperature jump experimenst with nanometre space resolution using rhodamine 101 anti-Stokes fluorescence from nanoseconds to milliseconds for precise measurements of temperature changes in liquid microenvironment

THESES

C B Brady
Spectroscopy and kinetics of some iron (II) spin crossovers in solution and other media
Ph D, Queen's University Belfast

D Koutsogeorgis
Laser processing of transparent conductive coatings
Ph D, Nottingham Trent University

J Neal
A Brillouin light scattering investigation of ultra-thin epitaxial Fe films grown on singular and vicinal GaAs substrates
Ph D, University of Salford

S J Pfauntsch
Developments in soft X-ray laboratory systems for microscopy and cellular probing
Ph D, University of London

F W Vergeer
Photo- and redox activation of homo- and heteronuclear transition metal clusters
Ph D, University of Amsterdam

A Wellner
Fabrication and properties of nanostructured gold and silicon films
Ph D, University of Birmingham

Laser Science and Developments

JOURNAL PUBLICATIONS, BOOKS AND PUBLISHED PROCEEDINGS

P Matousek, M Towrie, A W Parker
Fluorescence background suppression in Raman spectroscopy using combined Kerr gated and shifted excitation Raman difference techniques
J Raman Spectr 33 (4) 238-242 (2002)

K Osvay, G Kurdi, J Klebniczki, M Csatari, I N Ross, E J Divall, C J Hooker, A J Langley
Broadband amplification of ultraviolet laser pulses
Appl Phys B 74 (9) S163-S169 (2002)

I N Ross, M Csatari, S Hutchins
High-performance diode-pumped Nd:YLF amplifier
Appl Opt 42 (6) 1040-1047 (2003)

I N Ross, P Matousek, G H C New, K Osvay
Analysis and optimization of optical parametric chirped pulse amplification
JOSA B 19 (12) 2945-2956 (2002)

CONFERENCE PRESENTATIONS

CLEO 2002, Long Beach, USA (May 2002)

P Matousek, I Ross, J Collier, C Hernandez-Gomez, M Towrie, A Langley, C Danson, D Neely, D Pepler, B Wyborn, C Aldis, S Hancock
Multi-petawatt optical parametric chirped pulse amplification (OPCPA)

IQEC/LAT 2002, Moscow, Russia (June 2002)

I N Ross, P Matousek, J L Collier
The current status and future prospects for optical parametric chirped pulse amplification

Panel Membership and CLF Structure

PANEL MEMBERSHIP

VULCAN AND ASTRA SCHEDULING ADVISORY PANEL 2002/03

Professor D D Burgess (Chairman)
Imperial College, London

Dr D Riley deputising for Professor C L S Lewis
Department of Pure and Applied Physics
Queen's University of Belfast

Professor J Wark
Physics Department
Oxford Universsity

Dr K Krushelnick
Plasma Physics Group
Imperial College

Mr C N Danson (Secretary)
Central Laser Facility
CCLRC Rutherford Appleton Laboratory

Dr P A Norreys
Central Laser Facility
CCLRC Rutherford Appleton Laboratory

Professor G J Pert
Department of Physics
University of York

Professor K W D Ledingham
Department of Physics
University of Strathclyde

Observers
Dr D Neely
Central Laser Facility
CCLRC Rutherford Appleton Laboratory

Dr J L Collier
Central Laser Facility
CCLRC Rutherford Appleton Laboratory

LASERS *for* SCIENCE FACILITY PANEL 2002/03

Dr R Bisby (Chairman)
Department of Biological Sciences
University of Salford

Professor J A Cairns
Department of Electronic Engineering & Physics
University of Dundee

Dr R Devonshire
Department of Chemistry
Sheffield University

Dr I P Clark (Secretary)
Central Laser Facility
CCLRC Rutherford Appleton Laboratory

Professor K G McKendrick
Department of Chemistry
Herriot-Watt University

Professor W R Newell
Department of Physics & Astronomy
University College London

Research Council Representatives:
Dr A McCaig
B. Raven
EPSRC
Dr C Thompson
BBSRC

CLF EURO EXPERIMENTS PANEL 2002/03

Professor C L S Lewis (Chairman)
Department of Pure and Applied Physics
Queen's University of Belfast

Professor C Fotakis
Institute of Electronic Structure and Laser
FORTH, Greece

Professor D Phillips
Department of Chemistry
Imperial College

Dr S W Botchway (Secretary)
Central Laser Facility
CCLRC Rutherford Appleton Laboratory

Mr C N Danson (Contract Manager)
Central Laser Facility
CCLRC Rutherford Appleton Laboratory

Dr G Matthieussent
Laboratoire Physique Gaz et Plasmas, Universite Paris XI -
CNRS, France

Professor J Meyer-ter-Vehn
Max-Planck-Institut für Quantenoptik
Garching, Germany

Dr Karel Rohlena
Institut of Physics
Prague

Professor J Kossanyi
CNRS – Laboratoire des Materiaux Moléculaires
Thiais, France

CENTRAL LASER FACILITY STRUCTURE 2002/03

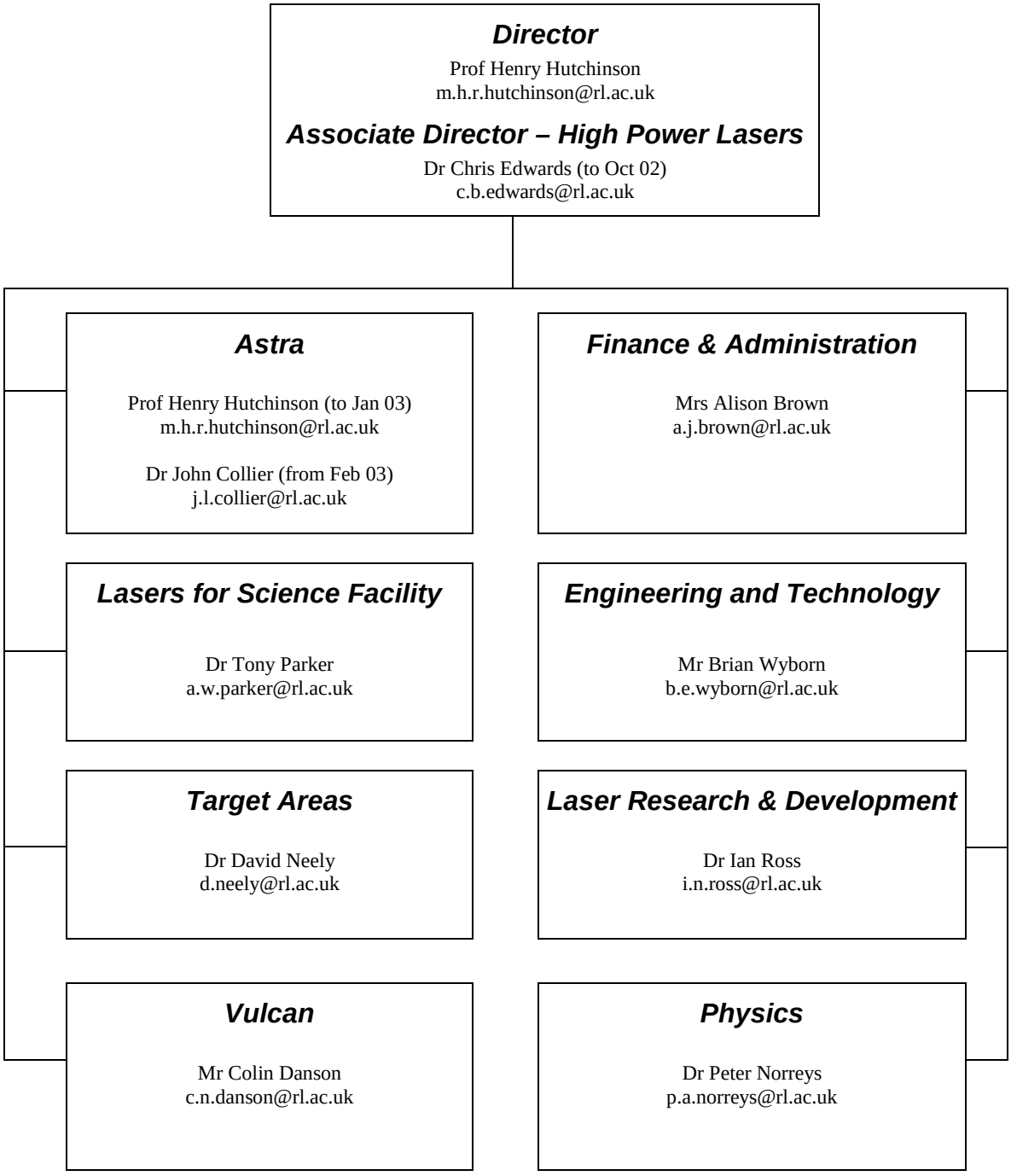

Author Index